ASME
SETTING THE STANDARD

Transactions of the ASME, Journal of Heat Transfer (ISSN 0022-1481) is published monthly by The American Society of Mechanical Engineers, Three Park Avenue, New York, NY 10016. Periodicals postage paid at New York, NY and additional mailing offices. POSTMASTER: Send address changes to Transactions of the ASME, Journal of Heat Transfer, c/o THE AMERICAN SOCIETY OF MECHANICAL ENGINEERS, 22 Law Drive, Box 2300, Fairfield, NJ 07007-2300. **CHANGES OF ADDRESS** must be received at Society headquarters seven weeks before they are to be effective. Please send old label and new address.

Journal of Heat Transfer

Published Monthly by ASME

VOLUME 132 • NUMBER 7 • JULY 2010

RESEARCH PAPERS

(Contents continued on inside back cover)

This journal is printed on acid-free paper, which exceeds the ANSI Z39.48-1992 specification for permanence of paper and library materials. ♾™
♻ 85% recycled content, including 10% post-consumer fibers.

Journal of Heat Transfer **Volume 132, Number 7** **JULY 2010**

MAX JAKOB AWARD PAPER

TECHNICAL BRIEFS

The ASME Journal of Heat Transfer is abstracted and indexed in the following:

Applied Science and Technology Index, Chemical Abstracts, Chemical Engineering and Biotechnology Abstracts (Electronic equivalent of Process and Chemical Engineering), Civil Engineering Abstracts, Compendex (The electronic equivalent of Engineering Index), Corrosion Abstracts, Current Contents, E & P Health, Safety, and Environment, Ei EncompassLit, Engineered Materials Abstracts, Engineering Index, Enviroline (The electronic equivalent of Environment Abstracts), Environment Abstracts, Environmental Engineering Abstracts, Environmental Science and Pollution Management, Fluidex, Fuel and Energy Abstracts, Index to Scientific Reviews, INSPEC, International Building Services Abstracts, Mechanical & Transportation Engineering Abstracts, Mechanical Engineering Abstracts, METADEX (The electronic equivalent of Metals Abstracts and Alloys Index), Petroleum Abstracts, Process and Chemical Engineering, Referativnyi Zhurnal, Science Citation Index, SciSearch (The electronic equivalent of Science Citation Index), Theoretical Chemical Engineering

Analysis of Microheat Pipes With Axial Conduction in the Solid Wall

Yew Mun Hung[1]
e-mail: hung.yew.mun@eng.monash.edu.my

Kek-Kiong Tio
e-mail: kktio@mmu.edu.my

Faculty of Engineering and Technology,
Multimedia University,
75450 Melaka, Malaysia

A one-dimensional, steady-state model of a triangular microheat pipe (MHP) is developed, with the main purpose of investigating the thermal effects of the solid wall on the heat transport capacity of an MHP. The energy equation of the solid wall is solved analytically to obtain the axial temperature distribution, the average of which over the entire length of the MHP is simply its operating temperature. Next, the liquid phase is coupled with the solid wall by a heat transfer coefficient. Then, the continuity, momentum, and energy equations of the liquid and vapor phases are, together with the Young–Laplace equation, solved numerically to yield the heat and fluid flow characteristics of the MHP. The heat transport capacity and the associated optimal charge level of the working fluid are predicted for different operating conditions. Comparison between the models with and without a solid wall reveals that the presence of the solid wall induces a change in the phase change heat transport by the working fluid, besides facilitating axial heat conduction in the solid wall. The analysis also highlights the effects of the thickness and thermal conductivity of the solid wall on its axial temperature distribution. Finally, while the contribution of the thermal effects of the solid wall on the heat transport capacity of the MHP is usually not dominant, it is, nevertheless, not negligible either.
[DOI: 10.1115/1.4000947]

Keywords: microheat pipe, axial conduction, solid wall, phase change, heat transport capacity

1 Introduction

Owing to their various applications, either proposed or implemented, microheat pipes (MHPs) have attracted considerable interest since they were first proposed by Cotter [1] in the 1980s. Today, the literature consists of several review articles [2–6] and a large number of analytical studies, such as those of Tio and coworkers [7–9], Kim et al. [10], Suman and Hoda [11], and Do et al. [12], to name just a few of the works published in the past decade. However, the great majority of the literature only deals with the working fluid of an MHP, without taking into account the effects of axial conduction in the solid wall. On the other hand, these effects may be significant, judging from the conclusion drawn by Maranzana et al. [13] for mini- and microchannels. While there exist a few studies which include the effects of the thermophysical properties of the solid wall, such as those of Suman and Hoda [11] and Do et al. [12], many important issues remain unaddressed. In this paper, we shall therefore attempt to investigate some of these issues, as a first step in a series of systematic studies which incorporate the thermal effects of the solid wall.

Figure 1 is a schematic illustration of the heat and fluid flows inside an MHP. A portion of the heat applied to the MHP over its evaporator section is conducted axially through the solid wall toward the condenser section; the remaining part is transferred to the liquid phase, which is confined to the corner regions by the action of surface tension, and is taken up as the latent heat of evaporation. The resulting vapor then flows through the adiabatic section, over which no heat transfer occurs between the MHP and its surroundings, and toward the condenser section, where the vapor condenses and releases the latent heat of evaporation. The released heat then flows from the MHP into the surroundings through the condenser section, which effectively serves as the heat sink for both the heat conducted in the solid and the heat released by the condensing vapor. In this paper, we shall assume that the heat fluxes entering and leaving the MHP are, respectively, distributed uniformly over the evaporator and condenser sections; however, the model developed based on this assumption can be very easily modified for cases of nonuniform fluxes. Associated with the evaporation and condensation of the working fluid of an MHP is the continual axial variation of the liquid-vapor interface along its entire axis. Since the liquid volume fraction at the evaporator section is less than that at the condenser section, the radius of curvature of the liquid-vapor interface at the evaporator is also less than that at the condenser. Due to the action of capillarity, this results in a drop in the liquid pressure, going from the condenser to the evaporator. This drop in pressure (and, for the orientation of the MHP shown in Fig. 1, gravity as well) then serves as the agent which drives the condensate back to the evaporator, where it begins a new cycle of phase change and circulation.

To investigate the heat and fluid flows described above, a one-dimensional, steady-state model of an MHP has been developed. In this model, the cross-sectional variation of a variable, such as the temperature of the solid wall or the velocity of the liquid phase, is assumed to have been properly integrated to yield an averaged quantity which varies only along the axis of the MHP. As the main purpose of this paper is to obtain as clear an exposition as possible of the effects of axial heat conduction in the solid wall of an MHP, several simplifying assumptions will, obviously, be required for the liquid and vapor phases of its working fluid. Thus, following the common practice in the existing literature, we shall assume a uniform temperature for both the liquid and vapor. Moreover, axial conduction and convection in the liquid are ignored, so that, at a given axial location, the heat transfer from the solid to the liquid is taken up as the latent heat of evaporation, and the liquid-to-solid heat transfer is solely provided by the conden-

[1]Present address: School of Engineering, Monash University, 46150 Bandar Sunway, Malaysia.

Contributed by the Heat Transfer Division of ASME for publication in the JOURNAL OF HEAT TRANSFER. Manuscript received November 14, 2008; final manuscript received December 11, 2009; published online April 22, 2010. Assoc. Editor: Jayathi Murthy.

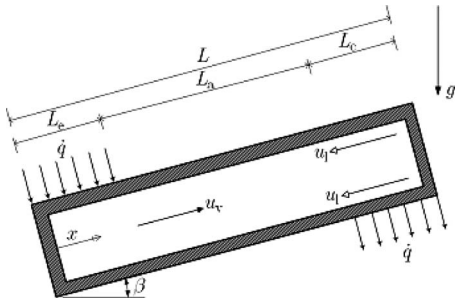

Fig. 1 A schematic diagram of an inclined microheat pipe, β being its angle of inclination

sation of the vapor phase. As in previous studies, such as those of Tio and co-workers [7–9], the uniform temperature of the liquid and vapor will be regarded as the operating temperature of the MHP, and all the relevant physical properties of the solid, liquid, and vapor are evaluated at this temperature. While the temperature of the solid varies along the axis of the MHP, in order to drive the axial conduction in the solid wall, its properly weighted averaged value must be equal to the temperature of the liquid, since there is no net heat transfer between them. The present model, in which there is neither dryout nor flooding along the axis of the MHP, yields the result that the simple, nonweighted average temperature of the solid is equal to that of the liquid, which, as mentioned earlier, is taken as the operating temperature of the MHP. This is of practical significance, because it allows us to determine the operating temperature by measuring the solid temperature at various axial locations and then taking the average.

From a practical viewpoint, one of the most important issues concerning the operation of an MHP is the optimal amount of its working fluid so that it can be loaded with the maximum possible heat transport rate. Like the conventional heat pipes, the performance of an MHP is also bounded by the various possible limitations such as capillary, sonic, entrainment, and viscous limits. For a horizontal MHP, it has been shown by Babin et al. [14], who investigated a horizontal trapezoidal MHP with water as the working fluid and operating at the temperature range of 25–100°C, that the capillary limit is the one that controls the maximum possible heat transport rate. In this paper, we shall, therefore, be concerned with the capillary limit only.

The MHP selected for our study has a cross section in the shape of an equilateral triangle, of width w equal to 1.04 mm, a wall thickness of $t_s=0.14$ mm, and a total length of 50 mm, encompassing three sections, i.e., evaporator, adiabatic, and condenser sections. Unless stated otherwise, the numerical results presented in this paper are meant for this particular MHP, whose geometric specifications are given in Table 1. This MHP is, in terms of the cross-sectional area, equivalent to the trapezoidal heat pipe studied by Babin et al. [14]. In order to elucidate the effects of the solid wall, three types of solid materials of significantly different thermal conductivities are considered in this paper: copper, nickel, and monel. While the thermophysical properties of the working fluid play an important role in the heat transport capacity of an MHP [9], we shall, for the sake of simplicity, be concerned with water only in our numerical results.

Table 1 Dimensions of a triangular MHP

L	50.0 mm
L_a	24.6 mm
L_e	12.7 mm
L_c	12.7 mm
w	1.04mm
t_s	0.14mm

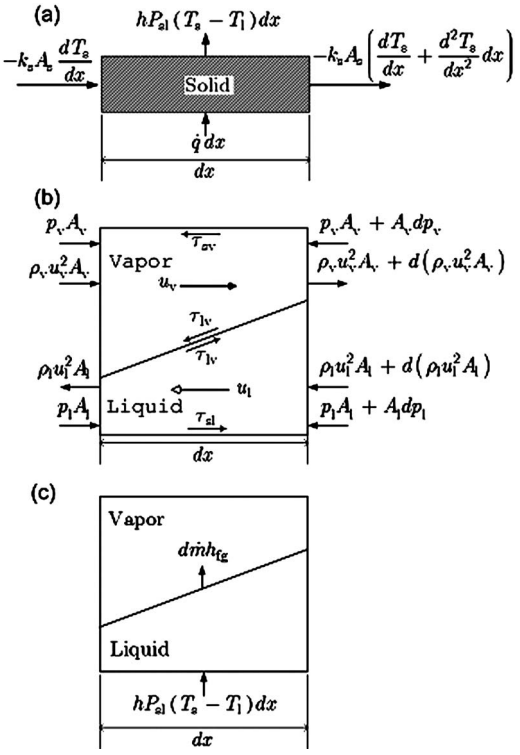

Fig. 2 Schematic infinitesimal control volumes for the derivation of governing equations. (*a*) Energy equation for conduction in the solid wall. (*b*) Momentum equations for liquid and vapor flows. (*c*) Energy equation for evaporation in the liquid domain.

2 Governing Equations

As mentioned previously, a steady one-dimensional model of a triangular MHP will be utilized in this study. This model is developed from the first principles and takes into account the MHP's solid wall as well as the liquid and vapor phases of its working fluid. The application of energy conservations to the solid wall and the liquid phase, momentum and mass conservations to both liquid and vapor phases, and the Young–Laplace capillary equation to the liquid-vapor interface then yields a set of governing equations for the model.

First, we consider the axial temperature distribution of the solid wall. Assuming steady-state conditions and then applying the principle of energy conservation to the control volume depicted in Fig. 2(*a*), we can derive the ordinary differential equation governing the axial temperature of the solid wall as

$$k_sA_s\frac{d^2T_s}{dx^2} - hP_{sl}(T_s - T_l) + \dot{q} = 0 \tag{1}$$

where T_s and T_l are the solid and liquid temperatures, k_s is the thermal conductivity of the solid, A_s is the cross-sectional area of the solid wall, and P_{sl} is the length of the solid-liquid interface of the cross section at a given axial position x. As depicted in Fig. 1, the coordinate x is measured from the evaporator end of the MHP. In Eq. (1), $\dot{q}$ denotes the rate of heat transfer per unit axial length between the MHP and its surroundings, whereas h is the heat transfer coefficient between the solid wall and the liquid phase of the working fluid. This coefficient is related to the Nusselt number through the formula

$$\mathrm{Nu} = \frac{hD_{H,l}}{k_l} \tag{2}$$

where k_l is the thermal conductivity of the liquid phase, and $D_{H,l}$ is the cross-sectional hydraulic diameter of the liquid phase which

takes into account the solid-liquid interface only. For a hydrodynamically and thermally developed laminar duct flow, the Nusselt number is generally a constant of order one [15]. In the particular case of pipes of equilateral triangle cross section, the Nusselt number is equal to 3 for constant heat flux, but is equal to 2.35 for uniform wall temperature. In the absence of theoretical or experimental results which are readily applicable to the present study, some reasonable approximations must be employed. Since the situations encountered here fall between the two extreme cases of uniform wall temperature and uniform wall heat flux, the Nusselt number throughout the present study is taken to be 2.68, which is equal to the arithmetic mean of the two extreme Nusselt numbers.

While the Nusselt number is a fixed constant irrespective of the type of solid wall material, the Biot number

$$\mathrm{Bi} = \frac{hD_{H,l}}{k_s} = \left(\frac{k_l}{k_s}\right)\mathrm{Nu} \tag{3}$$

is a constant which depends on the type of wall material. For the three materials selected for our study, copper, nickel, and monel, the Biot numbers are 0.00441, 0.0198, and 0.0897, respectively. As will be seen later, the Biot number may serve as an indicator of the importance of the thermal effects of the solid wall on the heat transport capacity of an MHP.

Denoting ϑ as the difference between the solid and liquid temperatures, i.e., $\vartheta = T_s - T_l$, we can rewrite Eq. (1) as

$$\frac{d^2\vartheta}{d\hat{x}^2} - \lambda^2\vartheta + \Theta = 0 \tag{4}$$

where

$$\lambda^2 = \frac{C_{sl}^2}{4}\left(\frac{k_l}{k_s}\right)\left(\frac{L^2}{A_s}\right)\mathrm{Nu} \tag{5}$$

and

$$\hat{x} = \frac{x}{L} \tag{6}$$

is the dimensionless axial coordinate originating from the evaporator end, L being the total length of the MHP. The constant C_{sl} in Eq. (5) is a geometrical parameter which incorporates the effect of the contact angle, and is given in the Appendix. During a steady-state operation, the rate of the heat energy entering the MHP through its evaporator must be equal to that leaving through its condenser. Therefore, the quantity Θ in Eq. (4), which accounts for the rate of heat transport $\dot{Q}$ (i.e., the load on the MHP), can be written as

$$\Theta = \begin{cases} \Theta_e = \dfrac{\dot{Q}L^2}{k_s A_s L_e}, & 0 \le \hat{x} \le \dfrac{L_e}{L} \\ 0, & \dfrac{L_e}{L} \le \hat{x} \le 1 - \dfrac{L_c}{L} \\ \Theta_c = -\dfrac{QL^2}{k_s A_s L_c}, & 1 - \dfrac{L_c}{L} \le \hat{x} \le 1 \end{cases} \tag{7}$$

assuming that the heat fluxes entering and leaving the MHP are uniformly distributed over the entire lengths of the evaporator (L_e) and the condenser (L_c), respectively. As Eq. (4) is a second order differential equation, two boundary conditions are required to obtain the solution for $\vartheta = T_s - T_l$. They are

$$\left.\frac{d\vartheta}{d\hat{x}}\right|_{\hat{x}=0} = \left.\frac{d\vartheta}{d\hat{x}}\right|_{\hat{x}=1} = 0 \tag{8}$$

We note that these adiabatic boundary conditions have been prescribed to ensure that the rates of heat energy entering and leaving the MHP are indeed the same and equal to $\dot{Q}$.

Integrating Eq. (4) piecewise, imposing the requirement of continuity of temperature and heat flux at $\hat{x} = L_e/L$ and $\hat{x} = 1 - L_c/L$, and then applying the boundary conditions (8), we obtain

$$\vartheta = T_s - T_l = \begin{cases} C_e(e^{-\lambda\hat{x}} + e^{\lambda\hat{x}}) + \dfrac{\Theta_e}{\lambda^2}, & 0 \le \hat{x} \le \dfrac{L_e}{L} \\ C_{a1}e^{-\lambda\hat{x}} + C_{a2}e^{\lambda\hat{x}}, & \dfrac{L_e}{L} \le \hat{x} \le 1 - \dfrac{L_c}{L} \\ C_c(e^{\lambda(2-\hat{x})} + e^{\lambda\hat{x}}) + \dfrac{\Theta_c}{\lambda^2}, & 1 - \dfrac{L_c}{L} \le \hat{x} \le 1 \end{cases} \tag{9}$$

where

$$C_{a2} = \frac{\Theta_c(e^{-\lambda L_c/L} - e^{\lambda L_c/L}) + \Theta_e(e^{-\lambda(1-L_e/L)} - e^{-\lambda(1+L_e/L)})}{2\lambda^2(e^{\lambda} - e^{-\lambda})} \tag{10}$$

$$C_{a1} = \frac{2\lambda^2 C_{a2} + \Theta_e(e^{\lambda L_e/L} - e^{-\lambda L_e/L})}{2\lambda^2} \tag{11}$$

$$C_c = \frac{\lambda^2(C_{a2}e^{\lambda(1-L_c/L)} + C_{a1}e^{-\lambda(1-L_c/L)}) - \Theta_c}{\lambda^2 e^{\lambda}(e^{\lambda L_c/L} + e^{-\lambda L_c/L})} \tag{12}$$

$$C_e = \frac{\lambda^2(C_{a2}e^{\lambda L_e/L} + C_{a1}e^{-\lambda L_e/L}) - \Theta_e}{\lambda^2(e^{\lambda L_e/L} + e^{-\lambda L_e/L})} \tag{13}$$

For a given MHP of known geometrical parameters and types of solid and working fluid, the constants C_{a2}, C_{a1}, C_c, and C_e can be calculated, one after another in the order stated here, using Eqs. (10)–(13), provided that the operating temperature is specified. The averaged temperature of the solid over the entire length of the MHP, $\overline{T_s}$, is given by

$$\overline{T_s} = \int_0^1 T_s(\hat{x})d\hat{x} \tag{14}$$

While $\overline{T_s}$ can be obtained by substituting Eq. (9) into Eq. (14), it is, perhaps, more instructive to consider the differential equation governing the axial temperature distribution of the solid. Integrating Eq. (4) over the entire length of the MHP, we obtain

$$\left.\frac{d\vartheta}{d\hat{x}}\right|_{\hat{x}=1} - \left.\frac{d\vartheta}{d\hat{x}}\right|_{\hat{x}=0} - \lambda^2\int_0^1 [T_s(\hat{x}) - T_l]d\hat{x} + \int_0^1 \Theta d\hat{x} = 0 \tag{15}$$

Obviously, the second integral on the left side of Eq. (15) is zero, since the heat energy entering the MHP through its evaporator section must be equal to that leaving through the condenser section. On account of Eq. (8), Eq. (15) then reduces to

$$\overline{T_s} = T_l \tag{16}$$

As mentioned previously, we shall adopt the common practice in the literature of regarding the temperature of the working fluid of an MHP as its operating temperature. It then follows from Eq. (16) that this temperature is simply the nonweighted average of the solid temperature. This point is of considerable practical significance because it provides a firm theoretical basis for the experimental determination of the operating temperature of an MHP.

To derive the equations governing liquid and vapor flows inside an MHP, we begin with the principle of momentum conservation, application of which to the infinitesimal control volume depicted in Fig. 2(*b*) yields the ordinary differential equations

$$\rho_l\frac{d}{dx}(A_l u_l^2) = -A_l\frac{dp_l}{dx} + \tau_{sl}P_{sl} + \tau_{lv}P_{lv} - g\rho_l A_l \sin\beta \tag{17}$$

and

$$\rho_v \frac{d}{dx}(A_v u_v^2) = -A_v \frac{dp_v}{dx} - \tau_{sv} P_{sv} - \tau_{lv} P_{lv} - g\rho_v A_v \sin\beta \quad (18)$$

In these equations, A_j, ρ_j, u_j, and p_j are the cross-sectional area, density, velocity, and pressure of phase j, respectively, g is the gravitational acceleration, and β is the angle of inclination of the MHP. The shear stress τ at the solid-liquid (sl), solid-vapor (sv), and liquid-vapor (lv) interfaces is given by [15]

$$\tau_{ij} = \frac{\rho_j u_j^2 f}{2}, \quad f = \frac{K}{\mathrm{Re}_j} \quad (i = s,l; \quad j = l,v; \quad i \neq j) \quad (19)$$

where the dimensionless quantity f is the friction factor. The Reynolds number Re_j is defined based on the hydraulic diameter $D_{H,j}$ as

$$\mathrm{Re}_j = \frac{\rho_j u_j D_{H,j}}{\mu_j} \quad (20)$$

where μ_j is the dynamic viscosity of phase j. For laminar flows, the constant K in Eq. (19) is a function of the cross-sectional geometry. Since the MHP under investigation has a cross section in the shape of an equilateral triangle and the liquid phase is confined to the corner regions, it is reasonable to approximate the value of K for the liquid domain with the value of 13.3 for a triangular duct. For all the cases studied in this paper, the cross section of the vapor domain varies from practically an equilateral triangle, for which $K=13.3$, at the evaporator end to the one resembling a circle, for which $K=16$, at the condenser end. (In the special case of zero contact angle between the liquid-vapor interface and the solid wall, the cross section of the vapor domain at the condenser end is a circle.) In view of this, we select for the vapor domain $K=14.7$, which is the average of 13.3 and 16. During a steady-state operation of an MHP, there is no mass accumulation anywhere along its axis. It then follows from the principle of mass conservation that there is no net flow of matter through any cross section of the MHP. This, in turn, requires the equality of the mass flow rates of liquid and vapor at any axial position, i.e.,

$$\rho_l u_l A_l = \rho_v u_v A_v = \dot{m} \quad (21)$$

where $\dot{m}$ is the mass flow rate of liquid and vapor through a given cross section of the MHP. In addition to Eqs. (17) and (18), the pressure of the two phases, p_l and p_v, must also satisfy the Young–Laplace capillary equation

$$p_l - p_v = -\frac{\sigma}{r} \quad (22)$$

where r is radius of curvature of the liquid-vapor interface, and σ is the surface tension, which is assumed to be constant throughout this interface. In Eq. (22), we have considered the curvature in the cross-sectional plane only and ignore that in the longitudinal plane. This is justified by the fact that the former is dominant over the latter, as the cross-sectional length scales of an MHP are much smaller than its axial length scales. Differentiating both sides of Eq. (22), we then obtain

$$\frac{dp_l}{dx} - \frac{dp_v}{dx} = \frac{\varpi\sigma}{2A^{1/2}s^{3/2}} \frac{ds}{dx} \quad (23)$$

where A is the cross-sectional area of the MHP's channel, s is the volume fraction occupied by the liquid phase, and ϖ is an angular parameter (see the Appendix).

The governing equations can be rendered nondimensional by utilizing the following dimensionless variables:

$$\hat{x} = \frac{x}{L}, \quad s = \frac{A_l}{A}, \quad 1 - s = \frac{A_v}{A}, \quad \hat{m} = \frac{\dot{m}}{\dot{Q}L/h_{fg}L_e} = \frac{\dot{m}}{\dot{m}_{\mathrm{ref}}}, \quad \hat{p} = \frac{p_j}{\sigma/A^{1/2}} \quad (24)$$

Then, combining Eqs. (17), (18), (21), and (23) together with the expressions for the geometrical parameters given in the Appendix, we obtain the following ordinary differential equation:

$$\frac{ds}{d\hat{x}} = \frac{s^{3/2}}{\varpi}\left\{ \mathrm{We}\left[\frac{1}{\varepsilon(1-s)} \frac{d}{d\hat{x}}\left(\frac{\hat{m}^2}{1-s} \right) - \frac{1}{s}\frac{d}{d\hat{x}}\left(\frac{\hat{m}^2}{s} \right) \right] + \mathrm{Ca}[(f\ \mathrm{Re}_l)F(s) + \gamma(f\ \mathrm{Re}_v)G(s)]\hat{m} - \mathrm{Ga}\sin\beta \right\} \quad (25)$$

where the capillary number Ca, gravity number Ga, Weber number We, kinematic viscosity ratio γ, and density ratio ε are defined, respectively, as

$$\mathrm{Ca} = 2\left(\frac{L}{A^{1/2}} \right)\left[\frac{\mu_l(\dot{m}_{\mathrm{ref}}/\rho_l A)}{\sigma} \right] \quad (26)$$

$$\mathrm{Ga} = 2\left(\frac{L}{A^{1/2}} \right)\left[\frac{g(\rho_l - \rho_v)A}{\sigma} \right] \quad (27)$$

$$\mathrm{We} = \frac{2\rho_l(\dot{m}_{\mathrm{ref}}/\rho_l A)^2 A^{1/2}}{\sigma} \quad (28)$$

$$\gamma = \frac{\mu_v \rho_l}{\mu_l \rho_v} = \frac{\nu_v}{\nu_l} \quad (29)$$

$$\varepsilon = \frac{\rho_v}{\rho_l} \quad (30)$$

The two functions in Eq. (25), $F(s)$ and $G(s)$, are functions of s which can be expressed as

$$F(s) = \frac{C_{sl}^2}{8s^2} \quad (31)$$

$$G(s) = \frac{[NwA^{-1/2} + (C_{lv} - C_{sl})s^{1/2}][NwA^{-1/2} + C_{lv}s^{-1/2} - C_{sl}s^{1/2}]}{8(1-s)^3} \quad (32)$$

where N is the number of corners of a cross section ($N=3$ for the triangular cross section considered in this paper) and w is its side length. The geometrical parameters C_{lv} and C_{sl} are given in the Appendix. The dimensionless mass flow rate $\hat{m}$ (see Eqs. (24) and (25)) is readily obtained by considering the energy conservation of the liquid phase. Ignoring the axial conduction and convection, the thermal energy entering the liquid phase from the solid wall is then assumed to diffuse toward the liquid-vapor interface, where it is taken up as the latent heat of evaporation. Under this assumption, which is depicted schematically in Fig. 2(c), the principle of energy conservation can be expressed as

$$\frac{d\hat{m}}{d\hat{x}} = \eta\vartheta \quad (33)$$

where

$$\eta = \frac{\lambda^2 k_s A_s}{\dot{m}_{\mathrm{ref}} h_{fg} L} \quad (34)$$

and h_{fg} is the latent heat of evaporation of the working fluid. As given by Eq. (33), the mass flow rate depends solely on the axial distribution of the solid wall temperature, which was previously obtained as Eq. (9). Therefore, Eq. (33) can be integrated, subject to the "initial condition" $\hat{m}(0)=0$, to yield the dimensionless mass flow rate profile as follows:

$$\hat{m} = \begin{cases} \dfrac{\eta}{\lambda}\left[C_e(e^{\lambda\hat{x}} - e^{-\lambda\hat{x}}) + \dfrac{\Theta_e \hat{x}}{\lambda} \right], & 0 \le \hat{x} \le \dfrac{L_e}{L} \\ \dfrac{\eta}{\lambda}(C_{a2}e^{\lambda\hat{x}} - C_{a1}e^{-\lambda\hat{x}} + K_1), & \dfrac{L_e}{L} \le \hat{x} \le 1 - \dfrac{L_c}{L} \\ \dfrac{\eta}{\lambda}\left[C_c(e^{\lambda\hat{x}} - e^{\lambda(2-\hat{x})}) + \dfrac{\Theta_c \hat{x}}{\lambda} + K_2 \right], & 1 - \dfrac{L_c}{L} \le \hat{x} \le 1 \end{cases} \tag{35}$$

where

$$K_1 = C_e(e^{\lambda L_e/L} - e^{-\lambda L_e/L}) + C_{a1}e^{-\lambda L_e/L} - C_{a2}e^{\lambda L_e/L} + \frac{\Theta_e L_e}{\lambda L} \tag{36}$$

$$K_2 = C_e(e^{\lambda L_e/L} - e^{-\lambda L_e/L}) + C_{a1}(e^{-\lambda L_e/L} - e^{-\lambda(1-L_c/L)}) + C_{a2}(e^{\lambda(1-L_c/L)} - e^{\lambda L_e/L}) + C_c(e^{\lambda(1+L_c/L)} - e^{\lambda(1-L_c/L)}) + \frac{\Theta_e L_e + \Theta_c(L - L_c)}{\lambda L} \tag{37}$$

Equation (25) is a first order, nonlinear ordinary differential equation, and will be solved numerically using the fourth order Runge–Kutta method with a step size of 0.001, which has been tested to be sufficiently small to yield accurate results. In this paper, we shall be concerned with the heat transport capacity $\dot{Q}_{\text{cap}}$ of an MHP, which is the maximum possible load that the MHP can carry without the occurrence of dryout and flooding. As pointed out by Tio et al. [7], an MHP which is filled with the optimal amount of working fluid and loaded with $\dot{Q}_{\text{cap}}$ will operate under the condition of simultaneous onsets of dryout at its evaporator end and flooding at its condenser end. In view of these, the integration of Eq. (25) is carried out subject to the "initial condition" of $s(0)=s_{\text{cl}}$, which corresponds to the onset of dryout at the evaporator end. Throughout our study, we shall adopt the value of $s_{\text{cl}}=0.0001$ instead of the mathematical condition of $s(0)=0$, in order to avoid the occurrence of singularity in Eq. (25). This is justified since, as first pointed out by Longtin et al. [16], the actual value of s_{cl} is immaterial as long as it is less than a certain threshold value; moreover, it is found in this study that $\dot{Q}_{\text{cap}}$ is not sensitive to changes in s_{cl} for $s_{\text{cl}}<0.004$ and that $\dot{Q}_{\text{cap}}$ changes by less than 1% in response to the reduction of s_{cl} from 0.004 to 0.0001. To achieve the onset of flooding at the condenser end, we adjust the heat input $\dot{Q}$ for the integration of Eq. (25) until we satisfy the condition $s(1)=s_{\text{fl}}$, where s_{fl} is the liquid volume fraction which corresponds to the onset of flooding, and is given in terms of the contact angle θ and the half corner angle as

$$s_{\text{fl}} = \frac{\varpi^2 \tan\phi}{4\cos^2(\phi+\theta)} \tag{38}$$

The iteration is carried out in steps of $\Delta\dot{Q}=0.0001$ W, which is roughly 10^{-4} times the heat transport capacity of a typical MHP [7,14], and stopped when the condition $s(1)=s_{\text{fl}}$ is reached, in which case the corresponding $\dot{Q}$ is the heat transport capacity $\dot{Q}_{\text{cap}}$. Once the liquid volume fraction s is obtained, the charge level M of the MHP can be easily determined. In dimensionless form, it is given by

$$\hat{M} = \frac{M}{AL\rho_l} = \varepsilon + (1-\varepsilon)\int_0^1 s(\hat{x})d\hat{x} \tag{39}$$

The integral in Eq. (39) must be evaluated numerically, and in the present study, Simpson's rule is selected for its simplicity and accuracy. In our calculations, we made use of the book by Dunn and Reay [17] for the thermophysical properties of all the solids and working fluid, except monel, for which the handbook by Perry and Green [18] was consulted.

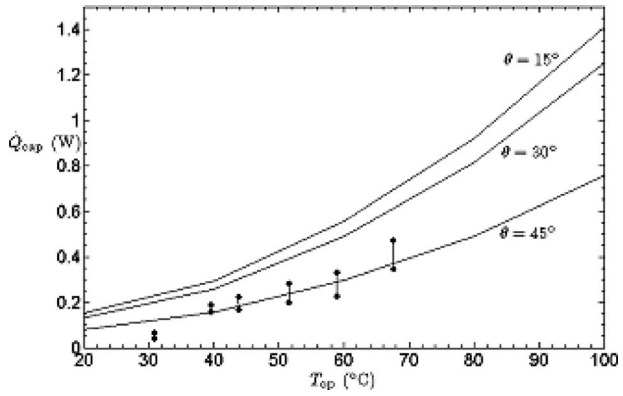

Fig. 3 Heat transport capacity $\dot{Q}_{\text{cap}}$ of a copper MHP as a function of the operating temperature T_{op} for different values of contact angle. Experimental data from Ref. [14] are included.

3 Results and Discussion

The main concern of this paper is the heat transport capacity of a microheat pipe together with the effects of the thermophysical properties of its solid wall. Before we embark on the investigation of the roles played by the solid wall, we must, however, establish first the validity of the MHP model employed in the study. A sensitivity study reveals that the heat transport capacity $\dot{Q}_{\text{cap}}$ is insensitive to the variations of the Nusselt number within the range of 2.35 and 3, for the extreme cases of uniform wall temperature and uniform wall heat flux, respectively. For the copper-water microheat pipe of Table 1 optimally operating at 60°C, the discrepancy between the heat transport capacity in the present model and the heat transport capacities obtained for both cases of uniform wall temperature and uniform wall heat flux is negligibly small, being less than 0.7% and 0.6%, respectively. This justifies the selection of a mean value of the two extreme Nusselt numbers in the present model, as discussed in Sec. 2.

In Fig. 3, we plot the heat transport capacity as a function of the operating temperature, the contact angle θ between the liquid phase and the solid wall being a parameter; the corresponding optimal charge levels are shown in Fig. 4. For comparison, the experimental data reported by Babin et al. [14] for a copper trapezoidal MHP, of a cross-sectional area equivalent to that of the present study and filled with 32 mg of water, are also included in Fig. 3. We observe that the theoretical and experimental results agree qualitatively, in the sense that both of them show the same trend of heat transport rate increasing with the operating tempera-

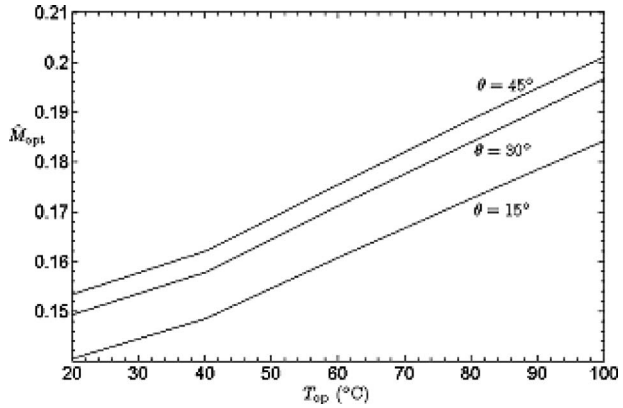

Fig. 4 Optimal charge level $\hat{M}_{\text{opt}}$ corresponding to the heat transport capacity $\dot{Q}_{\text{cap}}$ of Fig. 3, as a function of the operating temperature T_{op} for different values of contact angle

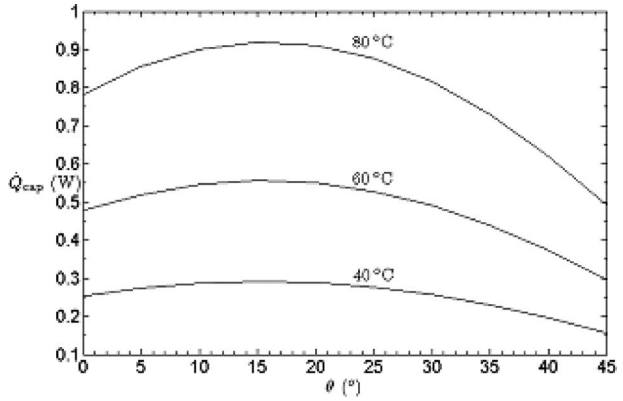

Fig. 5 Heat transport capacity $\dot{Q}_{cap}$ of a copper MHP as a function of contact angle θ, the operating temperature T_{op} being a parameter

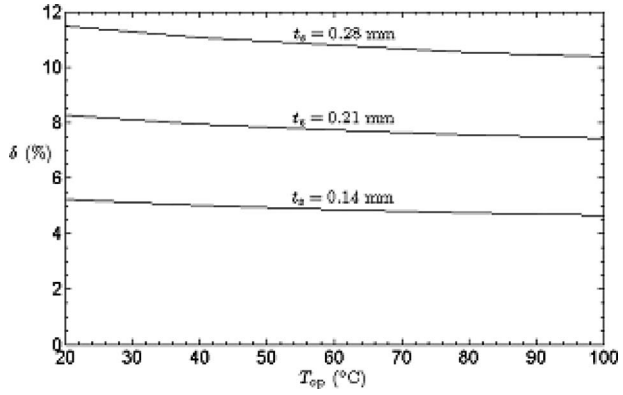

Fig. 6 Relative difference between $\dot{Q}_{cap}$ and $\dot{Q}^*_{cap}$, δ, as a function of the operating temperature T_{op} of a copper MHP, the solid wall thicknesses t_s being a parameter

ture. Moreover, both sets of results also agree well on the order of magnitude of the heat transport rate. However, it would be meaningless to draw further quantitative comparisons between them. This follows from the fact that we are comparing MHPs of different cross-sectional shapes, albeit of the same cross-sectional area, and that the heat transport capacity of an MHP is very sensitive to its cross-sectional shape [19].

In Figs. 3 and 4, and, in fact, throughout the present study, the contact angle with which the liquid-vapor interface touches the solid wall is assumed to be uniform throughout an MHP. This assumption is, needless to say, an ideal approximation only, since the wetting of solids by liquids is a complex phenomenon [20]. Nevertheless, it is still useful to investigate further the effects of the contact angle on the heat transport capacity of an MHP. In Fig. 5, we plot the heat transport capacity $\dot{Q}_{cap}$ as a function of the contact angle θ, the operating temperature being a parameter. For a given operating temperature, we observe that the heat transport capacity increases as the contact angle is increased from zero until a threshold value of θ is reached, beyond which the heat transport capacity decreases with an increasing contact angle. A similar trend was also observed by Tio et al. [7], in whose study the thermal effects of the solid wall are not taken into account. They point out that the existence of this threshold contact angle is due to the balance between two opposite trends. While an increase in the contact angle results in an increase in the charge level $\hat{M}_{opt}$ (Fig. 4 and Fig. 9(*b*) of reference [7]), providing capillarity with more liquid to perform its task, the strength of capillarity actually decreases. For small contact angles, the positive effect of increasing $\hat{M}_{opt}$, in response to an increase in the contact angle, outweighs the negative effect of decreasing capillarity; however, beyond the threshold contact angle, the strength of capillarity is so diminished that an increase in $\hat{M}_{opt}$ cannot compensate for the further decrease in capillary strength, thus resulting in a decrease in $\dot{Q}_{cap}$. From Fig. 5, we observe that this threshold contact angle is roughly equal to 15 deg. In the absence of definitive and readily useful information on how the contact angle varies inside an MHP, we shall therefore assume, in what follows, that the contact angle is constant and equal to 15 deg throughout an MHP.

As mentioned earlier, the primary objective of this paper is to examine the effects of the solid wall on the performance of an MHP. To this end, we first compare the heat transport capacity predicted by our model, $\dot{Q}_{cap}$, and that obtained by a similar model without the solid wall, $\dot{Q}^*_{cap}$. For the latter, uniform heat fluxes are also prescribed over its evaporator and condenser sections. In the absence of the solid wall, these fluxes are those entering and leaving the liquid phase directly, and correspond to the heat transport capacity $\dot{Q}^*_{cap}$. Moreover, they give rise to the dimensionless mass flow rate

$$\hat{m} = \begin{cases} \hat{x}, & 0 \le \hat{x} \le \dfrac{L_e}{L} \\ \dfrac{L_e}{L}, & \dfrac{L_e}{L} \le \hat{x} \le 1 - \dfrac{L_c}{L} \\ \dfrac{L_e}{L_c}(1-\hat{x}), & 1 - \dfrac{L_c}{L} \le \hat{x} \le 1 \end{cases} \tag{40}$$

which is considerably simpler than its counterpart given in Eq. (35). Substituting Eq. (40) into Eq. (25) and then solving the latter, $\dot{Q}^*_{cap}$ is obtained in the same manner as that for $\dot{Q}_{cap}$. Here, we note that the behavior of $\dot{Q}^*_{cap}$ with respect to the operating temperature is qualitatively similar to that of $\dot{Q}_{cap}$ depicted in Fig. 3. To compare the two heat transport capacities, $\dot{Q}_{cap}$ and $\dot{Q}^*_{cap}$, we consider their relative difference δ, which is defined as follows:

$$\delta = \frac{\dot{Q}_{cap} - \dot{Q}^*_{cap}}{\dot{Q}_{cap}} \tag{41}$$

In Fig. 6, this difference is plotted as a function of the operating temperature, the thickness of the solid wall being a parameter. We observe that the model without a solid wall underpredicts the heat transport capacity of an MHP. While δ, interpreted here as the error incurred by the exclusion of the solid wall, decreases slightly with the operating temperature, it becomes greater as the wall thickness is increased. For a solid wall thickness of $t_s = 0.14$ mm, δ is about 5% over the temperature range of 20–100°C. When the thickness is increased by 50% to $t_s = 0.21$ mm, δ increases to about 8%. Finally, doubling the wall thickness to $t_s = 0.28$ mm results in an error of approximately 11%. Although the fractional error δ for a given wall thickness decreases with the operating temperature, the absolute error, $\dot{Q}_{cap} - \dot{Q}^*_{cap}$, actually increases if the operating temperature is increased, as can be deduced from Figs. 3 and 6. For instance, the absolute error for a wall thickness of $t_s = 0.14$ mm increases from about 0.0079 W to roughly 0.066 W when the operating temperature is increased from 20°C to 100°C. As observed earlier, the relative error δ at a fixed operating temperature increases with the wall thickness t_s. This simple observation then allows us to deduce from the formula

$$\frac{\dot{Q}_{\text{cap}} - \dot{Q}^*_{\text{cap}}}{\dot{Q}^*_{\text{cap}}} = \frac{\delta}{1-\delta} \tag{42}$$

that the absolute error, $\dot{Q}_{\text{cap}} - \dot{Q}^*_{\text{cap}}$, also increases with the wall thickness, as does the heat transport capacity. Although our observation that both the relative error δ and absolute error $\dot{Q}_{\text{cap}} - \dot{Q}^*_{\text{cap}}$ increase with the solid wall thickness is based on a rather limited range of thickness values, this observation is, as will be seen later, valid for all values of t_s. While we are not yet able to draw a conclusion from our discussion so far that the solid wall of an MHP must always be included in the calculation of its heat transport capacity, for we have only examined one type of material, we can, nevertheless, assert that the solid wall cannot be casually excluded either. We shall examine later the effects of different solid materials.

The fact that our model of an MHP with a solid wall predicts a larger heat transport capacity than the one without a solid wall is, of course, not surprising, since the presence of the solid wall provides an additional mode of heat transport: axial heat conduction in the solid. However, we should not simply equate the difference in the heat transport capacities of these models to the rate of heat conduction in the solid wall. Indeed, we do not know at this point if this axial conduction is the sole effect introduced by the presence of the solid wall. To address this issue, we must actually calculate the net rate of the axial heat conduction in the solid. For this purpose, we first note that a portion of the thermal energy which enters an MHP through its evaporator section is used for phase change, while the remaining portion is conducted in the solid wall toward the condenser section. For the heat transport capacity, we therefore write

$$\dot{Q}_{\text{cap}} = \dot{Q}_p + \dot{Q}_c \tag{43}$$

where $\dot{Q}_p$ is that portion of $\dot{Q}_{\text{cap}}$ which enters the liquid phase from the solid wall and is taken up as the latent heat of evaporation, and $\dot{Q}_c$ is the remaining portion of $\dot{Q}_{\text{cap}}$ which is conducted in the solid wall toward the condenser section. Obviously

$$\dot{Q}_p = \int_{x=0}^{x=0.5L} hP_{sl}(T_s - T_l)dx = \frac{\lambda^2 k_s A_s}{L} \int_{\hat{x}=0}^{\hat{x}=0.5} \vartheta d\hat{x} \tag{44}$$

We note that the upper limits of $x=0.5L$ and $\hat{x}=0.5$ in these integrals are the result of symmetry: uniform heat flux over the evaporator and condenser sections of equal lengths. Substitution of Eq. (44) into Eq. (43) then allows us to determine $\dot{Q}_c$. Subtracting $\dot{Q}^*_{\text{cap}}$ from both sides of Eq. (43), we obtain

$$\dot{Q}_{\text{cap}} - \dot{Q}^*_{\text{cap}} = \dot{Q}_c + (\dot{Q}_p - \dot{Q}^*_{\text{cap}}) \tag{45}$$

In MHP models which do not take into account the thermal effects of the solid wall, the heat transport from one end to the other end of the MHP is entirely carried out by phase change. In view of this, we may interpret the $\dot{Q}^*_{\text{cap}}$ on the left side of Eq. (45) as the heat transport capacity but that on the right side as the rate of thermal energy taken up by phase change (i.e., evaporation). Then, Eq. (45) simply states that the error in the heat transport capacity incurred by neglecting the thermal effects of the solid wall of an MHP is equal to the sum of the rate of axial conduction in the solid and the change in the rate of heat transport by evaporation induced by the presence of the solid wall. To examine further the contributions of these two components, we introduce the variables $\tilde{\delta}_c$ and $\tilde{\delta}_p$, given respectively by

$$\tilde{\delta}_c = \frac{\dot{Q}_c}{\dot{Q}_{\text{cap}} - \dot{Q}^*_{\text{cap}}} \tag{46}$$

and

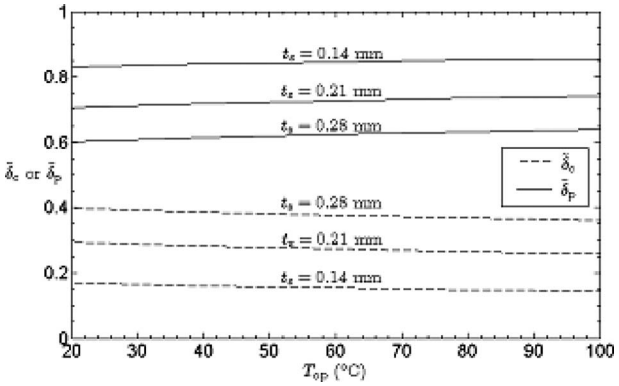

Fig. 7 Fractional errors contributed by axial solid conduction $\tilde{\delta}_c$ and change in phase change heat transport $\tilde{\delta}_p$ for a copper MHP as a function of the operating temperature T_{op}, the solid wall thickness t_s being a parameter

$$\tilde{\delta}_p = \frac{\dot{Q}_p - \dot{Q}^*_{\text{cap}}}{\dot{Q}_{\text{cap}} - \dot{Q}^*_{\text{cap}}} \tag{47}$$

so that Eq. (45) can be rewritten as

$$\tilde{\delta}_c + \tilde{\delta}_p = 1 \tag{48}$$

In Fig. 7, these variables are plotted as a function of the operating temperature, the solid wall thickness being a parameter. We observe that for a given wall thickness t_s, the fraction of error contributed by axial conduction in the wall, $\tilde{\delta}_c$, decreases with the operating temperature. However, this decrease is attributable to the rapid increase in the absolute error $\dot{Q}_{\text{cap}} - \dot{Q}^*_{\text{cap}}$, which increases with increasing operating temperature, as discussed earlier. In fact, simple calculations making use of Figs. 3, 6, and 7 reveal that the absolute rate of axial conduction in the solid wall, $\dot{Q}_c$, increases with the operating temperature. From Fig. 7, we observe that the fraction of the change in the heat transport rate by evaporation induced by the presence of the solid wall, $\tilde{\delta}_p$, increases with increasing operating temperature. As $\tilde{\delta}_p$ is always positive, the change induced in the heat transport rate by phase change, $\dot{Q}_p - Q^*_{\text{cap}}$, as clearly seen from Eq. (47), also intensifies when the operating temperature is increased. Since $\dot{Q}^*_{\text{cap}}$, as noted earlier, increases with the operating temperature, so does the actual rate of heat transport by phase change, $\dot{Q}_p$. For a fixed operating temperature, Fig. 7 shows that the variable $\tilde{\delta}_c$ increases with the wall thickness. Similar to the observation in Fig. 6, we also observe that $\dot{Q}_c$ increases with the wall thickness, as required by the formula

$$\frac{\dot{Q}_c}{Q^*_{\text{cap}}} = \frac{\delta\tilde{\delta}_c}{1-\delta} \tag{49}$$

which results from a simple manipulation of Eqs. (41) and (46). That $\dot{Q}_c$ increases with t_s is, of course, consistent with the universal observation that the rate of heat conduction increases with the area of the cross section through which the heat energy is conducted. Similarly, the change induced in the heat transport rate by phase change, $\dot{Q}_p - Q^*_{\text{cap}}$, is related to δ by the formula

$$\frac{\dot{Q}_p - Q^*_{\text{cap}}}{Q^*_{\text{cap}}} = \frac{\delta\tilde{\delta}_p}{1-\delta} \tag{50}$$

For a fixed operating temperature, although $\tilde{\delta}_p$ decreases with increasing solid wall thickness, a careful review of Figs. 7 and 6 as

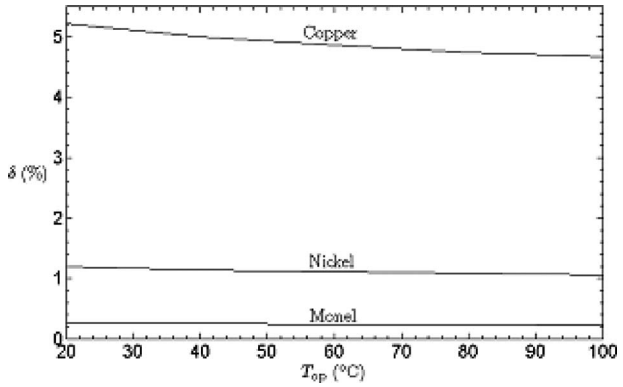

Fig. 8 Relative difference between $\dot{Q}_{cap}$ and $\dot{Q}^*_{cap}$, δ, as a function of the operating temperature T_{op} of an MHP with a solid wall thicknesses of t_s=0.14 mm and three different solid wall materials: copper, nickel, and monel

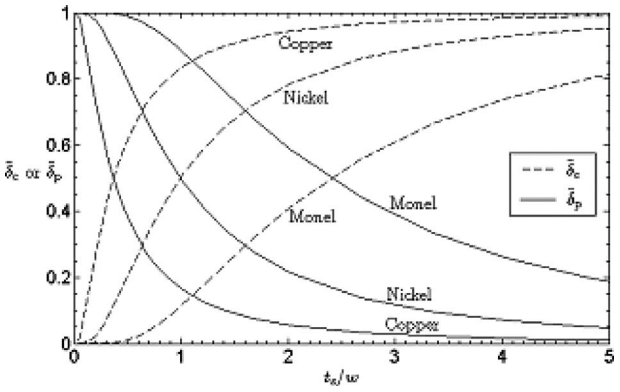

Fig. 9 Fractional errors contributed by axial solid conduction $\tilde{\delta}_c$ and change in phase change heat transport $\tilde{\delta}_p$ as a function of the solid wall thickness of MHPs of different solid materials. The MHPs are optimally charged for and operated at 60°C.

well as Eqs. (50) and (47) reveals that $\dot{Q}_p - Q^*_{cap}$ actually increases with increasing solid wall thickness. The fact that $\dot{Q}_p - Q^*_{cap}$ shares a similar trend with $\dot{Q}_c$ suggests that it may have its origin in axial solid conduction, a point that we shall explore later.

In Figs. 6 and 7, we have selected copper and water as the solid material and working fluid, respectively. To see further the thermal effects of the solid wall, we replace copper (k_s =394 W/m K) with two other solids of lower thermal conductivity: nickel (k_s=88 W/m K) and monel (k_s=19.4 W/m K). While a change in the solid material gives rise to changes in the variables δ, $\tilde{\delta}_c$, and $\tilde{\delta}_p$, their variations with the wall thickness and operating temperature of an MHP made of either nickel or monel are qualitatively similar to those depicted in Figs. 6 and 7 for a copper MHP. Nevertheless, it is still useful to compare MHPs of a fixed wall thickness (and geometry) but of different solid wall materials. To this end, we first see how the thermal conductivity of the solid affects the variable δ. From Fig. 8, we observe that δ increases as we go from monel to nickel and copper; moreover, the error δ associated with monel and nickel is negligible, but that associated with copper is not insignificant. Noting that copper has the highest thermal conductivity among these three solids and that δ increases with the solid wall thickness (Fig. 6), we conclude that the thermal effects of the solid wall on the heat transport capacity of an MHP can be ignored, if and only if the thickness and thermal conductivity of the solid wall are both sufficiently small. In view of Eq. (3), we may also conclude that for an MHP with a given geometry and working fluid, these thermal effects have an inverse relation with the Biot number.

To further investigate the effects of the thickness of the solid wall, the variables $\tilde{\delta}_c$ and $\tilde{\delta}_p$ are depicted in Fig. 9 as a function of the solid wall thickness of an MHP, its operating temperature being fixed at 60°C, for the three types of solid materials. For the case of a very thin solid wall, so that the error $\dot{Q}_{cap} - \dot{Q}^*_{cap}$ is very small, $\tilde{\delta}_p$ dominates over $\tilde{\delta}_c$, indicating that very little axial conduction takes place in the solid wall and that the effect of the solid wall manifests itself almost solely in the increase in heat transport by phase change. We observe from Fig. 9 that for a sufficiently thin solid wall of a fixed thickness, so that $\tilde{\delta}_p$ dominates over $\tilde{\delta}_c$, the degree of dominance is greater for a lower thermal conductivity, and vice versa. As the wall thickness is increased, the contribution of axial solid conduction to the error $\dot{Q}_{cap} - \dot{Q}^*_{cap}$ becomes more prominent, and eventually, $\tilde{\delta}_c$ starts to overtake $\tilde{\delta}_p$ at $\tilde{\delta}_c = \tilde{\delta}_p = 0.5$, beyond which $\tilde{\delta}_c$ dominates over $\tilde{\delta}_p$ for all solid materials. We term this particular solid wall thickness as the balanced-out thickness. We observe that this thickness is a function of the thermal conductivity of the solid wall material, and, as expected, is greater for a material of lower conductivity, and vice versa. Beyond the balanced-out thickness, $\tilde{\delta}_c$ becomes dominant over $\tilde{\delta}_p$, as both approach their respective asymptotes of $\tilde{\delta}_c$=1 and $\tilde{\delta}_p$=0. Moreover, for a given wall thickness, the degree of the dominance of $\tilde{\delta}_c$ over $\tilde{\delta}_p$ is greater for a wall material of higher thermal conductivity, and vice versa.

The existence of the asymptotes $\tilde{\delta}_c$=1 and $\tilde{\delta}_p$=0 is easily understood from Fig. 10, in which the rate of the axial conduction in the solid wall, $\dot{Q}_c$, and the rate of heat transport by phase change, $\dot{Q}_p$, are depicted as a function of the thickness of the solid wall of the MHP of Fig. 9 operating at 60°C. In the case of zero solid wall thickness, no axial conduction exists, and the heat transport capacity of the MHP is entirely carried by the phase change heat transport $\dot{Q}_p$. When the wall thickness is increased slightly, $\dot{Q}_p$ increases rapidly, with a higher rate for a solid of greater thermal conductivity, and vice versa. However, axial conduction in the solid wall remains negligible, although we can observe that, similar to $\dot{Q}_p$, it also increases with wall thickness, and that a larger $\dot{Q}_c$ is associated with a greater solid thermal conductivity, and vice versa. When the solid wall thickness reaches a certain threshold value, which is a function of the solid conductivity, axial solid conduction starts to exceed heat transport by phase change. Further increase in the wall thickness eventually results in a parabolic profile for axial solid conduction ($\dot{Q}_c$ is proportional to t_s^2, or, the

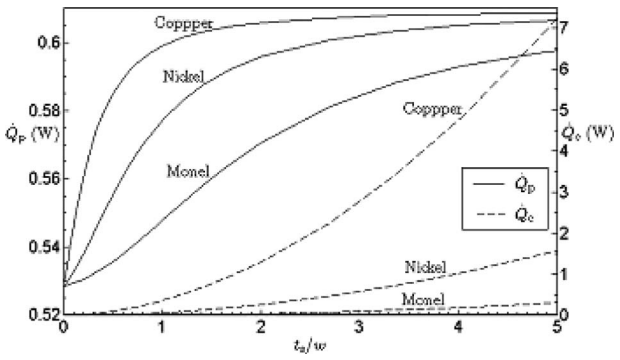

Fig. 10 Absolute rate of axial conduction in the solid wall $\dot{Q}_c$ and the absolute rate of heat transport by phase change $\dot{Q}_p$ as a function of the solid wall thickness of the MHPs of Fig. 9

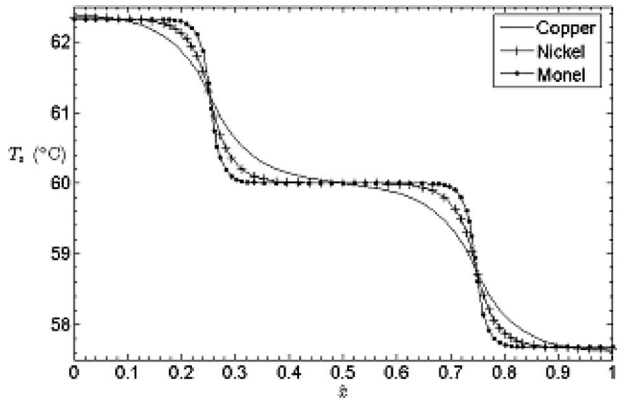

Fig. 11 Axial solid wall temperature profiles of MHPs of a solid wall thickness of t_s=0.14 mm and made of three different materials: copper, nickel, and monel. The MHPs are optimally charged and operated at 60°C.

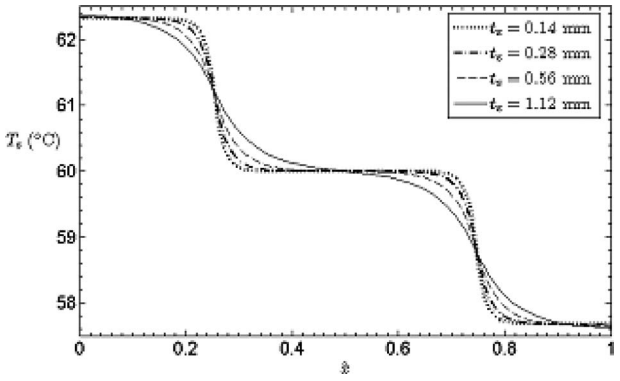

Fig. 12 Axial solid wall temperature profiles of monel MHPs of different values of solid wall thickness, all optimally charged for and operated at 60°C

cross-sectional area of the solid wall) and the heat transport by phase change approaching its maximum value; this scenario corresponds to $\tilde{\delta}_c$ and $\tilde{\delta}_p$ approaching their respective asymptotes of $\tilde{\delta}_c=1$ and $\tilde{\delta}_p=0$, as depicted in Fig. 9, and the heat transport capacity of the MHP being almost entirely carried by axial solid conduction with negligible fractional contribution by phase change. The fact that $\dot{Q}_p$ possesses an asymptote is, of course, not entirely unexpected, because it is limited by the onsets of dryout and flooding. However, that this asymptotic value depends on the type of solid wall material, being greater for the solid of higher conductivity and vice versa, and that $\dot{Q}_p$, in line with $\dot{Q}_c$, increases with the thickness of the solid wall and its conductivity suggest that further exploration is required. We continue, then, with the effects of solid thermal conductivity.

Figure 11 shows the axial solid temperature profiles of MHPs of a solid wall thickness of t_s=0.14 mm and optimally operated at 60°C; as usual, we consider three solid materials: copper, nickel, and monel. We note that these temperature profiles are consistent with those obtained experimentally by Lin et al. [21] and numerically by Do et al. [12]. For each of the three cases depicted in Fig. 11, we observe that a temperature drop of about 5°C, the actual value being greater for the solid of high conductivity and vice versa, occurs between the evaporator and condenser ends. This is noteworthy, in view of the commonly held notion that heat pipes are (nearly) isothermal heat transfer devices. Except for the 5°C temperature drop, the three temperature profiles in Fig. 11 are rather dissimilar. For an MHP made of monel, which has the lowest thermal conductivity among the three solid materials, each of the evaporator, condenser, and adiabatic sections has a uniform temperature distribution, except at the intersectional regions, where steep jumps in temperature are observed. That the core region of the adiabatic section of a monel MHP remains isothermal at 60°C, which is also the temperature of the liquid phase, implies that no heat energy is conducted through the adiabatic section, and that phase change heat transport, which takes place mostly over the evaporator and condenser sections only, is the sole agent responsible for the heat transport capacity. For a nickel MHP, the core region of the adiabatic section also remains isothermal at 60°C, so that no axial conduction passes through this section either. However, the extent of this core region is less than that of a monel MHP, allowing significant phase change to take place over the adiabatic section. While the phase change heat transport at the evaporator and condenser is reduced, compared with that of a monel MHP (see Fig. 11 and Eq. (44)), this reduction is apparently overcompensated by the increase in the phase change heat transport at the adiabatic section, resulting in a greater $\dot{Q}_p$ for the nickel MHP. For an MHP made of copper, which has the highest thermal conductivity among the three solid materials, the solid temperature decreases continuously from the evaporator end to the condenser end, indicating that axial conduction takes place inside the solid wall, from the evaporator end to the condenser end. This axial solid temperature distribution indicates that evaporation and condensation also take place at the adiabatic section so that its demarcations with the evaporator and condenser sections no longer exist. This observation is consistent with the proposition by Vadakkan et al. [22], who pointed out that there is no "adiabatic section" for a conventional flat heat pipe subjected to heating with multiple discrete heat sources.

Next, we turn our attention to the effect of the solid wall thickness on the axial temperature distribution. Figure 12 depicts the axial solid wall temperature profiles for a monel MHP operated at 60°C, the solid wall thickness being a parameter. When the solid wall thickness is small, i.e., t_s=0.14 mm, the constant temperature at the adiabatic section suggests that very little heat transfer takes place between the solid wall and the working fluid. However, when the solid wall thickness is increased eightfolds up to t_s=1.12 mm, the solid wall temperature is more evenly distributed, resembling the temperature profile of the MHP of high solid thermal conductivity and thin solid wall depicted in Fig. 11. Hence, a conclusion similar to that associated with Fig. 11 can be drawn. No sharp demarcation lines exist for the adiabatic section if the solid wall is thick enough, although its thermal conductivity may be low.

In our discussion so far, we have purposely concentrated on the heat transport capacity of a microheat pipe. This rate of heat transport is, as pointed out by Tio et al. [7], the maximum allowable load that can be applied to the MHP if it is to operate without dryout and flooding at a given operating temperature, and requires a specific temperature-dependent amount of working fluid. While this approach is suitable for analysis, the practical situation is more likely to involve MHPs with a fixed amount of working fluid and operating at a temperature which is determined by their ambient conditions. For an MHP with a fixed amount of working fluid, there are, in fact, only two independent operating conditions. This point is vividly illustrated in Fig. 13, which is simply a relation governing the rate of heat transport $\dot{Q}$, the operating temperature T_{op}, the temperature at the evaporator end T_0, and the temperature at the condenser end T_1 of the MHP of Table 1 optimally filled with water for the operating temperature of 60°C. Any point within the region comprising the upward sloping lines depicted in Fig. 13 represents an effective steady operation of the MHP, in the sense that no dryout and flooding take place. In practical situations, the temperatures at the evaporator and condenser ends can be physically measured, so that the heat transport rate and the operating temperature of the MHP can be determined

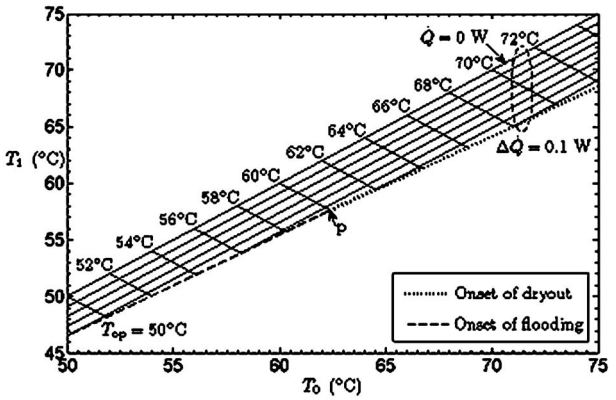

Fig. 13 A map of the relation governing the rate of heat transport $\dot{Q}$, the operating temperature T_{op}, and the temperatures at the evaporator and condenser ends, T_0 and T_1, of a copper MHP optimally charged for 60°C. The parallel lines of positive slope are lines of constant heat transport rate; those of negative slope are lines of constant operating temperature.

correspondingly from Fig. 13. For a fixed operating temperature, which can be maintained by coordinated variations of T_0 and T_1, an increase in $\dot{Q}$ requires an increase in T_0 and a decrease in T_1. However, $\dot{Q}$ cannot be increased beyond the maximum value given by the lines of onset of dryout or onset of flooding depicted in Fig. 13. Since the MHP is designed for 60°C, its operation at that temperature is limited by the simultaneous onsets of dryout and flooding represented by point P, where $\dot{Q}_{cap}=0.555$ W, $T_0=62.37$°C, and $T_1=57.63$°C. If this MHP is operated below 60°C, it will be overcharged with the working fluid [7]. In this case, the onset of flooding at the condenser end will be attained before the occurrence of dryout at the evaporator end with a value of $\dot{Q}$, which is lower than $\dot{Q}_{cap}$. We observe that this value of $\dot{Q}$ decreases with the operating temperature. On the other hand, if the MHP is operated above 60°C, it is considered to be undercharged with the working fluid [7], in which case the onset of dryout at the evaporator end will be reached before the occurrence of flooding at the condenser end with a value of $\dot{Q}$ which is higher than $\dot{Q}_{cap}$. Moreover, this value of $\dot{Q}$ increases with the operating temperature.

4 Conclusion

A mathematical model of an MHP has been developed to investigate, primarily, the thermal effects of the solid wall on the heat transport capacity. The heat transport capacity and optimal charge level of an MHP predicted in the present study would be a useful analytical tool for MHP design and performance analysis. The present investigation provides interesting insights into the thermal effects of the solid wall, which are commonly neglected in the existing literature, by comparing the models with and without a solid wall. Apart from facilitating axial solid conduction, the presence of the solid wall also affects the phase change heat transport by the working fluid, leading to an increase in the heat transport capacity of an MHP. Elaboration on the effects of the solid wall thermal conductivity on the axial solid conduction and phase change heat transport is presented by comparing MHPs with different solid wall materials. Based on the results from a variety of cases with different solid wall materials and thicknesses, it is concluded that the thermal effects of the solid wall on the heat transport capacity of an MHP can be ignored if and only if the thickness and thermal conductivity of the solid wall are both sufficiently small. The effects of the thickness and thermal conductivity of the solid wall on the axial temperature distribution of the solid wall are also examined. It is observed that the temperature is distributed more evenly over the entire length of an MHP if the thermal conductivity or thickness of the solid wall is sufficiently large. Associated with these conditions, evaporation and condensation of the working fluid also take place in the adiabatic section, especially at its outer regions, resulting in the disappearance of the lines of demarcation for the adiabatic section. Finally, a map has been constructed to relate the rate of heat transport, operating temperature, and the temperatures at the evaporator and condenser ends.

Nomenclature

A = cross-sectional area, m^2
Bi = Biot number, defined in Eq. (3)
C = constant, geometrical parameter
Ca = capillary number, defined in Eq. (26)
D_H = hydraulic diameter (m)
f = friction factor
Ga = gravity number, defined in Eq. (27)
g = gravitational acceleration (m/s^2)
h = heat transfer coefficient (W/m^2 K)
h_{fg} = latent heat of evaporation (J/kg)
K = constant
k = thermal conductivity (W/m K)
L = length of micro heat pipe (m)
M = mass of working fluid (kg)
$\hat{M}$ = charge level
$\hat{M}_{opt}$ = optimal charge level
$\dot{m}$ = mass flow rate (kg/s)
$\hat{m}$ = dimensionless mass flow rate
$\dot{m}_{ref}$ = reference mass flow rate, defined in Eq. (24) (kg/s)
N = number of corners
Nu = Nusselt number, defined in Eq. (2)
P = contact length (m)
p = pressure (N/m^2)
$\dot{Q}$ = heat transport rate (W)
$\dot{Q}_c$ = heat transport rate due to axial conduction in solid wall (W)
$\dot{Q}_{cap}$ = heat transport capacity (W)
$\dot{Q}_p$ = heat transport rate due to phase change of the working fluid (W)
$\dot{q}$ = rate of heat transfer per unit axial length
Re = Reynolds number, defined in Eq. (20)
r = meniscus radius of curvature
s = volume fraction occupied by liquid phase
T = temperature (°C)
t_s = wall thickness (m)
u = velocity (m/s)
We = Weber number, defined in Eq. (28)
w = side width of MHP
x = axial distance from evaporator end
$\hat{x}$ = dimensionless x

Greek Symbols

β = angle of inclination
γ = kinematic viscosity ratio, defined in Eq. (29)
δ = relative difference of heat transport capacity, defined in Eq. (41)
$\tilde{\delta}_c$ = fraction of error contributed by axial conduction in the wall, defined in Eq. (46)
$\tilde{\delta}_p$ = fraction of the change in the phase change heat transport rate, defined in Eq. (47)
ε = density ratio
η = coefficient as defined in Eq. (34)

Θ = quantity as defined in Eq. (7)
θ = contact angle (rad)
ϑ = solid and liquid temperature difference (°C)
λ = coefficient as defined in Eq. (5)
μ = dynamic viscosity (kg/s m)
ν = kinematic viscosity (m^2/s)
ϖ = angular parameter
ρ = density (kg/m^3)
σ = surface tension (N/m)
τ = shear stress (N/m^2)
ϕ = half corner angle (rad)

Subscripts

a = adiabatic section
c = condenser section
cl = capillary limit
e = evaporator section
fl = onset of flooding
l = liquid
lv = liquid-vapor interface
s = solid wall
sl = solid-liquid interface
sv = solid-vapor interface
v = vapor

Superscript

$*$ = without solid wall

Appendix

Several geometrical parameters are required in the governing conservation equations, such as the liquid and vapor cross-sectional area, A_l and A_v, respectively, the wall-liquid contact line length P_{sl}, the wall-vapor contact line length P_{sv}, the liquid-vapor contact line length P_{lv}, and the hydraulic diameter of the liquid phase and vapor phase, $D_{H,l}$ and $D_{H,v}$, respectively. These parameters depend on the contact angle θ and the half corner angle ϕ. Their relationships are expressed by the following equations:

$$A_l = As \tag{A1}$$

$$A_v = A(1-s) \tag{A2}$$

where A is the inside MHP cross-sectional area and s is the volume fraction occupied by the liquid phase, which can be related to the meniscus radius of curvature r by

$$s = \frac{(\varpi r)^2}{A} \tag{A3}$$

ϖ is the angular parameter defined as

$$\varpi = N^{1/2}\left[\frac{\cos\theta\cos(\phi+\theta)}{\sin\phi} + (\phi+\theta) - \frac{\pi}{2}\right]^{1/2} \tag{A4}$$

where N is the number of corners of a polygonal cross-sectioned MHP. The contact lengths between different phases are given by the following expressions:

$$P_{sl} = C_{sl}(As)^{1/2} \tag{A5}$$

$$P_{sv} = Nw - C_{sl}(As)^{1/2} \tag{A6}$$

$$P_{lv} = C_{lv}(As)^{1/2} \tag{A7}$$

where w is the width of one side of equilateral cross section. C_{sl} and C_{lv} are the geometrical constants, respectively, defined as

$$C_{sl} = \frac{2N^{1/2}}{\sin\phi}\left[\frac{\cos\theta}{\sin\phi\cos(\phi+\theta)} - \frac{\pi/2-(\phi+\theta)}{\cos^2(\phi+\theta)}\right]^{-1/2} \tag{A8}$$

$$C_{lv} = 2N^{1/2}\left[\frac{\pi}{2} - (\phi+\theta)\right]\left[\frac{\cos\theta\cos(\phi+\theta)}{\sin\phi} + (\phi+\theta) - \frac{\pi}{2}\right]^{-1/2} \tag{A9}$$

The hydraulic diameter of liquid phase, $D_{H,l}$, and the hydraulic diameter of vapor phase, $D_{H,v}$, are defined, respectively, as

$$D_{H,l} = \frac{4A_l}{P_{sl}} = \frac{4(As)^{1/2}}{C_{sl}} \tag{A10}$$

$$D_{H,v} = \frac{4A_v}{P_{sv}+P_{lv}} = \frac{4A(1-s)}{Nw + (C_{lv}-C_{sl})(As)^{1/2}} \tag{A11}$$

References

[1] Cotter, T. P., 1984, "Principles and Prospects for Micro Heat Pipes," *Proceedings of the Fifth International Heat Pipe Conference*, Tsukuba, Japan, pp. 328–335.
[2] Peterson, G. P., 1992, "Overview of Micro Heat Pipe Research and Development," Appl. Mech. Rev., **45**, pp. 175–189.
[3] Peterson, G. P., 1996, "Modeling, Fabrication, and Testing of Micro Heat Pipes," Appl. Mech. Rev., **49**, pp. S175–S183.
[4] Groll, M., Schneider, M., Sartre, V., Zaghdoudi, M. C., and Lallemand, M., 1998, "Thermal Control of Electronic Equipment by Heat Pipes," Rev. Gen. Therm., **37**, pp. 323–352.
[5] Sobhan, C. B., Rag, L. R., and Peterson, G. P., 2007, "A Review and Comparative Study of the Investigations on Micro Heat Pipes," Int. J. Energy Res., **31**, pp. 664–688.
[6] Suman, B., 2007, "Modeling, Experiment, and Fabrication of Micro-Grooved Heat Pipes: An Update," Appl. Mech. Rev., **60**, pp. 107–119.
[7] Tio, K.-K., Liu, C. Y., and Toh, K. C., 2000, "Thermal Analysis of Micro Heat Pipes Using a Porous-Medium Model," Heat Mass Transfer, **36**, pp. 21–28.
[8] Sugumar, D., and Tio, K.-K., 2006, "Thermal Analysis of Inclined Micro Heat Pipes," ASME J. Heat Transfer, **128**, pp. 198–202.
[9] Sugumar, D., and Tio, K.-K., 2009, "The Effects of Working Fluid on the Heat Transport Capacity of a Microheat Pipe," ASME J. Heat Transfer, **131**, p. 012401.
[10] Kim, S. J., Seo, J. K., and Do, K. H., 2003, "Analytical and Experimental Investigation on the Operational Characteristics and the Thermal Optimization of a Miniature Heat Pipe With a Grooved Wick Structure," Int. J. Heat Mass Transfer, **46**, pp. 2051–2063.
[11] Suman, B., and Hoda, N., 2005, "Effect of Variations in Thermophysical Properties and Design Parameters on the Performance of a V-Shaped Micro Grooved Heat Pipe," Int. J. Heat Mass Transfer, **48**, pp. 2090–2101.
[12] Do, K. H., Kim, S. J., and Garimella, S. V., 2008, "A Mathematical Model for Analyzing the Thermal Characteristics of a Flat Micro Heat Pipe with a Grooved Wick," Int. J. Heat Mass Transfer, **51**, pp. 4637–4650.
[13] Maranzana, G., Perry, I., and Maillet, D., 2004, "Mini- and Micro-Channels: Influence of Axial Conduction in the Walls," Int. J. Heat Mass Transfer, **47**, pp. 3993–4004.
[14] Babin, B. R., Peterson, G. P., and Wu, D., 1990, "Steady-State Modeling and Testing of a Micro Heat Pipe," ASME J. Heat Transfer, **112**, pp. 595–601.
[15] Bejan, A., 2004, *Convection Heat Transfer*, Wiley, Hoboken, NJ, Chap. 3.
[16] Longtin, J. P., Badran, B., and Gerner, F. M., 1994, "A One-Dimensional Model of a Micro Heat Pipe During Steady-State Operation," ASME J. Heat Transfer, **116**, pp. 709–715.
[17] Dunn, P. D., and Reay, D. A., 1994, *Heat Pipes*, Pergamon, New York.
[18] Perry, R. H., and Green, D. W., 1997, *Perry's Chemical Engineers' Handbook*, McGraw-Hill, New York.
[19] Sugumar, D., 2002, "Thermal Analysis of Micro Heat Pipes: Effects of Geometry, Type of Working Fluid, and Gravity," MS thesis, Multimedia University, Malaysia.
[20] de Gennes, P. G., 1985, "Wetting: Statics and Dynamics," Rev. Mod. Phys., **57**, pp. 827–863.
[21] Lin, L., Ponnappan, R., and Leland, J., 2002, "High Performance Miniature Heat Pipe," Int. J. Heat Mass Transfer, **45**, pp. 3131–3142.
[22] Vadakkan, U., Garimella, S. V., and Murthy, J. Y., 2004, "Transport in Flat Heat Pipes at High Heat Fluxes from Multiple Discrete Sources," ASME J. Heat Transfer, **126**, pp. 347–354.

Numerical Analysis of Convective Heat Transfer From an Elliptic Pin Fin Heat Sink With and Without Metal Foam Insert

Hamid Reza Seyf
Islamic Azad University,
Karaj Branch,
P.O. Box 31485-313,
Tehran, Karaj, 3158777878 Iran

Mohammad Layeghi
Assistant Professor
University of Tehran,
P.O. Box 31485-77871,
Tehran, Karaj, 3158777878 Iran
e-mail: mlayeghi@ut.ac.ir

A numerical analysis of forced convective heat transfer from an elliptical pin fin heat sink with and without metal foam inserts is conducted using three-dimensional conjugate heat transfer model. The pin fin heat sink model consists of six elliptical pin rows with 3 mm major diameter, 2 mm minor diameter, and 20 mm height. The Darcy–Brinkman–Forchheimer and classical Navier–Stokes equations, together with corresponding energy equations are used in the numerical analysis of flow field and heat transfer in the heat sink with and without metal foam inserts, respectively. A finite volume code with point implicit Gauss–Seidel solver in conjunction with algebraic multigrid method is used to solve the governing equations. The code is validated by comparing the numerical results with available experimental results for a pin fin heat sink without porous metal foam insert. Different metallic foams with various porosities and permeabilities are used in the numerical analysis. The effects of air flow Reynolds number and metal foam porosity and permeability on the overall Nusselt number, pressure drop, and the efficiency of heat sink are investigated. The results indicate that structural properties of metal foam insert can significantly influence on both flow and heat transfer in a pin fin heat sink. The Nusselt number is shown to increase more than 400% in some cases with a decrease in porosity and an increase in Reynolds number. However, the pressure drop increases with decreasing permeability and increasing Reynolds number. [DOI: 10.1115/1.4000951]

Keywords: heat sink, porous media, metallic foam, numerical method, finite volume

1 Introduction

Pin fin heat sinks are efficient heat transfer devices in many electric cooling applications including: CPU, transformer, and thyristor cooling. Due to the demand of many industries for systems providing higher heat dissipation per volume, a lot of research works have been done for improving performance of pin fin heat sinks. The efficiency of pin fin heat sinks can be improved by several techniques, which are purely convection based such as using larger fans; improving pin fins arrangements and shapes and increasing surface area of the heat sink. However, each of these techniques has some disadvantages and difficulties related to noise, manufacturing cost, and weight, respectively. Another effective method for heat transfer enhancement of heat sinks is using high conductive porous inserts such as metallic foams with appropriate properties and acceptable pressure drop along the heat sinks. However, there are limited researches about this topic in literature.

There are many researches on heat transfer in electronic cooling using pin fin heat sinks. A good literature review can be found in Ref. [1]. Sparrow et al. [2] studied the heat transfer performance of cylindrical fins in both staggered and inline arrangements. Sparrow and Kang [3] experimentally investigated pressure drop and heat transfer characteristics of longitudinal finned cross flow tube banks. They found that by attaching integral wake splitters at the rear of the tubes, heat transfer enhances noticeably. Constans et al. [4] carried out a theoretical and numerical study to determine a technique for optimization of a finned heat sink. In their works, heat transfer coefficients were obtained using empirical correlations. Moreover, a finite difference model was developed and an ellipsoid algorithm used for optimization. Shaukatullah et al. [5] measured the thermal performance of inline square pin fins and plate heat sinks for different fin heights, thicknesses, spacings, and angle of approaches for velocities under 5 m/s. Biber and Belady [6], Li et al. [7], and Dvinsky et al. [8] numerically studied fluid flow and heat transfer in heat sinks. Li et al. [7] investigated the flow resistance and heat transfer characteristics in rectangular ducts with staggered arrays of short elliptic pin fins. They reported higher heat transfer coefficients and smaller pressure drop in the range 44–58% for elliptic pins. Dvinsky et al. [8] found that for heat sinks with side and top clearance, up to half of the entered flow to the heat sink may leave it through the top and side. Jonsson and Moshfegh [9] experimentally characterized various plate-fin heat sinks for different dimensions and configurations allowing for variations in tip and side by-pass at different Reynolds numbers. Sara et al. [10] reported that if the angle of attack of pin fins decreases, a hot zone will be developed in front zone of pin fins and heat transfer rate increases. The computational fluid dynamics (CFD) simulations of Jonsson and Moshfegh [11] revealed the existence of a complex leakage flow from pin fins. They reported flow lost through the top, to balance inward flow from the sides. Saha and Acharya [12] numerically studied unsteady 3D flow and heat transfer in parallel-plate channel heat exchanger with periodic inline array of rectangular cylinders. The results show that when the flow become unsteady the thermal performance factor increases significantly. Kobus and Oshio [13] theoretically and experimentally studied the thermal performance of a pin fin array heat sink for pure natural convection and combined natural and forced convection. Peles et al. [14] investigated the effects of thermohydraulic and geometrical parameters on heat transfer, pressure drop, and total thermal resistance of a bank of micro pin fins. Recently, Sahiti et al. [15] numerically investigated the effect

Contributed by the Heat Transfer Division of ASME for publication in the JOURNAL OF HEAT TRANSFER. Manuscript received January 8, 2009; final manuscript received December 11, 2009; published online April 22, 2010. Assoc. Editor: Patrick H. Oosthuizen.

of pin fin cross-section on pressure drop and overall performance of pin fins arrays. Their results show that the elliptic pins offers highest heat transfer rate and lowest pressure drop for a given base area and the same energy input. Therefore, elliptic pins are more attractive than circular pins in heat sink applications. Naphon and Sookkasem [16] presented new experimental data on heat transfer characteristics of tapered cylindrical pin fin heat sinks under constant heat flux conditions for both inline and staggered arrangements. Yang et al. [17] conducted an experimental investigation of pin fin heat sinks having square, circular, and elliptic cross-sections. They reported that for the staggered arrangement by increasing fin density, the heat transfer coefficient increases for all three configurations. They also demonstrated that for a fixed pumping power and same surface area, elliptic pin fins in a staggered arrangement and circular pin fins in an inline arrangement possesses lower thermal resistance with respect to other configurations. Sahin and Demir [18] experimentally investigated the effects of various parameters on friction factor and heat transfer for a heat exchanger with square cross-section perforated pin fins. For perforating pin fins, their results show that at relatively low Reynolds numbers, decreasing interfin spacing and clearance ratios leads to an improvement in heat transfer performance.

Recently, forced convection through metallic foams has been proved to substantially enhance heat transfer rate. So, metallic foams are well suited for use in high performance compact heat exchangers and heat sinks used in electronic equipments [19]. Bastawros and co-workers [20,21] demonstrated that metal foams are good choices for heat removal in electronic cooling applications. Bastawros et al. [21] showed that a high performance cellular aluminum heat sinks such as aluminum foams have a heat removal about 2–3 times more than a pin fin array with only a moderate increase in pressure drop. Many experimental and numerical works that has been performed was aimed at application of porous media in heat transfer enhancement of heat exchangers at high Reynolds numbers [19]. Kim et al. [22] experimentally investigated the impact of porous fins on the pressure drop and heat transfer characteristics in plate-fin heat exchangers. They used six 6101 aluminum alloy foams of 10, 20, and 40 pore per inch (PPIs) with different porosities using water as the fluid. Both the friction factor and heat transfer were significantly affected by the permeability and the porosity of sample foam pins. They employed Forchheimer equation for the flow analysis and used the Darcy number, geometry, and Reynolds number to correlate the friction factor. Kim et al. [23] numerically studied the effect of anisotropy in effective conductivity and permeability on thermal performance of an aluminum-foam heat sink. Their results show that anisotropy in effective thermal conductivity and permeability changes the heat transfer rate significantly. Bhattacharya and Mahajan [24] presented experimental results on forced convection in finned metal foam heat sinks. Experiments were conducted on aluminum foams of 90% porosity with one, two, four, and six fins and two different pore sizes. They showed that when fins are incorporated in metallic foam, the heat transfer coefficient will increase up to six times the commercial finned heat sinks. Furthermore, they found that decreasing the PPI and increasing the number of fins will lead to heat transfer enhancement at a constant given pressure drop.

Kim et al. [25] conducted an experimental study to investigate heat transfer characteristics of an aluminum-foam heat sink. They found that employing aluminum-foam heat sink with low pore density will lead to lower thermal resistance and overall mass of electronic cooling device. Tadrist et al. [26] investigated the use of aluminum foams with porosities in the range of $\varepsilon > 0.9$ for compact heat exchangers. They determined the permeability and inertia coefficient experimentally. Hernández [27] experimentally investigated the flow and heat transfer in various metal foam heat sinks. Experimental data were compared with two available commercial heat sinks with various fin densities. The results show that metal foam heat sinks have lower thermal resistance and at a given operation point, the metal foam heat sinks perform better than conventional heat sinks. Mahdi et al. [28] experimentally made some comparisons between performance of CPU heat exchangers and aluminum-foam heat exchangers in natural convection using an industrial setup. Their results show that aluminum-foam CPU heat exchangers reduce the thermal resistance (more than 70%) and the overall weight. Shih et al. [29] studied the effect of height on the cooling performance of aluminum-foam heat sinks under the impinging-jet flow condition. They reported that by decreasing height to diameter ratio of aluminum-foam heat sinks from 0.92 to 0.15, the Nusselt number first increases and then decreases. Furthermore, by decreasing pore density and porosity, the Nusselt number increases and convective heat transfer enhances. Recently, Layeghi [30] numerically studied forced convective heat transfer from a staggered tube bundle with various low conductivity wooden porous media inserts at maximum Reynolds numbers 100 and 300. He showed that inserting wooden porous media between the tubes can increase heat transfer. Also, high conductivity porous media are very effective for heat transfer enhancement.

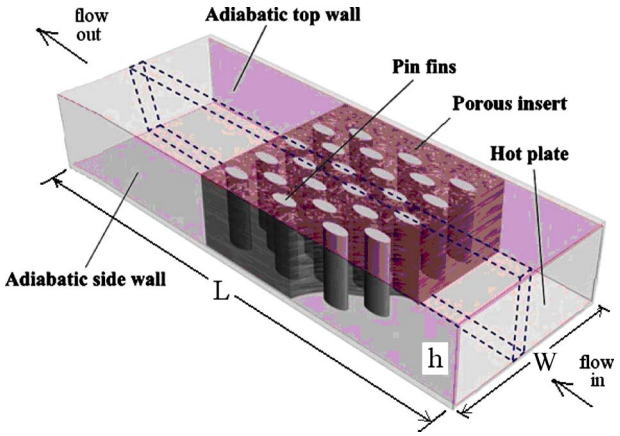

Fig. 1 Schematic of the elliptic pin fin heat sink

A complete 3D numerical analysis of elliptical pin fin heat sinks with metal foam inserts in laminar regime has not been accomplished so far. In this study, a numerical investigation has been performed to determine flow and heat transfer characteristics of elliptical pin fin heat sinks with and without metal foam inserts. The effects of metallic foam properties at various Reynolds numbers are studied numerically. It is shown that using metal foam inserts between void spaces of elliptic pin fin heat sinks causes both pressure drop and heat transfer increase. Therefore, careful attention is needed for the selection of metallic foam. It must have good heat transfer characteristics and acceptable pressure drop. In this study, more than 400% increase in the Nusselt number has been observed in some cases at high Reynolds numbers.

2 Governing Equations

Two sets of governing equations are used for the study of fluid flow and heat transfer around an elliptic pin fin heat sink with and without metal foam insert (Fig. 1). For Reynolds numbers less than 1000, Zukauskas [31] observed that fluid flow around a tube bank can be considered to be dominantly laminar.

The incompressible, laminar, steady state fluid flow and heat transfer around pin fins without metal foam insert is described by the classical Navier–Stokes equations, together with the mass conservation, and corresponding energy equation (Fig. 2).

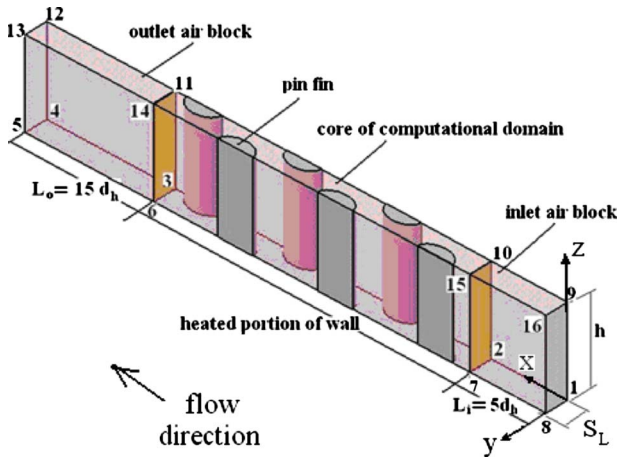

Fig. 2 Schematic of the computational domain, coordinate system, and boundary conditions

These equations are as follows.

Continuity

$$\nabla \cdot \boldsymbol{V} = 0 \tag{1}$$

Momentum equations:

$$\rho\left(\frac{\partial \boldsymbol{V}}{\partial t} + \boldsymbol{V} \cdot \nabla \boldsymbol{V}\right) = -\nabla p + \mu \nabla^2 \boldsymbol{V} \tag{2}$$

Energy

$$\rho c_p\left(\frac{\partial T}{\partial t} + \boldsymbol{V} \cdot \nabla T\right) = k\nabla^2 T + \mu\Phi \tag{3}$$

where in Eqs. (1)–(3), $\boldsymbol{V}=(u,v,w)$ is the flow velocity vector. p and T are flow pressure and temperature, respectively. c_p, ρ, and μ and k are specific heat at constant pressure, density, viscosity of the fluid, and thermal conductivity, respectively. Φ is dissipation function and it represents the time rate at which energy is being dissipated per unit volume through the action of viscosity. For an incompressible flow it is written as follows:

$$\Phi = \left\{2\left[\left(\frac{\partial u}{\partial x}\right)^2 + \left(\frac{\partial v}{\partial y}\right)^2 + \left(\frac{\partial w}{\partial z}\right)^2\right] + \left(\frac{\partial u}{\partial y} + \frac{\partial v}{\partial x}\right)^2 + \left(\frac{\partial v}{\partial z} + \frac{\partial w}{\partial y}\right)^2 + \left(\frac{\partial w}{\partial x} + \frac{\partial u}{\partial z}\right)^2\right\} \tag{4}$$

The steady state, laminar, and incompressible fluid flow and heat transfer in metal foam insert between fins by the assumption of isotropic saturated porous medium with constant properties and in local thermal equilibrium condition can be written as follows.

continuity

$$\nabla \cdot \boldsymbol{V} = 0 \tag{5}$$

momentum equations

$$\rho_f\left[\frac{1}{\varepsilon}\frac{\partial \boldsymbol{V}}{\partial t} + \frac{1}{\varepsilon}\nabla\left(\frac{\boldsymbol{V}\cdot\boldsymbol{V}}{\varepsilon}\right)\right] = -\nabla p + \frac{\mu}{\varepsilon\rho_f}\nabla^2\boldsymbol{V} - \frac{\mu}{K}\boldsymbol{V} - \frac{c_F\rho_f}{K^{1/2}}|\boldsymbol{V}|\boldsymbol{V} \tag{6}$$

energy equation

$$(\rho c)_m\frac{\partial T}{\partial t} + \rho_f c_p \boldsymbol{V}\cdot\boldsymbol{\nabla} T = \left[(k_{\text{eff}} + k_{D,x})\frac{\partial^2 T}{\partial x^2} + (k_{\text{eff}} + k_{D,y})\frac{\partial^2 T}{\partial y^2} + (k_{\text{eff}} + k_{D,z})\frac{\partial^2 T}{\partial z^2}\right] \tag{7}$$

where in Eqs. (5)–(7), $\boldsymbol{V}=(u,v,w)$ is the Darcy velocity vector and (u,v,w) are the Darcy velocity components, c_F the is dimensionless form-drag constant, T is the temperature, and p is the static pressure. Here, we assume $c_F=0.1$, which is an average value for many types of foams. ε and K are porosity and permeability of the porous medium, respectively. k_{eff} is the effective thermal conductivity of the porous medium. It is volume average of fluid and solid media conductivities, $k_{\text{eff}}=\varepsilon k_f+(1-\varepsilon)k_s$. Indices f and s refer to fluid and solid parts of the porous medium, respectively. $(\rho c)_m=(1-\varepsilon)(\rho c)_s+\varepsilon(\rho c_p)_f$ and $k_{D,x}$, $k_{D,y}$, and $k_{D,z}$ are the longitudinal and transverse thermal dispersion conductivities in x, y, and z directions, respectively. At high pore Reynolds numbers in nearly parallel flows, they can be correlated as a linear function of Peclet number. Since the porous medium assumed to be isotropic, $k_{D,x}=k_{D,y}=k_{D,z}=k_D$, the thermal dispersion can then be obtained by following equation

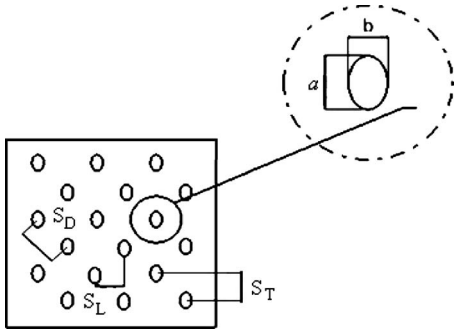

Fig. 3 Geometry and pin fin configuration of the problem

$$\frac{k_D}{k_f} = c_F \text{Pe}_m = \frac{c_T U_m d_p}{\alpha_f} \tag{8}$$

where in the above equation Pe_m is the Peclet number based on pore diameter d_p and mean velocity U_m. The coefficient c_T depends on porous medium structure and distance from solid walls. $\alpha_f=k_f/(\rho c_p)_f$ is the thermal diffusivity of the fluid.

For conjugate heat transfer from pin fins, each set of above equations should be solved together with solid energy equation for pins, which is

$$\nabla^2 T_s = 0 \tag{9}$$

where index s denotes the solid region of pin fin heat sinks.

3 Computational Domain and Boundary Conditions

The computational domain consists of pins defined as solid and surrounding fluid shown in Figs. 1 and 2. It has a height of h (equal to pin length), flow length L, and width S_L.

The inlet and outlet boundaries are placed upstream and downstream nearly 5 and 15 times the hydraulic diameter of the pin cross-section, respectively.

The elliptical pin fins with major diameter ($a=3$ mm), minor diameter ($b=2$ mm), and a height of 20 mm have been made by aluminum alloy ($\rho_{\text{Al}}=2719$ kg/m^3, $c_{\text{Al}}=871$ J/kg K, and $k_{\text{Al}}=237$ W/m K). The staggered arrangement is in form of an equilateral triangle with $S_T/b=1.25$, $S_L/a=1.75$, and $S_D/b=2.9$ where S_D, S_T, and S_L are the diagonal, transverse, and longitudinal distances between center of adjacent pin fins, respectively. Figure 3 shows the detail configuration of pin fins.

In order to investigate the physical characteristics of the heat transfer and fluid flow through pin fins, a combination of inlet, outlet, wall, and symmetry boundary conditions are applied in computational domain.

The channel and elliptical pin fin surfaces are treated as no-slip boundary conditions. Constant temperature boundary condition is applied on the heated wall ($T_w=343$ K) whereas the top wall is insulated. At the inlet, constant temperature ($T_{\text{in}}=293$ K) and a uniform profile are prescribed for velocity. At the outlet, the static

Table 1 boundary conditions for the computational domain (Fig. 2)

Boundary condition	u	v	w	T
Inlet (1-8-16-9) ($x=0$)	U_{in}	0	0	T_{in}
Inlet block(1-2-7-8), outlet block (3-4-5-6) ($z=0$)	0	0	0	$\partial T/\partial z=0$
Heated wall (2-3-6-7) ($z=0$)	0	0	0	T_w
Top wall (9-12-13-16) ($z=h$)	0	0	0	$\partial T/\partial z=0$
Symmetry (1-4-12-9) ($y=0$)	$\partial u/\partial y=0$	0	$\partial w/\partial y=0$	$\partial T/\partial y=0$
Symmetry (8-5-13-16) ($y=S_T$)	$\partial u/\partial y=0$	0	$\partial w/\partial y=0$	$\partial T/\partial y=0$
Outlet (4-12-13-15) ($x=L$)	$\partial u/\partial x=0$	$\partial v/\partial x=0$	$\partial w/\partial x=0$	$\partial T/\partial x=0$

pressure is fixed and the remaining flow variables are extrapolated from interior of computational domain. The same energy equation is used for both fluid as well as solid domain with higher conductivity and zero velocity within the elliptic pin fins. Since a conservative scheme is employed and the gird distribution tailored such that mesh boundaries lie along the edges of the pin fins, the energy conservation is satisfied automatically across the solid interface. The appropriate boundary conditions for the solution domain shown in Fig. 2 are given in Table 1.

4 Numerical Solution

Equations (1)–(3) and (5)–(7) are solved separately using a finite volume code based on collocated grid system. Figure 4 shows grid around pin fins. The grid consists of tetrahedral cells around pin fins and hexahedral cells in the upstream and downstream regions.

The governing equations (1)–(3) and (5)–(7) are integrated in each mesh cell and resulting integrals approximated using multidimensional linear reconstruction approach [32]. Numerical schemes used to obtain discretized equations are listed in Table 2.

Based on the finite volume approach, the SIMPLE [35] algorithm is employed to deal with the problem of velocity and pressure coupling and Rhie–Chow [36] interpolation technique is used to interpolate velocity components in discretized continuity equation.

Table 2 Numerical schemes used to obtain discretized equations

Transport equation term	Numerical scheme
Diffusive	Second-order centered [32]
Convective	QUICK [33]
Source	Midpoint rule integration [34]

Table 3 Properties and dimensions of heat sink used in code verification

No. of pins (N)	25	
Major diameter of pins (a)	3	mm
Minor diameter of pins (b)	2	mm
Height of pins (h)	20	mm
Longitudinal pitch	5.34	mm
Transverse pitch	11	mm
Triangular pitch	7.67	mm
Area of base plate	45×45 mm^2	
Thermal conductivity of Al	170 W m^{-1} K^{-1}	
Applied heat flux to the base plate	12,345.67 W m^{-2}	

For each Reynolds number and each porous medium, the calculations were performed with three different meshes; the sizes of grids were 111,280, 319,594, and 999,897. The results of Nusselt number and pressure drop were compared for all three meshes. It was found that a grid with 999,897 cells is sufficient to accurately predict the basic characteristics of flow and heat transfer with and without metal foam inserts.

To ensure the validity of numerical analysis, our numerical code must be validated. Unfortunately, there was not any experimental data in literature related to study of pin fin heat sinks with porous metal foam inserts. Therefore, the numerical code was validated against the experimental results of Yang et al. [17] for an elliptical pin fin heat sink without porous inserts with total number

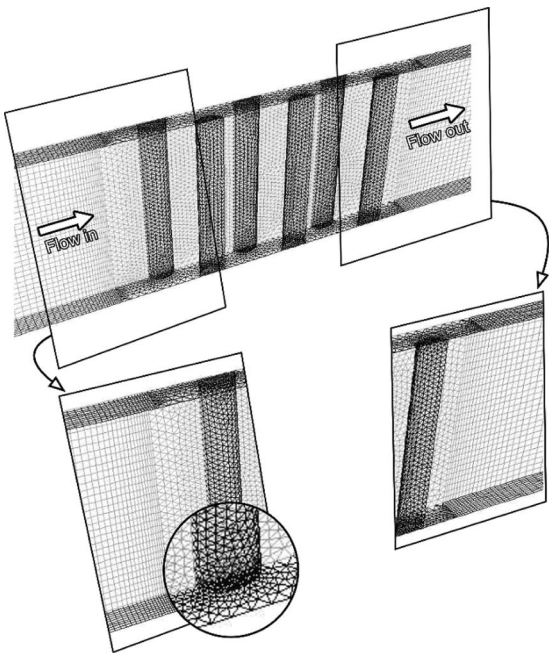

Fig. 4 computational grid around pin fins with details of inlet and outlet air blocks

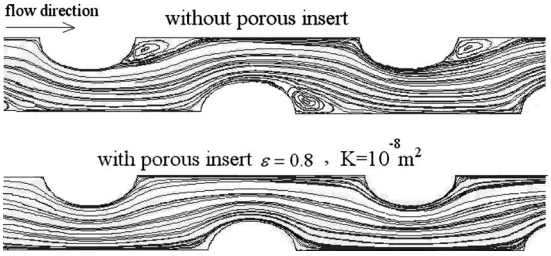

Fig. 5 Streamlines around pin fins with or without metal foam insert in the plane $z=10$ mm at Re=380

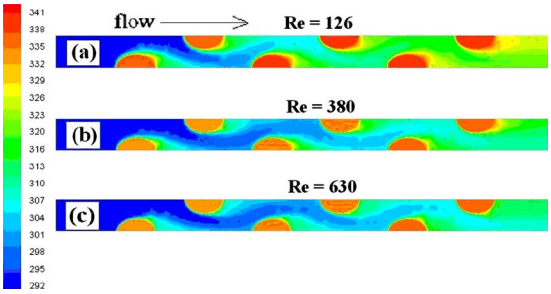

Fig. 6 The temperature contours around pin fins without metal foam insert at three different Reynolds numbers in the plane $z=10$ mm and Pr=0.71

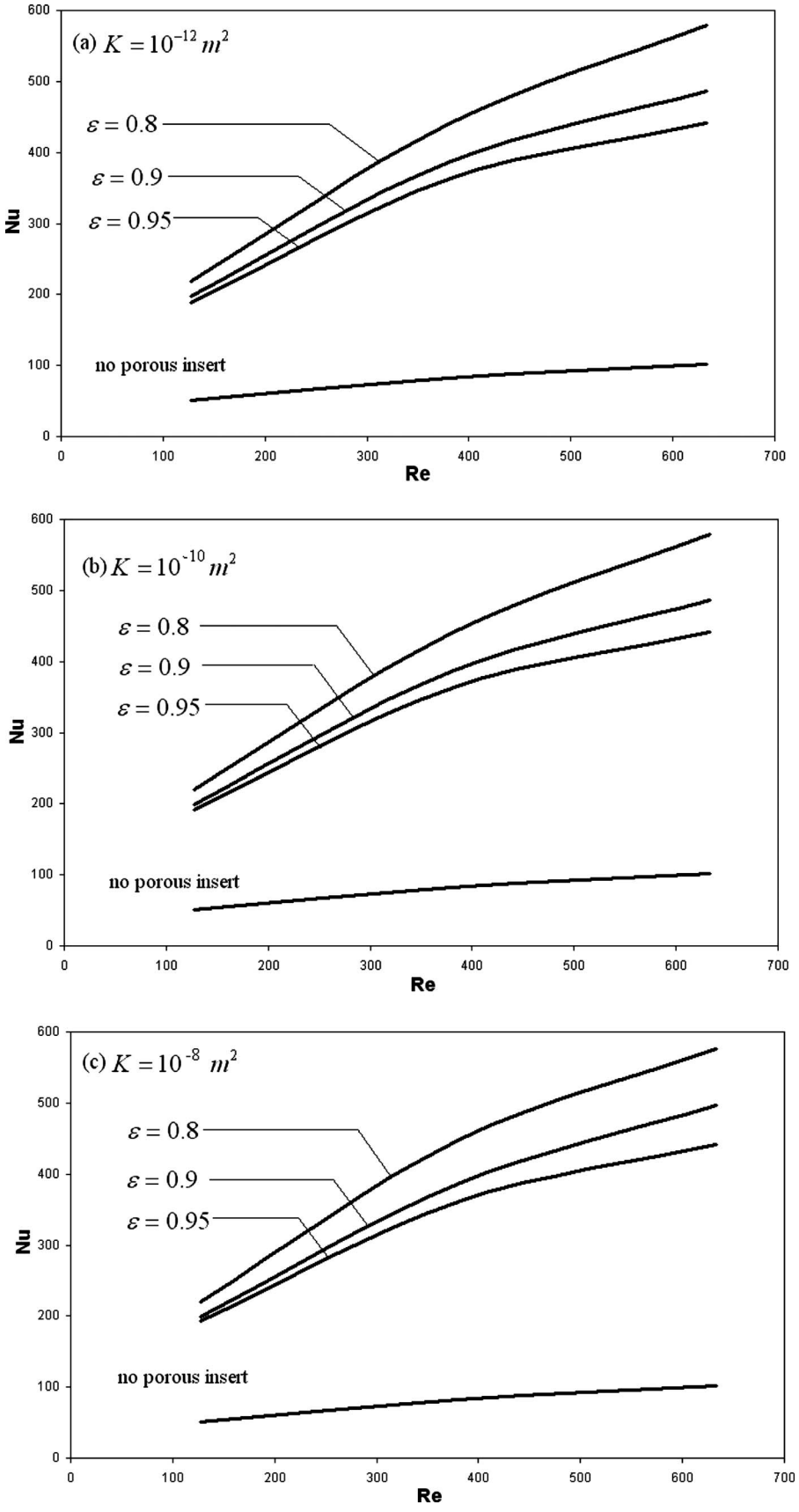

Fig. 7 Effect of porosity on the overall Nusselt number of the pin fin heat sink Pr=0.7

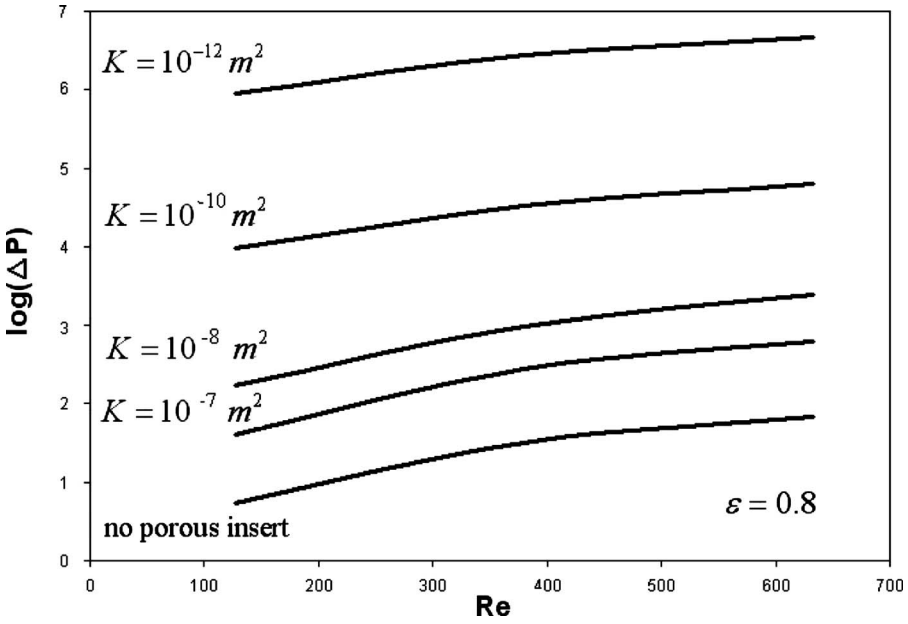

Fig. 8 Effect of permeability on pressure drop (in Pa) at various Reynolds numbers

of 25 pins. Table 3 shows the properties and dimensions of the heat sink used in the code validation. The maximum deviation between experimental and numerical data for Nusselt number and pressure drop were observed 19% and 15%, respectively.

The numerical solution is considered to be converged at an iteration in which the summation of absolute values of relative errors reduces four to five orders of magnitude. The relative error (RE) in numerical procedure is defined as

$$\mathrm{RE} = \sum_{\text{cells}} \left| \frac{\varphi^{n+1} - \varphi^{n}}{\varphi^{n}} \right|; \quad \varphi = u, v, w, T \tag{10}$$

where superscript n refers to the previous iteration. The overall energy and mass balance are checked as a second criterion for convergence, as well.

5 Results and Discussion

Numerical analysis consists of four parts in a range of Reynolds numbers 126 to 630. First, the streamlines and temperature contours are compared at three different Reynolds numbers. After that, the effect of porosity and permeability on the overall Nusselt number of pin fin heat sink is studied. Then, the effect of porosity and permeability on overall pressure drop is investigated. Finally, the effect of porosity and permeability on the efficiency of pin fin heat sink with metal foam insert is studied.

In this study, the temperature field and streamlines are three-dimensional, so these parameters are presented in a plane normal to z-axis. Figure 5 shows the streamlines around the second, third, and fourth pins in the plane $z = 10$ mm (pin half height) with or without metal foam insert.

It can be seen that in the presence of metal foam insert, the recirculation zones behind pins will be very smaller than the cases without metal foam insert. The streamlines in the other cases with metal foam insert have the same shape, as well. The investigation of the streamlines in the other cases shows that the separation of boundary layer takes place at different angle of attack depending on Reynolds number and structural properties of metal foam insert. It can also be seen that the fluid flow becomes fully developed soon after the second row for both cases with or without metal foam insert.

The temperature contours around pin fins without metal foam insert at three Reynolds numbers can be seen in Fig. 6.

It can be seen that temperature distribution changes with increasing Reynolds number. As the Reynolds number increases, the thermal boundary layer thickness on the pins decreases. However, the heat transfer from pin rows increases. Similar behavior can be seen for a pin fin heat sink with metal foam insert.

For the results presented in this paper, the validity of criteria given by Kim and Jang [37] for the local thermal equilibrium condition has been checked for cases with metal foam insert. Since the Reynolds and Prandtl numbers are not very high, this assumption was found to be valid for all cases with metal foam insert.

The heat transfer coefficient of pins in the array is calculated using the following equation:

$$h_{\text{pin}} = \frac{\dfrac{1}{A_{\text{pin}}} \displaystyle\int_{A_{\text{pin}}} \dot{q}_{\text{pin}} dA_{\text{pin}}}{\Delta T_{lm,\text{pin}}} \tag{11}$$

where A_{pin} and $\dot{q}_{\text{pin}}$ denote the area of the pin in contact with the fluid (wetted area) and the local heat flux from pin fins to the air, respectively. $\Delta T_{lm,\text{pin}}$ is the logarithmic temperature difference between the pins and the air and can be expressed as

$$\Delta T_{lm,\text{pin}} = \frac{(T_{\text{fp}} - T_{\text{in}}) - (T_{\text{lp}} - T_{\text{out}})}{\ln\left(\dfrac{T_{\text{fp}} - T_{\text{in}}}{T_{\text{lp}} - T_{\text{out}}}\right)} \tag{12}$$

where T_{fp}, T_{lp}, T_{in}, and T_{out} are the mean temperatures of the first pin wall, the temperature of the last pin wall, and the inlet and outlet bulk fluid temperatures, respectively. The heat transfer coefficient of the unpinned area is calculated by equation given below.

$$h_{\text{up}} = \frac{\dfrac{1}{A_{\text{uf}}} \displaystyle\int_{A_{\text{uf}}} \dot{q}_{\text{up}} dA_{\text{uf}}}{\Delta T_{lm}} \tag{13}$$

All parameters in Eq. (13) are similar to the parameters in Eq. (11) except the logarithmic temperature difference ΔT_{lm}, which is defined as

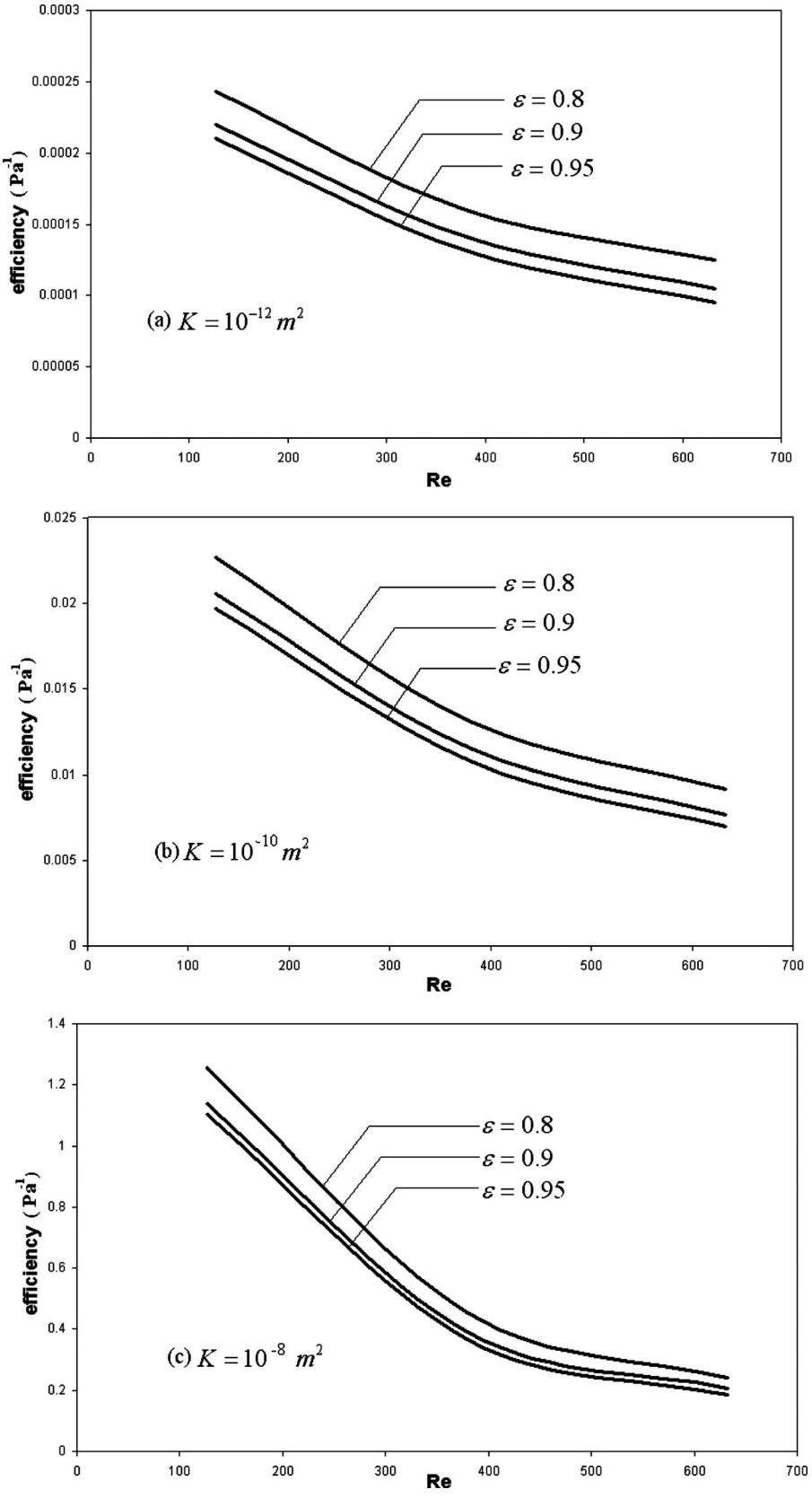

Fig. 9 Effect of porosity on the efficiency of the pin fin heat sink Pr=0.7

$$\Delta T_{lm} = \frac{(T_w - T_{\text{in}}) - (T_w - T_{\text{out}})}{\ln\left(\frac{T_w - T_{\text{in}}}{T_w - T_{\text{out}}}\right)} \tag{14}$$

where T_w is the wall temperature and the outlet and inlet bulk fluid temperatures are the temperatures at the end and beginning of the heated wall portion (Fig. 2).

The overall heat transfer coefficient of the pin array h_a can be calculated as

$$h_a = \frac{\frac{1}{A_b}\int_{A_b} \dot{q}_b dA_b}{\Delta T_{lm}} \tag{15}$$

where A_b is the area from where the heat comes in. Finally, the overall Nusselt number Nu of the pin fin heat sink is defined as follows:

$$\text{Nu} = \frac{h_a d_h}{k_f} \tag{16}$$

where d_h and k_f are the hydraulic diameter of the pin cross-section and fluid thermal conductivity, respectively.

The inlet bulk temperature is considered constant for all models (293 K), whereas the outlet bulk temperature is calculated from the following equation:

$$T_{\text{out}} = \frac{\int_{A_{\text{out}}} uTdA_{\text{out}}}{\int_{A_{\text{out}}} udA_{\text{out}}} \tag{17}$$

where A_{out} represents the outlet cross-section of the flow domain and u is the velocity in the flow direction.

Figure 7 shows the effect of porosity on the overall Nusselt number of the pin fin heat sink. It can be seen that Nusselt number for pin fin heat sinks with metal foam insert is higher than pin fin heat sink without metal foam insert. This is due to the effect of porous media in increasing heat transfer surface area and convection from the pin fins. It can also be seen that Nusselt number increases by decreasing the porosity of the metal foam insert.

The effect of permeability on pressure drop is shown in Fig. 8. It can be seen that pressure drop decreases by increasing permeability. This is due to the effect of porous insert, which limits the fluid flow movements between the pin fins.

For the performance assessment of the investigated pin fin heat sink with porous insert, the overall efficiency of the pin fin heat sink with porous insert is defined as

$$\text{efficiency} = \frac{\text{Nu}}{\Delta p} \tag{18}$$

where Δp is the total pressure drop along the heat sink. This parameter seems to be a reasonable one since metal foam insert usually increases both the pressure drop along the pin fin heat sink and total heat transfer from it. The best metal foam insert is one that provides maximum efficiency.

Figure 9 shows the effect of porosity on the efficiency of the pin fin heat sink for three permeabilities: $K=10^{-12}$ m^2, 10^{-10} m^2, and 10^{-8} m^2. It can be seen in Figs. 9(*a*)–9(*c*) that for each permeability, the efficiency increases by decreasing porosity from 0.95 to 0.8 and Reynolds number from 630 to 126. However, the best efficiency curve in Fig. 9 is obtained for $K=10^{-8}$ m^2. A comparison of results shows that the maximum thermal efficiency occurs at Re=126 for $\varepsilon=0.8$ and $K=10^{-7}$ m^2.

6 Conclusion

A numerical analysis of forced convective heat transfer from an elliptical pin fin heat sink with and without metal foam inserts has been conducted using three-dimensional conjugate heat transfer model. The pin fin heat sink model consists of six elliptical pin rows with 3 mm major diameter, 2 mm minor diameter, and 20 mm height. The Darcy–Brinkman–Forchheimer and classical Navier–Stokes equations and corresponding energy equations have been used in the numerical analysis of flow field and heat transfer in the heat sink with and without metal foam inserts, respectively. A finite volume code with point implicit Gauss–Seidel solver in conjunction with algebraic multigrid method has been used to solve the governing equations. The code has been validated thoroughly with published results for elliptical pin fin heat sinks without porous metal foam inserts. Different metallic foams with various porosities and permeabilities have been used in the numerical analysis. The effects of air flow Reynolds number and metal foam porosity and permeability on the overall Nusselt number, pressure drop, and the efficiency of heat sink have been investigated. Based on the results of the present study, the following conclusions can be drawn.

1. The heat transfer enhancement factors, Nu for the pin fin heat sink with metal foam inserts are higher than the pin fin heat sink without metal foam inserts for all investigated cases. This means that the use of metal foam inserts leads to an advantage of basis heat transfer enhancement.
2. The total Nusselt number increases with decreasing porosity of metal foam insert and the total pressure drop increases with decreasing permeability. Therefore, careful attention is needed in selecting appropriate metal foam inserts to obtain best efficiency.
3. Enhancement in efficiency increases with decreasing Reynolds number from 630 to 126. This means that metal foam inserts are more effective at lower Reynolds numbers.
4. The most important parameters affecting the heat transfer from the pin fin heat sink are Reynolds number and metal foam porosity and permeability. The maximum heat transfer rate observed at Re=630 for $\varepsilon=0.8$, which was about 400% more than that for a pin fin heat sink without metal foam insert. Also, the maximum thermal efficiency observed at Re=126 for $\varepsilon=0.8$ and $K=10^{-7}$ m^2

Nomenclature

A = area
a = major diameter of elliptical pin
b = minor diameter of elliptical pin
c_F = dimensionless form-drag constant
c_p = heat capacity of fluid at constant pressure
c_s = heat capacity of solid part of porous media at constant pressure
c_{AL} = heat capacity of aluminum at constant pressure
c_T = thermal dispersion constant
d_p = pore diameter
d_h = hydraulic diameter of the pin cross-section
h = heat sink height
h_a = overall heat transfer coefficient of the pin array
K = permeability of metallic foam
k = thermal conductivity
L = length of heat sink
Nu = pin array Nusselt number
P = pressure
Pe_m = Peclet number ($=\rho U_m d_p/\mu$)
Pr = Prandtl number ($=\mu c_p/k_f$)
$\dot{q}$ = heat flux
Re = Reynolds number ($=\rho U_{\text{in}} a/\mu$)
S = distance between pins
T = temperature
t = time
U_m = mean velocity in metallic foam
u = fluid velocity, Darcy velocity in x direction

$\boldsymbol{V}$ = velocity vector
v = fluid velocity, Darcy velocity in y direction
w = fluid velocity, Darcy velocity in z direction
W = width of heat sink
x = coordinate in x direction
y = coordinate in y direction
z = coordinate in z direction

Greek Symbols

α = thermal diffusivity
ε = porosity
μ = viscosity
Φ = viscous dissipation
ρ = density

Subscripts

b = base area
D = dispersion
eff = effective
f = fluid
in = inlet
L = longitudinal
Al = aluminum
out = outlet
s = solid
T = transverse
w = wall
x = in x direction
y = in y direction
z = in z direction

References

[1] Khan, W. A., 2004, "Modeling of Fluid Flow and Heat Transfer for Optimization of Pin Fin Heat Sinks," Ph.D. thesis, Department of Mechanical Engineering, Faculty of Engineering, Waterloo, ON, Canada.

[2] Sparrow, E. M., Ramsey, J. W., and Altemani, C. A. C., 1980, "Experiments on Inline Pin Fin Arrays and Performance Comparison With Staggered Arrays," ASME J. Heat Transfer, **102**, pp. 44–50.

[3] Sparrow, E. M., and Kang, S. S., 1985, "Longitudinally Finned Cross Flow Tube Banks and Their Heat Transfer and Pressure Drop Characteristics," Int. J. Heat Mass Transfer, **28**, pp. 339–350.

[4] Constans, E. W., Belegundu, A. D., and Kulkarni, A. K., 1994, "Optimization of a Pin Fin Sink: a Design Tool," CAFJCAD Application to Electronic Packaging, ASME EEP-Vol. 9, pp. 25–32.

[5] Shaukatullah, H., Storr, W. R., Hansen, B. J., and Gaynes, M. A., 1996, "Design and Optimization of Pin Fin Heat Sinks for Low Velocity Applications," *Proceedings of the 12th IEEE SEMI-THERM Symposium*, Austin, TX, pp. 151–163.

[6] Biber, C. R., and Belady, C. L., 1997, "Pressure Drop Predictions for Heat Sinks: What is the Best Method?" Advances in Electronic Packaging, ASME EEP-Vol. 19-2, pp. 1829–1835.

[7] Li, Q., Chen, Zh., Flechtner, U., and Warnecke, H. J., 1998, "Heat Transfer and Pressure Drop Characteristics in Rectangular Channels With Elliptic Pin Fins," Int. J. Heat Fluid Flow, **19**, pp. 245–250.

[8] Dvinsky, A., Bar-Cohen, A., and Strelets, M., 2000,"Thermofluid Analysis of Staggered and Inline Pin Fin Heat Sinks," *Proceedings of the Seventh IEEE Inter Society Conference on Thermal Phenomena (ITHERM)*, Las Vegas, NV, pp. 157–164.

[9] Jonsson, H., and Moshfegh, B., 2001, "Modeling of the Thermal and Hydraulic Performance of Plate Fin, Strip Fin, and Pin Fin Heat Sinks–Influence of Flow By-Pass," IEEE Trans. Compon. Packag. Technol., **24**, pp. 142–149.

[10] Sara, O. N., Pekdemir, T., Yapici, S., and Yilmaz, M., 2001, "Heat Transfer Enhancement in a Channel With Perforated Rectangular Blocks," Int. J. Heat Fluid Flow, **22**, pp. 509–518.

[11] Jonsson, H., and Moshfegh, B., 2002, "Enhancement of the Cooling Performance of Circular Pin Fin Heat Sinks Under Bypass Conditions," *Proceedings of the Eighth IEEE Inter Society Conference on Thermal Phenomena (ITHERM)*, San Diego, CA, pp. 425–432.

[12] Saha, A. K., and Acharya, S., 2003, "Parametric Study of Unsteady Flow and Heat Transfer in a Pin Fin Heat Exchanger," Int. J. Heat Mass Transfer, **46**, pp. 3815–3830.

[13] Kobus, C. J., and Oshio, T., 2005, "Development of a Theoretical Model for Predicting the Thermal Performance Characteristics of a Vertical Pin Fin Array Heat Sink Under Combined Forced and Natural Convection With Impinging Flow," Int. J. Heat Mass Transfer, **48**, pp. 1053–1063.

[14] Peles, Y., Kosar, A., Mishra, C., Kuo, C. J., and Schneider, B., 2005, "Forced Convective Heat Transfer Across a Pin Fin Micro Heat Sink," Int. J. Heat Mass Transfer, **48**, pp. 3615–3627.

[15] Sahiti, N., Lemouedda, A., Stojkovic, D., Durst, F., and Franz, E., 2006, "Performance Comparison of Pin Fin In-Duct Flow Arrays With Various Pin Cross Section," Appl. Therm. Eng., **26**, pp. 1176–1192.

[16] Naphon, P., and Sookkasem, A., 2007, "Investigation on Heat Transfer Characteristics of Tapered Cylinder Pin Fin Heat Sinks," Energy Convers. Manage., **48**, pp. 2671–2679.

[17] Yang, K. S., Chu, W. H., Chen, I. Y., and Wang, C. C., 2007, "A Comparative Study of the Airside Performance of Heat Sinks Having Pin Fin Configurations," Int. J. Heat Mass Transfer, **50**, pp. 4661–4667.

[18] Sahin, B., and Demir, A., 2008, "Performance Analysis of a Heat Exchanger Having Perforated Square Fins," Appl. Therm. Eng., **28**, pp. 621–632.

[19] Nield, D. A., and Bejan, A., 1992, *Convection in Porous Media*, 2nd ed., Springer, New York.

[20] Bastawros, A. F., 1998, "Effectiveness of Open-Cell Metallic Foams for High Power Electronic Cooling," ASME, New York, Vol. HTD-361-3/PID-3, pp. 211–217.

[21] Bastawros, A. F., Evans, A. G., and Stone, H. A., 1998, "Evaluation of Cellular Metal Heat Transfer Media," Harvard University Report No. MECH 325, Cambridge, MA.

[22] Kim, S. Y., Paek, J. W., and Kang, B. H., 2000, "Flow and Heat Transfer Correlations for Porous Fin in a Plate-Fin Heat Exchangers," ASME J. Heat Transfer, **122**, pp. 572–578.

[23] Kim, S. Y., Koo, J. M., and Kuznetsov, A. V., 2001, "Effect of Anisotropy in Permeability and Effective Thermal Conductivity on Thermal Performance of an Al-Foam Heat Sink," Numer. Heat Transfer, Part A, **40**(1), pp. 21–36.

[24] Bhattacharya, A., and Mahajan, R. L., 2002, "Finned Metal Foam Heat Sinks for Electronic Cooling in Forced Convection," ASME J. Electron. Packag., **124**(3), pp. 155–163.

[25] Kim, S. Y., Paek, J. W., and Kang, B. H., 2003, "Thermal Performance of Aluminum-Foam Heat Sinks by Forced Air Cooling," IEEE Trans. Compon. Packag. Technol., **26**(1), pp. 262–267.

[26] Tadrist, L., Miscevic, M., Rahli, O., and Topin, F., 2004, "About the Use of Fibrous Materials in Compact Heat Exchangers," Exp. Therm. Fluid Sci., **28**, pp. 193–199.

[27] Hernández, A. R. A., 2005, "Combined Flow and Heat Transfer Characterization of Open Cell Aluminum Foams," M.S. thesis, University of Puerto Rico, Mayagüez Campus.

[28] Mahdi, H., Lopez, P., Fuentes, A. A., and Jones, R., 2006, "Thermal Performance of Aluminum-Foam CPU Heat Exchangers," Int. J. Energy Res., **30**, pp. 851–860.

[29] Shih, W. H., Chiu, W. C., and Hsieh, W. H., 2006, "Height Effect on Heat Transfer Characteristics of Aluminum-Foam Heat Sinks," ASME J. Heat Transfer, **128**(6), pp. 530–537.

[30] Layeghi, M., 2008, "Numerical Analysis of Wooden Porous Media Effects on Heat Transfer From a Staggered Tube Bundle," ASME J. Heat Transfer, **130**(1), p. 014501.

[31] Zukauskas, A., 1987, "Heat Transfer From Tubes in Crossflow," *Advances in Heat Transfer*, J. P. Hartnett and Th. F. Irvine, eds., Academic, New York, Vol. 18.

[32] Barth, T. J., and Jesperson, D., 1989, "The Design and Application of Upwind Schemes on Unstructured Meshes," AIAA Paper No. 89-0366.

[33] Leonard, B. P., 1995, "Order of Accuracy of Quick and Related Convection–Diffusion Schemes," Appl. Math. Model., **19**, pp. 640.

[34] Mathur, S., and Murthy, J. Y., 1997, "A Pressure Based Method for Unstructured Meshes," Numer. Heat Transfer, Part B, **31**(2), pp. 195–215.

[35] Van Doormall, J. P., and Raithby, G. D., 1984, "Enhancements of the Simple Method for Predicting Incompressible Fluid Flow," Numer. Heat Transfer, Part A, **7**, pp. 147–163.

[36] Rhie, C. M., and Chow, W. L., 1983, "Numerical Study of Turbulent Flow Past and Airfoil With Trailing Edge Separation," AIAA J., **21**(11), pp. 1525–1532.

[37] Kim, S. J., and Jang, S. P., 2002, "Effects of the Darcy Number, Prandtl Number, and the Reynolds Number on Local Thermal Non-Equilibrium," Int. J. Heat Mass Transfer, **45**, pp. 3885–3896.

Proper Orthogonal Decomposition for Reduced Order Thermal Modeling of Air Cooled Data Centers

Emad Samadiani
e-mail: samadiani@gatech.edu

Yogendra Joshi
e-mail: yogendra.joshi@me.gatech.edu

G.W. Woodruff School of Mechanical Engineering,
Georgia Institute of Technology,
Atlanta, GA 30332

Computational fluid dynamics/heat transfer (CFD/HT) methods are too time consuming and costly to examine the effect of multiple design variables on the system thermal performance, especially for systems with multiple components and interacting physical phenomena. In this paper, a proper orthogonal decomposition (POD) based reduced order thermal modeling approach is presented for complex convective systems. The basic POD technique is used with energy balance equations, and heat flux and/or surface temperature matching to generate a computationally efficient thermal model in terms of the system design variables. The effectiveness of the presented approach is studied through application to an air-cooled data center cell with a floor area of 23.2 m^2 and a total power dissipation of 240 kW, with multiple turbulent convective components and five design variables. The method results in average temperature rise prediction error of 1.24°C (4.9%) for different sets of design variables, while it is ~150 times faster than CFD/HT simulation. Also, the effects of the number of available algebraic equations and retained POD modes on the accuracy of the obtained thermal field are studied.
[DOI: 10.1115/1.4000978]

Keywords: proper orthogonal decomposition, reduced order thermal modeling, data center

1 Introduction

Computational fluid dynamics/heat transfer (CFD/HT) is currently used to simulate convective transport in geometrically complex systems with multiple components. However, full-field methods are too time consuming and costly to examine the effect of multiple design parameters on the system thermal performance, especially for systems with multiple components and interacting physical phenomena. In this regard, compact or reduced models, which could run significantly faster than CFD/HT models with sufficient fidelity, are essential.

A representative example of a turbulent convective system with multiple components in need of reduced modeling is a data center. Data centers, as shown in Fig. 1, are computing infrastructure facilities that house arrays of electronic racks containing high power dissipation data processing and storage equipment whose temperatures must be maintained within allowable limits. The typical approach currently used for thermal management of data centers utilizes computer room air-conditioning (CRAC or AC) units that deliver cold air to the racks arranged in alternate cold/hot aisles through perforated tiles placed over an under-floor plenum, see Fig. 2. Aside from CFD/HT, simulation methods based on machine learning to predict the air temperature at discrete points, such as server inlets/outlets for a new heat load distribution among the data center racks, have been explored [1–6]. They simulate the effects of the system parameters on the temperature field in the data center based on some heuristic approaches. However, optimal thermal design of data centers with different configurations and thermal characteristics is possible only if a deterministic and rapid modeling of the temperature field is available in terms of the involved system parameters. Nie and Joshi [7] presented a reduced order modeling approach for steady turbulent convection in systems with connected domains and illustrated its application to an electronic rack. They suggested developing proper orthogonal decomposition (POD)-flux matching based reduced order model for each component separately and then combining the developed models using flow network modeling, standard SIMPLE algorithm, and boundary profile matching. Their method is only applicable for systems consisting of a series of nested subdomains [7].

In this paper, a POD based reduced order thermal modeling approach is presented to predict the effect of the involved parameters on the temperature field in complex systems, assuming the same POD temperature equation for the entire domain. A complex system here means a system consisting of multiple convective components. The physical phenomena in different components can interact internally and do not need to happen in a specific order. The key features of this paper include the following:

- using the basic POD technique with simple energy balance equations, heat flux matching [8], and/or surface temperature matching for temperature field generation
- conducting an explicit study on the effects of the retained POD modes and available thermal information on the accuracy of the POD based thermal field
- illustrating the approach to predict the temperature field within an entire operational air-cooled data center in terms of the involved design variables based on observations from the minimum required thermal sensors

In Sec. 2, the basic POD technique and its enhancement to simulate the temperature field in complex thermal-fluid systems are explained. In Sec. 3, the method is applied to an air-cooled data center cell with five design variables. The accuracy and computational speed of the POD generated temperature field for different test cases and scenarios are examined through comparison with CFD/HT results. The effects of the quantity of the input

Contributed by the Heat Transfer Division of ASME for publication in the JOURNAL OF HEAT TRANSFER. Manuscript received July 28, 2009; final manuscript received December 1, 2009; published online April 29, 2010. Assoc. Editor: Giulio Lorenzini.

Fig. 1 Data center and its multiscale nature

thermal information and number of components in the system on the POD based predictions are studied as well. Finally, the approach and results are reviewed in Sec. 4.

2 Reduced Order Thermal Modeling of Complex Systems

In Sec. 2.1, the basic POD technique is explained briefly, while more details can be found in Refs. [8–11]. Also, some recent modification on the basic POD technique for flow/thermal modeling can be found in Refs. [12–14]. In Sec. 2.2, enhancements to the POD based method to simulate the temperature field in complex systems are explained.

2.1 Proper Orthogonal Decomposition. The POD, also known as the Karhunen–Loeve decomposition, is a model reduction technique that expands a set of data on empirically determined basis functions for modal decomposition [8,10]. It can be used to numerically predict the temperature field more rapidly than full-field simulations. The temperature field is expanded into basis functions or POD modes:

$$T = T_0 + \sum_{i=1}^{m} b_i \psi_i \tag{1}$$

The POD has several properties that make it well suited for turbulent flows. First, the empirical determination of the basis functions makes this method well suited for nonlinear problems. Second, it captures more of the dominant dynamics for a given number of modes than any other linear decomposition [10]. Also, it has been shown experimentally that low-dimensional models using POD can well address the role of coherent structures in turbulence generation [10]. The general algorithm to generate a POD based reduced order thermal modeling in a system is illustrated in Fig. 3 and is explained in the following.

(a) Observation generation. In the first step, the design variables of the system are changed n times, and the temperature field for the entire domain is obtained by CFD/HT simulations, or detailed experimental measurements for each case. These thermal fields are called observations or snapshots. The reference field T_0 in Eq. (1) is typically calculated as the average of the observations.

(b) POD mode, ψ_i, calculation. The POD modes of a thermal system, ψ_i, can be calculated from observations. In Eq. (1), m is the number of retained POD modes in the decomposition, which can be 1 up to $n-1$, where n is the number of observations. Using the method of snapshots, each POD mode can be expressed as a linear combination of the linearly independent observations [10]:

$$\psi_i = \sum_{k=1}^{n} a_k (T_{\text{obs},k} - T_0) \tag{2}$$

where T_{obs} is a matrix of which each column, $T_{\text{obs},i}$, includes a complete temperature field data from an observation. An element of the reference temperature field, T_0, in Eqs. (1) and (2) is usually considered as the average of the all observed data for a field point. The weight coefficients, a_k, in Eq. (2) are obtained by solving the following n^*n eigenvalue problem:

$$\sum_{k=1}^{n} R(i,k) a_k = \lambda a_i, \quad i = 1, \ldots, n \tag{3}$$

where $R = (T_{\text{obs}} - T_0)^* \otimes (T_{\text{obs}} - T_0)/n$ [8–11]. For a given set of observations, n eigenvalues, λ_i, and their relevant eigenvectors are obtained from Eq. (3). Each eigenvector includes the weight coefficients, a_k, of the relative POD mode in Eq. (2), so n POD modes are finally calculated. The energy captured by each POD mode in the system is proportional to the relevant eigenvalue. The eigenvalues are sorted in a descending order, so the first POD modes in Eq. (1) capture larger energy compared with the later modes.

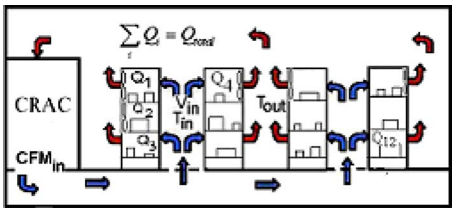

Fig. 2 Typical air-cooling system in data centers

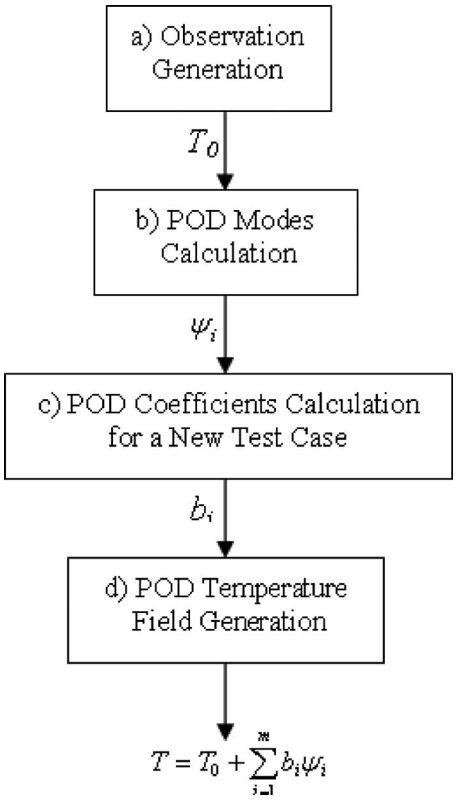

Fig. 3 General algorithm for POD temperature field generation

(c) POD coefficients, b_i, calculation for a new test case. This key step is where the POD can be used to create a reduced order thermal/fluid model as a function of the system design variables. Generally, there are three methods to calculate the POD coefficients b_i for a new test case with a new set of design variables.

(1) Galerkin projection of the system POD modes onto the governing equations. This results in a set of coupled nonlinear ordinary differential equations (ODEs) in time for transient systems, or a set of algebraic equations for steady state systems, to be solved for the POD coefficients. This method has been used to create reduced order models of transient temperature fields in terms of mostly one parameter such as Reynolds/Raleigh number [15–23]. The previous investigations have been either for prototypical flows (such as flow around a cylinder) or for simple geometries, such as channel flow where inhomogeneous boundary conditions are easily homogenized by the inclusion of a source function in the decomposition. Recently, POD has been used for development of transient reduced order modeling of air-cooled rooms [24]. Assuming a known velocity field, the transient 2D energy equation has been solved through POD method and Galerkin projection in terms of the air inlet temperature from the air-conditioning unit [24]. In the present paper, we are interested in developing a steady state thermal model for complex systems with several components in terms of multiple parameters without a need to the velocity field.

(2) Interpolation among modal coefficients. In steady state, the POD coefficients at a new set of design variables can be obtained by an interpolation between the weight coefficients at the observed variables to match a desired new variable value [22,25]. However, this method has been applied only for a system with one parameter and simple geometry such as the cavity flow [22,25]. Higher order multidimensional interpolation would be required to model more complex systems.

(3) Flux matching process. In the flux matching process [8,11], the coefficients b_i are obtained by applying Eq. (1) to some locally specified region, such as system boundaries to match the known mass or heat fluxes. Although the flux matching process has been used to develop reduced order models of the flow behavior in complex steady state systems successfully [7,9,11,26,27], it has been applied only for thermal modeling of a simple geometry of a channel with two isoheat flux blocks [7,8,27], with no consideration of complex 3D geometry.

(d) POD temperature field generation. With calculated T_0, ψ_i, and b_i for a new set of design variables, the corresponding temperature field for the test case can be generated inside the entire domain from Eq. (1) for different numbers of used POD modes, m.

2.2 POD Based Method for Thermal Modeling in Complex Systems. In this paper, the flux matching process in step (c) of the basic POD algorithm is enhanced to obtain a set of algebraic equations for complex 3D steady state systems with multiple convective components. Here, the algebraic equations are obtained simply through energy balance, heat flux matching [8], and/or surface temperature matching for all convective components of the complex system. Finally, all equations are subsequently solved together using the least-squares approach to obtain a single set of POD coefficients, assuming the same POD temperature equation for the entire domain. This method is explained in the following.

Having obtained the observations for the system, the eigenvalue problem in Eq. (3) is solved and POD modes for the entire domain are calculated through Eq. (2). Then, appropriate algebraic equations are obtained to calculate the POD coefficients by focusing on the key convective phenomena at each component or subsystem of the main system. These components are illustrated in Fig. 4. For case (a) in Fig. 4, the fluid temperature at a specific surface of the domain is kept at a known constant value of T_{const}. From Eq. (1), we get

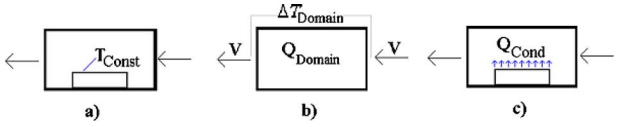

Fig. 4 Convective components in a complex system

$$T_{\text{const}} = \overline{T_0} + \sum_{i=1}^{m} b_i \overline{\psi}_{i,\text{surf}} \tag{4}$$

where $\overline{\psi}_{i,\text{surf}}$ and $\overline{T_0}$ are the average values of the temperature POD modes and temperature reference on the surface with a constant temperature. We get one algebraic equation for each constant temperature surface of the domain.

For components like case (b) in Fig. 4, one equation is obtained to satisfy the conservation of the energy across the domain. Applying the total energy balance across the inlet and outlet surfaces of the domain results in

$$Q_{\text{domain}} = \rho V A c_p \Delta T_{\text{domain}} \tag{5}$$

By separating the known and unknown variables and substituting Eq. (1) into Eq. (5), we obtain

$$\frac{Q_{\text{domain}}}{VA\rho c_p} = \Delta T_{\text{domain}} = \overline{T}_{0,\text{domain outlet}} - \overline{T}_{0,\text{domain inlet}} + \sum_{i=1}^{m} b_i (\overline{\psi}_{i,\text{domain outlet}} - \overline{\psi}_{i,\text{domain inlet}}) \tag{6}$$

where $\overline{\psi}_{i,\text{domain inlet}}$ and $\overline{\psi}_{i,\text{domain outlet}}$ are the average values of the temperature POD modes on the inlet and outlet surfaces of the domain of case (b) in Fig. 4, respectively. Also, $\overline{T}_{0,\text{domain inlet}}$ and $\overline{T}_{0,\text{domain outlet}}$ are the average values of the reference temperature, T_0, on the inlet and outlet surfaces of the domain, respectively. Sometimes, especially if the method is used for thermal modeling of real-world systems, the inlet velocity and/or heat load in case (b) of Fig. 4 is not known, but the temperature difference across the domain is measured and known instead. In this case, Eq. (6) can be still used to find the appropriate POD coefficients associated with the measured temperature difference.

For components like case (c) in Fig. 4, one equation is obtained by matching the heat flux at the surface with a constant heat flux.

$$q''_{\text{cond}} = -k \left. \frac{\partial T}{\partial n} \right|_{\text{wall}} \tag{7}$$

Since the flux function involves a gradient, substituting the POD temperature of Eq. (1) into Eq. (7) may produce large errors. To address this issue, a modal heat conduction function, $F_{i,\text{modal cond}}$, is defined in the POD space. All m modal heat conduction functions can be calculated together by [8]

$$F_{\text{modal cond}} = Q_{\text{cond obs}} \otimes (T_{\text{obs}} - T_0)^+ \otimes \psi \tag{8}$$

where $Q_{\text{cond obs}}$, a $1 \times m$ matrix, includes m observation surface heat inputs and $(\cdot)+$ is the Moore–Penrose pseudo-inverse giving the least-squares solution. This definition results in the following algebraic equation for this case [8]:

$$Q_{\text{cond}} = \sum_{i=1}^{m} b_i F_{i,\text{modal cond}} \tag{9}$$

After the algebraic equations have been obtained for all components of the system, they are solved together to find the associated POD coefficients for a new set of design variables. With calculated T_0, ψ_i, and b_i, the corresponding temperature field for the test case can be generated inside the entire domain from Eq. (1) for different numbers of used POD modes, m.

We should note that the number of obtained algebraic equations, s, can be less, equal to, or larger than the number of available POD modes, $n-1$. As mentioned before, n is the number of observations. Since we need at least the same number of equations as the number of unknown POD coefficients to avoid an underdetermined system of equations, the maximum possible number of POD modes to use, m in Eq. (1), is limited by the number of available equations N_{equation}, in addition to the number of available modes $n-1$. Accordingly, m can be 1 up to $N_{\text{max mode}}=\min(n-1, N_{\text{equations}})$ in this method. On the other hand, the number of available equations is limited by the number of convective components $N_{\text{components}}$ and available thermal information N_{info} for the components in the system. In fact, $N_{\text{equations}}$ is always equal to N_{info}, while N_{info} cannot be larger than $N_{\text{components}}$. This brings a limitation to the presented method whose effect on the results for a data center cell is studied in Secs. 3.3 and 3.4. While this limitation exists in the flux matching process [8] as well, it has not been explicitly studied in the previous applications of the POD method [7–9,11,26,27]. In Sec. 3, the method outlined above is applied to an air-cooled data center cell.

3 Illustration of Thermal Modeling Approach: A Data Center Example

The POD based method outlined in Sec. 2.2 is applied to an air-cooled data center cell with multiple convective components to simulate the temperature field as a function of CRAC unit air delivery velocity and rack heat loads. In Sec. 3.1, a case study with five design variables is defined. The accuracy and computational speed of the presented method in simulating the temperature field for different sets of design variables are examined in Sec. 3.2 through comparison with fine-mesh, full-domain CFD/HT results. The effects of the quantity of the known thermal information and number of components in the system on the POD solution are studied in Secs. 3.3 and 3.4, respectively.

3.1 Case Study Definition. The data center cell consists of 4 CRAC units and 32 electronic racks arranged symmetrically in four rows with cold-hot aisle configuration. Each CRAC unit takes in hot return air from the room and discharges cold air into a subfloor plenum for delivery to the data center through perforated tiles. Each rack is filled by six servers, each ~333 mm tall. To obtain the required observations for the POD algorithm, one-fourth of the representative data center and the plenum are simulated using the CFD/HT code, FLUENT v. 6.1. Turbulent flow and heat transfer are simulated assuming the k-ε model. The coefficients used are $C_{1\varepsilon}=1.44$, $C_{2\varepsilon}=1.92$, $C_{\mu}=0.09$, $\sigma_k=1$, $\sigma_{\varepsilon}=1.3$, and $\text{Pr}_t=0.85$. The geometry and model of this section of the data center is shown in Fig. 5. The height of the racks and CRAC unit are 2 m and the plenum is 0.86 m high. The air pressure drop through perforated flow tiles is modeled as a porous jump boundary condition. The tiles are assumed to be 20% open and 0.035 m thick with the relative pressure drop coefficient obtained from Fried and Idelchik [28]. Each server is modeled as a uniform volumetric heat source (Q'''_{server}) with a representative fan at its exit and a lumped pressure jump at its inlet, as shown in Fig. 5. The walls of all 48 servers are modeled as adiabatic surfaces. The CRAC unit is modeled with a constant inlet and exit velocity, discharging the cooling air into the plenum at 15°C. Also, the return air to the CRAC is assumed to be at a higher temperature, calculated through overall energy balance between the rack heat loads and the cooling air.

A mesh with 431,120 grid cells when compared with a 334,972 grid-cell mesh leads to only 0.35% change in the maximum temperature. The change for the 334,972 grid-cell mesh compared with a coarser mesh containing 182,000 grid cells was 23%. Therefore, the mesh with 431,120 grid cells is considered fine enough and used here for CFD/HT generation of observations.

To construct a POD based reduced order model of the temperature field, the rack heat loads and CRAC air flow rate are considered to change between 500 W and 30 kW and 1 m^3/s (2128 CFM) and 16.2 m^3/s (34,500 CFM), respectively. To reduce the number of design variables for illustration purposes, we assume that all six servers housed in a specific rack have the same heat load. Also, corresponding racks in each column are assumed to have the same heat load. This leads to five design variables for the case study of Fig. 5:

1. inlet air velocity of CRAC unit, V_{in}
2. heat load of racks A1 and B1, Q_1
3. heat load of racks A2 and B2, Q_2
4. heat load of racks A3 and B3, Q_3
5. heat load of racks A4 and B4, Q_4

3.2 POD Temperature Field for the Case Study. The method explained in Sec. 2.2 is followed to predict the temperature field for the case study. The CRAC velocity and rack heat loads are varied to generate 21 observed temperature fields throughout the data center cell. The design variables for these observations are collected in Table 1. The rack inlet air temperature is usually used for thermal design of data centers, with ASHRAE requiring that this be kept below 32°C [29]. The contours of the average of all 21 observations, T_0 in Eq. (1), at the inlets of racks A1–A4 and B1–B4 of the case study in Fig. 5 are shown in Figs. 6(*a*) and 6(*b*), respectively. It is seen that the dominant hot spots for the data center cell occur at the middle and top of the first rack. All 20 POD modes for the data center cell are calculated through Eqs. (3) and (2). As mentioned in Sec. 2.1, the energy captured by each POD mode in the system is proportional to the relevant eigenvalue in Eq. (3). The energy percentage captured by each POD mode is plotted versus the mode number in Fig. 7. The magnitude of the eigenvalue and the energy captured by each mode decreases sharply with the index of POD modes. The modes with largest eigenvalues take the shape of large scale smooth structures, e.g., see Fig. 8(*a*). The modes with large index numbers include small scale structures, such as the temperature boundary layer, e.g., Fig. 8(*b*). Figure 8 shows the contours of the first and last POD mode at the inlet surfaces of racks A1–A4 of the case study.

To obtain the appropriate algebraic equations to calculate the POD coefficients for a test case with new design variables, Eq. (6) associated with case (b) in Fig. 4 is applied to each server in the data center. As mentioned following Eq. (6), heat load and inlet air velocity for each server need to be known to obtain the POD coefficients and finally the temperature field for the new test case. Alternatively, as mentioned before, the temperature difference across each server for the new test case can be measured and used in Eq. (6), which is more practical in an operational data center. In this study, we use the temperature differences obtained by CFD/HT solution to verify the presented algorithm. In Sec. 3.3, the effect of the number of known temperature differences across servers on the predicted temperature field is discussed. Having applied Eq. (6) to all servers, N_{servers} equations are obtained; N_{servers} is 48 here. Similarly, the energy balance equation, Eq. (6), is applied for the CRAC unit with known total heat load of the data center and CRAC inlet velocity for the new test case. Also, the temperature field at the perforated tile surfaces is kept fixed at the known constant air discharge temperature by applying Eq. (5) for case (a) in Fig. 4. Ultimately, $(N_{\text{servers}}+1+1=50)$ equations are obtained to solve for 20 POD mode coefficients. All the obtained equations are solved together using least-squares approach to

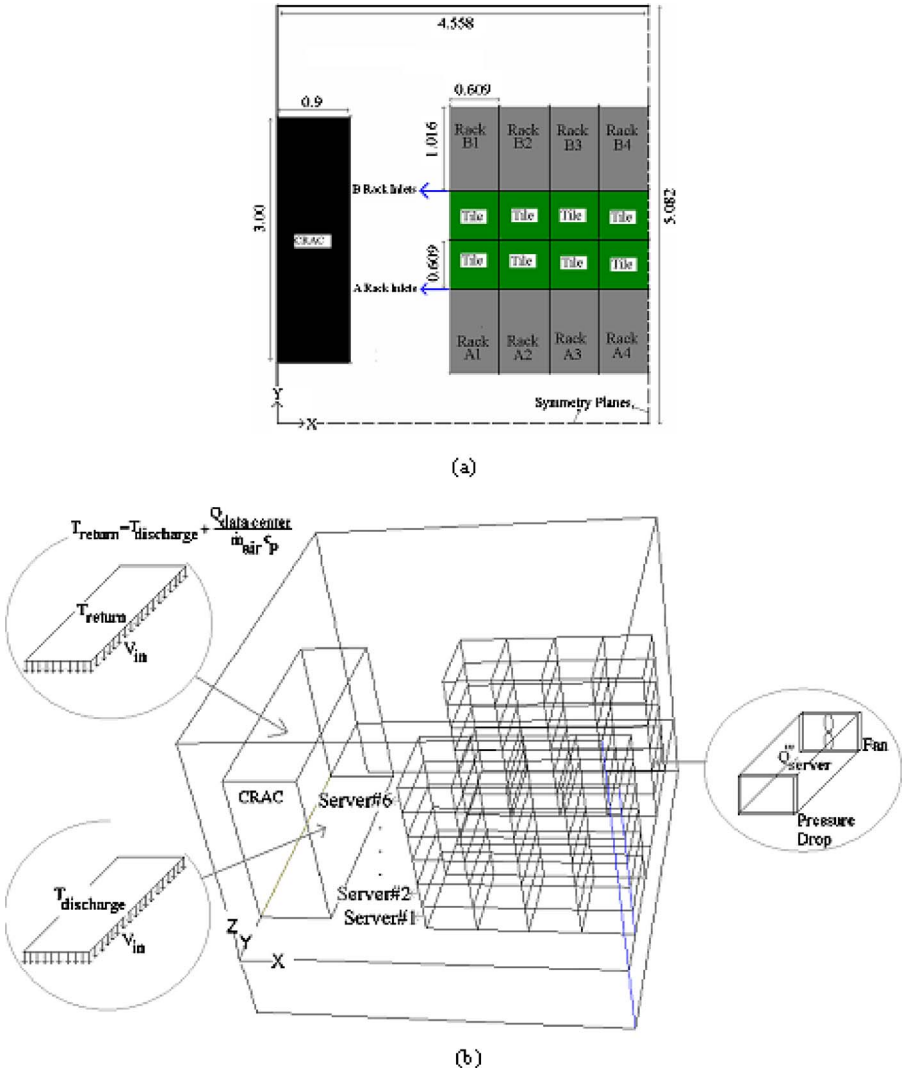

Fig. 5 Data center cell in the case study. (*a*) Top view: Dimensions are in m. (*b*) 3D model.

obtain a single set of POD coefficients for a new set of design variables.

POD coefficients associated with different modes, b_i, are shown in Fig. 9 for four arbitrary test cases, which are distinct from the observations. These coefficients have been obtained when all 20 modes are retained in the POD reconstruction in Eq. (1). It is seen that the value of POD coefficients decreases for modes with higher index and lower energy content. Also, the last mode coefficients are almost zero. So, the first few terms in the decomposition of Eq. (1) are dominant. Also, the changes in the POD coefficients after using approximately 10 modes are much less than the coefficient changes in the initial part of the graph in Fig. 9. It seems that the solution has been converged after approximately 10 modes.

To study the convergence of the solution with the number of used POD modes, the solution is first examined at the CRAC unit, perforated tile, and servers' boundaries, where the algebraic equations were obtained for. The effect of the number of retained POD modes in Eq. (1) on the error in the energy conservation at the system boundaries is shown in Fig. 10 for the four test cases. The differences between the right and left hand side terms in Eq. (5) for the perforated tile, and Eq. (6) for the 48 servers and one

Table 1 Design variables for the observations

	Observation No.																				
	1	2	3	4	5	6	7	8	9	10	11	12	13	14	15	16	17	18	19	20	21
V_{in}(m/s)	0.4	0.6	0.8	1	1.2	1.4	1.6	1.9	2.1	2.4	2.6	3	3.25	3.5	3.75	4	4.25	4.5	5	5.5	6
Q_1(kW)	1	2	4	5	7	6	11	4	12	30	21	17	4	14	15	10	10	21	21	29	20
Q_2(kW)	1	3	3	5	4	7	11	10	8	5	11	6	7	22	16	15	10	16	21	28	20
Q_3(kW)	1	2	1	5	8	8	11	12	19	5	7	22	10	20	16	20	30	27	21	16	25
Q_4(kW)	1	1	5	5	9	9	11	16	9	20	6	20	8	14	25	30	30	23	21	26	25

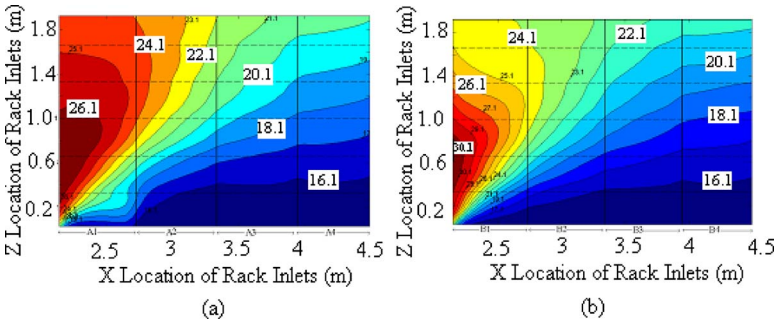

Fig. 6 Reference air temperature contours (°C) at the racks inlets: (*a*) racks A1–A4 and (*b*) racks B1–B4

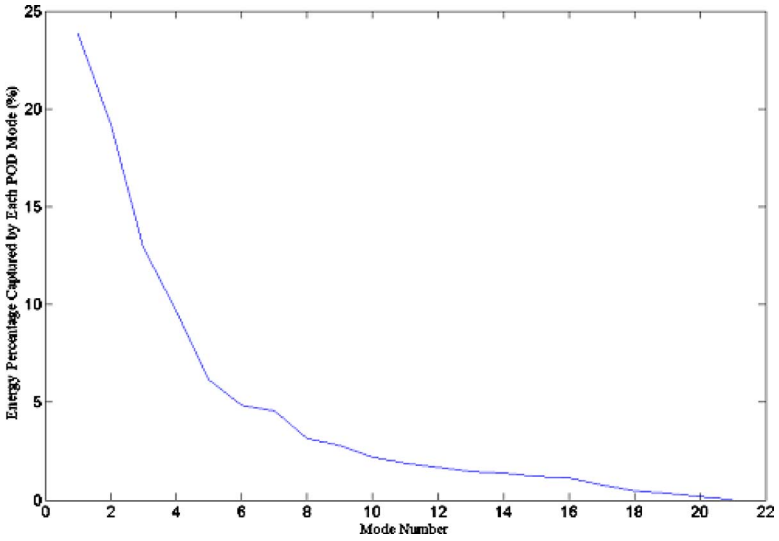

Fig. 7 Energy percentage (%) captured by each POD mode for the case study

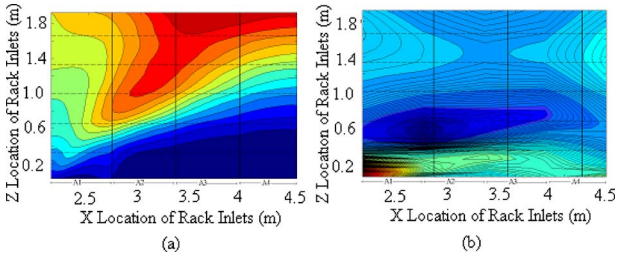

Fig. 8 Structures of the first and last POD mode at the inlets: (*a*) mode 1 and (*b*) mode 20

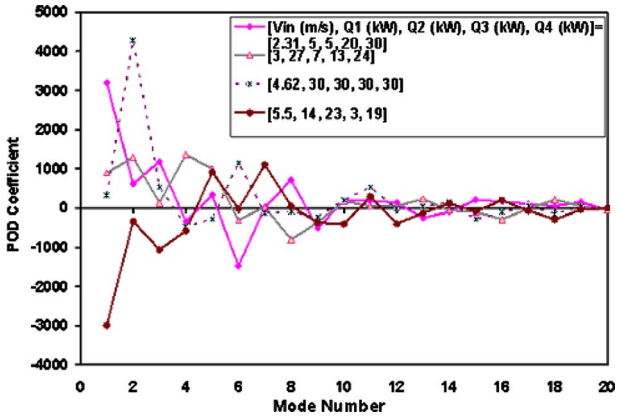

Fig. 9 POD coefficients of the associated modes for four test cases when all 20 modes are used in the POD reconstruction

CRAC unit, are calculated for each number of used modes. The average of these discrepancies is shown in Fig. 10 versus the number of used modes. It is seen that after approximately seven modes, the error becomes almost zero and adding more modes to the POD reconstruction does not have any effect on the energy conservation at the system boundaries. This is interesting considering that the available equations to satisfy, 50, is significantly larger than the number of modes and unknown POD coefficients. It shows that only seven POD modes are enough to satisfy all 50 energy conservation equations at the boundaries. However, the convergence of the POD solution at local points throughout the data center is more important.

To study the convergence of the obtained local temperatures with the mode numbers and also to examine the fidelity of the POD method, the POD temperatures are compared with full CFD/HT simulations. A mean error, $\overline{T}_{\text{error}}(x,y,z)$ (°C), is calculated by taking an average of the absolute values of the temperature difference between POD and full numerical predictions for all points:

$$T_{\text{error}}(x,y,z) = \left|T_{\text{POD}}(x,y,z) - T_{\text{Fluent}}(x,y,z)\right| \tag{10}$$

$$\overline{T}_{\text{error}}(x,y,z) = \frac{\sum_{i=1}^{N_{\text{nodes}}} T_{\text{error}}(x,y,z)}{N_{\text{nodes}}} \tag{11}$$

where N_{nodes} is the number of nodes/points in the domain, 431,120 for the data center cell in Fig. 5. The mean error is plotted for the

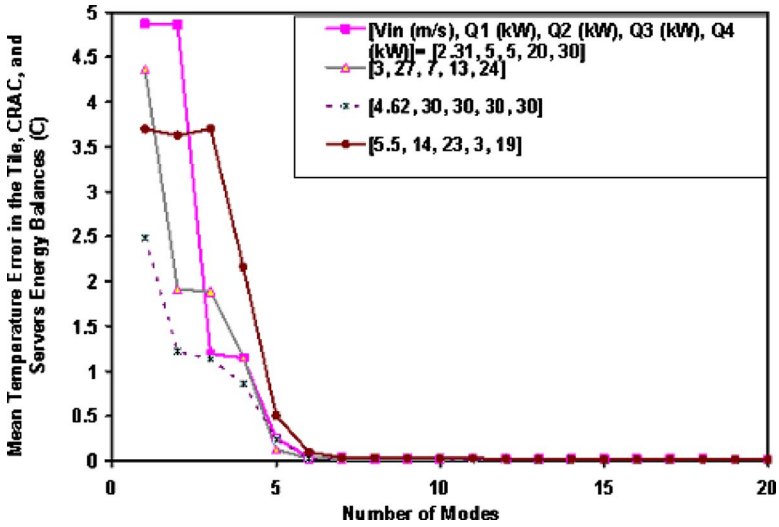

Fig. 10 Effect of the number of retained POD modes on the error (°C) in the energy conservation in the component boundaries of the data center cell for four test cases

four test case cases in Fig. 11 when the number of used POD modes changes from 1 to 20. Comparing Fig. 11 with Fig. 10 shows that while the temperature difference across the system components has converged after approximately seven modes, the local temperatures need approximately three additional modes to converge for the same test case. As shown in Fig. 11, the local temperatures converge after approximately ten modes. This is consistent with the relative flattening in the POD coefficient changes after approximately ten modes in Fig. 9, as discussed above. Also, the converged mean error for the entire domain for these cases is less than 1.4°C or 7.2%, as seen in Fig. 11.

To see if the POD method can predict the air temperatures at the rack inlets accurately for use in design decisions, the full-field predictions, POD simulations, and the POD temperature error are shown in Fig. 12 for racks A1–A4 for two test cases. The average error is less than 1.5°C, while the maximum local error is ~2.5°C for some small regions. Considering that the uncertainty in deployed sensor measurements can be around 1°C, the POD based method can be used effectively in solving data center thermal design problems. The mean error, the standard deviation in the error, and the mean relative error of the POD temperature field at all 431,120 points of the domain for six test cases, which are distinct from the observations, are tabulated in Table 2. The standard deviation and the mean relative error for each test case are defined by

$$T_{\text{std}} = \left(\frac{\sum_{i=1}^{N_{\text{nodes}}} (T_{\text{error}}(x,y,z) - \overline{T}_{\text{error}}(x,y,z))^2}{N_{\text{nodes}} - 1} \right)^{1/2} \tag{12}$$

$$\text{mean relative error} = \frac{\sum_{i=1}^{N_{\text{nodes}}} \frac{T_{\text{error}}(x,y,z)}{T_{\text{Fluent}}(x,y,z)} \times 100\%}{N_{\text{nodes}}} \tag{13}$$

In the relative error calculation, the temperatures are in °C. As seen in Table 2, the mean error in predicting temperature rise for the six test cases varies from 0.63°C or 2.4% to 2.13°C or 8.4%. The averages in the mean absolute and relative error for all cases are 1.24°C and 4.9% while the average standard deviation is

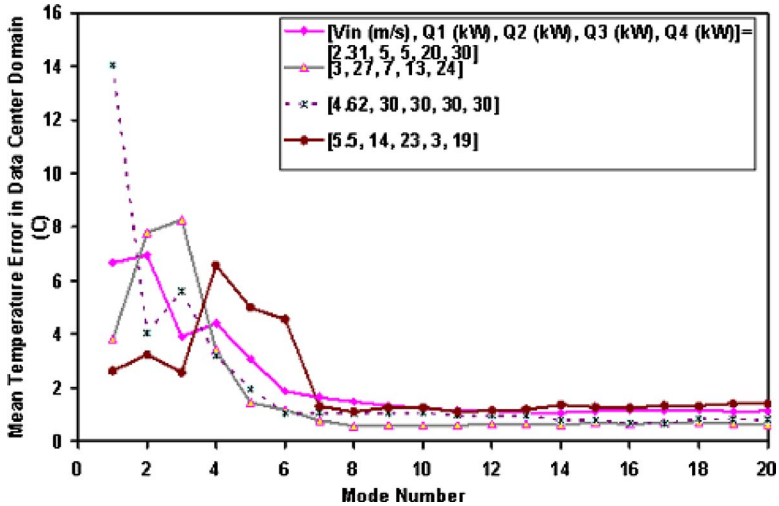

Fig. 11 Effect of the number of retained POD modes on the mean POD temperature error (°C) for the entire data center for four test cases

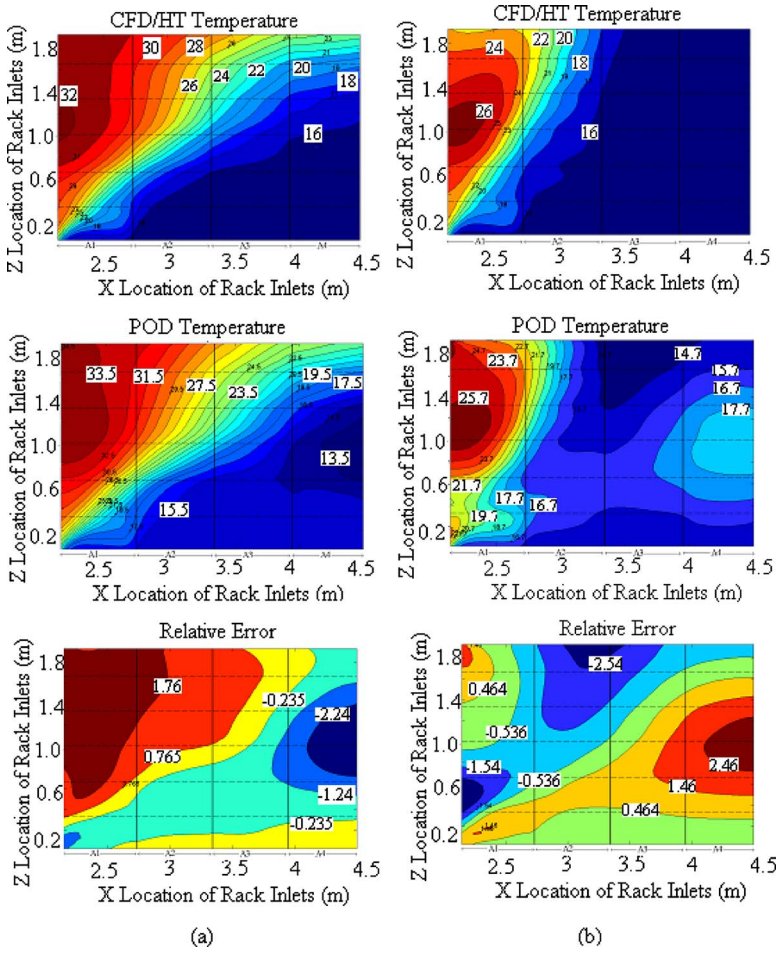

Fig. 12 Contours of CFD/HT temperature, POD temperature, and relative error (°C) at the inlets of racks A1–A4 for two test cases: (*a*) [2.31 m/s, 5 kW, 5 kW, 20 kW, 30 kW] and (*b*) [5.5 m/s, 14 kW, 23 kW, 3 kW, 19 kW]

Table 2 POD temperature error and its standard deviation compared with CFD/HT solution for six test cases

Case No.	[V_{in} (m/s), Q_1 (kW), Q_2 (kW), Q_3 (kW), Q_4 (kW)]	Mean relative error (%)	Mean error (C)	Standard deviation (C)
1	[1.5, 2, 30, 1, 3]	8.35	2.13	2.02
2	[2.31, 5, 5, 20, 30]	3.59	1.14	1.39
3	[3, 27, 7, 13, 24]	2.39	0.63	0.76
4	[4, 30, 29, 9, 28]	4.77	1.31	1.99
5	[4.62, 30, 30, 30, 30]	3.05	0.8	0.94
6	[5.5, 14, 23, 3, 19]	7.23	1.41	1.63
Average		4.90	1.24	1.46

Table 3 Specifications of scenarios 1–8 for the case study

	Scenario No.						
	1 and 5	2	3	4	6	7	8
No. of components per rack	6	6	6	6	3	2	1
No. of known temperature differences per rack	6	4 (for servers 1, 3, 4, and 6)	3 (for servers 1, 4, and 6)	2 (for servers 1 and 6)	3	2	1
No. of total components in data center ($N_{components}$)	50	50	50	50	26	18	10
No. of known thermal information (temperature differences) in data center (N_{info})	50	34	26	18	26	18	10
No. of total equations in data center ($N_{equations}$)	50	34	26	18	26	18	10
Maximum possible number of pod modes to use ($N_{max\ mode}$)	20	20	20	18	20	18	10

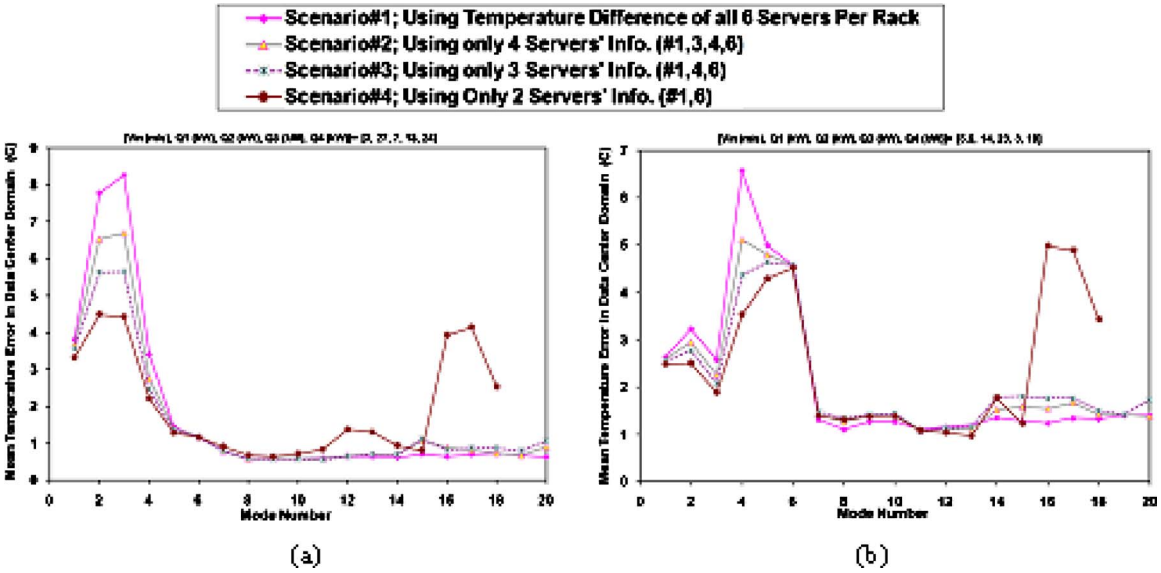

Fig. 13 Mean POD temperature error (°C) versus used mode number for scenarios 1–4: (*a*) test case of [3 m/s, 27 kW, 7 kW, 13 kW, 24 kW] and (*b*) test case of [5.5 m/s, 14 kW, 23 kW, 3 kW, 19 kW]

1.46°C. These values confirm that the presented POD method is reasonably accurate at the entire data center cell.

Regarding the computational speed of the POD based method, it should be noted that the POD based thermal model has only 20 DOFs, representing five orders of magnitude decrease compared with the CFD/HT model. The CFD/HT simulation takes ~2 h to obtain the temperature field for a new test case on a desktop computer with Xeon™ CPU, 2.8 GHz and 2.75 Gbytes of RAM. However, it takes only ~48 s to obtain the POD temperature field for the same test case on the same computing platform, which is ~150 times faster.

In the next section, the effect of the number of known temperature differences across the servers on the POD temperature results is studied.

3.3 Effect of the Known Thermal Information Quantity on the POD Result. In Sec. 3.2, it was shown that the POD based method can predict a new temperature field in the entire data

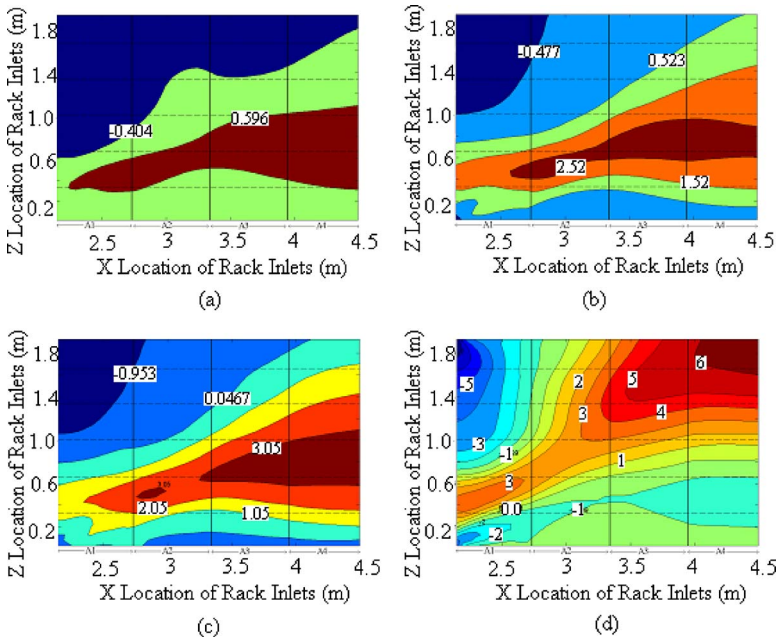

Fig. 14 Contours of POD temperature error (°C) at the inlets of racks A1–A4 for scenarios 1–4 for test case of [3 m/s, 27 kW, 7 kW, 13 kW, 24 kW]. The results have been obtained using all possible modes. (*a*) Scenario 1: thermal information for six servers per rack, a total of 50 equations and 20 modes. (*b*) Scenario 2: thermal information for four servers per rack, a total of 34 equations and 20 modes. (*c*) Scenario 3: thermal information for three servers per rack, a total of 26 equations and 20 modes. (*d*) Scenario 4: thermal information for two servers per rack, a total of 18 equations and 18 modes.

center cell of Fig. 5 with an average error of 5% if the temperature differences across all the servers are given as known information, in addition to the CRAC air velocity and discharge temperature. One interesting question is how the POD solution and error change if lesser thermal information about the components such as the server temperature differences is supplied. This information is useful in reducing the number of required thermal sensors at the server inlets/outlets in the operational data centers to be able to predict the entire temperature field with the lowest cost.

For this purpose, four different scenarios are considered, as listed in Table 3.

Scenario 1. Temperature differences for all six servers per rack in Fig. 5 are measured and given to the method. In this situation, $N_{\text{equations}}=N_{\text{info}}=50$. So, 50 equations are obtained to solve for the POD coefficients. The results are as presented in Sec. 3.2.

Scenario 2. Temperature differences for only four servers, servers 1, 3, 4, and 6 in Fig. 5 per rack are given to the POD method. So, there are $N_{\text{equations}}=N_{\text{info}}=34$ equations in this scenario.

Scenario 3. Temperature differences for only three servers, servers 1, 4, and 6 in Fig. 5 per rack are used and totally $N_{\text{equations}}=N_{\text{info}}=26$ equations are solved to obtain the POD coefficients.

Scenario 4. Temperature differences for only two servers, servers 1 and 6 in Fig. 5, per rack are given and totally $N_{\text{equations}}=N_{\text{info}}=18$ equations are solved to obtain the POD coefficients. In this scenario, the maximum possible number of retained modes in Eq. (1) is limited to 18 since $N_{\text{max mode}}=\min(n-1,N_{\text{equations}})$, as discussed in Sec. 2.2. In the previous scenarios, all $n-1=20$ modes can be used since $N_{\text{equations}}>n-1$.

The effect of the number of used modes on the mean error for the four scenarios is shown in Fig. 13 for two test cases. As seen in the figure, the solution starts to diverge when the number of used server temperature differences is reduced. However, complete divergence is only seen in scenario 4 when the information of only two servers per rack is used in the method. In Fig. 14, the error contours of the POD temperature field for one test case, when all possible modes are used, at the inlets of racks A1–A4, are shown for the four scenarios. It is seen that the error increases as the specified information is reduced. Also, the mean absolute and relative errors with the associated standard deviation are shown in Table 4 for the four scenarios and six test cases. As seen in the table, the average error for all test cases increases from 1.2°C (4.9%) to 1.45°C (5.7%), 2.5°C (10%), and 3.3°C (13.25%), as the number of known temperature differences decreases from 6 servers to 4, 3, and 2 per rack, respectively. In the results presented in Fig. 14 and Table 4, all possible modes, 20 for scenarios 1–3 and 18 for scenario 4, have been used in the POD reconstruction.

As seen in Fig. 13, the mean error in the POD solution for all scenarios reduces with the increase in the number of used POD modes until approximately ten modes. As seen in Fig. 7, the first ten modes capture 89.4% of the energy of the system. The last modes, as seen in Fig. 8(*b*), include small scale structures with low energy contribution to the system and fluctuate sharply throughout the domain. Adding these fluctuating fine modes to the first dominant modes in the POD reconstruction of Eq. (1) generally results in numerical error and solution divergence. When successive modes are added to the POD solution for the case study after ten modes, the contribution of the numerical error to the POD reconstruction starts to increase. However, there is a competition between the numerical error and the given thermal information at the boundaries. As seen in Fig. 14 and Table 4 for scenarios 1 and 2, when number of available equations to satisfy is much higher than the number of POD coefficients, the POD solution does not diverge by adding more modes. In these situations, the POD solution is enforced to satisfy the thermal information at many system interior boundaries and is not allowed to diverge. But, as the available information and number of equations decrease, approaching the number of used modes and unknown POD

Table 4 POD temperature errors for scenarios 1–4 with different known thermal information about the servers. The results have been obtained for six test cases using all possible modes.

		Scenario 1: using temperature difference of all six servers per rack, 50 equations and 20 modes		Scenario 2: using temperature difference of only four servers (1, 3, 4, and 6), 34 equations and 20 modes		Scenario 3: using temperature difference of only three servers (1, 4, and 6), 26 equations and 20 modes		Scenario 4: using temperature difference of only two servers (1 and 6), 18 equations and 18 modes	
Case No.	$[V_{\text{in}}$ (m/s), Q_1 (kW), Q_2 (kW), Q_3 (kW), Q_4 (kW)]	Mean error (C)	Mean relative error (%)	Mean error (C)	Mean relative error (%)	Mean error (C)	Mean relative error (%)	Mean error (C)	Mean relative error (%)
1	[1.5, 2, 30, 1, 3]	2.31	8.35	2.98	11.76	6.25	25.13	5.42	22.43
2	[2.31, 5, 5, 20, 30]	1.14	3.59	1.51	4.88	2.97	9.86	4.97	16.19
3	[3, 27, 7, 13, 24]	0.63	2.39	0.89	3.53	1.06	4.22	2.53	9.51
4	[4, 30, 29, 9, 28]	1.31	4.77	1.24	4.55	2.44	9.56	1.64	6.47
5	[4.62, 30, 30, 30, 30]	0.8	3.05	0.69	2.53	0.69	2.53	1.86	7.19
6	[5.5, 14, 23, 3, 19]	1.41	7.23	1.39	7.00	1.74	8.77	3.44	17.71
Average		1.24	4.90	1.45	5.71	2.52	10.01	3.31	13.25

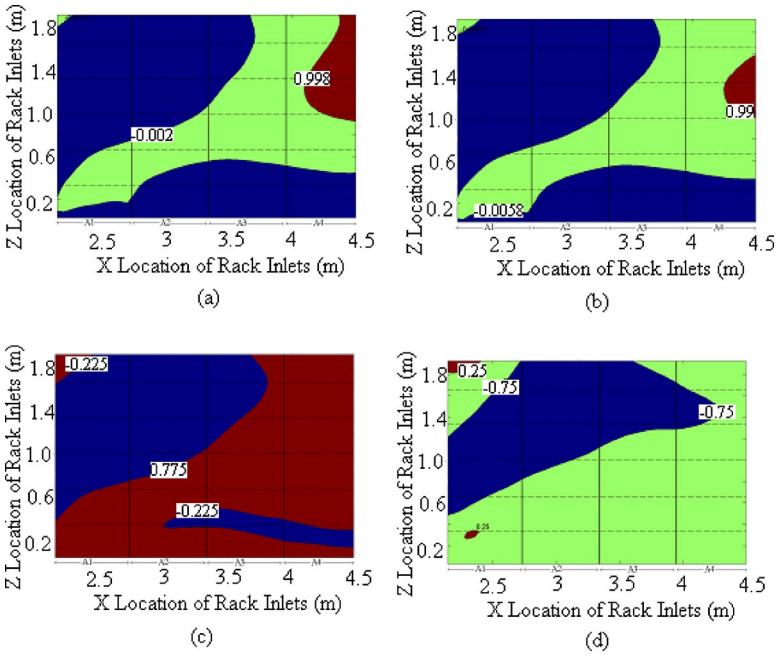

Fig. 15 Contours of POD temperature error (°C) at the inlets of racks A1–A4 for scenarios 1–4 for test case of [3 m/s, 27 kW, 7 kW, 13 kW, 24 kW]. The results have been obtained using only ten modes. (*a*) Scenario 1: thermal information for six servers per rack, a total of 50 equations and ten modes. (*b*) Scenario 2: thermal information for four servers per rack, a total of 34 equations and ten modes. (*c*) Scenario 3: thermal information for three servers per rack, a total of 26 equations and ten modes. (*d*) Scenario 4: thermal information for two servers per rack, a total of 18 equations and ten modes.

coefficients, the numerical error contribution, and as a result the solution divergence become larger. This can be seen by comparing the results for scenario 3 with 26 equations and scenarios 1 and 2 with 50 and 34 equations, respectively, in Fig. 14. In scenario 4, when the number of equations, 18, is equal to the number of used modes, the numerical error contribution becomes dominant and the solution diverges after approximately ten modes.

As discussed above and seen in Fig. 14, we can obtain a converged POD solution for all four scenarios using only ten modes. The temperature error contours, using only ten modes, for all scenarios are shown at the rack inlets for the same test case in Fig. 15. It is seen that the error is less than 1 °C in most of the regions at the rack inlets for all scenarios. Also, the mean absolute and relative errors with the standard deviation are shown in Table 5 for the four scenarios and six test cases, when only ten modes are used in the POD reconstruction. As seen in Table 5, the average error for all test cases increases slightly from 1.28 °C (5.05%) to 1.33 °C (5.23%), 1.38 °C (5.4%), and 1.58 °C (6.22%), as the number of server information equations decreases from 6 to 4, 3, and 2 per rack, respectively. It shows that even with temperature differences specified for only two servers per rack, the POD method can predict the temperatures at all 431,120 points in the data center with an average error of 6.2% if we know the number of required POD modes to reach a converged solution. This required POD mode number can be obtained directly from the POD solution through graphs such as Figs. 9 and 10 without a need to run and compare with CFD/HT solution.

3.4 Effect of the Number of System Components on the POD Result. As mentioned in Sec. 2.2, the maximum possible number of used POD modes is limited by the number of available algebraic equations in the presented method. This number is limited to the number of interior convective components or subsystems like the ones in Fig. 4, for which we can use energy balance equations, heat flux matching, and/or surface temperature matching. In this section, the effect of the number of these components in the main system on the POD solution is studied considering four new scenarios in the case study. These scenarios are listed in Table 3 and defined in the following.

Scenario 5. Each server in Fig. 5(*b*) is considered as a component for which Eq. (6) is applied. This results in six components per rack and totally $N_{\text{equations}}=N_{\text{info}}=50$ equations to solve for $N_{\max\ \text{mode}}=\min(n-1,N_{\text{equations}})=20$ mode coefficients. This scenario is the same as scenario 1 in Sec. 3.3 and the results are presented in Sec. 3.2.

Scenario 6. Two adjacent servers in each rack are assumed as one component. So, Eq. (6) is applied to only three components per rack. So, there are 26 equations in this scenario while the maximum possible number of used modes is 20.

Scenario 7. Each rack is assumed to have only two components. The combination of servers 1–3 in Fig. 5(*b*) makes one component as the combination of servers 4–6 do. So, there are two equations per rack and a total of 18 equations in the data center for this scenario. This reduces the possible number of used modes to only 18 since $\min(n-1,N_{\text{equations}})=18$.

Scenario 8. All six servers in each rack are assumed as one component. So, there is 1 equation per rack and a total of 10 equations in the data center in this scenario, while the possible number of used modes is only 10.

In scenarios 5–8, N_{info} is equal to $N_{\text{components}}$ since there is one specified temperature difference for each component. The effect of the number of used modes on the mean error for scenarios 5–8 is shown in Fig. 16 for four test cases. The trend of the results is very similar to the POD solution for scenarios 1–4 shown in Fig. 13 when the available server thermal information drove the number of available equations. In scenarios 5–8, the number of com-

Table 5 POD temperature errors for scenarios 1–4 with different known thermal information about the servers. The results have been obtained for six test cases using only ten modes.

Case No.	$[V_{in}$ (m/s), Q_1 (kW), Q_2 (kW), Q_3 (kW), Q_4 (kW)]	Scenario 1: using temperature difference of all six servers per rack, 50 equations and ten modes		Scenario 2: using temperature difference of only four servers (1, 3, 4, and 6), 34 equations and ten modes		Scenario 3: using temperature difference of only three servers (1, 4, and 6), 26 equations and ten modes		Scenario 4: using temperature difference of only two servers (1 and 6), 18 equations and ten modes	
		Mean error (C)	Mean relative error (%)	Mean error (C)	Mean relative error (%)	Mean error (C)	Mean relative error (%)	Mean error (C)	Mean relative error (%)
1	[1.5, 2, 30, 1, 3]	2.25	8.81	2.36	9.18	2.55	9.90	2.39	9.48
2	[2.31, 5, 5, 20, 30]	1.24	3.80	1.23	3.78	1.26	3.86	1.43	4.41
3	[3,27,7,13,24]	0.60	2.25	0.59	2.20	0.56	2.07	0.72	2.69
4	[4, 30,29,9,28]	1.27	4.86	1.30	4.74	1.29	4.74	2.37	9.12
5	[4.62, 30, 30, 30, 30]	1.07	4.08	1.09	4.17	1.16	4.47	1.18	4.50
6	[5.5, 14, 23, 3, 19]	1.27	6.49	1.44	7.33	1.44	7.37	1.38	7.12
Average		1.28	5.05	1.33	5.23	1.38	5.40	1.58	6.22

ponents drives the number of equations. By comparing the results in Fig. 16 with Fig. 13, the following statements can be made about the presented method.

(1) A converged and accurate temperature field in a complex system is generated only if the number of components, $N_{components}$, and given thermal information, N_{info}, is much larger than the maximum number of available modes, $N_{max\ mode}$, and the number of required dominant modes to capture the key physics of the system, $N_{dominant}$. As mentioned before, $N_{max\ mode}=\min(n-1, N_{equations})$. Also, $N_{dominant}\sim 10$ in this case study as discussed before. For scenarios 1, 2, and 5 in Figs. 13 and 16, $N_{equations}=N_{info}=50$, 34, and 50, respectively, which is much higher than $N_{max\ mode}=20$ and $N_{dominant}$. So, we have a converged and accurate solution for these scenarios.

(2) The solution starts to diverge when the number of equations $N_{equations}$, which is equal to the number of given thermal information N_{info} and always less than the number of components $N_{components}$, decreases and becomes closer to the maximum number of available POD modes $N_{max\ mode}$. This trend is seen in scenarios 3, 4, 6, 7, and 8 with $N_{equations}=N_{info}=26$, 18, 26, 18, and 10 available equations and $N_{max\ mode}=20$, 18, 20, 18, and 10 available modes to use, respectively. There are two situations for these scenarios.

   (a) If the number of available equations $N_{equations}$ is still higher than the number of required modes to capture the main physics of the system, $N_{dominant}\sim 10$ in this case study, the method gives accurate results if only the required modes $N_{dominant}$, and not all available modes $N_{max\ mode}$, are used in the POD reconstruction. This is seen for scenarios 3, 4, 6, and 7. As seen in Figs. 13 and 16, the POD solution using only ten modes for these scenarios has not started diverging yet and is accurate.

   (b) If the number of available equations $N_{equations}$ is very close to, or less than, the number of required dominant modes for the system $N_{dominant}$, the error changes nonlinearly with the number of used modes. In this situation, there is an optimal number of used modes to reach the minimum error in the solution. But, this optimal number changes on a case by case basis and cannot be determined in advance. This happens for scenario 8 in Fig. 16, when the number of components and available equations is equal to the number of required modes, i.e., 10.

4 Conclusion

CFD/HT methods are often too time consuming and costly to examine the effect of multiple design parameters on the system thermal performance, especially for complex systems with multiple components and interacting physical phenomena. In this paper, a POD based reduced order thermal modeling approach is presented to predict the temperature field in complex systems in terms of multiple design variables. In this method, the algebraic equations to solve for the POD coefficients are obtained simply through energy balance equations, heat flux matching, and/or surface temperature matching for all convective components. The method is applied to a data center cell with multiple turbulent convective components and five design variables. The method results in average temperature rise prediction error of 1.24°C (4.9%) for different sets of design variables, while it is ~150 times faster than CFD/HT simulation.

The solution convergence and accuracy of the presented method are shown to depend on the number of components and given thermal information about the system. It is shown that the POD results remain accurate for the case study even if the given thermal information at the component boundaries decreases by 67%, if we use the required dominant POD modes to capture the most important phenomena of the system. In fact, the method can predict the air temperatures at all 431,120 points in the data center

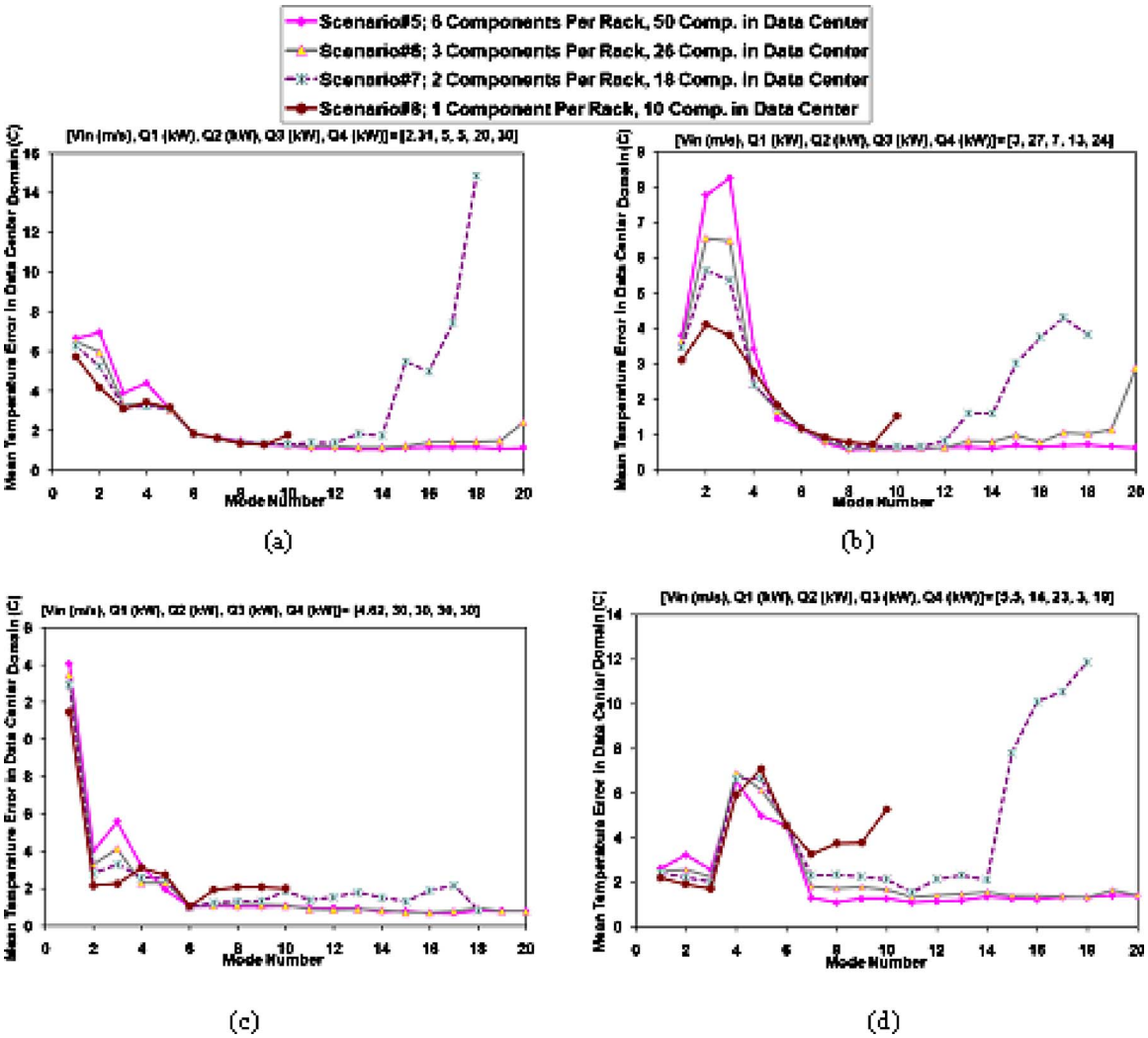

Fig. 16 POD mean temperature error (°C) versus used mode number for scenarios 5–8 for four test cases. Relevant test case is mentioned at the top of each plot.

cell with an average error of 6.2% even with known temperature differences for only two servers per rack. It is discussed how to obtain this required number of dominant modes in advance, based on the changes in the POD coefficients and component boundary thermal errors. Generally, the presented method can be used as a reliable and rapid predictor to obtain a new temperature field throughout the complex system, unless the number of components or available thermal information in the form of equations at the component boundaries is very close to or less than the number of dominant modes.

Acknowledgment

The authors acknowledge support of this research by the members of the Consortium for Energy Efficient Thermal Management (CEETHERM).

Nomenclature

a, b = modal weight coefficient
c_p = specific heat, J/kg K
k = thermal conductivity, W/m K
n = number of observations, $n=21$ in the case study
m = number of retained modes
$N_{\text{equations}}$ = number of total algebraic equations
$N_{\text{components}}$ = number of total components in domain
N_{info} = number of known thermal information in domain
$N_{\text{max mode}}$ = maximum possible number of POD modes to use
N_{dominant} = number of required dominant modes
P = pressure, Pa
Q = heat generation, W
T = temperature, K
V = average velocity on a surface, m/s

Greek Symbols

λ = eigenvalue
ρ = density, kg/m^3
ψ = POD mode

Subscripts

obs = observation
cond = conduction

Superscripts

$*$ = transpose
$+$ = pseudo-inverse

References

[1] Moore, J., Chase, J., Ranganathan, P., and Sharma, R., 2005, "Making Scheduling Cool: Temperature-Aware Workload Placement in Data Centers," *Proceedings of the Usenix Technical Conference*.

[2] Sharma, R. K., Bash, C., Patel, C. D., Friedrich, R. J., and Chase, J. S., 2003, "Balance of Power: Dynamic Thermal Management for Internet Data Centers," Technical Report No. HPL-2003-5.
[3] Moore, J., Chase, J., Farkas, K., and Ranganathan, P., 2005, "Data Center Workload Monitoring, Analysis, and Emulation," *Proceedings of the Eighth Workshop on Computer Architecture Evaluation Using Commercial Workloads*.
[4] Moore, J., Chase, J., and Ranganathan, P., 2006, "Weatherman: Automated, Online, and Predictive Thermal Mapping and Management for Data Centers," *Proceedings of the IEEE International Conference on Autonomic Computing (ICAC)*, pp. 155–164.
[5] Tang, Q., Gupta, S., and Varsamopoulos, G., 2008, "Energy-Efficient Thermal-Aware Task Scheduling for Homogeneous High-Performance Computing Data Centers: A Cyber-Physical Approach," IEEE Trans. Parallel Distrib. Syst., **19**(11), pp. 1458–1472.
[6] Moore, J., Chase, J., Ranganathan, P., and Sharma, R., 2005, "Making Scheduling Cool: Temperature-Aware Workload Placement in Data Centers," *Proceedings of the USENIX 2005 Annual Technical Conference*, pp. 61–75.
[7] Nie, Q., and Joshi, Y., 2008, "Reduced Order Modeling and Experimental Validation of Steady Turbulent Convection in Connected Domains," Int. J. Heat Mass Transfer, **51**(25–26), pp. 6063–6076.
[8] Rambo, J., and Joshi, Y., 2007, "Reduced-Order Modeling of Turbulent Forced Convection With Parametric Conditions," Int. J. Heat Mass Transfer, **50**(3–4), pp. 539–551.
[9] Rolander, N., 2005, "An Approach for the Robust Design of Air Cooled Data Center Server Cabinets," MS thesis, Georgia Institute of Technology, Atlanta, GA.
[10] Holmes, P., Lumley, J. L., and Berkooz, G., 1996, *Turbulence, Coherent Structures, Dynamical Systems and Symmetry*, Cambridge University Press, Cambridge, England.
[11] Rambo, J., 2006, "Reduced-Order Modeling of Multiscale Turbulent Convection: Application to Data Center Thermal Management," Ph.D. thesis, Georgia Institute of Technology, Atlanta, GA.
[12] Alonso, D., Velazquez, A., and Vega, J. M., 2009, "Robust Reduced Order Modeling of Heat Transfer in a Back Step Flow," Int. J. Heat Mass Transfer, **52**(5–6), pp. 1149–1157.
[13] Ilak, M., Rowley, C. W., and Rowley, C. W., 2008, "Modeling of Transitional Channel Flow Using Balanced Proper Orthogonal Decomposition," Phys. Fluids, **20**(3), p. 034103.
[14] Bogner, T., 2008, "General Variational Model Reduction Applied to Incompressible Viscous Flows," J. Fluid Mech., **617**, pp. 31–50.
[15] Ravindran, S. S., 2002, "Adaptive Reduced-Order Controllers for a Thermal Flow Using Proper Orthogonal Decomposition," SIAM J. Sci. Comput., **23**(6), pp. 1924–1942.
[16] Park, H. M., and Cho, D. H., 1996, "The Use of the Karhunen-Loeve Decomposition for the Modeling of Distributed Parameter Systems," Chem. Eng. Sci., **51**(1), pp. 81–98.
[17] Park, H. M., and Cho, D. H., 1996, "Low Dimensional Modeling of Flow Reactors," Int. J. Heat Mass Transfer, **39**(16), pp. 3311–3323.
[18] Sirovich, L., and Park, H. M., 1990, "Turbulent Thermal Convection in a Finite Domain: Part I. Theory," Phys. Fluids, **2**(9), pp. 1649–1657.
[19] Sirovich, L., and Park, H. M., 1990, "Turbulent Thermal Convection in a Finite Domain: Part II. Numerical Results," Phys. Fluids, **2**(9), pp. 1659–1668.
[20] Tarman, I. H., and Sirovich, L., 1998, "Extensions of Karhunen-Loeve Based Approximations of Complicated Phenomena," Comput. Methods Appl. Mech. Eng., **155**, pp. 359–368.
[21] Park, H. M., and Li, W. J., 2002, "Boundary Optimal Control of Natural Convection by Means of Mode Reduction," ASME J. Dyn. Syst., Meas., Control, **124**, pp. 47–54.
[22] Ding, P., Wu, X.-H., He, Y.-L., and Tao, W.-Q., 2008, "A Fast and Efficient Method for Predicting Fluid Flow and Heat Transfer Problems," ASME J. Heat Transfer, **130**(3), p. 032502.
[23] Hasan, N., and Sanghi, S., 2007, "Proper Orthogonal Decomposition and Low-Dimensional Modelling of Thermally Driven Two-Dimensional Flow in a Horizontal Rotating Cylinder," J. Fluid Mech., **573**, pp. 265–295.
[24] Sempey, A., Inard, C., Ghiaus, C., and Allery, C., 2009, "Fast Simulation of Temperature Distribution in Air Conditioned Rooms by Using Proper Orthogonal Decomposition," Build. Environ., **44**, pp. 280–289.
[25] Ly, H. V., and Tran, H. T., 2001, "Modeling and Control of Physical Processes Using Proper Orthogonal Decomposition," Math. Comput. Model., **33**, pp. 223–236.
[26] Rolander, N., Rambo, J., Joshi, Y., Mistree, F., and Allen, J. K., 2006, "Robust Design of Turbulent Convective Systems Using the Proper Orthogonal Decomposition," ASME J. Mech. Des., **128**, pp. 844–855.
[27] Nie, Q., and Joshi, Y., 2008, "Multiscale Thermal Modeling Methodology for Thermoelectrically Cooled Electronic Cabinets," Numer. Heat Transfer, Part A, **53**(3), pp. 225–248.
[28] Fried, E., and Idelchik, I. E., 1989, *Flow Resistance: A Design Guide for Engineers*, Hemisphere, New York.
[29] ASHRAE, 2004, "Thermal Guidelines for Data Processing Environments," American Society of Heating, Refrigeration, and Air-Conditioning Engineers.

Enhancement of Saturation Boiling of PF-5060 on Microporous Copper Dendrite Surfaces

Mohamed S. El-Genk[1]
Fellow ASME
Regents' Professor, Department of Chemical and Nuclear Engineering,
and Department of Mechanical Engineering,
University of New Mexico,
Albuquerque, NM 87131;
Director of Institute for Space and Nuclear Power Studies (ISNPS),
University of New Mexico,
Albuquerque, NM 87131
e-mail: mgenk@unm.edu

Amir F. Ali
Research Assistant, ISNPS,
University of New Mexico,
Albuquerque, NM 87131;
Department of Mechanical Engineering,
University of New Mexico,
Albuquerque, NM 87131

Experiments are performed to investigate saturation boiling of degassed PF-5060 dielectric liquid on microporous copper dendrite surface layers deposited on 10×10 mm^2 Cu substrates. The electrochemically deposited surface layers are of different thicknesses (145.6 μm, 46.3 μm, and 33.1 μm). The thickest layer gives the best results: the saturation CHF of 25.27 W/cm^2 occurs at a surface superheat of only 2.9 K and the maximum nucleate boiling heat transfer coefficient, h_{MNB}, near the end of the fully developed nucleate boiling region, is 8.76 W/cm^2 K. In addition, nucleate boiling ensues at a surface temperature slightly above saturation (<0.5 K), with no temperature excursion. The temperature excursions before initiating boiling on the 46.3 μm and 33.1 μm thick Cu nanodendrite surface layers are small (3.7 K and 6 K), corresponding to surface temperatures of ~55.1°C and 57.4°C, respectively. These temperatures are much lower than recommended (85°C) for reliable operation of most silicon electronics and central processor units. [DOI: 10.1115/1.4000975]

Keywords: pool boiling enhancement, copper nanodendrites, electrochemical deposition, electronics cooling, dielectric liquids

1 Introduction

The ever increasing transistor density and processing speed of computer chips and central processor units (CPUs) present several challenges: (a) removing the dissipated heat, up to 100 W per chip, at a reasonable junction temperature; (b) reducing the number and heat flux of the surface hot spots; and (c) mitigating the effect of the forming hot spots on shortening the service life of the chip or CPU. The temporal variation in the chip surface could be as much as 10°C, or even higher, and the hot-spot heat flux (>100 W/cm^2) could be two to three times the average value. These challenges can be dealt with effectively using immersion cooling by enhanced nucleate boiling of dielectric liquids on micro- and macroporous structured surfaces (e.g., Refs. [1–12]). Desirable attributes of immersion cooling using dielectric liquids include a relatively low surface or junction temperature, more uniform surface temperature, and attaining high heat transfer coefficient, with no or little excursion in the surface temperature before initiating boiling. The excursion in surface temperature is caused by the very low surface tension (Table 1) and high wetting of dielectric liquids. On plane copper surfaces, temperature excursions of as much as 15–25 K have been reported [8,9,13]. A large excursion in the surface temperature of the chip, beyond the recommended values for most silicon electronic devices and computer chips, reduces the service life and increases the failure frequency.

For immersion cooling with nucleate boiling, the critical heat flux (CHF) is a practical limit not to exceed; however, nominal operation is preferable at the maximum nucleate boiling heat transfer coefficient, h_{MNB}. This coefficient, which occurs near the end of the fully developed nucleate boiling region, is higher than at CHF and the corresponding surface temperature is also lower [3,8,9,13–15].

Typical pool boiling curves of dielectric liquids (Table 1) can be divided into three successive regions [3,8]: (a) the discrete-bubble region at low surface superheats, (b) the fully developed nucleate boiling region at intermediate surface superheats, and (c) the bubble coalescence region at high surface superheats, ending with CHF. The heat transfer coefficient in the fully developed nucleate boiling region is the highest. It reaches a maximum, h_{MNB}, near the end of this region before transitioning to region (c). In region (c), the nucleate boiling heat transfer coefficient, h_{NB}, decreases with increased surface superheat, until reaching CHF. At CHF, the nucleate boiling heat transfer coefficient is lower and the corresponding surface temperature, T_W, is higher than at h_{MNB}. This is because of the added resistance to the boiling heat transfer due to the lateral coalescence of the growing and rising vapor bubbles at and near the heated surface. Thus, for electronics cooling it is preferable to operate at or near h_{MNB}, on the left side of the pool boiling curve, where the surface superheat is low.

Micro- and macroporous surfaces, surfaces with re-entrant cavities, fabricated pores and microfins, porous, roughened, and microstructured surfaces, and applied microporous coatings have been shown to enhance nucleate boiling heat transfer of dielectric liquids [1,3,5,7,8,11,12,16–18]. This is in addition to increasing CHF and either eliminating or markedly reducing the excursion in the surface temperature before initiating boiling.

Recently the reported results on nucleate boiling enhancement using microporous copper nanodendrite surface layers have been very promising [4,6,10,19–23]. The microstructure of these surface layers is relatively complex. It consists of a repeated pattern of almost circular pores surrounded by a relatively dense structure of growing and branching copper nanodendrites (Fig. 1) [21].

The metal nanodendrite layers (<400 μm thick) are easily and inexpensively applied using electrochemical processes. The values of the controlled parameters during deposition affect not only the

[1]Corresponding author.

Contributed by the Heat Transfer Division of ASME for publication in the JOURNAL OF HEAT TRANSFER. Manuscript received June 2, 2009; final manuscript received November 24, 2009; published online April 28, 2010. Assoc. Editor: Satish G. Kandlikar.

Table 1 Best estimates of the physical properties of FC-72 and PF-5060 dielectric liquids at the local ambient pressure (ambient pressure in Albuquerque, NM)

Saturation properties	FC-72 (~0.085 MPa[a])	PF-5060 (~0.085 MPa[a])
Boiling point (°C)	51.5	51.4[b]
Freeze point (°C)	−90	−90
Ave. molecular weight (g/mol)	338	338
Liquid density (kg/m^3)	1619	1606
Vapor density (kg/m^3)	11.4	11.3
Liquid viscosity (kg/m s)	4.4×10^{-4}	4.6×10^{-4}
Liquid specific heat (J/kg K)	1094	1094
Latent heat of vaporization (kJ/kg)	96.4	96.4
Liquid thermal conductivity (W/m K)	0.054	0.054
Liquid surface tension (N/m)[c]	0.00864	0.010368

[a]Ambient pressure in Albuquerque, NM.
[b]In present work.
[c]Temperature dependent.

thickness, microstructure, volume porosity, and pore sizes but also the structural strength of the deposited microporous nanodendrite layers. These parameters include the deposition dc current density and time, the composition of the electrolyte solution, and the anode surface area and its separation distance from the copper substrate connected to the cathode (Table 2). The thickness of the deposited layer, typically 30–400 μm, depends on the values of the various parameters during deposition (Table 2), particularly the electrical current density, deposition time, and the concentration of $CuSO_4$ in the electrolyte solution [10,20].

Despite the encouraging preliminary results, little work has been reported on pool boiling of dielectric liquids such as FC-72 and PF-5060 (Table 1) on metal nanodendrite surface layers [4–6,10,19–22]. In addition, understanding the effects of the various electrochemical disposition parameters, such as the current density, deposition time, type, and amount of additives to the electrolyte solution, and the electrolyte composition on the mechanical strength of the deposited microstructure and its potential for enhancing nucleate boiling is nonconclusive. Thus, there is a need for investigating these effects, which is the focus of this work.

In the present work, the adhesion of the deposited Cu nanodendrite layers to the Cu substrates (Table 2) has been good. The mechanical strength and toughness of the deposited and structurally strengthened layers for resisting chipping and fracture increased with increased thickness. In addition, the reproducibility of the deposited structure in terms of mechanical strength and nucleate boiling heat transfer has been reasonable. Compared with other methods reported in the literature for fabricating microstructured, microfinned, and microporous surfaces and the application of microporous coatings, the electrochemical deposition process employed in the present work is very simple, well controlled, and could be used for the deposition on large surfaces of several centimeters in length scale. Preparation and cleaning of the Cu anode and Cu substrate (cathode) before starting the electrochemical deposition are critical for achieving good adhesion of the deposited layers and the reproducibility of the results.

The performed experiments investigated the enhancement in saturation boiling of PF-5060 dielectric liquid on 10×10 mm^2 copper substrate with Cu nanodendrite surface layers of different thickness, average pore size, and volume porosity (Table 2). Table 1 compares the physical properties of FC-72 and PF-5060 dielectric liquids at the local pressure in Albuquerque, NM.

A primary focus of this work is to determine the effects of the thickness and microstructure of the deposited Cu nanodendrite surface layers on enhancing saturation nucleate boiling of PF-5060 dielectric liquid, increasing the values of h_{MNB} and CHF,

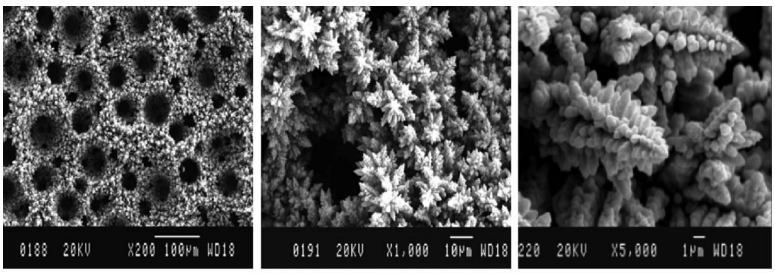

Fig. 1 SEM images of Cu nanodendrites deposited using high current density [21]

Table 2 Deposited surface layers of Cu nanodendrites

Layer	Electrolyte (mol/l)	Deposition current (A/cm^2)	Thickness (μm)/porosity (%)	Anode area (cm^2)/Sep. (cm)
1	0.8 $CuSO_4$, 1.5 H_2SO	3[a], 0.05[b]	145.6 ± 5.8 (94.5[a], 73.9[b])	5/2
2	0.4 $CuSO_4$, 1.5 H_2SO	3[a], 0.05[b]	46.3 ± 1.8 (92.2[a], 29.7[b])	5/2
3	0.4 $CuSO_4$, 1.5 H_2SO	3[a], 0.05[b]	33.1 ± 1.3 (93.8[a], 7.1[b])	5/2

[a]First deposition period.
[b]Second deposition period.

and decreasing the corresponding surface superheats, ΔT_{sat}, and the excursion in the surface temperature before initiating nucleate boiling.

2 Electrochemical Deposition

Microporous Cu nanodendrite layers are deposited onto Cu substrates measuring 10×10 mm^2 and 1.6 mm thick. The Cu substrate functions as the cathode during the process of electrochemical deposition. They are laid out parallel to the copper anode (4.5–5 cm^2 in surface area) and separated from it by 2 cm (Table 2). The cathode and the anode are fully immersed in the electrolyte solution of sulfuric acid and copper sulfate during the electrochemical deposition.

The area of the copper anode is much larger than that of the cathode to ensure that the rate of electrochemical deposition is uniform and not limited by the supply of Cu ions from the anode. During deposition, the cathode and the anode are connected to an external dc power supply, controlled by a PC, to adjust the supplied current density and monitor the disposition time. The electrochemical deposition of the copper nanodendrite surface layers is carried out in two successive steps. The initial thickness and microstructure of the deposited layers are established in the first period, during which the current density is kept constant at 3 A/cm^2, while varying the deposition time (25 s, 10 s, and 5 s for surface layers 1, 2, and 3) and the composition of the electrolyte solution (Table 2). The deposited microstructure is then structurally strengthened by continuing the electrochemical deposition for a subsequent, but much longer period (tens of minutes) at very low-current density ($\sim$50 mA/cm^2).

Initially, the bare surface of the 10×10 mm^2 Cu cathode substrate is in contact with the electrolyte solution, containing both Cu^{+2} and H^+. When the electric current is supplied to the electrochemical deposition cell, the process proceeds with two simultaneous reduction reactions at the anode and the cathode, respectively:

$$Cu^{+2} + 2e^{-1} \rightarrow Cu \quad \text{and} \quad 2H^{+1} + 2e^{-1} \rightarrow H_2 \tag{1}$$

2.1 First Deposition Period. During the first period of high current density (3 A/cm^2) electrochemical deposition, the rising columns of hydrogen bubbles generating at the cathode surface form circular macropores (Figs. 1(*a*) and 1(*b*)). These macropores are surrounded by a complex structure of branching Cu nanodendrites that grow onto the cathode Cu substrate (Figs. 1(*b*) and 1(*c*)). The continuous migration of copper and hydrogen ions, Cu^{+2} and H^+, through the electrolyte solution to the cathode surface sustains the electrochemical deposition process. Because the mobility of H^+ ions is higher than that of the Cu^{+2} ions, the former migrate to the cathode surface faster than the latter, increasing the generation rate of hydrogen bubbles at the cathode surface.

The initially deposited Cu nanodendrites provide new active reduction sites for incoming H^+ ions and the formation of hydrogen bubbles. The bubbles released from these sites are responsible for the growth of the nondendrite branches (Figs. 1(*b*) and 1(*c*)) and the increase in the average size of the macropores (Fig. 1(*a*)).

The departing hydrogen bubbles, from the cathode surface and the exposed surface of the Cu nanodendrites, coalesce forming larger bubbles, which sustain the open macropores in the deposited surface layers (Fig. 1(*a*)). The rising hydrogen bubbles not only sustain the open macropores in the depositing Cu nanodendrite structure but also increase the average diameter of the macropores with increased thickness of the deposited nanodendrite surface layer.

The columns of rising bubbles also produce the patterns of the macropores (Fig. 1(*a*)), a few to tens of microns in diameter, within the deposited Cu nanodendrite surface layers. On the other hand, the micropores within the Cu nanodendrite structure are very small, ranging from a fraction of a micron to a few microns in size (Figs. 1(*b*) and 1(*c*)).

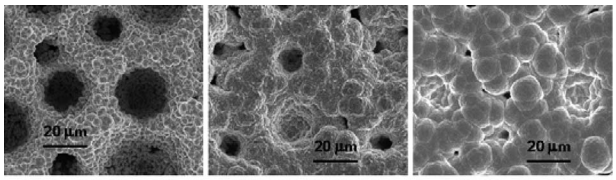

Fig. 2 SEM images of the structurally strengthened Cu Nanodendrite surface layers used in the present pool boiling experiments (500×).

Figures 1(*a*)–1(*c*) present the scanning electron microscope (SEM) images of Cu nanodendrite layers deposited using similar current density and deposition times as in the present work (Table 2). They clearly show the macropores surrounded by branches of Cu nanodendrite [21]. Increasing the thickness of the deposited Cu nanodendrite layer progressively increases the average size of the macropores in the deposited layers [10,20,21] but slightly changes the volume porosity, ranging from 92.2% to 94.5% (Table 2).

2.2 Second Deposition Period. Because of the very high volume porosity of the deposited Cu nanodendrite surface layers during the initial period of electrochemical disposition using high current density (Table 2), the resulting structurally is very delicate to handle. In order to structurally strengthen the deposited surface layer and improve its adhesion to the Cu substrate, the initial electrochemical deposition period (Table 2) is followed by a second, long deposition period (tens of minutes) at very low-current density of $\sim$5 mA/cm^2 (Table 2). During this period, the production rate of hydrogen bubbles is very low and infrequent to change the basic microstructure. The resulting microstructure is structurally rugged and excellent for handling in the boiling experiments. The strength of the structure comes at the expense of decreasing the volume porosity to $\sim$73.9%, 29.7%, and 7.1% for surface layers 1, 2, and 3, respectively (Table 2). Figures 2(*a*)–2(*c*) show the SEM images of the deposited and structurally strengthened Cu nanodendrite surface layers used in the present pool boiling experiments.

Comparing the images in Figs. 1 and 2 clearly indicates that the second period of very low-current electrochemical deposition, while strengthened the microstructure, masked the original nondendrites (Figs. 1(*b*) and 1(*c*)) and filled out some of the originally open macropores with Cu nanoparticle (Figs. 2(*a*)–2(*c*)). The filled out macropores effectively increase the surface area for nucleate boiling. The increase in surface area of the structurally strengthened layers is indicated by the large and deep depressions in the SEM images (Figs. 2(*a*)–2(*c*)), ranging from 30 μm to 50 μm in diameter in the surface layer 1, compared $<$30 μm in surface layers 2 and 3. Also the spacing of the filled out macropores in surface layer 1 is smaller than in surface layers 2 and 3. The combination of larger diameter and smaller spacing of the filled out macropores increases the effective area for boiling on layer 1 (Fig. 2(*a*)), compared with that for layer 2 (Fig. 2(*b*)). The least increase in the effective surface area appears to be that of surface layer 3 (Fig. 2(*c*)).

3 Test Section

The assembled test section (Fig. 3), measuring 30×30 mm^2 in outside dimensions, consists of a Teflon block with a 1.0 mm deep square cavity ($\sim10\times10$ mm^2) at the center of the top surface in which a high flux heating element is placed. The 10×10 mm^2 copper substrate with the deposited Cu nanodendrite surface layer is soldered to the top of the heating element (Fig. 3(*b*)).

The 1.6 mm thick copper substrate has two 0.6 mm diameter horizontal holes drilled on one side, $\sim$0.8 mm from the bottom, and halfway into the substrate (Fig. 3(*b*)). The measuring tips of

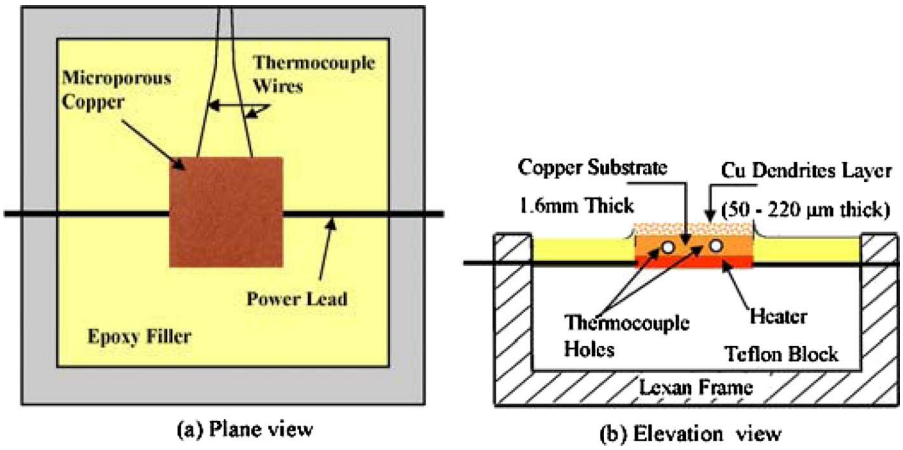

Fig. 3 Assembled test section

the two K-type thermocouples are securely attached to the inside of the holes using thermally conducting epoxy. The average reading of these thermocouples is taken as the average surface temperature for the purpose of constructing the pool boiling curves, after accounting for the temperature drop by conduction (<0.5 K) to the surface.

The Teflon block is encased in a Lexan frame with closed bottom (Fig. 3(*b*)). The shallow cavity on top of the Teflon block is filled with translucent epoxy adhesive, flush with the nanodendrite surface layer, to prevent bubbles nucleation at the edges and skewing the pool boiling curve (Fig. 3(*a*)).

4 Experimental Setup and Procedures

The test facility for conducting the boiling experiments is described in detail elsewhere [3,8,13,15] and a schematic is shown in Fig. 4. It is comprised of a hot water bath (B in Fig. 4) for maintaining the temperature of the PF-5060 liquid in the test vessel constant at saturation. The polycarbonate test vessel (C in Fig. 4) is immersed in the water bath and has a tightly sealed cover (D in Fig. 4). The hot water bath and the submerged cooling coils in the test vessel's pool (7 in Fig. 4) maintain its temperature within ± 0.5 K of the saturation temperature of PF-5060 liquid in the

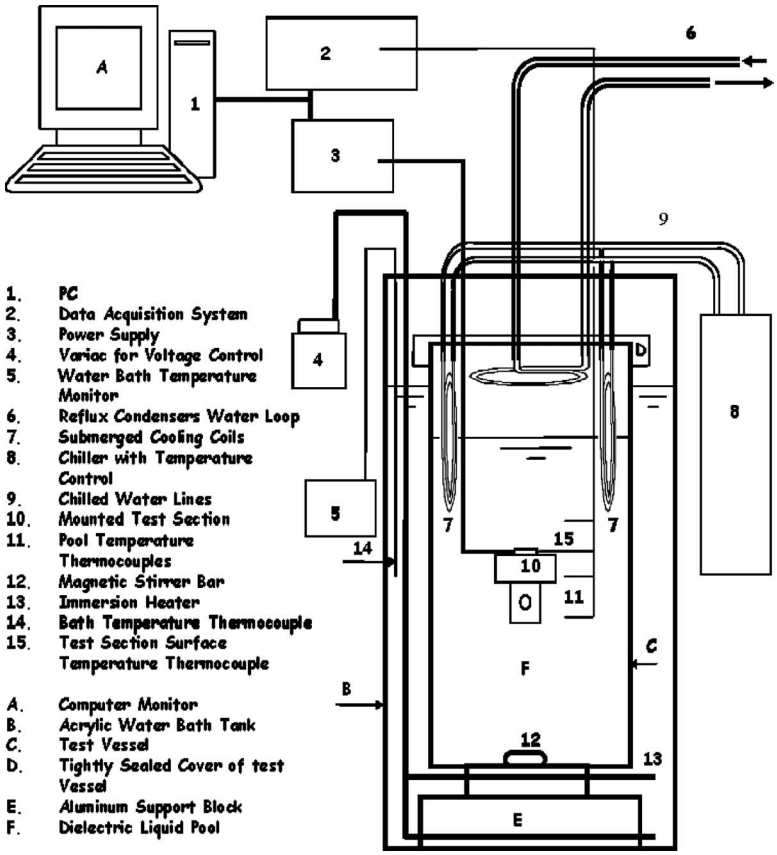

Fig. 4 A Schematic of the experimental setup

experiments (Table 1).

The magnetic stirrer at the bottom of test vessel (12 in Fig. 4) speeds up the outgassing and ensures uniform pool temperature prior to conducting the boiling experiments. Because of the high air solubility in PF-5060, it takes typically more than 2 h to adequately outgas the liquid pool in the test vessel, before conducting the experiments.

The water-cooled reflux condenser below the cover plate of the test vessel (D in Fig. 4) condenses the vapor generated by the test section, thus maintaining a constant liquid level in the pool above the test section surface (~8 cm). The temperature of the liquid pool in the vessel is monitored using four K-type thermocouples at different locations. The pool temperature in the experiments is taken as the average reading of the two thermocouples placed a few millimeters from the boiling surface (11 in Fig. 4).

The heat losses through the sides, top, and bottom of the assembled test section (Fig. 3) are calculated using the ANSYS finite element commercial software and found to be negligibly small [3,8,13,15]. Thus, the dissipated power from the uniformly heated, 10×10 mm^2 Cu nanodendrite surface layer is taken equal to that generated by the underlying heating element in the test section. This power is determined from the measured voltage across and the electric current provided to the heating element by a dc power supply (3 in Fig. 4). This power is used to determine the dissipated heat flux for the purpose of constructing the boiling curves.

In the experiments, the electrical power supplied to the heating element in the test section is increased slowly by incrementally increasing the applied voltage <0.02 V at a time. The size of the voltage increment decreases as the boiling curve approaches CHF to limit the temperature overshot associated with CHF. Following each incremental increase in the applied voltage to the heating element, the surface heat flux and the average surface temperature, after accounting for the temperature drop in the Cu substrate, are recorded when reaching a steady state. This is when the recorded difference between two successive measurements of the average surface temperature is within ±0.2 K. Each of these surface temperatures is the average of 30 readings of the two thermocouples embedded in the copper substrate (Fig. 3(*b*)).

When either of the two thermocouples in the copper substrate detects a rapid increase in temperature, in excess of 30 K in two consecutive steady state measurements, it is considered an indication of reaching CHF, and the experiment is terminated. These procedures protect the heating element in the test section from burning out when reaching CHF.

The estimated uncertainties in the present pool boiling experiments are ±0.2 K and ±0.10 V in the temperature and applied voltage measurements, $\pm2.2\%$ and $\pm3.9\%$ in the determined nucleate boiling heat flux and nucleate boiling heat transfer coefficient, $\pm2.3\%$ in the determined critical heat flux value using the procedures described earlier, and as much as 1–3 K in the surface temperature at CHF. These uncertainties are based on the methodology outlined in Ref. [24].

5 Experimental Results

The present experiments are conducted using degassed PF-5060 dielectric liquid to investigate saturation pool boiling on structurally strengthen, Cu nanodendrite surface layers (Figs. 2(*a*)–2(*c*)), deposited on 1.6 mm thick Cu substrates measuring 10×10 mm^2 in cross section. Because of the high elevation in Albuquerque, NM, the boiling point of this liquid in the experiments is 51.4°C (Table 1).

The structurally strengthened Cu nanodendrite surface layers are of different thicknesses (145.6 μm, 46.3 μm, and 33.1 μm), average macropore size, and volume porosity (Table 2). Compared with FC-72 dielectric liquid, the reported pool boiling experimental data for the PF-5060 liquid on plane, microporous, and microstructured surfaces are very few [18]. PF-5060 is relatively less expensive and has the same physical properties and saturation temperature as FC-72, except the surface tension is ~20% higher

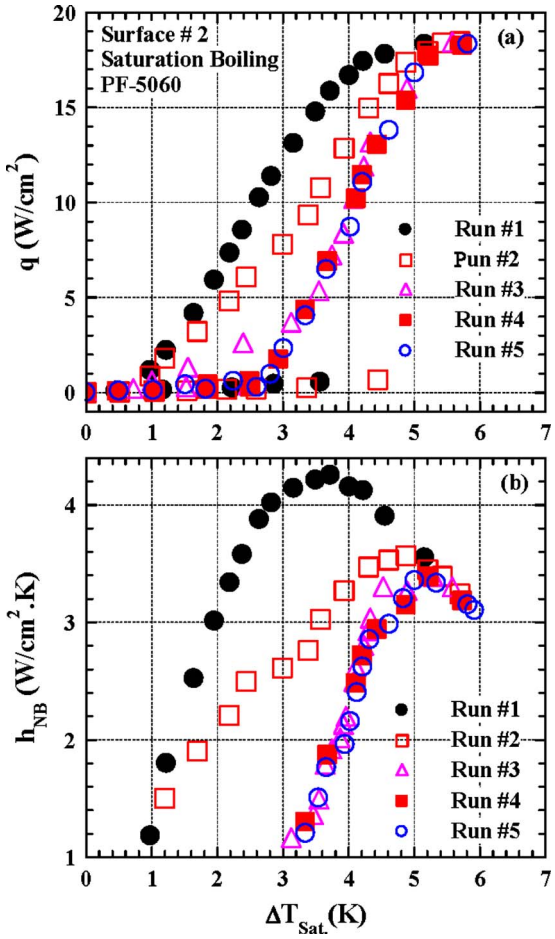

Fig. 5 Boiling and h_{NB} curves of PF-5060 on surface layer 2

(Table 1). The obtained saturation pool boiling and nucleate boiling heat transfer coefficient curves for the PF-5060 liquid on the structurally strengthened layer 1 are presented in Figs. 5(*a*) and 5(*b*).

The structurally strengthened surface layers (Figs. 2(*a*)–2(*c*)) are used individually in the experiments to investigate the effect on saturation pool boiling of PF-5060 dielectric liquid. The obtained pool boiling curves and those of nucleate boiling heat transfer coefficient, h_{NB}, are presented in Figs. 5–7. Figure 8 compares the results for surface layer 1 (Table 2) with those reported by others for saturation boiling of both FC-72 and PF-5060 on different microporous and microstructured surfaces.

5.1 Conditioning of Surface Layers. The best nucleate boiling heat transfer results of PF-5060 in the present experiments are when the Cu nanodendrite surface layers (Table 2) were used for the first time. Nucleate boiling on the thick surface layer in Fig. 2(*a*) (145.6 μm) starts consistently at a relatively small surface superheat (<0.3 K). On the thinner surface layers (Figs. 2(*b*) and 2(*c*)), nucleate boiling ensues following small excursions (<6 K) in surface temperature (Table 2, and Figs. 5–7).

When used for the first time, some layers require activation of the nucleation sites in the surface by performing the experiments first at a high heat flux for a short period of time. Subsequent to the surface activation, nucleate boiling typically begins at a low surface superheat or following a little excursion in surface temperature, depending on the thickness of the nanodendrite surface layer. Repeated experiments conditioned the surface layers. This is associated with a gradual decrease in the nucleate boiling heat flux, q, or shift of the pool boiling curves to higher surface superheats, decreasing the heat transfer coefficient, but not necessarily

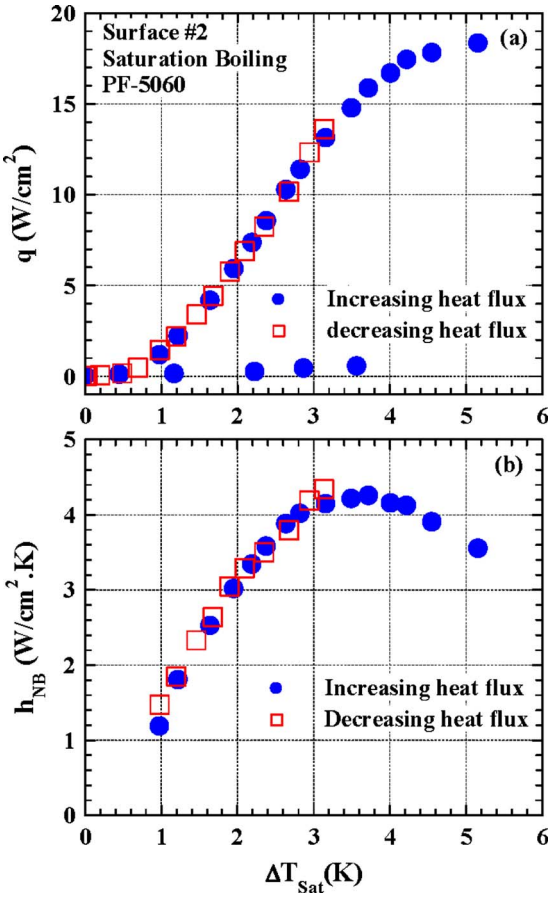

Fig. 6 Boiling hysteresis of PF-5060 on surface 2 (Table 2)

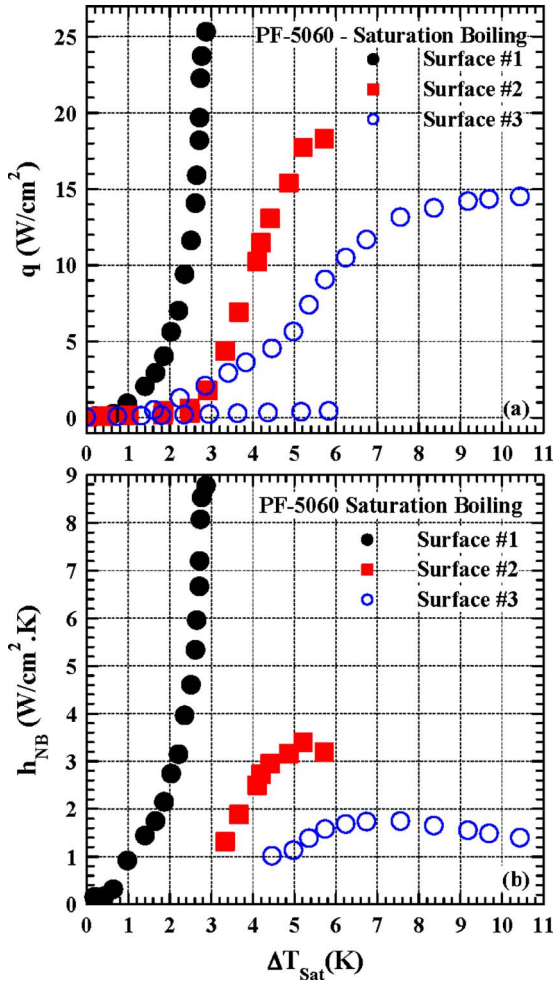

Fig. 7 Boiling and h_{NB} curves of PF-5060 on different Cu nanodendrite surface layers (Table 2)

CHF (Figs. 5–7).

After conducting several pool boiling experiments, each lasting typically 4–5 h, separated by cool down intervals of 2–14 h, the Cu nanodendrite surface layers become conditioned and the measured boiling curves are reproducible (Fig. 5(*a*)). As this figure indicates, the pool boiling curves of PF-5060 on the structurally strengthened (Fig. 2(*b*)) and conditioned nanodendrite surface layer 2 in test runs 3–5 are almost identical. The values of CHF, indicated by the last data points on the boiling curves in Figs. 5–7, and the corresponding surface superheats strongly depend on the thickness of the nanodendrite surface layer (Figs. 7 and 8). The saturation CHF of PF-5060 in the boiling experiments with surface layer 2 (Fig. 2(*b*)) is ~18.25 W/cm^2 (Fig. 5(*a*)) and as much as 25.27 W/cm^2 for the surface layer 1 (Fig. 7(*a*)). On plane copper, saturation boiling CHF for PF-5060 ranges from 13 W/cm^2 to 16 W/cm^2, depending on the surface roughness.

The nucleate boiling heat flux progressively increases with increased surface superheat until reaching CHF (Fig. 5(*a*)). The nucleate boiling heat transfer coefficient initially increases with increased surface superheat to a maximum, h_{MNB}, and then decreases with further increase in the surface superheat until reaching CHF (Fig. 5(*b*)). The h_{MNB}, occurring near the end of the fully developed nucleate boiling region, is much higher than at CHF and the corresponding surface superheat is typically lower than at CHF. For saturation boiling of PF-5060 on the conditioned surface layer 2 (Table 2 and Fig. 2(*c*)), h_{MNB}=3.35 W/cm^2 K and occurs at ΔT_{sat}=5.0 K, compared with 3.1 W/cm^2 K and 5.9 K at CHF (Figs. 5(*a*) and 5(*b*)).

5.2 Boiling Hysteresis. To examine boiling hysteresis in the present experiments, identical tests are conducted using the same Cu nanodendrite surface layers at the same conditions. The results for the conditioned surface layer 2 (Fig. 2(*b*)) are shown in Fig. 6. The boiling hysteresis is typically caused by the contribution of the thermal inertial of the surface and the metal substrate and the potential changes in the boiling process at the surface.

To quantify the boiling hysteresis in the experiments, the obtained pool boiling curves in separate tests using ascending order (or increasing heat flux) and descending order (or decreasing heat flux) of the input power to the test section are compared (Fig. 6). In the former, the input power to the heating element in the test section (Fig. 3) increases incrementally until reaching CHF, while in the latter, the experiment started at high heat flux (~14 W/cm^2) and the power to the heating element decreases incrementally.

Figures 6(*a*) and 6(*b*) for the structurally strengthened (Fig. 2(*b*)) and conditioned surface layer 2 show that the nucleate boiling heat flux and heat transfer coefficient curves obtained by incrementally increasing and decreasing the input power to the test section are almost identical. Thus, little or no boiling hysteresis exists in the present saturation boiling experiments (Table 2). These results are consistent with those of other pool boiling experiments conducted in our laboratory and reported by other investigators elsewhere using dielectric liquids such as FC-72 and HFE-7100 on different surfaces [1,3,9,13,22].

5.3 Effect of Surface Microstructure. The obtained saturation pool boiling and nucleate boiling heat transfer coefficient curves for PF-506 dielectric liquid on the structurally strengthened (Figs. 2(*a*)–2(*c*)) and conditioned surface layers 1–3 are compared

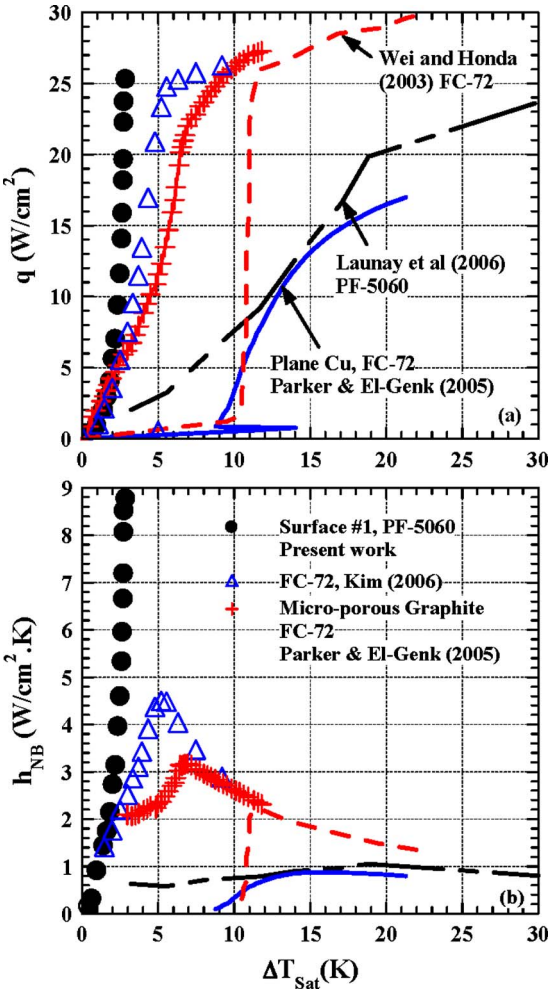

Fig. 8 Saturation boiling of FC-72 and PF-5060 on microstructured, microporous, and plane Cu surfaces

in Figs. 7(*a*) and 7(*b*). As shown in Figs. 7(*a*)–7(*c*), the best pool boiling heat transfer results, with the highest nucleate boiling heat transfer coefficients, are those for the structurally strengthened and conditioned surface layer 1 (Fig. 2(*a*)), followed by surface layers 2 and 3 (Figs. 2(*b*) and 2(*c*)). For the latter two layers, the slopes of the pool boiling curves and the CHF values are lower than for layer 1. The surface superheat, ΔT_{sat}, at CHF is also lower than on surface layer 1 (Fig. 7(*a*)). The saturation CHF for PF-5060 on surface layer 3 is 14.53 W/cm^2 and occurs at ΔT_{sat} = 10.9 K, compared with 18.25 W/cm^2 and 6.2 K on surface layer 2, and 25.27 W/cm^2 and 2.9 K on surface layer 1 (Fig. 7(*a*)).

The maximum saturation nucleate boiling heat transfer coefficient, h_{MNB}, for PF-5060, near the end of the fully developed nucleate boiling region, is highest on the structurally strengthened and conditioned surface layer 1 (8.76 W/cm^2 K) and occurs at the lowest surface superheat (2.9 K), compared with 3.4 W/cm^2 K and 5.0 K and 1.73 W/cm^2 K and 7.6 K on layers 2 and 3, respectively (Fig. 7(*b*)).

5.4 Comparison With Published Work. Figure 8 compares the present saturation boiling curve of PF-5060 dielectric liquid on surface layer 1 (Fig. 2(*a*)) with those reported for FC-72 on a Cu nanodendrite surface by Kim [22], silicon with micropin fins by Wei and Honda [25], and microporous graphite and plane copper by Parker and El-Genk [8], and for PF-5060 on silicon with carbon nanotube (CNT)-based pin fin arrays by Launay et al. [18]. The reported CHF for FC-72 by Wei and Honda [25] of

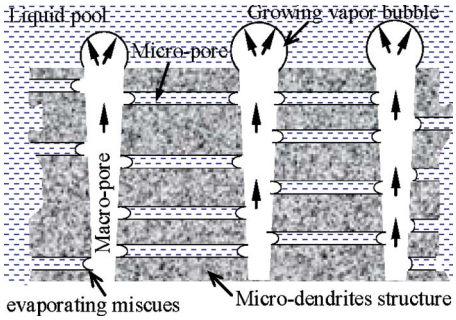

Fig. 9 An Illustration of pool boiling of dielectric liquid on Cu nanodendrite surface layers

29.8 W/cm^2 is the highest and that on plane copper of 17 W/cm^2 is the lowest. The CHF value reported by Kim [22] for FC-72 on a Cu nanodendrite surface layer is higher than the present value (25.27 W/cm^2) for PF-5060 (Fig. 8(*a*)) on the Cu nanodendrite surface layer 1 (Fig. 2(*a*)).

The present value of h_{MNB} for saturation boiling of PF-5060 on the structurally strengthened and conditioned Cu nanodendrite surface layer 1 of ~8.76 W/cm^2 K is significantly higher than that of Kim [22] (~4.5 W/cm^2.K) for FC-72 on a Cu nanodendrite surface. Both values are much higher than for FC-72 on plane copper (0.8 W/cm^2 K) [8] and occur at significantly lower surface superheats (Fig. 8(*b*)). The surface superheat at the maximum heat transfer coefficient, h_{MNB}, for PF-5060 in the present experiments (2.9 K) on surface layer 1 (Fig. 2(*a*)) is also much smaller than for FC-72 (5.1 K) on a Cu nanodendrite surface in Ref. [22] and on plane copper (~15 K) [8]. On a microporous graphite surface [8], the reported h_{MNB} for saturation boiling of FC-72 is 3.2 W/cm^2 K and occurs at surface superheat of 6.9 K (Fig. 8(*b*)).

5.5 Discussion. The open macropores within and the larger effective surface areas of the structurally strengthened Cu nanodendrite surface layers (Fig. 2) in the present experiments appear to be partially responsible for enhancing nucleate boiling heat transfer. The high volume porosity (Table 2) of the structurally strengthened surface layer 1 (Fig. 2(*a*)) compared with those of surface layers 2 and 3 (Figs. 2(*b*) and 2(*c*)) partially contributed to the enhanced nuclear boiling. The open macropores increase the circulating liquid from the overlaying pool through the fin dendrite structure by the capillary pressure developing at the liquid-vapor interface in the capillaries within the nanodendrite structure (Fig. 9). The average diameter of these capillaries could range from a fraction of a micron to a few microns (Fig. 1). The developing capillary pressure is proportional to the surface tension of the liquid and inversely proportional to the average radius of the capillaries within the nanodendrite structure (Figs. 1(*b*) and 1(*c*)). The evaporation of the liquid from the meniscus at the interface between the liquid feed capillaries and the vertical open macropores (Figs. 2 and 8) increases the vapor pressure in the macropores, forming growing bubbles at surface. When the size of these bubbles is large enough to overcome surface tension at the opening of the micropores, they detach from the surface by the buoyant force and other bubbles begin to grow at the same open macropores.

This may explains the very low surface superheat for initiating bubble nucleation on the surface of the Cu dendrite layers, particularly on layer 1 with the largest thickness and volume porosity (Table 2 and Fig. 2(*a*)). Thus, the number of the active nucleation sites on the surface could be close to that of the open macropores in the deposited and strengthened Cu dendrite layers (Fig. 2). The size and the number of the open macropores, as well as the effective surface areas, increase as the thickness of the deposited layer increases (Table 2 and Fig. 2). However, the relative contributions

of the increased surface areas in the second long period of deposition, the number and size of the open macropores and the large interconnected volume porosity of the dendrites with the deposited layers to the enhancement of nucleate boiling and CHF are not well understood at the present time and would be the subject of a future investigation by the authors.

For the thick and structurally strengthened surface layer 1 (Fig. 2(*a*)), CHF is apparently triggered by a dry-out in the liquid feed capillaries within the nanodendrite structure. However, for the thinner layers 2 and 3 (Figs. 2(*b*) and 2(*c*)), CHF could have been triggered by the lateral coalescence of growing and rising bubbles near the surface. This is suggested by the absence of the bubble coalescence region from the boiling curve for surface layer 1 and its presence in the boiling curves of the PF-5060 liquid on surface layers 2 and 3 (Figs. 5(*a*) and 7(*a*)).

6 Summary and Conclusions

Microporous Cu nanodendrite surface layers, 33.1–145.6 μm thick, are deposited using electrochemical processes on Cu substrates measuring 10×10 mm^2 in surface area and 1.6 mm thick. The thickness and microstructure of these surface layers depend on the current density used, duration of deposition, and the composition of the electrolyte solution (Table 2). In order to strengthen the structure of the deposited layers, the initial high current density (3 A/cm^2) electrochemical deposition process is followed by a long deposition period (tens of minutes) at a very low-current density of $\sim$5 mA/cm^2. The potential of the deposited and structurally strengthened Cu nanodendrites layer for enhancing nucleate boiling of degassed PF-5060 dielectric liquid is investigated experimentally at saturation condition. The thickest nanodendrite surface layer ($\sim$145.6 μm thick) gives the best boiling heat transfer results.

For PF-5060 on this surface layer (surface 1 in Table 2 and Fig. 2(*a*)), the saturation CHF of 25.27 W/cm^2 and h_{MNB} of 8.76 W/cm^2 K occur at ΔT_{sat} of only 2.9 K. The boiling heat transfer performance of the thinnest surface layer 3 of 33.1 μm thick (Fig. 2(*c*)) is inferior to surface layers 1 (Fig. 2(*a*)) and 2 (Fig. 2(*b*)). For surface layers 2 and 3, the saturation nucleate boiling heat transfer coefficient and CHF values are lower than on surface layer 1. The surface superheat at CHF is also higher than for surface layer 1 (Fig. 7(*a*)). The saturation CHF for PF-5060 on surface layer 3 is 14.53 W/cm^2 and occurs at ΔT_{sat}=10.9 K, compared with 18.25 W/cm^2 and 6.2 K on surface layer 2, and 25.27 W/cm^2 and 2.9 K on surface layer 1.

The maximum saturation nucleate boiling heat transfer coefficient, h_{MNB}, for PF-5060, near the end of the fully developed nucleate boiling region, is the highest on the structurally strengthened surface layer 1 (8.76 W/cm^2 K) and occurs at the lowest surface superheat (2.9 K), compared with 3.35 W/cm^2 K and 5.0 K and 1.73 W/cm^2 K and 7.6 K on the structurally strengthened surface layers 2 and 3, respectively. The temperature excursions before initiating boiling on layers 3 and 2 are 3.7 K and 6 K, which corresponds to surface temperatures of $\sim$55.1°C and 57.4°C, respectively. These temperatures are much lower than the maximum recommended (85°C) for the reliable operation of most silicon electronics and CPUs.

The present saturation boiling heat transfer results for PF-5060 dielectric on the 145.6 μm thick Cu nanodendrite surface layer (Fig. 2(*a*)) is very promising for cooling high power chips and CPUs, while keeping the junction temperature relatively low. The electrochemical deposition process is relatively simple and inexpensive; however, the reproducibility of results requires precise control of various parameters, such as deposition time, current density, the composition of the electrolyte solution, and the surface area of the anode and its separation distance form the Cu substrate (or cathode).

In the present experiments, the adhesion and strength of the Cu nanodendrite layers are good (Fig. 2). Planned future work will investigate the effects of surface orientation and liquid subcooling on the total thermal power removed from Cu nanodendrite surface layers by nucleate boiling and on CHF and h_{MNB} and the corresponding surface superheats.

The results reported in this paper could be very helpful for emerging cooling applications. The reported value of h_{MNB} on the structurally strengthened surface layer 1 (Fig. 2(*a*)) is significantly higher than previously reported by numerous investigators for dielectric liquids on nano- and microfinned and microstructured surfaces, microporous surfaces, and surfaces with microporous coatings. Furthermore, the present values of the surface superheat at h_{MNB} and CHF are significantly lower than reported on other surfaces, thus decreasing the temperature of the underlying CPU or high power computer chip. The present results also show that using 145.6 μm thick Cu nanodendrites surface layer that is structurally strengthened basically eliminates the surface temperature excursion before initiating nucleate boiling, a great advantage for electronics cooling applications of nucleate boiling of the highly wetting dielectric liquids. In addition to the high values of CHF and the maximum nucleate boiling heat transfer coefficient, the electrochemical processes used in the present work for depositing and structurally strengthening the nanodendrite surface layers are widely used commercially. Large surface layers could be easily deposited on metal substrates that are several centimeters in length scale for heat sinks.

Acknowledgment

This research is funded by the University of New Mexico's Institute for Space and Nuclear Power Studies.

Nomenclature

CHF = critical heat flux (W/cm^2)
h = heat transfer coefficient (W/cm^2 K)
q = heat flux (W/cm^2)
T = temperature (K)
ΔT_{sat} = $(T_W - T_{sat})$ (K)

Subscripts

MNB = maximum nucleate boiling
NB = nucleate Boiling
sat = saturation
W = boiling surface

References

[1] Arik, M., Bar-Cohen, A., and You, S. M., 2007, "Enhancement of Pool Boiling Critical Heat Flux in Dielectric Liquids by Microporous Coatings," Int. J. Heat Mass Transfer, **50**(5–6), pp. 997–1009.

[2] Yu, C. K., and Lu, D. C., 2007, "Pool Boiling Heat Transfer on Horizontal Rectangular Fin Array in Saturated FC-72," Int. J. Heat Mass Transfer, **50**, pp. 3624–3637.

[3] El-Genk, M. S., and Parker, J. L., 2008, "Nucleate Boiling of FC-72 and HFE-7100 on Porous Graphite at Different Orientations and Liquid Subcooling," Energy Convers. Manage., **49**(4), pp. 733–750.

[4] Furberg, R., Li, S., Palm, B., Toprak, M., and Muhammed, M., 2006, "Dendritically Ordered Nano-Particles in a Micro-Porous Structure for Enhanced Boiling," *Proceedings of the 13th International Heat Transfer Conference*, Sydney, Australia, Paper No. NAN-07.

[5] Kim, J. H., Kashinath, M. R., Kwark, S. M., and You, S. M., 2007, "Optimization of Microporous Structures in Enhanced Pool Boiling Heat Transfer of Saturated R-123, FC-72, and Water," ASME Paper No. HT2007-32339.

[6] Li, S., Furberg, R., Toprak, M. S., Palm, B., and Muhammed, M., 2008, "Nature-Inspired Boiling Enhancement by Novel Nanostructure Macroporous Surfaces," Adv. Funct. Mater., **18**, pp. 2215–2220.

[7] Nimkar, N. K., Bhavnani, S. H., and Jaeger, R. C., 2006, "Benchmark Heat Transfer Date for Microstructured Surfaces for Immersion-Cooled Microelectronics," IEEE Trans. Compon. Packag. Technol., **29**(1), pp. 89–97.

[8] Parker, J. L., and El-Genk, M. S., 2005, "Enhanced Saturation and Subcooled Boiling of FC-72 Dielectric Liquid," Int. J. Heat Mass Transfer, **48**, pp. 3736–3752.

[9] Rainey, K. N., and You, S. M., 2000, "Pool Boiling Heat Transfer From Plain and Microporous, Square Pin-Finned Surfaces in Saturated FC-72," ASME J. Heat Transfer, **122**, pp. 509–516.

[10] Shin, H. C., Dong, J., and Liu, M., 2003, "Nanoporous Structure Prepared by an Electrochemical Deposition Processes," Adv. Mater. (Weinheim, Ger.),

15(19), pp. 1610–1614.
[11] Vemuri, S., and Kim, K. J., 2005, "Pool Boiling of Saturated FC-72 on Nano-Porous Surface," Int. Commun. Heat Mass Transfer, **32**, pp. 27–31.
[12] Yu, C. K., Lu, D. C., and Cheng, T. C., 2006, "Pool Boiling Heat Transfer on Artificial Micro-Cavity Surfaces in Dielectric Fluid FC-72," J. Micromech. Microeng., **16**(10), pp. 2092–2099.
[13] El-Genk, M. S., and Bostanci, H., 2003, "Saturation Boiling of HFE-7100 From a Copper Surface, Simulating a Microelectronic Chip," Int. J. Heat Mass Transfer, **46**, pp. 1841–1854.
[14] Chang, J., You, S. M., and Haji-Sheikh, A., 1998, "Film Boiling Incipience at the Departure From Natural Convection on Flat, Smooth Surfaces," ASME J. Heat Transfer, **120**, pp. 402–409.
[15] Parker, J. L., and El-Genk, M. S., 2006, "Effect of Surface Orientation on Nucleate Boiling of FC-72 on Porous Graphite," ASME J. Heat Transfer, **128**, pp. 1159–1175.
[16] Webb, R. L., 2004, "Odyssey of the Enhanced Boiling Surface," ASME J. Heat Transfer, **126**, pp. 1051–1059.
[17] Jung, J.-Y., and Kwak, H.-Y., 2006, "Effect of Surface Condition on Boiling Heat Transfer From Silicon Chip With Submicron-Scale Roughness," Int. J. Heat Mass Transfer, **49**(23–24), pp. 4543–4551.
[18] Launay, S., Fedorov, A. G., Joshi, Y., Gao, A., and Ajayan, P. M., 2006, "Hybrid Micro-Nano Structured Thermal Interfaces for Pool Boiling Heat Transfer Enhancement," Microelectron. J., **37**, pp. 1158–1164.
[19] Albertson, C. E., 1977, "Boiling Heat Transfer Surface and Method," U.S. Patent No. 4,018,264.
[20] Shin, H.-C., and Liu, M., 2004, "Copper Foam Structures With Highly Porous Nanostructured Walls," Chem. Mater., **16**, pp. 5460–5464.
[21] Furberg, R., 2006, "Enhanced Boiling Heat Transfer From a Novel Nanodentritic Microporous Copper Structure," Ph.D. thesis, KTH School of Industrial Engineering and Management, Stockholm, Sweden.
[22] Kim, J. H., 2006, Enhancement of Pool Boiling Heat Transfer Using Thermally-Conductive Microporous Coating Techniques, Ph.D. thesis, UT, Arlington, TX.
[23] Bliss, F. E., Jr., Hsu, S. T., and Crawford, M., 1969, "An Investigation Into the Effects of Various Plating's on the Film Coefficient During Nucleate Boiling From Horizontal Tubes," Int. J. Heat Mass Transfer, **12**, pp. 1061–1072.
[24] Kline, S. J., 1985, "The Purposes of Uncertainty Analysis," ASME Trans. J. Fluids Eng., **107**, 153–160.
[25] Wei, J. J., and Honda, H., 2003, "Effect of Fin Geometry on Boiling Heat Transfer From Silicon Chips With Micro-Pin-Fins Immersed in FC-72," Int. J. Heat Mass Transfer, **46**, pp. 4059–4070.

Laminar Forced Convection Flow Past an In-Line Elliptical Cylinder Array With Inclination

Esam M. Alawadhi
Department of Mechanical Engineering,
Kuwait University,
P.O. Box 5969,
Safat, 13060 Kuwait
e-mail: esam@kuc01.kuniv.edu.kw

Laminar forced convection flow past an in-line elliptical cylinder array with inclination is simulated using the finite element method. The inclination of the elliptical cylinders is increased with the number of the cylinder in the array, 0 deg for the first cylinder and 90 deg for the last cylinder. The global objective of this research is to enhance the heat transfer out of the cylinders. A parametric study of heat exchanges between the cylinders and flow (expressed by the Nusselt number) is reported for Reynolds numbers between 125 and 1000, while the Prandtl number is fixed at 0.71. The results are compared with an elliptical cylinder array without inclination to assess the heat transfer enhancement. The problem is solved as transient, and a vortex shedding phenomenon is reported. The results indicated that the Reynolds number has a significant effect on the heat transfer out of the cylinders, and the inclination of the elliptical cylinders enhances heat transfer rate up to 238.59%, but pressure drop is increased as high as 700%. Also, skin-friction coefficient along the five cylinders' perimeter, plots of the velocity flow field, and temperature contours are presented. [DOI: 10.1115/1.4000061]

Keywords: elliptical cylinder array, forced convection flow, vortex shedding

1 Introduction

Flow past a cylinder array with various configurations has wide range of practical engineering applications such as in heat exchangers, boilers, condensers, and energy storage systems. The thermal performance of these systems is important in meeting the efficiency standards with low cost and environmental impact. On the other hand, flow past a cylinder array has been attracting the attention of many academic researchers because it contains interesting fluid dynamics phenomena such as flow instability, free-shear layer, flow separations, and vortex shedding, and many others.

Flow over a bank of circular tubes was addressed previously by many researchers. Zukauskas [1] studied the heat transfer from tubes in cross flow, and a correlation for the Nusselt number was presented for a wide range of Reynolds numbers. A finite element method was employed by Chen et al. [2] to solve the full Navier–Stokes and energy equations for a problem of flow around isothermal cylinders, and the Nusselt number and pressure were obtained over the entire cylinders surface. Optimum spacing between cylinders in cross-flow forced convection was determined by Stanescu et al. [3] based on experiments. Gowda et al. [4] simulated transient laminar flow past an in-line tube bank using the finite element method. In their work, the Nusselt number, pressure, and shear stress distributions around the surface of cylinders were determined. Mathematical model was developed by Wilson and Bassiouny [5] to simulate the laminar and turbulent flow around tube bank. In-line and staggered tube arrangements, as well as the single row of tubes, were studied, and the Nusselt number in case of staggered arrangement was higher than that of the in-line one in a low range of parallel spacing. Laminar two-dimensional steady cross flow in a bank of plain tubes in square and nonsquare in-line arrangements was investigated by El-Shaboury and Ormiston [6]. They indicated that the overall heat transfer was increased as the transverse pitch-to-diameter ratio was decreased and as the longitudinal pitch-to-diameter was increased.

The above studies indicated that the Reynolds number is the most important parameter that affects the heat exchange between the cylinders and flow. Obviously, increasing the Reynolds number increases the Nusselt number. However, the high Reynolds numbers condition cannot be implemented in many systems due to design strength and cost limitations. Therefore, researchers are concentrating their efforts on the heat transfer enhancement from the cylinders through the modification of the flow pattern. Destroying the hydrodynamics boundary layer and creating several separation and reattachment points at the cylinders' surface are the objectives of the flow modification technique. In this regards, researchers examined various techniques, such as using an array of delta-winglet vortex generator for in-line tubes [7], and this technique provided an overall heat transfer enhancement of about 32% but with a similar pressure drop penalty, or the surface area of the cylinders is increased by using fin. Annular-finned tube bundles in staggered and in-line were investigated by Mon and Gross [8], and the heat transfer coefficient was enhanced in the whole investigated parameter range. Instead of annular fins design, He et al. [9] studied plate fins, and they indicated that there was an optimum fin pitch at which the Nusselt number is maximized.

Another commonly used technique of heat transfer enhancement is to increase the cross-sectional area of the circular cylinders, such as using elliptical cylinders. The thermal characteristics of a single elliptical cylinder in a forced convection domain is extensively studied in literature, such as studying the effect of axial ratio on the distribution of the Nusselt number in laminar flow condition [10], the wake structure and hydrodynamic forces acting on an oscillating cylinder [11], heat transfer from a cylinder with variable angles of attack in fluctuating free stream condition [12], and mixed convection heat transfer from accelerated flow past a cylinder [13]. Studying fluid flow over a bank of elliptical cylinders was also accomplished experimentally and numerically. Flow of hot air across a single array of elliptical cylinders carrying cold water was experimentally investigated by Khan et al. [14]. The Nusselt number was increased with the Reynolds number in a power law fashion over the considered conditions. The

Contributed by the Heat Transfer Division of ASME for publication in the JOURNAL OF HEAT TRANSFER. Manuscript received December 13, 2008; final manuscript received July 23, 2009; published online April 22, 2010. Assoc. Editor: Ali Ebadian.

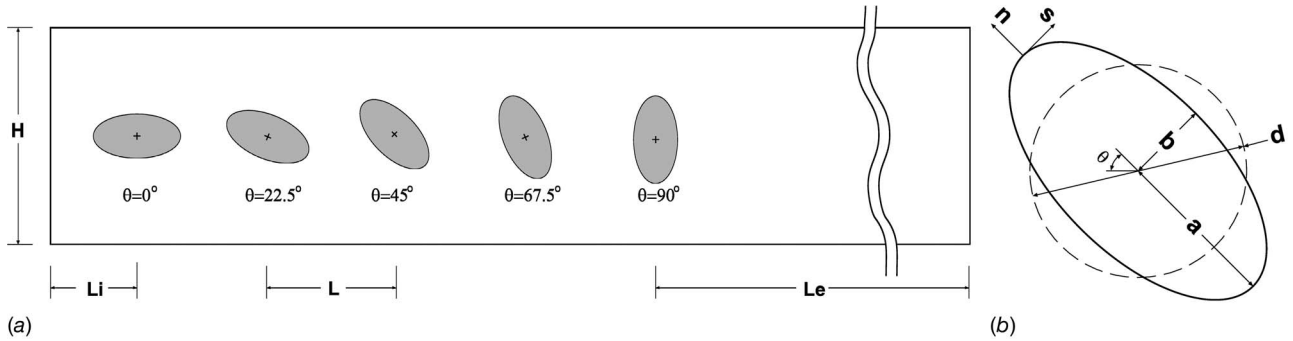

Fig. 1 (*a*) **Schematic diagrams of the elliptical cylinder array with inclination and** (*b*) **an inclined elliptical cylinder with the important geometrical parameters**

Nusselt number and drag coefficient for circular and elliptical cylinders were presented by Hasan and Siren [15] for the turbulent flow condition. It was found that the Nusselt number for the elliptical cylinders was close to that for equivalent circular cylinders for $\mathrm{Re}<4000$. However, the drag coefficient for elliptical cylinders was less than that for equivalent circular cylinders due to the slender shape of the elliptical cylinders. Matos et al. [16] enhanced heat transfer rate from finned elliptical cylinders using optimization techniques, while Tiwari et al. [17] used multiple delta-winglet type vortex generators in various configurations to improve heat transfer, and their results indicated that the Nusselt number was about 100% higher as compared with vortex generators case at a Reynolds number of 1000.

Previous results of flow past cylinder array [1–3] indicate that the heat flow out of the cylinders was drastically decreased with the number of cylinder in the row. The intercylinders are mostly exposed to the wake flow and less to core flow. This research presents a new technique to enhance heat transfer from five in-line elliptical cylinder array for laminar forced convection flow. The inclination of the elliptical cylinders is variable depending on its location in the array, and with this technique, the surface of the cylinders is exposed more to the flow and less to the wake flow. The local and average Nusselt numbers, distribution of skin friction along the five cylinders perimeter, and pressure drop are presented and compared with equivalent elliptical cylinder array without inclination to assess the effect of the inclination. To the best of the author's knowledge, the presented configuration was not address in literature before.

This paper is organized as follows: description of the considered model is illustrated in Sec. 2. The governing equations along with the boundary conditions, followed by the solution technique, are presented in Sec. 3. In Sec. 4, the validation and verification for the model are presented. Results, including fluid flow and heat transfer, are presented in Sec. 5. Finally, concluding remarks are made in the Sec. 6.

2 Model Description

The physical model consists of flow around an in-line five elliptical cylinder array, as illustrated in Fig. 1(*a*). The inclination of the elliptical cylinders increases with the number of the cylinder in the row: the first cylinder has 0 deg inclination while the last has 90 deg inclination. The fluid flow and heat transfer are solved as a transient problem to capture an expected vortex shedding street phenomenon. The working fluid is air, $\mathrm{Pr}=0.71$. Since the cylinders are tightly packed, it is assumed that no flow or heat transfer takes place in cross direction along the lateral boundaries. The length of the cylinders is typically long for heat exchangers, and therefore the flow field and heat transfer are considered to be two-dimensional, consisting of a single row. The elliptical cylinders have long and short semi-axes of (a) and (b), respectively. The inclination angle of the cylinders is θ, and Fig. 1(*b*) depicts an elliptical cylinder with the important geometrical parameters. The equation $(x/a)^2+(y,b)^2=1$ describes the surface curvature of the ellipse, and the ellipse's aspect ratio is defined as $AR=(b/a)$. The cross-sectional area of the cylinder is given by $A=(\pi ab)$. Hence, the elliptical cylinders have an equivalent diameter of $2\sqrt{ab}$. The total length of the channel is W, while the height of the channel is H. The center of the first cylinder is placed at a distance (L_i) from the channel's inlet, and center of the fifth cylinder is placed at a distance (L_e) from the exit. The distance between cylinders is L. To quantify the heat transfer enhancement due to the inclination, the results are compared with a corresponding elliptical cylinder array without inclination.

3 Mathematical Formulation and Numerical Method

Based on the characteristic scales of the average inlet velocity (u_i), equivalent diameter of the elliptical cylinder (d), dynamics pressure (ru_i^2), temperature difference (T_s-T_i), and time (H/u_i), the dimensionless variables are defined as follows:

$$u^*=\frac{u}{u_i},\quad v^*=\frac{v}{u_i},\quad x^*=\frac{x}{d},\quad y^*=\frac{y}{d},\quad P^*=\frac{P}{\rho u_i^2}$$

$$T^*=\frac{T-T_i}{T_s-T_i},\quad t^*=\frac{d}{d/u_i}$$

The two basic dimensionless groups describing the problem are the Reynolds (Re) and Prandtl (Pr) numbers, and they are defined as, respectively

$$\mathrm{Re}=\frac{\rho u_i d}{\mu},\quad \mathrm{Pr}=\frac{\mu C_p}{k}$$

Several assumptions are made to simplify the numerical simulations, and they are as follows.

a. The fluid flow is laminar and incompressible.
b. Natural convection effect of air is negligible.
c. The effect of viscous dissipation and radiation is not considered.

The problem is solved as a transient fluid flow and heat transfer. The governing equations of the mass, momentum, and energy are described in the following dimensionless form.

For mass conservation,

$$\frac{\partial u^*}{\partial x^*}+\frac{\partial v^*}{\partial y^*}=0 \tag{1}$$

For x-momentum conservation,

$$\frac{\partial u^*}{\partial t^*}+u^*\frac{\partial u^*}{\partial x^*}+v^*\frac{\partial u^*}{\partial y^*}=-\frac{\partial P^*}{\partial x^*}+\frac{1}{\mathrm{Re}}\left(\frac{\partial^2 u^*}{\partial x^{*2}}+\frac{\partial^2 u^*}{\partial y^{*2}}\right) \tag{2}$$

For y-momentum conservation,

$$\frac{\partial v^*}{\partial t^*} + u^*\frac{\partial v^*}{\partial x^*} + v^*\frac{\partial v^*}{\partial y^*} = -\frac{\partial P^*}{\partial y^*} + \frac{1}{\mathrm{Re}}\left(\frac{\partial^2 v^*}{\partial x^{*2}} + \frac{\partial^2 v^*}{\partial y^{*2}}\right) \tag{3}$$

For energy conservation,

$$\frac{\partial T^*}{\partial t^*} + u^*\frac{\partial T^*}{\partial x^*} + v^*\frac{\partial T^*}{\partial y^*} = \frac{1}{\mathrm{Re}\ \mathrm{Pr}}\left(\frac{\partial^2 T^*}{\partial x^{*2}} + \frac{\partial^2 T^*}{\partial y^{*2}}\right) \tag{4}$$

Due to the elliptic nature of the governing equations, the boundary conditions along the entire domain must be specified. At the inlet, uniform velocity is imposed, while the *y*-velocity component is assumed zero. The pressure is equal to zero at the exit. At the upper and lower walls, symmetry boundary conditions for flow and heat are specified. Uniform temperature distribution is specified at the inlet, and temperature gradient at the exit is equal to zero. No slip velocity boundary condition and constant temperature are imposed at the surface of the cylinders. The flow and thermal boundary conditions are described in the following mathematical expression.

At the inlet ($x^*=0; -1\le y^*\le 1$)

$$u^* = 1 \tag{5a}$$

$$v^* = 0 \tag{5b}$$

$$T^* = 0 \tag{5c}$$

At the exit ($x^*=W^*; -1\le y^*\le 1$)

$$P^* = 0 \tag{6a}$$

$$\frac{\partial T^*}{\partial x^*} = 0 \tag{6b}$$

At the lateral boundaries ($0\le x^*\le W$; $y^*=-1$, and $y^*=1$)

$$v^* = 0 \tag{7a}$$

$$\frac{\partial T^*}{\partial y^*} = 0 \tag{7b}$$

At the surface of the all elliptical cylinders

$$u^* = 0 \tag{8a}$$

$$v^* = 0 \tag{8b}$$

$$T^* = 1 \tag{8c}$$

The initial conditions, $t^*=0$, for the entire computational domain

$$T^* = u^* = v^* = 0 \tag{9}$$

The Nusselt number along the cylinders' surface is used to describe the heat flow out of them. The local Nusselt number is defined as

$$(\mathrm{Nu})_s = -\frac{1}{T_s^*}\frac{\partial T^*}{\partial n^*} \tag{10}$$

where n^* is the dimensionless coordinate normal to the surface. The temperature gradient at the cylinders' surface is defined as

$$\frac{\partial T^*}{\partial n^*} = \sqrt{\left(\frac{\partial T^*}{\partial x^*}\right)^2 + \left(\frac{\partial T^*}{\partial y^*}\right)^2} \tag{11}$$

The average Nusselt number is defined as

$$\mathrm{Nu} = \frac{1}{c}\oint (\mathrm{Nu})_s ds^* \tag{12}$$

where s^* is the dimensionless coordinate along the cylinders' surface, and c is the circumference of the ellipse

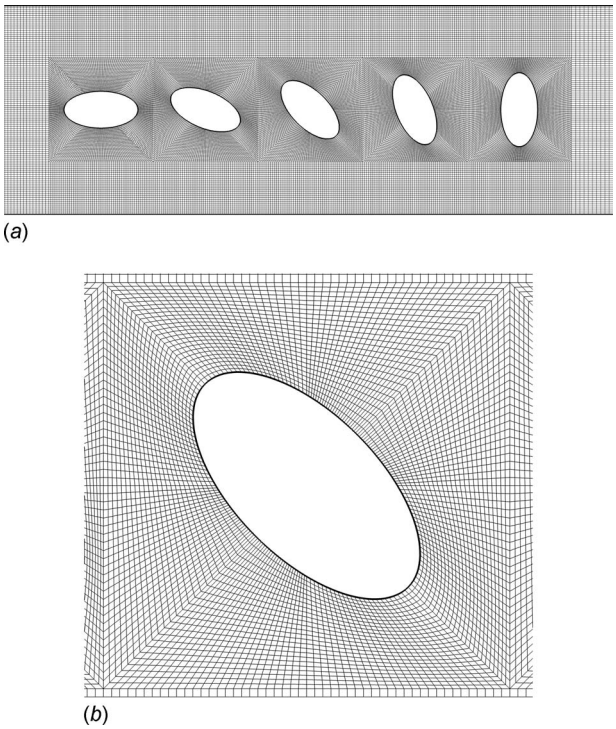

Fig. 2 (*a*) Finite element mesh near the six cylinder region and (*b*) a close-up view of the mesh at the third cylinder

$$c = \frac{\pi}{2}[3(a+b) - 2\sqrt{ab}] \tag{13}$$

The Nusselt number enhancement of the present configuration is evaluated by comparing the Nusselt number to elliptical cylinder array without inclination ($\theta=0$). The percentage of Nusselt number enhancement is defined as

$$(\mathrm{Nu})_{\mathrm{enh}} = \frac{\mathrm{Nu} - (\mathrm{Nu})_{\theta=0}}{(\mathrm{Nu})_{\theta=0}} \times 100 \tag{14}$$

where $(\mathrm{Nu})_{\theta=0}$ is the average Nusselt for an elliptical cylinder without inclination. The local skin-friction coefficient at the surface of cylinders is obtained using the following expression:

$$C_f = \left|\frac{1}{\mathrm{Re}}\left(\frac{\partial u^*}{\partial y^*} + \frac{\partial v^*}{\partial x^*}\right)\right| \tag{15}$$

The finite element method is utilized to solve the governing equations with linear quadrilateral elements. Figures 2(*a*) and 2(*b*) shows the finite element mesh near the five cylinder region and a close-up view of the mesh at third the cylinder, respectively. The numerical model consists of 60,000 elements and 61,071 nodes. The preconditional generalized minimum residual (PGMR) solver is employed to solve a set of discretization equations of energy and pressure, while the tridiagonal matrix algorithm (TDMA) solver is employed to solve the velocity fields. The relaxation factor of 0.5 was specified for all field variables. The selected solvers and advection formulation with relaxation factors stabilize the solution toward the convergence. The iterative solver was kept running until the sum of changes of a field variable calculated from the result between the current iteration and the previous iteration divided by the sum of the current values reaches the termination criterion, $\varepsilon = 10^{-6}$. The convergence criterion has the following form:

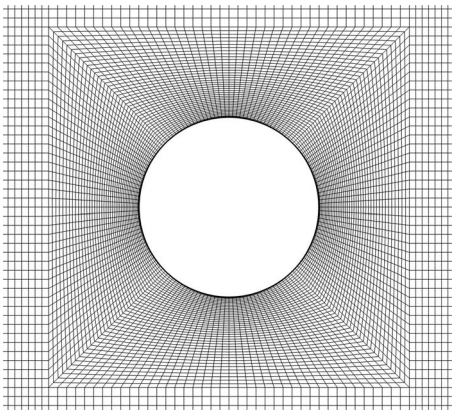

Fig. 3 The mesh near the cylinder surface of the model used for validation

$$\frac{1}{\left(\sum_{m=1}^{M}\varphi_m^i\right)}\sqrt{\sum_{m=1}^{M}(\varphi_m^i-\varphi_m^{i-1})^2}\leq\varepsilon \tag{16}$$

where the superscript i refers to the iteration number, subscript m is the node number, the M to the maximum node number, and φ is a field variable. Decreasing the value of termination criterion below the specified value does not cause any significant change in the result. All simulations were carried out using the dual Intel Xion 3.8 MHz processors workstation, and each simulation takes about 28.2 h.

4 Validation and Verification

The AIAA recommends a standard procedure for validation and verification of computational fluid mechanics analyses [18], and the present research implements the procedure to ensure that the obtained numerical results are accurate. The validation is the process of determining if computational results represent the real world, while the verification is the process of determining if computational results accurately represent the conceptual description of a model. To validate the numerical model, a uniform flow past a cylinder for a Reynolds number of 100 and 200 is simulated using the present finite element method. Flow over a single cylinder is commonly used in literature to validate a newly developed solution technique. A cylinder with dimensionless diameter of $d^*=1$ is placed in free stream, and the height and width of the computational domain are equal to $30\times d^*$ and $20\times d^*$, respectively. The cylinder is place in midheight at a distance $5\times d^*$ from the inlet. The working fluid is air with Pr=0.71. The mesh near the cylinder surface is shown in Fig. 3. The mesh is dense at the region near to the cylinder's surface to accurately capture the heat flow out of the cylinder. At the inlet, the uniform velocity profile is specified, and zero pressure is imposed at the exit. Symmetric boundary conditions are prescribed on the two lateral boundaries. Zero velocity components are specified on the surface of the cylinder. The problem is solved as transient, and the nondimensional time step of 0.05 is used in all runs. The initial condition for all field variables is equal to zero, and the simulation was kept running until a periodic condition for the vortex shedding process is established. The time history of the average pressure on the cylinder's surface is used to compute the Strouhal number, St $=f(d^*/u_i)$. The frequency is determined from the fast Fourier transform of the time history of the pressure. The Strouhal number was determined and tabulated with previously published numerical and experimental results for Re=100 and 200 in Table 1. For both the tested Reynolds numbers, Table 1 indicates that Strouhal numbers compare very well with the experimental result of Roshko [19], Norberg [20], and Williamson [21]. Additionally, the present results compare well with the numerical results of Meneghini et al. [22], Braza et al. [23], and Ding et al. [24]. To ensure that the discretization of the energy equation is correct and to ensure that the technique used to compute the average Nusselt number is precise, the average Nusselt number is determined. The surface temperature of the cylinder is equal to 1, while the flow inlet temperature is equal to zero. The present results for Re =100, 150, and 200 are compared with results from the experimental correlations by Zhuauskas [25], Knudsen and Katz [26], and Churchill and Benstein [27], and their equations are, respectively

Table 1 Comparison of the Strouhal number for a single cylinder for different values of the Reynolds number

	Strouhal number	
	Re=100	Re=200
Present study (num.)	0.163	0.196
Roshko [19] (exp.)	0.16–0.17	0.17–0.19
Norberg [20] (exp.)	0.168	0.18–0.197
Williamson [21] (exp.)	0.164	0.196
Meneghini et al. [22] (num.)	0.162	0.196
Braza et al. [23] (num.)	0.16	0.2
Ding et al. [24] (num.)	0.166	0.196

Table 2 Comparison of the average Nusselt number for a single cylinder for different values of the Reynolds number

	Nusselt number		
	Re=100	Re=150	Re=200
Present study	5.13	6.291	7.221
Zhuauskas [25]	5.1	6.246	7.212
Knudsen and Katz [26]	5.21	6.294	7.197
Churchill and Benstein [27]	5.184	6.292	7.228

$$\mathrm{Nu}=0.51\ \mathrm{Re}^{0.5} \tag{17a}$$

$$\mathrm{Nu}=0.683\ \mathrm{Re}^{0.466}\ \mathrm{Pr}^{0.333} \tag{17b}$$

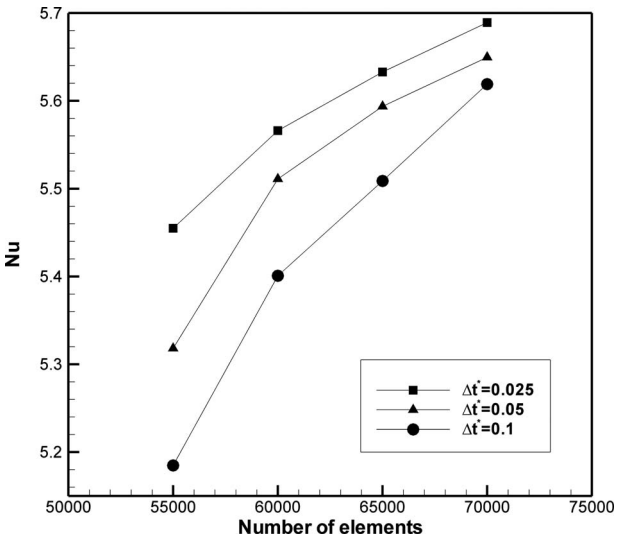

Fig. 4 The average Nusselt number for the third elliptical cylinder for different mesh sizes and time steps and for Re=500

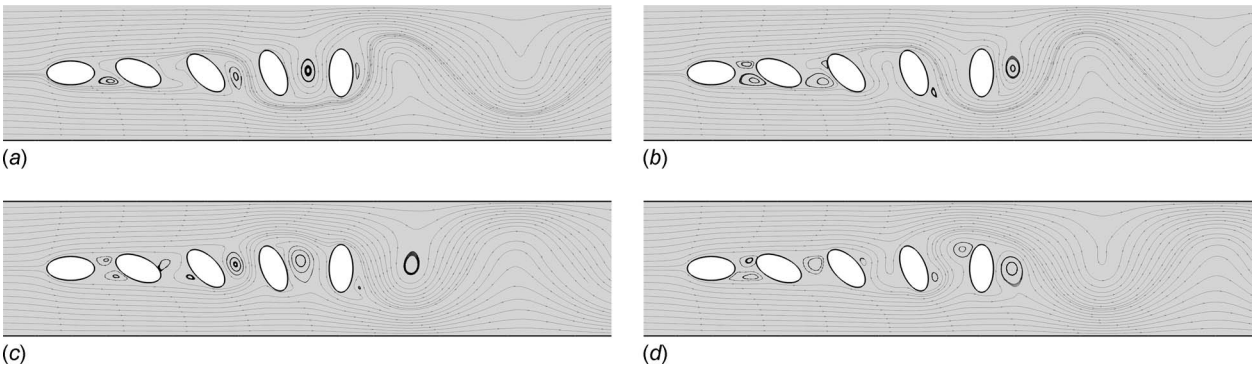

Fig. 5 Instantaneous velocity streamlines during a complete vortex shedding cycle for Re=500 and dimensionless time of t^*= (*a*) 0, (*b*) $\tau^*/4$, (*c*) $\tau^*/2$, and (*d*) $3\tau^*/4$

$$\mathrm{Nu} = 0.3 + \frac{0.62\ \mathrm{Re}^{1/2}\ \mathrm{Pr}^{1/3}}{[1+(0.4/\mathrm{Pr})^{2/3}]^{1/4}}\left[1+\left(\frac{\mathrm{Re}}{282{,}000}\right)^{5/8}\right]^{4/5} \quad (17c)$$

Table 2 shows the average Nusselt numbers for Re=100, 150, and 200 computed using the present finite element technique and those obtained from aforementioned correlations. For the examined Reynolds numbers, the average Nusselt number agrees very well with the three correlations with a maximum error of 1.56%. Hence, the results shown in Tables 1 and 2 validate the finite element method and technique used to calculate the Nusselt number.

The result of the numerical model can be significantly affected by the number of elements in the model and the selected time step. A model with a coarse mesh or using a large time step would defiantly result in less computational time, but the accuracy of the results is questionable. To ensure that the number of elements in the domain has no effect on the solution, the number of elements in the mesh presented in Fig. 2(*a*) is increased by 5000 and 10,000, and also decreased by 5000. Several sample runs confirmed that the channel exit length has no effect on the solution. Additionally, the four models are solved with three time steps of $\Delta t^*=0.025$, 0.05, and 0.1. The objective of this study is to determine the required element number and time step resulting in less computational time with an acceptable accuracy. The simulations are performed for Re=500, and the average Nusselt number is calculated for the third elliptical cylinder, and the results are presented in Fig. 4. As shown, having more elements than the base model would not significantly affect the results, and the difference between the 60,000 element and 70,000 element model is less than 3.25% with $\Delta t^*=0.025$. Also, using time step less than 0.05 would not significantly affect the results. Therefore, the numerical model is verified giving one confidence in the use of the present solution technique.

5 Results and Discussions

The thermal and fluid flow characteristics of flow over an inline elliptical cylinder array are presented. The range of the Reynolds number, $125 \le \mathrm{Re} \le 1000$, was selected because it is typical for energy systems and also to maintain laminar flow conditions [2–4]. The working fluid is air with Pr=0.7. The height of the computational domain is $H^*=4$, and distance between the cylinders is $L^*=2$. The distance between the inlet and the first cylinder is $L_i^*=4$, and the distance between the fifth cylinder and the exit is $L_e^*=14$. The ellipse's aspect ratio is equal to $AR=1/2$, and the equivalent diameter of the elliptical cylinders is $d^*=1$. The long and short semi-axes are $a^*=\sqrt{2}/2$ and $b^*=\sqrt{2}/4$, respectively. The inclination of the first, second, third, fourth, and fifth cylinders is 0 deg, 22.5 deg, 45 deg, 67.5 deg, and 90 deg, respectively. The simulation was kept running until a periodic condition for the vortex shedding process is established.

5.1 Flow Field and Temperature Contours. Figures 5(*a*)–5(*d*) show instantaneous velocity streamlines during a complete vortex shedding cycle for Re=500 and dimensionless time of $t^*=0$, $\tau^*/4$, $\tau^*/2$, and $3\tau^*/4$, where τ^* denotes one period of vortex shedding cycle. These figures show only a portion of the computational domain, $1 \le x^* \le 5$. Flow enters the channel from the left side and exits from the right side. Flow patterns, including the speed of the axial core flow and flow pattern between the

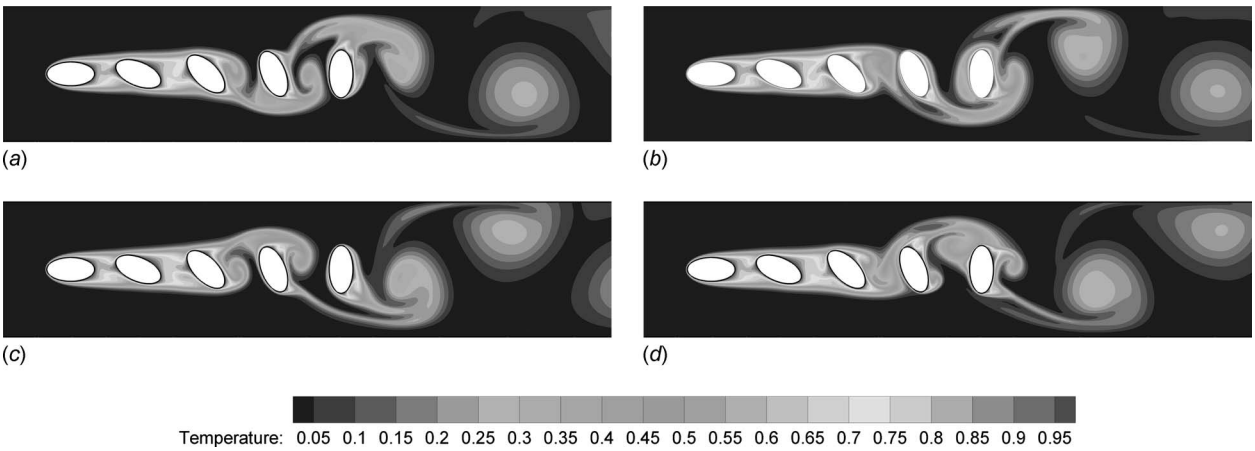

Fig. 6 time evaluation of temperature contours during a complete vortex shedding cycle for Re=500 and dimensionless time of t^*= (*a*) 0, (*b*) $\tau^*/4$, (*c*) $\tau^*/2$, and (*d*) $3\tau^*/4$

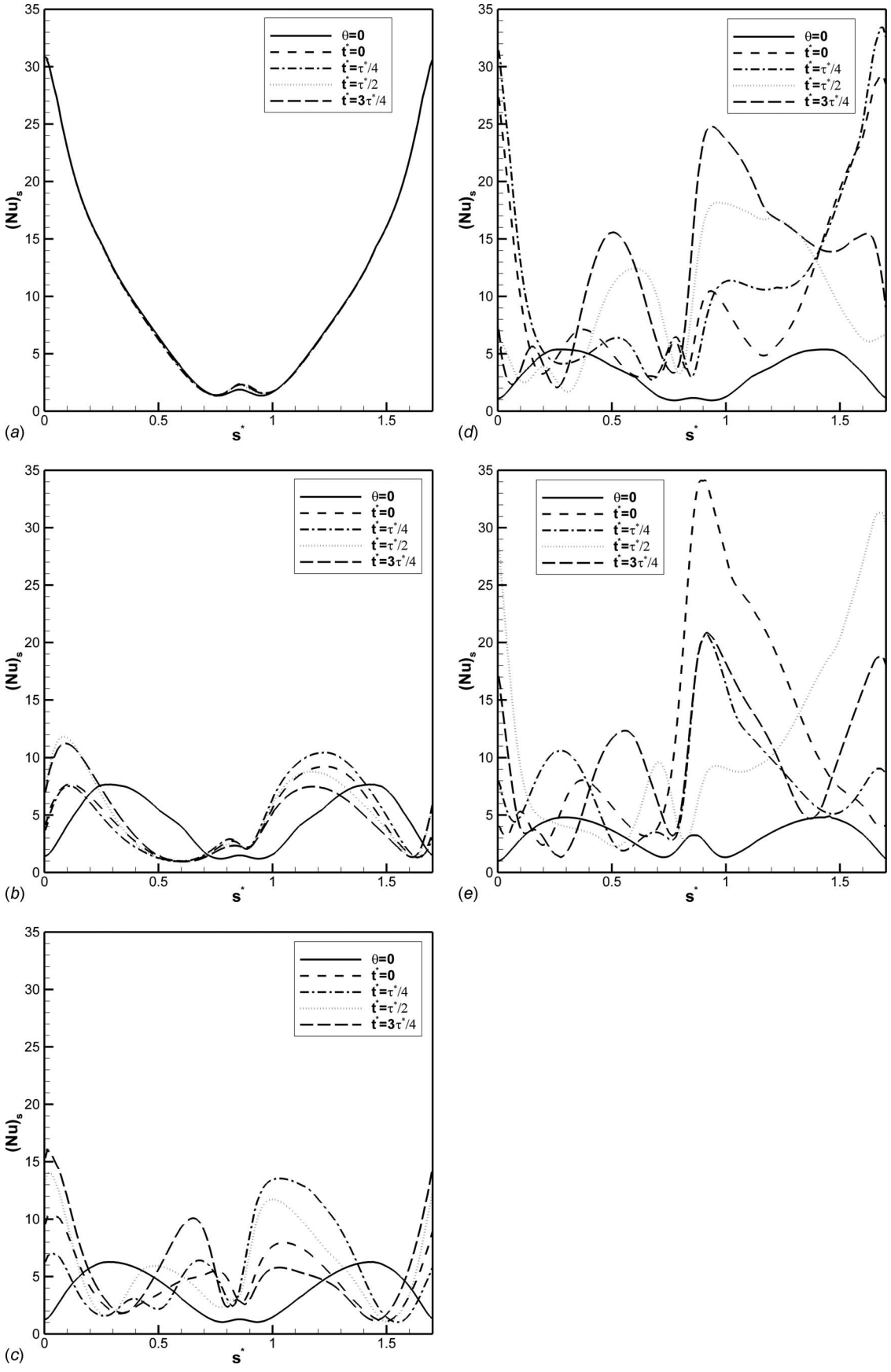

Fig. 7 Timewise variations in the local Nusselt number along the surface of the cylinders during a complete vortex shedding cycle cylinders for (*a*) cylinder 1, (*b*) cylinder 2, (*c*) cylinder 3, (*d*) cylinder 4, and (*e*) cylinder 5

Table 3 The average Nusselt number for the elliptical cylinder and percentage of the heat transfer enhancement (values in parentheses are in percent)

			Nusselt number ($(Nu)_{enh}$)			
Cylinder	C	m	Re=125	Re=250	Re=500	Re=1000
1	0.623	0.457	5.618 (0)	7.604 (0)	10.043 (0)	15.078 (2.30)
2	0.31	0.434	2.523 (0)	3.385 (0)	4.780 (3.89)	8.497 (36.57)
3	0.243	0.444	2.091 (0.25)	2.886 (2.67)	5.511 (42.97)	11.879 (126.44)
4	0.216	0.441	2.031 (11.59)	3.072 (25.53)	10.798 (222.82)	15.379 (238.59)
5	0.163	0.481	2.589 (53.55)	3.997 (74.96)	10.148 (216.1)	14.994 (227.98)

cylinders, have a significant effect on heat flow out of the cylinders. The inclination of the cylinders forces the core flow to bypass the region between the cylinders, simulating a nozzle effect and enhancing heat transfer. At the space between the first and second and second and third cylinders, no shedding of the vortices is observed, but the flow pattern varies rapidly. Vortices are formed then disappears during the cycle. The shear layer is separated from the fourth cylinder to form a vortex behind it, and after a while, this vortex detaches and impinges the fifth cylinder, initiating shedding process and drastically increases heat flow from the fourth and fifth cylinders. At the downstream, the shear layer is separated from the fifth cylinder to form a vortex street. Breath and death of vortices in the space between the cylinders and vortex shedding process enhance the heat flow from the cylinders by destroying the thermal boundary layer and reducing the thermal resistance by creating several separation and reattachment points.

Figures 6(*a*)–6(*d*) shows the time evaluation of temperature contours during a complete vortex shedding cycle for Re=500, and $t^*=0$, $\tau^*/4$, $\tau^*/2$, and $3\tau^*/4$, which correspond to the instantaneous streamlines shown in Figs. 5(*a*)–5(*d*). As shown, the flow pattern plays a major role in the distribution of the temperature contours, and varying the flow pattern causes the temperature contours to be time dependent. At dense isotherm regions, the heat transfer rate is expected to be high. The dense isotherm regions are visible from the contours, especially near the top and bottom sides of elliptical cylinders, which are directly exposed to the core flow. These sides have the thinner thermal boundary layer and then the highest heat transfer rate. In the downstream, the temperature contours with high values extend further due to the vortex shedding, and further away from the array, the fluid temperature decreases drastically because of the flow mixing.

5.2 Local and Average Nusselt Numbers. One of the main objectives in heat transfer analysis is to compute the local and average Nusselt numbers from the cylinders, $(Nu)_s$ and Nu, respectively. The effect of varying the inclination of the elliptical cylinders in the array can be best be evaluated by inspecting the local and average Nusselt number. Figure 7 shows the local Nusselt number along the five cylinders perimeter during a complete vortex shedding cycle using expression (10). The presented results are for Re=500 and $t^*=0$, $\tau^*/4$, $\tau^*/2$, and $3\tau^*/4$, which correspond to the instantaneous flow streamlines and temperature contours shown in Figs. 5(*a*)–5(*d*) and 6(*a*)–6(*d*), respectively. The distribution of the $(Nu)_s$ for elliptical cylinder without inclination is also presented in these figures to illustrate the effect of the inclination. The location of the origin of the dimensionless local coordinate system, s^* and n^*, is shown in Fig. 1(*b*). For the first elliptical cylinder, the distribution of the $(Nu)_s$ is nearly time independent and completely symmetrical, and the maximum $(Nu)_s$ occurs at the front stagnation point, while the minimum is at the rear stagnation point. In addition, the difference between the cylinder with and without inclination is negligible. However, the $(Nu)_s$ behind the first cylinder, $0.7 \le s^* \le 1.0$, slightly deviates during one cycle, showing the insignificant effect of the flow pattern variation between the first and second. For the other cylinders, the difference between the cylinder with and without inclination is evident. The variation in the $(Nu)_s$ coincides with the flow pattern variation in the space between the cylinders. The rate of heat transfer is greatest at the leading tip, which is the origin of the local coordinate system, and rear tip of the ellipse. The $(Nu)_s$ profile, featuring a double and triple hump structure, and their maximum values were significantly higher than elliptical cylinders without inclination, and the maximum values shift during the cycle. It is also observed that the $(Nu)_s$ variation intensifies with the number of cylinders in the array, while for the cylinders without inclinations, the $(Nu)_s$ decreases with the number of the cylinders in the array, showing a decreasing rate of heat transfer from the cylinders. As the cylinder inclined, its surface is exposed more to the low temperature of axial core flow, and the variation in flow pattern between the cylinder intensifies more, causing the location and stagnation and separation points to be displaced. When the inclination is introduced, the maximum $(Nu)_s$ is significantly increased with the number of cylinders in the array. For example, the maximum $(Nu)_s$ for the fourth cylinder is equal to 5.04 if the cylinder is not inclined, but with inclination, it reaches 33.5. The maximum $(Nu)_s$ for the second cylinder with inclination is enhanced by about 46% at $t^*=\tau^*/2$, and enhancement reaches about 600% for the fourth and fifth cylinders.

Table 3 shows the values of the integrated local Nusselt number over one vortex shedding cycle for all elliptical cylinders using expression (12), and the table shows the percentage of Nusselt number enhancement using expression (14). For the first cylinder, no significant heat transfer enhancement is observed over the entire range of Reynolds numbers. For the second cylinder, the enhancement is started at a Reynolds number of 500 and reaches 36.57% at Re=1000. For the third cylinder, the enhancement is started at a Reynolds number of 250 and reaches 42.97% and 126.44% at Re=500 and 1000, respectively. For the fourth and fifth cylinders, the enhancement reaches up to 238.59% for the fourth cylinder and reaches 227.98% for the fifth cylinder. The Strouhal number is calculated for Re=125, 250, 500, and 1000, and it is equal to 0.370, 0.385, 0.333, and 0.294, respectively. Table 3 also shows the values of C and m for the numerical correlation for the average Nusselt number as a function of Re, for each cylinder. The Nu is presented in the following expression:

$$\mathrm{Nu} = C\ \mathrm{Re}^m \tag{18}$$

5.3 Local Skin-Friction Coefficient and Pressure Drop. In Fig. 8, the local skin-friction coefficient, C_f, along the five cylinder perimeter during a complete vortex shedding cycle is depicted for Re=500 and $t^*=0$, $\tau^*/4$, $\tau^*/2$, and $3\tau^*/4$. The distribution of C_f for the elliptical cylinder without inclination is also presented in these figures to illustrate the effect of the inclination. For the first elliptical cylinder, the distribution of the C_f is nearly time independent and completely symmetrical, and the maximum C_f occurs at the upper and bottom surfaces of the ellipse where the flow velocity is maximum, while minimum at the front and rear stagnation points. In addition, the difference between the cylinder with and without inclination is negligible. However, the C_f behind the first cylinder, $0.6 \le s^* \le 1.1$, slightly deviates during one cycle,

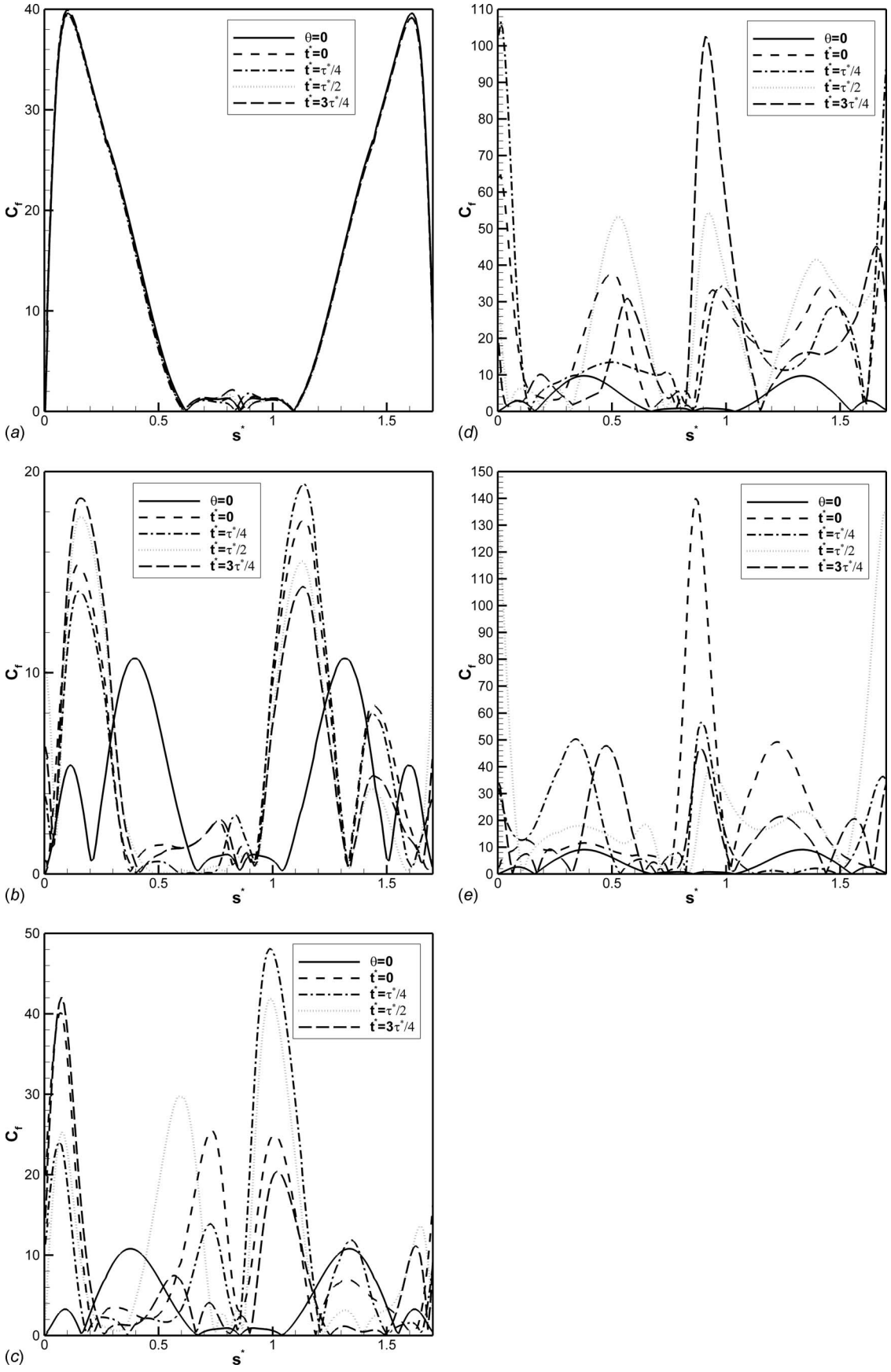

Fig. 8 Timewise variations in the local skin-friction coefficient along the surface of the cylinders during a complete vortex shedding cycle cylinders for (*a*) cylinder 1, (*b*) cylinder 2, (*c*) cylinder 3, (*d*) cylinder 4, and (e) cylinder 5

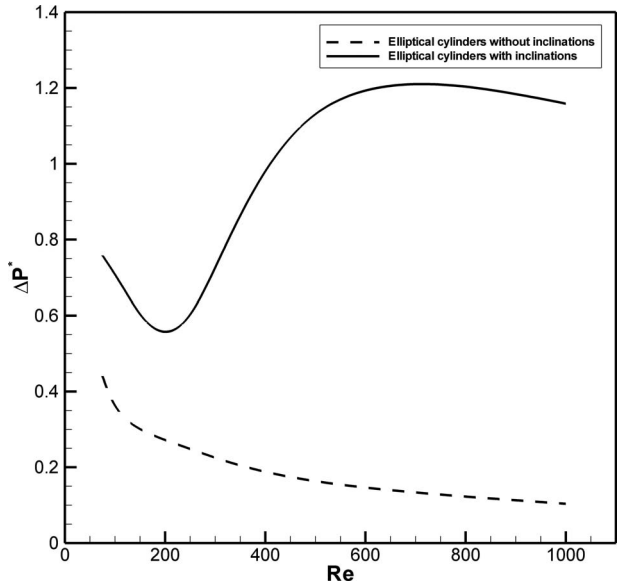

Fig. 9 The effect of the Reynolds number on the pressure drop across the channel for the elliptical cylinder array with and without inclination

showing the insignificant effect of the flow pattern variations between the first and second cylinders. Several interesting trends in the results for other cylinders are that several separation and reattachment points exist on the surface of the cylinders, and the location of separation and reattachment points are changed during one vortex shedding cycle. Also, the transient flow pattern causes a quite complicated variation in the C_f distribution. For the second cylinder, the inclination causes the C_f to increase for about 100% during the cycle and 1300% for the fifth cylinder. This significant increase in C_f has, however, a negative effect on the pressure drop and the required pumping power.

The pressure drop across the channel is determined for two examined cases: elliptical cylinder array with and without inclination. Figure 9 shows the dimensionless pressure drop for Re $=125-1000$. For the elliptical array without inclination, the pressure drop decreases with the increasing Reynolds number up to $\mathrm{Re}=600$ and then, it remains almost constant for the further increments with some tendency to decrease. Increasing the Reynolds number decreases the hydrodynamics boundary layer and, thus, significantly decreases shear stress and pressure drop. For the array with inclinations, the pressure initially deceases in the range of Reynolds number of $125\leq \mathrm{Re}\leq 250$ in a similar behavior of the cylinder array without inclinations. However, the pressure drop of the array with inclination is higher than the array with inclination case because the cross-sectional area of the channel gradually decreases. For $\mathrm{Re}>250$, the pressure drop is drastically increased to reach its maximum value of 1.2. The significant change in the flow pattern in the domain causes the pressure drop to increase. Moreover, the strength of the vortex shedding process is increased, and flow pattern variation between the cylinders becomes more intensive. The pressure drop increase can reach as high as 700% at $\mathrm{Re}=600$.

6 Conclusions

The finite element method is utilized to solve for the forced convection flow past an in-line elliptical cylinder array with inclination. The inclination of the first, second, third, fourth, and fifth cylinders is 0 deg, 22.5 deg, 45 deg, 67.5 deg, and 90 deg, respectively. The standard AIAA validation and verification procedure is performed to confirm the credibility of the present numerical results. The aim of this research is to enhance the heat transfer out of the elliptical cylinders. The range of the Reynolds number is $125\leq \mathrm{Re}\leq 1000$, while the Prandtl number is fixed at 0.71. The results are compared with an elliptical cylinder array without inclination to assess the heat transfer enhancement. The problem is solved as transient, and a vortex shedding phenomenon was reported. The results indicated that the Reynolds number has a significant effect on the heat transfer out of the cylinders, and the inclination of the elliptical cylinders enhances heat transfer for all cylinders except the first cylinder, and the enhancement can reach as high as 238.59%, but pressure drop increase can reach as high as 700%.

Nomenclature

AR = aspect ratio
C_p = heat capacity, kJ/kg K
C = constant for Eq. (18)
c = circumference of the ellipse, m
C_f = skin friction coefficient
d = diameter of a circular cylinder, m
f = frequency, 1/s
i = iteration number
k = thermal conductivity, W/m K
L = spacing between cylinders, m
L_i = distance between the first cylinder and inlet, m
L_e = distance between the last cylinder and exit, m
M = maximum node number
M = constant for Eq. (18)
Nu = average Nusselt number
$(\mathrm{Nu})_s$ = local Nusselt number
n = coordinate normal a surface, m
P = pressure $\mathrm{N/m^2}$
Pr = Prandtl number
Re = Reynolds number
St = Strouhal number
s = coordinate along a surface, m
T = temperature, K
t = time, s
u = velocity in the x-direction, m/s
v = velocity in the y-direction, m/s
W = width of the computational domain, m
x = x-coordinate, m
y = y-coordinate, m

Greek Symbols

ε = termination criterion
μ = viscosity, $\mathrm{N\,s/m^2}$
ρ = density, $\mathrm{kg/m^3}$
τ = period, s
φ = field variable
θ = inclination angle, deg

Subscripts

i = inlet
s = surface

Superscripts

i = iteration number
m = node number
* = dimensionless quantity

References

[1] Zukauskas, A., 1987, "Heat Transfer From Tubes in Cross Flow," Adv. Heat Transfer, **18**, pp. 87–157.
[2] Chen, C., Wong, K., and Cleaver, J., 1986, "Finite Element Solution of Laminar Flow and Heat Transfer of Air in a Staggered and an in-Line Tube Array," Int. J. Heat Fluid Flow, **7**, pp. 291–300.
[3] Stanescu, G., Fowler, A., and Bejan, A., 1996, "The Optimal Spacing of Cylinders in Free-Stream Cross-Flow Forced Convection," Int. J. Heat Mass Transfer, **39**, pp. 311–317.
[4] Gowda, Y., Patnaik, B., Narayana, P., and Seetharamu, K., 1998, "Finite Ele-

ment Simulation of Transient Laminar Flow and Heat Transfer Past an in-Line Tube Bank," Int. J. Heat Fluid Flow, **19**, pp. 49–55.
[5] Wilson, A., and Bassiouny, M., 2000, "Modeling of Heat Transfer for Flow Across Tube Banks," Chem. Eng. Process., **39**, pp. 1–14.
[6] El-Shaboury, A., and Ormiston, S., 2005, "Analysis of Laminar Forced Convection of Air Crossflow in in-Line Tube Banks With Non-Square Arrangements," Numer. Heat Transfer, Part A, **48**, pp. 99–126.
[7] Joadar, A., and Jacobi, A., 2007, "A Numerical Study of Flow and Heat Transfer Enhancement Using an Array of Delta-Winglet Vortex Generators in a Fin-and Tube Heat Exchanger," ASME J. Heat Transfer, **129**, pp. 1156–1166.
[8] Mon, M., and Gross, U., 2004, "Numerical Study of Fin-Spacing Effect in Annular-Finned Tube Heat Exchangers," Int. J. Heat Mass Transfer, **47**, pp. 1953–1964.
[9] He, Y., Tao, W., Song, F., and Zhang, W., 2005, "Three-Dimensional Numerical Study of Heat Transfer Characteristics of Pain Plate Fin-and-Tube Heat Exchangers From View Point of Field Synergy Principle," Int. J. Heat Fluid Flow, **26**, pp. 459–473.
[10] Faruquee, Z., Ting, D., Fartaj, A., Barron, R., and Carriveau, R., 2007, "The Effects of Axis Ratio on Laminar Fluid Flow Around an Elliptical Cylinder," Int. J. Heat Fluid Flow, **28**, pp. 1178–1189.
[11] Kocabiyik, S., and D'Alessio, S., 2004, "Numerical Study of Flow Around an Inclined Elliptical Cylinder Oscillating in Line With Incident Uniform Flow," Eur. J. Mech. B/Fluids, **23**, pp. 279–302.
[12] Ahmad, E., and Badr, H., 2002, "Mixed Convection From an Elliptical Tube at Different Angle of Attack Placed in a Fluctuating Free Stream," Heat Transfer Eng., **23**, pp. 45–61.
[13] D'Alessio, S., Saunders, M., and Harmsworth, D., 2003, "Forced and Mixed Convection Heat Transfer From Accelerated Flow Past an Elliptical Cylinder," Int. J. Heat Mass Transfer, **46**, pp. 2927–2946.
[14] Khan, M., Fartaj, A., and Ting, D., 2004, "An Experimental Characterization of Cross-Flow Cooling of Air Via an in-Line Elliptical Tube Array," Int. J. Heat Fluid Flow, **25**, pp. 636–648.
[15] Hasan, A., and Siren, K., 2007, "Comparison of External Surface Heat Transfer Coefficients for Circular and Oval Tubes," Heat Transfer Eng., **28**, pp. 640–644.
[16] Matos, R., Laursen, T., Vargas, J., and Bejan, A., 2004, "Three-Dimensional Optimization of Staggered Finned Circular and Elliptic Tubes in Forced Convection," Int. J. Therm. Sci., **43**, pp. 477–487.
[17] Tiwari, S., Maurya, D., Biswas, G., and Eswaran, V., 2003, "Heat Transfer Enhancement in Cross-Flow Heat Exchangers Using Tubes and Multiple Delta Winglets," Int. J. Heat Mass Transfer, **46**, pp. 2841–2856.
[18] AIAA, 1998, "Guide for the Verification and Validation of Computational Fluid Dynamics Simulations," Paper No. G-077-1998.
[19] Roshko, A., 1954, "On the Drag and Shedding Frequency of Two Dimensional Bluff Bodies," National Advisory Committee for Aeronautics, Washington, DC, NACA Technical Note No. 3169.
[20] Norberg, C., 2003, "Fluctuating Lift on a Circular Cylinder: Review and New Measurements," J. Fluids Struct., **17**, pp. 57–96.
[21] Williamson, C., 1991, "2-D and 3-D Aspects of the Wake of a Cylinder and Their Relation to Wake Computations," *Vortex Dynamics and Vortex Method* (Lectures in Applied Mathematics), Vol. 28.
[22] Meneghini, J., Saltara, F., and Ferrari, J., 2001, "Numerical Simulation of Flow Interference Between Two Circular Cylinders in Tandem and Side-by-Side Arrangement," J. Fluids Struct., **15**, pp. 327–350.
[23] Braza, M., Chassaing, P., and Ha, H., 1986, "Numerical Study and Physical Analysis of the Pressure and Velocity Field in the Near Wake of a Circular Cylinder," J. Fluid Mech., **165**, pp. 79–130.
[24] Ding, H., Shu, C., Yeo, Y., and Xu, D., 2007, "Numerical Simulation of Flows Around Two Circular Cylinders by Mesh-Free Least Square-Based Finite Difference Methods," Int. J. Numer. Methods Fluids, **53**, pp. 305–332.
[25] Zhuauskas, A., 1972, "Heat Transfer From Tubes in Cross-Flow," *Advances in Heat Transfer*, Vol. 8, Academic, New York.
[26] Knudsen, J., and Katz, D., 1958, *Fluid Dynamics and Heat Transfer*, McGraw-Hill, New York.
[27] Churchill, S., and Benstein, M., 1977, "A Correlating Equation for Forced Convection From Gases and Liquids to a Circular Cylinder in Crossflow," ASME J. Heat Transfer, **99**, pp. 300–306.

High Rotation Number Effect on Heat Transfer in a Triangular Channel With 45 deg, Inverted 45 deg, and 90 deg Ribs

Yao-Hsien Liu
Department of Mechanical Engineering,
National Chiao Tung University,
Hsinchu 30010, Taiwan
e-mail: yhliu@mail.nctu.edu.tw

Michael Huh
Department of Mechanical Engineering,
University of Texas at Tyler,
Tyler, TX 75799
e-mail: mhuh@uttyler.edu

Je-Chin Han
Department of Mechanical Engineering,
Turbine Heat Transfer Laboratory,
Texas A&M University,
College Station, TX 77843-3123
e-mail: jc-han@tamu.edu

Hee-Koo Moon
Solar Turbines Inc.,
San Diego, CA 92186

Heat transfer and pressure drop have been experimentally investigated in an equilateral triangular channel ($D_h = 1.83$ cm), which can be used to simulate the internal cooling passage near the leading edge of a gas turbine blade. Three different rib configurations (45 deg, inverted 45 deg, and 90 deg) were tested at four different Reynolds numbers (10,000–40,000), each with five different rotational speeds (0–400 rpm). The rib pitch-to-height (P/e) ratio is 8 and the height-to-hydraulic diameter (e/D_h) ratio is 0.087 for every rib configuration. The rotation number and buoyancy parameter achieved in this study were 0–0.58 and 0–2.3, respectively. Both the rotation number and buoyancy parameter have been correlated with predict the rotational heat transfer in the ribbed equilateral triangular channel. For the stationary condition, staggered 45 deg angled ribs show the highest heat transfer enhancement. However, staggered 45 deg angled ribs and 90 deg ribs have the higher comparable heat transfer enhancement at rotating condition near the blade leading edge region. [DOI: 10.1115/1.4000986]

Keywords: heat transfer, turbulence promoter, triangular channel, high rotation number

1 Introduction

The leading edge of the gas turbine blade is critical due to high heat load. Internal cooling technique can be applied by circulating compressed air through the multipass cooling cavities inside blade structure. Cooling channels with different geometry are applicable to different regions of the turbine blade, as shown in Fig. 1. It shows that the triangular-shaped channel and wedge-shaped channel can be applied to the leading edge and trailing edge of the blade, respectively. Internal cooling is influenced by the channel aspect ratio, turbulence promoter configurations, rotational and flow parameters. *Gas Turbine Heat Transfer and Cooling Technology* [1] provides in-depth information about the state of the art cooling techniques.

Early internal cooling research began with square or rectangular channels [2–5]; however, they are commonly used in the middle portion of the turbine blade. A triangular-shaped cooling channel is a more realistic design to fit the profile of the blade leading edge. Studies focused on triangular channels at stationary condition provide a good starting point to understand the heat transfer in leading edge cavities. The heat transfer and pressure drop measurements inside the triangular channel were in good agreement with the correlations developed for turbulent tube flow using the hydraulic diameter of the triangular duct as the tube diameter [6]. Metzger and Vedula [7] experimentally measured heat transfer in triangular channels with angled ribs on two walls. They studied three different rib angles and three different sets of rib orientations. For all the test configurations, 60 deg angled ribs produce higher heat transfer than 30 deg angled ribs, and $P/e=7.5$ rib spacing yield the best thermal performance (TP). Zhang et al. [8] tested heat transfer in a triangular duct with full and partial ribbed walls. They found that the heat transfer coefficients and friction factors in triangular ducts with partial ribbed walls (90 deg or 45 deg ribs) were 10% higher than those with fully ribbed walls. Haasenritter and Weigand [9] performed a numerical study of heat transfer in a rib-roughened triangular channel. The results show good agreement with the experimental data from Ref. [7]. Ahn and Son [10] studied heat transfer and pressure drop in a rib-roughened equilateral triangular channel with $P/e=4$, 8, and 16. They concluded that the $P/e=8$ had the best thermal performance with the Reynolds number from 10,000 to 70,000. Amro et al. [11] also experimentally investigated heat transfer inside a ribbed triangular channel. Considering the local as well as overall heat transfer enhancement and the friction factor, they concluded that 45 deg inclined ribs were the optimum. Not only the triangular channels have been studied, the trapezoidal channels with the similar shape also provide valuable information. Taslim et al. [12] measured heat transfer coefficients and friction factor in the trapezoidal channel by liquid crystal technique. They found that the roughening of the partition walls enhances the heat transfer coefficients on those walls but, more importantly, enhances heat transfer coefficients on the primary walls considerably. Takeishi et al. [13] performed an experimental and analytical study on the heat transfer and pressure drop in a triangular cooling channel with the gap between sidewall and ribs. The conclusion was optimizing the length of the gap enables the enhancement of the heat transfer around the trailing edge and to assure mean heat transfer in the while of the cooling flow passage.

In the actual turbine blade, the rotor blade is rotating and the effect of rotation in the cooling channels should be considered. The secondary flow induced by rotation has great impact in the smooth channel as well as in the ribbed channel. Dutta et al. [14] studied heat transfer in a two-pass rotating triangular duct with the rotation number from 0 to 0.22. They studied two channel orientations to the direction of rotation. For the radially outward flow in the first pass, the Nusselt number ratios increase with rotation on the trailing wall and reduce on the leading wall. Lee et al. [15] measured the heat transfer and pressure drop in a rotating equilateral triangular channel with three different rib arrangements: 45 deg, 90 deg, and 135 deg. The highest rotation number was 0.1 at

Contributed by the Heat Transfer Division of ASME for publication in the JOURNAL OF HEAT TRANSFER. Manuscript received August 8, 2009; final manuscript received November 1, 2009; published online April 29, 2010. Assoc. Editor: Frank Cunha.

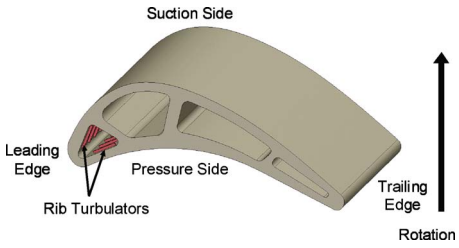

Fig. 1 Internal gas turbine blade cooling passage

Reynolds number of 10,000. They showed that the thermal performance for 45 deg and 135 deg angled ribs is very similar and both are higher than the 90 deg ribs.

The effect of rotation needs to be tested under high rotation numbers in order to simulate the actual engine condition. Currently, most of the data available in the high rotation number domain is limited to square or rectangular channel. Wagner et al. [16] performed heat transfer measurements inside a smooth square channel with radial outward flow in the first pass. The rotation number ranged from 0.00 to 0.48 in their studies. Wagner et al. [17] continued to investigate the heat transfer inside the second and third passage of the smooth square channel. The results from Refs. [16,17] showed that both the rotation number and density ratio (DR) caused large changes in heat transfer for radially outward flow but relatively small changes for radially inward flow. Johnson et al. [18] performed heat transfer measurements in a rotating square channel with ribs skewed to the flow and compared the results from the smooth channel. They found that heat transfer with skewed ribs is less sensitive to the buoyancy than the heat transfer inside the smooth channel or normal ribbed channel. Zhou et al. [19] investigated the heat transfer in a 4:1 channel under high rotation numbers from 0 to 0.6. They concluded that there is a critical rotation number where the trend of the heat transfer enhancement begins to reverse. Liou et al. [20] investigated the heat transfer in a rectangular channel ($AR=1:2$) with 45 deg angled ribs under high rotation numbers from 0 to 2. They found that the 45 deg staggered ribs generated overall heat transfer enhancement of 1.6–4.3 times higher than the Dittus–Boelter correlation in the Reynolds number range of 5000–15,000. Liu et al. [21] studied the heat transfer in a two-pass rectangular ($AR=1:4$) channel under high rotation numbers from 0 to 0.67. They found that the buoyancy parameter can be used to quantify the effect of rotation. Wright et al. [22] conducted heat transfer measurements in a wedge-shaped trailing edge channels under high rotation numbers from 0 to 1.0. It showed that the nondimensional rotation number and buoyancy parameter not only can be used in the rectangular channel but also valid in this wedge-shaped channel.

Liu et al. [23] investigated the heat transfer inside an equilateral triangular channel with a smooth and 45 deg angled ribbed surface. The objective is to do an extended research from the previous study [23], and the performance of different rib configurations inside this triangular cooling channel is compared. The details are as follows.

1. Investigate heat transfer distribution in the equilateral triangular ribbed channel under stationary and rotating conditions. Since the thermal load varies near the leading edge of the turbine blade, each surface of the channel is divided into two regions to provide local heat transfer distribution.
2. Study heat transfer and pressure drop inside the triangular channel with three different rib configurations (45 deg, inverted 45 deg, and 90 deg). The highest rotation number is 0.58 under the applicable Reynolds number of 10,000.
3. The Reynolds numbers, the rotational speeds, and the coolant-to-wall density ratios were varied in order to obtain a thorough understanding of the rotation number and buoyancy parameter effects. Correlation functions have been generated to predict the heat transfer enhancement.

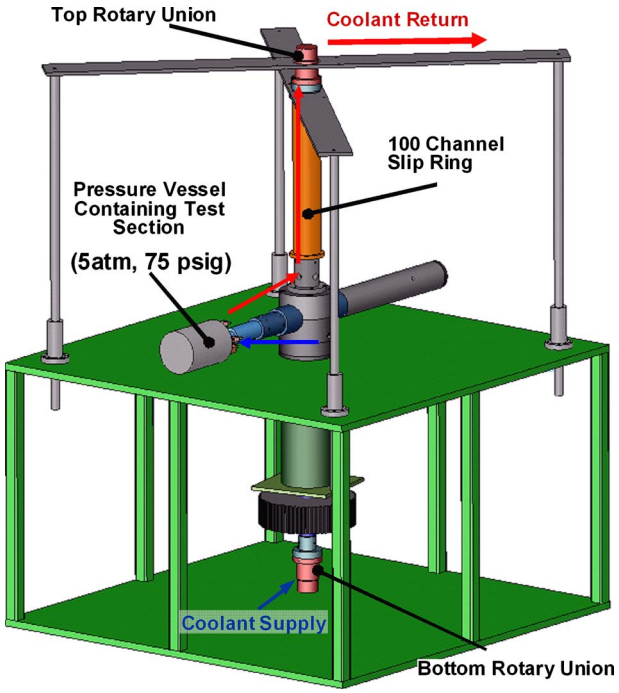

Fig. 2 Rotating facility

2 Experimental Setup

2.1 Rotating Facility. The study of heat transfer inside rotating cooling channel is performed in a rotating facility as shown in Fig. 2. Coolant air enters from the bottom of the rig through a rotary union into the hollow shaft. The air continues to travel through the hub to a rubber hose and goes into the pressure vessel containing the test section. After the air passes through the heated test section, the air goes through another rubber hose to the copper tubing inside slip ring. The copper tubing connects to another rotary union at the top of the slip ring. A needle valve is attached to the pipe to adjust the pressure of the flow loop. With the air pressurized at 5 times atmospheric pressure, the rotation number reached in this triangular channel is 0–0.58. A motor is used to drive the shaft with a frequency controller to control the rotational speeds from 0 rpm to 400 rpm. A 100 channel slip-ring is used as an interface to transfer the data reading from the rotating test section to the data acquisition system.

2.2 Triangular Channel With Ribs. The equilateral triangular test section used is shown in Fig. 3(*a*). The coolant air comes from a 1.27 cm diameter pipe into the inlet part. Two mesh screens were placed at the inlet part to help spread the flow. The thickness of the inlet part is 3.81 cm with the $L_e/D_h=2.09$. The inlet part has a slot with the same cross section as the triangular test section and is fully attached to the test section parts. The coolant flow goes radially outward into the test section and discharges into the cavity of the pressure vessel then back to the flow loop. Two pressure taps were placed at the inlet and another two pressure taps were placed at the outlet to measure the pressure drop across the test section.

The triangular test section consists of three parts: leading, trailing, and inner walls as shown in Fig. 3(*b*). These three pieces are made of Garolite and the thickness of each piece is 2.54 cm. The size of each copper plate is 1.35×1.11 cm^2 with the thickness of 0.476 cm. The copper plates on the leading and trailing surfaces were in staggered arrangement. The gaps between the copper plates were filled with silicon as an insulation layer. A blind hole

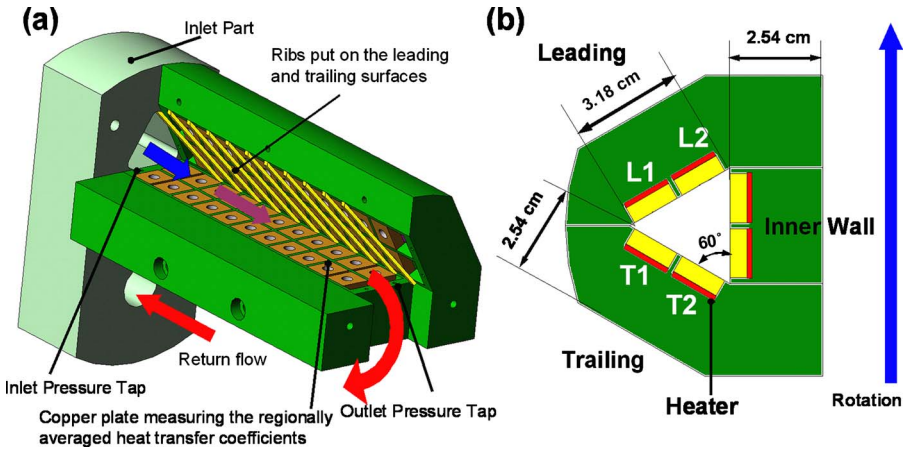

Fig. 3 (*a*) **Details of the triangular test section and** (*b*) **cross-sectional view of the test section**

was drilled in each copper plate and a thermocouple was glued in each hole with epoxy. Electric resistant heaters were placed beneath the copper plates in each row. The channel orientation was 90 deg to the direction of rotation.

In the current study, the ribs were glued on the leading and trailing surfaces with super glue. The square ribs were made of brass with the cross section of 1.59×1.59 mm^2. Three different rib configurations were tested with the same P/e ratio of 8 and e/D_h ratio of 0.087. Figure 4 shows these three rib configurations (45 deg angled, inverted 45 deg angled, and 90 deg orthogonal). Due to the staggered arrangement of the copper plates, the ribs on the leading surface and trailing surface were also staggered. In order to eliminate the conduction effects caused by the continuous ribs across different surfaces, insulation was filled between the gaps as shown in Fig. 4.

3 Data Reduction

3.1 Heat Transfer Measurement. As described with the experimental setup, regionally averaged heat transfer coefficients were measured in the current study. The heat transfer coefficients can be determined from Newton's Law of Cooling as demonstrated in Eq. (1).

$$h = \frac{\dot{Q}_{\text{net}}}{A(T_{w,x} - T_{b,x})} = \frac{\dot{Q}_{\text{in}} - \dot{Q}_{\text{loss}}}{A(T_{w,x} - T_{b,x})} \tag{1}$$

The net rate of heat transfer is determined from the difference of the power supplied to each resistance heater and the heat lost from the test section. The heat loss is determined by inserting the insulation material into the channel to eliminate natural convection. Power is supplied by the heaters, and the power required to reach a series of given temperatures is recorded. The power supplied to the heaters during this calibration is equivalent to the actual experimental heat loss. Separate heat loss calibrations are required for each rotational speed.

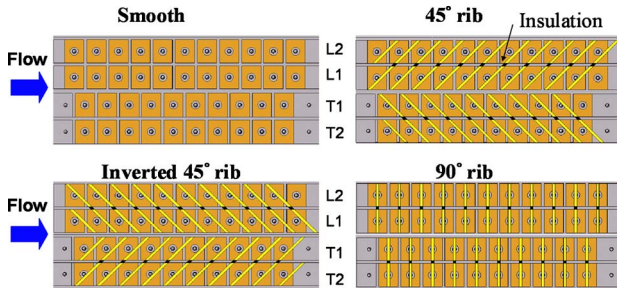

Fig. 4 Rib configurations of the current study

The regional wall temperature ($T_{w,x}$) is measured using the thermocouple fixed in each copper plate. The coolant bulk temperature at a specific location ($T_{b,x}$) in the channel is determined by the linear interpolation between the measured inlet and outlet temperatures. The Nusselt number is used to quantify the heat transfer enhancement (or declination) due to either the specific channel geometry or rotation. The Nusselt number ratio (Nu/Nu_o) is used to show the heat transfer enhancement relative to fully developed, turbulent heat transfer in a circular tube (Dittus–Boelter–McAdams correlation, Nu_o). Equation (2) shows this Nusselt number ratio.

$$\frac{\text{Nu}}{\text{Nu}_o} = \left(\frac{hD_h}{k}\right)\left(\frac{1}{0.023\ \text{Re}^{0.8}\ \text{Pr}^{0.4}}\right) \tag{2}$$

3.2 Friction Factor Ratio and Thermal Performance. The friction factor can be calculated from the pressure drop between the inlet and the outlet of the channel as shown in Eq. (3).

$$f = (\Delta P)/4\left(\frac{L}{D_h}\right)\frac{1}{2}\rho V^2 \tag{3}$$

The pressure difference (ΔP) is taken as the difference between the inlet pressure and outlet pressure readings. The frictional losses can then be calculated by dividing the fiction factor by the turbulent friction factor in a smooth tube as given by the Blasius equation. With the friction factor in a smooth tube defined as f_o, the friction factor ratio can be expressed in terms of the measured friction factor, and the smooth channel friction factor, as shown in Eq. (4).

$$f/f_0 = f/0.079\ \text{Re}^{-0.25} \tag{4}$$

Based on the heat transfer enhancement (Nu/Nu_o) and the frictional loss penalty (f/f_o), the TP for a given rib configuration can be calculated. Equation (6) shows the thermal performance based on the constant pumping power condition.

$$\text{TP} = (\text{Nu}/\text{Nu}_0)/(f/f_0)^{1/3} \tag{5}$$

3.3 Uncertainty Analysis. The experimental uncertainty for the presented results was calculated using the method developed and published by Kline and McClintock [24]. Air properties were taken based on the mean bulk air temperature. The uncertainty for the temperature measurement in the triangular channel is 0.3°C. The uncertainty of the Nusselt number ratio is approximately

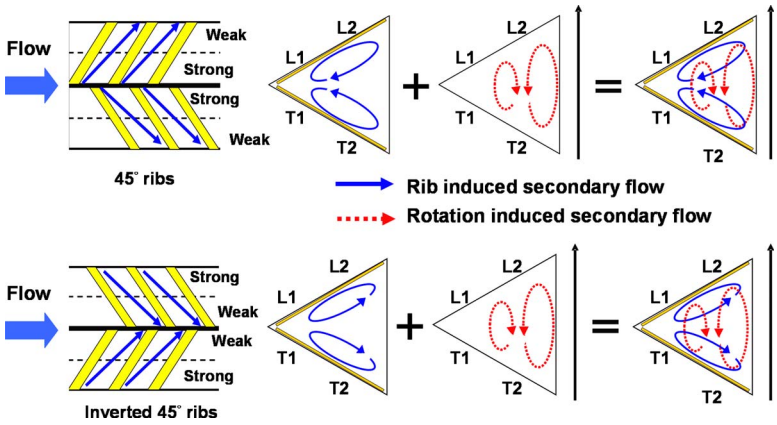

Fig. 5 Conceptual view of the rib and rotation induced secondary flow in a rotating ribbed channel

4.9% for the highest Reynolds number (Re=40,000). For the lowest Reynolds number (Re=10,000), the maximum uncertainty is approximately 9.8%. The maximum uncertainty for the pressure measurement is 9.7% at Re=10,000 and drops to 4.7% at Re =40,000.

4 Results and Discussion

4.1 Heat Transfer in the Stationary Channel. In the current experimental setup, it is in the developing flow condition because of the short entrance length (L_e/D_h=2.09). Heat transfer is enhanced and the baseline data comparisons were shown in the previous work [23]. Heat transfer is influenced by the channel geometry and the flow condition inside the stationary channel. Angled ribs induce secondary flow along the rib orientations as speculated in Fig. 5 and heat transfer distribution is altered. 45 deg angled ribs induced secondary flow goes from the rib leading region (L1 and T1) toward the rib trailing region (L2 and T2). The strength of this secondary flow decreases along the rib orientation and it tends to impinge on the rib leading region (L1 and T1). Therefore, the heat transfer enhancement is higher in the rib leading region (L1 and T1) than the rib trailing region (L2 and T2). For inverted 45 deg angled ribs, the secondary flow structure is reversed as the rib is inverted.

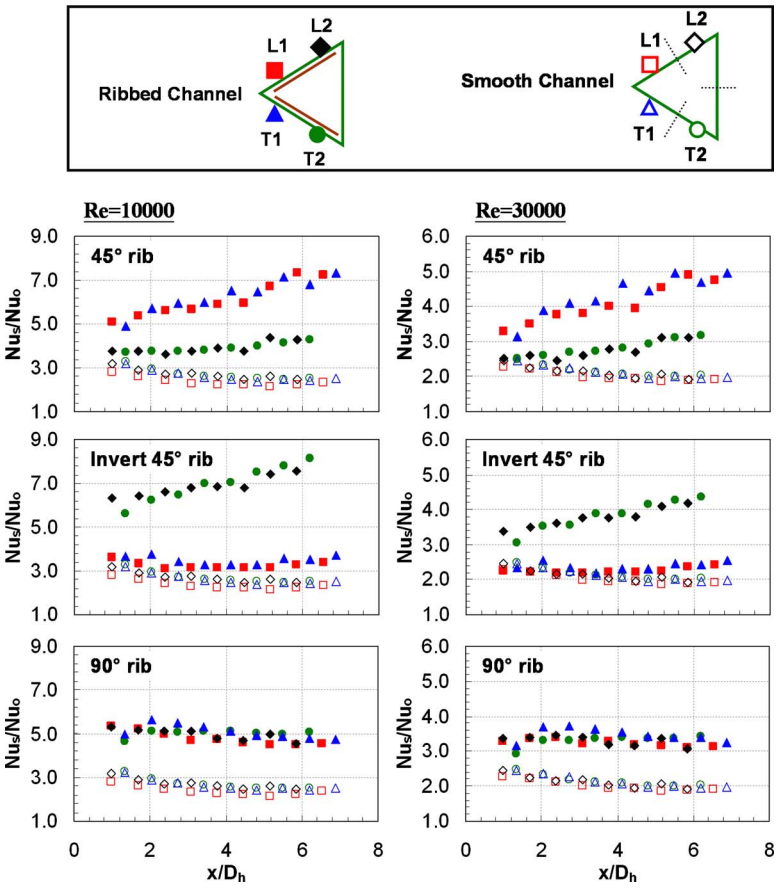

Fig. 6 Nusselt number ratio distribution in the stationary channel

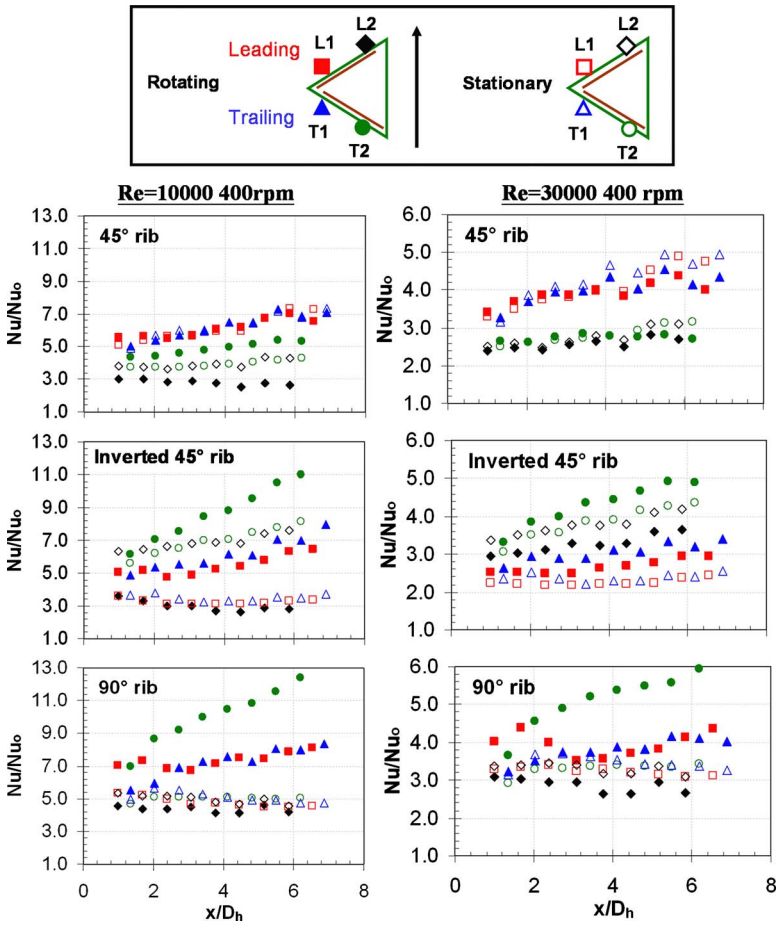

Fig. 7 Nusselt number ratio distribution in the rotating channel

Figure 6 shows the Nusselt number ratios (Nu/Nu_o) in the stationary channel with smooth case and ribbed cases. Two different Reynolds numbers of 10000 and 30000 are reported for each case. For the 45 deg ribbed channel, the heat transfer enhancement in the rib leading region (L1 and T1) is higher than the rib trailing region (L2 and T2). This is a good design for high heat load portion near the blade leading region. The angled rib induced secondary flow grows in strength as the flow goes over several additional ribs and the heat transfer is increased gradually along the streamwise direction. The Nusselt number ratio increases along the streamwise direction from 5.0 to 7.4 in L1 and T1 regions at Re=10,000. It increases along the streamwise direction from 3.8 to 4.3 in L2 and T2 regions at Re=10,000. The entire ribbed leading and trailing surfaces both have higher heat transfer than the smooth cases. However, as the Reynolds number increases from 10,000 to 30,000, the heat transfer enhancement by the ribs decreases. For the inverted 45 deg angled ribs, the rib induced secondary flow is reversed compared with the 45 deg angled ribs. Therefore, the higher heat transfer occurs on L2 and T2 surfaces while the lower heat transfer occurs on L1 and T1 surfaces. It shows the reversed heat transfer trend as compared with the 45 deg angled rib. Heat transfer is only slighted altered by the ribs on L1 and T1 surfaces and is smaller than L2 and T2 region. For 90 deg orthogonal ribs, heat transfer is influenced mainly due to ribs tripping the flow and the flow reattachment. There is no rib induced secondary flow along the rib orientation and heat transfer is more uniformly altered across the entire channel. The Nusselt number ratios (Nu/Nu_o) on these four regions are very similar and decrease gradually along the streamwise direction as shown in Fig. 6. At Reynolds number of 10,000, Nusselt number ratio on the leading surface (L1 and L2) decreases from 5.4 to 4.5 along the streamwise direction. The Nusselt number ratio is about 1.7 times higher than the smooth case at Re=10,000 and 1.5 times higher than the smooth surface at Re=30,000.

4.2 Heat Transfer in the Rotating Channel. Before the detailed discussion of the rotating results, it is necessary to describe the effect of rotation inside cooling channels. Two counter rotating vortices are generated due to Coriolis force during rotation. For the radially outward flow, rotation increases heat transfer on the trailing surface while decreases heat transfer on the leading surface. The structure of these two counter rotating vortices varies depending on the channel geometry and the channel orientation. Figure 5 shows this secondary flow pattern in the current study, which also involves the formation of the two counter rotating vortices. In a ribbed channel, the rib induced secondary flow interacts with the rotating induced secondary flow and the heat transfer behavior is affected by the combined effects from both as shown in Fig. 5. The effect of rotation is small and does not have significant impact on heat transfer on the rib leading surface (L1 and T1) because rib induced secondary flow dominates. While near the rib trailing surface (L2 and T2), the wide space allows the rotation induced secondary flow to develop freely and the effect of rotation is more obvious. With the ribs put on the leading and trailing surfaces, the Nusselt number ratio distributions in both the stationary and rotating channels (400 rpm) are shown in Fig. 7.

For 45 deg angled ribs, it has high heat transfer near L1 and T1 regions and the heat transfer improvement due to rotation is limited. While on the rib trailing region (L2 and T2), the effect of rotation is more obvious and enhances heat transfer on the trailing

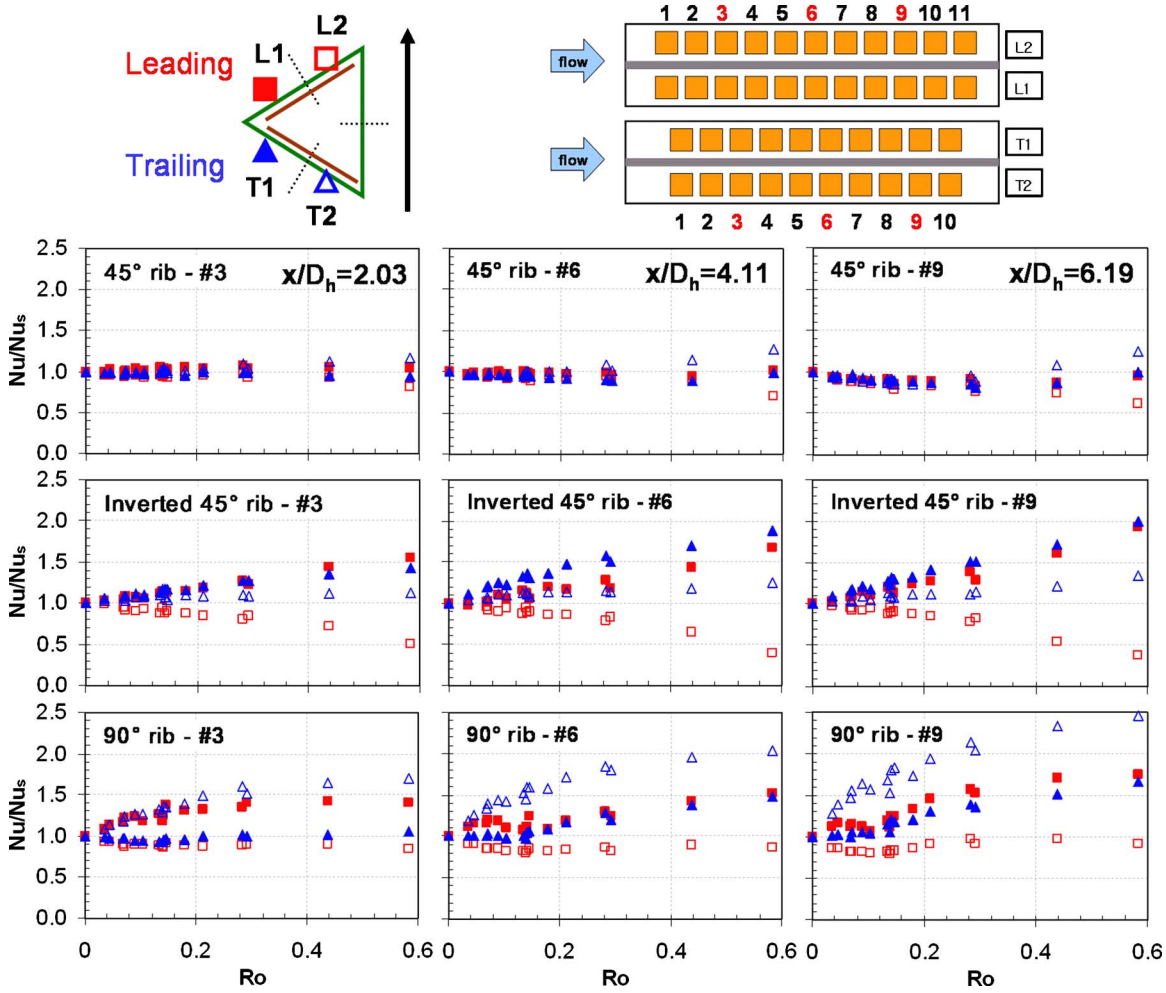

Fig. 8 Effect of rotation number on three different regions

surface while decreases heat transfer on the leading surface. On the L2 region, the rib induced secondary flow opposes the rotation induced secondary flow and produces lowest heat transfer.

It can be expected that the direction of rib induced secondary flow is reversed while the rotation induced secondary flow remains the same for the inverted 45 deg angled ribs. On the T2 surface, both the rib and rotation induced secondary flows interact together to enhance heat transfer and the highest heat transfer occurs due to the combined effects. Nusselt number ratio (Nu/Nu_o) increases from 6.0 to 11.0 along the streamwise direction at Re=10,000. Heat transfer on the T1 surface is slightly higher than the L1 surface due to effect of rotation but both higher than the stationary case. Therefore, the L1 surface has the lowest heat transfer at Re=30,000. However, the L2 surface has the lowest heat transfer at Re=10,000 due to stronger effect of rotation (higher rotation number).

Heat transfer is the highest on the T2 surface and the lowest on the L2 surface for 90 deg orthogonal ribs. The rotating heat transfer is mainly affected by the effect of rotation because there is no secondary flow along the rib orientation. Nusselt number ratio increases dramatically from 7.0 to 13.0 on the T2 surface along the streamwise direction at Re=10,000; however, it increases slightly on L1 and T1 surfaces from 7.0 to 8.4. Nu ratio on the L2 surface is the lowest and remains the same level along the streamwise direction. As the Reynolds number increases, the Nusselt number ratio (Nu/Nu_o) decreases and the difference between stationary and rotating results also decreases. Thus, the effect of rotation is reduced.

4.3 Rotation Number Effects. Rotation number is a ratio of Coriolis force to the bulk flow inertia force. By varying the rotational speed (Coriolis force) and the Reynolds number (flow inertia force), the contribution from these two factors should yield the same results. The rotation number is defined in Eq. (6).

$$\mathrm{Ro} = \frac{\Omega D_h}{V} \tag{6}$$

This nondimensional parameter is widely used to quantify the effect of rotation in the industry and academia. Heat transfer enhancement due to effect of rotation is represented by the ratio of the rotational Nusselt number to the stationary Nusselt number (Nu/Nu_s). Figure 8 shows this heat transfer enhancement (Nu/Nu_s) with Reynolds number from 10,000 to 40,000 and rotational speed from 0 rpm to 400 rpm. Three different regions (3, 6, and 9) in the streamwise direction (x/D_h=2.03, 4.11, and 6.19, respectively) are chosen to study the rotation number effects.

The Nusselt number ratios (Nu/Nu_s) with rotation number for 45 deg angled ribs are presented from region 3 to region 9. The heat transfer enhancements (Nu/Nu_s) on L1 and T1 surfaces are very similar, which indicate the effect of rotation is small and the rib induced secondary flow dominates. In region 3, Nusselt number ratio decreases gradually from 1.0 to 0.8 with the rotation number on the L2 surface and gradually increases from 1.0 to 1.2 with the rotation number on the T2 surface. When the flow moves downstream to regions 6 and 9, the difference between L2 and T2

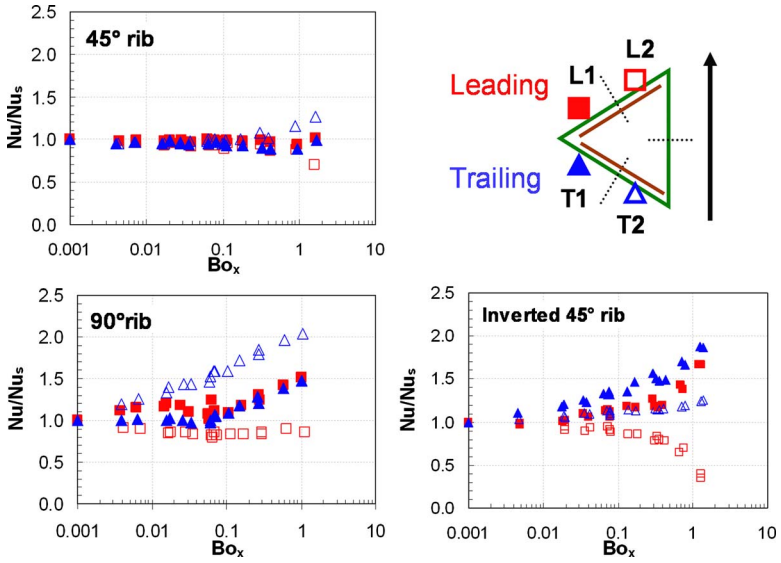

Fig. 9 Effect of Buoyancy Parameter on Nusselt number ratios at x/D_h =4.11

surfaces becomes larger than region 3. For 45 deg angled ribs, heat transfer enhancement/degradation due to effect of rotation is smallest among all the cases.

For inverted 45 deg angled ribs, heat transfer enhancements on all the surfaces increase with Ro except for the L2 surface. On L1 and T1 surfaces, Nusselt number ratio (Nu/Nu_s) increases from 1.0 to 1.5 in region 3 and from 1.0 to 2.0 in region 9 with rotation number. Heat transfer enhancement due to rotation is smaller near the entrance of the channel because of entrance effect. The Nusselt number ratio (Nu/Nu_s) on L1 and T1 surfaces is high due to low Nusselt number at stationary condition (Nu_s). On the T2 surface, heat transfer enhancement increases slightly with rotation number. Nu/Nu_s increases up to 1.1 in region 3 and 1.35 in region 9. Heat transfer enhancement due to rotation is smaller compared with L1 and T1 surfaces. Heat transfer on T2 surface is already high at stationary condition and thus enhancement due to rotation is limited. On the L2 surface, Nu/Nu_s decreases gradually down to 0.5 in region 3 and 0.4 in regions 6 and 9 with rotation number.

For 90 deg orthogonal ribs, heat transfer enhancement is the highest on the T2 surface and the lowest on the L2 surface. On the T2 surface, Nu/Nu_s increases with rotation number up to 1.7 in region 3 and 2.5 in region 9. For the L2 surface, heat transfer enhancement maintains the same level of 0.8 as rotation number increases and the effect of rotation in this region is minimal. The L2 surface has the lowest Nusselt number ratio due to rotation for all the ribbed cases. In region 3, Nu/Nu_s maintains the same level with rotation number on the T1 surface but increases with the rotation number on L1 surfaces. It is noted that Nu/Nu_s on the T1 surface is lower than the L1 surface due to staggered ribs near the entrance under rotating condition in region 3. In regions 6 and 9, Nu/Nu_s increases gradually with rotation number for L1 and T1 surfaces. For 90 deg orthogonal ribs, there is no significant heat transfer declination as rotation number increases; therefore, overall heat transfer gradually increases with rotation.

4.4 Buoyancy Parameter Effects. The buoyancy parameter is also a widely used nondimensional parameter to quantify the effect of rotation inside the gas turbine blade. The buoyancy force due to centrifugal force and temperature difference is important because of the high rotating speed and large temperature difference in the actual engines. The buoyancy parameter considers all factors affecting the effect of rotation: the density ratio (temperature difference), the rotation number, and the rotating radius. It is shown in Eq. (7).

$$\mathrm{Bo}_x = \left(\frac{\Delta\rho}{\rho}\right)_x (\mathrm{Ro})^2 \frac{R_x}{D_h} = \frac{T_{w,x} - T_{b,x}}{T_{f,x}} (\mathrm{Ro})^2 \frac{R_x}{D_h} \tag{7}$$

The local film temperature is defined as the average of the local wall temperature and the local bulk temperature as shown in Eq. (8).

$$T_{f,x} = (T_{w,x} + T_{b,x})/2 \tag{8}$$

In the current study, the region near the middle portion of the channel (x/D_h=4.11) is chosen to study the effect of buoyancy parameter on Nusselt number ratios (Nu/Nu_s). All the cases were tested at the coolant-to-wall DR of 0.11.

Figure 9 shows the Nusselt number ratio (Nu/Nu_s) for 45 deg, inverted 45 deg, and 90 deg ribs. For the 45 deg angled ribs, Nusselt number ratio (Nu/Nu_s) remains the same level on L1 and T1 surfaces as the buoyancy parameter increases. Heat transfer is enhanced slightly on the T2 surface while declined slightly on the L2 surface. Nusselt number ratio (Nu/Nu_s) increases up to about 1.3 in the T2 region while decreases down to about 0.7 in the L2 region at the maximum buoyancy parameter of 1.9. For 90 deg orthogonal ribs, Nusselt number ratio (Nu/Nu_s) maintains the same level as buoyancy parameter increases on the L2 surface. Nu/Nu_s increases with buoyancy parameter on L1, T1, and T2 surfaces. It is noted that there is no significant heat transfer degradation for all the regions. High heat transfer due to rotation can be expected at high buoyancy parameter for the 90 deg orthogonal ribs.

Two additional coolant-to-wall DRs of 0.13 and 0.15 were tested specifically for inverted 45 deg rib case to study the density ratio effects. Total of three different density ratios (0.11, 0.13, and 0.15) were plotted. On the leading surface, L1 increases with buoyancy parameter while L2 decreases with buoyancy parameter. For the entire trailing surface, Nusselt number ratio (Nu/Nu_s) increases with the buoyancy parameter as shown in the figure. The heat transfer enhancement on the T1 surface is higher than the T2 region. The data with different density ratios fit nicely into the curve. It shows that the density ratio, Reynolds number, and rotational speed can be varied independently but the results still can be correlated into a single curve by buoyancy parameter.

4.5 Average Heat Transfer. The Nusselt number ratios (Nu/Nu_o) were averaged along the streamwise direction for every surface (L1, T1, L2, and T2), as shown in Fig. 10. Results are

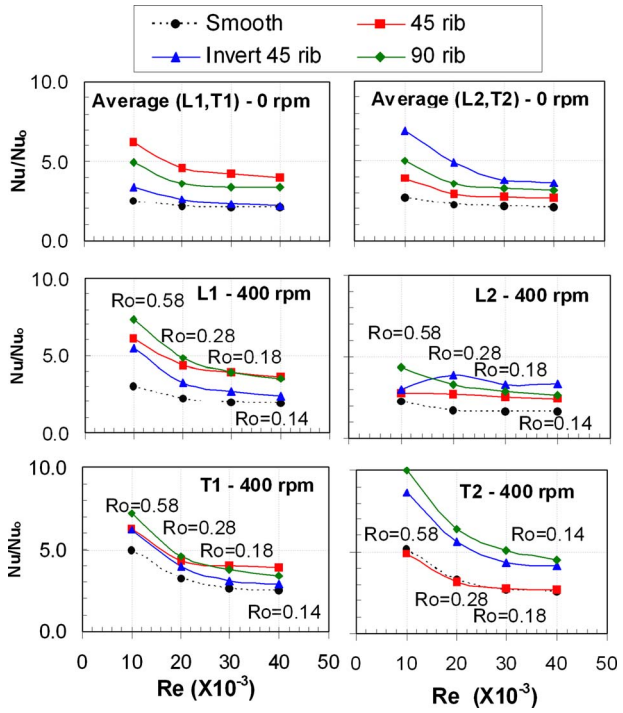

Fig. 10 Average heat transfer results at stationary and rotating conditions

compared between stationary and the highest rotational speed (400 rpm) to investigate the effect of rotation. The two regions (L1 and T1) can be used to represent the blade leading edge region of the gas turbine where high thermal load exists. At stationary condition, 45 deg rib has the highest heat transfer while the inverted 45 deg rib has the lowest heat transfer for average of the L1 and T1 surfaces. From this figure, we can conclude that although heat transfer for 45 deg rib is the highest at stationary case; heat transfer of 90 deg rib is comparable with 45 deg rib at rotating condition. The heat transfer enhancement level increases as Reynolds number decreases (rotation number increases). Inverted 45 deg rib has the highest heat transfer for the average of the L2 and T2 surfaces at stationary condition, as shown in Fig. 10. For rotating condition, inverted 45 deg and 90 deg rib have the comparable heat transfer enhancement on the L2 and T2 surfaces. It is

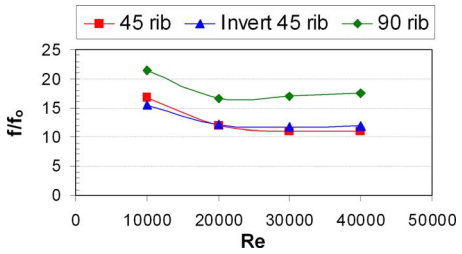

Fig. 11 Friction factor ratio of different rib configurations

noticed that the Nu ratio for 45 deg rib is the lowest on these surfaces and is very close to the smooth case on the T2 surface.

4.6 Friction Factor Ratio and Thermal Performance. One way to evaluate the performance of different ribs is to calculate the thermal performance for each rib configuration. In the current study, the pressure drop is measured for all the cases at stationary condition. The friction factor ratios are shown in Fig. 11. 90 deg rib has the higher friction factor ratio than the 45 deg and inverted 45 deg angled ribs.

Thermal performance near the leading edge of the turbine blade (L1 and T1 surfaces) and the total average at stationary condition are presented in Fig. 12. For the L1 and T1 surfaces, 45 deg rib has the highest thermal performance while inverted 45 deg rib has the lowest thermal performance at stationary condition. The total average thermal performance is based on the average Nusselt number ratios (Nu/Nu_o) from the leading and trailing surfaces. Angled ribs usually have higher thermal performance than the orthogonal ribs due to smaller pressure drop. Results show that 45 deg rib still has the best thermal performance and 90 deg rib has the worst thermal performance at stationary condition.

4.7 Correlations for Heat Transfer Enhancement. The average Nusselt number ratios (Nu/Nu_s) on the leading and trailing surfaces are plotted in Fig. 13. Each data point is the average of 18 points over the entire leading or trailing surfaces. The results are plotted with the rotation number and the average buoyancy parameter. The well-correlated curve shows that rotation number and buoyancy parameter can be used to predict the heat transfer enhancement inside this triangular channel with smooth and ribbed surfaces. It is well correlated for all the three rib cases by a power function with the maximum discrepancy within $\pm 6.8\%$. The constants for the correlation functions are shown in Table 1.

The results for 45 deg angled ribbed and smooth cases were

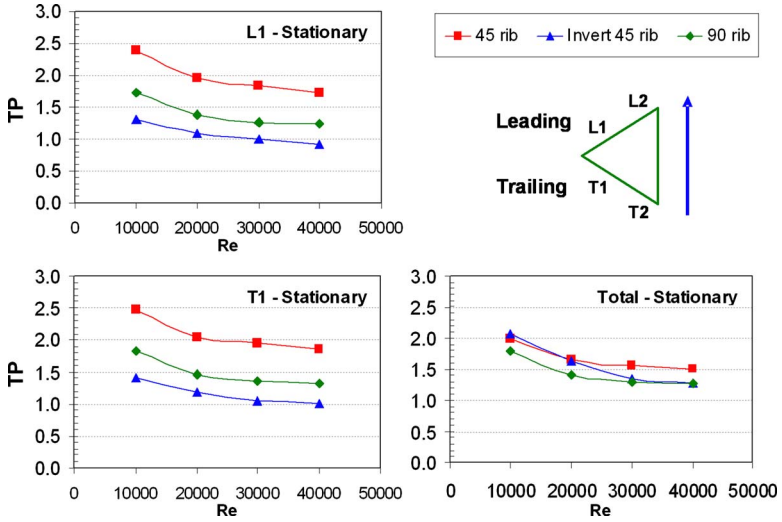

Fig. 12 Thermal performance comparison of L1, T1, and total average

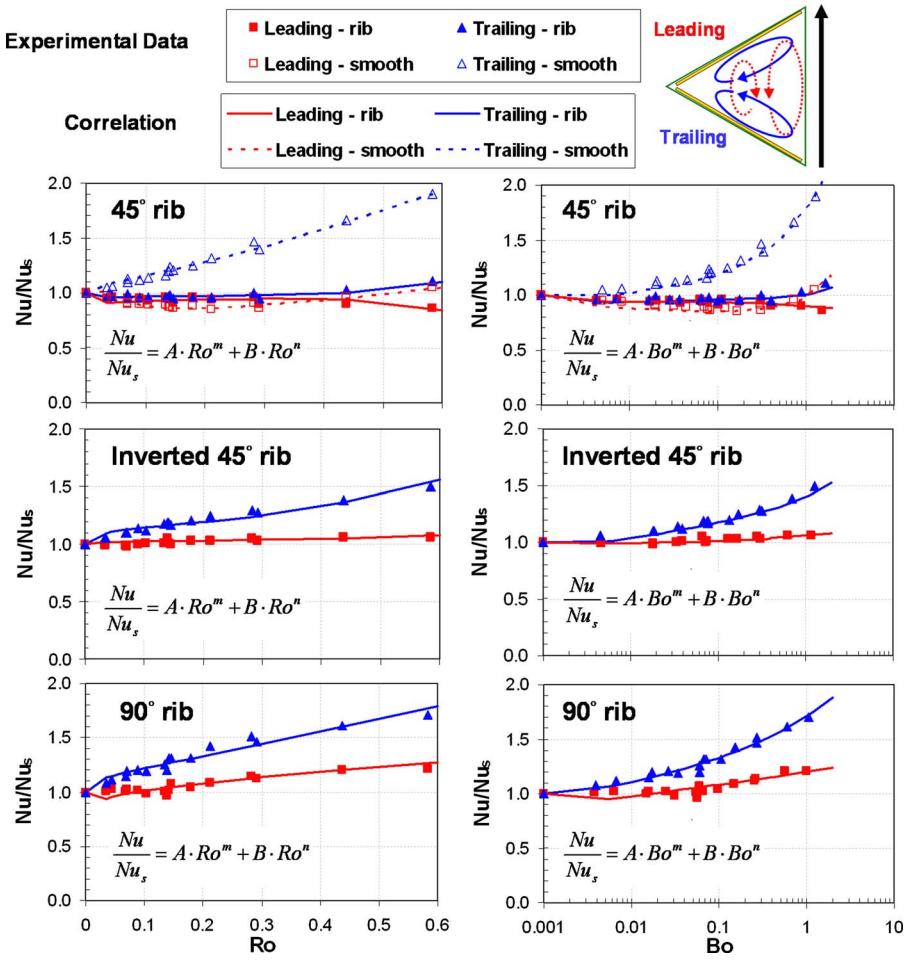

Fig. 13 Correlations for heat transfer enhancement

plotted together for comparison. The heat transfer enhancement due to rotation for the smooth case is higher than the 45 deg ribbed case. The heat transfer enhancement/degradation for the smooth case occurs at a lower rotation number and buoyancy parameter than the ribbed case. For the ribbed case, the Nu/Nu_s values on the leading and trailing surfaces are very close when rotation number is smaller than 0.3. After that, the Nusselt number ratios on the leading and trailing surfaces begin to diverge. Figure 13 also shows the Nu/Nu_s with the average buoyancy parameters. The trends are very similar to the plots with the rotation number. For the inverted 45 deg angled ribs, the average Nusselt number ratio (Nu/Nu_s) increases with rotation number and buoyancy parameter on both the leading and trailing surfaces. The Nu ratio (Nu/Nu_s) increases up to 1.5 on the trailing surface while only increases up to 1.1 on the leading surface as rotation number and buoyancy parameter increases. For 90 deg ribs, both the leading and trailing surface increase with rotation number and buoyancy parameter. Trailing surface has higher heat transfer enhancement than the leading surface. It shows that the heat transfer enhancement due to rotation for 90 deg rib is the highest among all the rib cases.

5 Conclusion

Heat transfer and pressure drop have been measured in a rotating equilateral triangular channel to model the cooling channel near the leading edge of the gas turbine blade. The results on the leading and trailing surfaces of the channel were reported. The

Table 1 Correlation coefficients for the heat transfer enhancement

	Ro				Bo			
	A	*m*	*B*	*n*	*A*	*m*	*B*	*n*
Leading—smooth	0.97	0.02	−10.00	7.50	0.80	−0.02	0.18	1.10
Trailing—smooth	0.50	−0.20	0.80	0.95	1.10	0.02	−0.20	0.25
Leading—45 deg rib	1.19	0.04	1.60	1.45	1.21	0.04	0.55	0.80
Trailing—45 deg rib	0.99	0.01	1.90	5.50	0.98	0.01	0.02	2.00
Leading—inverted 45 deg	1.05	0.01	0.50	5.50	0.90	−0.01	0.16	0.25
Trailing—inverted 45 deg	1.25	0.04	1.20	2.50	1.30	0.05	0.10	0.80
Leading—90 deg rib	1.10	0.05	0.35	1.05	1.41	0.06	−0.21	0.12
Trailing—90 deg rib	1.22	0.03	1.05	1.15	1.21	0.04	0.50	0.35

performance of three different rib cases (45 deg, inverted 45 deg, and 90 deg) as well as smooth case was studied. Regionally averaged heat transfer distribution reported in this study can help designer determine the rib configuration for internal cooling channels. The experiments were conducted under high rotation number and high buoyancy parameter to simulate the actual engine condition. The results can be correlated with different density ratios, Reynolds numbers, and rotational speeds by rotation number and buoyancy parameter. Based on the results reported, the following conclusion can be drawn.

(1) L1 and T1 surfaces are the most critical regions near the leading edge of the turbine blade. In these two surfaces, staggered 45 deg rib has the highest heat transfer enhancement (Nu/Nu_o) and TP at stationary condition; while staggered 45 deg rib and 90 deg rib have the higher comparable heat transfer enhancement (Nu/Nu_o) at rotating condition.
(2) On the L2 and T2 surfaces, inverted 45 deg rib has the highest heat transfer and thermal performance at stationary condition; inverted 45 deg rib and 90 deg rib show comparable heat transfer at rotating condition.
(3) 90 deg rib shows the highest friction factor ratio; 45 deg angled rib and inverted 45 deg angled rib have similar friction factor ratio.
(4) Rotation has more profound effects on heat transfer enhancement for 90 deg rib and inverted 45 deg angled rib than the 45 deg angled rib.

Acknowledgment

This research project has been funded by Solar Turbines Inc.

Nomenclature

A = area of the copper plate
D_h = channel hydraulic diameter
e = rib height
f = friction factor
f_o = fully developed friction factor in nonrotating, smooth pipe
h = regionally averaged heat transfer coefficient
k = thermal conductivity of the coolant
L = length of the heated portion of the test section
L_e = length of the unheated portion of inlet part
Nu = regionally averaged Nusselt number
Nu_o = Nusselt number of the fully developed turbulent flow in nonrotating smooth tube
P = rib spacing
Pr = Prandtl number of the coolant
Q_{loss} = heat loss through the wall
Q_{in} = heat input at the wall
R_x = local radius of rotation
Re = Reynolds number, $\rho V D_h/\mu$
Ro = Rotation number, $\Omega D_h/V$
$T_{w,x}$ = local wall temperature
$T_{b,x}$ = local coolant bulk temperature
$T_{f,x}$ = local film temperature $(=(T_{w,x}+T_{b,x})/2)$
V = bulk velocity in streamwise direction
α = rib angle of attack
ρ = density of the coolant
$(\Delta\rho/\rho)_x$ = local coolant-to-wall density ratio $(=(T_{w,x}-T_{b,x})/T_{f,x})$
Ω = rotational speed

References

[1] Han, J. C., Dutta, S., and Ekkad, S. V., 2000, *Gas Turbine Heat Transfer and Cooling Technology*, Taylor & Francis, New York.
[2] Han, J. C., 1984, "Heat Transfer and Friction in Channels With Two Opposite Rib-Roughened Walls," ASME J. Heat Transfer, **106**, pp. 774–781.
[3] Han, J. C., 1988, "Heat Transfer and Friction Characteristics in Rectangular Channels With Rib Turbulators," ASME J. Heat Transfer, **110**, pp. 321–328.
[4] Han, J. C., and Zhang, P., 1991, "Effect of Rib-Angle Orientation on Local Mass Transfer Distribution in a Three-Pass Rib-Roughened Channel," ASME J. Turbomach., **113**, pp. 123–130.
[5] Park, J. S., Han, J. C., Huang, Y., and Ou, S., 1992, "Heat Transfer Performance Comparisons of Five Different Rectangular Channels With Parallel Angled Ribs," Int. J. Heat Mass Transfer, **35**(11), pp. 2891–2903.
[6] Lowdermilk, W. H., Weiland, W. F., and Livingood, J. N. B., 1954, "Measurement of Heat Transfer and Friction Coefficients for Flow of Air in Noncircular Ducts at High Surface Temperatures," NACA RM E53J07.
[7] Metzger, D. E., and Vedula, R. P., 1987, "Heat Transfer in Triangular Channels With Angled Roughness Ribs on Two Walls," Exp. Heat Transfer, **1**, pp. 31–44.
[8] Zhang, Y. M., Gu, W. Z., and Han, J. C., 1994, "Augmented Heat Transfer in Triangular Ducts With Full and Partial Ribbed Walls," J. Thermophys. Heat Transfer, **8**(3), pp. 574–579.
[9] Haasenritter, A., and Weigand, B., 2001, "Heat Transfer in Triangular Rib-Roughened Channels," ASME Paper No. NHTC 2001-20245.
[10] Ahn, S. W., and Son, K. P., 2002, "Heat Transfer and Pressure Drop in the Roughened Equilateral Triangular Duct," Int. Commun. Heat Mass Transfer, **29**, pp. 479–488.
[11] Amro, M., Weigand, B., Poser, R., and Schnieder, M., 2007, "An Experimental Investigation of the Heat Transfer in a Ribbed Triangular Cooling Channel," Int. J. Therm. Sci., **46**, pp. 491–500.
[12] Taslim, M. E., Li, T., and Spring, S. D., 1998, "Measurements of Heat Transfer Coefficients and Friction Factors in Passages Rib-Roughened on All Walls," ASME J. Turbomach., **120**, pp. 564–570.
[13] Takeishi, K., Kitamura, T., Matsuura, M., and Shimizu, K., 2003, "Heat Transfer Characteristic of a Triangular Channel With Turbulence Promoter," *Proceedings of the International Gas Turbine Congress*, Tokyo, Japan, Paper No. TS-080.
[14] Dutta, S., Han, J. C., and Lee, C. P., 1995, "Experimental Heat Transfer in a Rotating Triangular Duct: Effect of Model Orientation," ASME J. Heat Transfer, **117**, pp. 1058–1061.
[15] Lee, D. H., Rhee, D. H., and Cho, H. H., 2006, "Heat Transfer Measurements in a Rotating Equilateral Triangular Channel With Various Rib Arrangements," ASME Paper No. GT 2006-90973.
[16] Wagner, J. H., Johnson, B. V., and Hajek, T. J., 1991, "Heat Transfer in Rotating Passages With Smooth Walls and Radial Outward Flow," ASME J. Turbomach., **113**, pp. 42–51.
[17] Wagner, J. H., Johnson, B. V., and Kopper, F. C., 1991, "Heat Transfer in Rotating Serpentine Passages With Smooth Walls," ASME J. Turbomach., **113**, pp. 321–330.
[18] Johnson, B. V., Wagner, J. H., Steuber, G. D., and Yeh, F. C., 1994, "Heat Transfer in Rotating Serpentine Passages With Trips Skewed to the Flow," ASME J. Turbomach., **116**, pp. 113–123.
[19] Zhou, F., Lagrone, J., and Acharya, S., 2004, "Internal Cooling in 4:1 AR Passages at High Rotation Numbers," ASME Paper No. GT 2004-53501.
[20] Liou, T. M., Chang, S. W., Hung, J. H., and Chiou, S. F., 2007, "High Rotation Number Heat Transfer of 45° Rib-Roughened Rectangular Duct With Two Channel Orientations," Int. J. Heat Mass Transfer, **50**, pp. 4063–4078.
[21] Liu, Y. H., Huh, M., Han, J. C., and Chopra, S., 2008, "Heat Transfer in a Two-Pass Rectangular Channel ($AR=1:4$) Under High Rotation Numbers," ASME J. Heat Transfer, **130**(8), p. 081701.
[22] Wright, L. M., Liu, Y. H., Han, J.-C., and Chopra, S., 2008, "Heat Transfer in a Trailing Edge, Wedge-Shaped Cooling Channels Under High Rotation Numbers," ASME J. Heat Transfer, **130**(7), p. 071701.
[23] Liu, Y. H., Huh, M., Rhee, D. H., Han, J. C., and Moon, H. K., 2008, "Heat Transfer in Leading Edge, Triangular Shaped Cooling Channels With Angled Ribs Under High Rotation Numbers," ASME Paper No. GT-2008-50344.
[24] Kline, S. J., and McClintock, F. A., 1953, "Describing Uncertainty in Single-Sample Experiments," Mech. Eng. (Am. Soc. Mech. Eng.), **75**, pp. 3–8.

Air-Side Heat-Transfer Enhancement by a New Winglet-Type Vortex Generator Array in a Plain-Fin Round-Tube Heat Exchanger

J. He
e-mail: jinghe2@illinois.edu

L. Liu
e-mail: lliu9@illinois.edu

A. M. Jacobi
e-mail: a-jacobi@illinois.edu

Department of Mechanical Science and Engineering,
University of Illinois,
1206 West Green Street,
Urbana, IL 61801

The impact of a vortex-generation technique for air-side heat-transfer improvement is experimentally investigated through full-scale wind-tunnel testing of a plain-fin round-tube heat exchanger under dry-surface conditions. Inspired by the formation locomotion of animals in nature, a new vortex generator (VG) array deployed in a "V" is proposed in the present work, aiming to create constructive interference between vortices. The array is composed of two delta-winglet pairs and placed at an attack angle of 10 deg or 30 deg. Its effectiveness is compared with a baseline configuration and two conventional single-pair designs placed at 30 deg, a small pair with half the area of the array and a large pair with the same area as the array. The frontal air velocity considered ranges from 2.3 m/s to 5.5 m/s, corresponding to a Reynolds number range based on the hydraulic diameter of 1400–3400. The experimental results show little impact of the 10 deg array and a moderate heat-transfer improvement of up to 32% for the small pair, both introducing additional pressure loss of approximately 20–40%. For the 30 deg array and the large pair, similar augmentation of 25–55% in air-side heat-transfer coefficient is obtained accompanied by average pressure drop penalties of 90% and 140%, respectively. Performance evaluation using the criteria of the modified area goodness factor and the volume goodness factor indicates the superiority of the heat exchanger enhanced by the 30 deg array among all the investigated VGs. The VG array is found more effective at comparatively low Reynolds numbers, representative of many heating, ventilation, air-conditioning, and refrigeration applications and compact heat-exchanger designs.
[DOI: 10.1115/1.4000988]

Keywords: heat exchanger, fin-and-tube, "V" formation, vortex generator, winglet array

1 Introduction

High heat-exchanger performance is crucial to meet efficiency standards with low cost and environmental impact in numerous end-use energy applications. In the liquid-to-air and phase-change heat exchangers typical to heating, ventilation, air-conditioning, and refrigeration (HVAC&R) systems, the air-side convective resistance is usually dominant, representing 75–90% of the total thermal resistance. Therefore, many techniques for improving heat-exchanger performance focus on the air-side surface. One promising method is the use of a passive flow manipulator known as vortex generator. In this method, winglike VGs are punched or mounted on a heat-transfer surface to generate longitudinal vortices. As the vortices are advected downstream by the main flow, they cause bulk fluid mixing, boundary-layer modification, and flow destabilization, and improve convective heat transfer. This enhancement approach has the advantage of low cost and ease of implementation, accompanied by a usually modest pressure drop penalty.

Vortex-enhanced channel flows have received considerable attention, because of their relevance to heat-exchanger geometries. Two commonly employed VG placements are the so called "common-flow-down" [1,2] and "common-flow-up" [3,4], as depicted in Fig. 1. The VGs are placed as a pair downstream of the tube in a common-flow-down configuration. The generated longitudinal vortex introduces high-momentum fluid of the main flow toward the fin surface behind the tube, thus improving the poor heat transfer in the wake as well as suppressing flow separation. Fiebig et al. [1] measured a 55–65% heat-transfer augmentation with corresponding 20–45% increase in the apparent friction factor for an inline arrangement of three tube rows. A 3D numerical simulation by Wu and Tao [2] took into account VG thickness, punched holes, and conjugate conduction and convection on the fin surface. For elements with three tube rows, the delta-winglet pairs at 30 deg enhanced the average Nusselt number by 16–20% and decreased pressure drop by 8–10% over a Reynolds number range 800–2000. Aside from the above-mentioned tube-wake manipulation of common-flow-down, the existence of the punched holes also contributes to a reduced pressure drop, albeit in a less important manner. Biswas et al. [5] performed computational analysis in a developing channel flow where a delta wing was either punched out of the wall or attached to the wall. The friction coefficients in the two cases were found to increase by 49% and 64%, respectively. By observation of a downwash velocity field in the presence of holes, the authors attributed the reduction in friction coefficient to the spiraling flow with less vortex strength. Rectangular winglet pairs were investigated by Leu et al. [6] for elements with three tube rows. Among all considered angles of attack, the 45 deg arrangement provided the best thermal-hydraulic performance and achieved area reduction ratio up to 25% using the variable geometry performance criteria by Webb and Kim [7]. The improvement was more pronounced for low-to-

Contributed by the Heat Transfer Division of ASME for publication in the JOURNAL OF HEAT TRANSFER. Manuscript received June 29, 2009; final manuscript received October 8, 2009; published online April 21, 2010. Assoc. Editor: S. A. Sherif.

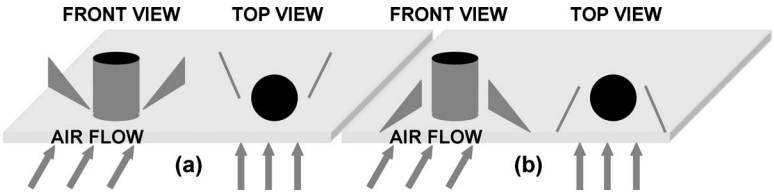

Fig. 1 Configuration of winglet-type VG on a fin surface: (*a*) common-flow-down and (*b*) common-flow-up

moderate Reynolds numbers (below 2000). VGs in a common-flow-up configuration are usually located further upstream relative to the tube, forming a nozzlelike flow passage together with the aft portion of the tube. By promoting fluid acceleration, this design is intended to delay separation on the tube surface and narrow the wake zone. Torii et al. [3] reported 10–20% augmentation in heat transfer and simultaneous 8–15% reduction in pressure drop for in-line tube banks. Note that in contrast to the results in Refs. [2,3], most studies [8–10] indicated heat-transfer enhancement accompanied by additional pressure loss, because the induced form drag of VGs generally dominates [9].

Due to the complexity of the underlying physics, most work in vortex generation has employed highly idealized geometries and flow conditions. There are very few results of full-scale implementation and testing of VGs in prototype heat exchangers under realistic operating conditions reported in the open literature. Elsherbini and Jacobi [11] evaluated the impact of leading-edge delta-wing VGs on a plain-fin-and-tube heat exchanger under dry-surface conditions. They obtained a 31% heat-transfer enhancement over the baseline, with modest pressure drop penalty of 10%. Wang et al. [12] compared air-side performance between delta-winglet VGs and wavy-fin surface in fin-and-tube heat exchangers under dry- and wet-surface conditions. According to their experiments, the performance of the VG surface relative to the wavy-fin surface improves with the number of tube rows. Under wet-surface conditions, the swirling motion above the VG surface causes better condensate drainage, which in turn induces lower pressure drop. Joardar and Jacobi [13] studied the effectiveness of delta-wing VGs in a compact flat-tube, louvered-fin heat exchanger typical to those used in automotive systems. Average heat-transfer increases of 21% for dry conditions and 23% for wet conditions were acquired with a pressure drop penalty below 7%. Sommers and Jacobi [14] evaluated the efficacy of longitudinal vortices as an air-side enhancement technique under frosting conditions. The examined delta-wing VGs were attached in an alternating single row, double row arrangement in a full-scale plain-fin-and-tube heat exchanger. For Reynolds numbers between 500 and 1300, the convective heat-transfer coefficient was found to increase by 60–93% with nearly identical core pressure drop. The enhanced frost density suggested that vortex-induced flow suppressed dendritic frost growth and hence produced a frost layer with a higher thermal conductivity. The first to-scale heat-exchanger application of winglets to generate a common-up-flow for tube-wake management was investigated by Joardar and Jacobi [4]. They assessed the overall heat transfer and pressure drop performance of a compact plain-fin-and-tube heat exchanger mounted with a single- or three-row VG set over a Reynolds number range 220–960. The three-row arrangement achieved a maximal heat-transfer increase of 69% with a pressure drop penalty of 26% at Re=960. Their study indicated the usefulness of multiple VG rows in improving the performance of fin-tube heat exchangers typically used in air-cooling and refrigeration applications.

It is established that apart from the aforementioned mechanisms, careful orientation and deployment of VGs can lead to further enhancement. Group movement of animals in specific formations is common in nature for a variety of benefits, among which hydrodynamic efficiency plays an important and sometimes dominant role. Typical examples include bird migration [15,16] (Fig. 2(*a*)), fish schooling [17] (Fig. 2(*b*)), and arthropod queues [18,19] (Fig. 2(*c*)). Lissaman and Shollenberger [15] applied aerodynamic theory to predict that 25 birds in a "V" formation could have a flight range increase of about 70% over a solo bird, with the trailing birds "riding" on the upwash of tip vortices generated from the upstream members. Fish swimming in a "diamond" pattern were found to exploit vortices shed by other fish in the school, thus achieving a significant decrease in locomotion cost [17]. Group movement of spiny lobsters [18] takes advantage of the fact that an object placed closely downstream of another usually results in a lower total drag than that when the two objects are separated far apart [20]. Such a collective behavior for mass migration was observed in the form of chainlike aggregation in a recently discovered fossil [19]. It is interesting to note a V-like or echelon (i.e., half V) formation among all these animal associa-

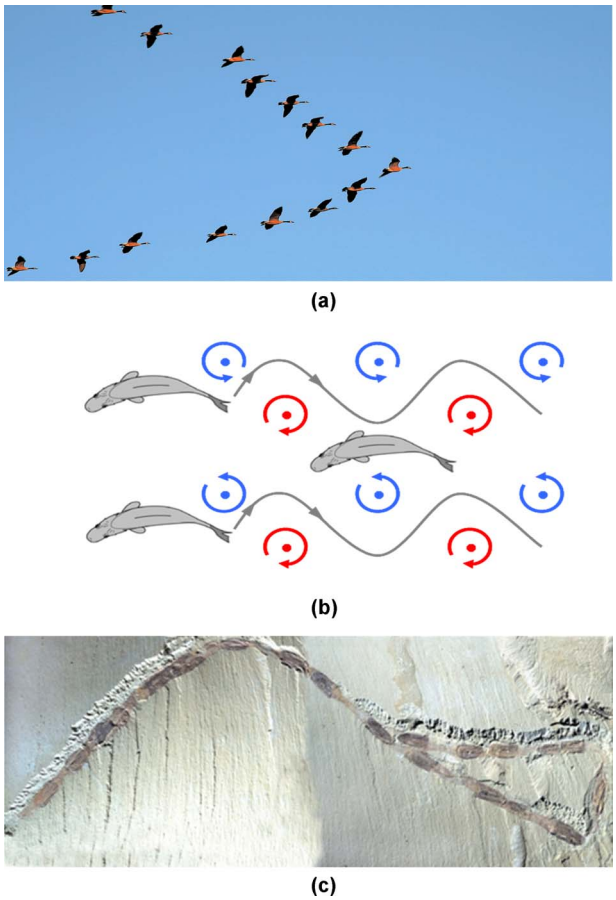

Fig. 2 (*a*) Migrating birds in V-formation (reproduced by courtesy of Tom Samoden, www.castlelakeestates.com/castlednn), (*b*) fish in a diamond-patterned school exploiting vortices (adopted from Ref. [17] with modification), and (*c*) fossilized collective behavior of shrimplike arthropods in a conga line (reproduced with permission from Ref. [19])

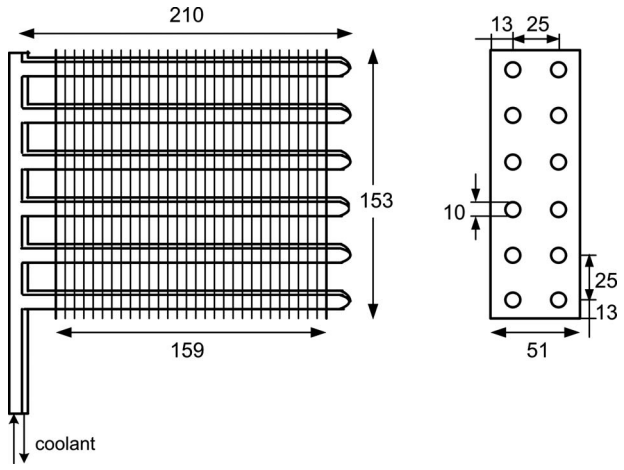

Fig. 3 Schematic of heat-exchanger configuration; all dimensions in millimeters

tions. A common presumption is that such shape adaptations have evolved for lowered power demands and improved energy efficiency, thereby promoting survival of the species in the Darwinian sense [21]. Although the inherent enhancement mechanisms may be different, the essential idea of grouping individuals in advantageous positions for favorable interaction could be utilized in human fluid-flow technology. As a preliminary realization, this study proposes a common-flow-up VG array deployed in a V to try to exploit the constructive inference between vortices. Its impact on the thermal-hydraulic performance of a plain-fin-and-tube heat exchanger is experimentally evaluated by full-scale wind-tunnel testing under dry-surface conditions, and compared with the baseline configuration and two conventional single-pair VG designs. The present work also aims to provide new and thus more complete experimental data on the performance of VG-enhanced heat exchangers, as such results are useful to assess the true potential of the vortex-enhancement strategy and reports in this area are limited in extant literature.

2 Experimental Methods

The baseline heat exchanger depicted in Fig. 3 has a collared fin-and-tube configuration with an inline tube arrangement. The fin spacing and thickness are 5.5 mm and 0.2 mm, respectively. With reference to Fig. 4, the proposed VG array is composed of two delta-winglet pairs, placed at the leading edge of the fins with an attack angle of 10 deg or 30 deg. The design follows the recommendation by Fiebig [10] that zero tip spacing was optimal for counter-rotating delta-winglet pairs. In addition, a preliminary investigation[1] suggested that the second pair being positioned immediately adjacent to the preceding one was as an appropriate arrangement. For each winglet, the height $b=3$ mm and the chord $c=6$ mm, which translates to an aspect ratio of $\Lambda=2$. More winglet pairs and higher attack angles are limited by the geometric confinement for the current specimen. Two single-pair VGs of the same height, placed at 30 deg, were included as well for the purpose of comparison. The small pair is identical to the leading pair of the array. The large pair has a chord twice the length of the single pair and thus has the same winglet area as the array. After the baseline tests were completed, a total number of 150 VGs (an array or either single pair shown in Fig. 3(*a*) referred to as one VG) were attached in the heat exchanger, resulting in less than 1% increase in the air-side heat-transfer area.

[1]Consisting of experiments in a parallel-plate channel flow—part of an ongoing research in this area.

Table 1 Test conditions

		Dry Operation
Air	Inlet dry bulb temperature (°C)	23.9
	Inlet relative humidity (%)	32
	Frontal air velocity (m/s)	2.3–5.5
Coolant	Inlet temperature (°C)	8.9
	Flow rate (kg/h)	196–492

A closed-loop wind tunnel [22] as illustrated in Fig. 5 was used to measure the heat transfer and pressure drop performance of the heat exchangers. The air flow was driven by an axial blower and passed through resistance heaters (to condition the air temperature), a flow nozzle (to measure air mass flow rate), a mixing chamber, honeycomb flow straighteners, screens, and a 9:1 area contraction before it reached the test section. A mixture of ethylene glycol (54.6% volume concentration) and water was supplied by a gear pump to cool the heat exchanger during the experiments. The coolant temperature was controlled using a chiller system, and a Coriolis-effect flow meter was used to measure its mass flow rate. A 6-junction, equally spaced thermocouple grid ($\pm 0.1°C$) and another 12-junction grid were used to detect the air temperatures at the inlet and downstream of the specimen, respectively. Immersion RTDs ($\pm 0.03°C$) were positioned at the inlet and outlet of the heat exchanger to record the coolant inlet and outlet temperatures. Air-side pressure drop across the heat exchanger was acquired with an electronic pressure transducer (± 0.2 Pa).

Test conditions of the present study are provided in Table 1. Experiments were conducted with a low relative humidity and relatively high coolant temperature to ensure no condensation occurred on the air-side surface. An experiment was initiated by circulating the air flow while bringing it to the desired temperature and frontal velocity. Coolant flow, which had also been preconditioned to the desired temperature, was then started to cool the heat exchanger. After a brief transient period (~ 15 min), a steady state was considered to prevail when all temperatures varied by less than the experimental uncertainty over a period of at least 3 min. Once an experiment reached the steady state, readings of the thermocouples, as well as all conditions, remained constant within their experimental uncertainty throughout the data collection period. Data were sampled at a rate of 1.0 Hz and averaged for subsequent analysis.

3 Data Interpretation

The temperature and flow-rate data sampled during an experiment were first used to determine the air-side heat-transfer coefficient. For the air and coolant flows, the heat-transfer rates at each side were calculated based on the mass flow rate and temperature change

$$Q_a = \dot{m}_a c_{p,a}(T_{a,i} - T_{a,o}) \tag{1a}$$

$$Q_c = \dot{m}_c c_{p,c}(T_{c,o} - T_{c,i}) \tag{1b}$$

A log-mean-temperature-difference (LMTD) method was employed to analyze the heat-transfer performance

$$UA_{\text{tot}} = \frac{Q_{\text{ave}}}{F \cdot \text{LMTD}} \tag{2}$$

In this equation, U is the overall heat-transfer coefficient and A_{tot} denotes the total air-side heat-transfer area (fin-and-tube). LMTD for counterflow was given by

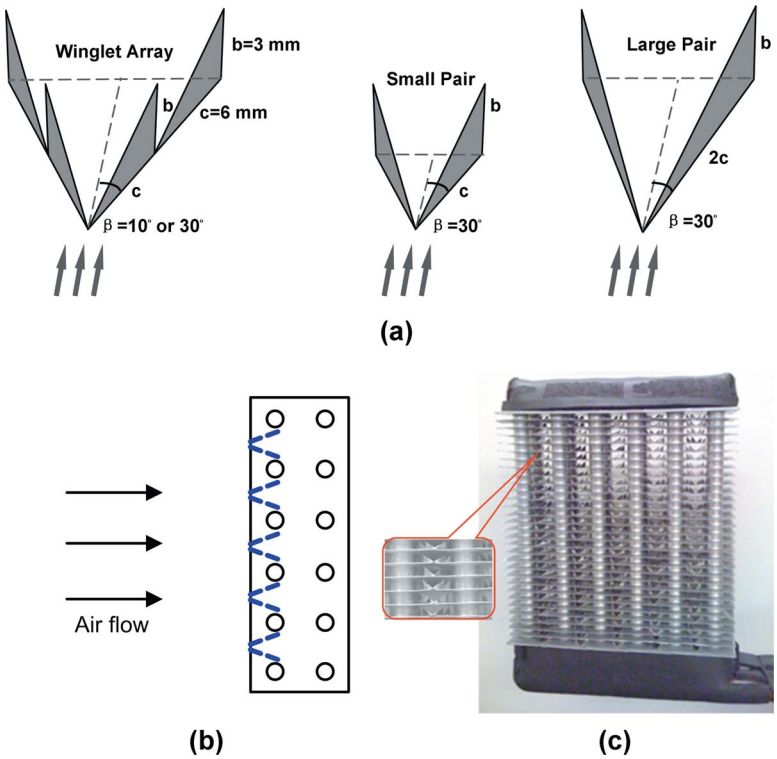

Fig. 4 (*a*) **Geometry of the proposed VG array and the single pair;** (*b*) **cross-sectional view and** (*c*) **photograph of the test heat exchanger with attached VGs at the leading edge**

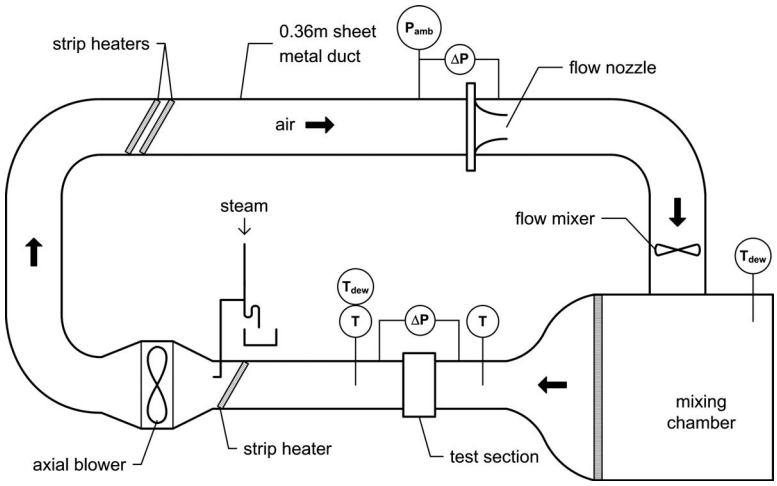

Fig. 5 Schematic of the wind tunnel used in the present work (adapted from Liu and Jacobi [22])

$$\text{LMTD} = \frac{(T_{a,i} - T_{c,o}) - (T_{a,o} - T_{c,i})}{\ln\left(\dfrac{T_{a,i} - T_{c,o}}{T_{a,o} - T_{c,i}}\right)} \tag{3}$$

and the correction factor F was very close to unity under operating conditions of this study. For the purpose of combined uncertainty minimization [23], Q_{ave} was estimated as the weighted average of the air-side and coolant-side heat-transfer rates using the following:

$$Q_{\text{ave}} = \omega_a Q_a + \omega_c Q_c \tag{4a}$$

where ω_a and ω_c are the weighting factors that depend on the uncertainties in the heat-transfer rates of the air side ξ_a and of the coolant side ξ_c as follows:

$$\omega_a = \frac{1/\xi_a^2}{1/\xi_a^2 + 1/\xi_c^2}, \quad \omega_c = \frac{1/\xi_c^2}{1/\xi_a^2 + 1/\xi_c^2} \tag{4b}$$

For all the data presented in this paper, the relative discrepancy between the air and coolant heat-transfer rates $|Q_a - Q_c|/Q_{\text{ave}}$ had an average value of 5% or less.

The overall thermal conductance (UA_{tot}) of the heat exchanger was then available from Eq. (2), and it could be related to the total thermal resistance through the following expression (where the contact resistance and fouling are assumed to be negligible):

$$\frac{1}{UA_{\text{tot}}} = R_c + R_{\text{cond}} + R_a \tag{5}$$

where R_c, R_{cond}, and R_a are the coolant-side convective resistance, tube wall conduction resistance, and air-side heat-transfer resistance, respectively,

$$R_c = \frac{D_i}{\mathrm{Nu}_c \; k_c A_c} \tag{6}$$

$$R_{\mathrm{cond}} = \frac{\ln\left(\frac{D_o}{D_i}\right) \cdot D_i}{2k_{\mathrm{Cu}} A_c} \tag{7}$$

$$R_a = \frac{1}{\eta_0 h_a A_{\mathrm{tot}}} \tag{8}$$

The conduction resistance across the tube wall was calculated assuming steady, 1D heat conduction as described in Eq. (7). In this study, R_{cond} was found to be less than 0.1% of the total resistance. The conduction resistance of a soldered collar is also negligible.

Because the coolant flow was divided into six circuits, the tube-side Reynolds number was always below 1000. Therefore, laminar flow prevailed and the following correlations [24] were adopted to evaluate the coolant-side convective Nusselt number:

$$\mathrm{Nu}_c = 1.86 \cdot \left(\frac{\mathrm{Re}_D \; \mathrm{Pr}_c}{L/D_i}\right)^{1/3} \cdot \left(\frac{\mu}{\mu_w}\right)^{0.14} \quad \text{for combined entry length} \tag{9a}$$

$$\mathrm{Nu}_c = 3.66 + \frac{0.0668(D_i/L)\mathrm{Re}_D \; \mathrm{Pr}_c}{1 + 0.04[(D_i/L)\mathrm{Re}_D \; \mathrm{Pr}_c]^{2/3}} \quad \text{for thermal entry length} \tag{9b}$$

where μ and μ_w are the coolant dynamic viscosities evaluated at the average fluid temperature and wall temperature, respectively. Equation (9) was applied by using Eq. (9*a*) for the portion of the tube over which hydrodynamic development occurred and Eq. (9*b*) over the rest of the tube, and finally taking the weighted average. As mentioned above, the coolant was a single-phase ethylene glycol/water mixture. The thermophysical properties of the mixture were calculated using correlations provided by the manufacturer, based on the measured coolant temperature and specific gravity.

The air-side resistance R_a in Eq. (8) is a combination of the resistance due to air-side convection from the tube and the fin surface areas. η_o is the overall surface efficiency defined as

$$\eta_o = 1 - \left(\frac{A_{\mathrm{fin}}}{A_{\mathrm{tot}}}\right) \cdot (1 - \eta_f) \tag{10}$$

The fin efficiency η_f was determined using the modified equations for plane fins, as suggested by Wang et al. [25],

$$\eta_f = \frac{\tanh(mr\phi)}{mr\phi} \tag{11a}$$

$$m = \sqrt{\frac{2h_a}{k_f \delta_f}} \tag{11b}$$

$$\phi = \left(\frac{R_{\mathrm{eq}}}{r} - 1\right) \cdot \left[1 + 0.35 \ln\left(\frac{R_{\mathrm{eq}}}{r}\right)\right] \tag{11c}$$

For inline tube layout,

$$\frac{R_{\mathrm{eq}}}{r} = 1.28 \cdot \frac{X_M}{r} \cdot \left(\frac{X_L}{X_M} - 0.2\right)^{1/2} \tag{11d}$$

Equations (1*a*), (1*b*), (2), (3), (4*a*), (4*b*), (5)–(8), (9*a*), (9*b*), (10), and (11*a*)–(11*d*) were programed with all the measured data into a commercial software package, engineering equation solver (EES), and the air-side heat-transfer coefficient h_a was determined in an iterative manner.

Data interpretation followed the methods detailed by the ARI Standard for fin-and-tube heat exchangers. Given the results of h_a, the Colburn j-factor is obtained from

$$j = \frac{\mathrm{Nu}_a}{\mathrm{Re}_{dh} \; \mathrm{Pr}_a^{1/3}} = \frac{h_a}{G c_{p,a}} \cdot \mathrm{Pr}_a^{2/3} \tag{12}$$

where the mass flux $G = \dot{m}_a / A_{\mathrm{min}}$ corresponds to the minimum free flow area. All the fluid properties were evaluated at the average values of inlet and outlet temperatures under the steady-state conditions. The nondimensional friction factor of the heat exchanger f is expressed as (excluding the negligible entrance and exit losses)

$$f = \frac{2\Delta P \rho_a}{G^2} \cdot \left(\frac{A_{\mathrm{min}}}{A_{\mathrm{tot}}}\right) - (1 + \sigma^2) \cdot \left(\frac{\rho_{\mathrm{up}}}{\rho_{\mathrm{down}}} - 1\right) \cdot \left(\frac{A_{\mathrm{min}}}{A_{\mathrm{tot}}}\right) \cdot \left(\frac{\rho_a}{\rho_{\mathrm{up}}}\right) \tag{13a}$$

with

$$\sigma = \frac{A_{\mathrm{min}}}{A_{\mathrm{front}}} \tag{13b}$$

and

$$\rho_a = \frac{\rho_{\mathrm{up}} + \rho_{\mathrm{down}}}{2} \tag{13c}$$

Two evaluation criteria were employed to assess the overall performance of the heat-exchanger specimen with and without VGs, i.e., the modified London area goodness factor ($j/f^{1/3}$ versus Re) and the volume goodness factor (heat-transfer coefficient versus pumping power per unit heat-transfer area). The pumping power PW required in the system is proportional to the core pressure drop across the heat exchanger

$$PW = \frac{\dot{m}_a \Delta P}{\rho_a} \tag{14}$$

Estimation of the uncertainties for all the calculated quantities followed the error-propagation methodology as described in NIST Technical Note 1297 [26], also utilizing the EES software.

4 Results and Discussion

4.1 Air-Side Thermal Performance. Enhanced thermal performance of the heat exchanger after attaching the VGs is compared with the baseline performance in Fig. 6, where the air-side heat-transfer coefficient h_a and the thermal resistance R_a are presented. The uncertainty in all figures is hereafter provided at representative points for better readability only. Using a 95% confidence interval and standard error-propagation analysis, the average uncertainties in h_a and R_a over the entire air velocity range were estimated to be 9.1% and 8.2%, respectively. The 10 deg VG array induces essentially no thermal improvement, as is observed that the differences in h_a and R_a from the baseline results are well within the experimental uncertainties. Such behavior indicates the ineffectiveness of the vortex-generation method at a relatively small attack angle due to the weak vortices produced. The small pair brings about a moderate heat-transfer augmentation of up to 32%. In contrast, both the 30 deg array and the large pair yield a 25–55% increase in the heat-transfer coefficient, and concurrently, a 22–35% reduction in the thermal resistance over the experimental range. The similar heat-transfer performance is consistent with established understanding of VG enhancement: Because of the same heights, chord lengths, and attack angles, the

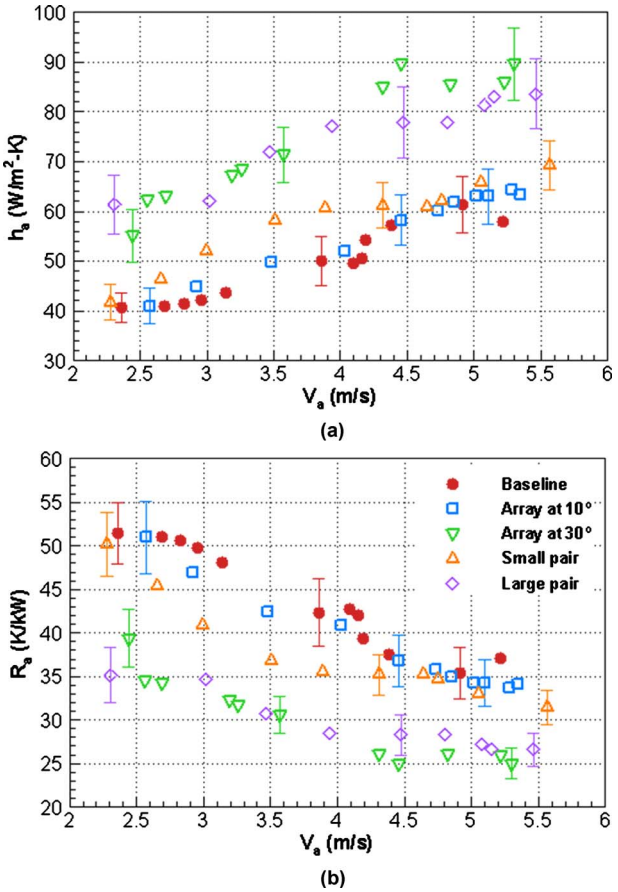

Fig. 6 Baseline and VG-enhanced thermal performance as a function of frontal air velocity: (*a*) air-side heat-transfer coefficient and (*b*) air-side thermal resistance

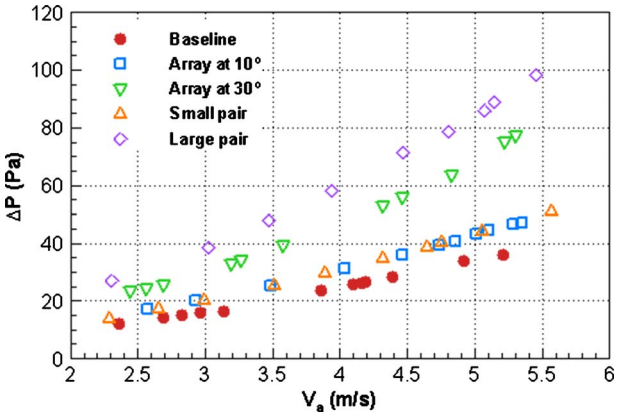

Fig. 7 Pressure drop across the heat exchanger with and without VGs

vortex strengths and affected areas for the two designs are expected to be close. The maximum enhancement can be seen to occur in the low velocity region. Recall that the VG-to-fin area ratio was calculated to be less than 1.0%. Therefore, the heat-transfer improvement for the enhanced fins can be mainly ascribed to the longitudinal vortices. Through enhancing bulk mixing, modifying the boundary layer, and potentially causing flow destabilization, the vortices result in a net effect of decreased air-side thermal resistance (and increased convective heat-transfer coefficient). The first two mechanisms are simply induced by the swirl and downwash motion of the longitudinal vortices. Evidence for the third mechanism was provided in an experimental study [9], which showed that the turbulence level increased from 0.8% of the incoming flow to above 10% four channel heights downstream of the winglet tips for $Re > 2200$ in a developing channel.

4.2 Core Pressure Drop. The core pressure drop ΔP across the heat exchanger with and without attaching VGs is presented in Fig. 7. The uncertainty in measured ΔP never exceeded 1.5% over the entire experimental range and thus is not shown in the plot. The pressure drop increases monotonically with the frontal air velocity, and the deviation from the baseline data after the addition of VGs becomes progressively more apparent for increasing velocities. This behavior confirms that the extra pressure loss associated with the use of VGs is predominately due to the form drag, which is proportional to the velocity square. The 10 deg array and the small pair exhibit similar additional pressure drop of 20–40%. By comparison, the 30 deg array causes a relatively severe pressure drop penalty of 80–110%. Nevertheless, the magnitude is still 40% lower than that of the large pair, even though the designs have the same attack angle and projected area. Representative streamlines in the wake behind a single delta winglet (winglet 1) computed by Ferrouillat et al. [27] using the large-eddy simulation (LES) turbulence model are illustrated in Fig. 8. It is clear that if a trailing winglet (winglet 2) is placed downstream following the proposed arrangement, the generated vortex by winglet 1 will transport high-momentum fluid toward the fin surface behind winglet 2, thus narrowing the wake zone and mitigating the pressure difference between the front and back of the winglet. The vortex strength of the trailing winglet is accordingly diminished. However, based on the heat-transfer results, this undesired effect may have been compensated by the simultaneously improved heat transfer in the wake, without impairing the overall thermal performance.

Note that the magnitude of extra pressure loss for the 30 deg array and the large pair is considerably larger than that reported by Joardar and Jacobi [4] (26–88% for delta-winglet pairs deployed in three rows). In addition to a higher Reynolds number range (1400–3400 versus 220–960), a larger attack angle (30 deg versus 15 deg), and a smaller flow depth (51 mm versus 178 mm) in this work, another cause is the difference in the VG location relative to the tubes. The current array was placed at the leading edge mainly due to the short flow passage of the test heat exchanger; whereas, a further downstream placement was adopted in the earlier work [4] to take advantage of tube-wake management. In particular cases [2,3], if the VGs are carefully designed and oriented such that reduction in the tube form drag outweighs the drag introduced by the VGs themselves, it is even possible to reduce the pressure

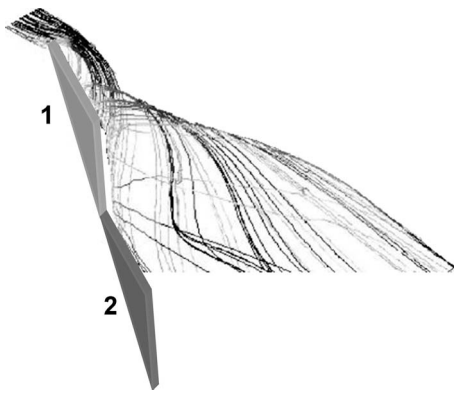

Fig. 8 Representative streamlines in the wake behind winglet 1 (without winglet 2) computed by the LES turbulence model [27] (adopted with modification). Winglet 2 was drawn to show the relative position of the trailing winglet to the preceding one in a VG array design.

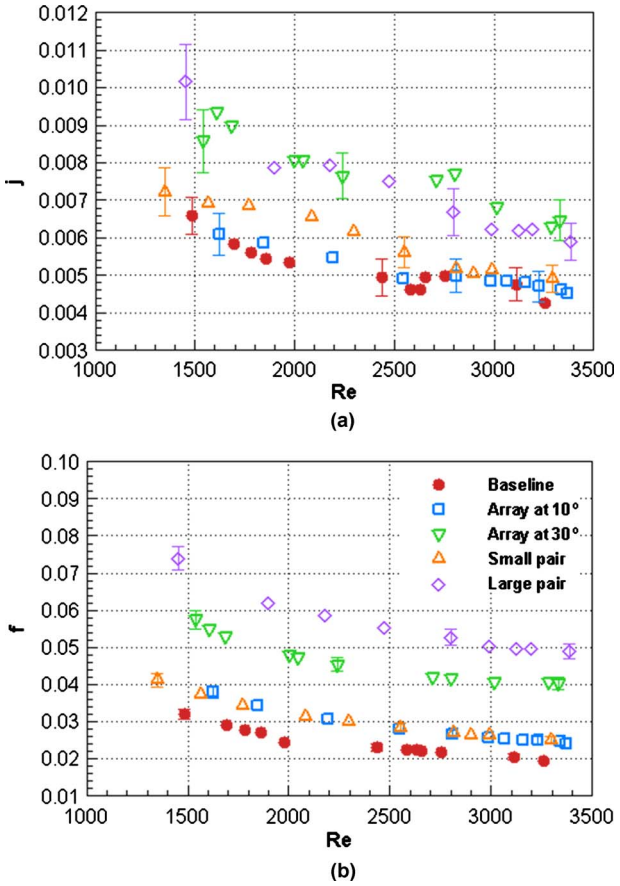

Fig. 9 (*a*) **Colburn *j*-factor and** (*b*) **friction factor versus air-side Reynolds number for the baseline and VG-enhanced heat exchanger**

drop as compared with the smooth heat exchanger without the generators. However, such a favorable configuration, if it exists, is definitely case dependent. Its determination is complicated by the numerous design parameters for a specific heat exchanger and VG type. The concern about the hydraulic performance in the presence of VGs may be alleviated by noting that the additional pressure drop is small relative to the overall losses in typical air-handling equipment for most HVAC&R systems. In point of fact, the incremental fan power required to overcome the pressure drop penalty for the 30 deg array was always below 5.0 W (calculated from Eq. (14)).

4.3 *j*- and *f*-Factors. The conventional representations of thermal-hydraulic performance in terms of the Colburn *j*-factor and *f*-factor are presented in Fig. 9, where similar enhancement characteristics as shown in h_a and ΔP are observed. The average increase in the *j*-factor is roughly 15% for the small pair, and 45% for the large pair and the 30 deg array. The latter two designs achieve heat-transfer augmentation far beyond the experimental uncertainty of 9.2% in the *j*-factor. The heat-transfer improvement is at the cost of a 25% increase in the *f*-factor for the small pair, 90% for the 30 deg array, and as high as 140% for the large pair. The uncertainty in the *f*-factor is about 4.0%.

4.4 Overall Performance Evaluation. The overall performance of the VG-enhanced heat exchanger is evaluated using the modified London area goodness factor ($j/f^{1/3}$ versus Re) and compared with the smooth heat exchanger in Fig. 10. Nearly all the data for the 10 deg array fall below the baseline points due to a similar heat-transfer performance and a larger pressure drop—the heat-exchanger performance is degraded. The results for the

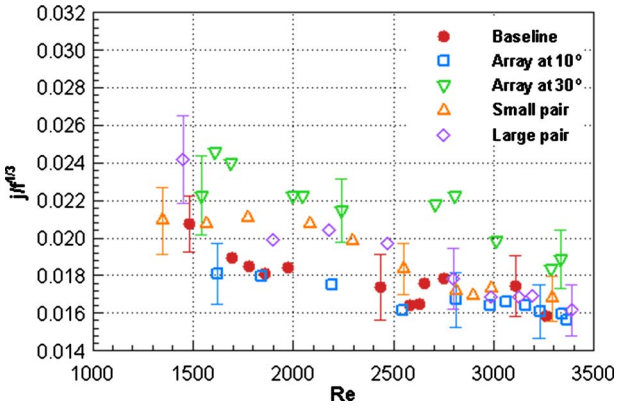

Fig. 10 Area goodness factor $j/f^{1/3}$ versus air-side Reynolds number for the baseline and VG-enhanced heat exchanger

pair designs (small and large) are seen to be close for $\mathrm{Re} \gtrsim 2000$. Both yield mild enhancement within the experimental uncertainty (9.1%). In contrast, the 30 deg array increases the modified area goodness factor by approximately 15–25% and demonstrates the best performance among all VG designs considered. The improvement is more prominent at low Reynolds numbers. By neglecting the density variation of air between upstream and downstream of the heat exchanger in Eq. (13*a*), and combining Eqs. (12), (13*a*), and (14) with the elimination of the mass flux *G*, a relation in the following form results (see also Ref. [7]):

$$\frac{\dfrac{j}{f^{1/3}}}{\left(\dfrac{j}{f^{1/3}}\right)_0} = \frac{\dfrac{hA_{\mathrm{tot}}}{(hA_{\mathrm{tot}})_0}}{\left(\dfrac{PW}{PW_0}\right)^{1/3} \cdot \left(\dfrac{A_{\mathrm{tot}}}{A_{\mathrm{tot},0}}\right)^{2/3}} \tag{15}$$

where the subscript "0" refers to the baseline quantities. Since the air-side resistance is the dominant part in Eq. (5), Eq. (15) may be approximated as

$$\frac{\dfrac{j}{f^{1/3}}}{\left(\dfrac{j}{f^{1/3}}\right)_0} \simeq \frac{\dfrac{Q}{Q_0}}{\left(\dfrac{PW}{PW_0}\right)^{1/3} \cdot \left(\dfrac{A_{\mathrm{tot}}}{A_{\mathrm{tot},0}}\right)^{2/3} \cdot \dfrac{\mathrm{LMTD}}{\mathrm{LMTD}_0}} \tag{16}$$

Significance of the enhancement in $j/f^{1/3}$ is then elucidated. By selecting one of the operational variables in the RHS of Eq. (16) as the desired objective subject to design constraints on the remaining variables, any of the four kinds of performance improvements as described by Webb and Kim [7] can be realized. From the viewpoint of "area goodness," the enhanced heat exchanger would require a smaller heat-transfer area to accomplish a given heat duty at the fixed pumping power if LMTD maintains constant. For the 30 deg array case, specifically, the average enhancement ratio of 1.21 was calculated to bring about 25% reduction in A_{tot}. As a result, the heat exchanger can be manufactured with less material, which allows more compactness and hopefully reduces cost. The size reduction also means a smaller volume of refrigerant will be used. This reduction could be a significant saving in the manufacture of refrigeration equipment.

Another commonly used evaluation criterion is the volume goodness factor, i.e., the air-side heat-transfer coefficient versus the pumping power per unit heat-transfer area. Such a comparison of the five configurations is presented in Fig. 11, where the 30 deg array exhibits the highest performance again. A higher volume goodness factor for a given heat exchanger may be interpreted as either larger heat duty under the operation of fixed pumping power or smaller pumping power required to fulfill fixed heat duty. The former enhancement can also be considered to reduce the required condensing pressure in a vapor-compression ma-

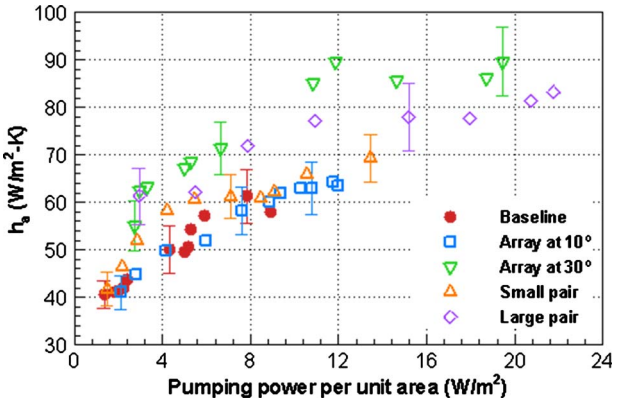

Fig. 11 Volume goodness factor, i.e., the air-side heat-transfer coefficient versus the pumping power per unit heat-transfer area for the baseline and VG-enhanced heat exchanger

chine, with attendant compressor power savings. The latter enhancement can be considered as a direct savings of fan power, although as pointed out earlier, core pressure drop is typically not large relative to the overall air-handling losses.

5 Summary and Conclusions

The thermal-hydraulic performance of a prototype plain-fin round-tube heat exchanger was experimentally evaluated before and after the implementation of four types of VGs: a new VG array deployed in a V at 10 deg or 30 deg and two conventional single-pair designs with one area being half of the other. The frontal air velocity ranged from 2.3 m/s to 5.5 m/s, corresponding to a Reynolds number range based on the hydraulic diameter of 1400–3400. The experimental results show little impact of the 10 deg array and a moderate heat-transfer improvement of up to 32% for the small pair, both introducing additional pressure loss of approximately 20–40%. For the 30 deg array and the large pair, similar augmentation of 25–55% in air-side heat-transfer coefficients is obtained, accompanied by average pressure drop penalties of 90% and 140%, respectively. Performance evaluation using the criteria of the modified area goodness factor and the volume goodness factor indicates the superiority of the heat exchanger enhanced by the 30 deg array among all the investigated VGs. The VG array is found more effective at comparatively low Reynolds numbers, representative of many HVAC&R applications and compact heat-exchanger designs.

The use of a V-array deployment of VGs was motivated by group locomotion of animals in nature as observed in bird migration, fish schooling, and arthropod queues, and was aimed at creating constructive interference between vortices. The two-row winglet configuration was employed for the test specimen and its geometry followed recommendations of prior work. Based on the heat transfer and core pressure drop results, it is conjectured that the vortex produced by the leading winglet reduces the wake zone of the trailing winglet and mitigates the pressure difference between its fore and aft sides. The overall performance of the heat exchanger is appreciably enhanced. The design may be further improved through optimization of winglet geometry (most likely by increasing appropriately the aspect ratio and winglet height relative to fin pitch) and placement. Due to the very large parametric space, no further effort was undertaken in this study to determine an optimal design. A computational analysis may be useful in determining a placement strategy that makes the best use of tube-wake management. Successful numerical investigations have been reported by Joardar and Jacobi [28] and, more recently, Chu et al. [29] for relevant fin-and-tube configurations with multiple rows of VGs. Both studies used the commercial CFD solver, FLUENT, and the results agreed well with the experimental data from Joardar and Jacobi [4]. Finally, it may be anticipated that in the practical design the winglets will likely be punched out of the fins, and the impact of the holes should also be assessed in any design optimization study.

Acknowledgment

This work was financially supported by the Air Conditioning and Refrigeration Center (ACRC) at the University of Illinois. The authors are grateful to Luvata Co. for providing the heat-exchanger samples, and to Tom Samoden for granting permission on the use of his photograph.

Nomenclature

A = heat-transfer area (m^2)
C_p = specific heat (J/kg K)
D = tube diameter (m)
F = correction factor, Eq. (2)
f = Fanning friction factor
G = mass flux at minimum flow area (kg/m^2 s)
h = heat-transfer coefficient (W/m^2 K)
j = Colburn j-factor
k = thermal conductivity (W/m K)
L = flow length (m)
$\dot{m}$ = mass flow rate (kg/s)
Nu = Nusselt number
PW = pumping power (W), Eq. (14)
Pr = Prandtl number
Q = heat-transfer rate (W)
R = thermal resistance (K/kW)
R_{eq} = equivalent radius for circular fin (m)
r = tube radius including collar fin thickness (m)
Re = Reynolds number
T = temperature (°C)
U = overall heat-transfer coefficient (W/m^2 K)
X_L = half longitudinal tube pitch (m)
X_M = half transverse tube pitch (m)

Greek Symbols

ΔP = core pressure drop across the heat exchanger (Pa)
δ = fin thickness (m)
η = fin efficiency
ρ = density (kg/m^3)
μ = dynamic viscosity (N s/m^2)
σ = surface ratio A_{min}/A_{front}
ω = weighting factor of heat-transfer rate, Eq. (4*a*)
ξ = uncertainty in heat-transfer rate, Eq. (4*b*)

Subscripts

a = air
ave = average
c = coolant
cond = heat conduction
Cu = copper
dh = hydraulic diameter
down = downstream of heat exchanger
f = fin
front = frontal area of heat exchanger
i = inlet, inside
min = minimum
o = outlet, outside, or overall in Eq. (10)
tot = total
up = upstream of the heat exchanger
w = wall

References

[1] Fiebig, M., Valencia, A., and Mitra, N. K., 1993, "Wing-Type Vortex Generators for Fin-and-Tube Heat Exchangers," Exp. Therm. Fluid Sci., **7**, pp. 287–295.

[2] Wu, J. M., and Tao, W. Q., 2007, "Investigation on Laminar Convection Heat Transfer in Fin-and-Tube Heat Exchanger in Aligned Arrangement With Longitudinal Vortex Generator From the Viewpoint of Field Synergy Principle," Appl. Therm. Eng., **27**, pp. 2609–2617.
[3] Torii, K., Kwak, K. M., and Nishino, K., 2002, "Heat Transfer Enhancement Accompanying Pressure-Loss Reduction With Winglet-Type Vortex Generators for Fin-Tube Heat Exchangers," Int. J. Heat Mass Transfer, **45**, pp. 3795–3801.
[4] Joardar, A., and Jacobi, A. M., 2008, "Heat Transfer Enhancement by Winglet-Type Vortex Generator Arrays in Compact Plain-Fin-and-Tube Heat Exchangers," Int. J. Refrig., **31**, pp. 87–97.
[5] Biswas, G., Deb, P., and Biswas, P., 1994, "Generation of Longitudinal Streamwise Vortices—A Device for Improving Heat Exchanger Design," ASME J. Heat Transfer, **116**, pp. 588–597.
[6] Leu, J. S., Wu, Y. H., and Jang, J. Y., 2004, "Heat Transfer and Fluid Flow Analysis in Plate-Fin and Tube Heat Exchangers With a Pair of Block Shape Vortex Generators," Int. J. Heat Mass Transfer, **47**, pp. 4327–4338.
[7] Webb, R. L., and Kim, N.-H., 2005, *Principles of Enhanced Heat Transfer*, 2nd ed., Taylor & Francis, New York.
[8] Jacobi, A. M., and Shah, R. K., 1995, "Heat Transfer Surface Enhancement Through the Use of Longitudinal Vortices: A Review of Recent Progress," Exp. Therm. Fluid Sci., **11**, pp. 295–309.
[9] Fiebig, M., 1995, "Embedded Vortices in Internal Flow: Heat Transfer and Pressure Loss Enhancement," Int. J. Heat Fluid Flow, **16**, pp. 376–388.
[10] Fiebig, M., 1998, "Vortices, Generators and Heat Transfer," Chem. Eng. Res. Des., **76**(2), pp. 108–123.
[11] Elsherbini, A., and Jacobi, A. M., 2002, "The Thermal-Hydraulic Impact of Delta-Wing Vortex Generators on the Performance of a Plain-Fin-and-Tube Heat Exchanger," HVAC&R Res., **8**, pp. 357–370.
[12] Wang, C. C., Chang, Y. J., Wei, C. S., and Yang, B. C., 2004, "A Comparative Study of the Airside Performance of Winglet Vortex Generator and Wavy Fin-and-Tube Heat Exchangers," ASHRAE Trans., **110**, pp. 53–57.
[13] Joardar, A., and Jacobi, A. M., 2005, "Impact of Leading Edge Delta-Wing Vortex Generators on the Thermal Performance of a Flat Tube, Louvered-Fin Compact Heat Exchanger," Int. J. Heat Mass Transfer, **48**, pp. 1480–1493.
[14] Sommers, A. D., and Jacobi, A. M., 2005, "Air-Side Heat Transfer Enhancement of a Refrigeration Evaporator Using Vortex Generation," Int. J. Refrig., **28**, pp. 1006–1017.
[15] Lissaman, P. B. S., and Shollenberger, C. A., 1970, "Formation Flight of Birds," Science, **168**, pp. 1003–1005.
[16] Weimerskirch, H., Martin, J., Clerquin, Y., Alexandre, P., and Jiraskova, S., 2001, "Energy Saving in Flight Formation," Nature (London), **413**, pp. 697–698.
[17] Weihs, D., 1973, "Hydromechanics of Fish Schooling," Nature (London), **241**, pp. 290–291.
[18] Bill, R. G., and Herrnkind, W. F., 1976, "Drag Reduction by Formation Movement in Spiny Lobsters," Science, **193**, pp. 1146–1148.
[19] Hou, X. G., Siveter, D. J., Aldridge, R. J., and Siveter, D. J., 2008, "Collective Behavior in an Early Cambrian Arthropod," Science, **322**, p. 224.
[20] Saleh, J., 2002, *Fluid Flow Handbook*, 1st ed., McGraw-Hill, New York.
[21] Bushnell, D. M., and Moore, K. J., 1991, "Drag Reduction in Nature," Annu. Rev. Fluid Mech., **23**, pp. 65–79.
[22] Liu, L., and Jacobi, A. M., 2009, "Air-Side Surface Wettability Effects on the Performance of Slit-Fin-and-Tube Heat Exchangers Operating Under Wet-Surface Conditions," ASME J. Heat Transfer, **131**, p. 051802.
[23] Park, Y., Liu, L., and Jacobi, A. M., 2010, "A Rational Approach for Combining Redundant, Independent Measurements to Minimize Combined Experimental Uncertainty," Exp. Therm. Fluid Sci., to be published.
[24] Incropera, F. P., and Dewitt, D. P., 2002, *Fundamentals of Heat and Mass Transfer*, 4th ed., Wiley, New York.
[25] Wang, C. C., Webb, R. L., and Chi, K. Y., 2000, "Data Reduction for Air-Side Performance of Fin-and-Tube Heat Exchangers," Exp. Therm. Fluid Sci., **21**, pp. 218–226.
[26] Taylor, B. N., and Kuyatt, C. E., 1994, "Guidelines for Evaluating and Expressing the Uncertainty of NIST Measurement Results," National Institute of Standards and Technology Technical Note 1297.
[27] Ferrouillat, S., Tochon, P., Garnier, C., and Peerhossaini, H., 2006, "Intensification of Heat-Transfer and Mixing in Multifunctional Heat Exchangers by Artificially Generated Streamwise Vorticity," Appl. Therm. Eng., **26**, pp. 1820–1829.
[28] Joardar, A., and Jacobi, A. M., 2007, "A Numerical Study of Flow and Heat Transfer Enhancement Using an Array of Delta-Winglet Vortex Generators in a Fin-and-Tube Heat Exchanger," ASME J. Heat Transfer, **129**, pp. 1156–1167.
[29] Chu, P., He, Y. L., and Tao, W. Q., 2009, "Three-Dimensional Numerical Study of Flow and Heat Transfer Enhancement Using Vortex Generators in Fin-and-Tube Heat Exchangers," ASME J. Heat Transfer, **131**, p. 091903.

Viscous Dissipation and Rarefaction Effects on Laminar Forced Convection in Microchannels

Arman Sadeghi

Mohammad Hassan Saidi[1]
e-mail: saman@sharif.edu

Center of Excellence in Energy Conversion (CEEC),
School of Mechanical Engineering,
Sharif University of Technology,
P.O. Box 11155-9567,
Tehran, Iran

Fluid flow in microchannels has some characteristics, which one of them is rarefaction effect related with gas flow. In the present work, hydrodynamically and thermally fully developed laminar forced convection heat transfer of a rarefied gas flow in two microgeometries is studied, namely, microannulus and parallel plate microchannel. The rarefaction effects are taken into consideration using first-order slip velocity and temperature jump boundary conditions. Viscous heating is also included for either the wall heating or the wall cooling case. Closed form expressions are obtained for dimensionless temperature distribution and Nusselt number. The results demonstrate that for both geometries, as Brinkman number increases, the Nusselt number decreases. However, the effect of viscous heating on the Nusselt number at greater values of Knudsen number becomes insignificant. In the absence of viscous heating, increasing values of Knudsen number lead to smaller values of Nusselt number. Furthermore, it is observed that viscous heating causes singularities in Nusselt number values. Also, asymmetry causes singularities in Nusselt numbers of both microannulus walls and the parallel plate wall having lower heat flux, even in the absence of viscous heating. For parallel plate microchannel, in the absence of viscous heating, Nusselt number of the wall having larger heat flux is an increasing function of the wall heat fluxes ratio.
[DOI: 10.1115/1.4001100]

Keywords: microchannel, slip flow, temperature jump, viscous dissipation, Knudsen number, laminar flow

1 Introduction

Microchannels are used for momentum and energy transfer in microdevices such as microheat exchangers for cooling of electronic circuits, reactors for separating biological cells, and micropumps used in inkjet printing. At macroscale, classical conservation equations are coupled with the corresponding wall boundary conditions. The boundary condition for the fluid over a solid surface is the generally accepted no-slip condition. However, when characteristic length scale of the device is comparable with gas mean free path, this assumption is no longer valid since the rarefaction effects are important. From a great deal of research, it is clear that continuum analyses are unable to predict flow properties in micronsize devices. An experimental investigation of gas flow in channels of 100 μm wide and ranging in depth from 0.5 μm to 20 μm was performed by Harley et al. [1], using nitrogen, helium, and argon gases. They found that correlations based on classical assumptions cannot predict flow characteristics in microchannels. An experimental investigation was carried out by Araki et al. [2] to study frictional characteristics of nitrogen and helium flows in microchannels with hydraulic diameter range of 3–10 μm. They concluded that the frictional resistance of gas flow in microchannel is smaller than that in the conventional-sized channel. Also, the experiments conducted by Arkilic and coworkers [3,4], Liu et al. [5], and Choi et al. [6] on the transport of gases in microchannels confirm the deviation from continuum approach at microscale.

The deviation of the state of the gas from continuum behavior is measured by the Knudsen number (Kn). For a microchannel, the Knudsen number is defined as $\mathrm{Kn}=\lambda/D_h$, where D_h is the channel hydraulic diameter and λ is the mean free path of gas molecules, given by $\lambda=\mu\sqrt{\pi/2RT\rho^2}$, where μ is the dynamic viscosity, R is the gas constant, and T and ρ are the temperature and density of the gas, respectively, [7]. Based on a classification given by Beskok and Karniadakis [8], gas flow can be categorized into four regimes according to its Knudsen number. For $\mathrm{Kn}<10^{-3}$, the gas is considered as a continuum while for $\mathrm{Kn}>10$ it is considered as a free molecular flow. In the Knudsen number ranging between 10^{-3} and 10, two different regimes exist: slip flow ($10^{-3}\leq\mathrm{Kn}\leq0.1$) and transition flow ($0.1<\mathrm{Kn}\leq10$). In general, there are several rarefaction effects, such as discontinuities of velocity and temperature on boundary, non-Newtonian components of stress tensor, non-Fourier heat flux, and formation of Knudsen boundary layer [9]. In the slip flow regime, deviations from the state of continuum are relatively small and the Navier–Stokes equations are still valid, except at the region next to the boundary, which is known as Knudsen boundary layer. The Knudsen boundary layer is significant only up to distances of the order of one mean free path from the wall [10]. So, besides velocity and temperature discontinuities at the wall, its effects are negligible in slip flow regime and the Navier–Stokes equations may be applied to the whole domain. The velocity and temperature discontinuities are incorporated into the solution as boundary conditions. Several forms of the slip boundary conditions have been proposed in literature, among them first- and second-order slip boundary conditions (based on Knudsen number). Although second-order slip boundary conditions are more accurate than the first-order conditions, however, first-order conditions are sufficiently accurate in slip flow regime [10]. This, accompanied by their simplicity to

[1]Corresponding author.

Contributed by the Heat Transfer Division of ASME for publication in the JOURNAL OF HEAT TRANSFER. Manuscript received January 31, 2009; final manuscript received January 12, 2010; published online April 22, 2010. Assoc. Editor: Satish G. Kandlikar.

use, has led to the wide use of first-order slip boundary conditions in literature. It is noteworthy that the measured friction factors obtained by Harley et al. [1], Araki et al. [2], Arkilic et al. [4], and Liu et al. [5] matched well with theoretical predictions assuming fully developed first-order slip flow.

The analytical study of internal slip flow has been confined to simple geometries. Hydrodynamic aspects of slip flow in the circular tube and parallel plate channel were studied by Kennard [11]. Ebert and Sparrow [12] determined the velocity distribution and pressure drop of slip flow in rectangular and annular ducts. More recently, Duan and Muzychka [13] performed an analytical analysis to describe fully developed laminar flow in elliptical microchannels. All the results in Refs. [11–13] showed that rarefaction effect decreases pressure drop in microchannels with respect to convectional channels for a given mass flow rate.

Also, some research works have been performed to study heat transfer characteristics of rarefied gas flow in microchannels. The problem of laminar slip flow in microtubes with uniform wall heat flux has been analytically studied by Ameel et al. [14]. They showed that as Knudsen number increases the fully developed Nusselt number decreases. Zhu et al. [15] performed a theoretical analysis for slip flow heat transfer in a parallel plate microchannel with constant but different wall heat fluxes. The analysis was accomplished by combining the solutions of two subproblems consisting of a microchannel with one wall being adiabatic and the other having constant heat flux. Tunc and Bayazitoglu [16] studied both hydrodynamically and thermally fully developed slip flow in rectangular microducts having constant wall heat flux, using integral transform method. Recently, Sadeghi et al. [17] performed a boundary layer analysis for simultaneously developing flow through parallel plate microchannels. The effects of Knudsen number on friction factor, Nusselt number, and entry length have been determined.

The numerical researches related to forced convection slip flow heat transfer in microchannels include simultaneously developing, thermally developing and also fully developed laminar flow through different microgeometries. Al-Nimr et al. [18] studied fully developed thermal behaviors of parallel flow microchannel heat exchanger. Thermally developing slip flow forced convection heat transfer in microtubes was numerically considered by Sun et al. [19]. Three different forms of the boundary condition, including constant wall temperature, constant wall heat flux, and linear variation in wall temperature were considered. Renksizbulut and co-workers [20,21] investigated simultaneously developing laminar flow and heat transfer in the entrance region of rectangular and trapezoidal channels with uniform wall temperature. A control-volume based numerical method was used to solve the Navier–Stokes and energy equations.

Viscous dissipation effects are typically significant only for high viscous flows or in presence of high gradients in velocity distribution. In macroscale, such high gradients occur in high velocity flows. In microscale devices, such as microchannels, however, because of small dimensions, such high gradients may occur even for low velocity flows. So for microchannels, the viscous dissipation should be taken into consideration. Viscous dissipation features as a source term in the fluid flow due to the conversion of kinetic motion of the fluid to thermal energy and causes the variation in the temperature distribution. The effects of viscous dissipation on the temperature field and ultimately on the friction factor were investigated by Koo and Kleinstreuer [22,23], using dimensional analysis and experimentally validated computer simulations. It was found that ignoring viscous dissipation could affect accurate flow simulations and measurements in microconduits. El-Genk and Yang [24] developed a semiempirical analytical expression for determining the influences of temperature rise due to the viscous dissipation on friction number in microtubes, which accounts for no-slip and slip at the wall. They demonstrated that with a slip, the friction number almost exponentially decreases as the channel diameter decreases. Tunc and Bayazitoglu [25] performed an analytical study to describe hydrodynamically fully developed and thermally developing slip flow in circular microchannels, considering viscous dissipation effects. Aydin and Avci [26] analytically studied fully developed laminar forced convective heat transfer of a Newtonian fluid in a microchannel between two parallel plates, considering viscous dissipation effects for both uniform wall temperature and uniform wall heat flux. The thermally developing case was studied by Jeong and Jeong [27], using the method of separation of variables. Their results showed that the Nusselt number decreases as Knudsen number or Brinkman number increases. Jiji [28] examined the effects of rarefaction, dissipation, curvature, and accommodation coefficients on flow and heat transfer characteristics in rotating microdevices. The problem was modeled as a cylindrical Couette flow with a rotating shaft and stationary housing.

Microannulus is a useful type of microchannels, which can be used as a micro heat exchanger. Such a geometry can also be found in cooling of high power resistive magnets, compact fission reactor cores, fusion reactor blankets, advanced space thermal management systems, and high density multichip modules in supercomputers and other modular electronics [29]. Duan and Muzychka [30] studied heat transfer characteristics of hydrodynamically and thermally fully developed laminar rarefied gas flow in annular microducts with constant wall heat fluxes, neglecting viscous heating effects. Avci and Aydin [31] studied the slip flow heat transfer in a microannulus for the special case of one wall being adiabatic and the other having constant heat flux, considering viscous heating effects. The effects of viscous heating, rarefaction and aspect ratio of annular geometry on Nusselt number were discussed.

From the above mentioned literature review, it is clear that there is still a lack of information about flow characteristics of a viscous dissipative rarefied gas in a microannulus with constant wall heat fluxes. The main objective of the present study is to analytically investigate hydrodynamically and thermally fully developed laminar forced convection heat transfer through annular microchannels with asymmetrically heated walls. A parallel plate microchannel is also considered separately, despite the fact that it is a special case of the annuli when the diameters ratio tends unity. This is because of its fundamental importance in small scale applications. The energy equation is solved using the previously obtained velocity distributions. The interactive effects of flow parameters on temperature field and Nusselt number are shown in graphical form and also discussed in detail.

2 Slip Velocity and Temperature Jump

As mentioned earlier because of velocity and temperature discontinuities on boundary, the fluid particles adjacent to the solid surface no longer attain the velocity and temperature of the solid surface. Therefore, the fluid particles have a tangential velocity, which is the slip velocity and a finite temperature difference, which is the temperature jump, at the solid surface. Using first-order slip boundary conditions, the slip velocity and temperature jump are, respectively, expressed as [32]

$$u_s = \frac{2 - F_m}{F_m} \mathrm{Kn} D_h \left(\frac{\partial u}{\partial n} \right)_w \tag{1}$$

$$T_s - T_w = \frac{2 - F_t}{F_t} \frac{2\gamma}{1 + \gamma} \frac{\mathrm{Kn} D_h}{\mathrm{Pr}} \left(\frac{\partial T}{\partial n} \right)_w \tag{2}$$

where u_s and T_s are the velocity and temperature of the gas at the wall, respectively, T_w is the wall temperature, Pr is the Prandtl number, γ is the heat capacity ratio, n is the normal direction exiting the wall, F_m is the tangential momentum accommodation coefficient, and F_t is the thermal accommodation coefficient.

The accommodation coefficients depend on various parameters that affect surface interaction, such as the magnitude and the direction of the velocity. It is shown that these coefficients are rea-

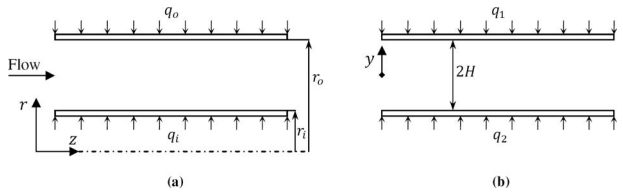

Fig. 1 Geometries of the ducts (*a*) microannulus and (*b*) parallel plate microchannel

sonably constant for a given gas and surface combination [33]. For light gases the accommodation coefficients may differ significantly from unity while for heavy gases they are close to unity. If one deals with a sufficiently heavy gas and with an ordinarily contaminated surface, one may assume the values of accommodation coefficients to be unity [34]. According to Hadjiconstantinou [10], for most engineering applications the values of accommodation coefficients are close to unity.

3 Analysis

Forced convection through annular and parallel plate microchannels is considered. Geometries of both ducts with the coordinate system are shown in Fig. 1. The flow is considered to be hydrodynamically and thermally fully developed, steady, laminar and having constant properties. The viscous heating is included but the axial heat conduction is assumed to be negligible, which requires the Peclet number (Pe) to be by far greater than unity [35]. The wall heat fluxes are assumed to be constant and different from each other. The directions of heat fluxes are positive while they are towards the fluid, otherwise they are negative. For microannulus, the outer and inner wall heat fluxes are given by q_o and q_i while q_1 and q_2 denote the upper and lower wall heat fluxes, respectively, for parallel plate microchannel.

3.1 Microannulus. For microannulus, the momentum equation in the z-direction and relevant boundary conditions are

$$\frac{1}{r}\frac{\mathrm{d}}{\mathrm{d}r}\left(r\frac{\mathrm{d}u}{\mathrm{d}r}\right)=\frac{1}{\mu}\frac{\mathrm{d}p}{\mathrm{d}z}=\text{constant} \tag{3}$$

$$u_{(r_i)}=\frac{2-F_m}{F_m}\mathrm{Kn}D_h\left(\frac{\mathrm{d}u}{\mathrm{d}r}\right)_{(r_i)}$$
$$u(r_o)=-\frac{2-F_m}{F_m}\mathrm{Kn}D_h\left(\frac{\mathrm{d}u}{\mathrm{d}r}\right)_{(r_o)} \tag{4}$$

in which $D_h=2(r_o-r_i)$. Using the following dimensionless parameters:

$$r^*=\frac{r}{r_o},\quad \beta=\frac{r_i}{r_o},\quad u^*=\frac{u}{U} \tag{5}$$

where U is the mean velocity, the dimensionless velocity distribution is [31]

$$u^*=(1-r^{*2}+2r_m^{*2}\ln r^*+A)/B \tag{6}$$

in which A and B are as follows:

$$A=4(1-\beta)(1-r_m^{*2})\frac{2-F_m}{F_m}\mathrm{Kn} \tag{7}$$

$$B=\frac{1}{2}\left[1-\beta^2-4r_m^{*2}\left(\frac{1}{2}+\frac{\beta^2}{1-\beta^2}\ln\beta\right)+2A\right] \tag{8}$$

where r_m^* represents the dimensionless radius and the maximum velocity occurs ($\mathrm{d}u/\mathrm{d}r=0$). It is given by

$$r_m^*=\frac{r_m}{r_o}=\left[\frac{(1-\beta^2)\left(1+4\dfrac{2-F_m}{F_m}\mathrm{Kn}\right)}{2\ln(1/\beta)-4\dfrac{2-F_m}{F_m}\mathrm{Kn}\left(\dfrac{\beta^2-1}{\beta}\right)}\right]^{1/2} \tag{9}$$

The conservation of energy including the effect of the viscous dissipation requires

$$u\frac{\partial T}{\partial z}=\frac{\alpha}{r}\frac{\partial}{\partial r}\left(r\frac{\partial T}{\partial r}\right)+\frac{v}{c_p}\left(\frac{\mathrm{d}u}{\mathrm{d}r}\right)^2 \tag{10}$$

and relevant boundary conditions are

$$T_{(r_i)}-T_{wi}=\frac{2-F_t}{F_t}\frac{2\gamma}{1+\gamma}\frac{\mathrm{Kn}D_h}{\mathrm{Pr}}\left(\frac{\partial T}{\partial r}\right)_{(r_i)}\quad\text{or}\quad -k\left(\frac{\partial T}{\partial r}\right)_{(r_i)}=q_i$$
$$T_{(r_o)}-T_{wo}=-\frac{2-F_t}{F_t}\frac{2\gamma}{1+\gamma}\frac{\mathrm{Kn}D_h}{\mathrm{Pr}}\left(\frac{\partial T}{\partial r}\right)_{(r_o)}\quad\text{or}\quad k\left(\frac{\partial T}{\partial r}\right)_{(r_o)}=q_o \tag{11}$$

We introduce dimensionless temperature as follows, which only depends on r for fully developed flow

$$\theta(r)=\frac{T-T_{so}}{\dfrac{(q_i+q_o)r_o}{k}} \tag{12}$$

Taking differentiation of Eq. (12) with respect to z gives

$$\frac{\partial T}{\partial z}=\frac{\mathrm{d}T_{so}}{\mathrm{d}z}=\frac{\mathrm{d}T_b}{\mathrm{d}z} \tag{13}$$

in which T_b is the bulk temperature. The term $\mathrm{d}T_b/\mathrm{d}z$, which is constant, can be obtained from energy balance between summation of energy generated by viscous heating and heat fluxes at the walls with the increase in internal energy of fluid. The energy equation is then modified into the following dimensionless form:

$$\frac{1}{r^*}\frac{\mathrm{d}}{\mathrm{d}r^*}\left(r^*\frac{\mathrm{d}\theta}{\mathrm{d}r^*}\right)=a-br^{*2}-\frac{c}{r^{*2}}+d\ln r^* \tag{14}$$

where a, b, c, and d are as follows:

$$a=\frac{1+A}{B}\left[\frac{2(\beta+\eta)}{(1+\eta)(1-\beta^2)}+8\frac{\mathrm{Br}}{B^2}\left(\frac{1+\beta^2}{4}-r_m^{*4}\frac{\ln\beta}{1-\beta^2}-r_m^{*2}\right)\right]+8\frac{\mathrm{Br}}{B^2}r_m^{*2} \tag{15}$$

$$b=\frac{1}{B}\left[\frac{2(\beta+\eta)}{(1+\eta)(1-\beta^2)}+8\frac{\mathrm{Br}}{B^2}\left(\frac{1+\beta^2}{4}-r_m^{*4}\frac{\ln\beta}{1-\beta^2}-r_m^{*2}\right)\right]+4\frac{\mathrm{Br}}{B^2} \tag{16}$$

$$c=4\frac{\mathrm{Br}}{B^2}r_m^{*4} \tag{17}$$

$$d=2\frac{r_m^{*2}}{B}\left[\frac{2(\beta+\eta)}{(1+\eta)(1-\beta^2)}+8\frac{\mathrm{Br}}{B^2}\left(\frac{1+\beta^2}{4}-r_m^{*4}\frac{\ln\beta}{1-\beta^2}-r_m^{*2}\right)\right] \tag{18}$$

where $\eta=q_o/q_i$ and Br is the Brinkman number given by

$$\mathrm{Br}=\frac{\mu U^2}{(q_i+q_o)r_o} \tag{19}$$

The thermal boundary conditions in the dimensionless form are written as

$$\left(\frac{d\theta}{dr^*}\right)_{(\beta)} = -\frac{1}{1+\eta}, \quad \theta_{(1)} = 0 \tag{20}$$

Using Eq. (14) and applying boundary conditions (20), the dimensionless temperature distribution is obtained as follows:

$$\theta(r^*) = \frac{a}{4}r^{*2} - \frac{b}{16}r^{*4} - \frac{c}{2}(\ln r^*)^2 + \frac{d}{4}(r^{*2}\ln r^* - r^{*2}) + e\ln r^* + f \tag{21}$$

where e and f are given below

$$e = -\frac{a}{2}\beta^2 + \frac{b}{4}\beta^4 + c\ln\beta - \frac{d}{4}(2\beta^2\ln\beta - \beta^2) - \frac{\beta}{1+\eta} \tag{22}$$

$$f = -\frac{a}{4} + \frac{b}{16} + \frac{d}{4} \tag{23}$$

Equation (21), which is in terms of T_{so}, can be transformed into an equation in terms of T_{wo}, using the following conversion formula:

$$\frac{T_{wo} - T_{so}}{\frac{(q_i + q_o)r_o}{k}} = \frac{2 - F_t}{F_t}\frac{4\gamma}{1+\gamma}\frac{\eta}{1+\eta}\frac{\mathrm{Kn}}{\mathrm{Pr}}(1-\beta) \tag{24}$$

Then Eq. (21) becomes

$$\theta^*(r^*) = \frac{T - T_{wo}}{\frac{(q_i + q_o)r_o}{k}} = \frac{T - T_{so}}{\frac{(q_i + q_o)r_o}{k}} - \frac{T_{wo} - T_{so}}{\frac{(q_i + q_o)r_o}{k}} = \frac{a}{4}r^{*2} - \frac{b}{16}r^{*4} - \frac{c}{2}(\ln r^*)^2 + \frac{d}{4}(r^{*2}\ln r^* - r^{*2}) + e\ln r^* + f - \frac{2 - F_t}{F_t}\frac{4\gamma}{1+\gamma}\frac{\eta}{1+\eta}\frac{\mathrm{Kn}}{\mathrm{Pr}}(1-\beta) \tag{25}$$

To obtain the Nusselt number, first the dimensionless bulk temperature θ_b^* must be calculated, which is given by

$$\theta_b^* = \frac{\int_\beta^1 u^*\theta^* r^* dr^*}{\int_\beta^1 u^* r^* dr^*} = \frac{2}{1-\beta^2}\left[\frac{1+A}{B}(g_1 - g_2) - \frac{1}{B}(g_3 - g_4) + \frac{2r_m^{*2}}{B}(g_5 - g_6)\right] + f - \frac{2 - F_t}{F_t}\frac{4\gamma}{1+\gamma}\frac{\eta}{1+\eta}\frac{\mathrm{Kn}}{\mathrm{Pr}}(1-\beta) \tag{26}$$

where

$$g_1 = \frac{1}{16}a - \frac{1}{96}b - \frac{1}{8}c - \frac{5}{64}d - \frac{1}{4}e \tag{27}$$

$$g_2 = \frac{a}{16}\beta^4 - \frac{b}{96}\beta^6 - \frac{c}{4}\beta^2\left[(\ln\beta)^2 - \ln\beta + \frac{1}{2}\right] + \frac{d}{4}\beta^4\left(\frac{\ln\beta}{4} - \frac{5}{16}\right) + \frac{e}{2}\beta^2\left(\ln\beta - \frac{1}{2}\right) \tag{28}$$

$$g_3 = \frac{1}{24}a - \frac{1}{128}b - \frac{1}{64}c - \frac{7}{144}d - \frac{1}{16}e \tag{29}$$

$$g_4 = \frac{a}{24}\beta^6 - \frac{b}{128}\beta^8 - \frac{c}{8}\beta^4\left[(\ln\beta)^2 - \frac{\ln\beta}{2} + \frac{1}{8}\right] + \frac{d}{24}\beta^6\left(\ln\beta - \frac{7}{6}\right) + \frac{e}{4}\beta^4\left(\ln\beta - \frac{1}{4}\right) \tag{30}$$

$$g_5 = -\frac{1}{64}a + \frac{1}{576}b + \frac{3}{16}c + \frac{3}{128}d + \frac{1}{4}e \tag{31}$$

$$g_6 = \frac{a}{16}\beta^4\left(\ln\beta - \frac{1}{4}\right) - \frac{b}{96}\beta^6\left(\ln\beta - \frac{1}{6}\right) - \frac{c}{4}\beta^2\left[(\ln\beta)^3 - \frac{3}{2}(\ln\beta)^2 + \frac{3}{2}\ln\beta - \frac{3}{4}\right] + \frac{d}{16}\beta^4\left[(\ln\beta)^2 - \frac{3}{2}\ln\beta + \frac{3}{8}\right] + \frac{e}{2}\beta^2\left[(\ln\beta)^2 - \ln\beta + \frac{1}{2}\right] \tag{32}$$

Based on definition, the Nusselt number is written as

$$\mathrm{Nu} = \frac{hD_h}{k} = \frac{q_w D_h}{k(T_w - T_b)} = \frac{2q_w}{q_i + q_o}\frac{1-\beta}{\theta_w^* - \theta_b^*} \tag{33}$$

Equation (33), for the inner and outer walls is, respectively, reduced to the following equations

$$\mathrm{Nu}_i = \frac{2}{1+\eta}\frac{1-\beta}{\theta_{wi}^* - \theta_b^*} \tag{34}$$

$$\mathrm{Nu}_o = -\frac{2\eta}{1+\eta}\frac{1-\beta}{\theta_b^*} \tag{35}$$

which θ_{wi}^* is given by

$$\theta_{wi}^* = \theta^*(\beta) + \frac{2 - F_t}{F_t}\frac{4\gamma}{1+\gamma}\frac{1}{1+\eta}\frac{\mathrm{Kn}}{\mathrm{Pr}}(1-\beta) \tag{36}$$

3.2 Parallel Plate Microchannel. For parallel plate microchannel, the momentum equation in z-direction and relevant boundary conditions may be written as

$$\frac{d^2u}{dy^2} = \frac{1}{\mu}\frac{dp}{dz} = \text{constant} \tag{37}$$

$$u_{(-H)} = \frac{2 - F_m}{F_m}\mathrm{Kn}D_h\left(\frac{du}{dy}\right)_{(-H)}, \quad u_{(H)} = -\frac{2 - F_m}{F_m}\mathrm{Kn}D_h\left(\frac{du}{dy}\right)_{(H)} \tag{38}$$

here $D_h = 4H$. The dimensionless velocity distribution then will be

$$u^* = \frac{3}{2}\left(\frac{1 - y^{*2} + 8\frac{2 - F_m}{F_m}\mathrm{Kn}}{1 + 12\frac{2 - F_m}{F_m}\mathrm{Kn}}\right) \tag{39}$$

in which $y^* = y/H$.

The energy equation in Cartesian coordinate and relevant boundary conditions are written as

$$u\frac{\partial T}{\partial z} = \alpha\frac{\partial^2 T}{\partial y^2} + \frac{v}{c_p}\left(\frac{du}{dy}\right)^2 \tag{40}$$

$$T_{(-H)} - T_{w2} = \frac{2 - F_t}{F_t}\frac{8\gamma}{1+\gamma}\frac{\mathrm{Kn}H}{\mathrm{Pr}}\left(\frac{\partial T}{\partial y}\right)_{(-H)} \quad \text{or} \quad -k\left(\frac{\partial T}{\partial y}\right)_{(-H)} = q_2$$
$$T_{(H)} - T_{w1} = -\frac{2 - F_t}{F_t}\frac{8\gamma}{1+\gamma}\frac{\mathrm{Kn}H}{\mathrm{Pr}}\left(\frac{\partial T}{\partial y}\right)_{(H)} \quad \text{or} \quad k\left(\frac{\partial T}{\partial y}\right)_{(H)} = q_1 \tag{41}$$

Similar to microannulus, the energy equation and thermal boundary conditions are made dimensionless. After required manipulations, they will take the following form:

$$\frac{d^2\theta}{dy^{*2}} = a - by^{*2} \tag{42}$$

Table 1 Comparison of Nusselt number values for microannulus at $\beta=0.2$ and $\eta\to\infty$

	Nu					
	Br=−0.1		Br=0.0		Br=0.1	
Kn	Present work	Ref. [31]	Present work	Ref. [31]	Present work	Ref. [31]
0.00	6.4516	6.4516	4.8826	4.8826	3.9274	3.9274
0.02	5.0669	5.0669	4.3530	4.3530	3.8154	3.8154
0.04	4.2784	4.2784	3.8950	3.8950	3.5746	3.5746
0.06	3.7348	3.7348	3.5082	3.5082	3.3075	3.3075
0.08	3.3255	3.3255	3.1824	3.1824	3.0512	3.0512
0.10	3.0016	3.0016	2.9067	2.9067	2.8176	2.8176

$$\theta_{(-1)}=0,\quad \left(\frac{\mathrm{d}\theta}{\mathrm{d}y^*}\right)_{(1)}=1 \tag{43}$$

where the dimensionless temperature has been defined as

$$\theta(y)=\frac{T-T_{s2}}{\dfrac{q_1 H}{k}} \tag{44}$$

and the coefficients a and b are given by

$$a=(1+8\mathrm{Kn})\left[\frac{3(1+\eta)}{4\left(1+12\dfrac{2-F_m}{F_m}\mathrm{Kn}\right)}+\frac{18\mathrm{Br}}{\left(1+12\dfrac{2-F_m}{F_m}\mathrm{Kn}\right)^3}\right] \tag{45}$$

$$b=\frac{3(1+\eta)}{4\left(1+12\dfrac{2-F_m}{F_m}\mathrm{Kn}\right)}+\frac{36\mathrm{Br}}{\left(1+12\dfrac{2-F_m}{F_m}\mathrm{Kn}\right)^2}+\frac{18\mathrm{Br}}{\left(1+12\dfrac{2-F_m}{F_m}\mathrm{Kn}\right)^3} \tag{46}$$

which $\eta=q_2/q_1$ and Brinkman number is given by

$$\mathrm{Br}=\frac{\mu U^2}{4q_1 H} \tag{47}$$

The solution of Eq. (42) subject to boundary condition (43) will be

$$\theta(y^*)=\frac{a}{2}y^{*2}-\frac{b}{12}y^{*4}+\left(1-a+\frac{b}{3}\right)y^*+1-\frac{3}{2}a+\frac{5}{12}b \tag{48}$$

and in terms of T_{w2}, the solution is

$$\theta^*(y^*)=\frac{T-T_{w2}}{\dfrac{q_1 H}{k}}=\frac{T-T_{s2}}{\dfrac{q_1 H}{k}}-\frac{T_{w2}-T_{s2}}{\dfrac{q_1 H}{k}}=\frac{a}{2}y^{*2}-\frac{b}{12}y^{*4}+\left(1-a+\frac{b}{3}\right)y^*+1-\frac{3}{2}a+\frac{5}{12}b-\frac{2-F_t}{F_t}\frac{8\gamma}{1+\gamma}\frac{\mathrm{Kn}}{\mathrm{Pr}}\eta \tag{49}$$

with the following conversion formula:

$$\frac{T_{w2}-T_{s2}}{\dfrac{q_1 H}{k}}=\frac{2-F_t}{F_t}\frac{8\gamma}{1+\gamma}\frac{\mathrm{Kn}}{\mathrm{Pr}}\eta \tag{50}$$

For parallel plate microchannel, the dimensionless bulk temperature is calculated as

$$\theta_b^*=\frac{\int_{-1}^{1}u^*\theta^*\mathrm{d}y^*}{\int_{-1}^{1}u^*\mathrm{d}y^*}=\frac{3}{4\left(1+12\dfrac{2-F_m}{F_m}\mathrm{Kn}\right)}\times\left[\left(1+8\frac{2-F_m}{F_m}\mathrm{Kn}\right)\left(2-\frac{8}{3}a+\frac{4}{5}b\right)-\frac{2}{3}+\frac{4}{5}a-\frac{16}{63}b\right]-\frac{2-F_t}{F_t}\frac{8\gamma}{1+\gamma}\frac{\mathrm{Kn}}{\mathrm{Pr}}\eta \tag{51}$$

and the Nusselt number is

$$\mathrm{Nu}=\frac{hD_h}{k}=\frac{q_w D_h}{k(T_w-T_b)}=4\frac{q_w/q_1}{\theta_w^*-\theta_b^*} \tag{52}$$

which is reduced to the following equations for the upper and lower walls

$$\mathrm{Nu}_1=\frac{4}{\theta_{w1}^*-\theta_b^*} \tag{53}$$

$$\mathrm{Nu}_2=-4\frac{\eta}{\theta_b^*} \tag{54}$$

in which θ_{w1}^* is given by

$$\theta_{w1}^*=(1-\eta)\left(1+\frac{2-F_t}{F_t}\frac{8\gamma}{1+\gamma}\frac{\mathrm{Kn}}{\mathrm{Pr}}\right) \tag{55}$$

4 Results and Discussion

Here, the interactive effects of flow parameters on temperature field and Nusselt number are analyzed. The results are obtained using constant values of Pr=0.71 and γ=1.4. Also, through this section the values of accommodation coefficients are assumed to be unity [36]. For microannulus the results are presented in the whole range of the aspect ratio of annular geometry ($0<\beta<1$), nevertheless it is worth mentioning that in practice, when the Knudsen number based on the inner radius is not small enough, there might be rarefaction effects inside, that could not be described by the Navier–Stokes equations. In order to validate the method of analysis developed here, we compare the results of both geometries for two limiting cases against those obtained by Avci and Aydin [31] as well as Jeong and Jeong [27]. Table 1 represents comparison of the Nusselt numbers obtained in the present study for microannulus with those given by Avci and Aydin [31] at $\eta\to\infty$. Note that at this condition, the inner wall behaves such as an adiabatic wall. Table 2 compares the present results for parallel plate microchannel against those of Jeong and Jeong [27] at symmetrically heating case. As seen for both cases, an excellent agreement with the above mentioned results is observed.

Figures 2 and 3 illustrate the distribution of dimensionless temperature for both geometries at different values of Brinkman number and the wall heat fluxes ratio for no-slip condition. For each

Table 2 Comparison of Nusselt number values for parallel plate microchannel at $\eta=1$

	Nu					
	Br=−0.1		Br=0.0		Br=0.1	
Kn	Present work	Ref. [27]	Present work	Ref. [27]	Present work	Ref. [27]
0.00	22.5806	22.5806	8.2353	8.2353	5.0360	5.0360
0.02	9.8755	9.8755	6.8411	6.8411	5.2331	5.2331
0.04	6.9151	6.9151	5.7551	5.7551	4.9284	4.9284
0.06	5.4775	5.4775	4.9282	4.9282	4.4790	4.4790
0.08	4.5859	4.5859	4.2912	4.2912	4.0321	4.0321
0.10	3.9631	3.9631	3.7909	3.7909	3.6331	3.6331

case, both positive and negative values of the wall heat fluxes are considered. Positive values of Brinkman number correspond to the wall cooling or the hot wall case while the opposite is true for negative values of Brinkman number. For each case, the viscous dissipation behaves like an energy source increasing the temperature of the fluid specially near the walls since the highest shear rates occur at these regions while it is zero at r_m^*. The effect of viscous dissipation for wall cooling is quite different from wall heating. In the absence of viscous dissipation, the distribution of dimensionless temperature is independent of whether the wall is heated or cooled. For symmetric cases, which correspond to $\eta=1$ and for the positive heat fluxes at the walls, the walls temperatures are greater than the bulk temperature. So increasing viscous dissipation will result in increasing the difference between the wall and the bulk temperature while the contrary is right for the case that the heat fluxes at walls are negative. For the cases that one wall is adiabatic, which correspond to $\eta=0$, the interpretation is more complicated. In these cases, for wall cooling, although the temperature of the nonadiabatic wall is greater than the bulk temperature but the adiabatic wall temperature is smaller than the bulk temperature, increasing by viscous heating rather than the bulk temperature. So the difference between the wall and the bulk temperature decreases. It can be deduced that there are values of η called $\eta_{c,i}$ and $\eta_{c,1}$ for which the temperatures of microannulus inner wall and the upper wall of parallel plate are equal to the bulk temperature of fluid. The value of η_c depends on Brinkman and Knudsen numbers as well as the aspect ratio of the annular geometry for microannulus. For $\eta_{c,i}<\eta$ and at wall cooling case, the inner wall temperature is smaller than the bulk temperature while

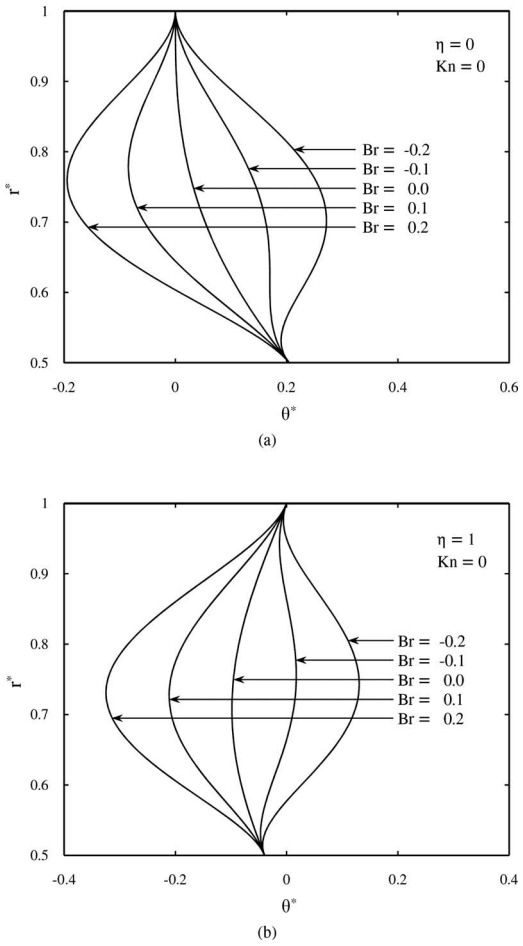

Fig. 2 Distribution of dimensionless temperature at different values of Brinkman number for microannulus with $\beta=0.5$ (*a*) $\eta=0$ and (*b*) $\eta=1$

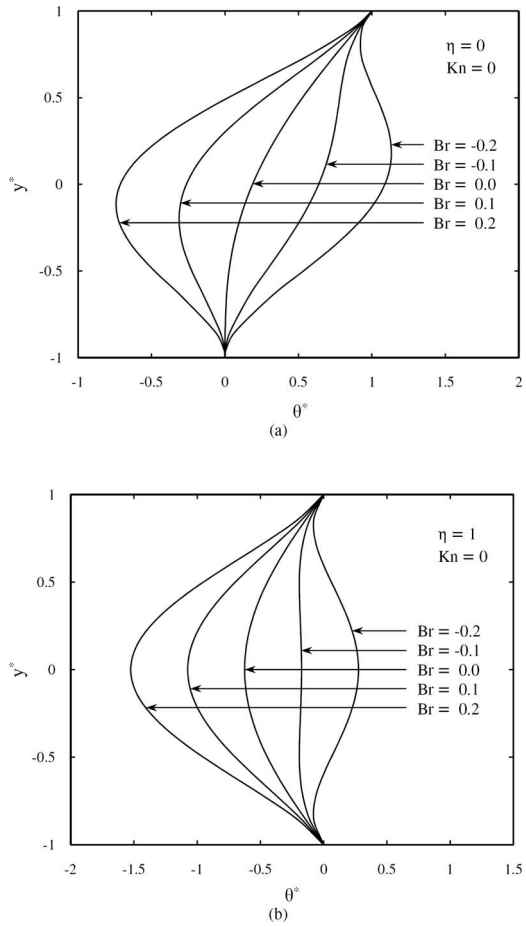

Fig. 3 Distribution of dimensionless temperature at different values of Brinkman number for parallel plate microchannel (*a*) $\eta=0$ and (*b*) $\eta=1$

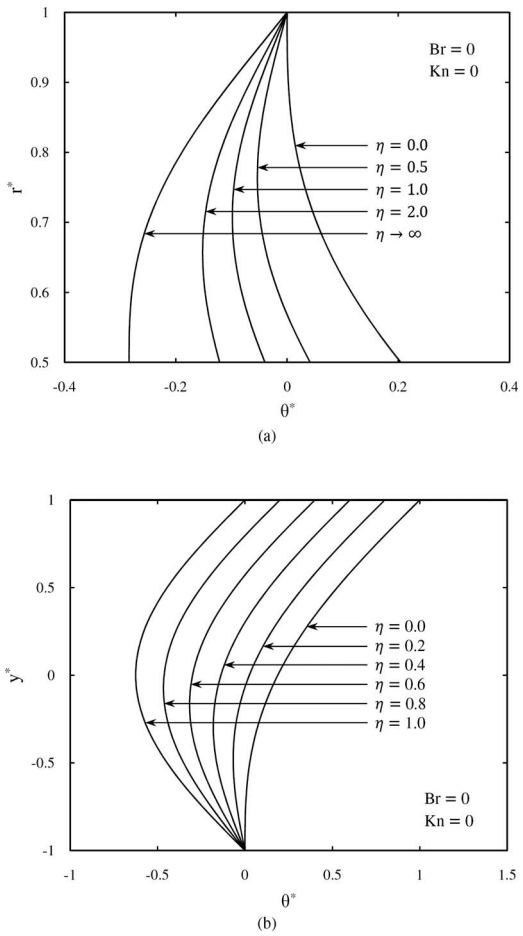

Fig. 4 Distribution of dimensionless temperature at different values of η (*a*) microannulus with β=0.5 and (*b*) parallel plate microchannel

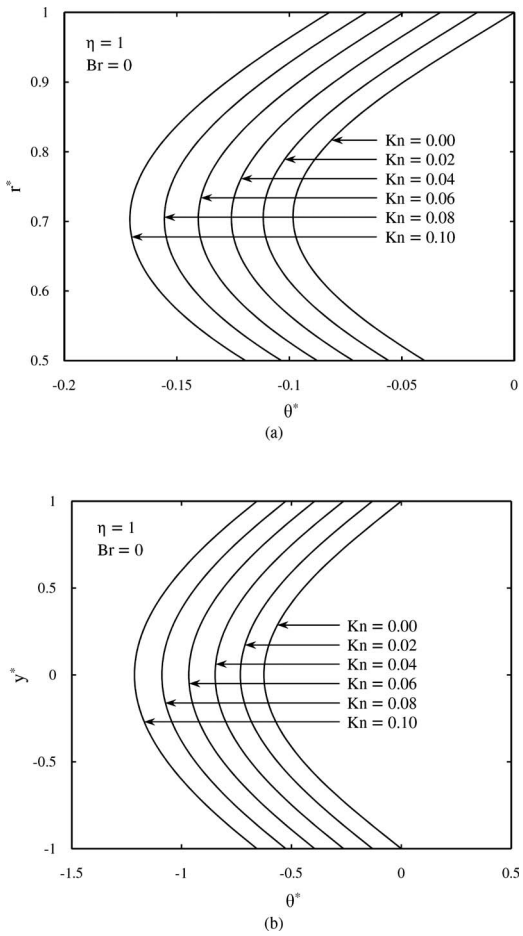

Fig. 5 Rarefaction effects on dimensionless temperature profile for no viscous heating case with symmetrically heating (*a*) microannulus with β=0.5 and (*b*) parallel plate microchannel

for $\eta < \eta_{c,i}$ it is vice versa. The corresponding critical values of η for the outer and lower walls are $\eta_{c,o}$ and $\eta_{c,2}$, respectively. The presence of η_c is more visible in Fig. 4, which exhibits the distribution of dimensionless temperature at different values of η for no-slip and no viscous heating case. For η=0, the dimensionless temperatures of the outer and lower walls are smaller than the dimensionless bulk temperature while the opposite is true at the upper limit of η, which is $\eta \to \infty$ for microannulus and η=1 for parallel plate microchannel.

In Fig. 5, the effects of slip velocity and temperature jump on dimensionless temperature profile for no viscous heating case is illustrated. For both cases, an increment in Knudsen number results in a decrease in nondimensional temperature profile. For microannulus, the minimum value of dimensionless temperature takes place at a point closer to the inner wall. This is due to the larger surface of outer wall, which leads to a larger influencing domain for the outer wall. Figure 6 demonstrates the effect of slip on distribution of dimensionless temperature in the presence of viscous dissipation for microannulus. As observed, at large values of Knudsen number, the shape of profile is very similar to that for no viscous heating case. For parallel plate microchannel, the case with viscous heating at wall cooling is similar to no viscous heating case while the dimensionless temperature profile at wall heating case, which is shown in Fig. 7, is very instructive. At no-slip condition, the dimensionless bulk temperature is positive while it reaches a negative value at Kn=0.1. Thus for a value of Knudsen number called Kn_c, which its value depends on Br and η, the dimensionless bulk temperature is zero. This, according to Eq. (54), will cause a singularity in the lower wall Nusselt values.

Figure 8 presents the Nusselt number values of the microannulus inner wall versus Knudsen number at different values of Brinkman number and the wall heat fluxes ratio. As observed, for η=0 and at wall cooling case, viscous dissipation decreases the Nusselt number. As discussed earlier, viscous heating increases the difference between the wall and the bulk temperature. Thus for a constant value of the wall heat flux, according to Eq. (33), the Nusselt number values decrease. For wall heating case, as ex-

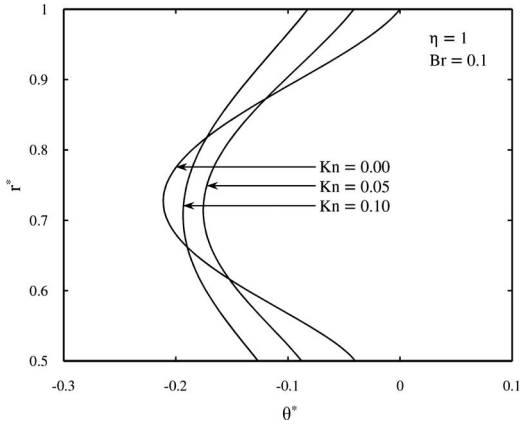

Fig. 6 Rarefaction effects on dimensionless temperature profile for microannulus with β=0.5

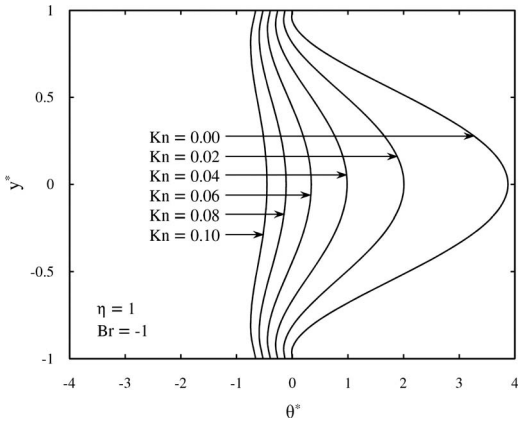

Fig. 7 Rarefaction effects on dimensionless temperature profile for parallel plate microchannel

pected, viscous heating leads to greater values of Nusselt number. Increasing values of Knudsen number result in decreasing the values of Nusselt number for wall heating case and also for no viscous heating case. However, for wall cooling case at small values of Knudsen number, an increment in Knudsen number leads to a larger amount of Nusselt while the opposite is true for larger values of Knudsen. For all cases, the effect of Brinkman number on Nusselt number becomes insignificant at larger values of Knudsen

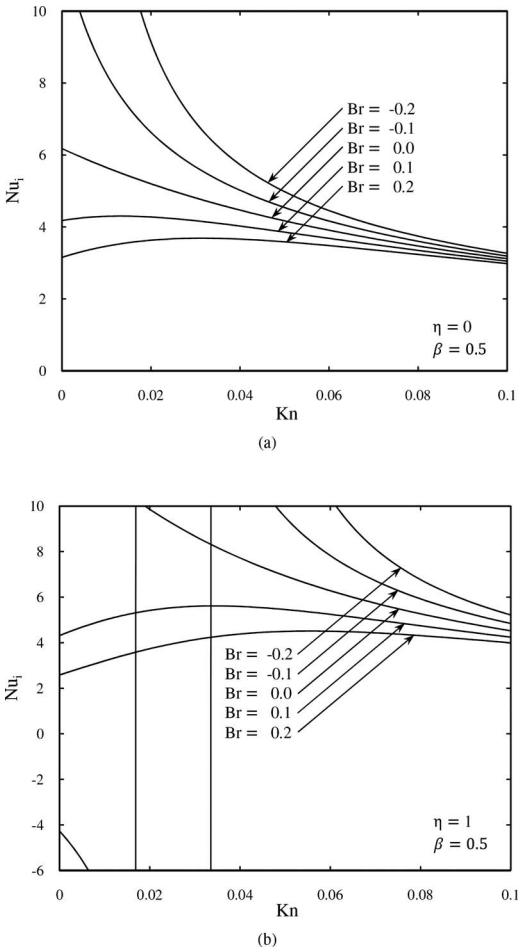

Fig. 8 Nusselt number values of the microannulus inner wall versus Knudsen number at different Brinkman numbers (*a*) $\eta=0$ and (*b*) $\eta=1$

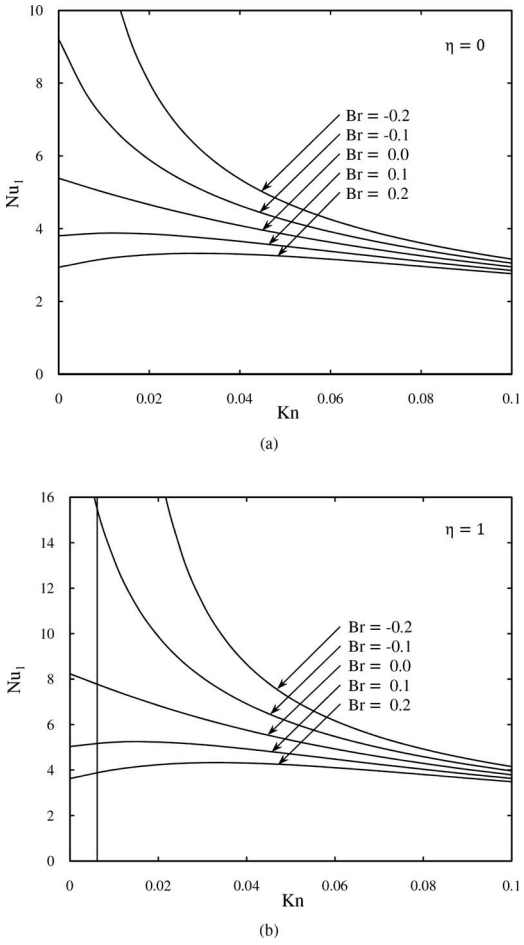

Fig. 9 Nusselt number values of the upper wall versus Knudsen number at different Brinkman numbers for parallel plate microchannel (*a*) $\eta=0$ and (*b*) $\eta=1$

number. This is due to the fact that the slip velocity tends to unify the velocity profile, which leads to smaller velocity gradients and consequently smaller shear rates, which ultimately reduces viscous heating effects. For $\eta=1$ and at wall heating cases, there are singularity points in Nusselt number values. For these cases, at no-slip condition, the wall temperature is larger than the bulk temperature. So the value of the Nusselt number is negative. As Kn increases, the velocity gradient and consequently viscous heating at the wall will be reduced, thus, the temperature difference between the wall and the bulk fluid reduces, which leads to a larger value of Nusselt number with negative sign. This trend lasts until the bulk temperature reaches the value of the wall temperature. At this point, which corresponds to the critical value of Knudsen number, called $Kn_{c,i}$, the heat transfer cannot be expressed in terms of Nusselt number and a singularity occurs in Nusselt number values. More increase in Knudsen number leads to a large value of Nusselt number with positive sign. Figure 9 exhibits the Nusselt number values of the parallel plate upper wall versus Knudsen number at different Brinkman numbers for two values of η. The results are similar to those for microannulus, including singularities in Nusselt number values. This trend was completely predictable, as the parallel plate is actually a special case of the annulus.

The effect of the wall heat fluxes ratio on Nusselt number of both microannulus walls for no viscous heating case is shown in Fig. 10. For the inner wall, at the beginning, increasing values of η result in increasing the value of Nusselt number. After the singularity points, the Nusselt number, which has a negative value,

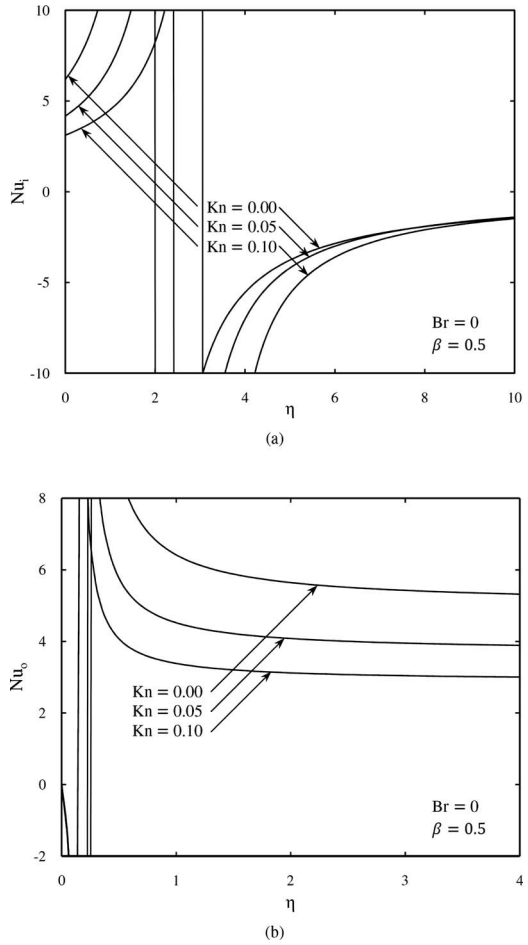

Fig. 10 Nusselt number values of microannulus versus η at different Knudsen numbers (*a*) inner wall and (*b*) outer wall

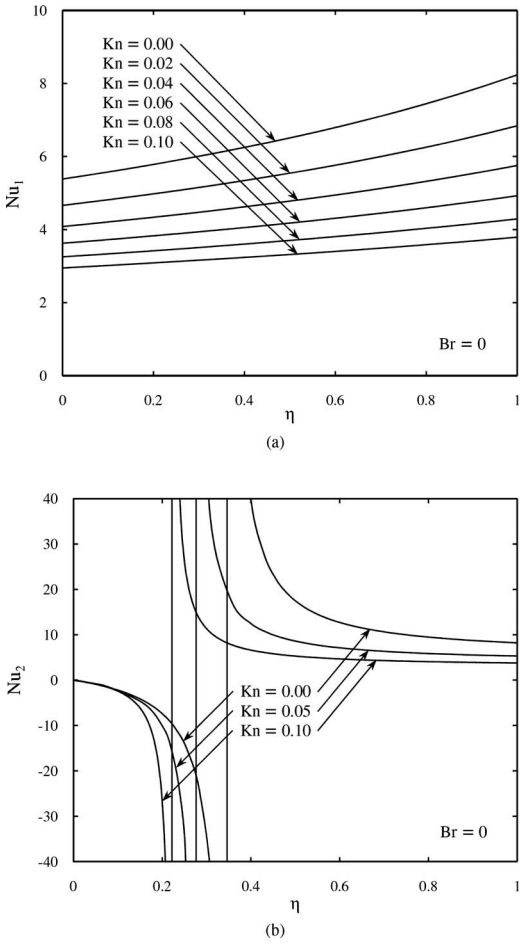

Fig. 11 Nusselt number values of parallel plate microchannel versus η at different Knudsen numbers (*a*) upper wall and (*b*) lower wall

decreases until it reaches zero when η goes to infinity. As expected, the Nusselt number of outer wall is zero at $\eta=0$. As η increases, the Nusselt number increases with a negative sign. After singularity points, the Nusselt number of the outer wall decreases until it reaches asymptotic values at large values of the wall heat fluxes ratio. The asymptotic values decrease as Knudsen number increases. Figure 11 presents Nusselt number versus η at different Knudsen numbers for both walls of parallel plate microchannel in the absence of viscous heating. For the upper wall, greater Nusselt numbers are achieved by increasing the wall heat fluxes ratio, nevertheless, at large values of Knudsen number, the effect of the wall heat fluxes ratio on Nusselt number becomes insignificant. The lower wall Nusselt number indicates a completely different trend. For the lower wall being adiabatic, as expected, the Nusselt number is zero. As η increases, the Nusselt number increases with a negative sign. After singularity points the Nusselt number decreases, until it reaches the value of the upper wall Nusselt number at $\eta=1$.

Figure 12 shows the Brinkman number dependency of the microannulus Nusselt numbers at different values of η for no-slip conditions. For both walls, there are singularities in the Nusselt number values, which depend on η. For large values of Brinkman number with either positive or negative signs, the Nusselt number values reach asymptotic values, which their values depend on η. For both walls, the asymptotic value is positive at positive values of Brinkman number while for negative values of Brinkman number, it is vice versa. The Brinkman number dependency of parallel plate Nusselt numbers is very similar to that for microannulus and it is omitted here in order to save space.

Figure 13 illustrates the Nusselt number values of both microannulus walls versus β at symmetric case for different Knudsen numbers in the absence of viscous heating. After singularity points, the Nusselt number values of the inner wall reduce as β increases. For the outer wall, increasing values of β result in increasing the Nusselt number. The reason is that as β increases, the influencing domain of the inner wall increases, which leads to a greater bulk temperature. So, the temperature difference between the outer wall and the bulk fluid decreases, which ultimately increases the Nusselt number of the outer wall. As expected, the Nusselt numbers of both walls coincide with each other at $\beta\rightarrow 1$, which corresponds to a parallel plate microchannel. The effect of β on Nusselt number is more pronounced at small values of Knudsen number while it becomes slighter at greater values of Kn.

The interactive effects of η and β on the Nusselt number values in the absence of viscous heating for no-slip conditions are shown in Fig. 14. For the inner wall and after singularity points, the influence of increasing values of η is to increase the Nusselt number. For the outer wall, at $\beta\rightarrow 0$, which corresponds to a circular microchannel, the value of the wall heat fluxes ratio does not affect the Nusselt number. For other values of β, the effect of increasing values of η is to decrease the Nusselt number values. At greater values of the wall heat fluxes ratio, the effect of β on Nusselt number becomes insignificant. This is due to the fact that for larger values of η, the outer wall dominates the temperature distribution. So, the increase in the inner wall surface does not notably affect heat transfer characteristics.

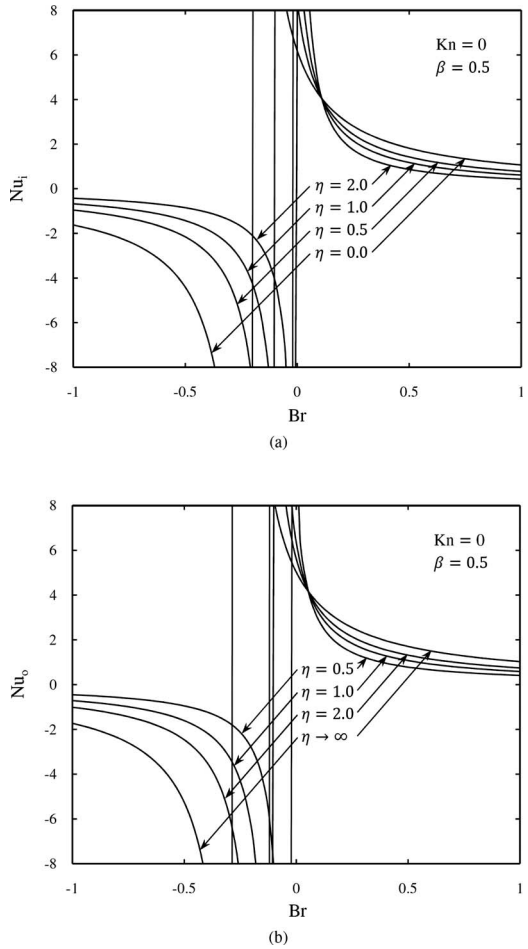

Fig. 12 Brinkman number dependency of microannulus Nusselt numbers at different values of η (*a*) inner wall and (*b*) outer wall

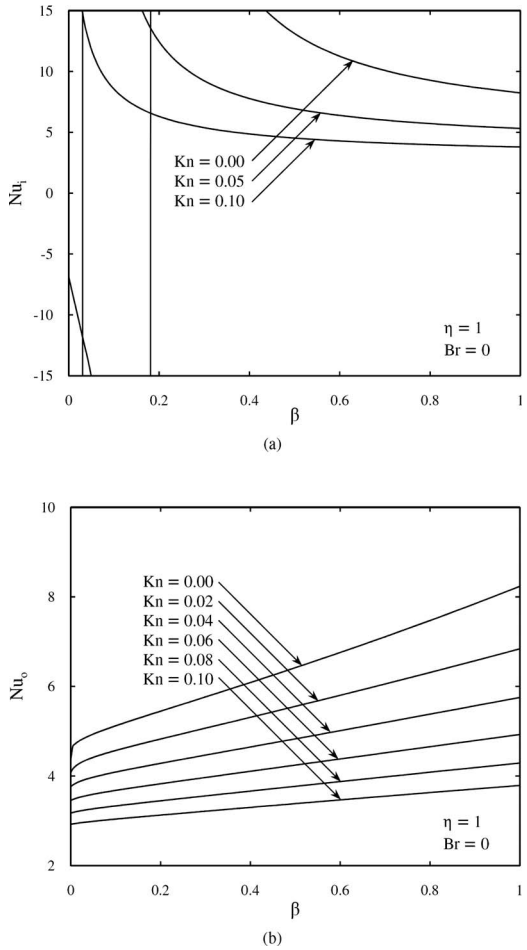

Fig. 13 Nusselt number values of microannulus versus β at different Knudsen numbers (*a*) inner wall and (*b*) outer wall

5 Conclusions

In this study, analytical solutions have been derived for laminar forced convection heat transfer of a viscous dissipative gas flow in two microgeometries, namely, microannulus and parallel plate microchannel. Flow was considered to be steady and both hydrodynamically and thermally fully developed. The rarefaction effects were taken into consideration using first-order slip velocity and temperature jump boundary conditions. The expressions for the dimensionless temperature and the Nusselt number in terms of flow parameters have been obtained. Some typical results of this study are as follows.

- For both geometries, as Brinkman number increases, the Nusselt number decreases. However the effect of viscous heating on the Nusselt number at greater values of Knudsen number becomes insignificant. This is due to slip velocity, which tends to unify the velocity profile and consequently causes smaller shear rates.
- In the absence of viscous heating, increasing values of Knudsen number lead to smaller values of Nusselt number.
- Viscous heating causes singularities in Nusselt number values.
- Asymmetry causes singularities in Nusselt numbers of both microannulus walls and also the parallel plate wall having lower heat flux, even in the absence of viscous heating.
- For parallel plate microchannel, in the absence of viscous heating, Nusselt number of the wall having larger heat flux is an increasing function of the wall heat fluxes ratio.
- At symmetric case and in the absence of viscous heating, as the aspect ratio of the annuli increases, the Nusselt number of the outer wall increases while the opposite is true for the inner wall. The effect of the aspect ratio on the Nusselt number is more notable at smaller values of Knudsen number and it becomes slighter at larger values of Knudsen.

Nomenclature

- Br = Brinkman number $(=\mu U^2/(q_i+q_o)r_o, \mu U^2/4q_1H)$
- c_p = specific heat at constant pressure (kJ kg^{-1} K^{-1})
- D_h = hydraulic diameter of channel $(=2(r_o-r_i), 4H)$
- F_m = momentum accommodation coefficient
- F_t = thermal accommodation coefficient
- h = heat transfer coefficient (W m^{-2} K^{-1})
- H = half of channel height (m)
- k = thermal conductivity (W m^{-1} K^{-1})
- Kn = Knudsen number $(=\lambda/D_h)$
- n = normal direction exiting the wall (m)
- Nu = Nusselt number $(=hD_h/k)$
- p = pressure (Pa)
- Pe = Peclet number (=Re Pr)
- Pr = Prandtl number $(=\upsilon/\alpha)$
- q = heat flux (W m^{-2})
- r = radial coordinate (m)
- r^* = dimensionless radial coordinate $(=r/r_o)$

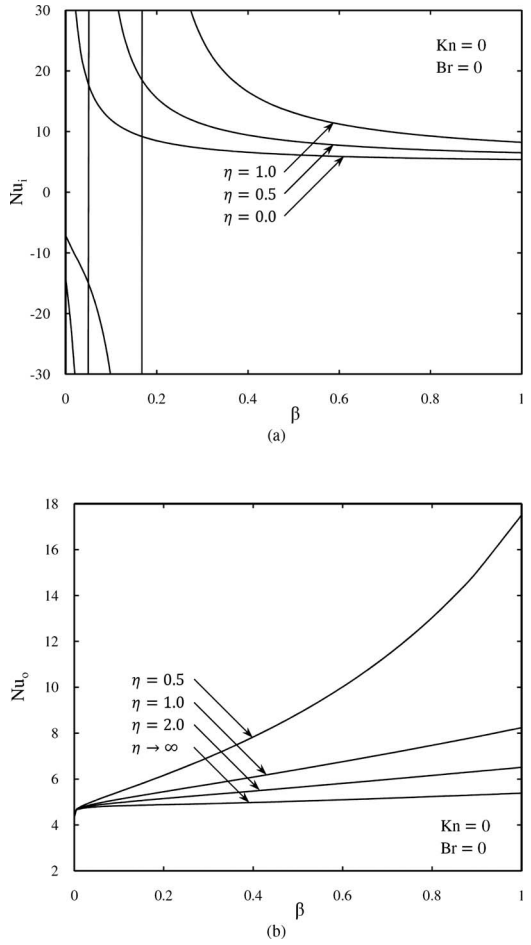

Fig. 14 Nusselt number values of microannulus versus β at different values of η (*a*) inner wall and (*b*) outer wall

r_m = the radius where the maximum velocity occurs (m)
r_m^* = dimensionless form of r_m ($=r_m/r_o$)
R = gas constant
Re = Reynolds number ($=UD_h/v$)
T = temperature (K)
u = axial velocity (m s^{-1})
u^* = dimensionless axial velocity ($=u/U$)
U = mean velocity (m s^{-1})
y = transverse coordinate (m)
y^* = dimensionless transverse coordinate ($=y/H$)
z = axial coordinate (m)

Greek symbols

α = thermal diffusivity (m^2 s^{-1})
β = aspect ratio of the annuli ($=r_i/r_o$)
γ = heat capacity ratio
η = wall heat fluxes ratio ($=q_o/q_i, q_2/q_1$)
θ = dimensionless temperature (Eqs. (12) and (44))
θ^* = dimensionless temperature (Eqs. (25) and (49))
λ = gas mean free path (m)
μ = dynamic viscosity (kg m^{-1} s^{-1})
v = kinematic viscosity (m^2 s^{-1})
ρ = density (kg m^{-3})

Subscripts

b = bulk
c = critical
i = inner wall
o = outer wall
s = fluid properties at solid surface
w = wall
1 = upper wall
2 = lower wall

References

[1] Harley, J., Huang, Y., Bau, H., and Zemel, J. N., 1995, "Gas Flow in Microchannels," J. Fluid Mech., **284**, pp. 257–274.
[2] Araki, T., Kim, M. S., Hiroshi, I., and Suzuki, K., 2002, "An Experimental Investigation of Gaseous Flow Characteristics in Microchannels," Microscale Thermophys. Eng., **6**, pp. 117–130.
[3] Arkilic, E. B., Breuer, K. S., and Schmidt, M. A., 1997, "Gaseous Slip Flow in Long Microchannels," J. Microelectromech. Syst., **6**, pp. 167–178.
[4] Arkilic, E. B., Breuer, K. S., and Schmidt, M. A., 2001, "Mass Flow and Tangential Momentum Accommodation in Silicon Micromachined Channels," J. Fluid Mech., **437**, pp. 29–43.
[5] Liu, J., Tai, Y. C., and Ho, C. M., 1995, "MEMS for Pressure Distribution Studies of Gaseous Flows in Microchannels," *Proceedings of IEEE, International Conference on Micro Electro Mechanical Systems*, Amsterdam, Netherlands, pp. 209–215.
[6] Choi, S. B., Barron, R. F., and Warrington, R. O., 1991, "Fluid Flow and Heat Transfer in Microtubes," *Proceedings of Micromechanical Sensors, Actuators, and Systems*, ASME, New York, Vol. 32, pp. 123–134.
[7] Kandlikar, S. G., Garimella, S., Li, D., Colin, S., and King, M. R., 2006, *Heat Transfer and Fluid Flow in Minichannels and Microchannels*, Elsevier, Oxford, U.K.
[8] Beskok, A., and Karniadakis, G. E., 1994, "Simulation of Heat and Momentum Transfer in Complex Micro-Geometries," J. Thermophys. Heat Transfer, **8**, pp. 647–655.
[9] Taheri, P., Torrilhon, M., and Struchtrup, H., 2009, "Couette and Poiseuille Microflows: Analytical Solutions for Regularized 13-Moment Equations," Phys. Fluids, **21**, p. 017102.
[10] Hadjiconstantinou, N. G., 2006, "The Limits of Navier Stokes Theory and Kinetic Extensions for Describing Small Scale Gaseous Hydrodynamics," Phys. Fluids, **18**, p. 111301.
[11] Kennard, E. H., 1938, *Kinetic Theory of Gases*, McGraw–Hill, New York.
[12] Ebert, W. A., and Sparrow, E. M., 1965, "Slip Flow in Rectangular and Annular Ducts," ASME J. Basic Eng., **87**, pp. 1018–1024.
[13] Duan, Z., and Muzychka, Y. S., 2007, "Slip Flow in Elliptic Microchannels," Int. J. Therm. Sci., **46**, pp. 1104–1111.
[14] Ameel, T. A., Wang, X. M., Baron, R. F., and Warrington, R. O., 1997, "Laminar Forced Convection in a Circular Tube With Constant Heat Flux and Slip Flow," Microscale Thermophys. Eng., **1**(4), pp. 303–320.
[15] Zhu, X., Xin, M. D., and Liao, Q., 2002, "Analysis of Heat Transfer Between Two Unsymmetrically Heated Parallel Plates With Microspacing in the Slip Flow Regime," Microscale Thermophys. Eng., **6**, pp. 287–301.
[16] Tunc, G., and Bayazitoglu, Y., 2002, "Heat Transfer in Rectangular Microchannels," Int. J. Heat Mass Transfer, **45**, pp. 765–773.
[17] Sadeghi, A., Asgarshamsi, A., and Saidi, M. H., 2009, "Analysis of Laminar Flow in the Entrance Region of Parallel Plate Microchannels for Slip Flow," *Proceedings of the Seventh International ASME Conference on Nanochannels, Microchannels and Minichannels, ICNMM2009*, Pohang, South Korea.
[18] Al-Nimr, M. A., Maqableh, M., Khadrawi, A. F., and Ammourah, S. A., 2009, "Fully Developed Thermal Behaviors for Parallel Flow Microchannel Heat Exchanger," Int. Commun. Heat Mass Transfer, **36**, pp. 385–390.
[19] Sun, W., Kakac, S., and Yazicioglu, A. G., 2007, "A Numerical Study of Single-Phase Convective Heat Transfer in Microtubes for Slip Flow," Int. J. Therm. Sci., **46**, pp. 1084–1094.
[20] Renksizbulut, M., Niazmand, H., and Tercan, G., 2006, "Slip-Flow and Heat Transfer in Rectangular Microchannels With Constant Wall Temperature," Int. J. Therm. Sci., **45**, pp. 870–881.
[21] Renksizbulut, M., and Niazmand, H., 2006, "Laminar Flow and Heat Transfer in the Entrance Region of Trapezoidal Channels With Constant Wall Temperature," ASME J. Heat Transfer, **128**, pp. 63–74.
[22] Koo, J., and Kleinstreuer, C., 2003, "Liquid Flow in Microchannels: Experimental Observations and Computational Analyses of Microfluidics Effects," J. Micromech. Microeng., **13**, pp. 568–579.
[23] Koo, J., and Kleinstreuer, C., 2004, "Viscous Dissipation Effects in Microtubes and Microchannels," Int. J. Heat Mass Transfer, **47**, pp. 3159–3169.
[24] El-Genk, M. S., and Yang, I. H., 2008, "Friction Numbers and Viscous Dissipation Heating for Laminar Flows of Water in Microtubes," ASME J. Heat Transfer, **130**, p. 082405.
[25] Tunc, G., and Bayazitoglu, Y., 2001, "Heat Transfer in Microtubes With Viscous Dissipation," Int. J. Heat Mass Transfer, **44**, pp. 2395–2403.
[26] Aydin, O., and Avci, M., 2007, "Analysis of Laminar Heat Transfer in Micro-Poiseuille Flow," Int. J. Therm. Sci., **46**, pp. 30–37.
[27] Jeong, H. E., and Jeong, J. T., 2006, "Extended Graetz Problem Including Streamwise Conduction and Viscous Dissipation in Microchannel," Int. J. Heat Mass Transfer, **49**, pp. 2151–2157.
[28] Jiji, L. M., 2008, "Effect of Rarefaction, Dissipation, and Accommodation Coefficients on Heat Transfer in Microcylindrical Couette Flow," ASME J. Heat Transfer, **130**, p. 042404.

[29] Adams, T. M., Abdel-Khalik, S. I., Jeter, S. M., and Qureshi, Z. H., 1998, "An Experimental Investigation of Single Phase Forced Convection in Microchannels," Int. J. Heat Mass Transfer, **41**, pp. 851–857.
[30] Duan, Z., and Muzychka, Y. S., 2008, "Slip Flow Heat Transfer in Annular Microchannels With Constant Heat Flux," ASME J. Heat Transfer, **130**(9), p. 092401.
[31] Avci, M., and Aydin, O., 2008, "Laminar Forced Convection Slip-Flow in a Micro-Annulus Between Two Concentric Cylinders," Int. J. Heat Mass Transfer, **51**, pp. 3460–3467.
[32] Beskok, A., Karniadakis, G. E., and Trimmer, W., 1996, "Rarefaction and Compressibility Effects in Gas Microflows," ASME J. Fluids Eng., **118**, pp. 448–456.
[33] Schaaf, S. A., 1963, "Mechanics of Rarefied Gases," *Encyclopedia of Physics, Fluid Dynamics II*, Vol. VII/2, Springer, Berlin, pp. 591–624.
[34] Sharipov, F., and Seleznev, V., 1998, "Data on Internal Rarefied Gas Flows," J. Phys. Chem. Ref. Data, **27**(3), pp. 657–706.
[35] Bejan, A., 1984, *Convection Heat Transfer*, Wiley, New York.
[36] Barron, R. F., Wang, X., Ameel, T. A., and Warrington, R. O., 1997, "The Graetz Problem Extended to Slip Flow," Int. J. Heat Mass Transfer, **40**(8), pp. 1817–1823.

Raman Thermometry Measurements and Thermal Simulations for MEMS Bridges at Pressures From 0.05 Torr to 625 Torr

Leslie M. Phinney[1]
e-mail: lmphinn@sandia.gov

Justin R. Serrano

Edward S. Piekos

John R. Torczynski

Michael A. Gallis

Allen D. Gorby

Engineering Sciences Center,
Sandia National Laboratories,
P.O. Box 5800,
Albuquerque, NM 87185-0346

This paper reports on experimental and computational investigations into the thermal performance of microelectromechanical systems (MEMS) as a function of the pressure of the surrounding gas. High spatial resolution Raman thermometry was used to measure the temperature profiles on electrically heated, polycrystalline silicon bridges that are nominally 10 μm wide, 2.25 μm thick, and either 200 μm or 400 μm long in nitrogen atmospheres with pressures ranging from 0.05 Torr to 625 Torr (6.67 Pa–83.3 kPa). Finite element modeling of the thermal behavior of the MEMS bridges is performed and compared with the experimental results. Noncontinuum gas effects are incorporated into the continuum finite element model by imposing temperature discontinuities at gas-solid interfaces that are determined from noncontinuum simulations. The results indicate that gas-phase heat transfer is significant for devices of this size at ambient pressures but becomes minimal as the pressure is reduced below 5 Torr. The model and experimental results are in qualitative agreement, and better quantitative agreement requires increased accuracy in the geometrical and material property values. [DOI: 10.1115/1.4000965]

Keywords: Raman thermometry, MEMS, finite element heat conduction simulations, noncontinuum gas-phase heat-transfer model, low-pressure effects, suspended microbridge

1 Introduction

The environmental conditions inside a packaged MEMS device dictate its performance and long-term reliability. Reducing packaging pressures below ambient decreases gas damping effects and gas-phase heat transfer and often is required to achieve the desired sensitivity for MEMS accelerometers, gyroscopes [1], ultrasonic sensors [2], infrared sensors [3], and bolometers [4]. Packaging microsystem devices at pressures lower than atmospheric dramatically affects their thermal performance since energy transfer to the environment is substantially reduced as the pressure is reduced.

In order to predict the performance and reliability of packaged MEMS devices, validated models of microsystems in varying environments are needed. Models of thermal performance of MEMS at varying pressures have been developed that account for noncontinuum gas-phase heat transfer at low pressures [5]; however, direct, spatially resolved, temperature measurements of MEMS structures in varying pressures were not available to validate the model results. Temperature measurements on MEMS at varying pressures are very challenging to obtain due to device sizes and access for diagnostic techniques. Lee et al. [6] used Raman thermometry to calibrate the temperature of a microcantilever heater with the dissipated electrical power at atmospheric pressure in air. They then measured the power dissipated as a function of pressure in air from 10^{-5} mbar to 10^{3} mbar and in helium from 10^{-3} mbar to 10^{3} mbar when the heater was operated at 673 K (1 mbar = 0.75 Torr = 100 Pa).

This study was undertaken to advance the understanding of thermal performance of packaged MEMS by experimentally and computationally determining temperature profiles at varying pressures on microbridges fabricated using sacrificial surface micromachining. The experimental methods are described, including the polycrystalline silicon (polysilicon) test structures, packaging of the test samples inside a Linkam stage, the gas control system used to vary the nitrogen atmosphere from 0.05 Torr (6.67 Pa) to ambient pressure, and Raman thermometry. Next, details for the numerical simulations are presented, including the noncontinuum gas model, material properties, and model geometry. The experimental and computational results are compared, and the effects of the environment on the thermal performance of a MEMS suspended bridge structure are discussed.

2 Test Structures

The SUMMiT V™ process [7,8] involves four structural *n*-type (phosphorous) polysilicon layers with a fifth layer as a ground plane. The polysilicon layers are separated by sacrificial oxide layers that are etched away during the final release step. The two topmost layers, Poly3 and Poly4, are nominally 2.25 μm in thickness, while the bottom two, Poly1 and Poly2, are nominally 1.0 μm and 1.50 μm in thickness, respectively. The ground plane, Poly0, is 0.30 μm in thickness and lies above a 0.80 μm layer of silicon nitride and a 0.63 μm layer of SiO_2. The sacrificial oxide layers between the structural layers are each roughly 2.0 μm thick.

Test structures used for the present study are fabricated from the Poly4 layer and are nominally 2.25 μm thick, 10 μm wide, and 200 μm or 400 μm long. The fixed-fixed bridges end at bond pads, layered structures that mechanically anchor the beam to the substrate and provide a location for wire bonding to the package. The wires are bonded to a 0.70 μm layer of aluminum

[1]Corresponding author.

Contributed by the Heat Transfer Division of ASME for publication in the JOURNAL OF HEAT TRANSFER. Manuscript received May 18, 2009; final manuscript received December 10, 2009; published online April 28, 2010. Assoc. Editor: He-Ping Tan.

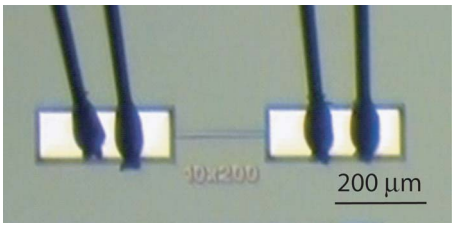

Fig. 1 Optical microscope image of a 10 μm wide × 200 μm long test structure fabricated using the SUMMiT V™ process. The bond pads are 100 μm wide and 300 μm long. Two wires bonded to each bond pad are visible in the image. The connections to the package are outside of the image.

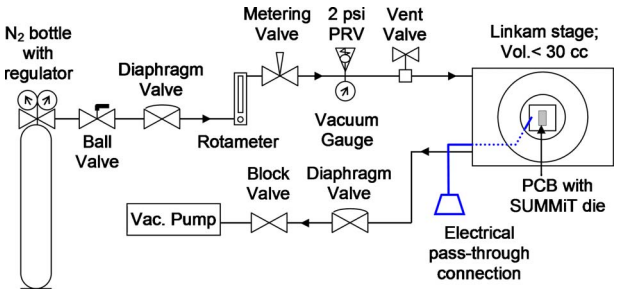

Fig. 2 Schematic of the layout of the vacuum and gas supply system for the experiments

that is deposited on top of the bond pad. Figure 1 is an image of a 10 μm wide, 200 μm long test structure with the bond pads and bond wires visible.

3 Experimental Methods

Temperature measurements were obtained with micro-Raman spectroscopy [9] using a Renishaw inVia Raman microscope. The microscope uses a 180 deg backscattering geometry and a 488 nm Ar^+ laser as the probe that produces a diffraction-limited spot of 560 nm in diameter when focused by a 50×, 0.50-numerical-aperture objective. The actual measurement diameter within the sample is larger, 1.70 μm, because of spreading of the probe laser within the sample. The Raman signal from the sample surface is collected through the objective, dispersed by a grating spectrograph, and detected with a back-side illuminated, thermoelectrically cooled charge coupled device (CCD) camera (Pixis 1024B, Princeton Instruments, Trenton, NJ). Dispersion of the Raman signal at the CCD is 0.57 cm^{-1}/pixel.

Laser power at the sample is attenuated to 65 μW to minimize localized heating of the sample that would otherwise introduce a bias into the temperature measurement. Minimal heating of the sample is confirmed by obtaining Raman spectra at decreasing laser powers from a room-temperature SUMMiT sample until no change in the Raman peak position was observed. Using scaling arguments presented by Kearney et al. [9], the power deposited on the probed location, assuming full absorption and a sample thermal conductivity of 30 W/m K (equivalent to SUMMiT polysilicon at 523 K), would amount to a temperature increase of 1.3 K; considering a silicon surface reflectivity of 39% [10], this value is likely closer to 0.8 K.

In the Raman process, photons from the incident probe light source interact with the optical phonon modes of the irradiated material and are scattered to higher (anti-Stokes) or lower (Stokes) frequencies from the probe line frequency. In the case of silicon and polysilicon, the scattered Raman light arises from the triply degenerate optical phonon at the Brillouin zone center. The resulting spectrum for the Stokes (lower frequency) Raman response has a single narrow peak at approximately 520 cm^{-1} from the laser line frequency at room temperature. Increases in temperature affect the frequency, lifetime, and population of the phonon modes coupled to the Raman process, leading to changes in the Raman spectra, namely, a shift in the peak position and broadening of the Raman peak. Both metrics are practical for temperature mapping of MEMS. However, while peak width is sensitive only to surface temperature, peak position is sensitive to both stress and temperature [9,11].

For thermometry of the test beams under varying-pressure conditions, a Linkam temperature-controlled thermal stage fitted with vacuum ports was used. A diagram of the layout of the vacuum system is shown in Fig. 2. The system used ultra-high-purity nitrogen gas as the purge gas and permitted control of the pressure inside the stage from ambient (nominally 625 Torr ± 10 Torr) to 0.010 Torr measured with a BOC Edwards Pirani gauge. The flow rate of nitrogen into the stage was maintained at 20 cc/min for pressures above 0.05 Torr, and at 6 cc/min for a pressure setting of 0.05 Torr. With a chamber volume of ~30 cc, the gas exchange rate inside the chamber is 1.5 min at all pressures, except for 0.05 Torr where it is about 5 min.

To provide electrical power to the test devices, the SUMMiT die was packaged on a printed circuit board (PCB) to which wire leads were soldered. Each bond pad on the beam structure is wire-bonded to two separate connections on the PCB to allow for four-point sensing of the voltage. Quick-disconnect connectors were used inside the stage to allow for easy exchange of parts. The PCB was placed in the center of a quartz crucible inside the stage and held in place with a vacuum-compatible carbon tape (Fig. 3). The heating ability of the stage was used to heat the sample to a temperature of 300–310 K to ensure a consistent substrate temperature for the measurements. The devices were powered with a Keithley 2400 source meter in a four-point sensing configuration, where the current is flowed through the outside connections and the voltage is measured across the inner ones.

Prior to performing the measurements on the test structures, a temperature calibration of the Raman response from the Poly4 layer was obtained by placing a die in a second temperature-controlled hot stage and acquiring Raman data over a temperature range 300–700 K. The sample used in the calibration was from the same fabrication run as those used in the validation measurements but was a different die. A Voigt function, which captures both the Lorentzian Raman line shape and the Gaussian instrument function, is fitted to the Raman spectral data to extract both the center position Ω and the full width at half maximum (FWHM) Γ_{Raman} of the Raman peak [9]. At different temperatures in the calibration

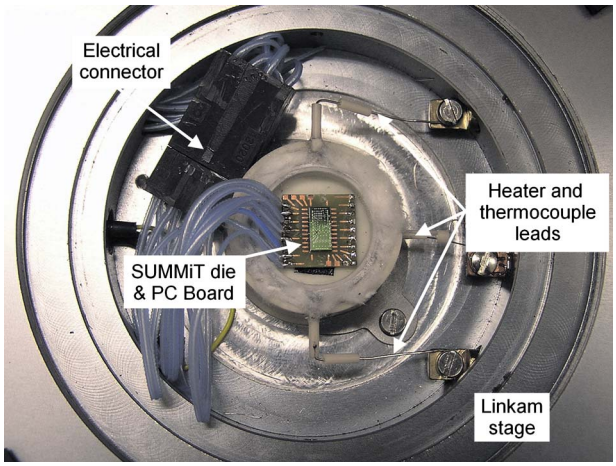

Fig. 3 Close-up of the packaged SUMMiT die inside the Linkam stage. The silicon die in the center of the square printed circuit board piece is 3.6 mm wide × 6.3 mm long.

range, six spectra are acquired from the sample and fitted, and the extracted peak position and peak width are then averaged and plotted as a function of temperature.

The data are then fitted to a calibration function that correlated the observed change in the Raman spectra to temperature. For the Raman peak position, the correlation is linear and is described by the expression

$$\Omega = \frac{\partial \Omega}{\partial T} T + \Omega_o \tag{1}$$

where $\partial\Omega/\partial T = -0.0239 \pm 0.00018$ cm^{-1}/K, T is in K, and $\Omega_o = 527.314$ cm^{-1}. For the Raman peak width (FWHM), the correlation is quadratic with temperature and is given by the expression

$$\Gamma_{\text{Raman}} = A(T+B)^2 + C \tag{2}$$

where $A = 5.129 \times 10^{-6}$ cm^{-1}/K^2, $B = 407.213$ K, and $C = 1.608$ cm^{-1}. Since the Poly4 fixed-fixed beams used in this study (Fig. 1) are anchored at both ends, thermal expansion during heating is constrained, and the beams are placed under compressive stress during their operation. For this reason, peak width is used as the metric for the test, and sample temperature is extracted using Eq. (2).

Two devices were tested for the validation measurements: a 10×200 μm^2 beam and a 10×400 μm^2 beam. The Raman temperature measurements were taken under five different pressure conditions (625 Torr, 50 Torr, 5 Torr, 0.5 Torr, and 0.05 Torr) for both geometries. The electrical currents used to power the devices were chosen so as to provide relatively consistent peak temperatures over the various pressures. The 10×200 μm^2 beam was tested under two current conditions that would provide peak temperatures of 400–450 K and 600 K, respectively; the 10×400 μm^2 beam was powered to provide a peak temperature of 450–500 K.

Error bars were calculated that represent the collective error in the measurement from the principal sources of uncertainty in the measurement, which are the accuracy of the peak width extraction and the error resulting from the temperature calibration. The peak width extraction through the curve fit was the largest source of uncertainty, with an uncertainty of ± 6.58 K over the temperature range explored in the samples, as determined by taking multiple spectra at a fixed temperature during the calibration. The error contribution from the temperature calibration curve (Eq. (2)) is ± 4.66 K. The contribution of system drift, although accounted for during the measurements by taking data from an unheated reference, is only ± 0.03 K for peak width measurements.

An additional source of uncertainty is the variation in the pressure of the system. For the system discussed above, the uncertainty in the pressure control is $\pm 1\%$ of the full scale for pressures below 100 Torr and 1 Torr for higher pressures. Here, full scale for the vacuum gauge is taken to be the next-highest power of 10 in Torr from the pressure reading (i.e., 10 Torr full scale for a 5 Torr pressure, with an uncertainty of ± 0.1 Torr). The corresponding temperature fluctuation due to these pressure variations is estimated to be no more than ± 3.5 K for all pressures and conditions based on the fluctuations observed in the voltage drop across the sample with the observed pressure fluctuations.

Assuming that these uncertainties are uncorrelated yields an uncertainty for the peak-width-based temperature measurement of ± 8.79 K. This total uncertainty is slightly lower than previously reported by Beechem et al. [11], namely, ~ 9 K rather than ~ 11 K, because of the increased number of acquisitions used and the increased signal level used.

4 Numerical Methods

Electrothermal simulations were performed for the experimentally investigated devices using CALORE. CALORE [12,13] is a massively parallel finite element method (FEM) thermal analysis application developed within the SIERRA analysis-code framework at Sandia National Laboratories under the Advanced Simulation and Computing (ASC) program of the National Nuclear Security Administration (NNSA). The present investigation builds on earlier research that used CALORE to investigate noncontinuum heat transfer in microsystems [14] by simulating a beam under user-specified volumetric heating. In the current work, steady-state heat conduction in the test structure and the surrounding gas is simulated, including thermal resistance due to the multilayer bond pads (detailed in Ref. [15]) and nonuniform Joule heating from a specified current due to a temperature-dependent electrical resistance.

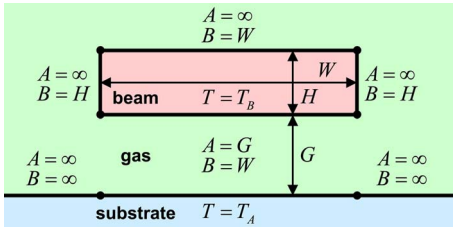

Fig. 4 Schematic of the gas heat-transfer model

Electrical heating problems are modeled in CALORE by loosely coupling two calculations: one that solves for the voltage distribution, and one that solves for the temperature distribution. The electrical calculation determines the Ohmic heating, which is then provided as a volumetric heat source in the temperature calculation. The temperature calculation determines the temperature distribution, which is then provided to the electrical calculation to calculate the temperature-dependent electrical conductivity.

Thermal MEMS devices fabricated using the SUMMiT V process have certain geometric features in common. These devices are composed of planar layers of uniform thickness that are separated from adjacent layers by gaps of uniform thickness, with perpendicular sides. Moreover, these devices employ long beams of rectangular cross section. Because of the large thermal conductivity of crystalline and polycrystalline silicon, the temperature of a heated beam is nearly uniform in each cross section, although the temperature can vary significantly along the length. Similarly, the substrate beneath a heated beam remains very nearly at the ambient temperature.

Extending the model of Gallis et al. [5] and based on the above observations, the paradigmatic microscale geometry for noncontinuum gas-phase heat-transfer model development is illustrated in Fig. 4. A beam of infinite length (out of the page) and finite width W and finite height (thickness) H is separated by a gap of uniform constant height G from a planar substrate of infinite length (out of the page) and infinite width. The beam cross section is at uniform constant elevated temperature T_B, and the substrate is at uniform constant ambient temperature T_A. The space between the beam and the substrate is filled with gas at uniform constant pressure $p = p_{\text{amb}}$ and spatially varying temperature T that approaches the ambient temperature T_A far from the beam.

The above geometry can be further broken down into a series of line segments of finite or infinite breadth that face either an identical parallel line segment at a fixed separation or else unbounded space. Thus, each line segment in Fig. 4 has a finite or infinite breadth B (the distance between its end points) and a finite or infinite separation A from a parallel segment. In Fig. 4, the separation A and the breadth B are given for each of the seven line segments in terms of the geometric lengths.

In the gas region, steady heat conduction is simulated using the temperature-dependent gas thermal conductivity K. When heat flows across a gas-solid interface, noncontinuum gas behavior causes the gas and solid temperatures to differ. The normal heat flux q can be related to the temperature difference across the interface ΔT in terms of a heat-transfer coefficient h [5] as follows:

Table 1 Aluminum, silicon dioxide, and silicon nitride properties (300 K)

Quantity	Al	Oxide	Nitride
Thermal conductivity (W/m K)	235	1.4	3.2
Electrical resistivity (Ω m)	0.028	-	-

$$q = h\Delta T \tag{3}$$

This expression provides a convenient means for expressing a noncontinuum effect in the continuum FEM simulations. At a boundary between gas and a solid, a temperature discontinuity can be maintained while satisfying conservation of energy by enforcing continuity of the flux. The magnitude of this discontinuity, which is assumed dependent solely on the gas conditions, is set by the heat-transfer coefficient h.

The following functional form of the heat-transfer coefficient is applied at all gas-solid interfaces shown in Fig. 4:

$$h = \left(1 + \frac{\zeta}{4}\right)\left(\frac{\sigma}{S_1 S_2}\right)\left(\frac{p\bar{c}}{T}\right) \tag{4}$$

$$S_1 = 2 - \sigma + \frac{\sigma}{1 + c_4(B/A) + c_5(B/\lambda)} \tag{5}$$

$$S_2 = 1 + \frac{c_1\sigma}{1 + c_2(\lambda/A) + c_3(\lambda/B)} \tag{6}$$

$$\lambda = \frac{2\mu}{\rho\bar{c}} \tag{7}$$

$$\bar{c} = \sqrt{\frac{8k_BT}{\pi m}} \tag{8}$$

and

$$\rho = \frac{mp}{k_BT} \tag{9}$$

Here, ζ is the number of molecular internal energy modes (2 for nitrogen), σ is the thermal accommodation coefficient (the probability between 0 and 1 that a gas molecule exchanges thermal energy when it reflects from a solid surface), S_1 and S_2 are order-unity dimensionless factors, A and B are the separation and breadth of a line segment, $\bar{c}$ is the molecular mean thermal speed, λ is the molecular mean free path, μ is the viscosity, ρ is the mass density, m is the molecular mass, k_B is the Boltzmann constant, and c_1–c_5 are positive dimensionless parameters that enable S_1 and S_2 to behave correctly in limiting regimes. The above functional form reproduces known gas heat-transfer behavior in the near-continuum and free-molecular regimes for parallel-plate and isolated-body geometries [5]. The parameters c_1–c_5 control the transitions between various limiting regimes. For nitrogen, their values are $c_1=0.167$, $c_2=0.599$, $c_3=1.23$, $c_4=0.32$, and $c_5=1.02$. Temperature-dependent thermophysical properties for nitrogen can be found in Ref. [16].

The test structure contains four materials: polycrystalline silicon (polysilicon), silicon dioxide (oxide), silicon nitride (nitride), and aluminum. The thermophysical properties of the materials other than polysilicon are obtained from published values and listed in Table 1. These materials are deposited using reasonably standard processes, and the effects of these processes on the quantities of interest in this work are reasonably small. Resistivity values are not provided for oxide and nitride because they are excluded from the electrical model.

The thermophysical properties for polysilicon vary strongly with processing conditions and with temperature and are critical to the current work. Thus, efforts were made to ensure appropriate values through comparisons with earlier measurements on SUMMiT polysilicon for the electrical resistivity r_s and the thermal conductivity K_s [15,17]. The resistivity values were found to be represented well by the following linear equation in temperature, where the temperature T is in K and the resistivity r_s is in Ω μm [18]:

$$r_s = 0.0232T + 13.6997 \tag{10}$$

The functional form of the thermal conductivity was determined from earlier measurements, and the offset was adjusted by performing simulations for a high-power, low-pressure, $10 \times 200\ \mu m^2$ beam for which the gas-phase transport is not significant (10.75 mW and 0.05 Torr). The resultant thermal conductivity is given as follows, where T is in K and K_s is in W/m K [18]:

$$K_s = \frac{1}{0.0066 + 0.00116(0.03T - 2)} - 6.5 \tag{11}$$

While the heated bridge portion of the test structure has a very simple geometry, the layers and geometry of the anchors are fairly complex [15]. These anchor points, also known as "bond pads" since the wires for electrical connections are bonded to them, have complex multilayer structures due to constraints imposed by the SUMMiT V manufacturing process. Because cross sections of the actual devices used in this work were not available, the geometry was built based on available computational models, with some input from measured quantities. The layer thicknesses were adjusted to bring the beam height above the substrate, 11.872 μm, into agreement with the interferometry measurements of the test structures used in the experiments. Figure 5 shows a cross section of a bond pad and base of a beam, and Table 2 lists the dimensions adopted for the computational model.

The gas heat conduction problem was solved on a mesh 100 μm wide and 50 μm tall. These dimensions were chosen by solving a steady-state, two-dimensional problem with a beam cross section held at 600 K. The domain boundaries were then placed such that the temperature gradient, and therefore the heat flux, fell below 1% of its magnitude at the beam surface at these locations, ensuring that placing insulating boundaries at these lo-

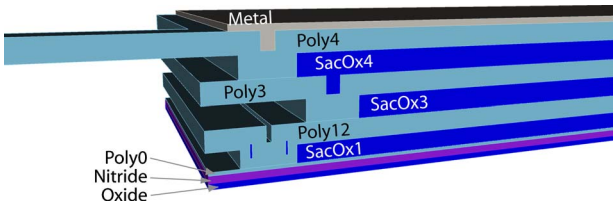

Fig. 5 Cross section showing the layers in the bond pad and base of the beam. Layer thicknesses are specified in Table 2.

Table 2 Geometric dimensions used in CALORE computational model

Layer thickness	Model value (μm)	Other lengths	Model value (μm)
Thermal oxide	0.630	Beam length (short)	200.00
Silicon nitride	0.800	Beam length (long)	400.00
Poly0	0.300	Beam width (both)	9.65
SacOx1	2.000	Bond pad x width	100.00
Poly12	2.260	Bond pad y width	41.00
SacOx3	2.461	Gas domain y width	100.00
Poly3	2.320	Gas domain z height	50.00
SacOx4	2.461		
Poly4	2.330		
Metal	0.700		

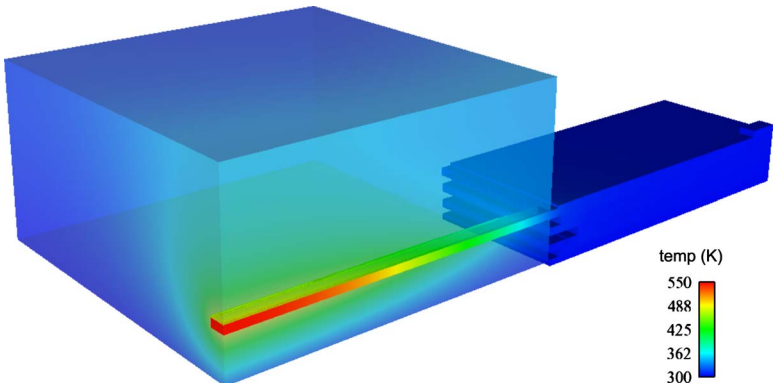

Fig. 6 Temperature field for a 200 μm long beam at 50 Torr (6.67 kPa) with an initial temperature of 304.15 K and operated at 12.41 mW with unity accommodation (Case 16)

cations would have little effect on the solution. The gas grid is truncated at the base of the beam because the temperature at this point is expected to be very near ambient, so there is little expected benefit in gridding between the layers at the forward edge of the bond pad.

Grids were constructed in three levels, with uniform refinement followed by localized refinement based on the gradient in voltage for the electrical grid. The coarse mesh contained 69,543, 244,665, and 959,916 elements for the electrical, solid, and gas grids, while the finest mesh contained 4,264,832, 15,472,640, and 35,318,496 elements. Most calculations were carried out on the medium grid, which contained 540,139, 1,941,115, and 4,436,064 elements. Computation times for the three grids for a typical calculation were 0.1 h, 1.3 h, and 5.9 h on 50 Infiniband-connected nodes of the Sandia "Thunderbird" cluster with two 3.6 GHz EM64T processors each. The typical calculation was for a 200 μm long beam at 50 Torr (6.67 kPa) with an initial temperature of 304.15 K and operated at 12.41 mW with a thermal accommodation coefficient of 0.3, the intermediate value considered. For this calculation, the temperature difference across the beam deviated from the finest grid value by 1.2% and 0.4% on the coarse and medium grids, respectively. The results computed on the medium grid are therefore very likely grid converged to well within the experimental error.

5 Results

Using the noncontinuum gas-phase heat-transfer model for the surface heat-transfer coefficient and the specified material properties and geometry, an example of typical model results for the temperature distribution in the beam and gas with an accommodation coefficient of unity is shown in Fig. 6 for a 200 μm long beam at 50 Torr with an initial temperature of 304.15 K and operated at 12.41 mW. Several features are visible in these results. First, the beam temperature is somewhat higher than that of the adjacent gas. This is a consequence of the noncontinuum gas-solid boundary condition. Second, the highest temperature, and most of the gas-phase heat transfer to the substrate, occurs at the beam center because the ends are cooled by conduction through the bond pad.

The combined gas-solid heat-transfer model described in Sec. 4 is applied to compute temperature profiles corresponding to the conditions for which the temperature profiles were measured. Figures 7 and 8 show the calculated and measured temperature profiles for the 200 μm and 400 μm beams, respectively. Each plot in each figure contains all model and experimental temperature profiles for the same beam length and the same gas pressure. The measured data are labeled by beam length, pressure, power, and measurement run or case number. Each 200 μm plot contains temperature profiles for two powers ("high" and "low"), whereas each 400 μm plot contains temperature profiles for only one power ("low"). The high-power and low-power conditions produce maximum temperatures of ~600 K and ~450 K, respectively. The 625 Torr, 200 μm plot is divided into two separate plots for reasons that will be discussed. The 625 Torr, 200 μm plot in Fig. 7(*e*) contains an additional power ("medium"). The colors red, green, and blue denote high, medium, and low, respectively.

The temperature measurements indicate that increasing the pressure by a factor of 10 from 0.05 Torr to 0.5 Torr hardly changes the temperature profiles and the corresponding powers. This is consistent with the results of Lee et al. [6] for which the dissipated power from a microcantilever heater at 673 K was fairly constant below 1 mbar (0.75 Torr) in air and helium atmospheres. This observation indicates that gas-phase heat transfer is negligible compared with solid-phase heat transfer at these low pressures. When the pressure is increased to 5 Torr, the power must be increased by about 4% to keep the peak of the temperature profile around 600 K, so gas-phase heat transfer is about 4% of solid-phase heat transfer at 5 Torr. A similar comparison indicates that gas-phase heat transfer is about 15% and 31% of solid-phase heat transfer at gas pressures of 50 Torr and 625 Torr, respectively. Thus, gas-phase heat transfer is significant for devices of this size at ambient pressure but becomes minimal as the pressure is reduced.

For each combination of beam length, gas pressure, and power, three model temperature profiles are presented in Figs. 7 and 8, corresponding to accommodation coefficients of 1.0, 0.3, and 0.0. A value of 1.0 produces the maximum gas heat transfer possible, a value of 0.0 produces no gas heat transfer, and the intermediate value of 0.3 is a low value compared with measurements [19,20].

As the pressure increases from 0.05 Torr to 0.5 Torr and to 5 Torr, the three model profiles for each condition are seen to separate, which indicates the increasing importance of gas heat transfer as the pressure increases although gas heat transfer is not large yet. The high-power model and experimental profiles in Figs. 7(*a*)–7(*c*) agree well. However, this agreement is not unexpected because the thermal conductivity model is calibrated to match the 0.05 Torr high-power profile and because gas heat transfer is still quite small below 5 Torr. For the low-power profiles in these plots, the model again slightly overpredicts the temperature rise near the beam ends and also slightly underpredicts the maximum temperature rise by a progressively greater amount as the pressure is increased.

As the pressure increases to 50 Torr, the agreement between the model and experimental profiles deteriorates, particularly for the low-power cases (Fig. 7(*d*)). At this pressure, the mean free path of gas molecules is about 1 μm, and is comparable to the beam thickness. This is the regime in which the gas-solid heat-transfer-

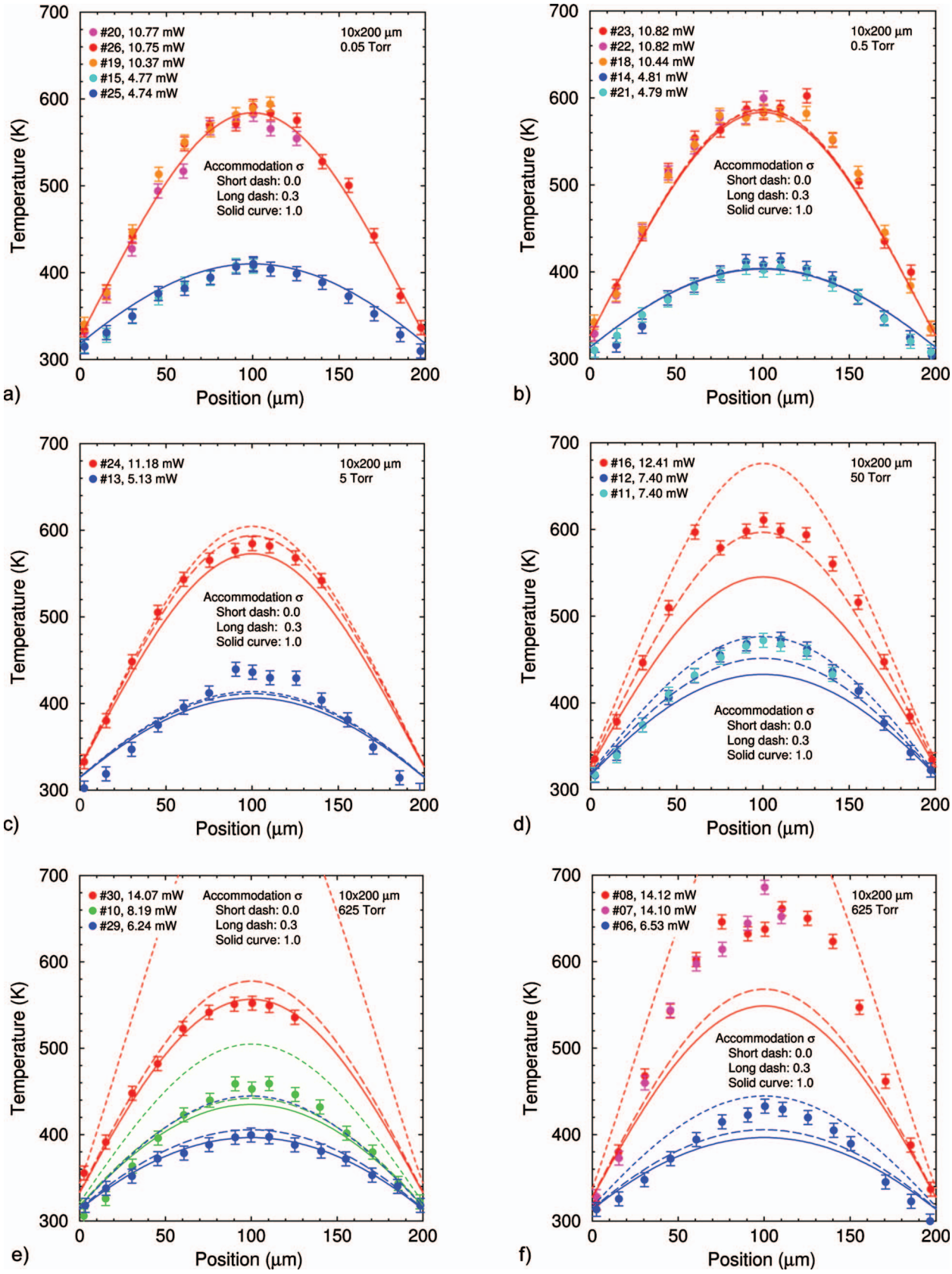

Fig. 7 Comparison of experimental (symbols) and simulation (lines) temperature profiles on 200 μm long beams at 0.05–625 Torr (6.67 Pa–83.3 kPa)

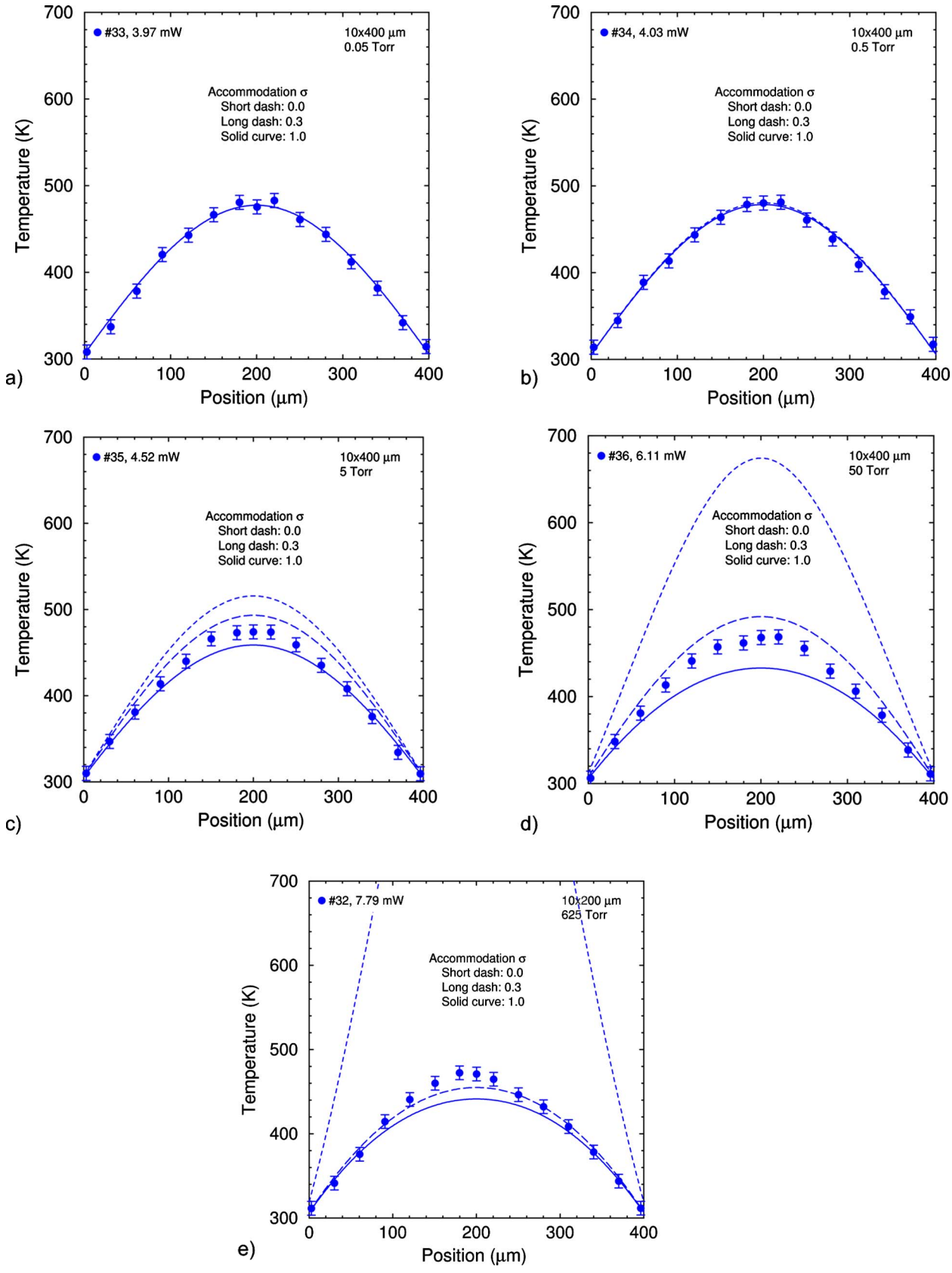

Fig. 8 Comparison of experimental (symbols) and simulation (lines) temperature profiles on 400 μm long beams at 0.05–625 Torr (6.67 Pa–83.3 kPa)

coefficient model is expected to be least accurate. However, the differences are more than what would be expected based on the comparisons of molecular and FEM gas simulations. An accommodation coefficient of 0.3 would represent the high-power profile well and the low-power profile marginally, but this value is much lower than expected [19,20].

The thermal conductivity of polysilicon depends strongly on the crystal structure, which can vary between processing runs and change over time, especially at high temperatures. Thus, the temperature-dependent thermal conductivity in Eq. (11) includes a temperature-independent offset selected to make the red model curve pass through the red symbols in Fig. 7(*a*). This high-power low-pressure case was used because the full temperature range is accessed and the gas heat transfer is essentially zero so that only the solid properties are important. This "calibrated" temperature-dependent thermal conductivity (Eq. (11)) lies within the reported measurement uncertainty (15%) and is used without modification in all the simulations.

This calibration approach can be assessed to some degree by examining the low-power low-pressure temperature profiles (blue values, Fig. 7(*a*)). The model predicts the maximum temperature rise reasonably well but systematically overpredicts the temperature rise near the beam ends. This difference is not as visible in the two low-pressure 400 μm cases (low-power) of Figs. 8(*a*) and 8(*b*), for which the simulation curves lie within the error bars for the entire temperature distribution.

Experimental artifacts are clearly visible in the two 625 Torr plots in Figs. 7(*e*) and 7(*f*). The maximum temperature rises of the profiles in Fig. 7(*f*) are roughly 40% larger than the corresponding values of the profiles in Fig. 7(*e*) despite the fact that the powers are almost identical. The experimental results in Fig. 7(*f*) are the first three data sets among those reported that were collected: Cases 6, 7, and 8. Given the difference in these data sets, something happened between Case 8 and Case 10 that altered the thermal behavior of the beams significantly and permanently.

At a pressure of 625 Torr (ambient), the experimental profiles are divided into two groups: Cases 10 and 29–30 (Fig. 7(*e*)) and Cases 6–8 (Fig. 7(*f*)). The model and experimental profiles agree well for Cases 10 and 29–30 but differ for Cases 6–8. Again, this is not a defect of the model; rather, the experimental results differ significantly between themselves. Since the model is calibrated using Case 26, it is reasonable that the model agrees more closely with the later cases than with the earliest cases.

For most low-power profiles in Fig. 7, the model overpredicts the experimental temperatures near the beam ends and underpredicts the experimental maximum temperature rise. One possibility suggested by this observation is that the experimental thermal conductivity is larger at ambient temperature but decreases more rapidly with increasing temperature than the thermal conductivity used in the model.

The model and experimental 400 μm temperature profiles are in reasonable agreement although the agreement degrades as the gas pressure is increased as seen in Fig. 8. These profiles are all low-power and are similar to those of the 200 μm beams.

6 Conclusions

This paper reports the first spatially resolved Raman temperature profiles for polysilicon MEMS, suspended 10 μm wide microbridges with lengths of 200 μm and 400 μm in nitrogen atmospheres at pressures varying from 0.05 Torr to 625 Torr (6.67 Pa–83.3 kPa). Temperature profiles are also computationally obtained using a finite element code, CALORE, with a heat-transfer coefficient at gas-solid surfaces derived from the noncontinuum gas-phase heat-transfer model. The experimental and simulation results indicate that at pressures below 0.5 Torr the gas-phase heat transfer is negligible compared with solid conduction. As the pressure increases above 0.5 Torr, the gas-phase heat transfer becomes more significant. For polysilicon MEMS structures at ambient pressures, gas-phase heat transfer significantly impacts the thermal performance. The measured and simulated temperature profiles are in qualitative agreement in the present study. Quantitative agreement between experimental and simulated temperature profiles requires accurate knowledge of temperature-dependent thermophysical properties' values, device geometries, and thermal accommodation coefficients.

Acknowledgment

Sandia is a multiprogram laboratory operated by Sandia Corporation, a Lockheed-Martin Co., for the U.S. Department of Energy's National Nuclear Security Administration under Contract No. DE-AC04-94AL85000.

Nomenclature

A = distance from one wall to the nearest parallel wall, m
B = distance from one corner to the other of finite-extent wall, m
A, B, C = constants in Eq. (2)
$\bar{c}$ = molecular mean thermal speed, m/s
$c_1 - c_5$ = positive dimensionless parameters in Eqs. (5) and (6)
h = heat-transfer coefficient at gas-solid interface, $W/(m^2\ K)$
k_B = Boltzmann constant, 1.380658×10^{-23} J/K
K = gas thermal conductivity, W/(m K)
K_s = solid thermal conductivity, W/(m K)
m = mass of gas molecules, kg
p = gas pressure, Pa
r_s = electrical resistivity, $\Omega\ \mu$m
S_1, S_2 = factors in the heat-transfer coefficient h (unity or larger)
T = temperature, K
V = voltage, V

Greek Symbols

Γ_{Raman} = FWHM of the Raman peak, cm^{-1}
ζ = number of internal energy modes of gas molecules (non-negative)
λ = mean free path of gas molecules, m
μ = gas viscosity, Pa s
ρ = gas mass density, kg/m^3
σ = thermal accommodation coefficient (0–1)
Ω = center frequency of the Raman peak, cm^{-1}
Ω_o = initial center frequency of the Raman peak, cm^{-1}

References

[1] Kim, J.-S., Lee, S.-W., Jung, K.-D., Kim, W.-B., Choa, S.-H., and Ju, B.-K., 2008, "Quality Factor Measurement of Micro Gyroscope Structure According to Vacuum Level and Desired Q-Factor Range Package Method," Microelectron. Reliab., **48**, pp. 948–952.

[2] Xuecheng, J., Ladabaum, I., Degertekin, F. L., Calmes, S., and Khuri-Yakob, B. T., 1999, "Fabrication and Characterization of Surface Micromachined Capacitive Ultrasonic Immersion Transducers," J. Microelectromech. Syst., **8**(1), pp. 100–114.

[3] Eriksson, P., Andersson, J. Y., and Stemme, G., 1997, "Thermal Characterization of Surface-Micromachined Silicon Nitride Membranes for Thermal Infrared Detectors," J. Microelectromech. Syst., **6**(1), pp. 55–61.

[4] Nagapriya, K. S., Raychaudhuri, A. K., Jain, V. K., Jalwania, C. R., and Kumar, V., 2003, "Effect of Ambient on the Thermal Parameters of a Micromachined Bolometer," Appl. Phys. Lett., **82**(16), pp. 2721–2723.

[5] Gallis, M. A., Torczynski, J. R., and Rader, D. J., 2007, "A Computational Investigation of Noncontinuum Gas-Phase Heat Transfer Between a Heated Microbeam and the Adjacent Ambient Substrate," Sens. Actuators A, **134**(1), pp. 57–68.

[6] Lee, J., Wright, T. L., Abel, M. R., Sunden, E. O., Marchenkov, A., Graham, S., and King, W. P., 2007, "Thermal Conduction From Microcantilever Heaters in Partial Vacuum," J. Appl. Phys., **101**, p. 014906.

[7] MEMS Technologies Department, 2008, "SUMMiT V™ Five Level Surface Micromachining Technology Design Manual, Version 3.1a," Sandia Report No. SAND2008-0659P, Sandia National Laboratories, Albuquerque, NM.

[8] Sniegowski, J. J., and de Boer, M. P., 2000, "IC-Compatible Polysilicon Surface Micromachining," Annu. Rev. Mater. Sci., **30**, pp. 299–333.
[9] Kearney, S. P., Phinney, L. M., and Baker, M. S., 2006, "Spatially Resolved Temperature Mapping of Electrothermal Actuators by Surface Raman Scattering," J. Microelectromech. Syst., **15**(2), pp. 314–321.
[10] Aspnes, D. E., and Studna, A. A., 1983, "Dielectric Functions and Optical Parameters of Si, Ge, GaP, GaAs, GaSb, InP, InAs, and InSb From 1.5 to 6.0 eV," Phys. Rev. B, **27**(2), pp. 985–1009.
[11] Beechem, T., Graham, S., Kearney, S. P., Phinney, L. M., and Serrano, J. R., 2007, "Simultaneous Mapping of Temperature and Stress in Microdevices Using Micro-Raman Spectroscopy," Rev. Sci. Instrum., **78**(6), p. 061301.
[12] Bova, S. W., Copps, K. D., and Newman, C. K., 2006, "Calore: A Computational Heat Transfer Program, Volume 1: Theory Manual," Sandia Report No. SAND2006, Sandia National Laboratories, Albuquerque, NM.
[13] Calore Development Team, 2008, "Calore: A Computational Heat Transfer Program, Volume 2: User Reference Manual, Version 4.6," Sandia Report No. SAND2008-0098P, Sandia National Laboratories, Albuquerque, NM.
[14] Torczynski, J. R., Wong, C. C., Piekos, E. S., Gallis, M. A., Rader, D. J., and Bainbridge, B. L., 2005, "Modeling Microscale Heat Transfer Using Calore," Sandia Report No. SAND2005-5979, Sandia National Laboratories, Albuquerque, NM.
[15] Phinney, L. M., Piekos, E. S., and Kuppers, J. D., 2007, "Bond Pad Effects on Steady State Thermal Conductivity Measurement Using Suspended Micromachined Test Structures," ASME Paper No. IMECE2007-41349.
[16] White, F. M., 1984, *Heat Transfer*, Addison-Wesley, Reading, MA.
[17] Phinney, L. M., Kuppers, J. D., and Clemens, R. C., 2006, "Thermal Conductivity Measurements of SUMMiT V Polycrystalline Silicon," Sandia Report No. SAND2006-7112, Sandia National Laboratories, Albuquerque, NM.
[18] Torczynski, J. R., Gallis, M. A., Piekos, E. S., Serrano, J. R., Phinney, L. M., and Gorby, A. D., 2008, "Validation of Thermal Models for a Prototypical MEMS Thermal Actuator," Sandia Report No. SAND2008-5749, Sandia National Laboratories, Albuquerque, NM.
[19] Saxena, S. C., and Joshi, R. K., 1989, *Thermal Accommodation and Adsorption Coefficients of Gases* (CINDAS Data Series on Material Properties Vol. II-1), C. Y. Ho, ed., Hemisphere, New York.
[20] Trott, W. M., Rader, D. J., Castañeda, J. N., Torczynski, J. R., and Gallis, M. A., 2009, "Measurement of Gas-Surface Accommodation," *Rarefied Gas Dynamics: 26th International Symposium*, American Institute of Physics, Melville, NY.

Thermal Wave Based on the Thermomass Model

Zeng-Yuan Guo[1]
e-mail: demgzy@tsinghua.edu.cn

Quan-Wen Hou

Department of Engineering Mechanics,
Key Laboratory for Thermal Science and Power
Engineering of Ministry of Education,
Tsinghua University,
Beijing 100084, China

*In times comparable to the characteristic time of the energy carriers, Fourier's law of heat conduction breaks down and heat may propagate as waves. Based on the concept of thermomass, which is defined as the equivalent mass of phonon gas in dielectrics, according to the Einstein's mass-energy relation, the phonon gas in the dielectrics is described as a weighty, compressible fluid. Newton mechanics has been applied to establish the equation of state and the equation of motion for the phonon gas as in fluid mechanics, because the drift velocity of a phonon gas is normally much less than the speed of light. The propagation velocity of the thermal wave in the phonon gas is derived directly from the equation of state for the phonon gas, rather than from the relaxation time in the Cattaneo–Vernotte (CV) model (Cattaneo, C., 1948, "Sulla Conduzione Del Calore," Atti Semin. Mat. Fis. Univ. Modena, **3**, pp. 83–101; Vernotte, P., 1958, "Paradoxes in the Continuous Theory of the Heat Equation," C. R. Acad. Bulg. Sci., **246**, pp. 3154–3155). The equation of motion for the phonon gas gives rise to the thermomass model, which depicts the general relation between the temperature gradient and heat flux. The linearized conservation equations for the phonon gas lead to a damped thermal wave equation, which is similar to the CV-wave equation, but with different characteristic time. The lagging time in the resulting thermal wave equation is related to the wave velocity in the phonon gas, which is approximately two orders of magnitude larger than the relaxation time adopted in the CV-wave model for the lattices. A numerical example for fast transient heat conduction in a silicon film is presented to show that the temperature peaks resulting from the thermomass model are much higher than those resulting from the CV-wave model. Due to the slower thermal wave velocity in the phonon gas, by as much as one order of magnitude, the damage due to temperature overshooting may be more severe than that expected from the CV-wave model.* [DOI: 10.1115/1.4000987]

Keywords: thermal wave, thermomass, short pulse laser heating, heat conduction in silicon film

1 Introduction

Heat motion through conductors is generally characterized by the empirical heat conduction law proposed by Fourier [1] in 1822 as

$$q = -k\nabla T \tag{1}$$

where T is the temperature, q is the heat flux, and k is the thermal conductivity. Fourier's law has been widely applied in various engineering fields. However, for fast transient heat conduction, Fourier's law leads to an infinite velocity of heat propagation since the resulting diffusion equation is parabolic by nature.

Based on the two-fluid model, Tisza [2] and Landau [3] predicted the existence of propagating temperature waves in superfluid helium, which was detected by Peshkov in 1944 [4]. Associated with the rapid development of material processing by pulsed sources, Fourier's law was shown to be inadequate in modeling laser processing of materials [5,6] and high frequency response in IC chips [7]. Intense efforts were thus put forth since 1950s to better understand the limitations of Fourier's law in view of the fast transition of thermodynamic states. Such efforts are not only crucial for more accurate predictions of temperature during the short-time transient, they are also critical for assuring the quality of laser processing of materials and the reliability of electronic devices with high power density.

The problems caused by the infinite velocity of heat propagation triggered many attempts to improve Fourier's law. Cattaneo [8], Vernotte [9], and Morse and Feshbach [10] proposed a new heat flux model, often termed Cattaneo–Vernotte (CV) model, to replace Fourier's law

$$q + \tau_{CV}\frac{\partial q}{\partial t} = -k\nabla T \tag{2}$$

where τ_{CV} is the relaxation time and t is the time. Taking the derivative of Eq. (2) and combining the result with the energy equation under the assumption that all thermophysical properties are constant, it results in

$$\frac{\partial^2 T}{\partial t^2} + \frac{1}{\tau_{CV}}\frac{\partial T}{\partial t} = \frac{a}{\tau_{CV}}\nabla^2 T \tag{3}$$

where a is the thermal diffusivity.

Equation (3) is hyperbolic due to the additional term of the second order derivative of temperature with respect to time. The nonzero value of τ_{CV} makes the heat propagation velocity finite [11]. Heat propagation thus evolves from a diffusion phenomenon to a wave phenomenon, with a finite velocity of heat propagation being $(a/\tau_{CV})^{1/2}$. Brorson et al. [12] proved that the velocity of heat propagation is finite by measuring the duration for a heat pulse to travel through a metallic film. The CV model is more general than Fourier's model because it may describe the thermal wave phenomena in the ultrafast transient. It reduces to Fourier's law, as the relaxation time τ_{CV} is very small, which implies an excessively large thermal wave velocity, in comparison with the characteristic dimension of the conductor. Further extensions of the CV model were also proposed, including the single-phase-

[1]Corresponding author.

Contributed by the Heat Transfer Division of ASME for publication in the JOURNAL OF HEAT TRANSFER. Manuscript received August 19, 2009; final manuscript received October 21, 2009; published online April 29, 2010. Assoc. Editor: Frank Cunha.

lagging (SPL) model [13,14] and the dual-phase-lagging (DPL) model [13–15]. More detailed information can be found in Refs. [11,13–19].

Nernst [20] suggested that, as early as 1917, heat has "inertia" and it can oscillate under some circumstances. In 1931, Onsager [21] recognized that Fourier's law only provides an approximation in describing the heat conduction process, neglecting the time needed for acceleration of heat flow. Thus, the time derivative of heat flux in Eq. (2) implies that heat flux has inertia, namely, it takes time to vary. These statements bear the concept of inertia for heat or heat flux, but they do not provide a quantitative description of the inertia and its effects on heat transport behavior. A quantitative description of heat inertia requires the concept of mass introduced in heat transport. Based on the mass-energy relation of Einstein's relativity theory, Tolman [22] showed that the heat has weight. Later, Eckart [23] and Landau and Lifshitz [24] derived a similar conclusion. Their approaches, however, were focused on the effect of the weight of heat on the thermodynamic properties only. Recently, Cao and Guo [25] used the concept of the mass of heat to describe the inertia of heat in heat transport, and proposed a thermomass (TM) model for heat conduction.

In this paper, extending the thermomass model, we derive a damped wave equation for transient heat conduction in dielectrics, which has intrinsically different physical contexts than the CV-wave model. Comparisons on the heat propagation behavior and the characteristic times between the two wave-based models are conducted.

2 Thermomass Model

2.1 Concept of Thermomass. In order to better describe the motion of the phonon gas in dielectrics, we need to introduce a physical quantity, the equivalent mass of the phonon gas. According to Einstein's special theory of relativity, the relativistic momentum of a particle at velocity u is

$$P_{\text{rel}} = \frac{M_R u}{\sqrt{1 - u^2/c^2}} \tag{4}$$

where c is the light speed and M_R denotes the rest mass of the particle. The relativistic momentum can be interpreted to mean that a moving particle undergoes an increase in mass, that is, the relativistic mass and energy are given, respectively, by

$$M_{\text{rel}} = \frac{M_R}{\sqrt{1 - u^2/c^2}} \tag{5}$$

$$E_{\text{rel}} = M_{\text{rel}} c^2 = \frac{M_R c^2}{\sqrt{1 - u^2/c^2}} \tag{6}$$

With $u \ll c$, Eqs. (5) and (6) can be simplified, respectively, to

$$M_{\text{rel}} = M_R + \tfrac{1}{2} M_R u^2/c^2 \tag{7}$$

$$E_{\text{rel}} = M_R c^2 + \tfrac{1}{2} M_R u^2 \tag{8}$$

where $M_R u^2/2$ is the kinetic energy of the particle in Newtonian mechanics, and $M_R u^2/(2c^2)$ is the increased mass due to particle motion, which can be referred to as the equivalent mass of the particle kinetic energy. For moving ideal gas molecules in a stationary container, Feynman et al. [26] indicated that, "when the gas is heated, the speed of the molecules is increased, and the mass is also increased and the gas is heavier." Likewise, the dielectrics become heavier at higher temperature, and when the velocities of the lattice thermal vibration (characterized by phonons) are much less than the light speed, the increased mass of dielectrics due to thermal vibration is approximately

$$M_h = \frac{E_{RD}}{c^2} \tag{9}$$

where E_{RD} is the sum of the thermal vibration energy of all rest mass lattices and M_h is then called the thermomass of lattice, or the equivalent mass of the phonon gas in dielectrics. Hence, the relativistic mass of the phonon gas is

$$M_{\text{rel}} = M_R + M_h \tag{10}$$

It should be noted that the increased mass due to motion is very small compared with the rest mass of particles and is usually neglected in particle or fluid dynamics, if the particle velocity is much less than the light speed. This is because the increased mass due to motion moves always with the rest mass of particles. However, the thermomass of lattice, or the equivalent mass of the phonon gas, though it is tiny compared with the rest mass of lattices, must be taken into account during heat conduction, because the equivalent mass of the phonon gas is able to move independently of the rest mass of lattices.

2.2 State Equation of Phonon Gas. The state equation of phonon gas was deduced from the Debye state equation by Guo et al. [27]. The Debye state equation for solids [28] is

$$p = -\frac{\partial E_R}{\partial V} + \frac{\gamma E_{RD}}{V} \tag{11}$$

in which p is the pressure, V is the volume, γ is the Grüneisen constant, and E_R and E_{RD} denote the potential and thermal vibration energies of the rest mass of lattice, respectively. The second term in Eq. (11) can be called the thermal pressure because it represents the thermal vibration induced pressure. When the solid temperature is higher than the Debye temperature, the thermal pressure of the rest mass of lattice has the following simple expression:

$$p_R = \frac{\gamma E_{RD}}{V} = \frac{\gamma M_R C T}{V} \tag{12}$$

where C is the specific heat per unit mass. If the thermomass of lattice is taken into account and Eq. (10) is used, we then have the thermal pressure of the relativistic mass of lattice

$$p_{\text{rel}} = p_R + p_h = \frac{\gamma (M_R + M_h) C T}{V} \tag{13}$$

and the thermal pressure of the equivalent mass of phonon gas

$$p_h = \frac{\gamma C M_h T}{V} = \left(\frac{\gamma c^2}{\rho} \right) \rho_h^2 \tag{14}$$

where ρ is the density of dielectrics. Equation (14) is the state equation of phonon gas, where the density of the phonon gas, or the thermomass density, is

$$\rho_h = \frac{M_h}{V} = \frac{\rho C T}{c^2} \tag{15}$$

For silicon at room temperature, the phonon gas pressure p_h is about 2×10^{-3} Pa, and the thermomass density is about 5×10^{-9} kg/m^3.

In summary, the concept of thermomass shows that the phonon gas, unlike the heat concept in the caloric theory, is the weighty and compressive fluid. The phonon gas flow in the dielectrics, where the rest mass of lattice acts as the skeleton, resembles the gas flow in the porous medium.

2.3 Thermomass Model of Heat Conduction. Aharoni [29] proved that for the motion of an object at low velocities, the motion can be characterized by the classical Newton's laws once the concept of a relativistic mass is adopted. Therefore, we used Einstein's mass-energy relation only to determine the equivalent mass of a phonon gas in this paper, while Newton mechanics is adopted to describe the motion of the phonon gas because the

relativistic mass equals to the equivalent mass of the phonon gas, and the drift velocity of a phonon gas is normally much less than the speed of light. Since heat conduction in dielectrics is due to the motion of the phonon gas, in the one-dimensional case, the continuity and momentum equations can be written as in fluid mechanics

$$\frac{\partial \rho_h}{\partial t} + \frac{\partial (\rho_h u_h)}{\partial x} = 0 \tag{16}$$

$$\rho_h \left(\frac{\partial u_h}{\partial t} + u_h \frac{\partial u_h}{\partial x} \right) + \frac{\partial p_h}{\partial x} + f_h = 0 \tag{17}$$

where ρ_h, u_h, and p_h are the density, drift velocity, and pressure of the phonon gas. The first term in Eq. (17) represents the inertial force, the second is the driving force, and the third one, f_h, holds for the resistant force for the phonon gas motion. It should be noted that Eq. (16) is the thermomass conservation equation, which is identical with the thermal energy conservation equation in the kinetic theory of heat, while Eq. (17) is the thermomass momentum conservation equation, which is absent in the kinetic theory of heat.

The velocity of heat motion or the drift velocity of the phonon gas can be extracted from the quantity of heat flux

$$u_h = \frac{q}{\rho C T} \tag{18}$$

For the heat conduction in silicon at room temperature with a heat flux $q = 10^4$ W/m^2, the drift velocity is about 10^{-5} m/s only. The resistant force is linearly related to the phonon gas velocity, if u_h is not very large

$$f_h = \beta u_h \tag{19}$$

with $\beta = 2\gamma C(\rho C T)^2/(kc^2)$ [23].

Substituting Eqs. (15), (18), and (19) into Eq. (17), we can get the equation for one-dimensional heat conduction in dielectrics as follows:

$$\tau_{\mathrm{TM}} \frac{\partial q}{\partial t} - l\rho C \frac{\partial T}{\partial t} + l \frac{\partial q}{\partial x} - bk \frac{\partial T}{\partial x} + k \frac{\partial T}{\partial x} + q = 0 \tag{20}$$

where

$$\tau_{\mathrm{TM}} = \frac{k}{2\gamma \rho C^2 T} \tag{21}$$

$$l = \frac{qk}{2\gamma C(\rho C T)^2} = u_h \tau_{\mathrm{TM}} \tag{22}$$

$$b = \frac{q^2}{2\gamma \rho^2 C^3 T^3} \tag{23}$$

The quantities τ_{TM} and l have dimensions of time and length, respectively, while b is a dimensionless number less than unity and its physical meaning will be given later. For silicon at room temperature, τ_{TM} is on the order of 10^{-10} s. For the heat conduction with a heat flux $q = 10^4$ W/m^2, l is on the order of 10^{-15} m, and b is on the order of 10^{-15}. The first four terms on the left side of Eq. (20) result from the inertial effects, the fifth term represents the effect from the pressure gradient (driving force), and the sixth term results from the resistance as the phonon gas flows through the lattices. Equation (20), inheriting from the concept of mass of heat, which describes the general relation between the temperature gradient and the heat flux vector, is referred to as the thermomass model.

3 Thermal Wave Equation Based on the Thermomass Model

We assume that the phonon gas is initially at rest with uniform temperature or thermal pressure $p_{h,0}$ and with a uniform thermomass density $\rho_{h,0}$. If a small disturbance spreads through the phonon gas, we then have

$$\rho_h = \rho_{h,0} + \rho_h' \tag{24}$$

$$p_h = p_{h,0} + p_h' \tag{25}$$

$$u_h = u_h' \tag{26}$$

The suffix 0 represents the equilibrium state. The superscript $'$ represents the small perturbation. Assuming the equilibrium parameters almost do not change with time and space. Substituting Eqs. (24)–(26) into Eqs. (16) and (17), and ignoring the second order terms, we can get the linear perturbation equations

$$\frac{\partial \rho_h'}{\partial t} + \rho_{h,0} \frac{\partial u_h'}{\partial x} = 0 \tag{27}$$

$$\frac{\partial u_h'}{\partial t} + \frac{1}{\rho_{h,0}} \left(\frac{dp_h}{d\rho_h} \right)_0 \frac{\partial \rho_h'}{\partial x} + \frac{2\gamma}{a} \frac{\rho_{h,0}}{\rho} c^2 u_h' = 0 \tag{28}$$

Taking the derivative of Eq. (28) and combining with Eq. (27), we can get the wave equation for the thermomass density

$$\frac{\partial^2 \rho_h'}{\partial t^2} + \frac{2\gamma c^2 \rho_{h,0}}{a\rho} \frac{\partial \rho_h'}{\partial t} = \left(\frac{dp_h}{d\rho_h} \right)_0 \frac{\partial^2 \rho_h'}{\partial x^2} \tag{29}$$

Substituting Eqs. (15) and (24) into Eq. (29) leads to

$$\frac{\partial^2 T}{\partial t^2} + \frac{2\gamma c^2 \rho_{h,0}}{a\rho} \frac{\partial T}{\partial t} = \left(\frac{dp_h}{d\rho_h} \right)_0 \frac{\partial^2 T}{\partial x^2} \tag{30}$$

Equation (30) is a thermal wave (temperature wave) equation, with the second term on the left side being the resistance induced damping term. The coefficient in the front of the second derivative on the right side of Eq. (30) is the square of the thermal wave velocity

$$s_{\mathrm{TM}}^2 = \frac{dp_h}{d\rho_h} = 2\gamma C T \tag{31}$$

It can be seen that the thermal wave velocity can be obtained from the state equation of the phonon gas in the thermomass model, which is independent of the damping term in Eq. (30). The thermal wave equation represented by Eq. (30), in other words, has now been derived alternatively from the equations of motion along with the equation of state for the phonon gas. It does not follow the traditional approach of combining the energy equation with the constitutive relation for the CV-wave model. The thermomass model thus developed, therefore, justifies Fourier's earlier effort in unifying heat transfer and Newton's law of motion.

To compare these two models, we rewrite Eq. (30) as follows:

$$\frac{\partial^2 T}{\partial t^2} + \frac{1}{\tau_{\mathrm{TM}}} \frac{\partial T}{\partial t} = \frac{a}{\tau_{\mathrm{TM}}} \frac{\partial^2 T}{\partial x^2} \tag{32}$$

where

$$\tau_{\mathrm{TM}} = \frac{a\rho}{2\gamma c^2 \rho_{h,0}} = \frac{k}{2\gamma \rho C^2 T} \tag{33}$$

is the characteristic time in the thermomass model, and

$$\left(\frac{dp_h}{d\rho_h} \right)_0 = s_{\mathrm{TM}}^2 = \frac{2\gamma c^2 \rho_{h,0}}{\rho} = \frac{a}{\tau_{\mathrm{TM}}} \tag{34}$$

The linear equation (32) implies that the second to fourth inertial terms on the left of Eq. (20) have been neglected as follows:

$$\tau_{\mathrm{TM}}\frac{\partial q}{\partial t}+k\frac{\partial T}{\partial x}+q=0 \tag{35}$$

which is termed as the simplified thermomass model. This is because combining Eqs. (16) and (35) also leads to Eq. (32). Hence, Eq. (32) is the thermal wave equation based on the simplified thermomass model. Although the simplified thermomass model possesses a similar appearance to the CV model, it is worth noting that the physical meanings of their characteristic times are intrinsically different. The characteristic time τ_{CV} in the CV model is the relaxation time as the energy carriers approaching the thermodynamic equilibrium. The characteristic time τ_{TM} in the thermomass model, on the other hand, describes a lagging response, in time, between the heat flux (the drift velocity of the phonon gas) and the temperature gradient (the driving force of the phonon gas). Hence, their values and predicted wave propagation velocities are quite different. Furthermore, unlike the CV model, the general thermomass model does not reduce to Fourier's law for steady heat conduction.

Postulating that the temperature gradient and heat flux vector occur at different instants of time, in correlation to the wave theory of heat conduction, Tzou [13–15] put forward the phase lag model to describe heat conduction with a single-phase delay as

$$q(r,t+\tau)=-k\nabla T(r,t) \tag{36}$$

where τ is the time delay between the temperature gradient vector and the heat flux vector. The first-order expansion of Eq. (36) with respect to t results in the expression

$$q(r,t)+\tau\frac{\partial q}{\partial t}(r,t)=-k\nabla T(r,t) \tag{37}$$

The one-dimensional form of Eq. (37) is identical to Eq. (35). This implies that the characteristic time τ_{TM} in the thermomass model is equivalent to the phase lag between the temperature gradient and the heat flux in the single-phase-lag model. Chester [30] estimated the relaxation time τ of phonon transport from the kinetic point of view

$$\tau=\frac{3a}{v_s^2}=\frac{a}{s^2} \tag{38}$$

where v_s is the sound speed and s is the thermal wave velocity. It is evident that both the relaxation time τ_{CV} in the CV model and the relaxation time τ in Chester's work are related to the sound speed in solid, whereas the lagging time τ_{TM} in the thermomass model is related to the sound speed in gas. As indicated in Ref. [25], phonon gas flows through dielectrics in ways analogous to gas flows through porous media. Consequently, there exist two sound waves in a porous medium [31]: the faster wave propagating in the solid phase and the slower wave propagating in the fluid phase. In correspondence, the thermal wave occurring in the phonon gas is the slower wave, while the sound wave occurring in the dielectrics is the faster wave. Therefore, the characteristic time in the heat flux model should be the lagging time between the temperature gradient and the heat flux in the phonon gas, not the relaxation time or the mean free time for phonon transport through the lattices.

If the perturbation is not small, we cannot obtain the wave equation of a single parameter as Eq. (30) or Eq. (32). Equations (16) and (20) can be rewritten as

$$\begin{aligned}&\frac{\partial T}{\partial t}+\frac{1}{\rho C}\frac{\partial q}{\partial x}=0\\&\frac{\partial q}{\partial t}+\frac{(1-b)k}{\tau_{\mathrm{TM}}}\frac{\partial T}{\partial x}+\frac{2l}{\tau_{\mathrm{TM}}}\frac{\partial q}{\partial x}=-\frac{q}{\tau_{\mathrm{TM}}}\end{aligned} \tag{39}$$

where

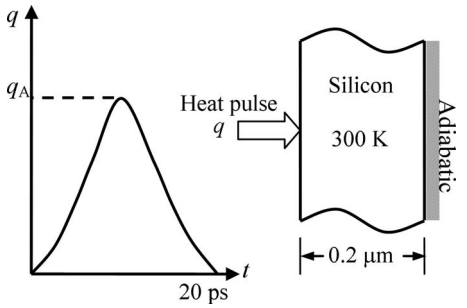

Fig. 1 The schematic diagram of system

$$b=\frac{1}{2\gamma CT}\left(\frac{q}{\rho CT}\right)^2=\left(\frac{u_h}{s_{\mathrm{TM}}}\right)^2\equiv(\mathrm{Ma}_h)^2 \tag{40}$$

b is the square of the Mach number (the ratio of drift velocity to the thermal wave velocity) of the phonon gas. Equation (39) is hyperbolic. Its characteristic equation is

$$\begin{vmatrix}0-s_D & \dfrac{1}{\rho C}\\ \dfrac{(1-b)k}{\tau_{\mathrm{TM}}} & \dfrac{2l}{\tau_{\mathrm{TM}}}-s_D\end{vmatrix}=0 \tag{41}$$

That is,

$$-s_D\left(\frac{2l}{\tau_{\mathrm{TM}}}-s_D\right)=\frac{(1-b)k}{\rho C\tau_{\mathrm{TM}}} \tag{42}$$

Solving Eq. (42), we can get the transport velocity of the thermal disturbance

$$s_D=\frac{q}{\rho CT}\pm\sqrt{\frac{a}{\tau_{\mathrm{TM}}}}=u_h\pm s_{\mathrm{TM}} \tag{43}$$

The first term is the drift velocity of the phonon gas, and the second term is the thermal wave velocity in the phonon gas.

If the coefficients in Eq. (39) are assumed constant, we can get a single equation of temperature as

$$\frac{\partial T}{\partial t}+\tau_{\mathrm{TM}}\frac{\partial^2 T}{\partial t^2}=(1-b)a\frac{\partial^2 T}{\partial x^2}-2l\frac{\partial^2 T}{\partial t\,\partial x} \tag{44}$$

Compared with CV model, Eq. (44) has an additional term, i.e., the last term on the right side, and an additional coefficient $(1-b)$ appearing in the first term on the right side. These additional terms all arise from the inertial force of the thermomass. Based on Eq. (44), we can get the same transport velocity of thermal disturbance as in Eq. (43).

4 Difference in Wave Behaviors Predicted by the Thermomass Model and CV Model

In order to quantitatively compare the wave behaviors predicted by the thermomass model and the CV model, numerical simulations on propagation velocity and temperature response are performed for a silicon nanofilm of 0.2 μm thickness at room temperature heated by a heat pulse on the left boundary, with the right boundary thermally insulated. Its schematic diagram is shown in Fig. 1. The heat pulse on the left boundary can be expressed as

$$q(0,t)=\begin{cases}q_A\times\dfrac{1}{2}\left(1-\cos\left(\dfrac{2\pi t}{t_0}\right)\right), & t<t_0\\ 0, & t\geq t_0\end{cases} \tag{45}$$

where $q_A=5\times10^{11}$ W/m^2 and $t_0=20$ ps. The property of silicon at room temperature used in the simulation is shown in Table 1.

Figures 2–4 show the temperature responses predicted by different heat flux models. In Fig. 2, the wave propagation predicted

Table 1 Thermal properties of silicon used in the computation at 300 K

ρ (g/cm^3)	k (W/m K)	C (J/kg K)	γ	v_s (m/s)
2.33	163	657	1.96	8433

by the simplified thermomass model is dominant over diffusion in the whole domain, while in Fig. 3, the heat pulse predicted by the CV model transports like a wave at the very beginning only (in 20 ps), and then the diffusion dominates the heat transport as the time increases. This is because the characteristic time of heating (2×10^{-11} s) is larger than the relaxation time in the CV model ($\tau_{CV}=4.65\times10^{-12}$ s), and much smaller than the lagging time in the thermomass model ($\tau_{TM}=1.38\times10^{-10}$ s). The thermal transport velocity in Fig. 2 (878 m/s) is much lower than that predicted by the CV model in Fig. 3 (4785 m/s). The much faster heat transport predicted by the CV model leads to the much lower local temperature peak shown in Fig. 3 than that predicted by the thermomass model, as shown in Figs. 2 and 4. As a result, the overheating damage of materials is more severe than that predicted by the CV-wave model. The temperature response predicted by the thermomass model is given in Fig. 4. Since the drift velocity of phonon gas is already comparable to the thermal wave velocity, the heat transport velocity predicted by the general thermomass model is higher than that predicted by the simplified thermomass model, but is still much lower than that predicted by the CV model on the one hand, and the temperature wave becomes unsymmetrical with the wave front leaning to the heat propagation direction on the other hand.

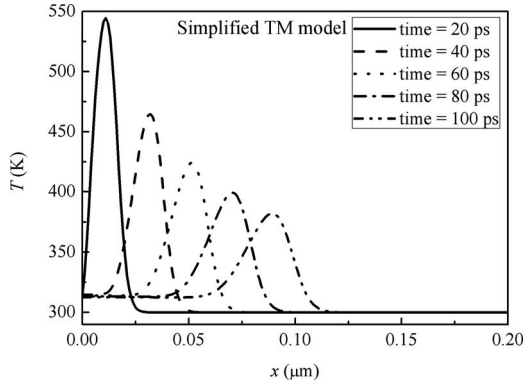

Fig. 2 Temperature response in silicon film based on the simplified thermomass model

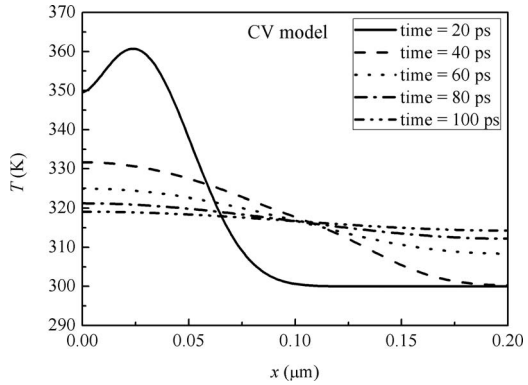

Fig. 3 Temperature response in silicon film based on CV model

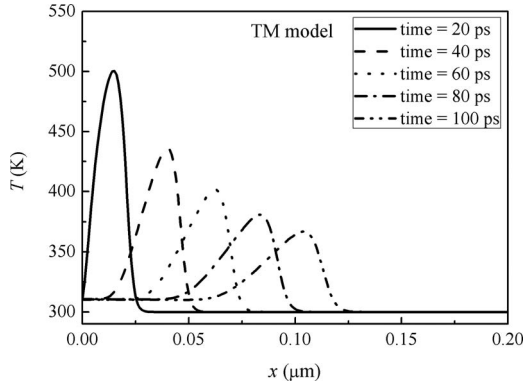

Fig. 4 Temperature response in silicon film based on the thermomass model

5 Conclusions

Based on the concept of thermomass defined by the mass-energy relation in Einstein's special relativity, the phonon gas in the dielectrics is a weighty, compressible fluid. Newton mechanics can be applied to describe the motion of the phonon gas (heat conduction in dielectrics) because the drift velocity of a phonon gas is normally much less than the speed of light. Hence, the mass and momentum conservation equations of the phonon gas can be written as in fluid mechanics, which leads to the thermomass model depicting the general relation between the temperature gradient and heat flux.

Unlike the traditional approach combining the energy equation with the constitute relation for the CV-wave model, the thermal wave equation has been derived in terms of the linearization of the mass and momentum conservation equations of the phonon gas, and the propagation velocity of the thermal wave in the phonon gas can be derived directly from the equation of state for the phonon gas, which is independent of the characteristic time. The characteristic time in different models, either the lagging time or the relaxation time, is the function of the resistance (thermal conductivity) of the phonon gas.

The wave equation based on the simplified thermomass model is similar to the wave equation based on the CV model, but with different characteristic times. The characteristic time τ_{CV} in the CV model is the relaxation time as the energy carriers approaching the thermodynamic equilibrium, while the characteristic time τ_{TM} in the thermomass model describes a lagging response, in time, between the heat flux and the temperature gradient.

In view of the fact that the phonon gas (thermomass) flows through dielectrics just like that the gas flows through porous medium, and there are two kinds of wave in the porous medium (the fast wave propagates in the solid and the slow wave propagates in the gas), the characteristic time related to the thermal wave in the phonon gas should be the lagging time, rather than the relaxation time for phonon transport.

Since the wave velocity predicted by the CV model is one order of magnitude larger than that predicted by the thermomass model, the temperature peaks resulting from the wave behavior in the thermomass model are much higher than those resulting from the CV-wave model. Finally, the overheating damage in laser processing of dielectric materials may be more severe than that expected from the CV-wave model.

Nomenclature

a = thermal diffusivity
b = dimensionless parameter in thermomass model
c = speed of light
C = heat capacity per unit mass
E_{rel} = relativistic energy

E_R = potential of the rest mass of lattice
E_{RD} = thermal vibration energy of the rest mass of lattice
f_h = resistant force for the phonon gas motion
k = thermal conductivity
l = parameter with unit of length in thermomass model
M_h = increased mass due to thermal vibration (thermomass)
M_{rel} = relativistic mass
M_R = rest mass
Ma_h = Mach number of the phonon gas
p = pressure
p_h = thermal pressure of phonon gas
$p_{h,0}$ = thermal pressure of phonon gas at equilibrium
p_h' = thermal pressure perturbation of phonon gas
p_{rel} = thermal pressure of the relativistic mass of lattice
p_R = thermal pressure of the rest mass of lattice
P_{rel} = relativistic momentum
q = heat flux
q_A = peak value of heat pulse
r = position
s = thermal wave velocity
s_D = transport velocity of thermal disturbance
s_{TM} = thermal wave velocity in thermomass model
T = temperature
t = time variable
t_0 = existing time of heat pulse
u = velocity
u_h = drift velocity of phonon gas
u_h' = drift velocity perturbation of phonon gas
V = volume
v_s = sound speed
x = x space variable
β = friction coefficient for motion of phonon gas
γ = Grüneisen constant
ρ = density of dielectrics
ρ_h = density of phonon gas
$\rho_{h,0}$ = density of phonon gas in equilibrium
ρ_h' = density perturbation of phonon gas
τ = relaxation time or time delay between the temperature gradient vector and the heat flux vector
τ_{CV} = relaxation time in CV model
τ_{TM} = characteristic time in thermomass model

References

[1] Fourier, J., 1955, *Analytical Theory of Heat*, Dover, New York.
[2] Tisza, L., 1938, "The Thermal Superconductivity of Helium II and the Statistics of Bose-Einstein," Compt. Rend., **207**, pp. 1035–1037.
[3] Landau, L., 1941, "Theory of the Superfluidity of Helium II," Phys. Rev., **60**(4), pp. 356–358.
[4] Peshkov, V., 1944, ""Second Sound" in Helium II," J. Phys. (USSR), **8**, p. 381.
[5] Stritzker, B., Pospieszczyk, A., and Tagle, J. A., 1981, "Measurement of Lattice Temperature of Silicon During Pulsed Laser Annealing," Phys. Rev. Lett., **47**(5), pp. 356–358.
[6] Torii, S., and Yang, W. J., 2005, ""Heat Transfer Mechanisms in Thin Film With Laser Heat Source," Int. J. Heat Mass Transfer, **48**(3–4), pp. 537–544.
[7] Guo, Z. Y., and Xu, Y. S., 1995, "Non-Fourier Heat Conduction in IC Chip," ASME J. Electron. Packag., **117**(3), pp. 174–177.
[8] Cattaneo, C., 1948, "Sulla Conduzione Del Calore," Atti Semin. Mat. Fis. Univ. Modena, **3**, pp. 83–101.
[9] Vernotte, P., 1958, "Paradoxes in the Continuous Theory of the Heat Equation," C. R. Acad. Sci., **246**, pp. 3154–3155.
[10] Morse, P. M., and Feshbach, H., 1953, *Methods of Theoretical Physics*, McGraw-Hill, New York.
[11] Joseph, D. D., and Preziosi, L., 1989, "Heat Waves," Rev. Mod. Phys., **61**(1), pp. 41–73.
[12] Brorson, S. D., Fujimoto, J. G., and Ippen, E. P., 1987, "Femtosecond Electronic Heat-Transport Dynamics in Thin Gold-Films," Phys. Rev. Lett., **59**(17), pp. 1962–1965.
[13] Tzou, D. Y., 1989, "On the Thermal Shock Wave Induced by a Moving Heat Source," ASME J. Heat Transfer, **111**, pp. 232–238.
[14] Tzou, D., 1992, "Thermal Shock Phenomena Under High-Rate Response in Solids," *Annual Review of Heat Transfer*, Hemisphere, Washington, DC, pp. 111–185.
[15] Tzou, D. Y., 1996, *Macro-to Microscale Heat Transfer: The Lagging Behavior*, Taylor & Francis, Washington, DC.
[16] Joseph, D. D., and Preziosi, L., 1990, "Addendum to the Paper "Heat Waves" [Rev. Mod. Phys. 61, 41 (1989)]," Rev. Mod. Phys., **62**(2), pp. 375–391.
[17] Özişik, M. N., and Tzou, D. Y., 1994, "On the Wave Theory in Heat-Conduction," ASME J. Heat Transfer, **116**(3), pp. 526–535.
[18] Haji-Sheikh, A., Minkowycz, W. J., and Sparrow, E. M., 2002, "Certain Anomalies in the Analysis of Hyperbolic Heat Conduction," ASME J. Heat Transfer, **124**(2), pp. 307–319.
[19] Cheng, L., Xu, M., and Wang, L., 2008, "Single- and Dual-Phase-Lagging Heat Conduction Models in Moving Media," ASME J. Heat Transfer, **130**(12), p. 121302.
[20] Nernst, W., 1917, *Die Theoretischen Grundlagen Des Neuen Wärmesatzes*, Knapp, Halle.
[21] Onsager, L., 1931, "Reciprocal Relations in Irreversible Processes. I," Phys. Rev., **37**(4), pp. 405–426.
[22] Tolman, R. C., 1930, "On the Weight of Heat and Thermal Equilibrium in General Relativity," Phys. Rev., **35**(8), pp. 904–924.
[23] Eckart, C., 1940, "The Thermodynamics of Irreversible Processes III Relativistic Theory of the Simple Fluid," Phys. Rev., **58**(10), pp. 919–924.
[24] Landau, L. D., and Lifshitz, E. M., 1959, *Fluid Mechanics*, Pergamon, London.
[25] Cao, B. Y., and Guo, Z. Y., 2007, "Equation of Motion of a Phonon Gas and Non-Fourier Heat Conduction," J. Appl. Phys., **102**(5), p. 053503.
[26] Feynman, R. P., Leighton, R. B., and Sands, M., 1964, *Lectures on Physics*, Addison-Wesley, Reading, MA.
[27] Guo, Z. Y., Cao, B. Y., Zhu, H. Y., and Zhang, Q. G., 2007, "State Equation of Phonon Gas and Conservation Equations for Phonon Gas Motion," Acta Phys. Sin., **56**, pp. 3306–3311.
[28] Tien, C. L., and Lienhard, J. H., 1979, *Statistical Thermodynamics*, Hemisphere, Washington, DC.
[29] Aharoni, J., 1985, *The Special Theory of Relativity*, Dover, New York.
[30] Chester, M., 1963, "Second Sound in Solids," Phys. Rev., **131**(5), pp. 2013–2015.
[31] Carcione, J. M., and Ouiroga-Goode, G., 1996, "Full Frequency-Range Transient Solution for Compressional Waves in a Fluid-Saturated Viscoacoustic Porous Medium," Geophys. Prospect., **44**(1), pp. 99–129.

Numerical Studies on Microwave Heating of Thermoplastic-Ceramic Composites Supported on Ceramic Plates

Tanmay Basak[1]
e-mail: tanmay@iitm.ac.in

Sankaran Durairaj

Department of Chemical Engineering,
Indian Institute of Technology,
Madras Chennai 600036, India

A detailed theoretical analysis has been carried out to study efficient microwave assisted heating of thermoplastic (Nylon 66) slabs via polymer-ceramic-polymer composite attached with ceramic plate at one side. The ceramic layer or plate is chosen as Al_2O_3 or SiC. The detailed spatial distributions of power and temperature are obtained via finite element simulation. It is found that uniform heating with enhanced processing rate may occur with specific thickness of Al_2O_3 composite, whereas SiC composite leads to enhanced processing rate with higher thermal runaway for thick Nylon samples attached with Al_2O_3 plate. SiC composite is effective due to enhanced processing rate, whereas Al_2O_3 is not effective due to reduced processing rate for thin samples attached with Al_2O_3 plate. For samples attached with SiC plate, thermal runaway is reduced by SiC composite, whereas that is not reduced by Alumina composite. Current study recommends efficient heating methodologies for thermoplastic substances with ceramic composite to achieve a higher processing rate with uniform temperature distribution.
[DOI: 10.1115/1.4000948]

Keywords: microwave heating, thermoplastics, Nylon 66, polymer composites, ceramics

1 Introduction

Microwave heating is advantageous over conventional heating methods due to brief start up time, internal heating, high efficiency, and rapid processing. The propagation of microwaves within a material depends on dielectric properties (dielectric loss and dielectric constant) of the material. Microwave propagation leads to "volumetric heat generation" within dielectrics and microwaves are used extensively for various thermal processing applications [1–10]. There is an increase in demand for processing of polymeric materials in a cost-effective way. A significant amount of research involves heating of polymers for various applications [11–17]. Microwave processing can improve the properties of the material as well based on internal and selective heating [18,19]. Microwave have been used for polymer processing in various applications [20–22]. Microwave heating also finds application in vulcanization of rubber [21,23]. A few more applications of microwaves in polymer industries are welding and molding of thermoplastics [22]. Microwave heating may also be used in thermoforming of plastics. A significant amount of earlier works reported that application of microwave in polymer processing is advantageous than that of conventional heating methods [18,21–25]. However, microwave heating of polymers is still in laboratory scale and it is not industrially wide spread.

Microwave heating of polymers need further attention due to temperature dependent dielectric properties. Note that the temperature dependent dielectric properties of polymer may lead to thermal runaway within the sample and that may result in degradation of the polymer [26]. Also, some of the thermoplastics are transparent to microwave due to the less dielectric loss [27,28]. Note that fillers can be used to improve the power absorption within the polymer sample [29]. However, adding a filler may affect the property of the material considerably. Another option for processing low loss material is to heat the material using some conventional method until it becomes a significant absorber of microwave [26]. However, heating with some other source may not be as efficient as microwave. In addition, the thermal runaway of a system is important to design an efficient heating strategy. Therefore a theoretical model is necessary to understand the efficient processing of the polymer sample.

A few theoretical models on microwave heating have been reported by earlier workers [30–41]. Ayappa et al. [30] carried out a detailed theoretical analysis on modeling of microwave heating in 1D slabs and 2D cylinders. The energy balance equation with a volumetric source term, which may be governed by Lambert's exponential law or Maxwell's equation, form the basis for the heating models of microwave. The constructive and destructive interferences of microwaves within samples cause nonuniform heating and the maxima in power or resonances due to microwave propagation were analyzed by Ayappa et al. [31]. Microwave heating of food materials (beef, oil, and water) with ceramic and metallic supports was investigated recently in detail by Basak and Priya [35,36].

Earlier models mostly involve constant dielectric and thermal properties except a few studies [37–40]. The dielectric property of a polymeric material is in general function of temperature. Thus energy balance equation is coupled with Maxwell equation and both equations have to be solved simultaneously. Ayappa and coworkers [37,38] developed the model with temperature dependent thermal and dielectric properties for 1D slab and 2D cylinders using finite element model. Even though temperature dependent dielectric and thermal properties are common in industrial processing, there are no detailed investigations to address the efficient microwave heating and processing of polymeric samples with temperature dependent dielectric and thermal properties.

The thermoplastic samples may give thermal runaway effect or transparency to microwaves due to their temperature dependent dielectric properties. Note that in molding or processing of polymer, the polymer sample is placed on a foreign material or the

[1]Corresponding author.

Contributed by the Heat Transfer Division of ASME for publication in the JOURNAL OF HEAT TRANSFER. Manuscript received December 1, 2008; final manuscript received November 18, 2009; published online April 22, 2010. Assoc. Editor: He-Ping Tan.

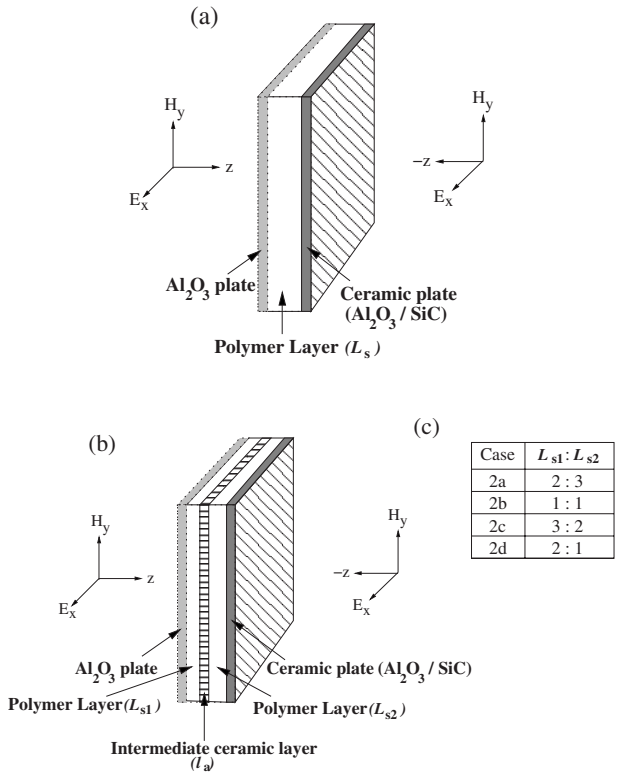

Case	$L_{s1} : L_{s2}$
2a	2 : 3
2b	1 : 1
2c	3 : 2
2d	2 : 1

Fig. 1 Schematic illustration of sample exposed to a plane electromagnetic wave: (*a*) polymer sample with ceramic plate (case 1) and (*b*) discrete polymer sample with ceramic plate (cases 2a-2d). (*c*) The chart for thickness ratios of cases 2a-2d. Note that the continuous or discrete sample is attached with ceramic plate either at the left side or right side. The dotted lines with plate denote the case with ceramic plate attached at left face and solid line with plate denote the case with attached plate at right face only.

sample may be kept on a plate or container and this may influence the microwave heating quality considerably. In the current study, the polymer sample is attached with ceramic (Al_2O_3/SiC) plate at one side. To overcome the major drawbacks in microwave heating, instead of continuous sample, one can also discretize the sample into two pieces and process it in the presence of intermediate ceramic layer between them and such studies are yet to appear in literature. The intermediate ceramic layer composited with polymer sample may play significant role to reduce the thermal runaway or to enhance the processing rate.

The current study is based on microwave heating of polymer-ceramic composites attached with ceramic plate, as seen in Figs. 1(*a*) and 1(*b*). Nylon 66 has been used as sample for this study. In general, ceramic can withstand high temperature and also possess high thermal conductivity. Therefore, ceramics may be the perfect choice to use as an intermediate layer [35]. Note that the thickness of ceramic plate is fixed as 0.2 cm. The thickness of the intermediate layer has been varied to obtain optimal choice of heating. As discussed earlier, there are two major issues in microwave processing of thermoplastics: thermal runaway effect and less power absorption. The analysis is carried out for various discrete sample ratios with one side or both sides microwave incidence corresponding to various thicknesses of intermediate layer. The optimal cases are highlighted in results and discussion section.

2 Theory

2.1 Electric Field in a Composite Slab. Microwaves are assumed to be uniform plane electromagnetic waves. Electric and magnetic fields lie in the *x*-*y* plane and vary in the direction of propagation (*z*-axis), as shown in Figs. 1(*a*) and 1(*b*). The current study involves continuous slab (case 1), as shown in Fig. 1(*a*), and discrete samples with intermediate ceramic layers (case 2), as shown in Fig. 1(*c*).

Table 1 Dielectric and thermal properties of materials

$P = a_0 + a_1T + a_2T^2 + a_3T^3 + a_4T^4$ (T in K)				
Property	Variables	Nylon 66 [38 and 37]	Alumina [41]	SiC [41]
Dielectric constant $P = \kappa'$	f, GHz	3	2–3	2–3
	a_0	16.727	10.8	26.66
	a_1	−0.10279		
	a_2	2.4192×10^{-4}		
	a_3	-1.7592×10^{-7}		
	f, GHz	3	2–3	2–3
Dielectric loss $P = \kappa''$	a_0	84.16	0.1566	27.99
	a_1	−1.0011		
	a_2	4.4563×10^{-3}		
	a_3	-8.8029×10^{-6}		
	a_4	6.5208×10^{-9}		
Specific heat $P = C_p$ ($J\ kg^{-1}\ K^{-1}$)	a_0	349.02	1046	3300
	a_1	0.4738		
Thermal conductivity, k ($W\ m^{-1}\ K^{-1}$)	a_0	0.43	26	40
Density, ρ ($kg\ m^{-3}$)	a_0	1200	3750	3100

Lateral dimensions (along *x*-axis and *y*-axis) are assumed to be very large compared to the total thickness of continuous/discrete samples (along *z*-axis including ceramic layer) and similar modeling assumptions are also found in earlier literatures [37]. Based on the assumptions, one-dimensional slab has been considered. The wave propagation due to uniform electric field (E_x), given by Maxwell's equation is

$$\frac{d^2E_x}{dz^2} + \kappa^2(T)E_x = 0 \tag{1}$$

where E_x lies in *x*-*y* plane. In Eq. (1), $\kappa(T) = (\omega/c)\sqrt{\kappa'(T) + i\kappa''(T)}$ is the propagation constant, which depends on dielectric constant, $\kappa'(T)$ and dielectric loss $\kappa''(T)$. Note that $\omega = 2\pi f$, where f is the frequency of the electromagnetic wave and c is the velocity of light. It may also be noted that the temperature dependency of the properties may be represented by polynomial functions (see Table 1). Note that dielectric properties for Nylon 66 correspond to frequency 3000 MHz. In an n multilayered sample, the electric field for lth layer obtained from Eq. (1) is

$$\frac{d^2E_{x,l}}{dz^2} + \kappa_l^2(T)E_{x,l} = 0 \tag{2}$$

where $z_{l-1} \le z \le z_l$ and $l = 1, \ldots, n$. The boundary conditions at the interface are

$$\left.\begin{aligned} E_{x,l} &= E_{x,l+1} \\ \frac{dE_{x,l}}{dz} &= \frac{dE_{x,l+1}}{dz} \end{aligned}\right\} \begin{aligned} l &= 1, \ldots, n-1 \\ z &= z_1, \ldots, z_{n-1} \end{aligned} \tag{3}$$

Here, $z_1, z_2, \ldots, z_{n-1}$ denote the interface positions. The boundary conditions at the outer face of the composite slab are [37]

$$\frac{dE_x}{dz} + ik(T)E_x = 2ik(T)E_L e^{-ik(T)L}, \quad z = z_1 = -L \tag{4}$$

and

$$\frac{dE_x}{dz} - ik(T)E_x = -2ik(T)E_R e^{-ik(T)L}, \quad z = z_n = L \tag{5}$$

The power absorption in lth layer (either polymer sample or ceramic)

$$q_l(z,T) = \frac{1}{2}\omega\epsilon_0\kappa_l''(T)E_{x,l}(z)E_{x,l}^*(z) \tag{6}$$

where * denotes the complex conjugate.

2.2 Modeling: Microwave Heating. Heat transport in a dielectric material during microwave radiation is due to a combined effect of volumetric heat generation and conduction. The unsteady-state one-dimensional energy balance for microwave heating is

$$\frac{\partial H}{\partial t} = \frac{\partial}{\partial z}\left[k(T)\frac{\partial T}{\partial z}\right] + q(z,T) \tag{7}$$

where

$$H = \rho C_p(T)(T - T_0) \tag{8}$$

where ρ, $C_p(T)$, T_0, $k(T)$, and $q(z,T)$ are the density, specific heat, initial temperature, thermal conductivity, and volumetric heat source term, respectively. The temperature dependent properties are obtained from earlier work [30] and various coefficients are given in Table 1. Note that the volumetric heat generation term $q(z,T)$ is defined in Eq. (6). The energy balance equation for lth layer in n multilayered sample consisting of polymer samples and ceramic is represented as

$$\frac{\partial H_l}{\partial t} = \frac{\partial}{\partial z}\left[k_l(T)\frac{\partial T_l}{\partial z}\right] + q_l(z,T), \quad l = 1, \ldots, n \tag{9}$$

The initial condition is

$$T_l = T_0, \quad l = 1, \ldots, n \tag{10}$$

and the boundary conditions are

$$k_1(T)\frac{\partial T_1}{\partial z} = h(T_1 - T_\infty), \quad z = z_1 \tag{11}$$

and

$$-k_{n-1}(T)\frac{\partial T_{n-1}}{\partial z} = h(T_{n-1} - T_\infty), \quad z = z_{n-1} \tag{12}$$

The interface conditions between various layers are

$$\left.\begin{aligned} T_l &= T_{l+1} \\ k_l(T)\frac{\partial T_l}{\partial z} &= k_{l+1}(T)\frac{\partial T_{l+1}}{\partial z} \end{aligned}\right\} \begin{aligned} l &= 2, \ldots, n-2 \\ z &= z_2, \ldots, z_{n-2} \end{aligned} \tag{13}$$

Microwave power $q_l(z,T)$ is a function of electric field and temperature as given in Eq. (6). The nonlinear coupled wave propagation and energy balance equation (Eqs. (2) and (9)) with appropriate boundary and interface conditions (Eqs. (3)–(5) and (11)–(13)) are solved simultaneously as discussed by Ayappa et al. [30] and Basak and Priya [35].

Galerkin finite element method is used to solve the energy balance and electric field equations simultaneously with appropriate boundary conditions. The interface conditions for energy balance and electric field equations due to multiple phases are automatically satisfied via an interface element common to two phases. At the interface node, the field variable and fluxes are continuous as discussed by Ayappa et al. [37]. To discretize the time domain, Crank–Nicholson method is used and the nonlinear residual equations are solved using Newton–Raphson method. Due to the lack of a good initial guess to begin the Newton scheme, a small time step $\Delta t = 1 \times 10^{-4}$ s was used at the first time step. Unless specified otherwise, $\Delta t = 0.5$ s was used for subsequent steps. Typically, 25–50 quadratic elements (15–35 elements for polymer sample and 10–15 elements for ceramic layer) have been used for entire slab. It was found that the maximum difference for the values of the unknowns at the nodes was less than 1% when the values were compared for 25 and 50 elements. For constant dielectric properties, the analytical solution of Eq. (2) is available [30,35] and the power distribution can be obtained without solving the energy balance equation [30,35]. The validation of current simulation strategy has been done by comparing the power distribution with the available analytical solution for constant dielectric material [30]. The comparisons are in good agreement and they are not shown for the brevity of the manuscript.

The discrete sample assembly consists of two polymer sample layers with an intermediate ceramic layer (Al_2O_3 and SiC) and the thickness of ceramic layer (l_a) is varied within 0.05–0.3 cm. Various ratios of discrete polymer samples ($L_{s1}:L_{s2}$) have been investigated. It may be noted that four suitable ratios or cases 2a–2d (2:3, 1:1, 3:2, and 2:1), as shown in Fig. 1(*c*), have been chosen for each type of incidence. Note that the thickness of ceramic plate is fixed as 0.2 cm. The analysis is carried out for type 1 (3.0 W cm^{-2} and 0 W cm^{-2} as left and right side incidence, respectively) and type 2 (1.5 W cm^{-2} and 1.5 W cm^{-2} as left and right incidence, respectively) incidences. The heat transfer coefficient at the outer faces is assumed to be 2 W m^{-2} K^{-1} for all computations. The initial temperature of the continuous/discrete (including ceramic layer) sample is 300 K.

3 Results and Discussion

3.1 Effect of Ceramic Plates for Continuous Polymer Samples. Four sample thicknesses such as 0.25 cm, 1 cm, 2 cm, and 5 cm have been selected as four length scales, LI, LII, LIII, and LIV, respectively. This section summarizes the role of ceramic plate for various length scales (LI–LIV) corresponding to type 1 and type 2 incidences. Note that the processing time corresponds to the time at which the average temperature of the sample reaches 375 K ($\pm 1\%$). The thermal runaway within polymer sample is quantified by ΔT_p, which is the difference between maximum and minimum temperature within sample. Figs. 2(*a*) and 2(*b*) illustrate processing time and temperature difference (ΔT_p), respectively, versus thickness of the polymer sample with and without ceramic plates corresponding to type 1 incidence. It is interesting to note that SiC plate leads to smallest processing time with largest ΔT_p irrespective to length scales. Note that sample attached with Alumina plate at right side leads to largest processing time for LI and LII length scales, whereas the processing time for LIII and LIV length scales corresponding to Alumina at right side are lesser than the processing time of sample without plate. It may also be noted that Alumina plate at left side leads to lesser processing time as compared to that of sample with Alumina at right side for LI and LII length scales, whereas the processing time is higher for Alumina plate at left side with LIII and LIV length scales. It may be noted that ΔT_p for LI length scale is almost identical for Alumina plate at left and right sides, whereas that is higher for Alumina plate at left side corresponding to LII length scale. On the other hand, ΔT_p for Alumina plate at left side is less than that of Alumina plate at right side corresponding to LIII and LIV length scales. However, ΔT_p with Alumina plate (both at left as well as right sides) lies between ΔT_p of samples without plate and ΔT_p with SiC plate.

Figures 2(*c*) and 2(*d*) illustrate processing time and temperature difference, respectively, versus thickness of the polymer sample with various ceramic plates corresponding to type 2 incidence. It is interesting to note that the variations for processing time and ΔT_p with SiC plate are qualitatively similar to that of type 1 incidence for LI, LII, and LIV length scales, whereas ΔT_p for LIII length scale is lesser for SiC plate. It is important to note that processing time and ΔT_p corresponding to Alumina plate at left and right sides are identical for type 2 incidence. Note that the processing time for LI–LIII length scales with Alumina plate is

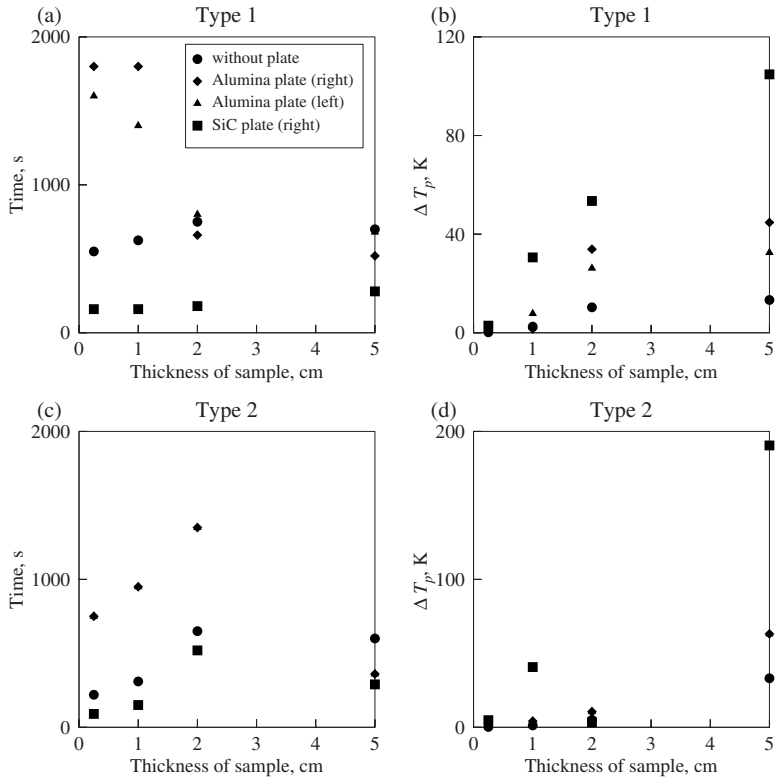

Fig. 2 Processing time; temperature difference for continuous sample versus sample thickness (L_S) with/without ceramic plates corresponding to type 1 incidence ((*a*) and (*b*)) and type 2 incidence ((*c*) and (*d*))

higher than that of sample without plate, whereas the processing time is less with Alumina plate for LIV length scale. However, similar to type 1 incidence, ΔT_p value of Alumina plate (both at left as well as right sides) lies between that without plate and that with SiC plate except for LIII length scales. It is found that, the ceramic plate influences the microwave heating quality considerably with type 1 and type 2 incidences. Based on the analysis, it is inferred that the choice of plate is crucial for particular length scale. Overall, SiC plate is optimal for smaller sample thickness and Alumina plate (right or left) is optimal for larger sample thickness corresponding to both type 1 and type 2 incidences. In order to analyze the efficient processing strategy, the influence of intermediate ceramic layer or composite has been investigated further for all sample thicknesses with various plate assemblies.

3.2 Comprehensive Characteristics on Efficient Heating Strategies. This section summarizes the role of intermediate ceramic material in a ceramic—Nylon composite for various length scales (LI–LIV) with cases 2a–2d on efficient heating. The role of ceramic—Nylon 66—composite on efficient heating of Nylon 66 sample attached with ceramic plate may be examined based on two factors: processing time (to attain an average temperature of 375 K) and thermal runaway.

3.2.1 Composite Sample Attached With Alumina Plate at Right Side. Figures 3(*a*)–3(*d*) illustrate the processing time (t) and temperature difference (ΔT_p) versus intermediate Alumina layer thickness (l_a) for all the cases (case 2a–2d) corresponding to LI–LIV due to type 1 incidence. Note that the temperature difference or the degree of thermal runaway for each polymer layer is shown in Figs. 3(*a*)–3(*d*). Figure 3(*a*) illustrates that the processing time increases sharply with l_a for LI length scale. It is interesting to note that ΔT_p for first layer increases with increase in Alumina layer thickness (l_a) corresponding to case 2b–2d, whereas ΔT_p is almost constant for case 2a. In contrast, ΔT_p for the second layer decreases to $l_a=0.075$ cm and thereafter ΔT_p increases to a certain level leading to a constant value at higher l_a. However, Nylon 66—Alumina assembly may not be recommended for LI thickness corresponding to type 1 incidence based on sharp increase in processing time with l_a.

On the other hand, variation in ΔT_p for LII length scale is quite different from that for LI. Figure 3(*b*) shows that processing time increases with increase in l_a. However, the rate of increase is less as compared to LI length scale. It is found that ΔT_p for the first layer decreases with the increase in l_a (Fig. 3(*b*)). In contrast, ΔT_p for second layer has a minima at $l_a=0.05$ cm and thereafter that increases to a certain level at higher l_a. The discrete polymer samples with Alumina composite do influence heating qualities or degree of thermal runaway. It is observed that case 2b may be the optimal choice as ΔT_p for case 2b is less for both the layers corresponding to lesser l_a. However, the optimal heating should be carried out with smaller values for l_a as processing time increases with l_a.

Figure 3(*c*) illustrates that the processing time for LIII is constant up to $l_a=0.1$ cm, thereafter processing time increases slightly with l_a for most of the cases. It is interesting to observe that the processing time is invariant with l_a for case 2d. It may be noted that ΔT_p for the second layer decreases with the increase in l_a for cases 2a–2d. On the other hand, ΔT_p for the first layer sharply decreases to $l_a=0.075$ cm for all the cases (case 2a–2d) and thereafter ΔT_p decreases for cases 2a and 2b, whereas that increases for cases 2c and 2d. It may also be noted that ΔT_p for the first layer is larger for case 2d and smaller for case 2a. Based on the two layers, it may be inferred that case 2a with $l_a=0.05-0.1$ cm may be the optimal choice of heating samples with LIII length scale.

Figure 3(*d*) illustrates the characteristics for LIV length scale. The processing time for cases 2a and 2b decreases with l_a, whereas that increases slightly for cases 2c and 2d. Note that ΔT_p

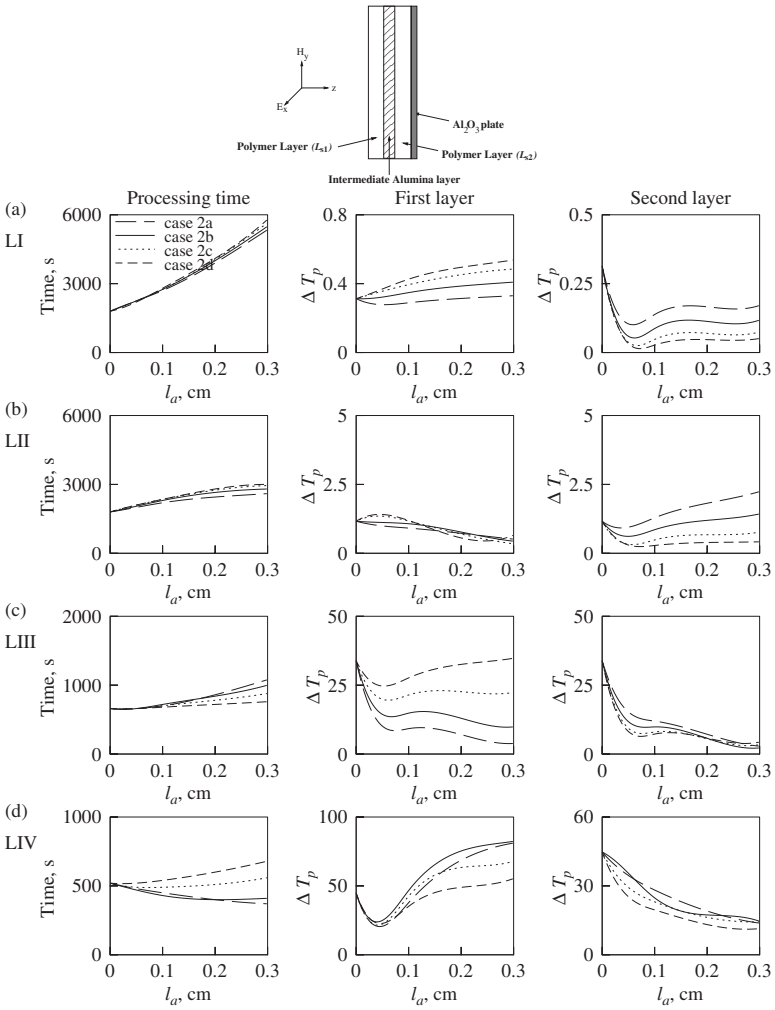

Fig. 3 Processing time; temperature difference for first and second polymer layers versus intermediate layer thickness (l_a) for all cases corresponding to Nylon 66 attached with Alumina plate at right side due to one side incidence. Note that Alumina is composited as intermediate layer corresponding to (*a*) LI, (*b*) LII, (*c*) LIII, and (*d*) LIV length scales.

distribution for the second layer is qualitatively similar to that for LIII length scale, whereas, ΔT_p for first layer decreases to $l_a = 0.05$ cm and thereafter ΔT_p increases with l_a for all the cases (case 2a–2d). It is interesting to note that ΔT_p is minimum for case 2d for all the values of l_a. However, based on processing time corresponding to case 2d, small value of l_a is preferable. Overall, it may be inferred that case 2d with $l_a = 0.05$ cm may be the optimal choice of heating. It is also important to note that compared to other thickness, LIV has less processing time, which implies that with the same power, thick sample can be processed in a faster rate compared to a thin sample. Based on the detailed analysis, it is observed that, Nylon 66—Alumina composite with $l_a = 0.05$ cm corresponding to case 2d for LIV may be the optimal strategy for efficient processing. However, the thermal runaway is significant for LIV thickness.

Similar analysis has been carried out for samples due to type 2 microwave incidence (figures not shown). It is interesting to observe that, the results are quite different from type 1 incidence, as seen in Fig. 3. Note that the processing time sharply increases with increase in l_a for LI–LIII length scales. On the other hand, the processing time for LIV length scale corresponding to cases 2a and 2b decreases with l_a, whereas that increases slightly corresponding to cases 2c and 2d. Note that ΔT_p for the first layer decreases to $l_a = 0.075$ cm and thereafter ΔT_p increases to a certain level leading to a constant value at higher l_a of all length scales (LI–LIV). It is also observed that, ΔT_p for second layer decreases with increase in l_a. It is interesting to note that ΔT_p for LIV length scale is minimum for case 2d for all the values of l_a. However, case 2d with small value of l_a is preferable based on processing time. Based on two layers, it may be inferred that case 2d with $l_a = 0.05$ cm may be the optimal choice of heating. Although processing time is lesser but ΔT_p is higher for type 2 incidence as compared to type 1 incidence corresponding to LI, LII and LIV length scales. In contrast, the processing time is higher and ΔT_p is lesser for LIII length scale. Based on detailed analysis, Nylon 66—Alumina composite with $l_a = 0.05$ cm corresponding to case 2d for LIV length scale may be the optimal strategy for efficient processing with type 2 incidence.

Simulations have also been carried out to study the processing time (t) and temperature difference (ΔT_p) versus intermediate SiC layer thickness (l_a) for all the cases (case 2a–2d) corresponding to LI–LIV due to type 1 incidence (figures not shown). Common to all length scales (LI–LIV), it is found that there is a sharp decrease in the processing time to $l_a = 0.075$ cm, thereafter that increases and attains further a constant value at larger l_a. It is also found that, the temperature difference (ΔT_p) for both the layers following similar qualitative variations with l_a, exhibits maximum

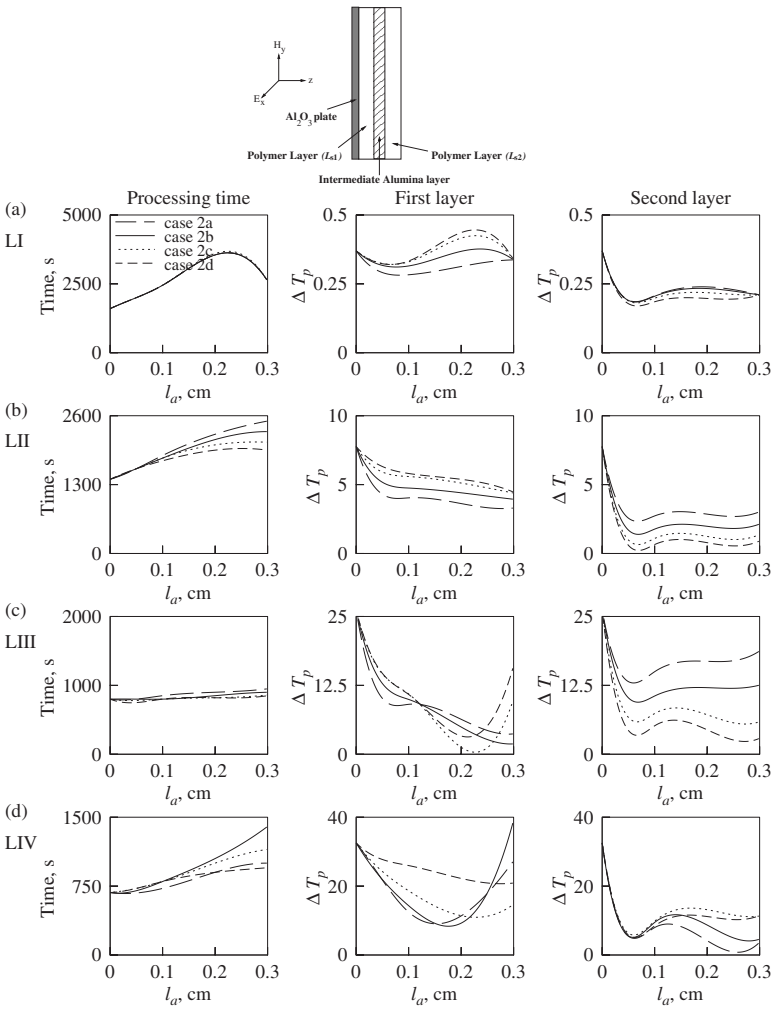

Fig. 4 Processing time; temperature difference for first and second polymer layers versus intermediate layer thickness (l_a) for all cases corresponding to Nylon 66 attached with Alumina plate at left side due to one side incidence. Note that Alumina is composited as intermediate layer corresponding to (*a*) LI, (*b*) LII, (c) LIII, and (*d*) LIV length scales.

values within $l_a < 0.1$ cm for all length scales. The maxima of ΔT_p for smaller length scales (LI and LII) are within 25 K, whereas the maxima of ΔT_p reaches around 80–150 K for LIII and LIV samples. It was found that case 2d with $l_a = 0.3$ cm may be the optimal choice for processing samples of LI and LII length scales, whereas LIII or LIV may not be optimal choices based on larger thermal runaway. Similar analysis has been carried out for type 2 incidence corresponding to SiC intermediate layer (figures not shown) and it is found that, the results are qualitatively similar to that of type 1 incidence as discussed above. However, compared to type 1 incidence, type 2 incidence has lesser processing time and higher ΔT_p values. Overall, the intermediate SiC layer may not be recommended based on larger thermal runaway especially for larger sample thicknesses.

3.2.2 Composite Sample Attached With Alumina Plate at Left Side. Figures 4(*a*)–4(*d*) illustrate the processing time (t) and temperature difference (ΔT_p) versus intermediate Alumina layer thickness (l_a) for all the cases (case 2a–2d) corresponding to LI–LIV due to type 1 incidence. Figure 4(*a*) illustrates that the processing time increases sharply up to $l_a = 0.23$ cm and thereafter that decreases for LI length scale. It is interesting to note that ΔT_p within first layer decreases to $l_a = 0.1$ cm and thereafter that either increases or shows nonmonotonic trend with l_a corresponding to all the cases (case 2a–2d). On the other hand, ΔT_p within second layer decreases to $l_a = 0.08$ cm and thereafter ΔT_p increases to a certain level leading to a constant value at higher l_a. However, Nylon 66—Alumina assembly or discrete samples may not be recommended for LI thickness corresponding to type 1 incidence based on sharp increase in processing time with l_a for $l_a \leq 0.2$ cm. Figure 4(*b*) illustrates that processing time for LII length scale also sharply increases with increase in l_a. It is found that ΔT_p for the first layer decreases with l_a (Fig. 4(*b*)). On the other hand, ΔT_p for second layer has a minima at $l_a = 0.08$ cm and thereafter that increases to a certain level. Based on two layers, it is observed that case 2a with $l_a = 0.05$ cm may be the optimal choice for processing LII length scale.

Figure 4(*c*) illustrates that the processing time for LIII is almost invariant with l_a for all the cases. It may be noted that ΔT_p for the first layer decreases with the increase in l_a for all cases. On the other hand, ΔT_p for the second layer sharply decreases to $l_a = 0.075$ cm for all the cases (case 2a–2d) and thereafter ΔT_p increases and later attains a constant value at higher l_a. Based on the two layers, it is observed that case 2d with $l_a = 0.05$ cm may be preferred for LIII length scale. However, ΔT_p for the first layer is significantly large and hence LIII may be recommended with very small l_a ($l_a = 0.05$ cm). Figure 4(*d*) illustrates that the processing

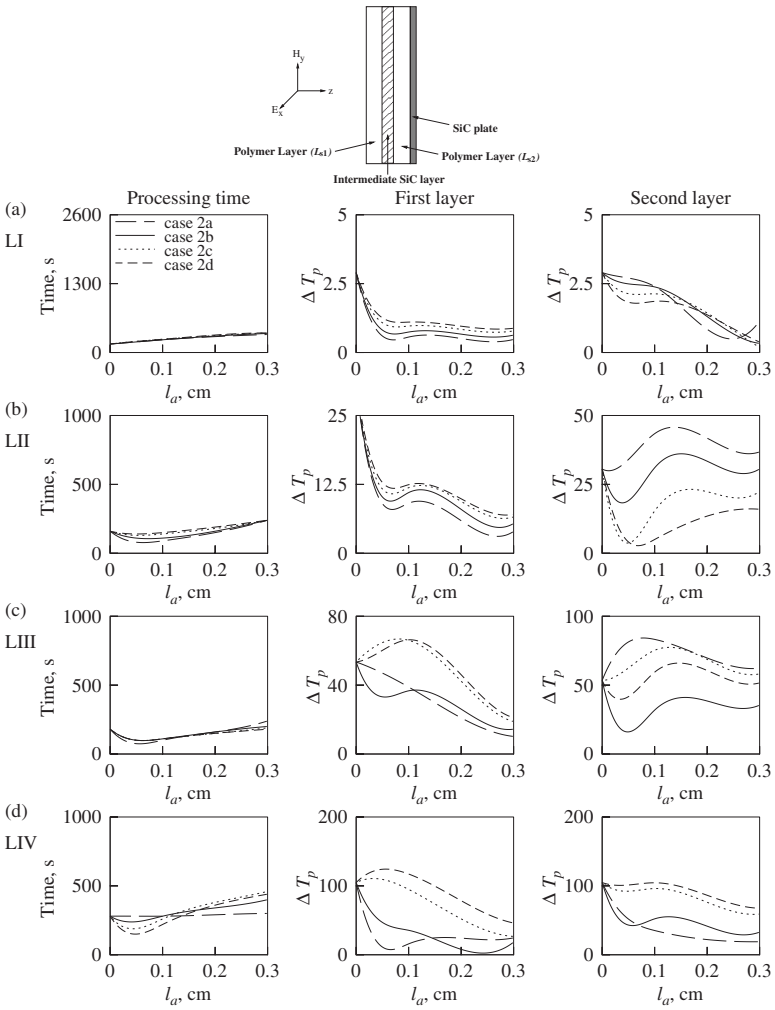

Fig. 5 Processing time; temperature difference for first and second polymer layers versus intermediate layer thickness (l_a) for all cases corresponding to Nylon 66 attached with SiC plate at right side due to one side incidence. Note that SiC is composited as intermediate layer corresponding to (*a*) LI, (*b*) LII, (*c*) LIII, and (*d*) LIV length scales.

time increases with l_a for LIV length scale. It may be noted that ΔT_p for first layer corresponding to cases 2a and 2c decreases to $l_a = 0.15–0.25$ cm and thereafter ΔT_p increases with l_a, whereas ΔT_p decreases with increase in l_a for case 2d. Similarly, ΔT_p for second layer decreases to $l_a = 0.08$ cm, thereafter that increases at higher values of l_a. Based on two layers, it may be inferred that case 2a or 2b with $l_a = 0.15$ cm may be preferred. Similar to LIII length scale, ΔT_p is large for first layer and hence LIV may not be an optimal choice. Similar analysis has been carried out with intermediate SiC layer as well (figures not shown). It is observed that intermediate SiC layer reduces the processing time considerably for all the length scales. However, ΔT_p corresponding to first layer of LIII and LIV length scales is large for all l_a. Note that the intermediate SiC layer may be useful for LI and LII length scales based on lesser processing time.

3.2.3 Composite Sample Attached With SiC Plate at Right Side. Simulations were carried out to illustrate the processing time (t) and temperature difference (ΔT_p) versus intermediate Alumina layer thickness (l_a) for all the cases (case 2a–2d) corresponding to LI–LIV due to type 1 incidence (figures not shown). It was observed that the processing time is almost invariant with l_a for LI and LII length scales, whereas processing time increases with l_a for all cases in larger sample thicknesses (LIII and LIV). The temperature difference (ΔT_p) distributions for all cases (case 2a–2d) corresponding to first layer have similar qualitative trend for LI as well as for LII length scales. It is interesting to note that ΔT_p within first layer decreases with Alumina layer thickness (l_a) to 0.08 cm thereafter that is invariant with respect to l_a. In contrast, ΔT_p for the second layer increases with l_a. However, case 2d corresponding to second layer has less ΔT_p for smaller l_a values corresponding to LI and LII length scales. The temperature difference (ΔT_p) for the second layer is found to be quite large for all cases in larger length scales (LIII and LIV). Overall, Alumina—polymer composite attached with SiC plate for LI–LIV length scales is found to be not optimal based on higher thermal runaway. Thus, Alumina-polymer composite attached with SiC plate may not be optimal strategy for microwave heating. Simulations have also been carried out for type 2 incidence (figures not shown) and the results are qualitatively similar to that of type 1 incidence.

Figures 5(*a*)–5(*d*) illustrate the processing time (t) and temperature difference (ΔT_p) versus intermediate SiC layer thickness (l_a) for all the cases (case 2a–2d) corresponding to LI–LIV due to type 1 incidence. It is interesting to note that ΔT_p is very high for continuous samples, whereas ΔT_p is reduced to a greater extent for samples composited with SiC layer. Figures 5(*a*) and 5(*b*)

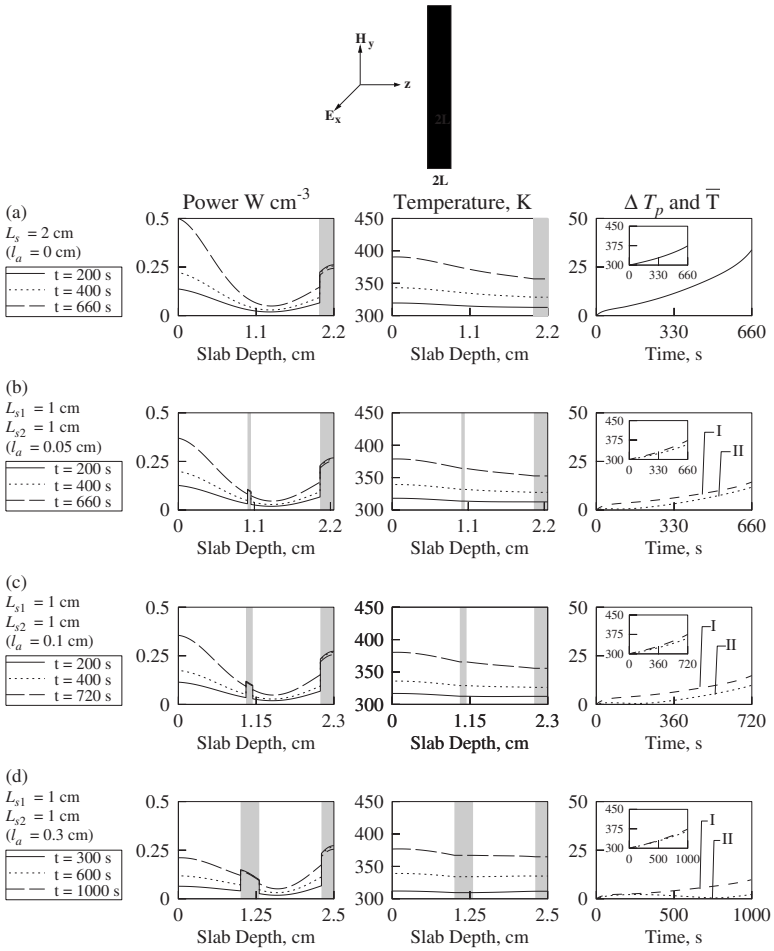

Fig. 6 Power, temperature, and temperature difference (ΔT_p) distributions for LIII length scale of Nylon 66 attached with Alumina plate at right side and with Alumina as intermediate layer corresponding to case 2b due to one side incidence with (*a*) l_a=0 cm, (*b*) l_a=0.05 cm, (*c*) l_a=0.1 cm, and (*d*) l_a =0.3 cm. The shaded regime denotes intermediate Alumina layer and Alumina plate. The symbols I and II in last column of figures represent first layer (- - -) and second layer (···), respectively, to illustrate ΔT_p and $\bar{T}$. The inset shows average temperature ($\bar{T}$) versus *t*.

illustrates that processing time varies slightly with l_a for all the cases (case 2a–2d) corresponding to LI and LII length scales. Note that small value of l_a is preferred based on the increase in processing time. It may also be noted that ΔT_p for first layer decreases to l_a=0.08 cm and thereafter ΔT_p is almost invariant with l_a for LI, whereas ΔT_p for second layer decreases with increase in l_a for all the cases. On the other hand, ΔT_p for first layer decreases to l_a=0.08 cm and thereafter ΔT_p decreases after reaching a maximum value around l_a=0.13 cm with LII length scale. Note that ΔT_p for second layer decreases to l_a=0.06 cm; thereafter ΔT_p increases with increase in l_a for all the cases for LII. Based on the two layers, case 2d with l_a=0.08 cm may be the optimal strategy for processing both LI and LII length scale.

Figures 5(*c*) and 5(*d*) illustrate that processing time for LIII and LIV length scale decreases with l_a to 0.1 cm; thereafter that slightly increases with increase in l_a. It is interesting to observe that ΔT_p is large for smaller values of l_a. However, there is a decrease in ΔT_p at larger l_a (l_a=0.3 cm) especially with case 2b but still ΔT_p is significantly high. Hence, SiC—polymer composite may be recommended for LI–LII length scales with smaller l_a. On the other hand, larger l_a may be preferred for larger sample thickness (LIII and LIV) with the slight increase in processing time compared to continuous sample.

In general, ΔT_p is reduced for samples with ceramic composite as compared to continuous sample. Hence, instead of processing a continuous sample one can use ceramic composite to reduce the thermal runaway.

3.3 Spatial Characteristics of Power and Temperature: Illustrative Test Cases. In the previous section, the role of optimal thickness of intermediate composite layer for polymer—ceramic composite has been discussed for samples attached with various ceramic plates. It is important to know effect of intermediate layer on power absorption and spatial temperature distribution within the sample. Hence, spatial distribution has been illustrated for few specific length scales to understand further the importance of ceramic composite.

3.3.1 Alumina Plate at Right Side. Figures 6(*a*)–6(*d*) illustrate the distributions of spatial power (q) and temperature (T), overall heating effect ($\bar{T}$) and temperature difference (ΔT_p) for cases 1 and 2b ($L_{s1}:L_{s2}$=1:1) corresponding to LIII (L_s=2 cm) due to type 1 incidence. Note that Nylon sample is attached with Alumina plate at right side of the sample (shaded region) and inter-

mediate Alumina layer (shaded region) is composited within two Nylon slabs, as seen in Figs. 6(*b*)–6(*d*). Overall, the heating effects are demonstrated by average heating rate ($d\overline{T}/dt$), as seen in inset plots, and ΔT_p denotes the difference between the maximum and minimum values of temperature within the sample layer, as shown in the third column of figures. Initially, the simulations are carried out for continuous samples, as seen in Fig. 6(*a*). It is interesting to observe that there is a maxima in power at the exposed face of the sample and a minima in power occurs near the center of the sample for all time labels. Note that the maxima in power is due to constructive interference of propagating waves, whereas the minima in power is due to destructive interference. It may be noted that the power absorption in the Alumina layer is almost invariant for all time labels, as seen commonly in Fig. 6(*a*)–6(*d*). It is observed that the temperature and power distributions are coupled as the dielectric loss is a nonlinear function of temperature (see Table 1). Therefore, power absorption is larger as heating progresses. It is observed that, temperature distribution decreases from exposed to unexposed face for all time labels. The temperature difference (ΔT_p) and the average temperature ($\overline{T}$) versus time are also shown in Fig. 6(*a*) panel. The inset plot shows that $\overline{T}$ reaches 375 K at $t=660$ s. It is interesting to observe that ΔT_p increases with time, which is direct consequence of high power absorption in the exposed face. Next, we will demonstrate the role of two discrete samples with identical total length (L_s) on the efficient heating of polymer samples.

Figure 6(*b*) illustrates distribution for case 2b with $l_a=0.05$ cm. Simulations are shown up to 660 s, which corresponds to average temperature around 375 K. Note that overall processing time with intermediate Alumina layer is almost identical to that of sample without intermediate layer. Similar to continuous sample, power absorption is maximum at the left face of first layer, whereas that is maximum at the right face of the second sample layer. It is interesting to note that the power absorption in the intermediate Alumina layer is small compared to the power absorption in Alumina plate at the right face. It may be noted that the power distribution within polymer sample is qualitatively similar to that of case 1. The temperature distribution is qualitatively similar to case 1 as discussed earlier. The temperature difference (ΔT_p) and the average temperature ($\overline{T}$) versus time are also shown in Fig. 6(*b*) panel. Note that ΔT_p values for the first and second layers are shown separately in the plot. The inset plot shows that $\overline{T}$ reaches 375 K at $t=660$ s and there is only slight difference between $\overline{T}$ of the two layers. It is interesting to observe that at 660 s, ΔT_p for first and second layers are less compared to that of ΔT_p for continuous sample. It may be inferred that the composite Alumina—Nylon samples with $l_a=0.05$ cm is advantageous for efficient heating as thermal runaway is reduced.

Figures 6(*c*) and 6(*d*) illustrate the power and temperature characteristics for $l_a=0.1$ and 0.3 cm, respectively. Figure 6(*c*) shows heating characteristics of up to $t=720$ s, whereas Fig. 6(*d*) illustrates heating characteristics of to $t=1000$ s. It is interesting to note that power and temperature distributions in Figs. 6(*c*) and 6(*d*) illustrate the common features of maxima and minima, as seen in Fig. 6(*b*). It is interesting to observe that ΔT_p distribution for first and second layers corresponding to $l_a=0.1$ cm (Fig. 6(*c*)) is qualitatively similar to that of $l_a=0.05$ cm (see Fig. 6(*c*)). In contrast, ΔT_p corresponding to $l_a=0.3$ cm has very less value for second layer (Fig. 6(*d*)). Although ΔT_p for $l_a=0.1$ and 0.3 cm is less as compared to $l_a=0$ cm, the processing time is high and hence these cases may not be preferred.

Test cases were also performed with Alumina intermediates for LIV samples and case 2a in presence of type 2 microwave incidence, which corresponds to microwave incidence at both sides (figures not shown). It is interesting to observe that a maxima in power occurs near the center of the sample and there is also an additional local maxima at left face of the sample for all time labels. It is also found that, the power absorption is larger at later stages of heating as discussed in earlier cases. The temperature distribution within samples is almost uniform at initial stages of heating and thereafter, temperature increases near the center of the sample due to larger power absorption at the center. Although a maxima in temperature occurs at the center for smaller l_a but additional maxima in temperature is also found to occur near the left side for larger l_a. Note that overall processing time with Alumina layer is less than that with continuous sample but the temperature difference (ΔT_p) is found to be quite high, especially for second layer.

A representative case study has been carried out with SiC intermediate for LIII samples attached with Alumina plate at right side involving case 2d in presence of type 1 incidence (figures not shown). It is interesting to note that large maxima in power absorption occurs within the SiC intermediate due to high dielectric loss of SiC, whereas power absorption is less by one order of magnitude within the sample as well as Alumina layer. Due to high power absorption within SiC layer, the processing rate is high with SiC intermediate. It was found that processing time with SiC intermediate varies within 220–260 s, whereas the time is around 660 s for a continuous sample. Similar to continuous sample, power absorption is maximum at the left face of first layer, whereas that is minimum at the right face of the second sample layer. It may also be noted that temperature distribution is almost uniform in first layer, whereas that of second layer decreases toward the right face. It is interesting to observe that at later stage of processing, ΔT_p for the first and second layers are less compared to that of ΔT_p for continuous sample. It is also interesting to note that ΔT_p for first layer decreases with time. Although processing time is less for $l_a=0.1$ and 0.3 cm, ΔT_p for second layer is high as compared to $l_a=0$ cm and $l_a=0.05$ cm. The processing of Nylon samples with SiC intermediate with case 2d may be preferred as the thickness of second layer is quite small.

3.3.2 Alumina Plate at Left Side. Figures 7(*a*)–7(*d*) illustrate the distributions for case 1 and case 2d ($L_{s1}:L_{s2}=2:1$) corresponding to LIII due to type 1 incidence. It may be noted that Alumina layer (shaded region) is composited within two Nylon slabs attached with Alumina plate (shaded region) at left side, as seen in Figs. 7(*a*)–7(*d*). The simulation results are shown for continuous samples, as seen in Fig. 7(*a*). It may be noted that the simulations are shown up to 800 s. It is interesting to observe that power absorption is maximum at right face of the polymer sample. It is also observed that, the power absorption in the Alumina plate is significant. The temperature distribution in Fig. 7(*a*) is maximum at the right face and decreases toward the left face. It is interesting to observe that ΔT_p is high and leads to thermal runaway for continuous samples attached with Alumina plate.

Figure 7(*b*) shows distribution for case 2d with $l_a=0.05$ cm and simulations are shown up to 750 s. Note that overall processing time with Alumina composite is less than that with continuous sample. It is interesting to note that power and temperature distributions follow similar qualitative trend to that of continuous sample. Note that the power absorption within the Alumina plate is larger than that within polymer sample. It is interesting to note that ΔT_p value is less as compared to that of continuous sample. Figures 7(*c*) and 7(*d*) illustrate the power and temperature characteristics for $l_a=0.1$ cm and 0.3 cm, respectively. Note that the power and temperature distributions of $l_a=0.1$ cm follow similar qualitative trend, as seen in Fig. 7(*b*). In contrast, the power absorption in the first layer is larger with large gradient and the power absorption in the second layer is smaller than that with $l_a=0.1$ cm. It is interesting to note that as l_a increases, the magnitude of power absorption in the Alumina plate decreases and the power absorption in the first layer increases. Note that larger l_a corresponds to higher ΔT_p and less processing rate. Based on the detailed spatial distribution analysis of case 1 and case 2d, l_a

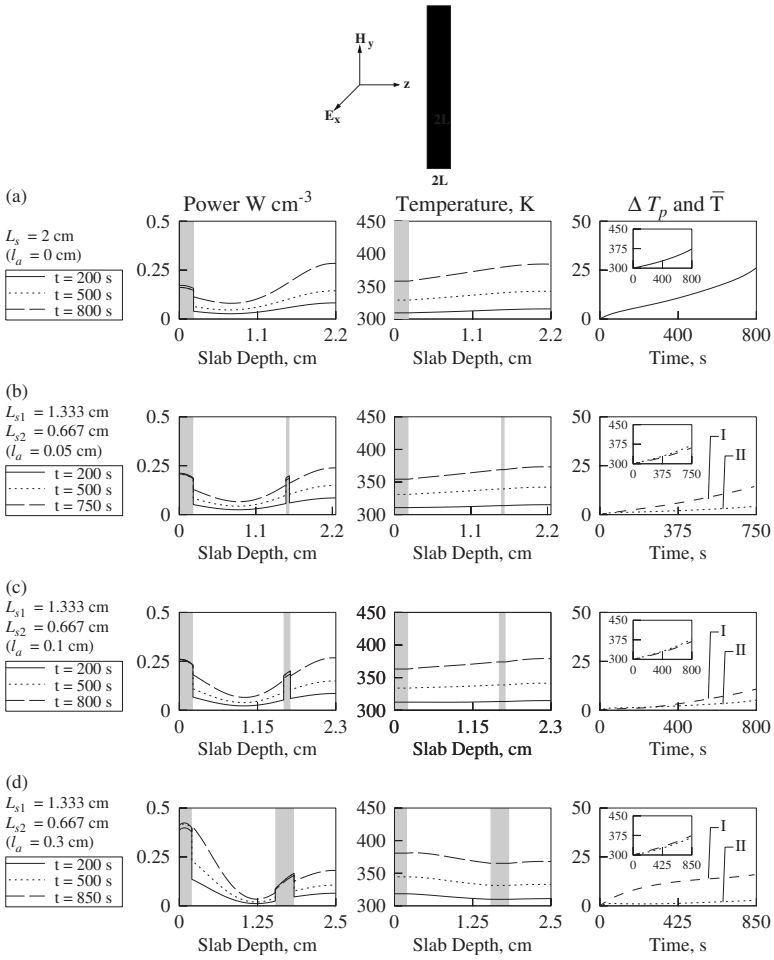

Fig. 7 Power, temperature, and temperature difference (ΔT_p) distributions for LIII length scale of Nylon 66 attached with Alumina plate at left side and with Alumina as intermediate layer corresponding to case 2d due to one side incidence with (*a*) l_a=0 cm, (*b*) l_a=0.05 cm, (*c*) l_a=0.1 cm, and (*d*) l_a =0.3 cm. The shaded regime denotes intermediate Alumina layer and Alumina plate. The symbols I and II in last column of figures represent first layer (- - -) and second layer (···), respectively, to illustrate ΔT_p and $\bar{T}$. The inset shows average temperature ($\bar{T}$) versus *t*.

=0.05 and 0.1 cm is the optimal Alumina layer thickness for microwave processing of LIII length scale of Nylon 66 sample attached with Alumina plate at left face corresponding to type 1 incidence.

3.3.3 SiC Plate at Right Side. Simulation studies have also been carried out for sample attached with SiC at right side (figures not shown). It is interesting to observe that a maxima in power occurs near the right face of the sample and there is also an additional local maxima at left face of the sample for all time labels. It may be noted that the power absorption in the SiC plate is maximum. The temperature distribution is maximum near the SiC plate and decreases toward the left face. Note that high temperature near the SiC plate is due to direct consequence of high power absorption in the SiC layer. It is interesting to observe that ΔT_p is very high and may lead to thermal runaway for continuous samples attached with SiC plate. The power and temperature distribution of sample—Alumina composite follow similar qualitative trend to that continuous sample for all values of l_a. Although ΔT_p is reduced for first layer with Alumina intermediate composite, ΔT_p of second layer is almost same as that of continuous sample. It may be noted that first layer has uniform temperature distribution compared to second layer. It is interesting to note that as l_a increases, the magnitude of power absorption in the SiC layer decreases and the power absorption in the first layer increases. Although larger l_a corresponds to lower ΔT_p in the first layer, the processing rate, and ΔT_p of second layer remains a critical issue. Hence, Alumina composite may not be recommended for samples attached with SiC plate at right side. In contrast, intermediate SiC composite leads to lesser ΔT_p for both the layers corresponding to all the length scales. It may be noted that the processing time is almost invariant with l_a. Based on the analysis it is found that, SiC intermediate composite is recommended for samples attached with SiC plate at right side.

4 Conclusions

Extensive analysis has been carried out on microwave heating for continuous Nylon 66 samples as well as discrete samples composited with various ceramic layers (Al_2O_3 and SiC) attached with ceramic plate due to microwave incidence at one side and both sides. The coupled energy balance equation and electric field equations are solved using Galerkin finite element method for temperature dependent dielectric and thermal properties. Initially, the analyses are carried out for various thickness of polymer samples and the few length scales have been chosen as case stud-

Case Studies	Optimal processing strategy
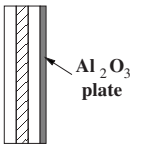	● Alumina composite may be recommended for LIII and LIV length scales. ● SiC composite may be recommended for LI–LIII length scales. ● Smaller l_a is preferred for Alumina and larger l_a is preferred for SiC composite.
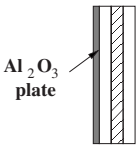	● Alumina composite may be recommended for LII–LIV length scales. ● SiC composite may be recommended for LI and LII length scales. ● Smaller l_a is preferred for LI–LIII of Alumina whereas larger l_a is preferred for LI–LII of SiC and LIV of Alumina composite.
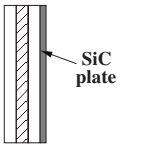	● Alumina composite may not be recommended for LI–LIV length scales. ● SiC composite may be recommended for LI–LIV length scales. ● Smaller l_a is preferred for LI–LIII length scales whereas larger l_a is preferred for LIV length scale corresponding to SiC composite.

Fig. 8 The optimal processing strategies for sample-ceramic composites attached with various ceramic plates

ies to study the efficient microwave heating with the inclusion of ceramic composites within two discrete polymer samples. The role of discrete samples in microwave heating has been best illustrated via processing time and temperature difference versus ceramic layer thickness (l_a) with each type of microwave incidence for all the cases. Influence of ceramic layer thickness for discrete samples has been studied for various discrete sample ratios (cases 2a–2d) corresponding to each length scale (LI–LIV). The processing time and temperature difference are found to be a strong function of ceramic layer thickness, discrete sample ratios and types of microwave distribution.

Discrete samples corresponding to various length scales (LI–LIV) have been studied in detail for specific cases with spatial distributions of power and temperature. In general, for thin Nylon samples ($L_S \leq 1$ cm), SiC layer may be preferred over Alumina based on smaller processing time. For thick Nylon samples ($L_S > 1$ cm), Alumina layer is preferred over SiC based on ΔT_p as well as processing time. SiC composites enhance the processing rate with little increase in temperature difference for thin Nylon samples, whereas Alumina composite reduces both processing time and ΔT_p for thick Nylon samples. The optimal strategy for processing of samples with various ceramic plates has been outlined in Fig. 8. Overall, thin layer of composite minimize the processing time as well as ΔT_p whereas larger thickness of composite increase processing time but ΔT_p may be reduced. Choice of intermediate layer thickness for optimal heating of discrete samples is very critical for a particular discrete samples ratio and type of incidence. This concept of microwave heating of discrete samples may be effectively implemented in polymer industries for thermoforming, melting, molding, vulcanizing, and many more within a customized oven based on uniform plane wave propagation.

Acknowledgment

The authors would like to thank the anonymous reviewers for critical comments and suggestions, which improved the quality of the manuscript.

Nomenclature

Bi = Biot number
C_p = specific heat capacity, J kg^{-1} K^{-1}
c = velocity of light, m s^{-1}
E_x = electric field intensity, V m^{-1}
f = frequency, Hz
h = heat transfer coefficient, W m^{-2} K^{-1}
H = enthalpy, J m^{-3}
H_y = magnetic field intensity, Amp m^{-1}
k = thermal conductivity, W m^{-1} K^{-1}
L = half-slab thickness, m
L_S = sample thickness, m
L_{S1} = first layer thickness, m
L_{S2} = second layer thickness, m
l_a = intermediate ceramic layer, m
q = microwave source term, W m^{-3}
t = time, s
T = temperature, K
T_0 = initial temperature, K
T_∞ = ambient temperature, K
ΔT_p = temperature difference, K
$\bar{T}$ = average temperature, K
z = distance, m

Greek Symbols

ϵ_0 = free space permittivity, F m^{-1}
κ = propagation constant
κ' = relative dielectric constant
κ'' = relative dielectric loss
κ^* = relative complex dielectric properties
ρ = density, kg m^{-3}
ω = angular frequency, rad s^{-1}

Subscripts

l = layer number

References

[1] Cola, B. A., Amama, P. B., Xu, X. F., and Fisher, T. S., 2008, "Effects of Growth Temperature on Carbon Nanotube Array Thermal Interfaces," ASME J. Heat Transfer, **130**(11), p. 114503.
[2] Huo, Y., and Li, B. Q., 2005, "Boundary/Finite Element Modeling of Three-Dimensional Electromagnetic Heating During Microwave Food Processing," ASME J. Heat Transfer, **127**(10), pp. 1159–1166.
[3] Rattanadecho, P., Aoki, K., and Akahori, M., 2002, "Experimental Validation

of a Combined Electromagnetic and Thermal Model for a Microwave Heating of Multi-Layered Materials Using a Rectangular Wave Guide," ASME J. Heat Transfer, **124**(5), pp. 992–996.
[4] Ratanadecho, P., Aoki, K., and Akahori, M., 2002, "Influence of Irradiation Time, Particle Sizes, and Initial Moisture Content During Microwave Drying of Multi-Layered Capillary Porous Materials," ASME J. Heat Transfer, **124**(1), pp. 151–161.
[5] Wang, Z. H., and Shi, M. H., 1998, "The Effects of Sublimation-Condensation Region on Heat and Mass Transfer During Microwave Freeze Drying," ASME J. Heat Transfer, **120**(3), pp. 654–660.
[6] Zeng, X., and Faghri, A., 1994, "Experimental and Numerical Study of Microwave Thawing Heat-Transfer for Food Materials," ASME J. Heat Transfer, **116**(2), pp. 446–455.
[7] Bubnovich, V., Villarreal, C., and Reyes, A., 2008, "Computer Simulation of the Drying of Seeds and Vegetables in a Discontinuous Fluidized Bed," Numer. Heat Transfer, Part A, **54**(3), pp. 255–278.
[8] Zhu, J., Kuznetsov, A. V., and Sandeep, K. P., 2007, "Numerical Modeling of a Moving Particle in a Continuous Flow Subjected to Microwave Heating," Numer. Heat Transfer, Part A, **52**(5), pp. 417–439.
[9] Kelen, A., Ress, S., Nagy, T., Pallai-Varsanyi, E., and Pintye-Hodi, K., 2006, ""3D Layered Thermography" Method to Map the Temperature Distribution of a Free Flowing Bulk in Case of Microwave Drying," Int. J. Heat Mass Transfer, **49**(5-6), pp. 1015–1021.
[10] Rattanadecho, P., 2004, "Theoretical and Experimental Investigation of Microwave Thawing of Frozen Layer Using a Microwave Oven (Effects of Layered Configurations and Layer Thickness)," Int. J. Heat Mass Transfer, **47**(5), pp. 937–945.
[11] Wu, H. X., Li, F., Lin, Y. H., Cai, R. F., Wu, H. X., Tong, R., and Qian, S. X., 2006, "Fullerene-Functionalized Polycarbonate: Synthesis Under Microwave Irradiation and Nonlinear Optical Property," Polym. Eng. Sci., **46**(4), pp. 399–405.
[12] So, H. W., and Taube, A., 2004, "Numerical Investigation of the Influence of Material Properties and Adhesive Layer Thickness on the Heating Efficiency of Microwave Curing of an Adhesive-Bonded Joint," Polym. Eng. Sci., **44**(8), pp. 1414–1418.
[13] So, H. W., and Taube, A., 2004, "Simulation and Experimental Study of Microwave Heating of Single Lap Adhesive-Bonded Polypropylene Joint," Polym. Eng. Sci., **44**(4), pp. 728–735.
[14] Wu, C. Y., and Benatar, A., 1997, "Microwave Welding of High Density Polyethylene Using Intrinsically Conductive Polyaniline," Polym. Eng. Sci., **37**(4), pp. 738–743.
[15] Lu, C. M., Cheng, M. M. C., Benatar, A., and Lee, L. J., 2007, "Embossing of High-Aspect-Ratio-Microstructures Using Sacrificial Templates and Fast Surface Heating," Polym. Eng. Sci., **47**(6), pp. 830–840.
[16] Riha, P., Hadac, J., Slobodian, P., Saha, P., Rychwalski, R. W., and Kubat, J., 2007, "Effect of Aging Time on the Volumetric and Enthalpic Glass Transition of *a*-PMMA Upon Heating," Polymer, **48**(25), pp. 7356–7363.
[17] Chen, M., Siochi, E. J., Ward, T. C., and Mcgrath, J. E., 1993, "Basic Ideas of Microwave Processing of Polymers," Polym. Eng. Sci., **33**(17), pp. 1092–1109.
[18] Chen, M., Hellgeth, J. W., Ward, T. C., and Mcgrath, J. E., 1995, "Microwave Processing of 2-Phase Systems—Composites and Polymer Blends," Polym. Eng. Sci., **35**(2), pp. 144–150.
[19] Jullien, H., Petit, A., and Merienne, C., 1996, "The Microwave Reaction of Phenyl Glycidyl Ether With Aniline on Inorganic Supports: A Model for the Microwave Cross-Linking Of Epoxy Resins," Polymer, **37**(15), pp. 3319–3330.
[20] Papargyris, D. A., Day, R. J., Nesbitt, A., and Bakavos, D., 2008, "Comparison of the Mechanical and Physical Properties of a Carbon Fibre Epoxy Composite Manufactured by Resin Transfer Moulding Using Conventional and Microwave Heating," Compos. Sci. Technol., **68**(7-8), pp. 1854–1861.
[21] Sombatsompop, N., and Kumnuantip, C., 2006, "Comparison of Physical and Mechanical Properties of NR/Carbon Black/Reclaimed Rubber Blends Vulcanized by Conventional Thermal and Microwave Irradiation Methods," J. Appl. Polym. Sci., **100**(6), pp. 5039–5048.
[22] Kathirgamanathan, P., 1993, "Microwave Welding of Thermoplastics Using Inherently Conducting Polymers," Polymer, **34**(14), pp. 3105–3106.
[23] Chabinsky, I. J., 1983, "Practical Applications of Microwave-Energy in the Rubber Industry," Elastomerics, **115**(1), pp. 17–20.
[24] Raj, J. M., Ranganathaiah, C., and Ganesh, S., 2008, "Interfacial Modifications in PS/PMMA and PVC/EVA Blends by E-Beam and Microwave Irradiation: A Free Volume Study," Polym. Eng. Sci., **48**(8), pp. 1495–1503.
[25] Jullien, H., and Valot, H., 1983, "Behavior of Film Forming Polymers in a Microwave Electric-Field," Polymer, **24**(7), pp. 810–814.
[26] Moriwaki, S., Machida, M., Tatsumoto, H., Kuga, M., and Ogura, T., 2006, "A Study on Thermal Runaway of Poly(Vinyl Chloride) by Microwave Irradiation," J. Anal. Appl. Pyrolysis, **76**(1–2), pp. 238–242.
[27] Bur, A. J., 1985, "Dielectric-Properties of Polymers at Microwave Frequencies—A Review," Polymer, **26**(7), pp. 963–977.
[28] Riddle, B., Baker-Jarvis, J., and Krupka, J., 2003, "Complex Permittivity Measurements of Common Plastics Over Variable Temperatures," IEEE Trans. Microwave Theory Tech., **51**(3), pp. 727–733.
[29] Harper, J., Price, D., and Zhang, J., 2007, "Use of Fillers to Enable the Microwave Processing of Polyethylene," J. Microwave Power Electromagn. Energy, **40**(4), pp. 219–227.
[30] Ayappa, K. G., Davis, H. T., Crapiste, G., Davis, E. A., and Gordon, J., 1991, "Microwave-Heating—An Evaluation of Power Formulations," Chem. Eng. Sci., **46**(4), pp. 1005–1016.
[31] Ayappa, K. G., Davis, H. T., Barringer, S. A., and Davis, E. A., 1997, "Resonant Microwave Power Absorption in Slabs and Cylinders," AIChE J., **43**(3), pp. 615–624.
[32] Barringer, S. A., Davis, E. A., Gordon, J., and Ayappa, K. G., 1995, "Microwave-Heating Temperature Profiles for Thin Slabs Compared to Maxwell and Lambert Law Predictions," J. Food Sci., **60**(5), pp. 1137–1142.
[33] Basak, T., and Ayappa, K. G., 1997, "Analysis of Microwave Thawing of Slabs With Effective Heat Capacity Method," AIChE J., **43**(7), pp. 1662–1674.
[34] Basak, T., 2004, "Role of Resonances on Microwave Heating of Oil-Water Emulsions," AIChE J., **50**(11), pp. 2659–2675.
[35] Basak, T., and Priya, A. S., 2005, "Role of Ceramic Supports On Microwave Heating of Materials," J. Appl. Phys., **97**(8), p. 083537.
[36] Basak, T., and Priya, A. S., 2005, "Role of Metallic and Ceramic Supports on Enhanced Microwave Heating Processes," Chem. Eng. Sci., **60**(10), pp. 2661–2677.
[37] Ayappa, K. G., Davis, H. T., Davis, E. A., and Gordon, J., 1991, "Analysis of Microwave-Heating of Materials With Temperature-Dependent Properties," AIChE J., **37**(3), pp. 313–322.
[38] Ayappa, K. G., Davis, H. T., Davis, E. A., and Gordon, J., 1992, "2-Dimensional Finite-Element Analysis of Microwave-Heating," AIChE J., **38**(10), pp. 1577–1592.
[39] De Wagter, C., 1984, "Computer Simulation Predicting Temperature Distributions Generated by Microwave Absorption in Multilayered Media," J. Microwave Power Electromagn. Energy, **19**(2), pp. 97–106.
[40] Jolly, P., and Turner, I., 1990, "Non-Linear Field Solutions of One-Dimensional Microwave Heating," J. Microwave Power Electromagn. Energy, **25**(1), pp. 3–15.
[41] Chatterjee, A., Basak, T., and Ayappa, K. G., 1998, "Analysis of Microwave Sintering of Ceramics," AIChE J., **44**(10), pp. 2302–2311.

Numerical Determination of Radiative View Factors Using Ray Tracing

T. Walker

S.-C. Xue

G. W. Barton
e-mail: gbarton@usyd.edu.au

School of Chemical and Biomolecular Engineering,
University of Sydney,
New South Wales 2006, Australia

A ray-tracing method is presented for numerically determining radiative view factors in complex three-dimensional geometries. This method uses a set of "primitive" shapes to approximate the required geometry together with a Monte Carlo simulation to track the fate of randomized rays leaving each surface. View factors were calculated for an operational fiber drawing furnace using both numerical integration and ray-tracing methods. Calculated view factor profiles were essentially identical above a ray density of 10^5 per unit area. Run times for the ray-tracing method were considerable longer, although the setup time to describe a new geometry is very short and essentially independent of system complexity. [DOI: 10.1115/1.4000974]

Keywords: radiative heat transfer, view factor, ray tracing, Monte Carlo method, polymer optical fiber

1 Introduction

Figure 1 shows an arbitrarily orientated surface A_i having a constant total hemispherical emissivity ε_i and temperature T_i. Of the total radiant energy leaving this surface in all directions ($\varepsilon_i \sigma_0 T_i^4 A_i$, where σ_0 is the Stefan–Boltzmann constant), only a fraction will reach a second arbitrarily orientated surface A_j. This fraction ($F_{i\text{-}j}$) is defined as the view factor, a term that is consistent with the fact that its value is dependent only on the geometrical orientation of the two participating surfaces. A view factor can thus be expressed (and calculated) as follows:

$$F_{i\text{-}j} = \frac{1}{A_i} \int \left(\int \frac{\cos\,\theta_i \cos\,\theta_j}{\pi S_{i\text{-}j}^2} dA_j \right) dA_i \tag{1}$$

where dA_i and dA_j are differential elements within the two surfaces with $S_{i\text{-}j}$ being the length of the connecting line between the two, while θ_i and θ_j are the respective angles between the connecting line and the normal vectors ($\mathbf{n}_i$ and $\mathbf{n}_j$) to each surface.

Evaluation of view factors is straightforward provided that $S_{i\text{-}j}$, $\cos\,\theta_i$, and $\cos\,\theta_j$ can be expressed in terms of the geometrical parameters that define the two participating surfaces and the necessary integration performed. For radiative exchange between an infinitesimal and a finite surface, only a single area integration is needed. However, if two finite surfaces are involved, then a double area integral is required. Because of the importance of radiative heat transfer in a wide variety of applications, compilations of analytical or tabulated results (often in terms of dimensionless geometrical parameters) are available in the literature [1]. In some cases, an unknown view factor can be generated from known factors by making use of view factor algebra [2].

The present work was motivated by the need to calculate the radiative heat transfer within an operational furnace used to heat a polymer preform sufficiently to be drawn to fiber. Here the available view factor compilations were of limited use due to the geometric complexity of our drawing furnace, and the fact that once the glass transition temperature is reached then the shape of the deforming preform becomes a strong function of the thermal conditions within the furnace. Initially all view factors were determined using numerical integration for the case of a cylindrical (i.e., nondeforming) preform and used in a heat transfer model of the drawing furnace with close agreement being obtained between simulated and experimental (measured at the preform surface and center) temperature profiles. These view factors are presented later to confirm the accuracy of results obtained using an alternative ray-tracing method.

The remainder of this paper is thus structured as follows. Section 2 presents the concept of ray-tracing and how "primitives" can be used to calculate view factors. The tapered cylinder primitive is presented in detail, as this is used in calculating view factors for the case where a cylindrical preform is drawn to fiber. Section 3 presents view factor results for both the nondeforming preform and the tapering preform cases. In the former case, both numerical integration and ray tracing are used, while in the latter only ray tracing is employed. This section also compares the relative merits of the two methods.

2 Ray Tracing

Ray tracing is a widely used technique in optics whereby the path of a photon or "ray" is followed through a three-dimensional (3D) environment from its point of origin to its final destination. This technique has been employed to solve diverse problems from the generation of images with a high degree of photorealism [3,4] to complex radiative heat transfer modeling [5–10]. In the present context, ray tracing may be adapted to calculate the view factor between objects through its implementation within a Monte Carlo simulation [11]. Essentially a large number of rays are "fired" from random points on a given object at random angles into the 3D environment with the first object that each ray intersects being recorded. The view factor between any two objects may be defined as the fraction of rays leaving one object that reaches the other.

Accurate view factor estimation here requires that careful attention be paid to a number of computational issues, the two most important being the distribution of (random) points on the emitting surface and their (random) emission into the 3D environment.

The major strength of ray tracing as a tool for numerically estimating view factors is that its application is essentially independent of the complexity of the 3D geometry that defines the system. By comparison, alternatives such as numerical integration become increasingly challenging with geometrical complexity.

Contributed by the Heat Transfer Division of ASME for publication in the JOURNAL OF HEAT TRANSFER. Manuscript received May 31, 2009; final manuscript received November 26, 2009; published online April 28, 2010. Assoc. Editor: He-Ping Tan.

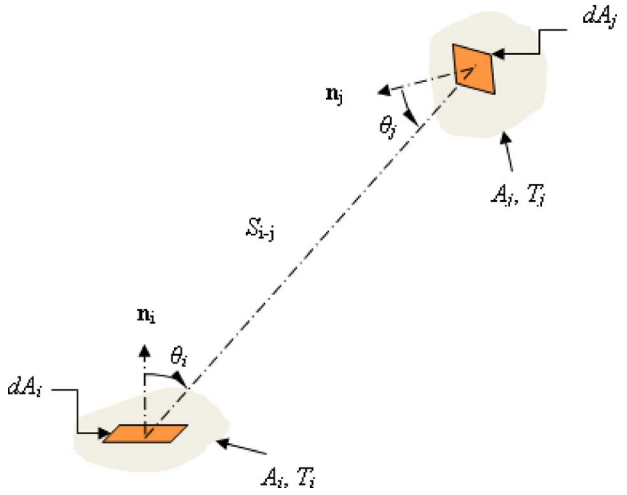

Fig. 1 Configuration for radiative heat exchange between two finite surfaces

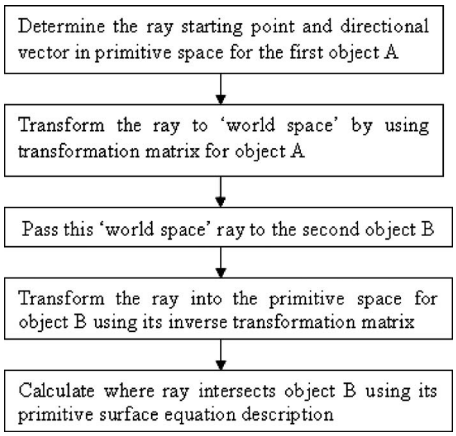

Fig. 2 Procedure for transforming a ray to find ray-object intersection

In passing, it should be noted that although the focus of this paper is on the use of ray tracing in view factor calculation, the technique can be conceptually expanded to calculate net radiative heat transfer within any complex 3D enclosure [12]. Here each ray emitted from a surface is taken as representing a "packet" of thermal energy that is either absorbed (and possibly re-emitted) or reflected when impinging on a second surface. However, it must be said that our (unpublished) case studies have shown this to be a computationally demanding approach.

2.1 Use of Primitives in Ray Tracing. Ray tracing is not a new approach for calculating view factors with a literature dating back some 40 years [13,14]. However, most approaches advocate that any object within a system be described via a mesh which maps to its surface [11,15,16]. While this approach reduces the complexity of calculating suitable ray launch positions and launch directions, it can introduce representational errors in terms of adequately modeling an object's curvature and requires a robust discretization algorithm.

A more elegant approach is to approximate any 3D geometry as a composite created from a modest set of simpler generic shapes (e.g., cylinder, cone, sphere, and plane). Each such primitive is described not in terms of a meshing arrangement but rather by a set of surface equations. Any primitive may be manipulated via affine transformations that allow it to be scaled, rotated, and transposed in 3D space to provide an infinite set of options while requiring a computational method for just a single shape. Thus any complex 3D geometry may be constructed as a collection of affine transformed primitives with such an approach being widely used in the computer-based multimedia industry as previously noted [3,4].

Intuitively, it might be expected that rays are created and traced in "world space," that is, the space where an actual object is approximated by a composite of (affine transformed) 3D primitives. However, such an approach increases the complexity of the ray-tracing implementation as it necessitates calculation of each ray's starting point and directional vector within the transformed space. It is computationally far more efficient to calculate a ray's starting point and launch direction in the primitive space, and subsequently transform the ray to perform the appropriate calculations. This ray transformation procedure is shown schematically in Fig. 2 for the case where the objective is to determine whether a ray from one object (A) intersects with a second object (B).

In this way, it is possible to describe a wide variety of 3D geometries in terms of a small number of primitive shapes and to use these compact descriptions to calculate the required view factors. For example, a polymer preform that is being drawn to fiber can be described in terms of a stack of tapered cylinders. The description of this primitive is thus considered next.

2.2 Tapered Cylinder Primitive. The primitive here is a cylinder with a base radius of 1 and a variable upper radius. As such, it can be used to model a wide range of shapes from a cylinder, through a conical frustum, to a cone. The "surface equation" for this primitive when its base is centered on the origin in the x-y plane and it extends along the z axis to a height of 1 is as follows:

$$x^2 + y^2 - (1 + (s-1)z)^2 = 0 \tag{2}$$

where s is the radius of the upper surface such that $0 \le s \le 1$.

When ray tracing is used to calculate view factors, it is essential to ensure an even distribution of ray starting points from the surface. For a simple cylinder (for which $s=1$), ray starting points can be defined in terms of the azimuthal angle (ϕ) as follows:

$$z = \chi \tag{3}$$

$$x = r_z \cos(\phi) \tag{4}$$

$$y = r_z \sin(\phi) \tag{5}$$

where χ is a random number between 0 and 1, r_z is the radius of the cylinder at z (here $r_z=1$), and ϕ is a random angle between 0 and $2p$.

However, for a tapered cylinder, it is no longer possible to simply use a random number to represent the z coordinate but rather a random surface area fraction ($0 \le A_f \le 1$) is selected. As the base radius and height for this primitive are both unity, A_f can be expressed as the following function of z:

$$A_f = \frac{z(1 + r_z)}{(1 + s)} \tag{6}$$

where $r_z = 1 + (s-1)z$ is the radius of the tapered cylinder at the point z.

Substituting for r_z in Eq. (6) gives a quadratic equation whose positive solution gives a random z coordinate distribution which reflects the changing surface area of the tapered cylinder:

$$z = \frac{\sqrt{1 - A_f + A_f^2} - 1}{s - 1} \tag{7}$$

The coordinates defining the starting point of any ray on this tapered cylinder are thus

$$r_z = 1 + (s-1)z \tag{8}$$

$$x = r_z \cos(\phi) \tag{9}$$

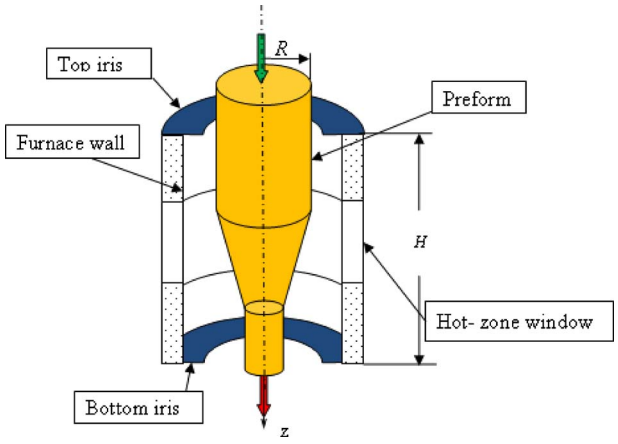

Fig. 3 Schematic diagram of fiber drawing furnace

$$y = r_z \sin(\phi) \tag{10}$$

The second issue is calculation of the ray directional vector, which is achieved by assuming azimuthal symmetry and calculating a hemispherical distribution as suggested by Farmer and Howell [12]. This distribution is rotated in such a way that it lies parallel to the surface of the tapered cylinder. The angle (θ) by which the directional distribution needs to be rotated around the x-axis is simply given by

$$\theta = \tan^{-1}(1 - s) \tag{11}$$

Applying this transformation and rotating around the z-axis by the random angle ϕ, a ray's directional vector may be determined as follows:

$$\begin{bmatrix} x_{\text{dir}} \\ y_{\text{dir}} \\ z_{\text{dir}} \end{bmatrix} = \begin{bmatrix} x\cos(\phi) - \sin(\phi) \times (y\cos(\theta) - z\sin(\theta)) \\ x\sin(\phi) + \cos(\phi) \times (y\cos(\theta) - z\sin(\theta)) \\ y\sin(\theta) - z\cos(\theta) \end{bmatrix} \tag{12}$$

It should be noted that this method generates a uniform directional distribution and thus is unsuitable for cases involving materials whose emissive characteristics deviate significantly from the underlying gray body assumption.

Using a ray's starting point and directional vector, as defined by Eqs. (9), (10), and (12), ensures that the calculated view factors are unbiased by any shape change, which in the present case would occur as the preform tapers and is drawn to fiber.

In applying the ray-tracing approach, a key computational parameter is the ray density ρ (i.e., the rays launched per unit area) to be used. Once this is set, the total number of rays used is simply the product of the surface area of the transformed (into "world space") tapered cylinder and the chosen ray density. Noting that rotation and translation do not affect surface area, the following formula can be used to give the surface area of a tapered cylinder that has been transformed by scaling factors a and b in the x and y directions, respectively:

$$A = \frac{\pi(1+s)}{s}\sqrt{\frac{s(a^2+b^2)}{2}} \tag{13}$$

3 View Factor Results for Fiber-Drawing Furnace

In order to evaluate the performance of ray tracing, it was used to determine the view factors needed in modeling the heat transfer within a fiber drawing furnace. Figure 3 is a schematic representation of an operational furnace used to fabricate microstructured polymer optical fibers (mPOFs). Such fibers owe their light-guiding properties to a pattern of holes that runs the length of the fiber. Here the required pattern is created by drilling holes into a monolithic block referred to as the preform. This is then drawn to fiber in a relatively low temperature furnace where heat transfer to the preform occurs by both convection and radiation. A critical issue in mPOF fabrication is the extent of deformation undergone by the hole structure as the preform is heated (above the polymer's glass transition temperature) and drawn to fiber. Details on mPOF fabrication are provided in the recent literature [17].

In Fig. 3, the preform enters at the top of the furnace through an adjustable iris while drawn fiber leaves at the bottom through a second iris. Six external halogen lamps (under on-off control) provide radiant heating through a central quartz "hot-zone" window with the rest of the furnace being well insulated. The preform surface is heated by thermal radiation (both through the quartz window and by reradiation from the furnace walls) and by convection induced within the furnace. In the present view factor determination context, two cases were considered. In the first, the furnace was operated such that the preform never exceeded its glass transition temperature and thus never underwent any neck-down in diameter. Here all relevant view factors were determined by numerical integration of Eq. (1). As noted, very good agreement was obtained between experimental temperature measurements and results from a fully conjugate heat transfer model where convective heat transfer was estimated using commercial computational fluid dynamics software.

In the second case considered (for which experimental measurements were not available), it was assumed that the preform was raised above its glass transition temperature and that the resultant preform neckdown could be described by the "slender body" approximation [18]. Here the preform radius (r) as a function of distance from the furnace entrance (z) is given by

$$r = R\exp\left(\frac{z\ln(D_r)}{2H}\right) \tag{14}$$

where D_r is the draw ratio (set by furnace operating conditions), H is the height of the furnace (0.18 m), and R is the initial preform radius (0.006 m).

In the latter case, determining all relevant view factors by numerical integration would be a time-consuming exercise. However, calculating these view factors using ray tracing is scarcely more involved than for the case where the preform diameter remains unchanged. The two D_r values chosen (9 and 900) gave exit to inlet radius ratios (i.e., r/R) that ranged from a modest to a substantial preform neckdown (33.33% and 3.33%, respectively).

3.1 Constant Diameter Preform. Although not required by this implementation of ray tracing, the preform and furnace walls were each discretized using 180 "slices" to allow a direct comparison of the view factors with those obtained via numerical integration (which used this level of discretization to ensure that the results were grid independent). Additionally, ray densities (ρ) of 10^4 and 10^5 per unit area were used to assess the impact of this key parameter on the ray-tracing results. As expected, increasing the ray density improved the "accuracy" of the ray-tracing results with excellent agreement between the two methods being achieved at the higher ρ value.

Results are given in Figs. 4–6 where in each case the view factors calculated by numerical integration and ray tracing are shown as solid lines and discrete symbols, respectively. Although all possible view factors for this furnace enclosure were determined, values are only given here between the preform surface and the furnace wall (observed from three different axial positions $z = 0.0095$, 0.0895, and 0.1695 of one surface to the entire other surface or to itself) to provide a direct comparison between the two methods. Here $F_{p\text{-}f}$ refers to the view factor from a position on the preform surface to the furnace wall, $F_{f\text{-}f}$ refers to the view factor from a position on the furnace wall to itself, and so on. The z values chosen show the essential geometric symmetry of a system that comprises a constant diameter cylinder located along the axis of a cylindrical enclosure. Under conditions where the

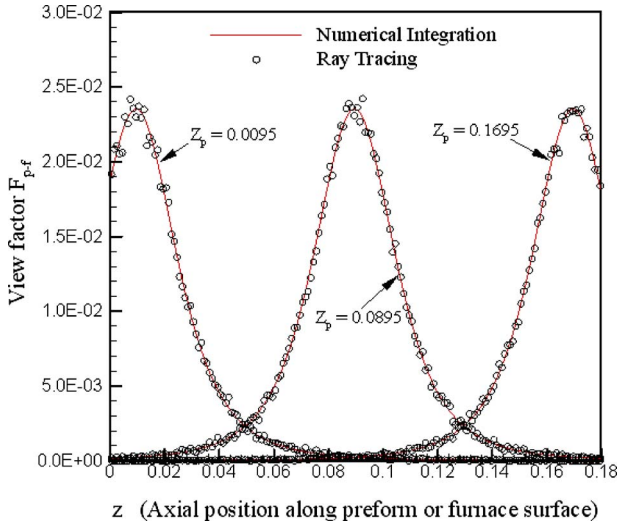

Fig. 4 View factors from three positions (z_p=0.0095, 0.0895, 0.1695) on the preform to the furnace wall (ρ=10^4 per unit area; cylindrical preform)

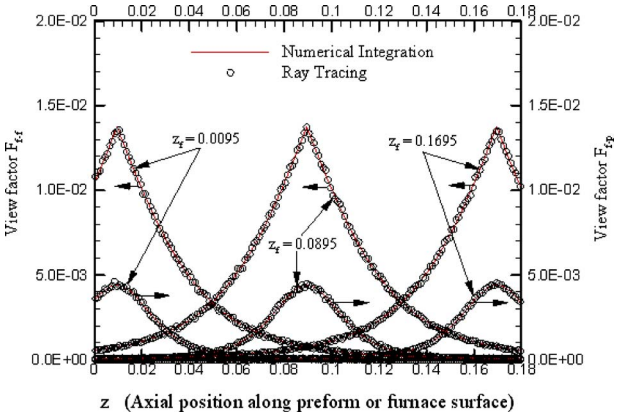

Fig. 6 View factors from three positions (z_f=0.0095, 0.0895, 0.1695) on the furnace wall to the preform surface (left) and itself (right) (ρ=10^5 per unit area; cylindrical preform)

preform undergoes neckdown, however, this symmetry is broken, as discussed in Sec. 3.2.

The accuracy of the view factor calculations is implied by both the close agreement between all F_{i-j} profiles obtained from the numerical integration and ray-tracing methods and the "sum rule" where the total of the view factors for each surface within the enclosure is essentially unity. Using these view factors, it is possible to determine the radiative heat transfer, using the net radiation method [2,19], between a stationary, finite length, solid preform, and the furnace surfaces where the heating wall is at a uniform temperature, and the top and bottom irises are either insulated or treated as black surfaces. For this case, if the aspect ratio of the cylindrical preform is large enough, the net radiative heat flux profile over the central section of the preform surface should approximate that for the limiting case of two infinitely long concentric cylinders. Figure 7 shows the results when a stationary polymethylmethacrylate (PMMA) preform (R=6 mm with a constant hemispherical total emissivity e_p of 0.90; initially at a uniform temperature of 293 K) is heated inside a furnace (with a constant emissivity e_w of 0.885, a height H of 180 mm, and a radius R_w of 32 mm; uniform wall temperature T_w of 373 K). Note that here the net heat flux for the preform has been scaled by the emitted flux q_b from a black surface with the same uniform wall temperature, that is, by $q_b = \sigma_0 T_w^4$, while the axial length has been scaled by H. As expected with an aspect ratio for the cylindrical preform of 30, when both irises are treated as insulated surfaces, the net radiative heat flux over the middle portion of the preform surface is consistent with the analytical result for two infinitely long concentric cylinders. However, if both irises are treated as black surfaces, then, due to heat lose thought the irises, the overall net radiative heat flux to the preform surface is reduced along the length of the preform, with the reduction becoming more marked when approaching the ends of the preform.

3.2 Reducing Diameter Preform. A constant diameter preform may be thought of as having a draw ration (D_r) of unity. As D_r is increased, so the amount of preform neckdown increases. View factors within the drawing furnace were calculated for two D_r values (9 and 900) using a ray density of 10^5 per unit area. The

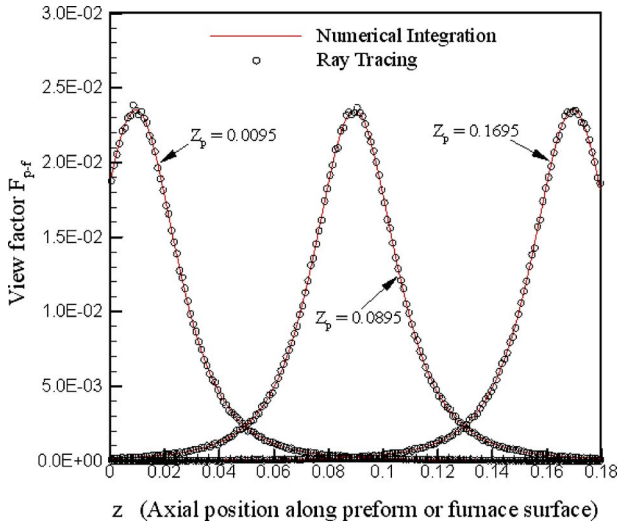

Fig. 5 View factors from three positions (z_p=0.0095, 0.0895, 0.1695) on the preform to the furnace wall (ρ=10^5 per unit area; cylindrical preform)

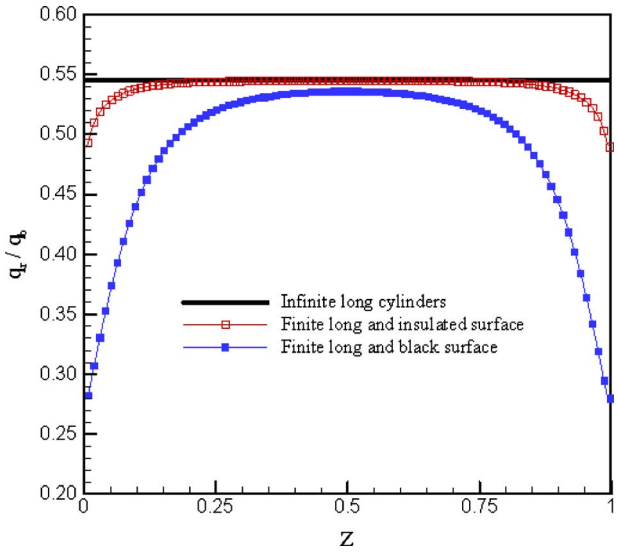

Fig. 7 Net radiative heat flux profiles along a stationary cylindrical preform within a furnace with a uniform heating wall temperature; two different thermal boundary conditions are used for the irises

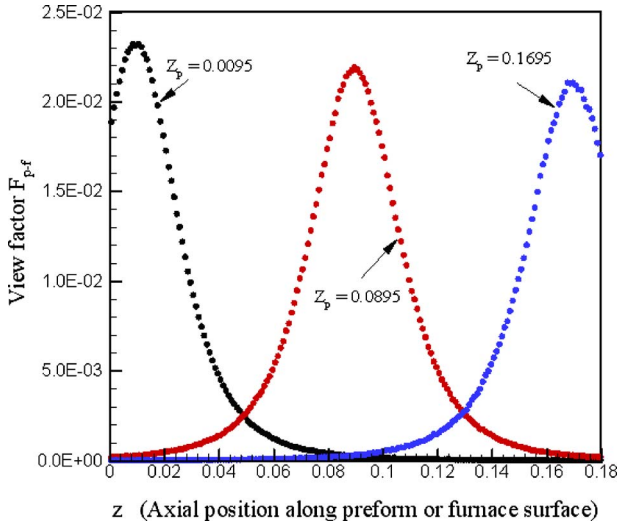

Fig. 8 View factors from three positions (z_p=0.0095, 0.0895, 0.1695) on the preform to the furnace wall (ρ=10^5 per unit area; D_r=9)

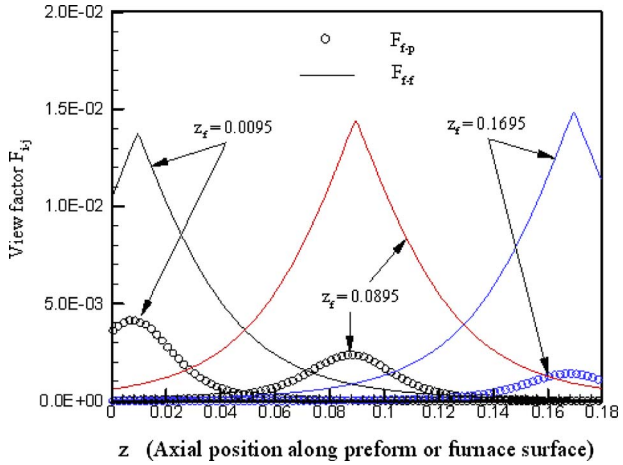

Fig. 10 View factors from three positions (z_f=0.0095, 0.0895, 0.1695) on the furnace wall to the preform and to itself (ρ=10^5 per unit area; D_r=9)

profiles presented in Figs. 8–11 correspond to those given in Figs. 5 and 6 for the constant diameter case.

Figures 5, 8, and 9 show the view factor profiles from the same positions on the preform surface to the furnace wall for three different D_r values (1, 9, and 900). The amount of preform thinning increases with D_r and the form of the view factor profile changes as the system geometry becomes less longitudinally symmetrical. Similar changes with preform thinning are apparent in Figs. 6, 10, and 11, where view factor profiles from three different positions on the furnace wall to both the preform surface ($F_{f\text{-}p}$) and itself ($F_{f\text{-}f}$) are given.

3.3 Computational Efficiency. It took ~5 s (using an AMD Althon 64 processor, 2.21 GHz, 2.0 Gbytes of RAM) to perform a complete set of view factor calculations for the draw furnace with a constant diameter preform using numerical integration at a level of discretization necessary to ensure grid independence. By comparison, the view factor profiles for a slender body preform with a draw ratio of 900 took 44.2 h when run on a comparable computer and a ray density (10^5 per unit area) that provided acceptable accuracy. This difference must, however, be weighted against the considerable time (several man months) taken in carrying out the necessary analysis and coding for the numerical integration case [20], the fact that it was not felt to be cost effective to extend this approach to the general deforming preform case, and the very modest time taken to set up a new case using the ray-tracing approach. No attempt was made in this study to speed up the ray-tracing calculations using either faster hardware or more sophisticated numerical techniques. In the latter category, constrained maximum likelihood smoothing appears to have promise [21], although its implementation would result in a significant nonlinear programming problem, somewhat at odds with the relative simplicity of the coding required for ray tracing built around the use of primitives.

Finally, it should be noted that if numerical integration is used, then the extent of the geometric discretization is primarily set by the need to ensure that the computed view factors are grid independent. By comparison, the discretization used in ray tracing is set simply by the resolution required in any given view factor profile. Thus in the present calculations, 180 cylindrical slices

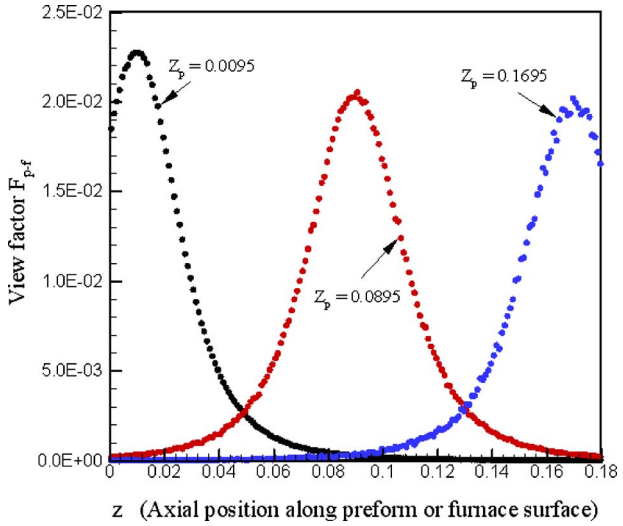

Fig. 9 View factors from three positions (z_p=0.0095, 0.0895, 0.1695) on the preform to the furnace wall (ρ=10^5 per unit area; D_r=900).

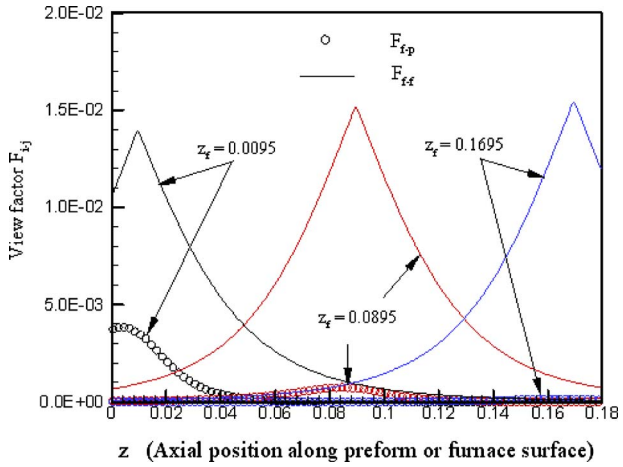

Fig. 11 View factors from three positions (z_f=0.0095, 0.0895, 0.1695) on the furnace wall to the preform and to itself (ρ=10^5 per unit area; D_r=900)

(either constant or tapered) were used to describe the preform simply for ease of comparison with the numerical integration results.

4 Conclusions

The determination of view factors for complex 3D geometries can be a challenge. In some cases, especially those that exhibit a measure of geometric symmetry, it is possible to employ numerical integration techniques, although considerable analysis is generally required and care needs to be taken in the discretization employed. Ray tracing is an alternative numerical approach that does not rely on any detailed geometric analysis. In the version employed in this study, 3D geometries are constructed using a set of primitive shapes. A subsequent Monte Carlo simulation (in which the "fate" of randomized rays leaving a surface are collated) is used to determine the required view factors. Although run times for ray-tracing calculations are significantly longer than for numerical integration, the "setup" time for a problem using ray-tracing is essentially independent of geometric complexity, making this a highly attractive approach for generic view factor software.

References

[1] Howell, J. R., 2008, "A Catalog of Radiation Heat Transfer Configuration Factors," 2nd ed., http://www.me.utexas.edu/~howell/index.html

[2] Siegel, R., and Howell, J. R., 2001, *Thermal Radiation Heat Transfer*, 4th ed., Taylor & Francis, New York.

[3] Hill, F. S., 2001, *Computer Graphics Using Open GL*, 2nd ed., P. Hall, ed., Prentice-Hall, Englewood Cliffs, NJ.

[4] Shirley, P., Sung, K., Brunvand, E., Davis, A., Parker, S., and Boulos, S., 2008, "Fast Ray-Tracing and the Potential on Graphics and Gaming Courses," Comput. Graph., **32**, pp. 260–267.

[5] Farmer, J., 1995, "Improved Algorithms for Monte Carlo Analysis of Radiative Heat Transfer in Complex Participating Medium," Ph.D. thesis, University of Texas, Austin, TX.

[6] Wang, A., and Modest, M. F., 2006, "Photon Monte Carlo Simulation for Radiative Transfer in Gaseous Media Represented by Discrete Particle Fields," ASME J. Heat Transfer, **128**, pp. 1041–1049.

[7] Steward, F. R., and Cannon, P., 1971, "The Calculation of Radiative Flux in a Cylindrical Furnace Using the Monte Carlo Method," Int. J. Heat Mass Transfer, **14**, pp. 245–262.

[8] Fan, T., and Fedorov, A. G., 2002, "Apparent Radiative Properties and Radiation Scattering by a Semi-Transparent Hemispherical Shell," ASME J. Heat Transfer, **124**, pp. 1088–1094.

[9] Hu, L., Schmidt, A., Narayanaswamy, A., and Chen, G., 2004, "Effect of Periodic Structures on Coherence Properties of Blackbody Radiation," ASME J. Heat Transfer, **126**, pp. 786–792.

[10] Xia, X. L., Shuai, Y., and Tan, H. P., 2005, "Calculation Techniques With the Monte Carlo Method in Stray Radiation Evaluation," J. Quant. Spectrosc. Radiat. Transf., **95**, pp. 101–111.

[11] Vujičić, M. R., Lavery, N. P., and Brown, S. G. R., 2006, "View Factor Method Using the Monte Carlo Method and View Factor Sensitivity," Commun. Numer. Methods Eng., **22**, pp. 197–203.

[12] Farmer, J. T., and Howell, J. R., 1998, "Comparison of Monte Carlo Strategies for Radiative Transfer in Participating Media," Adv. Heat Transfer, **31**, pp. 333–429.

[13] Howell, J. R., 1968, "Application of Monte Carlo to Heat Transfer Problems," Adv. Heat Transfer, **5**, pp. 1–52.

[14] Campbell, P. M., 1967, "Monte Carlo Method for Radiative Transfer," Int. J. Heat Mass Transfer, **10**, pp. 519–527.

[15] Vueghs, P., de Koning, H. P., Pin, O., and Beckers, P., 2009, "Use of Geometry in Finite Element Thermal Radiation Combined With Ray Tracing," J. Comput. Appl. Math. (in press).

[16] Sakai, S., and Maruyama, S., 2003, "A Fast Approximated Method for Radiative Exchange for Combined Heat Transfer Simulation," Numer. Heat Transfer, Part B, **44**, pp. 473–487.

[17] Large, M. C. J., Poladian, L., Barton, G. W., and van Eijkelenborg, M. A., 2008, *Microstructured Polymer Optical Fiber*, Springer, New York.

[18] Xue, S.-C., Tanner, R. I., Barton, G. W., Lwin, R., Large, M. C. J., and Poladian, L., 2005, "Fabrication of Microstructured Optical Fibers, Part I: Problem Formulation and Numerical Modeling of Transient Draw Process," J. Lightwave Technol., **23**(7), pp. 2245–2254.

[19] Xue, S.-C., Poladian, L., Barton, G. W., and Large, M. C. J., 2006, "Radiative Heat Transfer in Preforms for Microstructured Optical Fibres," Int. J. Heat Mass Transfer, **50**(7–8), pp. 1569–1579.

[20] Lee, S. H.-K., and Jaluria, Y., 1995, "The Effects of Geometry and Temperature Variations on the Radiative Transport During Optical Fiber Drawing," J. Mater. Process. Manuf. Sci., **3**, pp. 317–331.

[21] Daun, K. J., Morton, D. P., and Howell, J. R., 2005, "Smoothing Monte Carlo Exchange Factors Through Constrained Maximum Likelihood Estimation," ASME J. Heat Transfer, **127**, pp. 1124–1128.

Hervé Thierry Tagne Kamdem
Department of Physics,
Faculty of Sciences,
Green Energy Technology and Heat Transfer,
University of Dschang,
P.O. Box 67,
Dschang, Cameroon

Dominique Doermann Baillis
Centre de Thermique de Lyon (CETHIL),
UMR 5008 CNRS,
Institut des Sciences Appliquées de Lyon (INSA-Lyon),
Université Claude Bernard-Lyon 1,
Bâtiment Sadi Carnot,
69621 Villeurbanne, France
e-mail: dominique.baillis@insa-lyon.fr

Reduced Models for Radiative Heat Transfer Analysis Through Anisotropic Fibrous Medium

Reduced models for radiative heat transfer analysis through anisotropic medium are presented and evaluated. The models include two equivalent heat transfer models through isotropic medium using isotropic or Henyey–Greenstein scattering phase functions with arithmetic or weighted means radiative properties calculated over all incident direction and an anisotropic model with directional radiative properties coupled to an isotropic scattering phase function or directional anisotropically scattering phase function. The pertinence of the models is investigated by solving coupled conduction/radiation heat transfer through a slab of anisotropic fibrous medium with fiber randomly oriented in the plan parallel to the boundaries. Good agreements on heat fluxes and thermal conductivity are obtained for reduced anisotropic models and for reduced equivalent isotropic models with weighted mean radiative properties. [DOI: 10.1115/1.4000994]

Keywords: anisotropic medium, isotropic medium, fibrous, scattering phase function, Henyey–Greenstein, conduction, radiation

1 Introduction

Insulation barriers such as porous ceramics and fibrous media are made of randomly oriented not asymmetric particles. Radiative heat transfer through such highly anisotropic media are complex due to the scattering and absorption coefficients, depending on the direction of the radiation, and the scattering phase function, depending on both the incident radiation and the angle between the incident and the outgoing radiations [1–6]. The particle orientations greatly influence the radiative heat transfer through insulation medium. For example, the thermal conductivity of an insulation medium can be reduced by half if the particles are randomly oriented in plane parallel to the medium boundaries instead of to be randomly oriented in space [7].

Heat transfer through highly anisotropic media such as fibrous medium takes place by conduction through air-filled interstices and the solid material, and by radiation propagating in air and interacting with solid. Thus, to improve the thermal efficiencies of fibrous insulation materials, it is crucial to reduce these heat transfer mechanism. Different concepts for reducing gas conduction have been proposed by many researchers but they are impractical and/or expensive to implement [8]. Consequently, it is preferable to better understand and to control the thermal radiation in order to improve the efficiency of the insulation medium.

The radiative heat transfer models in isotropic insulation materials have been discussed intensively in the literature [8–13]. In these materials, the radiative properties are independent of incident radiation and the radiative heat transfer is described by an integrodifferential equation. Although significant efforts have been made to understand the radiative heat transfer through isotropic insulation medium, simple radiative models are often used by engineers for radiative heat transfer analysis [14]. In this case, the first order of the spherical harmonic method and the diffusion approximation has been largely used due to their simplicity and compatibility with standard methods for the solution of the energy equation [15–19]. However, the lowest spherical harmonic approximation performs poorly in the optically thin limit, while the diffusion approximation describes asymptotically accurately the radiative heat transfer process only in the optically thin limit. Other simple radiative methods commonly used by engineers for radiative heat transfer analysis are the Rosseland diffusion [7,20] and the two flux models [21–24]. Since the radiative transfer through anisotropic materials such as fibrous medium is more complex due to the dependence of the radiative properties on the incident radiation direction and the particle orientation, using previous approximate analytical solution to reduce the complexity of the problem can introduce great error of about 20–60% [7]. These errors can be due to the choice of the equivalent isotropic radiative properties used in the approximate analytic models.

Most researchers prefer to use simple scattering phase function in order to reduce the radiative heat transfer problem. The isotropic and the Henyey–Greenstein scattering phase functions are widely used to simplify the scattering phase function of isotropic semitransparent medium [25–28]. These phase functions depend only on the angle between the incident and scattering radiations, while the phase function of anisotropic media depends on both the incident radiation and the angle between the incident and the scattering radiation. It is then questionable to use these phase functions in modeling radiative heat transfer through anisotropic media such as fibrous media.

The aim of this paper is to study the reduced models for radiative analysis through anisotropic fibrous media. It is interesting to obtain such models for several reasons. First of all, the application of the full solution to analyze heat transfer through anisotropic fibrous insulation is more time consuming and difficult to implement. Then, since the experimental radiative properties are obtained from inverse method using approximate scattering phase functions, such as Henyey–Greenstein phase function, the current results can provide a justification or limitation of using such approximate phase functions.

In this study, we are particularly interested in the use of isotropic and Henyey–Greenstein scattering phase functions to reduce the anisotropic scattering of the medium and/or the equivalent isotropic medium assumption to model radiative heat transfer though anisotropic fibrous insulation. The first results obtained in a previous work [28] tend to show that radiative heat transfer in anisotropic fibrous medium can be modeled by a radiative heat transfer through equivalent isotropic medium that scatters isotropically. In this current paper, we extend the validity of the Henyey–Greenstein scattering phase function usually used for iso-

Contributed by the Heat Transfer Division of ASME for publication in the JOURNAL OF HEAT TRANSFER. Manuscript received August 29, 2009; final manuscript received October 29, 2009; published online May 5, 2010. Assoc. Editor: He-Ping Tan.

tropic media to model scattering phase function of anisotropic medium. The fibers in the medium are randomly oriented in a plane parallel to the boundaries and combined radiation/conduction heat transfer through a slab of anisotropic fibrous medium is investigated.

2 Heat Transfer in Anisotropic Medium

A plane parallel absorbing, emitting, scattering anisotropic medium is considered. The temperatures T_1, T_2 are imposed at boundaries. The governing equations of this coupled conduction/radiation one dimensional problem are the followings.

2.1 The Conduction Equation. The steady state thermal behavior within a homogenous semitransparent medium can be found by solving the energy equation [29]

$$\frac{\partial}{\partial y}\left(k_c \frac{\partial T}{\partial y}\right) = \int_0^\infty \frac{dq_{r,\lambda}}{dy} d\lambda \tag{1}$$

where k_c is the thermal conductivity and $q_{r,\lambda}$ is the spectral radiative heat flux. The boundaries conditions associated with this equation are

$$T(y) = T_1 \quad \text{at} \quad y = 0$$

$$T(y) = T_2 \quad \text{at} \quad y = \ell y \tag{2}$$

2.2 The Radiative Transfer Equation. The radiative problem for an absorbing, emitting, anisotropically scattering plane-parallel anisotropic medium is given by the relation [26]

$$\mu \frac{\partial I_\lambda(y,\Delta)}{\partial y} = \sigma_{a,\lambda}(\Omega) I_{b,\lambda} - \sigma_{e,\lambda}(\Omega) I_\lambda(y,\Delta) + \frac{1}{4\pi}\int_{4\pi} \sigma_{s,\lambda}(\Omega') P_\lambda(\Omega' \to \Omega) I_\lambda(y,\Delta') d\Omega' \tag{3}$$

where $P(\Omega', \Omega)$ is the scattering phase function normalized according to the relations

$$\frac{1}{4\pi}\int_{4\pi} \sigma_s(\Omega) P_\lambda(\Omega', \Omega) d\Omega = \sigma_s(\Omega')$$

$$\frac{1}{4\pi}\int_{4\pi} P_\lambda(\Omega', \Omega) d\Omega = 1 \tag{4}$$

The black boundaries conditions associated with Eq. (3) are given by

$$L(0,\Delta) = L_{\lambda,b}(T_1)$$

$$L(\ell y,\Delta) = L_{\lambda,b}(T_2) \tag{5}$$

with $L_{\lambda,b}(T)$ the blackbody intensity [26]

By integrating the radiative transfer equation (3)overall incident direction $\int_{4\pi} \cdots d\Omega$ and using the normalized phase function conditions (4), the divergence of the radiative heat flux is obtained:

$$\frac{dq_{r,\lambda}}{dy} = 4\pi \overline{\sigma}_{a,\lambda} L_{b,\lambda}[T(y)] - \int_{4\pi} \sigma_{a,\lambda}(\Omega) L_\lambda(y,\Delta) d\Omega \tag{6}$$

where the radiative heat flux and the arithmetic mean absorption coefficient are given, respectively, by

$$q_{r,\lambda} = \int_{4\pi} L_\lambda(y,\Delta) \mu d\Omega \tag{7}$$

$$\overline{\sigma}_{a,\lambda} = \int_{4\pi} \sigma_{a,\lambda}(\Omega) d\Omega / 4\pi \tag{8}$$

The dependence of the radiative properties on the incident direction increases the difficulty in the solution of the coupled conduction/radiation equation and especially for some wavelengths for which the scattering phase function can present high forward peak, oscillatory behavior, and backscattering depending of the direction of the radiation. Different models have been developed to reduce the solution of the radiative transfer equation and can be classified in two groups considering the scattering phase function of the models: isotropic and anisotropic scattering models.

2.2.1 Reduced Isotropic Models. Radiative heat transfer analysis in semitransparent medium is greatly reduced when the isotropic scattering phase function is adopted to simplify the scattering phase function of the medium. Using this phase function required a scaling of the medium radiative properties. The scaling properties can be obtained from the transport approximation if the medium scatters forward, from the scaling group methodology or from an equivalent problem through the use of the P1 approximation [30–32]. For anisotropic medium, three isotropic scaling models can be defined depending on the assumption made on the medium radiative properties [28]

The mean isotropic scaling (MIS) model. In this case, the radiative properties of an equivalent isotropic medium, which scatters isotropically, are assumed to be arithmetic mean over all incident radiation direction of the radiative properties of the anisotropic medium. The extinction and scattering coefficients, and the scattering albedo are defined, respectively, as

$$\overline{\sigma}_e^* = (1 - \overline{\omega g})\overline{\sigma}_e \tag{9}$$

$$\overline{\sigma}_s^* = (1 - \overline{g})\overline{\sigma}_s \tag{10}$$

$$\overline{\omega}^* = \overline{\omega}(1 - \overline{g})/(1 - \overline{\omega g}) \tag{11}$$

where the arithmetic mean absorption, extinction, and scattering coefficients, and albedo and asymmetry mean factors are given, respectively, by

$$\overline{\sigma}_{\{a,e,s\}} = \int_{4\pi} \sigma_{\{a,e,s\}}(\Omega) d\Omega / 4\pi \tag{12}$$

$$\overline{\omega} = \overline{\sigma}_s / \overline{\sigma}_e \tag{13}$$

$$\overline{g} = \int_{4\pi} g(\Omega) d\Omega / 4\pi \tag{14}$$

with $-1 \le g(\Omega) \le 1$ the bias scattering factor or the directional asymmetric factor defined by the relation [25,30]

$$g(\Omega) = \frac{1}{4\pi}\int_{4\pi} P(\Omega, \Theta) \cos\Theta d\Omega_s \tag{15}$$

where $\Omega_s \equiv (\psi, \Theta)$ is the scattering solid angle of coordinates consisting of the azimuthal and the scattering angles, respectively.

The P1 isotropic scaling (P1IS) model. In this case, the radiative properties of the equivalent isotropic medium, which scatter isotropically, are weighted mean over all incident radiation direction of radiative properties of the anisotropic medium

$$\sigma_{e,\mathrm{P1}}^* = \sigma_{eeq}(1 - \omega_{\mathrm{eq}} g_{\mathrm{P1}}) \tag{16}$$

$$\omega_{\mathrm{P1}}^* = \omega_{\mathrm{eq}}(1 - g_{\mathrm{P1}})/(1 - \omega_{\mathrm{eq}} g_{\mathrm{P1}}) \tag{17}$$

with the equivalent radiative properties given as

$$\sigma_{e,\mathrm{eq}} = \int_{4\pi} \sigma_e(\Omega) \mu^2 d\Omega / \int_{4\pi} \mu^2 d\Omega \tag{18}$$

$$\sigma_{s,\mathrm{eq}} = \sigma_{e,\mathrm{eq}} - \overline{\sigma_a}, \quad \overline{\sigma_a} = \int_0^1 \sigma_a(\mu) d\mu \tag{19}$$

$$\omega_{\mathrm{eq}} = \sigma_{s,\mathrm{eq}}/\sigma_{e,\mathrm{eq}} \tag{20}$$

$$g_{\mathrm{eq}} = \int_{4\pi} \sigma_s(\Omega) g(\Omega) \mu^2 d\Omega / \sigma_{s,\mathrm{eq}} \int_{4\pi} \mu^2 d\Omega \tag{21}$$

The directional isotropic scaling (DIS) model. In this case, the radiative properties of the medium are anisotropic and the scaled parameters of the isotropic scattering problem are defined as

$$\sigma_e^*(\Omega') = [1 - \omega(\Omega') g(\Omega')] \sigma_e(\Omega') \tag{22}$$

$$\omega^*(\Omega') = \frac{\omega(\Omega')[1 - g(\Omega')]}{[1 - \omega(\Omega') g(\Omega')]} \tag{23}$$

2.2.2 Reduced Anisotropic Scattering Models. Many approximate functions have been proposed to simplify the scattering phase function of isotropic medium [26,27]. These include the development of the scattering phase function in a series of Legendre polynomials, the delta-M scattering phase, the Henyey–Greenstein phase function, and its combinations. The simplification of the scattering phase function of anisotropic medium has received few attention in the literature probably due to the complex description of the phase function of such medium. In our knowledge, only Heino et al. [33] studied this case. The applicability of Legendre polynomials, the delta-M scattering phase, and combination of Henyey–Greenstein phase function to reduce the scattering function of isotropic medium is a difficult task and requires great computational times in order to calculate all the scattering moments involve in the scattering phase function. To overcome these difficulties, some researchers prefer to approximate the phase function by a simple Henyey–Greenstein scattering phase function because it depends only on one parameter, the asymmetric factor [25–28]. Note that this phase function is very useful in inverse method to determine radiative properties. Therefore, we choose the Henyey–Greenstein phase function to represent the anisotropic scattering behavior. The Henyey–Greenstein scattering phase function is defined by the relation

$$P_{\mathrm{HG}}(\Theta) = \frac{1 - g^2}{(1 + g^2 - 2g \cos\Theta)^{3/2}} \tag{24}$$

with the asymmetric factor defined as [18,26]

$$g = \frac{1}{2} \int_{4\pi} P(\Theta) \cos\Theta d\Omega_s \tag{25}$$

As noted by Lee and Buckius [31], scaling is the process by which two problems that are not in the same class of problems are made to belong to the same class by suitable transformation of variables. Therefore, the scaling processes can concern the anisotropic radiative properties and/or the anisotropic scattering phase function of the medium. In this current section, we propose two reduced scaling isotropic radiative transfer models and an anisotropic radiative transfer model.

The mean anisotropic Henyey–Greenstein model [$\mathrm{HG}(\overline{g})$]. The radiative heat transfer through an anisotropic medium is assumed to be equivalent to a radiative transfer problem through an isotropic medium with mean radiative properties calculated over all directions (Eqs. (12) and (13)) and an anisotropic Henyey–Greenstein scattering phase function of asymmetric factor defined by Eq. (14).

The P1 anisotropic Henyey–Greenstein model [$\mathrm{HG}(g_{\mathrm{P1}})$]. As it was presented in a previous paper [28], the P1 differential equation for anisotropic medium is independent of the incident direction:

$$\frac{d^2 q'}{d\tau'^2} - 3(1 - \omega_{\mathrm{eq}} g_{\mathrm{eq}})(1 - \omega_{\mathrm{eq}}) \tau_{\ell y}^2 q' = 4(1 - \omega_{\mathrm{eq}}) \tau_{\ell y} \left. \frac{dL_b'}{d\tau'} \right|_{\mathrm{AM}} \tag{26}$$

where the dimensionless parameters are defined by

$$\tau' = \tau/\tau_{\ell y} \tag{27}$$

$$\tau_{\ell y} = \sigma_{e,\mathrm{eq}} \ell y \tag{28}$$

If we assume a radiative transfer through an isotropic medium with a Henyey–Greenstein scattering phase function, the P1 radiative differential equation has the same form as Eq. (26). Thus, the relations to scale a radiative heat transfer through an anisotropic medium to a radiative transfer through an equivalent isotropic medium with a Henyey–Greenstein scattering phase functions are

$$(1 - \omega g) \sigma_e \ell y|_{\mathrm{IM}} \equiv (1 - \omega_{\mathrm{eq}} g_{\mathrm{eq}}) \sigma_{e,\mathrm{eq}} \ell y|_{\mathrm{AM}} \tag{29}$$

$$(1 - \omega) \sigma_e \ell y|_{\mathrm{IM}} \equiv (1 - \omega_{\mathrm{eq}}) \sigma_{e,\mathrm{eq}} \ell y|_{\mathrm{AM}} \tag{30}$$

where IM and AM denote the isotropic medium and the anisotropic medium, respectively.

The radiative properties of the equivalent isotropic medium, with Henyey–Greenstein scattering phase function, are therefore

$$\sigma_{e,\mathrm{IM}} = \sigma_{e,\mathrm{eq}} \tag{31}$$

$$\omega_{\mathrm{IM}} = \omega_{\mathrm{eq}} \tag{32}$$

$$g_{\mathrm{IM}} = g_{\mathrm{eq}} = g_{\mathrm{P1}} \tag{33}$$

with the isotropic equivalent properties $\sigma_{e,\mathrm{eq}}$, ω_{eq}, and g_{eq} defined, respectively, by Eqs. (18), (20), and (21).

The directional anisotropic Henyey–Greenstein (DHG) model. We propose to extend the Henyey–Greenstein phase function (Eq. (24)) to an anisotropic medium. We suggest a directional Henyey–Greenstein scattering phase function: the Henyey–Greenstein scattering phase function for each scattering direction with the asymmetry factor equal to the bias scattering factor of the scattering direction,

$$P_{\mathrm{DHG}}(\Omega, \Theta, g) = \frac{1 - g^2(\Omega)}{[1 + g^2(\Omega) - 2g(\Omega)\cos\Theta]^{3/2}} \tag{34}$$

It is obvious that for an isotropic medium, the bias scattering factor is identical for all directions and the directional Henyey–Greenstein scattering phase function is equal to the classical Henyey–Greenstein scattering phase function.

3 Radiative Properties of Fibrous Medium

The knowledge on the radiative properties of anisotropic fibrous medium is usually based on the theory of light scattering by small particles [1,7]. From this theory, the extinction, the scattering, and the absorption coefficients, and the scattering phase function are given, respectively, by

$$\sigma_{\{e,s\},\lambda}(\Omega) = \int_0^\infty \int_{O_f} C_{\{e,s\}}(\Omega, O_f) L_f dO_f dr \tag{35}$$

$$\sigma_{a,\lambda}(\Omega) = \sigma_{e,\lambda}(\Omega) - \sigma_{s,\lambda}(\Omega) \tag{36}$$

$$P_{s,\lambda}(\Omega', \Omega) \frac{\int_0^\infty \int_{O_f} C_{s,\lambda}(\Omega, O_f) p_\lambda(\Omega', \Omega, O_f) L_f dO_f dr}{\int_0^\infty \int_{O_f} C_{s,\lambda}(\Omega', O_f) L_f dO_f dr} \tag{37}$$

where $C_{\{e,s\}}$ the extinction and the scattering cross section are given by the Mie theory [34–36], L_f is the total length of fibers with size comprised between r and $r+dr$, and the scattering phase function of a single fiber is defined as [1,7]

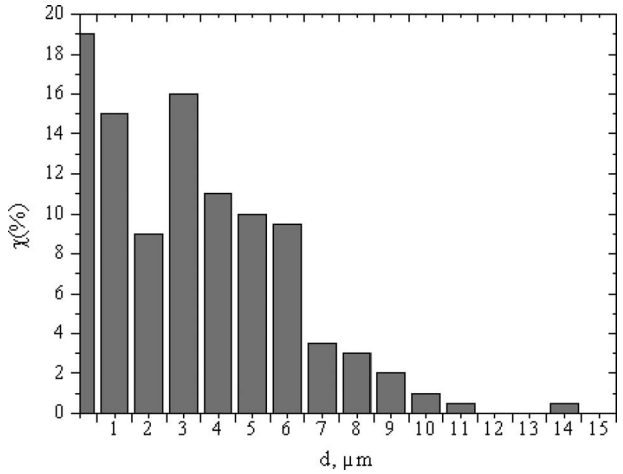

Fig. 1 Size distribution for silica fibers

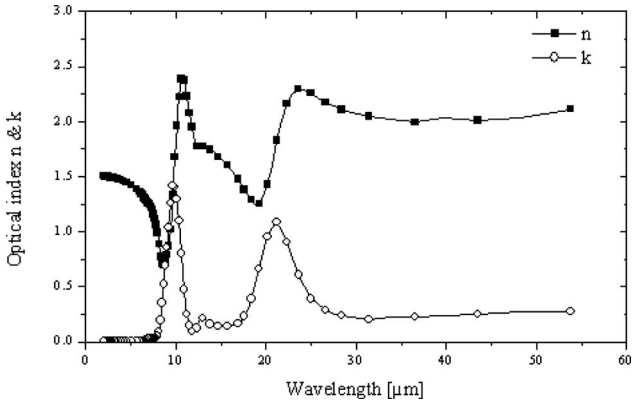

Fig. 2 Optical properties of the silica sample

$$p_\lambda(\phi,\Theta) = \frac{4\lambda i(\Theta,\phi)/\pi^2 C_{s,\lambda}(m\alpha,\phi)}{\sqrt{(1-\cos\Theta)(1+\cos\Theta-2\sin^2\phi)}} \tag{38}$$

where $i(\Theta,\phi)$ is the scattering intensity given by the Mie theory [34–36]. The scattering angle Θ is related to radiation and fiber coordinates in the medium by the relations [1,7]

$$\cos\eta = (\cos\Theta - \sin^2\phi)/\cos^2\phi \tag{39}$$

$$\cos\Theta = \cos\theta\cos\theta' + \sin\theta\sin\theta'\cos(\varphi-\varphi') \tag{40}$$

For fibers randomly oriented in plane parallel to the boundaries, the fiber function orientation and the total fiber length in a unit volume are defined, respectively, as [1,7,21,37]

$$dO_f = \delta(\theta_f - \theta_{fi})d(\varphi_f - \varphi_i)/\pi \tag{41}$$

$$L_f = f_v/\pi r^2 \tag{42}$$

In order to use the approximate models, it is necessary to define the bias scattering of fibrous medium. In a previous paper [28], we found that this parameter is proportional to the bias scattering factor of a single fiber

$$g(\Omega) = \frac{\int_0^\infty\int_{O_f} C_{s,\lambda}(\Omega,O_f)\langle\cos\Theta\rangle L_f(r)dO_f dr}{\int_0^\infty\int_{dO_f} C_{s,\lambda}(\Omega,O_f)L_f(r)dO_f dr} \tag{43}$$

with $\langle\cos\Theta\rangle$ the bias scattering factor of a single fiber [28,38],

$$\langle\cos\Theta\rangle = \frac{2\lambda}{\pi^2 C_{s,\lambda}(\phi)}\int_0^\pi i(\phi,\eta)(\sin^2\phi + \cos^2\phi\cos\eta)d\eta \tag{44}$$

4 Results and Discussion

In this section, the results of steady-state coupled conduction/radiation heat transfer results in anisotropic silica fibrous media using full solution and approximated models are presented. The conduction heat transfer through the silica fibrous insulation medium is described by Eq. (1) where the thermal conductivity is calculated according to the relation [39]

$$k_c = 0.2572T^{0.81} + 0.0527\rho_m^{0.91}(1 + 0.13\times10^{-2}\ \mathrm{T})\ \ \mathrm{mW/mK} \tag{45}$$

The fibers in the medium are randomly oriented in the plane parallel to the boundaries with temperatures $T_1 = 286$ K and $T_2 = 306$ K. The size distribution histogram of fibers in the medium obtained using scanning electron microscopy is given by Fig. 1. The radiative properties from the Mie theory are calculated by using the effective radius [40,41]:

$$r_{32} = \frac{\sum_{i=1}^{N\mathrm{dis}} r_i^3 N_i(r_i)}{\sum_{i=1}^{N\mathrm{dis}} r_i^2 N_i(r_i)} = \sum_{i=1}^{N\mathrm{dis}} r_i\chi_i \tag{46}$$

where $N(r)$ the number of fiber particle per unit volume with radius between r and $r+dr$ is given by the relation

$$N_i(r_i) = \frac{\chi_i f v}{\pi r_i^2} \tag{47}$$

Three silica fibrous samples of thickness 4.0 cm with densities 11.25 kg/m^3, 25 kg/m^3, and 50 kg/m^3 are studied and the silica fiber density is 2520 kg/m^3. The composition of the samples is 60–65% of SiO_2, 14–16% of Na_2O, 7–10% of CaO, 4–7% of B_2O_3, and 2–4% of Al_2O_3 and MgO. The optical properties of these samples (Fig. 2) required to calculate the radiative properties have been supplied by Saint-Gobain industry. In Table 1, the different fibrous samples characteristics are given.

4.1 Anisotropic Silica Medium Radiative Properties. The radiative properties of the silica fibrous medium, the extinction and scattering coefficients, the scattering phase function, and the bias scattering factor, were obtained using the Mie theory. Figures 3 and 4 show the representative behavior of the extinction and scattering coefficients, and the asymmetry factor of equivalent isotropic medium calculated from arithmetic mean and weighted mean. It can be observed that the difference between the two equivalent isotropic mean properties increases with increase wavelength. This implies that the silica fibrous medium is more anisotropic at high wavelengths.

Figures 5–7 illustrate a comparison of the theoretical radiative properties of equivalent isotropic medium and anisotropic medium at wavelength $\lambda = 29.41$ μm. From these figures, great differences on radiative properties between the full Mie model and simplified models can be observed. The presence of backscattering in the scattering phase function of the anisotropic medium for some incident direction can be noted (Fig. 7).

Table 1 Fibrous samples characteristics

Sample	Thickness (cm)	Density (kg/m^3)	Porosity (%)	Effective radius (μm)
Sple1	4.0	11.25	99.55	1.85
Sple2	4.0	25.00	99.01	1.85
Sple3	4.0	50.00	98.02	1.85

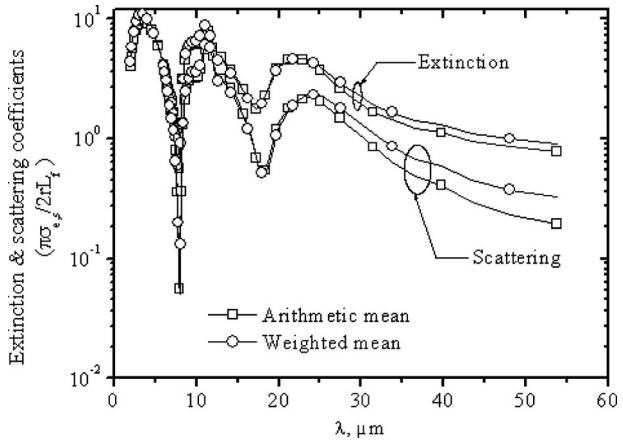

Fig. 3 Extinction and scattering coefficients of equivalent isotropic media

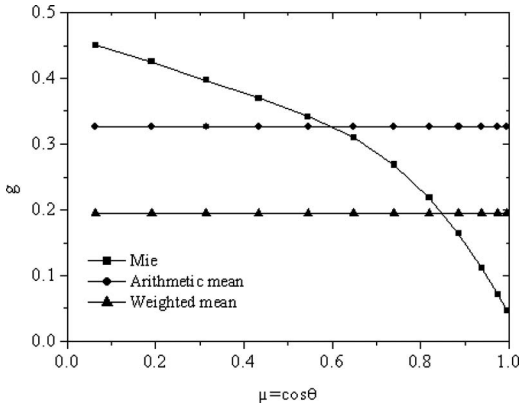

Fig. 6 Bias scattering factor of silica fibrous medium at wavelength $\lambda=29.41$ μm: isotropic medium versus anisotropic medium

4.2 Heat Fluxes in Anisotropic Silica Fibrous Medium. For the three samples, the conduction problem is solved using a tridiagonal-matrix algorithm obtained from a control volume discretization of the spatial domain in 200 unit grid. The radiative heat transfer problems were solved using the discrete ordinate method with the spatial discretization grid of the conduction problem. The fully radiative transfer problem requires high order of discrete ordinates than reduced radiative problems. Sixty directions are used to have the solution of the full problem, while the solution of the reduced models can be obtained with 24 discrete ordinates. These directions and spatial discretization have been used to obtain the heat fluxes in the silica insulation medium.

Figures 8–10 illustrate a comparison between the full solution of coupled conduction/radiative problem in anisotropic medium and the solution obtained for the reduced models. The comparison of the total heat fluxes shows a discrepancy between the full solution and the reduced models based on the equivalent isotropic medium using the arithmetic mean radiative properties. This deviation is due to the difference on the radiative heat fluxes. The relative error between the full solution and the equivalent isotropic reduced models with arithmetic mean radiative properties are greater or equal to 10%. The use of models with higher anisotropic scattering does not induce an amelioration of the accuracy as the difference between equivalent isotropic models using arithmetic mean properties with isotropic and Henyey–Greenstein scattering phase is inferior to than 2%.

A good agreement between the fully radiative solutions, reduced anisotropic models, and reduced equivalent isotropic models using weighted mean properties is observed. The larger relative errors between these models are ≅2% for both reduced models using isotropic or Henyey–Greenstein scattering phase function. The same conclusions can be observed for the two other samples of different densities (Figs. 9 and 10). They confirm that reduced anisotropic models and reduced equivalent isotropic mod-

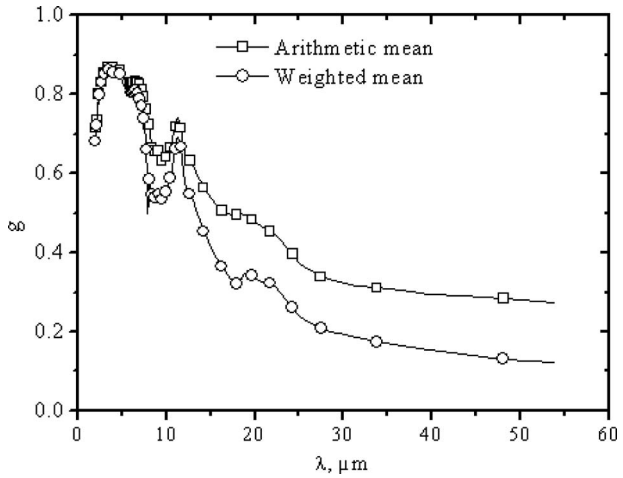

Fig. 4 Asymmetric factor of equivalent isotropic media

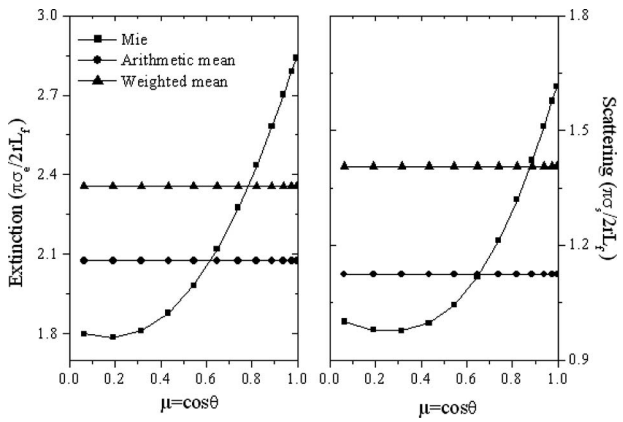

Fig. 5 Extinction and scattering coefficients of silica fibrous medium at wavelength $\lambda=29.41$ μm: isotropic medium versus anisotropic medium

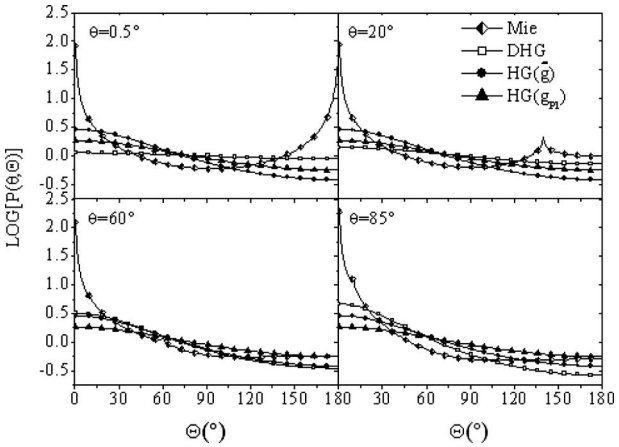

Fig. 7 Scattering phase function of silica fibrous medium at wavelength $\lambda=29.41$ μm: isotropic medium versus anisotropic medium

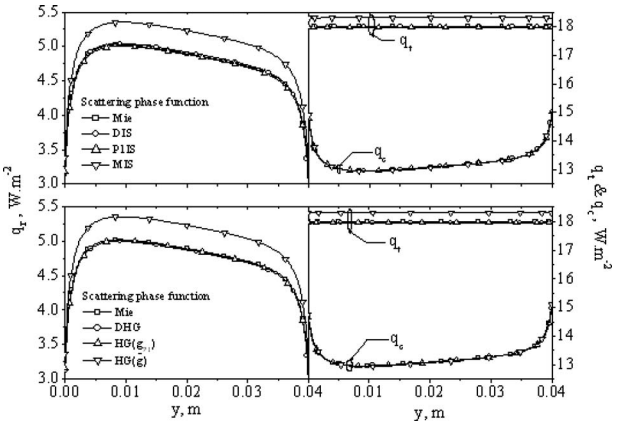

Fig. 8 Heat fluxes of anisotropic silica medium of sample 1: Mie solution versus reduced radiative models

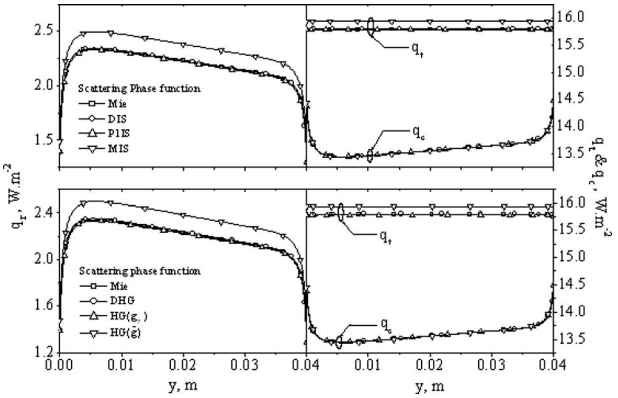

Fig. 9 Heat fluxes of anisotropic silica medium of sample 2: Mie solution versus reduced radiative models

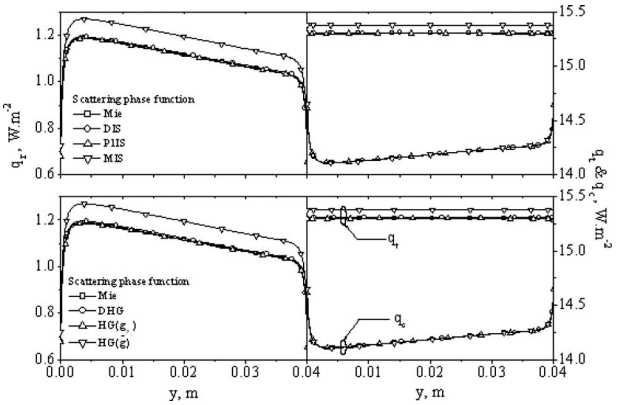

Fig. 10 Heat fluxes of anisotropic silica medium of sample 3: Mie solution versus reduced radiative models

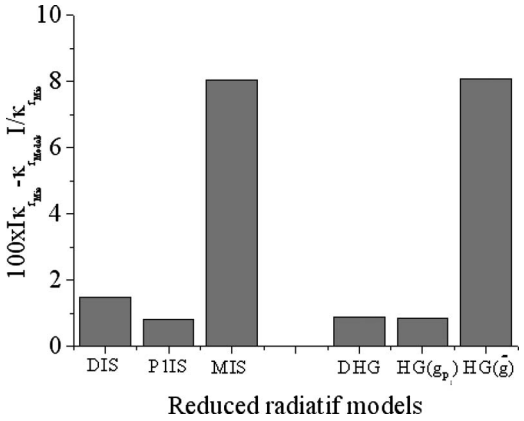

Fig. 11 Relative errors between Mie solution and reduced models on thermal radiative properties of sample 2

els using weighted mean radiative properties are appropriate and allow simplifying the radiative problem in anisotropic fibrous insulation medium.

4.3 Experimental and Theoretical Thermal Conductivities of Anisotropic Silica Fibrous Media. The theoretical "apparent thermal conductivities" are computed and compared with the experimental apparent thermal conductivities obtained from hot plate apparatus. The relative errors between the full solution and approximate models on "thermal radiative conductivities" for sample 2 are given on the histogram of Fig. 11. High errors are observed on the predicted thermal radiative conductivities calculated from equivalent radiative heat transfer models through an isotropic medium with arithmetic mean radiative properties: models MIS and HG($\overline{g}$). The errors are equal or larger than 10%.

The comparisons between the experimental and predicted apparent thermal conductivities are given in Table 2. Good agreement is observed between the experimental and predicted apparent thermal conductivities. At room temperature. radiative transfer is not preponderant and the full and reduced models are appropriate to calculate the apparent thermal conductivities.

5 Conclusion

Thus, this current work show that radiative heat transfer through anisotropic medium can be analyzed using simplified models through anisotropic medium or equivalent isotropic medium with weighted mean radiative properties with isotropic scattering or Henyey–Greenstein anisotropic scattering phase function. The comparisons with the fully radiative heat transfer solution reveal that equivalent models using the arithmetic mean radiative properties are less appropriate to simplify radiative analysis through anisotropic medium. The major results and conclusions of this study concern the following.

Table 2 Comparison between experimental and predicted "apparent thermal conductivities"

	Thermal conductivity (mW/m K)							
		Scattering phase function						
			Isotropic			Henyey–Greenstein		
Sample (porosity)	Expt.	Mie	DIS	P1IS	MIS	DHG	HG(g_{p1})	HG($\overline{g}$)
Sple1(11.25)	40.0	36.11	35.98	35.92	36.58	35.89	35.92	36.59
Sple 2(25.0)	33.3	31.64	31.58	31.55	31.86	31.48	31.55	31.87
Sple 3(50.0)	31.4	30.63	30.61	30.60	30.76	30.68	30.60	30.76

- The applicability of the extension of the Henyey–Greenstein scattering phase function of isotropic medium to anisotropic medium.
- The radiative heat transfer through anisotropic medium can be analyzed by an equivalent radiative heat transfer through isotropic medium with Henyey–Greenstein phase function assuming that equivalent isotropic radiative properties are weighted mean over all incident directions.
- It is also important to note the good agreement between the apparent thermal conductivities predicted by the full solution, the reduced models, and the experimental data at room temperature.

Acknowledgment

The authors wish to acknowledge Saint-Gobain industry, Rantigny, for supplying samples and optical characteristics of the silica fibers. The authors also wish to express their gratitude to Dr. R. Coquard for useful discussion and for his assistance in making the experiments.

Nomenclature

d = fiber diameter
f_v = fiber volume fraction
g = asymmetry factor
I = radiative intensity
I_b = blackbody intensity
k = index of absorption
L = total length of fibers
n = index of refraction
P = phase function
q = radiative heat flux
r = fiber radius
y = thickness, optical depth
HG = Henyey–Greenstein
T = temperatures

Greek Symbols

δ = delta function
ϕ = incident angle
η = fiber azimuth angle
φ = azimuth angle
κ = thermal conductivity
$\mu = \cos\theta$ = direction cosine in y direction,
θ = polar angle
σ = radiative coefficient
σ_b = Stefan–Boltzmann constant
ω = albedo
Ω = ordinate direction
Θ = scattering angle

Superscripts

$-$ = mean variables
* = scaled variable
$'$ = scattering direction

Subscripts

c = conductive
e = extinction
eq = equivalent
r = radiative
s = scattering
t = total
f = fiber
P1 = P1 scaling
1,2 = boundaries of the medium

References

[1] Lee, S. C., 1986, "Radiative Heat Transfer Through a Fibrous Medium: Allowance for Fiber Orientation," J. Quant. Spectrosc. Radiat. Transf., **36**(3), pp. 253–263.
[2] Boulet, P., Jeandel, G., and Morlot, G., 1993, "Model of Radiative Transfer in Fibrous Media-Matrix Method," Int. J. Heat Mass Transfer, **36**(18), pp. 4287–4297.
[3] Asllanaj, F., Jeandel, G., and Roche, J. R., 2001, "Numerical Solution of Radiative Transfer Equation Coupled With Nonlinear Heat Conduction Equation," Int. J. Numer. Methods Heat Fluid Flow, **11**(5), pp. 449–473.
[4] Milandri, A., Asllanaj, F., Jeandel, G., and Roche, J. R., 2002, "Heat Transfer by Radiation and Conduction in Fibrous Media Without Axial Symmetry," J. Quant. Spectrosc. Radiat. Transf., **74**, pp. 585–603.
[5] Zhang, C., Kribus, A., and Ben-Zvi, R., 2002, "Effective Radiative Properties of a Cylinder Array," ASME J. Heat Transfer, **124**(1), pp. 198–200.
[6] Kamdem-Tagne, H. T., 2008, "Etude du transfert thermique dans les milieu poreux anisotropes. Application aux isolants thermiques en fibres de silice," Ph.D. thesis, Institut des Sciences Appliquées de Lyon, Lyon, France.
[7] Lee, S. C., and Cunnington, G. R., 2000, "Conduction and Radiation Heat Transfer in High Porosity Fiber Thermal Insulation," J. Thermophys. Heat Transfer, **14**(2), pp. 121–136.
[8] Tong, T. W., and Tien, C. L., 1980, "Analytical Models for Thermal Radiation in Fibrous Insulations," J. Therm. Insul., **4**, pp. 27–44.
[9] Viskanta, R., and Mengüc, M. P., 1989, "Radiative Transfer in Dispersed Media," Appl. Mech. Rev., **42**(9), pp. 241–259.
[10] Cheng, Q., and Zhou, H.-C., 2007, "The DRESOR Method for a Collimated Irradiation on an Isotropically Scattering Layer," ASME J. Heat Transfer, **129**(5), pp. 634–645.
[11] Baillis, D., and Sacadura, J. F., 2000, "Thermal Radiation Properties of Dispersed Media: Theoretical Prediction and Experimental Characterization," J. Quant. Spectrosc. Radiat. Transf., **67**, pp. 327–363.
[12] Yuen, W. W., 2008, "Definition and Evaluation of Mean Beam Lengths for Applications in Multidimensional Radiative Heat Transfer: A Mathematically Self-Consistent Approach," ASME J. Heat Transfer, **130**(11), p. 114507.
[13] Joseph, D., Perez, P., El Hafi, M., and Cuenot, B., 2009, "Discrete Ordinates and Monte Carlo Methods for Radiative Transfer Simulation Applied to Computational Fluid Dynamics Combustion Modeling," ASME J. Heat Transfer, **131**(5), p. 052701.
[14] Yuen, W. W., and Cunnington, G., 2007, "Radiative Heat Transfer Analysis of Fibrous Insulation Materials Using the Zonal-gef Method," J. Thermophys. Heat Transfer, **21**(1), pp. 105–113.
[15] Dombrovsky, L. A., 1996, "Quartz-Fiber Thermal Insulation: Infrared Radiative Properties and Calculation of Radiative-Conductive Heat Transfer," ASME J. Heat Transfer, **118**, pp. 408–414.
[16] Galaktionov, A. V., Petrov, V. A., and Stepanov, S. V., 1994, "Combined Radiative-Conductive Heat Transfer in High-Temperature Fibrous Insulation of Reusable Orbital Space Vehicles," High Temp., **32**(3), pp. 375–381.
[17] Zverev, V. G., Gol'din, V. D., and Nazarenko, V. A., 2008, "Radiative-Conductive Heat Transfer in Fibrous Heat-Resistant Insulation Under Thermal Effect," High Temp., **46**(1), pp. 108–114.
[18] Modest, M. F., and Yang, J., 2008, "Elliptic PDE Formulation and Boundary Conditions of the Spherical Harmonics Method of Arbitrary Order for General Three-Dimensional Geometries," J. Quant. Spectrosc. Radiat. Transf., **109**, pp. 1641–1666.
[19] Hassanzadeh, P., and Raithby, G. D., 2009, "The Efficient Iterative Solution of the P_1 Equation," ASME J. Heat Transfer, **131**(1), p. 014504.
[20] Doermann, D., and Sacadura, J. F., 1996, "Heat Transfer in Open Cell Foam Insulation," ASME J. Heat Transfer, **118**, pp. 88–93.
[21] Andersen, F. M. B., and Dyrboel, S., 1998, "Modelling Radiative Heat Transfer in Fibrous Materials: The Use of Planck Mean Properties Compared to Spectral and Flux-Weighted Properties," J. Quant. Spectrosc. Radiat. Transf., **60**(4), pp. 593–603.
[22] Jeandel, G., Boulet, P., and Morlot, G., 1993, "Radiative Transfer Through a Medium of Silica Fibres Oriented in Parallel Planes," Int. J. Heat Mass Transfer, **36**(2), pp. 531–536.
[23] Dombrovsky, L., Randrianalisoa, J., and Baillis, D., 2006, "Modified Two-Flux Approximation for Identification of Radiative Properties of Absorbing and Scattering Media From Directional-Hemispherical Measurements," J. Opt. Soc. Am. A, **23**(1), pp. 91–98.
[24] Wu, H., Fan, J., and Du, N., 2007, "Thermal Energy Transport Within Porous Polymer Materials: Effects of Fiber Characteristics," J. Appl. Polym. Sci., **106**, pp. 576–583.
[25] Henyey, L. G., and Greenstein, J. L., 1941, "Diffuse Radiation in the Galaxy," Astrophys. J., **93**, pp. 70–83.
[26] Siegel, R., and Howell, J. R., 2002, *Thermal Radiation Heat Transfer*, 4th ed., Taylor & Francis, London.
[27] Modest, F. M., 2003, *Radiative Heat Transfer*, McGraw-Hill, New York.
[28] Kamdem-Tagne, H. T., and Baillis, D. D., 2005, "Radiative Heat Transfer Using Isotropic Scaling Approximation: Application to Fibrous Medium," ASME J. Heat Transfer, **127**, pp. 1115–1123.
[29] Ozisik, M. N., 1973, *Radiative Transfer and Interactions With Conduction and Convection*, Wiley, New York.
[30] McKellar, H. J., and Box, M. A., 1981, "The Scaling Group of the Radiative Transfer Equation," J. Atmos. Sci., **38**, pp. 1063–1068.
[31] Lee, H., and Buckius, R. O., 1982, "Scaling Anisotropic Scattering in Radiation Heat Transfer for a Planar Medium," ASME J. Heat Transfer, **104**, pp. 68–75.
[32] Guo, Z., and Maruyama, S., 1999, "Scaling Anisotropic Scattering in Radiative Transfer in Three-Dimensional Nonhomogeneous Media," Int. Commun. Heat Mass Transfer, **26**(7), pp. 997–1007.

[33] Heino, J., Arridge, S., Sikora, J., and Somersalo, E., 2003, "Anisotropic Effects in Highly Scattering Media," Phys. Rev. E, **68**, pp. 031908.
[34] Lind, A. C., and Greeenberg, J. M., 1966, "Electromagnetic Scattering for Obliquely Oriented Cylinders," J. Appl. Phys., **37**(8), pp. 3195–3303.
[35] Kerker, M., 1969, *The Scattering of Light and Other Electromagnetic Radiation*, Academic Press, New York.
[36] Dombrovsky, L. A., 1996, *Radiation Heat Transfer in Disperse Systems*, Begell House, New York.
[37] Yamada, J., Kurosaki, Y., and Take-Uchi, M., 1992, "Radiation Transfer in a Fibrous Medium With Fiber Orientation," *Developments in Radiation Heat Transfer*, Vol. 203, ASME, New York, pp. 63–70.
[38] Marschall, J., and Milos, F. S., 1997, "The Calculation of Anisotropic Extinction Coefficients for Radiation Diffusion in Rigid Fibrous Ceramics Insulations," Int. J. Heat Mass Transfer, **40**(3), pp. 627–634.
[39] Banner, D., Klarsfeld, S., and Langlais, C., 1989, "Temperature Dependence of the Optical Characteristic of Semitransparent Porous Media," High Temp. - High Press., **21**, pp. 347–354.
[40] Hansen, J. E., and Travis, L., 1974, "Light Scattering in Planetary Atmospheres," Space Sci. Rev., **16**, pp. 527–610.
[41] Brewster, M. Q., 1992, *Thermal Radiative Transfer and Properties*, Wiley, New York.

Direct Numerical Simulation of Near Field Thermal Radiation Based on Wiener Chaos Expansion of Thermal Fluctuating Current

Sy-Bor Wen
Department of Mechanical Engineering,
Texas A&M University,
3123 TAMU,
College Station, TX 77843-3123

A methodology is proposed, which is capable of determining the near field thermal radiation based on the Wiener chaos expansion. The approach has no explicit constraints on the geometry and temperature distributions of the system and can be easily included with classical electrodynamics simulations. A specific application is made for the near field thermal radiation between two plates and the results are in very good agreement with the classical solutions obtained from Green's function method. Also, by comparing the resulting solutions with the solutions from Green's function method, a new point of view for interpreting the results for the near field thermal radiation in terms of a chaos expansion is provided. [DOI: 10.1115/1.4000995]

Keywords: near field thermal radiation, Wiener chaos expansion, fluctuation-dissipation theory, thermal fluctuating current

1 Introduction

Following the dramatic progress of nanoscience and nanotechnology, devices can have characteristic lengths, which are much shorter than the characteristic wavelength of thermal radiation. As a result, evanescent waves and wave interference become important in thermal radiation, which are not considered in the traditional ray based radiative thermal analysis. In order to determine nanoscale radiative heat transfer in the near field [1–11] or nanoscale [12–18] thermal radiation, analyses have been proposed and they represent an important area in thermal science. In the near field thermal radiation analysis, thermal radiation is considered as electromagnetic waves rather than based on particle features (i.e., photons) as in ray analysis. Therefore, the transport of the near field thermal radiation can be described by Maxwell's equations [19], which includes evanescent waves and wave interference. It has been shown that the near field thermal radiation can result in a large enhancement in energy transport compared with large scale thermal radiation. Also, coherent and directional thermal radiation can be achieved with well organized nanostructures [20,21].

Early work on the near field thermal radiation can be traced to Rytov's early work for radiophysics in 1989 [22], which relates the random thermal fluctuating currents inside a source to the emitted radiation. In Rytov's analysis, the radiative heat flux is obtained from Poynting vectors by solving Maxwell's equations with random thermal fluctuating currents as source terms in Ampere's circuit equation. The amplitude of random thermal fluctuating currents is determined from the fluctuation-dissipation theorem as a function of temperature [1,3,12,18]. Analyses starting from Rytov's approach have been successful in analyzing the near field thermal radiation with different materials. Most of these analyses consider the near field thermal radiation between two planes or two spheres for which closed-form dyadic Green's functions of the electric field are available. The existence of analytical expression of dyadic Green's function of the electric field for the geometry considered is a prerequisite for Rytov's approach. Analytical forms of dyadic Green's functions do not exist for general geometric configurations. In order to study the near field thermal radiation for complex nanodevices, a more general near field thermal radiation analysis methodology without explicitly evaluating dyadic Green's functions of the entire nanodevice should be developed.

Because of the strong electromagnetic wave behavior for the near field thermal radiation, numerical methods for the propagation of electromagnetic field (e.g., finite different time domain method (FDTD), finite different frequency domain method (FDFD), and so on) are potentially alternative methods for simulating the near field thermal radiation without explicitly involving dyadic Green's functions of the electric field. Compared with classical electrodynamics simulations designed for coherent radiation situations [23], a simulation for thermal radiation with Maxwell's equations should also be able to determine incoherent randomly thermal fluctuating currents and the resulting incoherent thermal radiation from different locations. For studying the spatially incoherent current sources, any two point sources in the material, which cause thermal radiation, should radiate independently of each other. This definition by itself can be used as the direct technique for determining the spatially incoherent thermal sources [24]. In direct analysis, zero correlation between the contributions from any two thermal current point sources can be achieved by separately analyzing the structure with each point source and adding the individual contributions for the total thermal radiation intensity [25]. While this technique accurately analyzes the incoherent source, it is very time consuming because it requires one simulation of the entire structure for each point source at each wavelength considered. The simulation time can be unacceptably long even for a simple near field thermal radiation configuration and no result has been published based on the direct analysis to the author's knowledge.

In this study, an alternative method, which can efficiently determine the near field thermal radiation, is proposed by first obtaining the eigenmodes of randomly fluctuating thermal currents

Contributed by the Heat Transfer Division of ASME for publication in the JOURNAL OF HEAT TRANSFER. Manuscript received October 1, 2009; final manuscript received November 10, 2009; published online May 5, 2010. Review conducted by He-Ping Tan.

in the medium using the Wiener chaos expansion (WCE) method [24,26,27]. The net near field thermal radiation is equal to the summation of the thermal radiation resulting from all of the different eigenmodes of randomly fluctuating thermal currents determined by solving the corresponding Maxwell equations. In addition to $>\sim 6$ orders of magnitude improvement over the direct numerical simulation of the near field thermal radiation, numerical simulations based on the eigenmodes of randomly fluctuating thermal currents can partially recover the form of the corresponding analytical solutions if they are available. Sections 2 and 3 give definitions of the eigenmodes of randomly fluctuating thermal currents and the techniques for obtaining them with the WCE. Then, a specific case, namely, the near field thermal radiation between two closely separated plates, is studied. Numerical simulation for the near field thermal radiation between two closely separated plates based in the eigenmodes of the near field thermal radiation is included along with a comparison with analytical solutions.

2 Theory

2.1 Wiener Chaos Expansion for Stochastic Maxwell's Equation. For steady-state thermal radiation of a specified wavelength, propagation of the associated electromagnetic waves is described by electromagnetic theory with the four quantities $\vec{E}$, $\vec{D}$, $\vec{B}$, and $\vec{H}$ (where $\vec{E}$ is the electric field, $\vec{D}$ is the electric displacement, $\vec{B}$ is the magnetic induction, and $\vec{H}$ is the magnetic field). Time harmonic Maxwell's equations provide relations among the above four quantities as follows [9,10]:

$$\nabla \cdot \vec{D} = 0 \tag{1}$$

$$\nabla \cdot \vec{B} = 0 \tag{2}$$

$$\nabla \times \vec{E} = -j\omega\mu\vec{H} \tag{3}$$

$$\nabla \times \vec{H} = j\omega\varepsilon\vec{E} + \vec{J}_{\text{thermal}} \tag{4}$$

where ω is the specific frequency, ε is the dielectric constant, and $\vec{J}_{\text{thermal}}$ is the random thermal fluctuating current due to thermal induced fluctuation.

A thermal fluctuating current $\vec{J}_{\text{thermal}}$ occurs in a material when the temperature is greater than 0 K [14,18]. Although the mean value of the thermal fluctuating current is zero (i.e., $\langle \delta j_j(\vec{r},\omega)\rangle = 0$), the autocorrelation of the fluctuating current is not zero, which produces net emission from the material. The autocorrelation function of the thermal fluctuating current can be expressed in terms of the dielectric constant of a material according to the fluctuation-dissipation theorem (in the frequency domain) [3,12,18]

$$\langle J_j(\vec{r},\omega)J_k^*(\vec{r},\omega)\rangle = J(\omega)^2 = \frac{\omega\varepsilon_0}{\pi}\varepsilon''\Theta\delta(\omega-\omega')\delta(\vec{r}-\vec{r}')\delta_{jk} \tag{5}$$

where $\Theta = \hbar\omega/[\exp(\hbar\omega/k_BT_1)-1]$, ε'' is the imaginary part of the dielectric function of the material, ε_o is the permittivity of vacuum, $\hbar$ is the reduced Planck constant, k_B is the Boltzmann constant, and δ_{jk} is the Kronecker delta. The spatially incoherent fluctuating thermal current source, compare with Eq. (5), results in spatially incoherent electromagnetic waves, which is an important characteristic of thermal radiation. A direct method to determine the incoherent emission is to numerically solve the emission of a nanodevice from each location at each specified wavelength by freezing the thermal current of the radiative material but the position of interest. By repeating all of the positions of the nanodevice, the simulation, and the summing up of the radiation intensities, the total thermal emission and energy transport of within the nanodevice can be determined (direct method). The number of simulations for each specified thermal wavelength is equal to the number of spatial grids of the simulation in the direct method. For the near field thermal radiation, large numbers of spatial grids are required to obtain the continuous near field thermal radiation. For example, $\sim 10^5$ grids are used in Sec. 2.2 in order to simulate the near field thermal radiation between two infinite plates. The large number of calculations is a shortcoming of the detailed direct method in the simulation of the near field thermal radiation.

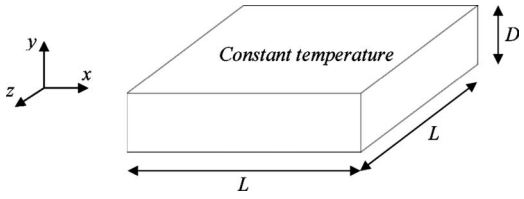

Fig. 1 Square plate used for the eigenmode $\phi_{ijk}(\vec{r})$ analysis

To reduce the simulation time and to provide insights for the phenomena, the WCE method is used to determine the spatially incoherent thermal radiation. To proceed, $\vec{J}_{\text{thermal}}$ is first assumed to be a separable function of space and time

$$\vec{J}_{\text{thermal}} = dW(\vec{r})V(t) \tag{6}$$

where $V(t)$ is a deterministic function representing the time variation in the thermal current source and $dW(\vec{r})$ is the derivative of a white noise signal representing the independent spatial randomness in the $\vec{r}$ direction. For the steady-state near field thermal radiation, $V(t)$ is a constant that is equal to J_ω and is determined from Eq. (5).

According to the WCE theorem [24,26,27], by choosing any orthogonal basis function $\phi_{ijk}(\vec{r})$ (e.g., the Fourier series basis function), a set of independent standard Gaussian random variables ξ_i can be introduced such that

$$\xi_{ijk} = \int_0^{\vec{r}} \phi_{ijk}(\vec{r})dW(\vec{r}) \quad i,j,k = 1,2,\ldots, \tag{7}$$

with

$$dW(\vec{r}) = \sum_i \sum_j \sum_k \xi_{ijk}\phi_{ijk}(\vec{r})$$

and $\phi_{ijk}(\vec{r})$ designated as the eigenmode of the random thermal fluctuating current. As a result, the random fluctuating thermal current can be expressed as

$$\vec{J}_{\text{thermal}} = \left[J_\omega \sum_i \sum_j \sum_k \xi_{ijk}\phi_{ijk}(\vec{r})\right]\hat{I}, \quad \hat{I} = \hat{x}+\hat{y}+\hat{z} \tag{8}$$

Because the expected value $\langle \xi_{ijk}\xi_{i'j'k'}\rangle = \delta_{ii'}\delta_{jj'}\delta_{kk'}$, the contributions of each eigenmode of the random thermal fluctuating current are independent. Therefore, when the random thermal fluctuating current is decomposed into its eigenmode $\phi_{ijk}(\vec{r})$ and then substituted into Eq. (4), the original stochastic partial differential equation (PDE) is reduced to a set of deterministic PDEs. The total near field thermal radiation intensity is the sum of the radiation intensities from each eigenmode of the random thermal fluctuating current.

2.2 Eigenmode $\phi_{ijk}(\vec{r})$ for the Random Thermal Fluctuating Current Within a Square Plate of Finite Thickness and Uniform Temperature. In this section, the eigenmode $\phi_{ijk}(\vec{r})$ for a random thermal fluctuating current within a square plate of finite thickness D and constant temperature (Fig. 1) is studied. Then, in Sec. 2.3, the analysis is expanded to obtaining eigenmode $\phi_{ijk}(\vec{r})$ for a random thermal fluctuating current of a plate with thickness D but infinite in the x and z directions of the infinitely large. The eigenmode $\phi_{ijk}(\vec{r})$ for a random thermal fluctuating current within an infinite plate of finite thickness is the basis for comparing the

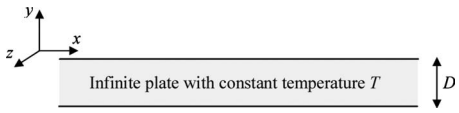

Fig. 2 Geometric of the infinite plane used for the eigenmode $\phi_{ijk}(\vec{r})$ analysis. The size of the plate is not limited in both the *x* and *z* directions.

WCE method proposed in this study with existing analytical solution from dyadic Green's functions.

Sets of sinusoidal orthonormal basis functions are used for the WCE in the *x*, *y*, and *z* directions. For the *y* direction expansion, the plate has a finite thickness *D* and a Fourier cosine series is applied to expand the fluctuation current in the *y* directions ($0 \le y \le D$). From Ref. [23]

$$\phi_0(y) = \frac{1}{\sqrt{D}}$$

$$\phi_l(y) = \sqrt{\frac{2}{D}}\cos\left[\frac{l\pi y}{D}\right] \quad l = 1,2,3,\ldots, \tag{9}$$

For the *x* direction expansion, the orthonormal complex Fourier series is applied to expand the fluctuation current in the *x* direction ($-L/2 \le x \le L/2$)

$$\phi_0(x) = \frac{1}{\sqrt{L}}$$

$$\phi_m(x) = \sqrt{\frac{2}{L}}\exp\left[\frac{i2m\pi x}{L}\right] \quad m = \pm 1, \pm 2, \pm 3, \ldots, \tag{10}$$

Similarly, eigenmodes for the random thermal fluctuating current in the *z* direction ($-L/2 \le z \le L/2$) are expressed as

$$\phi_0(z) = \frac{1}{\sqrt{L}}$$

$$\phi_n(z) = \sqrt{\frac{2}{L}}\exp\left[\frac{i2n\pi z}{L}\right] \quad n = \pm 1, \pm 2, \pm 3, \ldots, \tag{11}$$

The eigenmode of the random thermal fluctuating current of the entire square plate is a product of the eigenmodes in the *x*, *y*, and *z* directions, and can be expressed as $\phi_{lmn}(x,y,z) = \phi_l(y)\phi_m(x)\phi_n(z)$. The set of deterministic PDEs to be solved for obtaining the total thermal radiation within the square plate are

$$\nabla \cdot \vec{D}_{lmn} = 0$$

$$\nabla \cdot \vec{B}_{lmn} = 0$$

$$\nabla \times \vec{E}_{lmn} = -j\omega\mu\vec{H}_{lmn} \tag{12}$$

$$\nabla \times \vec{H}_{lmn} = j\omega\varepsilon\vec{E}_{lmn} + J_\omega\phi_{lmn}\hat{I}$$

The radiation intensity due to each eigenmode is the Poynting vector [28]

$$\vec{S}_{lmn}(x,y,z) = \tfrac{1}{2}\mathrm{Re}(\vec{E}_{lmn} \times \vec{H}_{lmn}^{\,*}) \tag{13}$$

2.3 Eigenmode $\phi_{ijk}(\vec{r})$ for the Random Thermal Fluctuating Current Within an Infinite Plate of Finite Thickness and Constant Temperature. Starting with Eqs. (10)–(12), the product of the eigenmodes of the random thermal fluctuating current in all directions (Fig. 2) can be expended as follows when $L \to \infty$:

$$\phi_{0K_xK_z} = \frac{1}{\pi\sqrt{D}}\exp(iK_x x)\exp(iK_z z)$$

$$\phi_{lK_xK_z} = \frac{1}{\pi}\sqrt{\frac{2}{D}}\cos\left[\frac{l\pi y}{D}\right]\exp(iK_x x)\exp(iK_z z) \quad l = 1,2,3,\ldots, \tag{14}$$

with $K_x = 2\pi m/L$, $K_z = 2\pi n/L$. To evaluate the near field thermal radiation intensity at a specified wavelength and temperature $W(\omega)$, Eq. (12) has to be solved again to obtain the Poynting vectors $\vec{S}(\phi_{lK_xK_z})$ for different eigenmodes $\phi_{lK_xK_z}$. Then

$$\vec{W}(\omega) = \sum_{l=0}^{\infty}\int_{-\infty}^{\infty}\int_{-\infty}^{\infty}\vec{S}(\phi_{aK_xK_z})dK_x dK_z \tag{15}$$

From Eq. (14), the product of eigenmodes in the *x* and the *z* axes yields (multiplier and multiplicand have the same format)

$$\exp(iK_x x)\exp(iK_z z) = \exp[i(K_x x + K_z z)] = \exp(iKr) \tag{16}$$

Thus, the combined $\exp(iK_x x)\exp(iK_z z)$ modes contribute the same amount of thermal radiation as pure separate eigenmodes modes in the *x* and *z* directions with $K = \sqrt{K_x^2 + K_z^2}$ and $r = (K_x/\sqrt{K_x^2 + K_z^2})x + (K_z/\sqrt{K_x^2 + K_z^2})z$.

Thus, the eigenmodes of the thermal fluctuating current for an infinite plate of finite thickness and constant temperature become

$$\phi_{0K} = \frac{1}{\pi\sqrt{D}}\exp(iKr)$$

$$\phi_{lK} = \frac{1}{\pi}\sqrt{\frac{2}{D}}\cos\left[\frac{a\pi y}{D}\right]\exp(iKr) \quad l = 1,2,3,\ldots, \tag{17}$$

The set of deterministic PDEs to be solved for obtaining the total thermal radiation in the plate are

$$\nabla \cdot \vec{D}_{lK} = 0$$

$$\nabla \cdot \vec{B}_{lK} = 0$$

$$\nabla \times \vec{E}_{lK} = -j\omega\mu\vec{H}_{lK} \tag{18}$$

$$\nabla \times \vec{H}_{lK} = j\omega\varepsilon\vec{E}_{lK} + J_\omega\phi_{lK}\hat{I}$$

The radiation intensity due to each eigenmode is the Poynting vector

$$\vec{S}_{lK}(x,y,z) = \tfrac{1}{2}\mathrm{Re}(\vec{E}_{lK} \times \vec{H}_{lK}^{\,*}) \tag{19}$$

The corresponding thermal radiation intensity is

$$\vec{W}(\omega) = \sum_{l=0}^{\infty}\int_0^{\infty} 2\pi\vec{S}(\phi_{lK})KdK = \int_0^{\infty}\left[2\pi\sum_{l=0}^{\infty}\vec{S}(\phi_{lK})\right]KdK \tag{20}$$

3 Results and Discussion

The WCE method for the near field thermal radiation simulation is proposed to determine heat transfer between two closely separated infinite plates (confer Fig. 3). The 2D FDFD method [29–32] is used to solve Maxwell's equations for different eigenmodes of the random thermal fluctuating current, as given in Eq. (16).

It is noted that *s* polarization radiation is induced by the *z* direction random thermal fluctuating current and *p* polarization radiation is induced by the *x* and *y* directions randomly thermal fluctuating currents.

An analytical solution exists for radiative heat transfer between two semi-infinite plates (Fig. 4) [13,14,18]

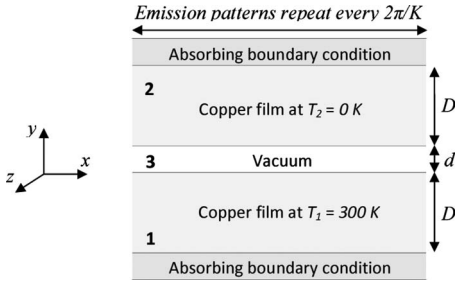

Fig. 3 Geometry for the FDFD simulation for the near field thermal radiation under a specified wave number *K* and an eigenmode of the random thermal fluctuating current ϕ_{lK}. *D* =150 nm, *d*=10 nm, infinite length.

$$W(T_1,T_2) = \frac{4}{\pi^2}\int_0^\infty [\Theta(\omega,T_1)-\Theta(\omega,T_2)]d\omega \int_0^\infty |e^{i\gamma_3 d}|^2 \times \left[\underbrace{\frac{|\gamma_3|^2}{|1-r_{31}^s r_{32}^s e^{2\gamma_3 di}|^2}\frac{\mathrm{Re}(\gamma_1)\mathrm{Re}(\gamma_2)}{|(\gamma_3+\gamma_1)(\gamma_3+\gamma_2)|^2}}_{s \text{ polarized radiation}} + \underbrace{\frac{|\varepsilon_3|^2|\gamma_3|^2}{|1-r_{31}^p r_{32}^p e^{2\gamma_3 di}|^2}\frac{\mathrm{Re}(\varepsilon_1\gamma_1^*)\mathrm{Re}(\varepsilon_2\gamma_2^*)}{|(\varepsilon_1\gamma_3+\varepsilon_3\gamma_1)(\varepsilon_2\gamma_3+\varepsilon_3\gamma_2)|^2}}_{p \text{ polarized radiation}} \right] KdK \tag{21}$$

where r_{ij}^s and r_{ij}^p denote the Fresnel reflection coefficients between region *i* and *j*, for *s* and *p* polarizations, and $\gamma_j=\sqrt{(\varepsilon_j\omega^2/c^2-K^2)}$ [4,18]. The spectral emission power per unit wave number *K* can be obtained from Eq. (21) as

$$W(T_1,T_2,\omega,K) = W(T_1,T_2,\omega,K)_{s \text{ polarization}} + W(T_1,T_2,\omega,K)_{p \text{ polarization}}$$

with

$$W(T_1,T_2,\omega,K)_{s \text{ polarization}} = \frac{4}{\pi^2}[\Theta(\omega,T_1)-\Theta(\omega,T_2)] \times |e^{i\gamma_3 d}|^2 \frac{|\gamma_3|^2}{|1-r_{31}^s r_{32}^s e^{2\gamma_3 di}|^2}\frac{\mathrm{Re}(\gamma_1)\mathrm{Re}(\gamma_2)}{|(\gamma_3+\gamma_1)(\gamma_3+\gamma_2)|^2}$$

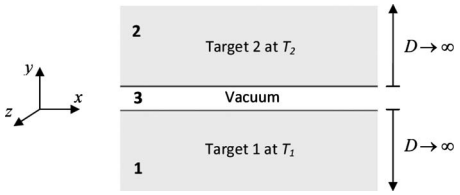

Fig. 4 Geometry for the thermal radiation described by an analytical solution with Green's function method

$$W(T_1,T_2,\omega,K)_{p \text{ polarization}} = \frac{4}{\pi^2}[\Theta(\omega,T_1)-\Theta(\omega,T_2)] \times |e^{i\gamma_3 d}|^2 \frac{|\varepsilon_3|^2|\gamma_3|^2}{|1-r_{31}^p r_{32}^p e^{2\gamma_3 di}|^2}\frac{\mathrm{Re}(\varepsilon_1\gamma_1^*)\mathrm{Re}(\varepsilon_2\gamma_2^*)}{|(\varepsilon_1\gamma_3+\varepsilon_3\gamma_1)(\varepsilon_2\gamma_3+\varepsilon_3\gamma_2)|^2} \tag{22}$$

The solution between plates of semi-infinite thickness (confer Fig. 4) provides a standard for comparison with the numerical simulation (confer Fig. 3) whenever the optical thicknesses of the plates are large (optically thick).

Comparing Eq. (20) with the analytical solution Eq. (21), it is manifested that both solutions involve integration over the wave number *K*. In the WCE expression, the sinusoidal eigenmode of the thermal fluctuating currents in the *x*-*z* plane is specified with a wave number *K* in the *x*-*z* direction (confer Eq. (16)). The sinusoidal plane current source, based on the classical electrodynamics theory [28], generates plane waves with a wave number *K* in the *x*-*z* direction. Summing the transmission of the resulting plane waves with different wave numbers in the *y* direction (i.e., carrying out the summation within the bracket of Eq. (20)) should recover the analytical solution Eq. (22) [33], i.e.,

$$W(T_1,T_2,\omega,K) = \left[2\pi \sum_{l=0}^{\infty} \bar{S}(\phi_{lK}) \right]$$

Thus, even starting from different approaches with different points of view (i.e., the Green's function method versus the WCE expansion), both approaches yield the same result. The equality provides the following relation (it is also obvious by comparing Eq. (20) with Eq. (22)):

$$\underbrace{2\pi\sum_{l=0}^{\infty} S_y(\phi_{lK})_{j_z}}_{\text{using WCE}} = \underbrace{\frac{4}{\pi^2}[\Theta(\omega,T_1)-\Theta(\omega,T_2)]|e^{i\gamma_3 d}|^2 \frac{|\gamma_3|^2}{|1-r_{31}^s r_{32}^s e^{2\gamma_3 di}|^2}\frac{\mathrm{Re}(\gamma_1)\mathrm{Re}(\gamma_2)}{|(\gamma_3+\gamma_1)(\gamma_3+\gamma_2)|^2}}_{\text{using dyadic Green's function}}$$

$$\underbrace{2\pi\sum_{l=0}^{\infty} S_y(\phi_{lK})_{j_x \& j_y}}_{\text{using WCE}} = \underbrace{\frac{4}{\pi^2}[\Theta(\omega,T_1)-\Theta(\omega,T_2)]|e^{i\gamma_3 d}|^2 \frac{|\varepsilon_3|^2|\gamma_3|^2}{|1-r_{31}^p r_{32}^p e^{2\gamma_3 di}|^2}\frac{\mathrm{Re}(\varepsilon_1\gamma_1^*)\mathrm{Re}(\varepsilon_2\gamma_2^*)}{|(\varepsilon_1\gamma_3+\varepsilon_3\gamma_1)(\varepsilon_2\gamma_3+\varepsilon_3\gamma_2)|^2}}_{\text{using dyadic Green's function}} \tag{23}$$

Equation (23) is used to compare the results from the proposed WCE approach with the analytical solution. The following condition is examined: thicknesses of upper and lower planes *D* are 150 nm. The space between the two plates *d* is 10 nm. Yee's grid [23] is applied in the simulation with $\Delta x=2\pi/(50K)$ nm and $\Delta y=0.25$ nm. It is noted that the grid dimension in the *x* direction is adjustable because 20–50 divisions of a wave period are sufficient for most electrodynamics simulations [23]. The plate temperatures

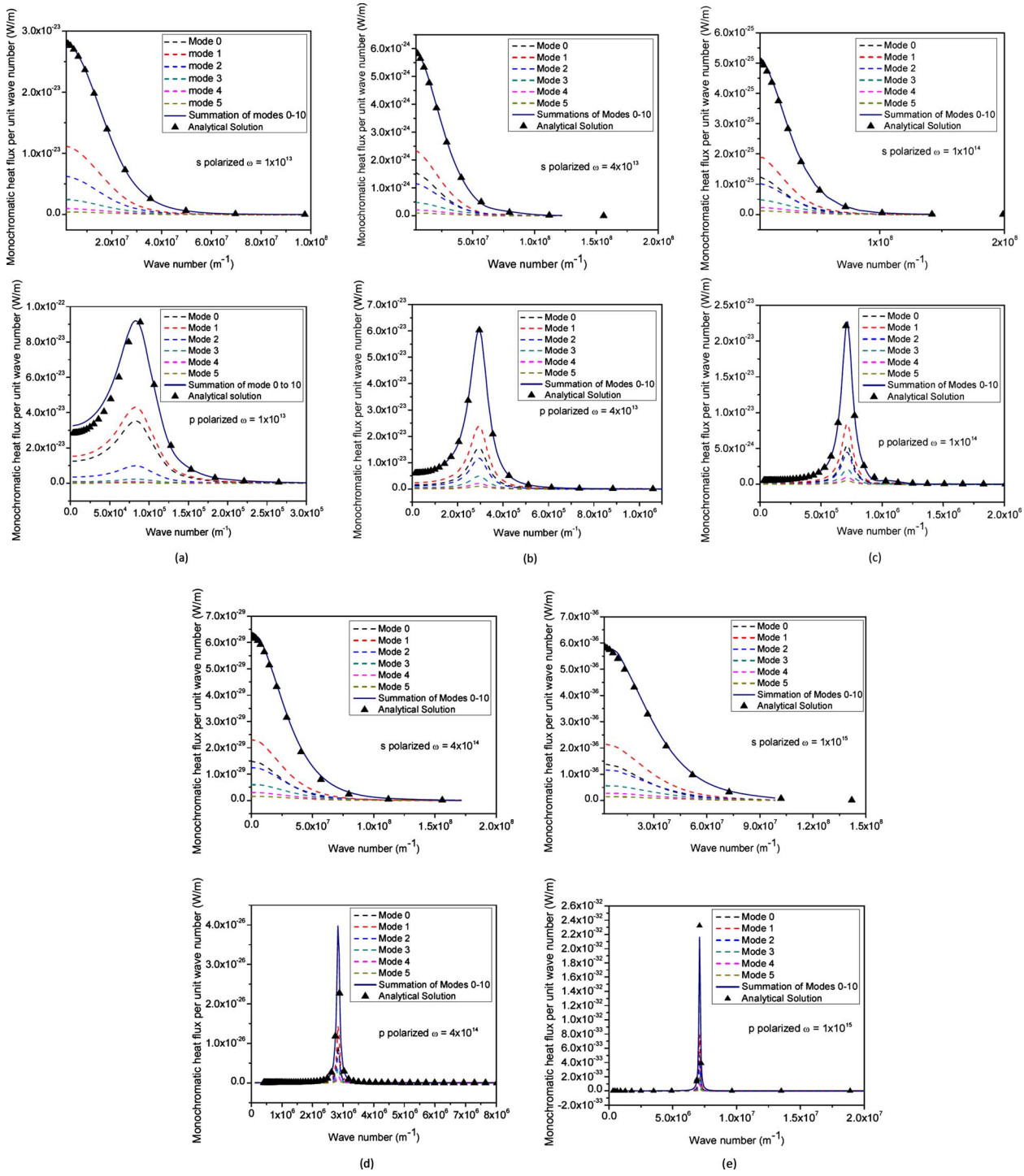

Fig. 5 Comparison between WCE (simulated) and dyadic Green's function (analytic) approaches for the near field monochromatic *S* and *P* polarized thermal emission intensities per unit wave number in the *x-z* plane between two thin gold plates (150 nm) with a separation distance of 10 nm when (*a*) $\omega=10^{13}$ rad/s, (*b*) $\omega=4\times10^{13}$ rad/s, (*c*) $\omega=10^{14}$ rad/s, (*d*) $\omega=4\times10^{14}$ rad/s, and (*e*) $\omega=10^{15}$ rad/s

are 300 K and 0 K (confer Fig. 3). The preconditioned generalized minimal residual method (GMRES) [34] is adopted to solve the large sparse linear system resulting from the FDFD simulation. Gold is selected as the plate material with its dielectric function described by the Drude model as

$$\varepsilon'(\omega) = 1 - \frac{\omega_p^2}{\Gamma^2 + \omega^2}, \quad \varepsilon''(\omega) = \frac{-\omega_p^2\Gamma}{\omega(\Gamma^2 + \omega^2)} \tag{24}$$

where $\omega_p = 1.71\times10^{16}$ rad/s and $\Gamma = 4.05\times10^{13}$ rad/s [35].

The numerical results are shown in Figs. 5(*a*)–5(*e*) and 6 are in very good agreement with the analytical solution for the monochromatic radiation intensity distributions in *s* and *p* polarizations for different wave numbers *K* (Figs. 5(*a*)–5(*e*)) along with the total spectral radiation intensity for different ω (Fig. 6). It is also found from Figs. 5(*a*)–5(*e*) that 5–10 eigenmodes in the *y* direction are sufficient to obtain the converged spectral radiation intensity (i.e., additional higher order eigenmodes provides $<0.1\%$ variation in the calculated results) in *s* and *p* polarizations under

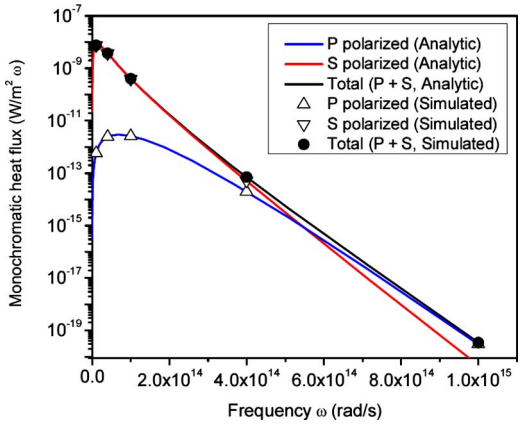

Fig. 6 Comparison between WCE (simulated) and dyadic Green's function (analytic) approaches for the near field *S* and *P* polarized along with total thermal emission intensities between two thin gold plates (150 nm) with a separation distance of 10 nm under different frequencies

different wave number K. Note that ~4 CPU hours (Intel Pentium 4 2.8 GHz single core) is required for simulating each monochromatic radiation intensity distribution presented in Figs. 5(*a*)–5(*e*).

The difference between the numerical and analytical results in the emission distribution in K domain for low emission frequencies ($<=10^{13}$ rad/s) at low wave numbers is related to the thickness D of the plate. The analytical solution is valid for semi-infinitely thick plates. However, the plate thickness D utilized in the simulation is only 150 nm, which is not sufficient to approximate semi-infinite plates especially for lower frequencies when the absorption coefficient of EM waves is reduced (i.e., optical thin). When the plate thickness is doubled from 150 nm to 300 nm, the differences between the numerical and analytical results are significantly reduced (Figs. 5(*a*) and 7). However, it is noted that more eigenmodes are required for an accurate simulation when the plates are thicker. Deviations between the results from WCE and dyadic Green's function method were also observed at high frequencies ($>=10^{15}$ rad/s, Fig. 5(*e*)). Deviations at high frequencies are mainly due to the spatial steps utilized in the simulation. Much smaller steps are required for simulating high frequency behaviors of thermal radiation because of the reduction in EM wavelengths at higher frequencies.

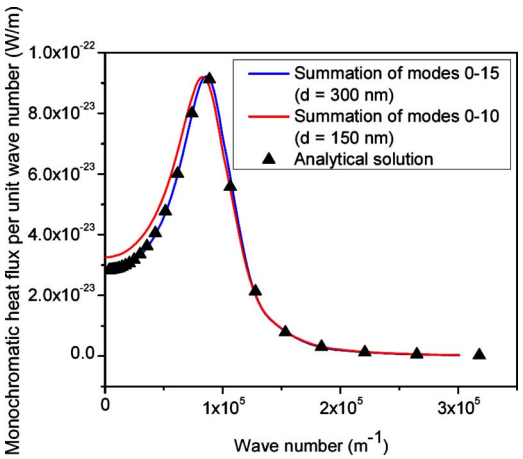

Fig. 7 Comparison between WCE and dyadic Green's function approaches for the near field thermal radiation between two 300 nm gold plates with a separation distance of 10 nm when $\omega=1\times10^{13}$ rad/s

4 Conclusions

Decomposing the random thermal fluctuating current of a material into its eigenmodes with the WCE, the thermal radiation from a material can be determined by solving a set of deterministic PDEs from Maxwell's equations. Thus, a direct simulation for the near field thermal radiation can be achieved. A specific study of the near field thermal radiation between two plates, which is one of the few conditions an analytical solution exists, is carried out for examining the validity of the proposed WCE methodology. Very good agreement between WCE methodology and the analytical solution from dyadic Green's function is obtained in this demonstration. The proposed method also provides results in a reasonable computation time. Furthermore, the method yields a physical understanding of the near field thermal radiation in terms of orthogonal eigenmodes of thermal fluctuating currents. Based on this understanding, geometric symmetry can be utilized to further simplify the simulation (e.g., reducing a 3D simulation to 2D). It is also pointed out that the proposed simulation based on the eigenmodes of thermal fluctuating currents has no explicit limitations on the geometry of the thermal radiation system. Also, temperature gradients and transient conditions can be directly incorporated into the proposed method for evaluating the near field thermal radiation. It is expected that a wide range of the near field thermal radiation problems can be studied utilizing the proposed methodology.

Acknowledgment

This work is supported by the National Science Foundation (Grant No. CBET 0845794) and the startup fund from Texas A&M University at College Station. The author thanks the fruitful discussion and comments from Dr. Ralph Greif in the University and California at Berkeley.

Nomenclature

$\vec{B}$ = magnetic induction, N/A m
$\vec{D}$ = electric displacement, C/m^3
DW = derivative of a white noise signal
$\vec{E}$ = electric field, V/m
$\vec{H}$ = magnetic field, A/m
$\vec{J}_{\text{thermal}}$ = thermal fluctuating current density, A/m^2
K = wave number, m^{-1}
k_B = Boltzmann constant, 1.38×10^{-23} m^2 kg/s^2 K
$\vec{r}$ = position of interest, m
$\vec{S}$ = Poynting vector, W/m^2
T = temperature, K
W = near field thermal radiation intensity at a specified wavelength and temperature, W/m^2 ω

Greek Symbols

δ_{jk} = Kronecker delta
ε_o = permittivity of vacuum, 8.854×10^{-12} F/m
ε' = real part of a relative dielectric constant
ε'' = imaginary part of a relative dielectric constant
ϕ = eigenmode for a random thermal fluctuating current
$\hbar$ = reduced Planck constant, 1.054×10^{-34} J s
Γ = reciprocal relaxation time in the Drude model, s^{-1}
ω = angular frequency, rad/s
ω_p = plasma frequency in Drude model, rad/s
ξ_{ijk} = standard Gaussian random variables

References

[1] Narayanaswamy, A., Shen, S., and Chen, G., 2008, "Near-Field Radiative Heat Transfer Between a Sphere and a Substrate," Phys. Rev. B, **78**, p. 115303.
[2] Hu, L., Narayanaswamy, A., Chen, X. Y., and Chen, G., 2008, "Near-Field

Thermal Radiation Between Two Closely Spaced Glass Plates Exceeding Planck's Blackbody Radiation Law," Appl. Phys. Lett., **92**, p. 133106.
[3] Narayanaswamy, A., and Chen, G., 2008, "Thermal Near-Field Radiative Transfer Between Two Spheres," Phys. Rev. B, **77**, pp. 075125.
[4] Francoeur, M., and Menguc, M. P., 2008, "Role of Fluctuational Electrodynamics in Near-Field Radiative Heat Transfer," J. Quant. Spectrosc. Radiat. Transf., **109**, pp. 280–293.
[5] Francoeur, M., Menguc, M. P., and Vaillon, R., 2008, "Near-Field Radiative Heat Transfer Enhancement via Surface Phonon Polaritons Coupling in Thin Films," Appl. Phys. Lett., **93**, p. 043109.
[6] Lee, B. J., and Zhang, Z. M., 2008, "Lateral Shifts in Near-Field Thermal Radiation With Surface Phonon Polaritons," Nanoscale Microscale Thermophys. Eng., **12**, pp. 238–250.
[7] Domingues, G., Volz, S., Joulain, K., and Greffet, J. J., 2005, "Heat Transfer Between Two Nanoparticles Through Near Field Interaction," Phys. Rev. Lett., **94**, p. 085901.
[8] Yannopapas, V., and Vitanov, N. V., 2007, "Fluctuational Electrodynamics in the Presence of Finite Thermal Sources," Phys. Rev. Lett., **99**, p. 053901.
[9] Modest, M., 2003, *Radiative Heat Transfer*, Academic, San Diego.
[10] Siegel, R., and Howell, J., 2001, *Thermal Radiation Heat Transfer*, Taylor & Francis, New York.
[11] Park, K., Basu, S., King, W. P., and Zhang, Z. M., 2008, "Performance Analysis of Near-Field Thermophotovoltaic Devices Considering Absorption Distribution," J. Quant. Spectrosc. Radiat. Transf., **109**, pp. 305–316.
[12] Volokitin, A. I., and Persson, B. N. J., 2007, "Radiative Heat Transfer and Noncontact Friction Between Nanostructures," Phys. Usp., **50**, pp. 879–906.
[13] Volokitin, A. I., and Persson, B. N. J., 2001, "Radiative Heat Transfer and Vacuum Friction Between Nanostructures," Phys. Low-Dimens. Semicond. Struct., **5–6**, pp. 151–172.
[14] Volokitin, A. I., and Persson, B. N. J., 2001, "Radiative Heat Transfer Between Nanostructures," Phys. Rev. B, **63**, p. 205404.
[15] Lee, B. J., Park, K., and Zhang, Z. M., 2007, "Energy Pathways in Nanoscale Thermal Radiation," Appl. Phys. Lett., **91**, p. 153101.
[16] Chapuis, P. O., Laroche, M., Volz, S., and Greffet, J. J., 2008, "Radiative Heat Transfer Between Metallic Nanoparticles," Appl. Phys. Lett., **92**, p. 201906.
[17] Pendry, J. B., 1999, "Radiative Exchange of Heat Between Nanostructures," J. Phys.: Condens. Matter, **11**, pp. 6621–6633.
[18] Mulet, J. P., Joulain, K., Carminati, R., and Greffet, J. J., 2002, "Enhanced Radiative Heat Transfer at Nanometric Distances," Nanoscale Microscale Thermophys. Eng., **6**, pp. 209–222.
[19] Luo, C. Y., Narayanaswamy, A., Chen, G., and Joannopoulos, J. D., 2004, "Thermal Radiation From Photonic Crystals: A Direct Calculation," Phys. Rev. Lett., **93**, p. 213905.
[20] Greffet, J.-J., Carminati, R., Joulain, K., Mulet, J.-P., Henkel, C., Mainguy, S., and Chen, Y., 2003, "Coherent Spontaneous Emission of Light Due to Surface Waves," Optical Nanotechnologies: The Manipulation of Surface and Local Plasmons, **88**, pp. 163–182.
[21] Carminati, R., and Greffet, J. J., 1999, "Near-Field Effects in Spatial Coherence of Thermal Sources," Phys. Rev. Lett., **82**, pp. 1660–1663.
[22] Rytov, S. M., Kravtsov, Y. A., and Tatarskii, V. I., 1989, *Principles of Statistical Radiophysics*, Springer-Verlag, Berlin.
[23] Taflove, A., and Hagness, S. C., 2005, *Computational Electrodynamics: The Finite-Difference Time-Domain Method*, Artech, Norwood.
[24] Badieirostami, M., Adibi, A., Zhou, H. M., and Chow, S. N., 2007, "Model for Efficient Simulation of Spatially Incoherent Right Using the Wiener Chaos Expansion Method," Opt. Lett., **32**, pp. 3188–3190.
[25] Hanamura, K., and Kameya, Y., 2008, "Spectral Control of Thermal Radiation Using Rectangular Micro-Cavities on Emitter-Surface for Thermophotovoltaic Generation of Electricity," J. Therm. Sci. Technol., **3**, pp. 33–44.
[26] Hou, T. Y., Luo, W., Rozovskii, B., and Zhou, H. M., 2006, "Wiener Chaos Expansions and Numerical Solutions of Randomly Forced Equations of Fluid Mechanics," J. Comput. Phys., **216**, pp. 687–706.
[27] Lototsky, S. V., and Rozovskii, B. L., 2006, "Wiener Chaos Solutions of Linear Stochastic Evolution Equations," Ann. Probab., **34**, pp. 638–662.
[28] Jackson, J. D., 1998, *Classical Electrodynamics*, Wiley, New York.
[29] Margengo, E. A., Rappaport, C. M., and Miller, E. L., 1999, "Optimum PML ABC Conductivity Profile in FDFD," IEEE Trans. Magn., **35**, pp. 1506–1509.
[30] Rappaport, C. M., and McCartin, B. J., 1991, "FDFD Analysis of Electromagnetic Scattering in Anisotropic Media Using Unconstrained Triangular Meshes," IEEE Trans. Antennas Propag., **39**, pp. 345–349.
[31] Xu, F., and Wu, K., 2009, "A Compact 2-D Finite-Difference Frequency-Domain Method Combined With Implicitly Restarted Arnoldi Technique," IEEE Trans. Microwave Theory Tech., **57**, pp. 1129–1135.
[32] Xu, F., Zhang, Y. L., Hong, W., Wu, K., and Cui, T. J., 2003, "Finite-Difference Frequency-Domain Algorithm for Modeling Guided-Wave Properties of Substrate Integrated Waveguide," IEEE Trans. Microwave Theory Tech., **51**, pp. 2221–2227.
[33] Sipe, J. E., 1987, "New Green-Function Formalism for Surface Optics," J. Opt. Soc. Am. B, **4**, pp. 481–489.
[34] Saad, Y., 2003, *Iterative Methods for Sparse Linear Systems*, Society for Industrial and Applied Mathematics, Philadelphia.
[35] Chapuis, P. O., Volz, S., Henkel, C., Joulain, K., and Greffet, J. J., 2008, "Effects of Spatial Dispersion in Near-Field Radiative Heat Transfer Between Two Parallel Metallic Surfaces," Phys. Rev. B, **77**, p. 035431.

Airflow and Cooling in a Data Center

Suhas V. Patankar
Professor Emeritus
Department of Mechanical Engineering,
University of Minnesota,
Minneapolis, MN 55455;
President
inInnovative Research, Inc.,
Plymouth, MN 55447
e-mail: patankar@inres.com

This paper deals with the distribution of airflow and the resulting cooling in a data center. First, the cooling challenge is described and the concept of a raised-floor data center is introduced. In this arrangement, cooling air is supplied through perforated tiles. The flow rates of the cooling air must meet the cooling requirements of the computer servers placed next to the tiles. These airflow rates are governed primarily by the pressure distribution under the raised floor. Thus, the key to modifying the flow rates is to influence the flow field in the under-floor plenum. Computational fluid dynamics (CFD) is used to provide insight into various factors affecting the airflow distribution and the corresponding cooling. A number of ways of controlling the airflow distribution are explored. Then attention is turned to the above-floor space, where the focus is on preventing the hot air from entering the inlets of computer serves. Different strategies for doing this are considered. The paper includes a number of comparisons of measurements with the results of CFD simulations. [DOI: 10.1115/1.4000703]

Keywords: data center, electronics cooling, raised floor, under-floor flow, simulation, computational fluid dynamics

1 Introduction

1.1 What is a Data Center? We live in a computer age. We search for information on the Internet. We reserve e-tickets for airline travel and get our boarding passes on a computer. Stocks are traded on computers and people use online banking. When we use a credit card, the transaction is instantaneously verified and approved. All major retail merchants offer online shopping. Large companies have their inventory, purchase orders, invoices, and all accounting computerized. Medical records are stored on computers. We use email and text messaging to communicate with others. The modern cell phone is a small computer that communicates with the rest of the world. The list goes on.

Whereas the *visible* transaction takes place at the "point of sale" on a personal computer or a small device, the whole mechanism can function only if all the relevant data is held at one place and processed at a very fast speed. Therefore, behind the small visible devices (such as a desktop computer, a laptop, or a cell phone) are large and powerful computer servers located in one place. For a credit-card or stock-trading company, it is common to have a large room (of the size 70×70 m^2) housing over 2000 server racks (each 1×1 m^2 and 2 m tall). There are also *colocation* facilities, where different companies can place a few server racks each for their own use. Such a huge computer room is called a "data center." It has become an essential part of any modern-day large business.

The most important requirement for a data center is its uninterrupted, zero-downtime operation. An interruption caused by equipment failure would entail costly repairs and replacement. But even more serious is the cost of business interruption; the business may lose thousands or even millions of dollars for every minute of downtime.

For uninterrupted operation, two things are crucial: power and cooling. Uninterrupted power is assured by having several backup sources of power that can be automatically brought on line as soon as a power failure is detected. Cooling is a more complex issue, which is discussed in this paper.

1.2 The Cooling Challenge. Each server rack in a data center consumes electrical energy and dissipates a large amount of heat in the range of 2–20 kW. For the electronics to function properly, it needs to be cooled and kept at an acceptable temperature level. Overheating may cause the equipment to malfunction, melt, or burn; but more commonly, safety devices on the server racks will detect high temperatures and shut down the equipment. It is this interruption that presents a serious problem for a data center and needs to be prevented.

Normally, cooling air enters a server rack through the front face and hot air exits from the rear face. In a large room, in which 2000 server racks may be spread all over the room, it is not easy to supply cooling air to each rack. This task is accomplished by a clever concept called the *raised-floor* data center. The server racks are installed on a tile floor that is raised 0.3–0.6 m (12–24 in.) above the real solid floor. Air-conditioners are used to pump cold air into the space below the raised floor. The floor tiles are removable and some of the solid tiles can be replaced by perforated tiles or grilles to permit the cold air to enter the above-floor space. By locating perforated tiles at the foot of the server racks, cooling air is delivered to them. The hot air then finds its way back to the air-conditioners.

The raised-floor arrangement gives unlimited flexibility. If the layout of the server racks is changed, all that is needed is to rearrange the perforated tiles so that cooling air is delivered at the new locations of the server racks. Since there is no permanent ducting, no elaborate dismantling or construction is necessary.

The raised-floor design makes it possible to create, but does not guarantee, proper cooling of the server racks. How much cold air do we need? How does it distribute in the whole data center? Are we meeting the *individual demands* of all server racks? Does the cold air introduced at the floor level reach to the top of the 2-m tall server rack? Can the hot air coming out of one rack enter the inlet of another rack and damage its cooling? These questions will be addressed in this paper.

Cooling a data center in its current configuration is a difficult challenge in itself. But data centers are dynamic; their equipment layout continually needs to change. Business conditions require that new server racks are installed and the old ones are removed. Typically, ten percent of the equipment in a data center is replaced *each month*. The cooling design has to keep pace with this frequent change.

The common practice to meet this challenge is trial-and-error

Contributed by the Heat Transfer Division of ASME for publication in the JOURNAL OF HEAT TRANSFER. Manuscript received March 30, 2009; final manuscript received November 11, 2009; published online April 27, 2010. Editor: Yogesh Jaluria.

and "overkill." One detects hot spots and tries to force cold air there by placing more perforated tiles. If that fails, an extra air-conditioner is installed in the hope of removing the hot spots. It is estimated that the amount of cooling air used in most data centers is 2.5 times the required amount. So, there is a good opportunity for saving on air-conditioning equipment and energy. Whereas until now uninterrupted operation was the only focus (and data centers were ready to spend any amount of resources to achieve it), the current economic climate has shifted the focus to energy conservation. A "green data center" is a new goal in addition to the zero-downtime operation.

1.3 The Criterion for Acceptable Cooling in a Data Center. Manufacturers of computer servers design their equipment with a certain allowable maximum inlet temperature. This value is around 24°C (75°F). The air-conditioners in a data center usually supply cold air at 13°C (55°F). If the 13°C cold air enters the servers, there is no difficulty in satisfying the manufacturer's criterion. As we will see later, the cold air does not always enter at all the inlet locations on the server rack. Often, the hot air exhausted by the rack finds its way to the inlet of the same rack or some other rack. This is how the cooling in a data center is compromised.

1.4 Methods to Meet the Cooling Challenge. As in any complex engineering situation, the cooling in a data center has been conventionally handled by accumulated experience (including some rules of thumb), field measurements, and ad hoc design changes. A number of specialized cooling products have been introduced in recent years, but their evaluation for specific situations is costly and time-consuming. The need for a more scientific approach is quite obvious.

1.5 Role of CFD Simulation. Cooling in a data center is an excellent application for Computational Fluid Dynamics (CFD). It offers a new paradigm for meeting the cooling challenge. One can create a computer model of the whole data center, complete with the raised floor, air-conditioning units, perforated tiles, and server racks. The CFD simulation then provides a detailed distribution of air velocity, pressure, and temperature throughout the room. The simulation can be used to analyze an existing data center, but more importantly, any *proposed* layout for a new or reconfigured data center. One can detect hot spots in a simulation (before they arise in reality) and explore ways of mitigating them. As already mentioned, data centers are dynamic environments; their equipment layout changes frequently. A CFD simulation provides invaluable help in planning the changes and ensuring proper cooling.

1.6 Available Literature. Archival literature on airflow management in data centers is rather scarce. Only in recent years, this topic has created strong scientific and practical interest. A brief overview of the available literature is given below.

Seymour [1] applied CFD analysis to show temperature and flow distributions in an atrium. Awbi and Gan [2] used CFD to predict airflow and temperature distributions within offices. Kiff [3] presented the results of a CFD analysis of rooms populated with telecommunications equipment. Bullock and Phillip [4] performed a CFD simulation for the Sistine Chapel renovation project. Schmidt [5] compared CFD results with measurements of temperature and velocity fields in an office-size data processing room. Cinato et al. [6] describe a tool to optimize the energy consumption of the environmental systems that provide cooling to telecommunication rooms. Quivey and Bailey [7] have presented results based on a CFD model for a Lawrence Livermore Data Center.

Kang et al. [8], on the basis of some CFD calculations, proposed a simplified model that assumes the whole volume under the raised floor to be at a *uniform* pressure. The entire flow system is then represented as a network of flow resistances. The results from this simplified model did agree well with CFD results for a particular small data center. However, as will be shown later in this paper, the assumption is not valid for most practical configurations.

In a subsequent study, Schmidt et al. [9] allowed the pressure variations in the under-floor space, but used a depth-averaged model to convert the three-dimensional problem into a two-dimensional one. For the cases they considered, a good agreement with measurements was demonstrated. However, later investigations have shown that the depth-averaged model is adequate when the height of the raised floor is small (normally less then 0.15 m or 6 in.). Practical data centers have floor heights in the range of 0.3–0.75 m. As a result, even this simplification is not acceptable and one must perform the full three-dimensional computation.

Schmidt [10] and Schmidt and Cruz [11,12] have studied the inlet temperatures to server racks in a data center. Patel et al. [13,14] describe application of CFD modeling to data centers and evaluate some specific overhead-cooling solutions. A detailed analysis of the flow in the under-floor space and the factors affecting it is presented by Karki et al. [15,16] and Patankar and Karki [17]; in Ref. [16], computed results are compared with measurements of airflow through the perforated tiles. Guggari et al. [18] describe ways of optimizing data center layout. As the concerns about data center cooling became more important, Bash et al. [19] outlined the research needs in this area.

Temperature and flow rate measurements in an actual data center are reported by Schmidt [20]. Later in this paper, this study will be used to provide a sample validation of CFD simulation. The issue of distributed leakage through the raised floor is addressed by Radmehr et al. [21] and Karki et al. [22]; they report airflow measurements and corresponding CFD analysis. Van Gilder and Schmidt [23] consider the factors that govern the uniformity of airflow through the perforated tiles.

Whereas the full three-dimensional CFD analysis of the under-floor airflow yields useful results, a one-dimensional idealization of the flow can be used to get valuable insight. Karki and Patankar [24] have derived such a one-dimensional model and provided an analytical solution of the governing equations. The validity of the model is demonstrated with reference to a full three-dimensional CFD solution.

The interaction of the air stream emerging from a perforated tile with the internal fans in a front-to-rear server rack is analyzed by Radmehr et al. [25]. They determine the conditions for which the inlet flow is essentially unaffected by the pressure variations in the inlet stream.

1.7 Scope of the Paper. The purpose of this paper is to describe some interesting physical behavior in the airflow and cooling in a data center. Many physical effects are explained with the help of CFD simulation. Most of the material is taken from the papers mentioned above, where further details can be found.

A complete consideration of the flow and heat transfer in a data center would include both the under-floor and above-floor spaces. This paper initially focuses on the flow in the under-floor space and the resulting airflow rates through the perforated tiles. Although the under-floor space appears to be insignificant, it is here that the cooling battle is primarily won or lost. If we are able to deliver the required amount of airflow at the foot of each server rack, proper cooling is essentially assured. If we fail to satisfy this requirement, any attempted remedy in the above-floor space is usually ineffective.

The flow in the under-floor space is influenced by various factors such as the layout of perforated tiles, their open area, the height of the raised floor, and under-floor obstructions. A number of simple case studies are described to illustrate these effects.

The above-floor space brings its own unique behavior and surprises. These are explained through a number of examples. It is shown that the main challenge in the above-floor space is to ensure that the hot exhaust air from a server rack does not enter the inlet of the same rack or some other rack. Various strategies used for ensuring this are described.

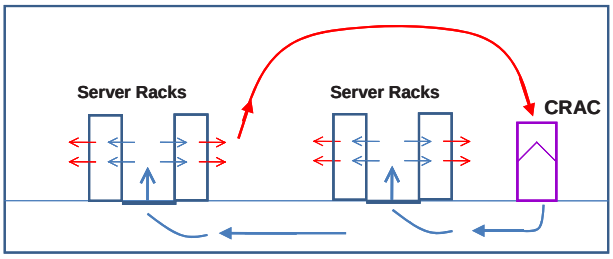

Fig. 1 A raised-floor data center

The paper is written in an introductory style so that the readers who are not intimately familiar with data centers can get a good appreciation of the scientific and practical issues pertaining to cooling in a data center.

2 Fundamentals of a Raised-Floor Data Center

2.1 The Overall Arrangement. Figure 1 shows an outline of a raised-floor data center. On the right, a down-flow air-conditioning unit is placed on the raised floor. It draws the hot air in the room into its top face and supplies cold air from its bottom into the under-floor space. Such an air-conditioner is called a computer room air-conditioner (CRAC) by the data center community. The cold under-floor air enters the above-floor space through perforated tiles that are placed at the foot of the server racks. The racks, in turn, draw in this air through their front face and exhaust hot air from the rear face. The hot air finally returns to the top of the air-conditioning unit (CRAC).

2.2 The Hot Aisle/Cold Aisle Concept. To eliminate the possibility that the hot air exhausted by one rack would enter the inlet of another rack, data centers are often laid out in the "hot aisle/cold aisle" arrangement, which is shown in Fig. 2. This arrangement was suggested by Sullivan [26] and has become a standard practice in data centers. The so-called cold aisle has the perforated tiles. The server racks are placed on both sides of the cold aisle such that their inlets face the cold aisle. As a result, the exhausts from two neighboring rows of racks emerge into the hot aisle. Of course, there is no reason to place any perforated tiles in the hot aisle. The hot air collected there simply returns to the CRAC unit, without entering (hopefully) into the inlet of any server rack.

Figure 3 shows a photograph of a cold aisle in a data center. The unit at the back is a CRAC. The inlets of the server racks are

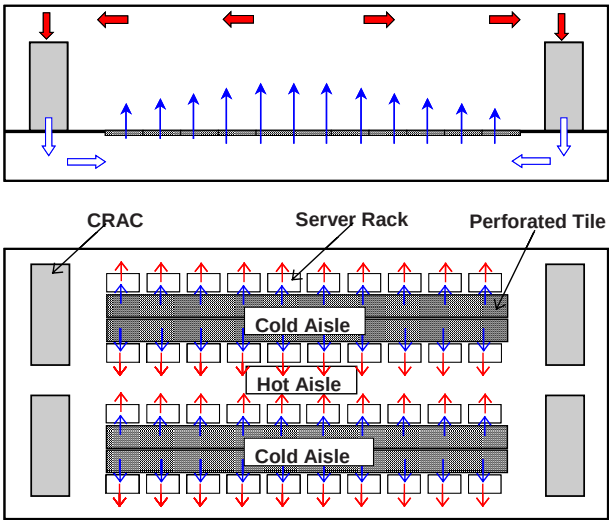

Fig. 2 The hot aisle/cold aisle arrangement

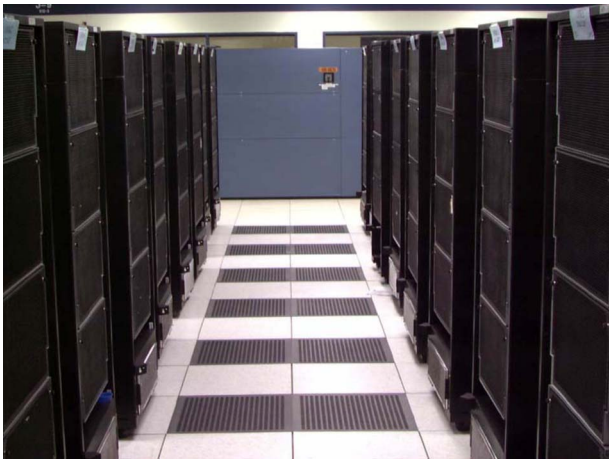

Fig. 3 The cold aisle in a data center

seen on both sides. The raised floor is made up of tiles. Many tiles in the cold aisle are perforated. It is through these tiles that cold air is supplied for the cooling of the racks.

2.3 Importance of Supplying the Required Airflow to Each Server Rack. A server rack has internal fans that draw a known amount of airflow rate. Also, as mentioned before, the cooling of the rack is designed on the basis of a *maximum acceptable inlet temperature*. If the actual inlet temperature exceeds this value, overheating occurs, which may lead to malfunction or automatic shutdown.

To ensure that cold air enters the rack, the airflow rate from the perforated tile at the foot of the rack has to be equal to (or greater than) the airflow rate demanded by the internal fans in the rack. Figures 4 and 5 illustrate this concept via simplified examples. In both cases, each rack dissipates 2 kW of heat and requires an airflow rate of 0.15 m^3/s. In Fig. 4, the airflow supplied at the

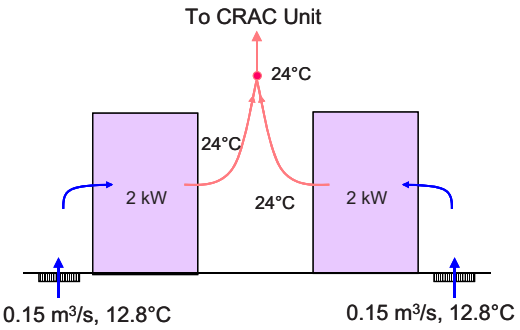

Fig. 4 Required airflow supplied

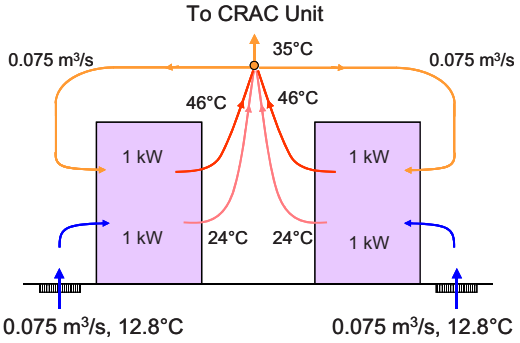

Fig. 5 Insufficient airflow

perforated tile is indeed 0.15 m^3/s. This meets the demand of the server rack. The cold air is supplied at 12.8°C, it heats up to 24°C, and this hot air returns to the CRAC unit. Since the temperature entering the rack is 12.8°C, which is well below the acceptable inlet temperature, proper cooling is assured.

As will be shown later, it is not always possible to control the amount of airflow emerging from each perforated tile. Figure 5 shows the case in which insufficient airflow is supplied from the perforated tile. Whereas the rack requires 0.15 m^3/s, the perforated tile supplies only half that amount. This reduced flow is sufficient to cool the bottom half of the rack. The cooling airflow needed by the top half is now taken from the "hot" air returning to the CRAC unit. This air has resulted from the mixing of the exhaust air at 24°C from the bottom half of the rack with the much hotter air emerging from the top half of the rack. The result is that the maximum inlet temperature to the rack is 35°C, which may be unacceptable for many electronics designs. (The idealized picture in Fig. 5 assumes that the exhausts of the top and bottom halves of the rack are well mixed to the temperature of 35°C. In reality, if such perfect mixing does not take place, even hotter air is likely to enter the inlet of the top half of the rack.)

These simple examples lead to a very important conclusion. The key to good cooling is to supply the *required amount of cold airflow* at the foot of each server rack. If this is done, satisfactory cooling is assured. If this cannot be done, cooling difficulties arise and then they are usually very hard to overcome.

2.4 Airflow in the Under-Floor Space. Since the airflow rate emerging from each perforated tile holds the key to successful cooling, we turn our attention to what controls the distribution of airflow through the perforated tiles. Interestingly, it is not what happens *above* the raised floor but what happens *below* the raised floor that determines the flow through the perforated tiles. Thus, the fluid mechanics of the tiny (and usually invisible) space below the raised floor controls the success or failure of cooling in a data center. From a computational point of view, this is good news. If the CFD simulation is limited to the under-floor space, the calculation domain is small and a fast solution is possible. Yet, this small computational effort leads to the most valuable information needed for the cooling of the data center.

2.5 Flow Through the Perforated Tiles. The perforated tiles used in a data center have a large number of small circular holes. Such a tile is usually characterized by the percentage open area; the most common perforated tiles have 25% open area. The flow resistance of the perforated tiles can be obtained from well-known pressure-drop correlations for such plates. The pressure drop Δp across a perforated tile is expressed as

$$\Delta p = K(0.5\rho V^2)$$

where V is the velocity approaching the perforated tile, ρ is the density of air, and K is the flow resistance factor (the "K factor"). An empirical formula for K, based on a large number of measurements, is given by Idelchik [27]

$$K = \frac{1}{F^2}(1 + 0.5(1 - F)^{0.75} + 1.414(1 - F)^{0.375})$$

where F is the fractional open area of the perforated tile. For a 25% open tile, this formula gives $K = 42.8$.

Figure 6 shows the variation in the pressure drop Δp with the volumetric airflow rate through the perforated tile for tiles of 6%, 11%, and 25% open area, as given by the above formula. For the case of 25% open tile, experimental data are also shown in the figure. The curve given by the formula is in good agreement with the data. (This figure assumes that the tiles are 2×2 ft^2, which is the common size used in the US. The size in other countries is 0.6×0.6 m^2, which is not very different.)

Table 1 gives, for the 25% open tile, the values of the airflow rates through the tile and the corresponding pressure drops. Practical flow rates through perforated tiles are of the order of 0.25 m^3/s, for which the pressure drop is about 12 Pa. That this value of the pressure drop is rather small is relevant for the discussion below.

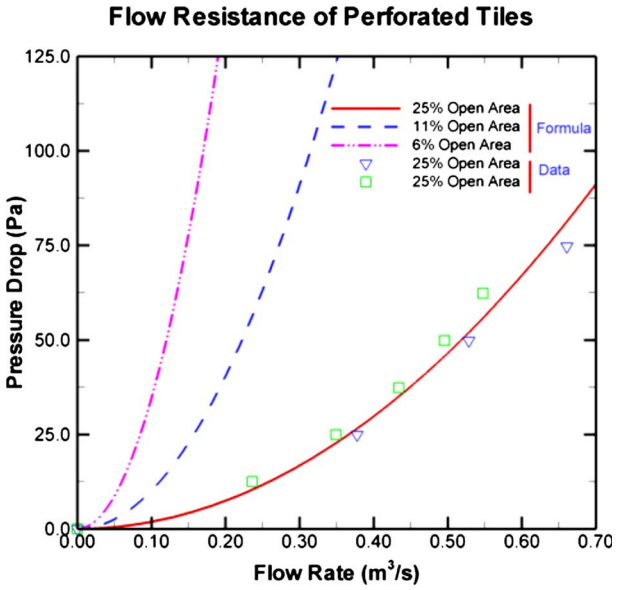

Fig. 6 Pressure drop as a function of the airflow rate for perforated tiles

2.6 Behavior of the CRAC Unit. The flow emerging from the perforated tiles originates at the CRAC unit. Usually, the flow is directed vertically downwards from one or more blowers in the CRAC. It impinges on the solid floor (usually called the subfloor), turns 90 deg, moves horizontally in the under-floor space, and emerges from the perforated tiles wherever they are placed. The CRAC blowers deliver a rated airflow; 5 m^3/s is a typical value.

Does the actual amount of airflow from a CRAC unit depend on the number of perforated tiles and their percent open area? Interestingly, for all practical purposes, a CRAC unit can be regarded as a constant-flow device that delivers that same amount of airflow rate for different numbers, layouts, and open areas of the perforated tiles.

To understand this conclusion, we need to examine the various pressure drops that the CRAC blower is required to overcome. These include the pressure drop in:

- The filter and cooling coils in the CRAC unit. (This is known as the internal static and is usually in the range 250–500 Pa.)
- The impingement and turning on the subfloor. (This is known as the external static and is usually in the range 100–200 Pa.)
- The perforated tiles (about 12 Pa, as seen above).

Table 1 Pressure drop for a 25% open tile at different airflow rates

Airflow rate (m^3/s)	Pressure drop (Pa)
0.05	0.47
0.10	1.87
0.15	4.21
0.20	7.48
0.25	11.7
0.30	16.8

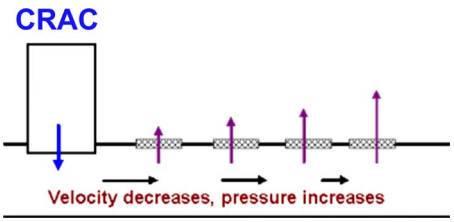

Fig. 7 Maldistribution of airflow and its cause

It is now obvious that the perforated tiles represent only a small fraction of the flow resistance experienced by the CRAC blower. Therefore, for all practical purposes, the CRAC unit gives *nearly the same flow rate* for different numbers, layouts, and open areas of the perforated tiles. (This is an important conclusion and it is often not understood even by experienced people in the data center field. They attempt to increase the flow rate from perforated tiles by using 40% open tiles instead of 25% open. As seen above, this action changes only the tiny pressure drop across the perforated tiles. Since the other two major pressure drops remain the same, the CRAC unit delivers essentially the same total flow rate.)

2.7 Surprising Airflow Distribution Through the Perforated Tiles. As seen in Fig. 3, different perforated tiles are at different distances from the CRAC unit. Does the airflow distribute uniformly through different perforated tiles? At first sight, we may conclude that, as we go way from the CRAC unit (which is the source of air), the airflow through the perforated tiles diminishes. Actually, the flow distributes in a surprising and counterintuitive manner. The perforated tiles that are farthest way from the CRAC unit get the largest flow. The airflow through the tiles close to the CRAC unit is quite small.

Figure 7 shows the so-called maldistribution of airflow in a schematic manner. The reason for this maldistribution is also explained in the figure. The mechanism is similar to the maldistribution that occurs in manifolds [28,29]. In Fig. 7, if we consider the velocity of the under-floor air in the horizontal direction, this velocity must decrease as air escapes through the perforated tiles. The Bernoulli equation would then imply that the pressure increases as we go away from the CRAC unit. The airflow rate through the perforated tiles depends on the pressure drop. Since the tiles on the right experience a greater pressure drop, they deliver more airflow. (This assumes that the pressure above the raised floor is nearly uniform. This is a valid assumption and has been verified by measurements and computation.)

2.8 An Early Validation. The above discussion explains the maldistribution in a qualitative sense. To verify its quantitative accuracy, a simple experiment [9] was conducted at IBM Corporation in Poughkeepsie, NY. The experimental setup is shown in Fig. 8. This includes a small data center with two CRACs and many perforated tiles. For the initial tests, the CRAC unit on the left was turned off. Then, only the unit on the right supplies cold air to all the perforated tiles. The airflow from each perforated tile was measured and compared with the airflow rate predicted by a CFD simulation of the under-floor space. The comparison is

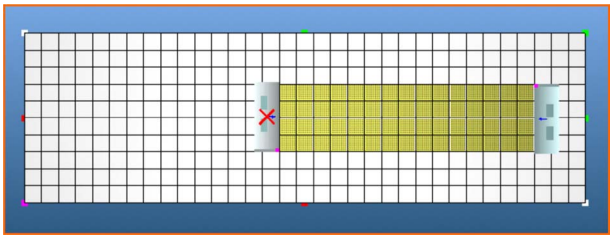

Fig. 8 Layout for a small test data center

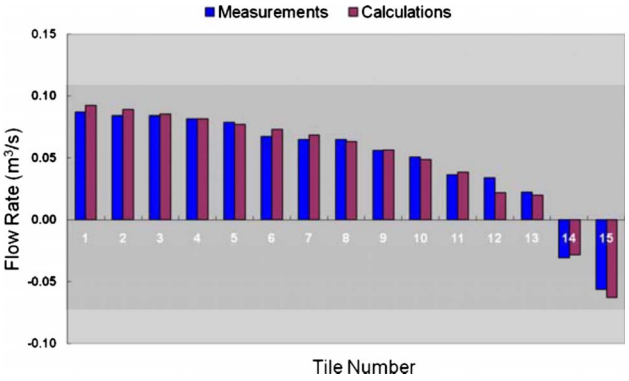

Fig. 9 Comparison of measured and calculated airflow rates (the tiles are numbered from left to right)

shown in Fig. 9. The maldistribution is clearly visible. For tiles 14 and 15, which are closest to the CRAC unit, the flow is actually negative. The flow can be seen to increase rapidly for smaller tile numbers (which are further away from the CRAC unit). The agreement between the measurements and calculation is very satisfactory.

2.9 Further Validations. The prediction of airflow rates through the perforated tiles by CFD simulation has been validated by comparison with measurements in a number of data centers. A typical example is shown in Figs. 10 and 11. Here Fig. 10 shows the layout of the data center, while Fig. 11 displays the comparison of calculated and measured airflow rates through the perforated tiles. These figures, which are directly taken from Ref. [16], contain "ft" as length units and "CFM" as the unit of volumetric flow rate through the perforated tiles. (If necessary, the unit conversion can be accomplished rather easily.) Once again, the computed results can be seen to agree quite well with the measured values.

3 Factors Affecting the Airflow Distribution

3.1 Relationship Between the Flow Field in the Plenum and Flow Rates Through Perforated Tiles. As we have seen before, the flow rate through a perforated tile depends on the pressure drop across the tile, that is, the difference between the plenum pressure just below the tile and the ambient pressure above the raised floor. Pressure variations above the raised floor are generally small compared with the pressure drop across the perforated tiles. Thus, relative to the plenum, the pressure just above the perforated tiles can be assumed to be uniform. The flow rates, therefore, depend primarily on the pressure levels in the

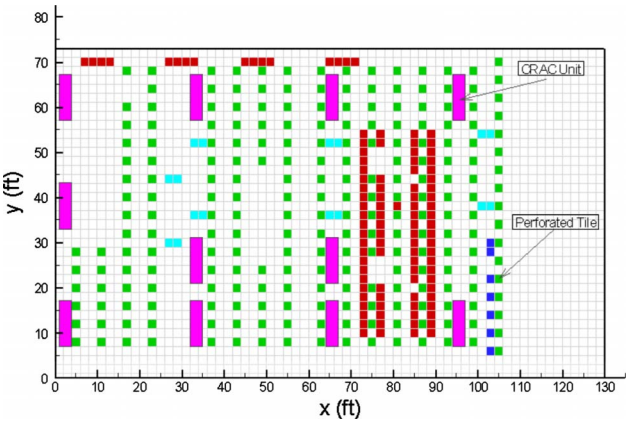

Fig. 10 Layout of a data center

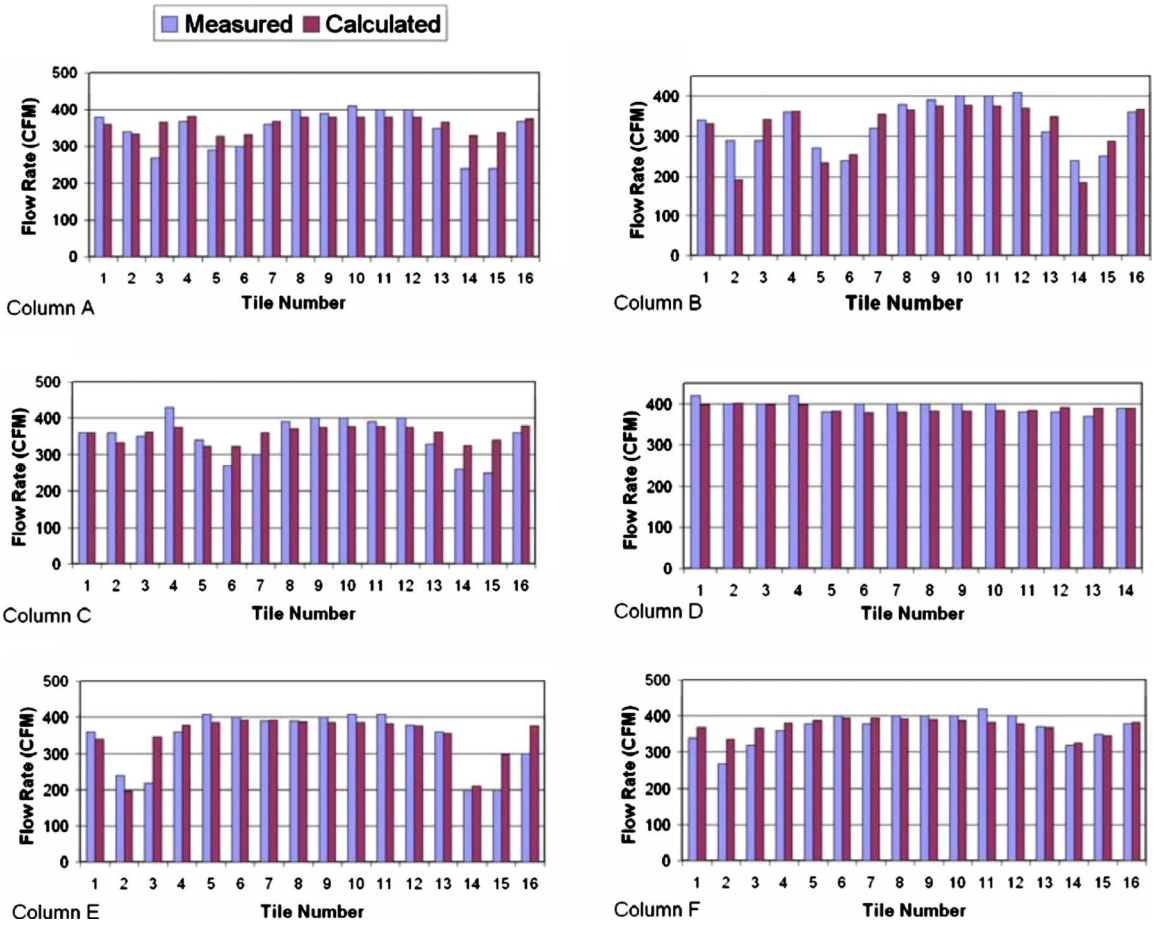

Fig. 11 Comparison of measured and calculated airflow rates

plenum, and the nonuniformity in the airflow distribution is caused by the pressure variations in the horizontal plane under the raised floor.

For the nonuniformity in the airflow distribution to be significant, the horizontal pressure variations (or change in velocity heads) must be comparable to the pressure drop across the perforated tiles. This condition is satisfied if the area available for horizontal flow in the plenum is comparable to or less than the total open area of the perforated tiles.

3.2 Parameters Considered. The key to controlling the airflow distribution is the ability to influence the pressure variation in the plenum. For specified (horizontal) floor dimensions and total flow rate, the effect of the following parameters is significant:

- plenum height
- open area of perforated tiles

Plenum height. The plenum height has a major influence on the horizontal velocity and pressure distributions in the plenum. As the plenum height increases, the velocities decrease and the pressure variations diminish, leading to a more uniform airflow distribution.

Open area of perforated tiles. As the open area of perforated tiles is reduced, the pressure drop across the tiles increases and, at some point, becomes much larger compared with the horizontal pressure differences under the raised floor. Under these conditions, all perforated tiles experience essentially the same pressure drop and the airflow distribution becomes nearly uniform.

3.3 The Base Case. The effect of these parameters on the airflow distribution will be illustrated with reference to the simple configuration shown in Fig. 12. This layout uses the conventional hot aisle/cold aisle arrangement, with the perforated tiles placed in the cold aisles. The CRAC units are also located in the cold aisles. The server racks are arranged on both sides of the cold aisles, with their intake sides facing the cold aisles. The hot aisles are formed between the back ends of two rows of server racks. The cooling air exiting the perforated tiles is sucked in by the internal fans of the racks, heats up as it moves through the racks, and is exhausted from the back of the racks into the hot aisles. From the hot aisles, the heated air returns to the inlets of the CRAC units. Due to symmetry, only a portion of the data center around one CRAC unit needs to be considered; this portion is shown in Fig. 12.

Thus, the base configuration under consideration here consists of a CRAC unit and two rows of perforated tiles, each containing 15 tiles with 25% open area. The CRAC unit delivers 4.72 m^3/s (10,000 CFM) of cold air. The under-floor plenum height is

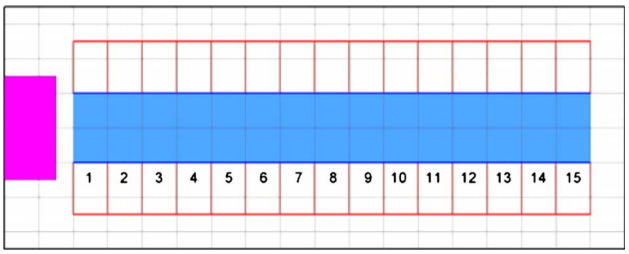

Fig. 12 The base case

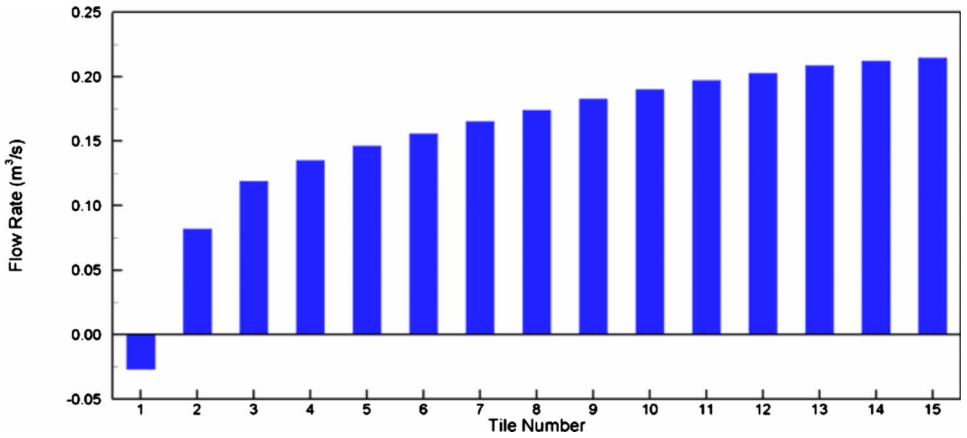

Fig. 13 Flow rates through perforated tiles for the base case

0.3048 m (12 in.). The tile size is 2×2 ft^2. The overall dimensions of this part of the data center are 36×14 ft^2 (10.97×4.27 m^2).

The distribution of airflow rates for this configuration is shown in Fig. 13. The flow rates are smaller near the CRAC unit and increase toward the opposite wall. There is actually a reverse flow through the perforated tiles next to the CRAC unit.

Figure 14 shows the velocity vectors and the pressure distribution on the horizontal plane just under the raised floor. The cold air exiting the CRAC unit impinges on the subfloor and expands horizontally. In the impingement region, the pressure levels are high, and they decrease rapidly as the air rushes out of these regions. As we move away from the CRAC unit, since the cold air is exiting the plenum, the horizontal velocity diminishes and the pressure rises. Note that the pressure under the perforated tiles next to the CRAC unit is negative (that is, *below* the pressure in the above-floor space) and produces a reverse flow through these tiles.

3.4 Effect of the Plenum Height. To illustrate the effect of plenum height on the airflow rates, the height for the base configuration is varied from 6 in. (0.1524 m) to 24 in. (0.6096 m).

The flow rates for different plenum heights are shown in Fig. 15. It can be seen that the nonuniformity in flow rates is most pronounced for plenum height of 6 in. (0.1524 m) and diminishes as the height is increased. The intensity of reverse flow through the perforated tiles next to the CRAC unit also weakens as the plenum height is increased. Note that the curves for the plenum heights of 18 (0.4572 m) and 24 in. (0.6096 m) are almost coincident. This implies that, once the plenum height is large enough, any further increase does not affect the flow distribution. In Fig. 15, even for the 24-in. (0.6096 m) height, the flow distribution is not quite uniform. This is due to the complex flow and lateral spreading in the vicinity of the CRAC unit.

Figures 16 shows the velocity vectors and pressure distribution on a horizontal plane just under the raised floor for plenum height of 6 in. (0.1524 m) For this smaller plenum height, the pressure variations are more significant (compared with Fig. 14), with an extensive region of negative pressure near the CRAC unit. Figure 17 shows the same plot for plenum height of 24 in. (0.6096 m). Here, the pressure distribution is much more uniform; the variations are limited to a small region near the CRAC unit. These pressure plots explain the airflow distribution shown in Fig. 15.

3.5 Effect of the Open Area of Perforated Tiles. To illustrate the effect of the open area of perforated tiles, the open area in the base configuration is varied from 10% to 60%.

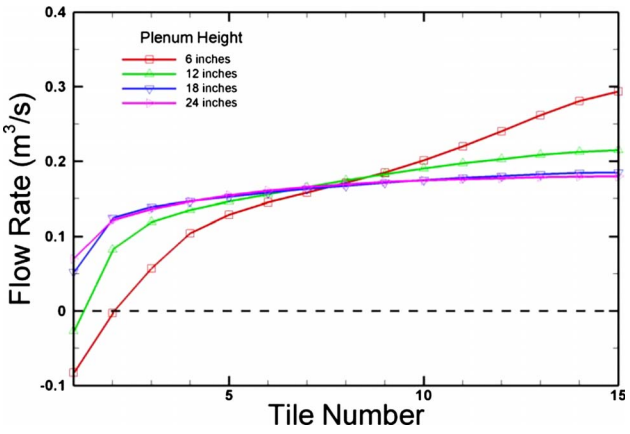

Fig. 15 Effect of plenum height on the airflow distribution

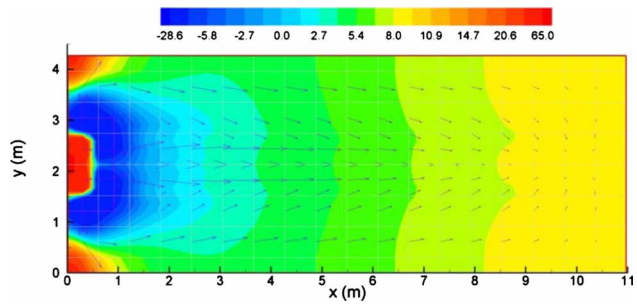

Fig. 14 Pressure distribution and velocity vectors under the raised floor for the base case (plenum height=12 in. (0.3048 m); the pressure values are in Pa)

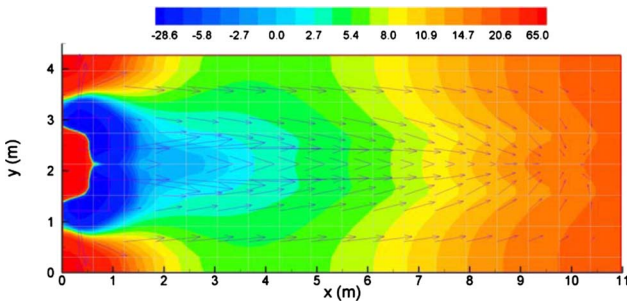

Fig. 16 Pressure distribution and velocity vectors under the raised floor for plenum height=6 in. (0.1524 m) (the pressure values are in Pa)

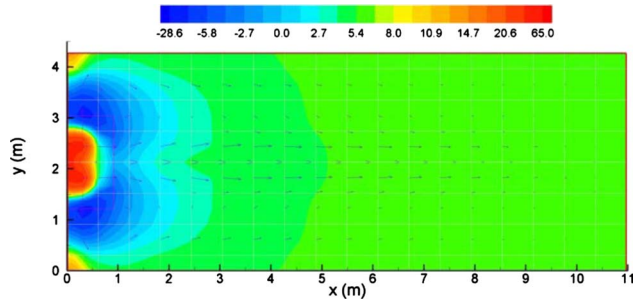

Fig. 17 Pressure distribution and velocity vectors under the raised floor for plenum height=24 in. (0.6096 m) (the pressure values are in Pa)

The airflow distributions for different open areas are shown in Fig. 18. For a fixed layout and plenum height, the nonuniformity in flow rates diminishes as the open area is reduced. A reduction in the open area also reduces the likelihood of reverse flow near the CRAC units. Note that there is no reverse flow for open area of 15% and 10%.

It may appear that using highly restrictive tiles (such as 10% open) is a good way of making the airflow distribution uniform. However, there is an undesirable side effect. At smaller open areas, the pressure levels in the plenum increase, and a large proportion of cold air escapes through extraneous openings on the floor, e.g., openings around cables and pipes and other leakage paths. (The flow resistance of these openings now becomes comparable to the flow resistance of the perforated tiles.) This wasted air will not be available for cooling of equipment.

3.6 One-Dimensional Idealization. The CFD simulations shown above are based on a three-dimensional analysis of velocity and pressure in the under-floor space. However, for the simple configuration chosen here, the significant variations are only in the x direction (left to right). For modest heights of the plenum, the variations in the vertical direction (between the subfloor and the raised floor) are usually small. In the y direction, significant variations are found only near the CRAC unit. Based on these observations, it is possible to construct a one-dimensional model of the situation designated above as the base case. Such a model has been described by Karki and Patankar [24]. In this model, the whole family of solutions is dependent on only two dimensionless parameters, which are

$$\text{pressure variation parameter, } \Psi = \frac{\eta}{\sqrt{K}}$$

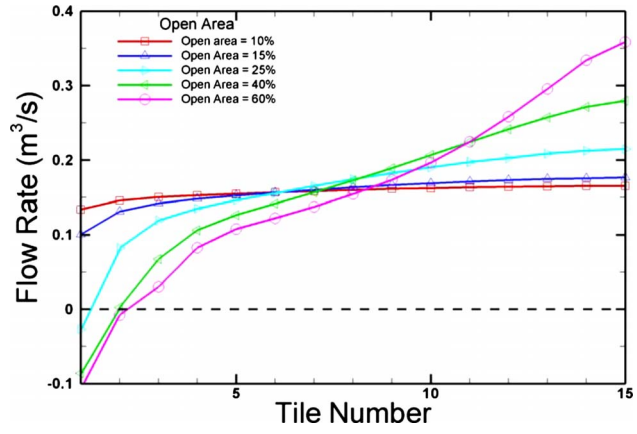

Fig. 18 Effect of open area of perforated tiles on the airflow distribution

$$\text{frictional resistance parameter, } \Phi = \frac{4fL}{d_h}$$

In the definition of Ψ, η is a geometrical factor defined as the ratio of the total area of perforated tiles A_{tile} to the cross-sectional area of the plenum (width $\times$ height) A_{cs}, that is,

$$\eta = \frac{A_{\text{tile}}}{A_{\text{cs}}}$$

The hydraulic diameter d_h appearing in the definition of Φ is taken as twice the plenum height. The friction coefficient f includes contributions from wall shear stress and the flow resistance of support structures and other distributed obstructions in the plenum.

A further simplification is possible by recognizing that, whereas Ψ is an important parameter, the frictional parameter of Φ is usually small and can be set equal to zero. Under these conditions, the governing one-dimensional differential equations can be solved to get an *analytical* exact solution. This solution reduces the complex problem of airflow in the under-floor space to a simple formula, which has surprisingly good validity.

While considering this simplification, we must remember that it applies to the simple configuration shown in Fig. 12. Whereas we get valuable guidance, understanding, and insight form the idealized model, it cannot be directly applied to real data centers with complex layouts, several CRAC units with intersecting flow streams, and irregular distribution of perforated tiles.

4 Leakage Through the Raised Floor

In practical data centers, the raised floor is not quite an impermeable surface as one would normally assume in an analysis. There are deliberate openings made in the tiles to bring cables to the server racks. (In fact, historically, the raised-floor arrangement was as much for bringing electrical connections as for supplying cooling air.) In addition, there are always small gaps between individual floor tiles. The leakage area due to these gaps is estimated to be 0.2% of the floor area.

In a normal data center, about 10% of the floor area is occupied by perforated tiles. If we assume that these tiles are 25% open, then the open area of the perforated tiles is 2.5% of the floor area. For this case, the leakage area mentioned above is 8% the total open area. If we reduce the number of perforated tiles on the floor, then the leakage area becomes an even larger proportion of the total open area.

If we ignore the leakage area, then we would expect that, as the number of perforated tiles decreases, the plenum pressure would increase and the average airflow rate through each perforated tile would be larger. These expectations are qualitatively in agreement with actual measurements, but quantitatively the pressure rise and the increase in airflow rate are not found to be as high. The reason for the discrepancy is the leakage area. As the number of perforated tiles decreases, the leakage area becomes comparable to the open area of the perforated tiles. As a result, the leakage airflow must be taken into account while estimating the plenum pressure and the average airflow rate through each perforated tile.

A detailed study of the effect of leakage is presented by Radmehr et al. [21] and Karki et al. [22]. The study includes careful measurements performed in a data center with and without distributed leakage from the floor. The measurements are also compared with the results of CFD simulations.

5 Effect of Under-Floor Obstructions

5.1 Types of Under-Floor Obstructions. In the under-floor space in a data center, usually there are many pipes, cables, structural beams, and other objects. Their presence reduces the area available for the airflow and creates nonuniformities in the pressure distribution. These are substantial effects and must be in-

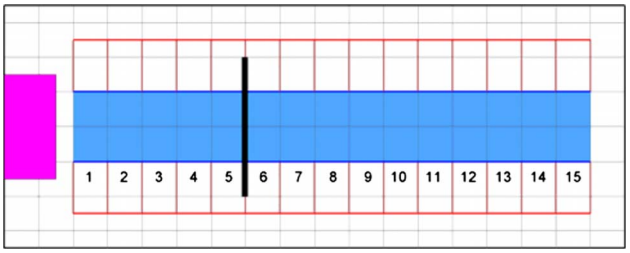

Fig. 19 A circular pipe as an under-floor obstruction (only the centerline of the pipe is shown)

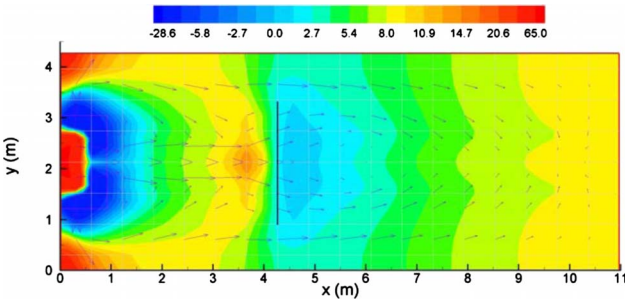

Fig. 21 Pressure distribution and velocity vectors under the raised floor for the case of the circular-pipe obstruction (the pressure values are in Pa)

cluded in a CFD simulation.

In addition to the obstructions that are present for other reasons (bringing in chilled water or electrical power), we can consider placing deliberate obstructions for the purpose of controlling the airflow distribution. This is an inexpensive way of getting the desired flow distribution. This concept will be illustrated in this section.

5.2 Effect of a Circular Pipe as an Obstruction. As a demonstration of how an under-floor obstruction influences the airflow distribution through the perforated tiles, a modification to the base case is considered. As shown in Fig. 19, a circular pipe of 6-in. (0.15 m) diameter is placed in the under-floor space as an obstruction. (Only the centerline of the pipe is shown in the figure. In the 12-in. height of the raised floor, the pipe is placed on the solid subfloor leaving a 6-in. clearance above it.) Fig. 20 shows the resulting airflow distribution through the perforated tiles. The corresponding velocity vectors and pressure distribution just under the raised floor are displayed in Fig. 21. In general, the pipe allows the pressure to build up in the upstream region. So, the flow rates close to the CRAC unit are not as small as in the base case. In the immediate upstream region of the pipe, air velocity increases (due to the blockage caused by the pipe) and pressure falls. Then, there is a further lowering of the pressure on the downstream side of the pipe. Thereafter, the pressure gradually builds up as the horizontal flow velocity diminishes. These pressure changes are reflected in the airflow distribution through the perforated tiles.

5.3 Use of Inclined Partitions. As mentioned above, deliberate obstructions can be used to control the airflow distribution. A convenient obstruction is a vertical partition placed in the under-floor space. The flow misdistribution in the base case occurs because the horizontal flow velocity deceases as the air emerges from the perforated tiles. If this velocity can be kept uniform (by deceasing the area available for the under-floor flow), then the pressure would remain uniform. Consequently, a uniform airflow distribution can be achieved through the perforated tiles.

Figure 22 shows the base case modified by the placement of two inclined partitions in the under-floor space. The partitions attempt to reduce the available area for the horizontal flow in a linear fashion. However, in order to avoid intersecting the final perforated tiles, the final area at the right end is kept finite and not made zero. The resulting airflow distribution through the perforated tiles is presented in Fig. 23, along with the distribution for the no-partition case. It can be seen that the use of the inclined partitions leads to a much more uniform airflow distribution compared with the base case. The only nonuniformities are in the region close to the CRAC unit (due to the rather complex flow there) and at the right end (due to our inability to make the area reduce to zero).

There is a valid criticism of the use of solid impermeable partitions that lead to closed regions in the under-floor space. For a data center with many CRAC units, the possibility of failure of one of the CRAC units is always present. In absence of solid partitions, other CRAC units would supply some of the air to the perforated tiles that are normally supplied by the failed CRAC unit. Solid partitions (such as the inclined ones used in Fig. 22) prevent such cross transfer and are likely to turn a normal failure into a catastrophic one.

From this point of view, a perforated plate can be a more suitable partition. A perforated partition does not completely stop the flow through it; however, the extra flow resistance offered by the partition can be used to discourage the flow in one place and consequently to encourage the flow in other places. The use of perforated partitions is discussed next.

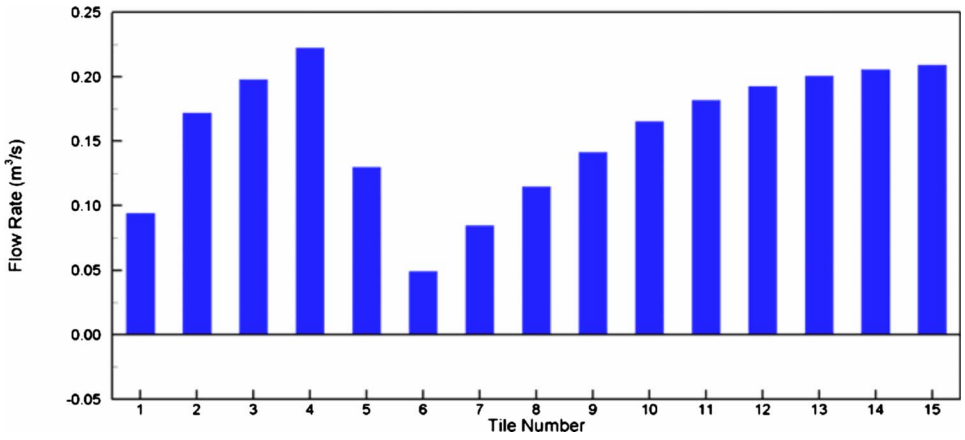

Fig. 20 Flow rates through perforated tiles as affected by the circular-pipe obstruction

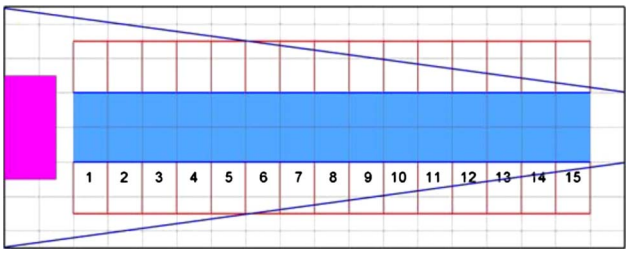

Fig. 22 Use of inclined partitions in the under-floor space

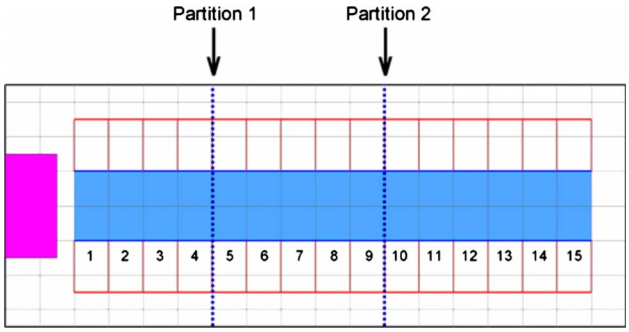

Fig. 24 Use of perforated partitions in the under-floor space

5.4 Use of Perforated Partitions. The flow maldistribution in the base case delivers large airflow rates through the perforated tiles located far way from the CRAC unit. The flow distribution can be made more uniform by placing perforated partitions normal to the horizontal flow so that the flow will be somewhat discouraged from moving fast to the downstream region. This concept is shown in Fig. 24 with two proposed locations for the partitions. The required percent open area of the partitions will be determined by computational experiments.

In Fig. 25, the results of airflow distribution are shown for the case of the two perforated partitions set at 70% and 30% open, respectively. Also shown for reference are the results for the no-partition case. It can be seen that the use of the partitions has increased the airflow in the tiles near the CRAC unit. At each partition location, there is a drop in the airflow rate due to the pressure drop across the partition. Actually, the "discouragement" of the flow is so strong that the six tiles furthest away from the CRAC unit have a rather small flow through them. To get a uniform flow, we need to adjust the percent open area of the partitions. However, if we do desire a large airflow for tiles 1–9 and a small airflow for tiles 10–15, then the current arrangement is quite satisfactory. In general, the perforated partitions can be used to get any *desired* distribution of airflow rates, not just a uniform distribution.

Figure 26 shows a further attempt with the partitions set at 75% and 50%. The airflow distribution has improved, but is still not quite uniform. The case in Fig. 27 uses partitions at 80% and 65% open area. The resulting airflow distribution is quite uniform. In fact, except for tile 1 (which is affected by the very complex flow in the vicinity of the CRAC unit), all other tiles give nearly the same airflow.

6 Above-Floor Effects

6.1 The Main Consideration. As already mentioned above, in a data center, the goal of cooling is to ensure that the maximum inlet temperature to any server rack does not exceed the allowable inlet temperature. The purpose of measurement and/or simulation in the above-floor space is to verify whether this requirement is satisfied. The primary cause of high inlet temperatures is insufficient airflow supplied through the perforated tile at the foot of the server rack. If the airflow demand of the rack cannot be met by the perforated tile, the upper part of the rack draws in hot air. To illustrate this, a small section of a data center is shown in Fig. 28, in which insufficient cooling airflow is supplied. For this situation, the calculated inlet temperatures for the racks are displayed in Fig. 29. (The color scale used for plotting the temperature contours is included in Fig. 29. The same color scale is used for all the remaining figures that show a temperature distribution. For this reason, the color scale is not repeated in those figures.) Since the cooling airflow is insufficient, all racks have hot air entering the tops of their inlets. Figure 30 shows where this hot air originates. It is the hot exhaust of the rack that gets recirculated into the inlet when the cooling air is insufficient. This was shown earlier in Fig. 5 via a simple example.

If sufficient cooling airflow is supplied at the foot of the server rack, usually there is no reason for unsatisfactory cooling. However, there are special locations and circumstances in which hot air can enter the inlets even when sufficient cold airflow is supplied at the perforated tiles. Some of these are described below.

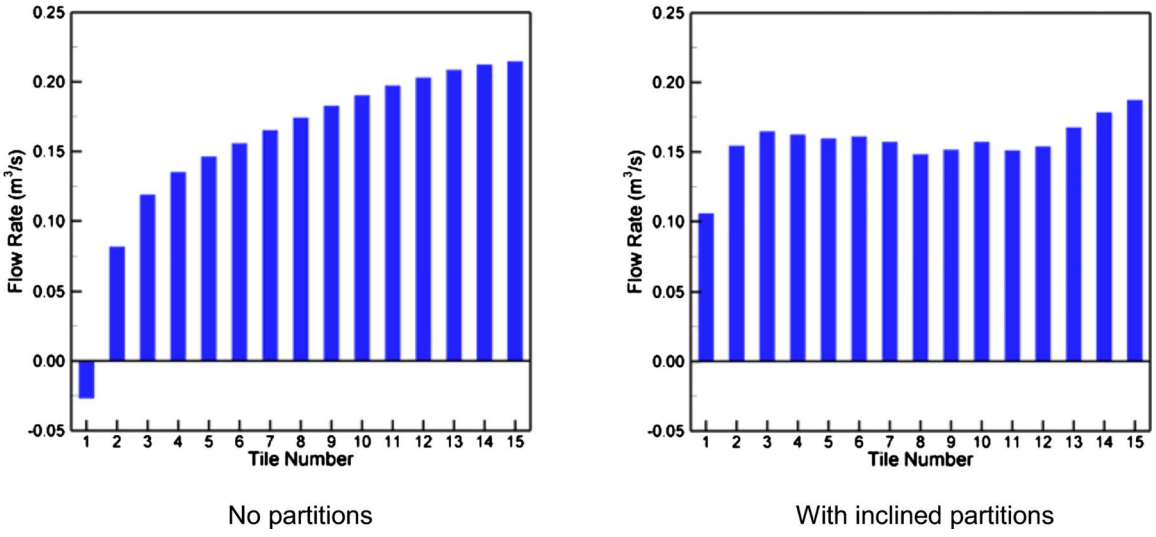

Fig. 23 Airflow distribution with and without inclined partitions

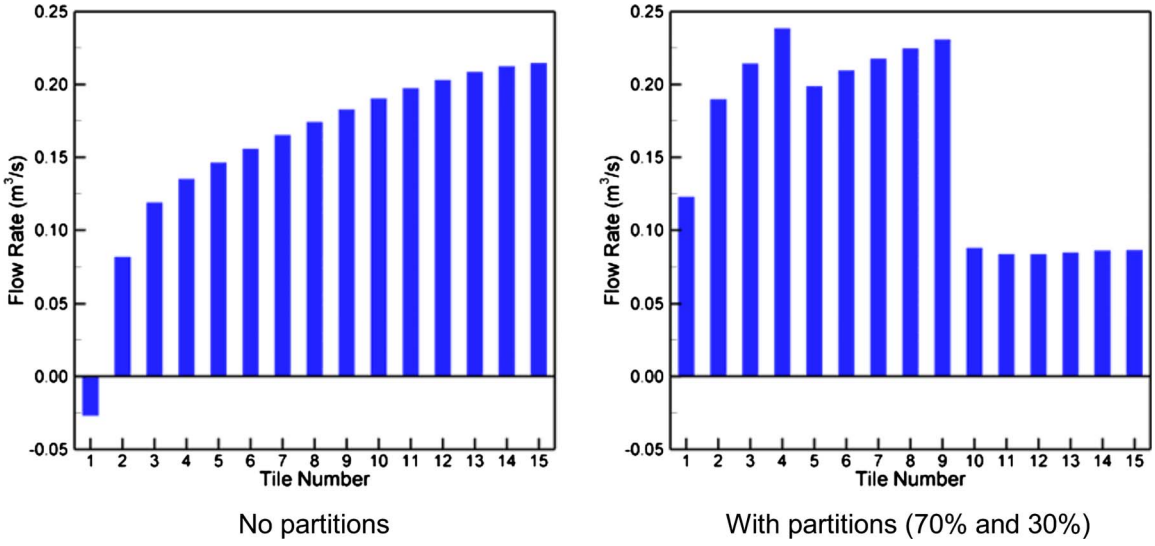

Fig. 25 Airflow distribution with and without perforated partitions (70% and 30%)

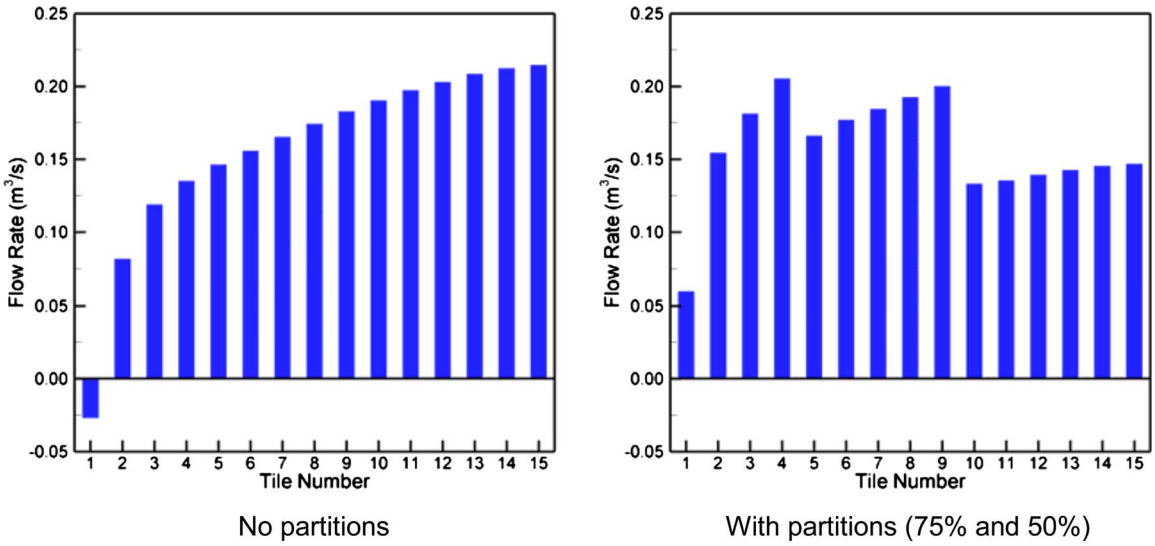

Fig. 26 Airflow distribution with and without perforated partitions (75% and 50%)

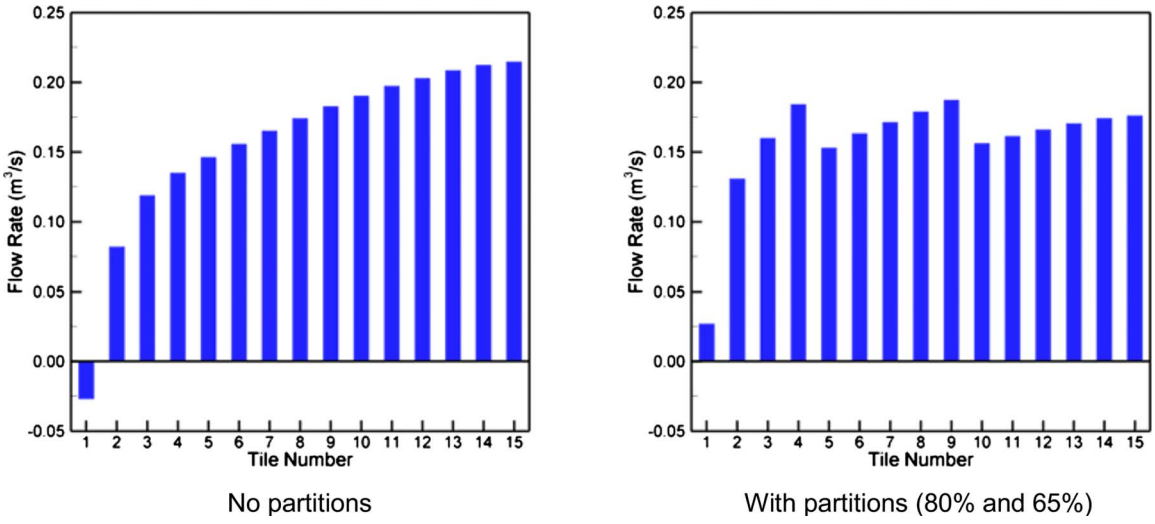

Fig. 27 Airflow distribution with and without perforated partitions (80% and 65%)

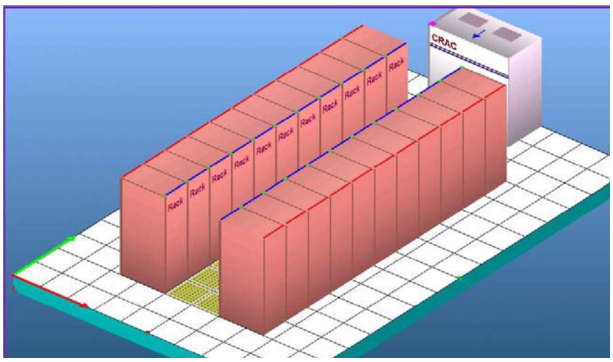

Fig. 28 A simple data center model with one CRAC, several racks, and perforated tiles (insufficient cooling airflow)

6.2 End Effects. Suppose that in Fig. 28, the airflow was increased to meet the demands of the racks. The corresponding calculated inlet temperatures are displayed in Fig. 31. It can be seen that most of the racks in the middle have acceptable low inlet temperatures over the whole inlet face. However, higher inlet temperatures are seen for the racks near the CRAC unit and also for the racks furthest away from the CRAC unit. The behavior near the CRAC is easy to understand. As we have seen before, the usual maldistribution of airflow leads to small airflow rates at the perforated tiles near the CRAC. This insufficient cooling flow leads to the higher inlet temperatures for the racks in that region. Far away from the CRAC unit, the perforated tiles deliver the

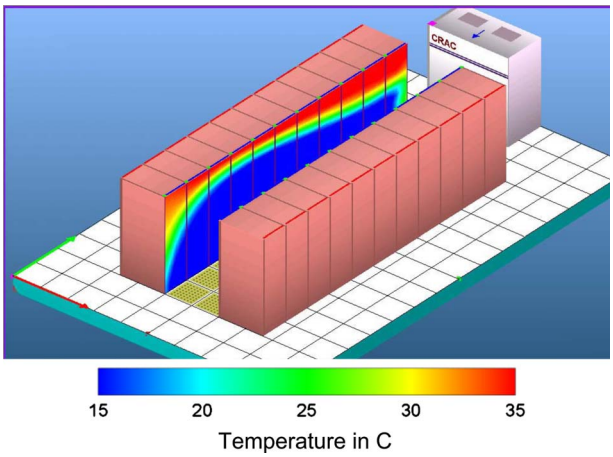

Fig. 29 Temperature distribution on the inlet faces of the racks (insufficient cooling airflow)

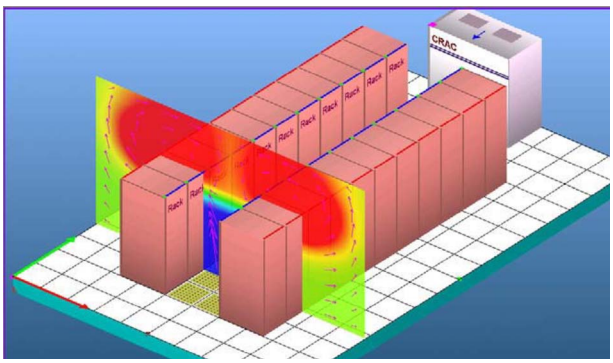

Fig. 30 Temperature distribution and velocity vectors on a plane (insufficient cooling airflow)

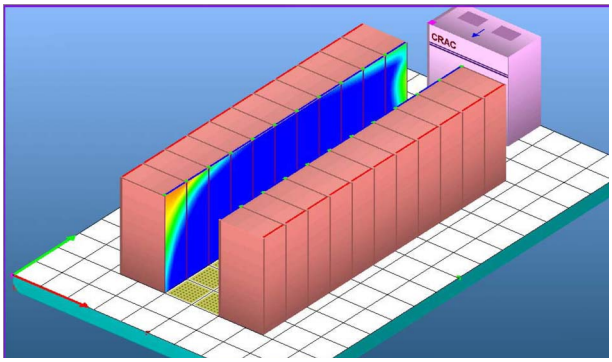

Fig. 31 Temperature distribution on the inlet faces of the racks with increased cooling airflow

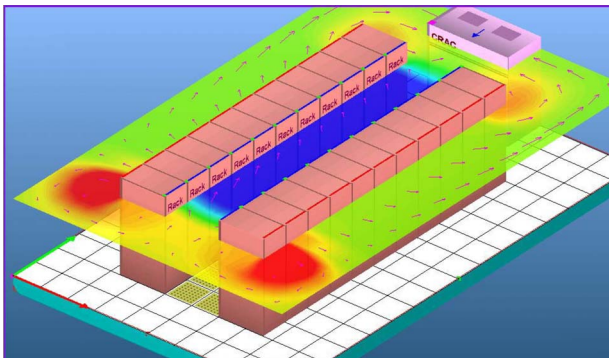

Fig. 32 Temperature distribution and velocity vectors on a horizontal plane

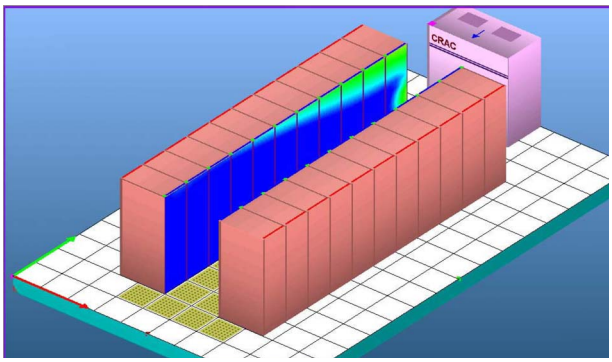

Fig. 33 Temperature distribution on the inlet faces of the racks with an air curtain

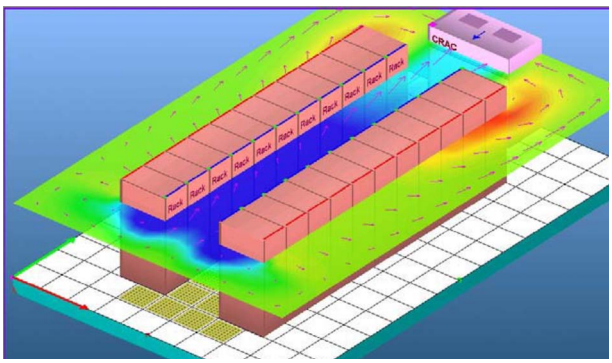

Fig. 34 Temperature distribution and velocity vectors on a horizontal plane (with an air curtain)

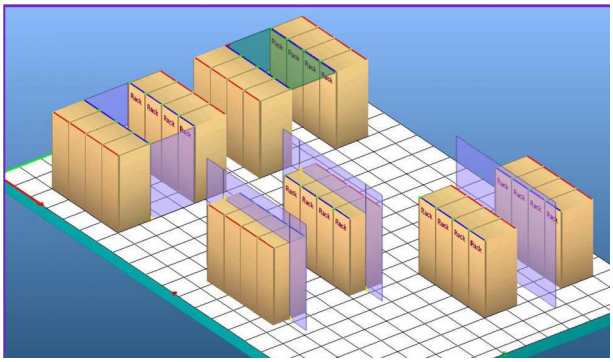

Fig. 35 Use of partitions to prevent hot air from entering the inlets of the racks

highest airflow rates. So, at first glance, the behavior of the racks in that region is difficult to understand. Figure 32 shows a plot of temperature distribution on a horizontal plane near the top of the racks. Although the perforated tiles in the end region (away from the CRAC) deliver sufficient flow, the hot exhaust air finds its way around the last rack and enters the rack inlets.

One quick remedy for this effect is shown in Fig. 33. Here, additional perforated tiles are placed in the end region to create an air curtain of cold air. The corresponding inlet temperatures in Fig. 33 can be seen to be an improvement over the distribution in Fig. 31. Figure 34 shows how the air curtain is effective in preventing the recirculation of hot air into the rack inlets.

6.3 Gaps Between the Racks. Normally, the racks are placed in a row in a contiguous manner. However, occasionally, there may be gaps between them. For example, in practice, gaps are created by *removing* a rack from a row. It is easy to see that the gaps provide additional places where the "end effects" can be observed. Hot air from the back of the racks can enter the cold aisle through the gaps and influence the inlet temperatures of the

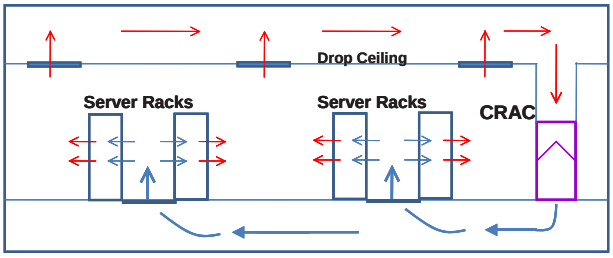

Fig. 36 A schematic of the drop-ceiling arrangement

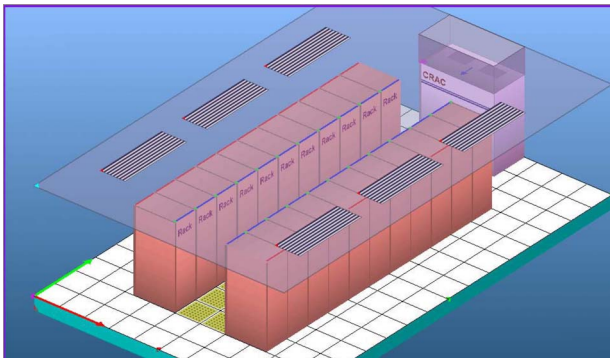

Fig. 37 Use of the drop ceiling

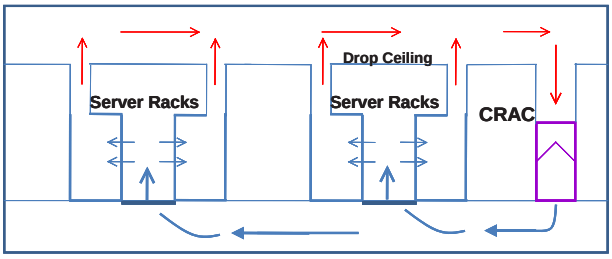

Fig. 38 A schematic of ducted racks with drop ceiling

racks. An obvious remedy is to close the gaps by using impermeable plates or partitions.

6.4 High-Velocity Flow Through the Perforated Tiles. The heat loads of modern server racks can be very high (10–20 kW) and the corresponding airflow demand may be of the order of 1.0 m^3/s. At these flow rates, air emerges from the perforated tile at a velocity of 3 m/s. When this high-velocity stream flows over the inlet face of the rack, would the cooling air enter the rack or simply flow past it? This is a valid concern. Radmehr et al. [25] considered this issue and performed a detailed analysis of the situation. It was shown that the high-velocity airflow does create a low-pressure region at the bottom of the rack. This means that the server fans in the bottom region deliver a lower flow rate compared with the uniform-pressure environment. Fortunately, this flow reduction is not large. The results in the paper indicate that, for realistic values of the flow resistance inside a server rack and for common fan curves, the flow reduction at the bottom of the rack is less than 15%.

6.5 Use of Above-Floor Partitions. The success of cooling in a data center depends on keeping the hot air away from the inlets of the server racks. This can be partially arranged by placing solid partitions in appropriate places. Figure 35 shows some possible arrangements. In the two configurations at the back, the top or the sides of the cold aisle are closed. This would prevent hot air entering the cold aisle from the top or from the side. The arrangement in the middle tries to prevent both top and side recirculation.

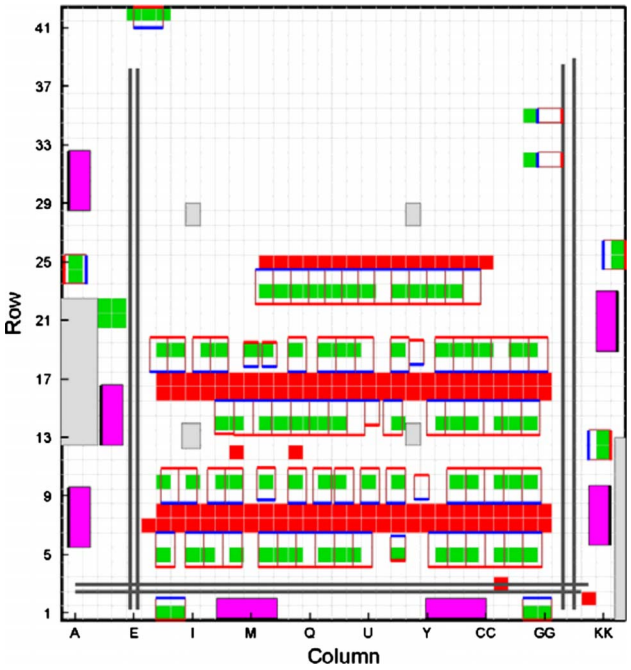

Fig. 39 Layout of the NCEP data center

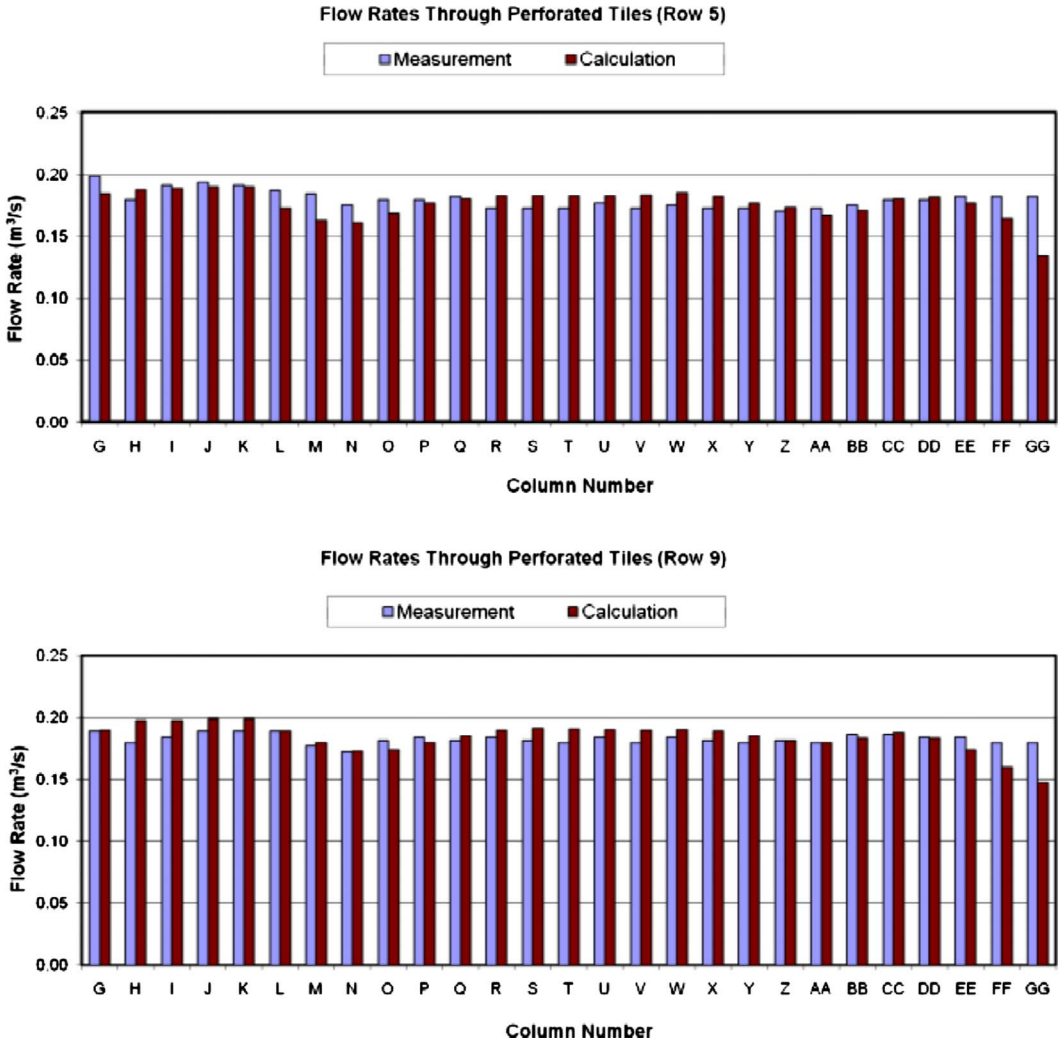

Fig. 40 Comparison of measured and computed airflow rates through perforated tiles

The arrangement at the right of the figure is an attempt to deal with the effects of a bad original layout. In this layout, the hot exhaust from one set of racks blows into the inlet faces of the next set of racks. (The hot aisle/cold aisle arrangement is not used.) The partition between the two rows of racks helps to keep the hot air away from the next set of inlets.

The use of partitions is an inexpensive way of keeping the hot air away from the inlets of the racks. An ultimate use of partitions is the arrangement known as the ceiling plenum or the use of a drop ceiling. This is described next.

6.6 Drop Ceiling. Figure 36 shows a schematic of the drop-ceiling arrangement, in which a false ceiling is created below the real ceiling. Above the hot aisles, vents are placed in the drop ceiling to take the hot air to the space above the drop ceiling. From this space, the hot air is ducted to the top of the CRAC units. A three-dimensional picture of the use of the drop ceiling is shown in Fig. 37. This arrangement creates a near-perfect separation between the hot and cold air and ensures satisfactory cooling.

6.7 Ducted Racks. Some designs go one step further. Instead of using vents above the hot aisle to capture the hot air, exhaust ducts are attached to the racks to transport hot air to the space above the drop ceiling. This arrangement is schematically shown in Fig. 38. It guarantees complete separation between hot and cold air. As long as the *total* amount of required airflow is supplied through the perforated tiles, proper cooling of all racks is assured. The flow distribution through the perforated tiles is no more important. The cold air can be supplied anywhere in the room; it will find its way to the inlets of the racks without getting "diluted" by any hot air.

6.8 Concerns About the Ducted Solutions. Although the need for reliable and assured cooling has made the arrangements like drop ceiling and ducted racks quite popular, they create some concerns. Originally, the attractions of the raised-floor design were its simplicity and flexibility. One could easily move server racks to new locations and simply place perforated tiles next to them to provide cooling air. No ducting was involved. The use of a drop ceiling requires ducting of the return airflow to the CRAC units. This makes it difficult to relocate the CRACs. Moving any racks to new locations requires the relocation of the vents on the drop ceiling in addition to the movement of perforated tiles.

The use of ducted racks presents additional problems. Relocating the racks is now even more difficult. Further, the flow rate provided by the CRAC blowers should match the flow rate demanded by the internal fans in the server racks. Otherwise, the spaces above and below the drop ceiling will be at very different pressures. This will cause the CRAC blowers and the server fans to operate at abnormal conditions. If, for the same set of CRACs, one adds or removes a number of server racks, a significant disparity in flow rates will arise.

These problems can be partially handled by (i) ensuring that the total flow rate provided by the CRACs is always equal to or greater than the airflow demanded by the server fans and (ii) pro-

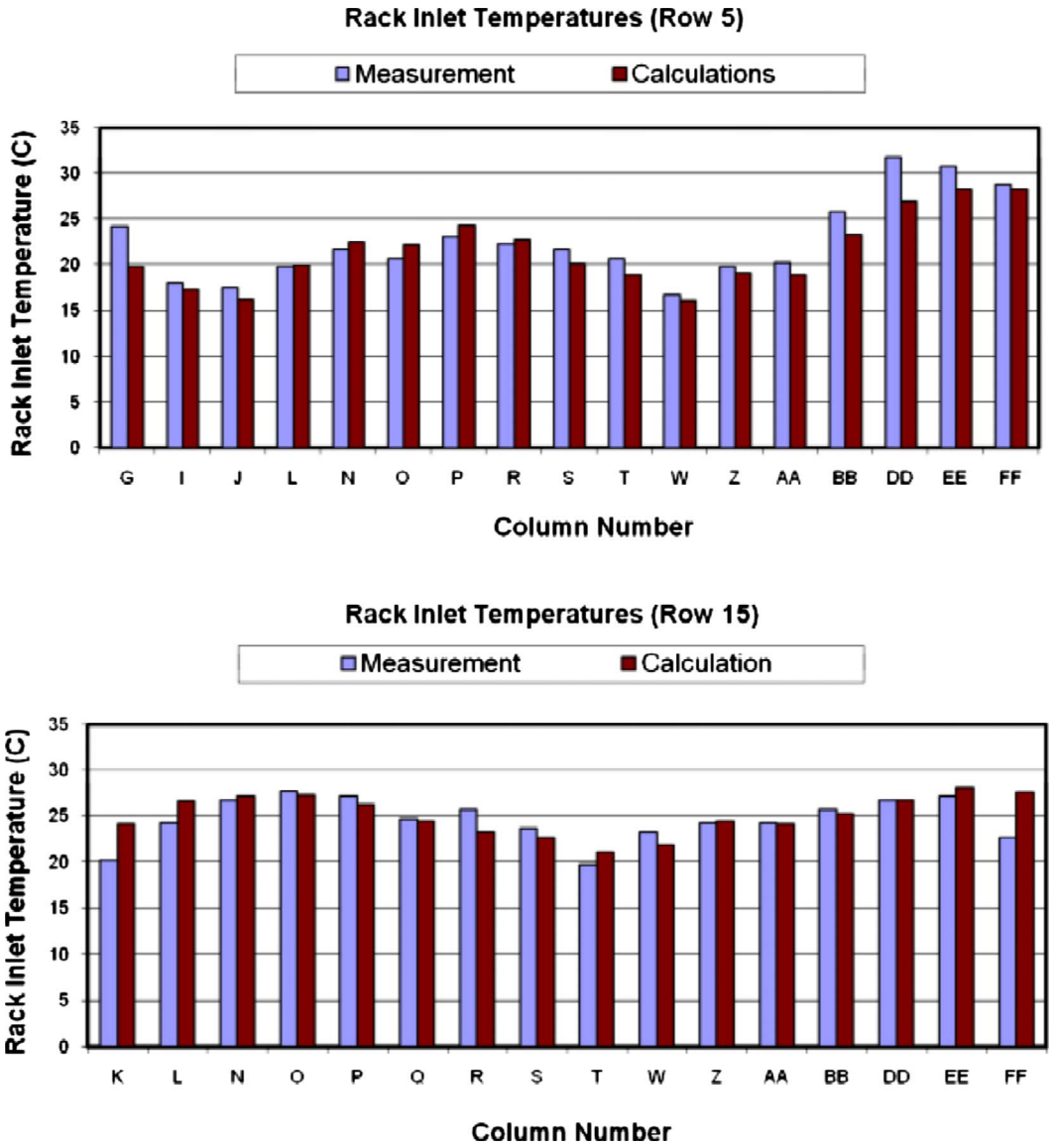

Fig. 41 Comparison of measured and computed temperatures at the rack inlets

viding vents in the drop ceiling (in addition to the ducted returns from the racks). The excess cold airflow will pass through these vents and will help to reduce the pressure difference between the spaces above and below the drop ceiling.

The most serious concern is what happens when one or more CRAC units fail. Then the above-mentioned matching of the flow rates does not hold any more. Since the airflow exhausted by the server fans cannot be handled by the remaining CRAC units, hot air will flow from the space above the drop ceiling into the room below through the extra vents provided. This hot air can directly enter the server racks causing a catastrophic failure.

6.9 Advanced Cooling Solutions. The increasing demands on data centers have led to a number of unconventional cooling solutions. These include in-row coolers, rear-door heat exchangers, and overhead-cooling units. An in-row cooler is similar to a rack and is placed in the middle of a row of racks. It draws in hot air from its back side (from the hot aisle), internally cools it, and exhausts cold air into the cold aisle. This cold air then enters the inlets of the surrounding server racks. A rear-door heat exchanger is mounted literally as a rear door for a rack. The normal hot exhaust from the rack is cooled in this heat exchanger so that the exhaust air is at an acceptably low temperature. This eliminates any hot-air streams in the data center and ensures proper cooling. There are also overhead-cooling units that draw in hot air from the hot aisle, cool it, and blow cold air downwards into the cold aisle.

6.10 A Non-Raised-Floor Data Center. Nearly all the discussion in this paper has focused on a raised-floor data center, which represents the most common design. However, there are non-raised-floor data centers used for special applications. For example, telecommunications equipment is so heavy that often it cannot be conveniently mounted on a raised floor. When there is no raised floor, the cooling air may come from upflow CRAC units (as opposed to the downflow units used in a raised-floor environment), from overhead ducts, and from the advanced cooling solutions mentioned above.

7 Validation of Above-Floor Simulation

As a sample of how computed results agree with measurements, a comparison with the measurements by Schmidt [20] is shown here. Figure 39 shows the layout of a data center at the National Center for Environmental Protection (NCEP), Bethesda, MD. Figure 40 gives a plot of computed and measured flow rates through the perforated tiles in selected rows. Figure 41 presents the com-

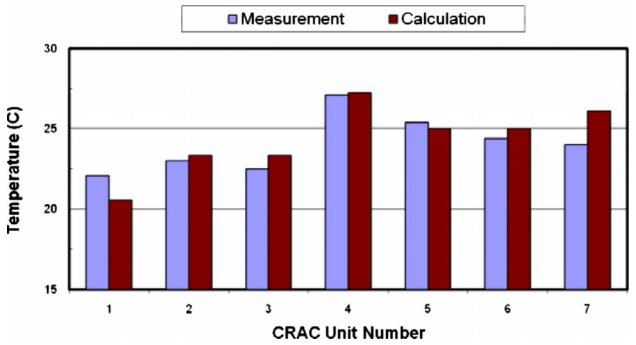

Fig. 42 Comparison of measured and computed return temperatures for the CRAC units

parison of computed and measured temperatures at the rack inlets at a height of 1.68 m (5.5 ft) from the floor (for selected rows). Finally, Fig. 42 compares the computed and measured values of the CRAC return temperatures for the seven CRAC units in the data center. In general, the agreement can be seen to be very good.

8 Work of the ASHRAE TC 9.9 Committee

This paper has described various fundamental and practical challenges in cooling a data center. To make a concerted effort on resolving many technical issues and to provide leadership and standardization, the Technical Committee TC 9.9 (Mission Critical Facilities, Technology Spaces, and Electronic Equipment) was established in 2002 under the auspices of American Society of Heating, Refrigerating, and Air-Conditioning Engineers (ASHRAE). The committee has representatives from over 110 organizations, which include manufacturers and users of data center equipment, consulting companies, and related agencies. The committee has made important contributions to ASHRAE handbooks and has published seven books [30–36] in the ASHRAE Datacom Series on topics directly related to data centers. These books represent a valuable resource for cooling and related issues in a data center.

9 Concluding Remarks

This paper has dealt with a number of issues pertaining to the airflow and cooling in data centers. For a raised-floor data center, the flow field in the under-floor space holds the key to the distribution of airflow through the perforated tiles. If the airflow demand of each server rack is met by supplying the required airflow at the foot of the rack, proper cooling is, in general, assured. The airflow distribution through the perforated tiles is governed by the pressure variation under the raised floor. This is affected by the height of the raised floor, the locations of the CRAC units, the layout of the perforated tiles, their open area, and the presence of under-floor obstructions. Whereas some obstructions are present as a practical necessity, deliberate placement of obstructions (such as perforated partitions) can be used to influence the flow field in a desirable way.

In the above-floor space, the goal is to prevent any hot-air stream from reaching the inlets of the server racks. This is primarily achieved by supplying sufficient cold air at the perforated tiles. In addition, air curtains, partitions, drop ceiling, and ducted racks can be used to achieve a separation between the hot and cold air streams. In special circumstances, advanced cooling solutions that provide localized cooling can be used.

Cooling in a data center is a topic of enormous practical importance. It also leads to many physical, mathematical, and computational issues that are very fascinating.

Acknowledgment

The author would like to thank his colleague Dr. Kailash C. Karki for his significant help in the preparation of this paper.

Nomenclature

A_{tile} = total area of the perforated tiles
A_{cs} = cross-sectional area of the plenum
d_h = hydraulic diameter
f = friction factor
F = fractional open area for the perforated tile
K = pressure-loss factor
L = streamwise distance
p = pressure
V = velocity approaching the perforated tile
η = area ratio
ρ = density of air
Φ = frictional resistance parameter
Ψ = pressure variation parameter

References

[1] Seymour, M., 1992, "Dynamic Design on Atria," *Building Services*, Chartered Institution of Building Services Engineers (CIBSE), pp. 27–29.
[2] Awbi, H. B., and Gan, G., 1994, "Prediction of Airflow and Thermal Comfort in Offices," ASHRAE J., **36**(2), pp. 17–21.
[3] Kiff, P., 1995, "A Fresh Approach to Cooling Network Equipment," *British Telecommunications Engineering*, Institution of British Telecommunications Engineers, London.
[4] Bullock, C. E., and Phillip, F., 1996, "The Sistine Chapel: HVAC Design for Special-Use Buildings," ASHRAE J., **38**(4), pp. 49–58.
[5] Schmidt, R. R., 1997, "Thermal Management of Office Data Processing Centers," InterPack '97, Hawaii.
[6] Cinato, P., Bianco, C., Licciardi, L., Pizzuti, F., Antonetti, M., and Grossoni, M., 1998, "An Innovative Approach to the Environmental System Design for TLC Rooms in Telecom Italia," Intelec 98.
[7] Quivey, B., and Bailey, A. M., 1999, "Cooling of Large Computer Rooms—Design and Construction of ASCI 10 TeraOps," InterPack 1999, Maui, HI.
[8] Kang, S., Schmidt, R. R., Kelkar, K. M., Radmehr, A., and Patankar, S. V., 2001, "A Methodology for the Design of Perforated Tiles in Raised Floor Data Centers Using Computational Flow Analysis," IEEE Trans. Compon. Packag. Technol., **24**(2), pp. 177–183.
[9] Schmidt, R. R., Karki, K. C., Kelkar, K. M., Radmehr, A., and Patankar, S. V., 2001, "Measurements and Predictions of the Flow Distribution Through Perforated Tiles in Raised-Floor Data Centers," ASME Paper No. IPACK2001-15728.
[10] Schmidt, R. R., 2001, "Effect of Data Center Characteristics on Data Processing Equipment Inlet Temperatures," ASME Paper No. IPACK2001-15870.
[11] Schmidt, R. R., and Cruz, E., 2002, "Raised Floor Computer Data Center: Effect on Rack Inlet Temperatures of Chilled Air Exiting Both the Hot and Cold Aisles," IEEE 2002 Inter Society Conference on Thermal Phenomena, pp. 580–594.
[12] Schmidt, R. R., and Cruz, E., 2004, "Cluster of High-Powered Racks Within a Raised-Floor Computer Data Center: Effect of Perforated Tile Flow Distribution on Rack Inlet Temperatures," ASME J. Electron. Packag., **126**, pp. 510–518.
[13] Patel, C. D., Bash, C. E., Belady, C., Stahl, L., and Sullivan, D., 2001, "Computational Fluids Dynamics Modeling of High Compute Density Data Centers to Assure System Air Inlet Specifications," ASME Paper No. IPACK2001-15622.
[14] Patel, C. D., Sharma, R., Bash, C. E., and Beitelmal, A., 2002, "Thermal Considerations in Cooling Large Scale High Compute Data Centers," *ITHERM 2002, Proceedings of the Eighth Intersociety Conference on Thermal and Thermomechanical Phenomena in Electronic Systems*.
[15] Karki, K. C., Patankar, S. V., and Radmehr, A., 2003, "Techniques for Controlling Airflow Distribution in Raised-Floor Data Centers," ASME Paper No. IPACK 2003-35282.
[16] Karki, K. C., Radmehr, A., and Patankar, S. V., 2003, "Use of Computational Fluid Dynamics for Calculating Flow Rates Through Perforated Tiles in Raised-Floor Data Centers," HVAC&R Res., **9**(2), pp. 153–166.
[17] Patankar, S. V., and Karki, K. C., 2004, "Distribution of Cooling Airflow in a Raised-Floor Data Center," ASHRAE Trans., **110**(2), pp. 629–635.
[18] Guggari, S., Agonafer, D., Belady, C., and Stahl, L., 2003, "A Hybrid Methodology for the Optimization of Data Center Room Layout," Paper No. IPACK2003-35273.
[19] Bash, C. E., Patel, C. D., and Sharma, R. K., 2003, "Efficient Thermal Management of Data Centers—Immediate and Long-Term Research Needs," HVAC&R Res., **9**(2), pp. 137–152.
[20] Schmidt, R. R., 2004, "Thermal Profile of a High-Density Data Center—Methodology to Thermally Characterize a Data Center," ASHRAE Trans., **110**(2), pp. 635–642.

[21] Radmehr, A., Schmidt, R. R., Karki, K. C., and Patankar, S. V., 2005, "Distributed Leakage Flow in Raised-Floor Data Centers," ASME Paper No. IPACK2005-73273.
[22] Karki, K. C., Radmehr, A., and Patankar, S. V., 2007, "Prediction of Distributed Air Leakage in Raised-Floor Data Centers," ASHRAE Trans., **113**(1), pp. 219–226.
[23] Van Gilder, J., and Schmidt, R. R., 2005, "Airflow Uniformity Through Perforated Tiles in a Raised-Floor Data Center," ASME Paper No. IPACK2005-73375.
[24] Karki, K. C., and Patankar, S. V., 2006, "Airflow Distribution Through Perforated Tiles in Raised-Floor Data Centers," Build. Environ., **41**(6), pp. 734–744.
[25] Radmehr, A., Karki, K. C., and Patankar, S. V., 2007, "Analysis of Airflow Distribution Across a Front-to-Rear Server Rack," ASME Paper No. InterPack2007-33574, pp. 8–12.
[26] Sullivan, R. F., "Alternating Cold and Hot Aisles Provides More Reliable Cooling for Server Farms," a White Paper From the Uptime Institute, Incorporated, Santa Fe, NM.
[27] Idelchik, I. E., 1994, *Handbook of Hydraulic Resistance*, CRC, Boca Raton, FL.
[28] Bajura, R. A., and Jones, E. H., 1976, "Flow Distribution in Manifolds," ASME J. Fluids Eng., **98**, pp. 654–666.
[29] Majumdar, A. K., 1980, "Mathematical Modelling of Flows in Dividing and Combining Flow Manifolds," Appl. Math. Model., **4**, pp. 424–432.
[30] ASHRAE, 2004, *Thermal Guidelines for Data Processing Environments* (ASHRAE Datacom Series), ASHRAE, Atlanta, GA.
[31] ASHRAE, 2005, *Datacom Equipment Power Trends and Cooling Applications* (ASHRAE Datacom Series), ASHRAE, Atlanta, GA.
[32] ASHRAE, 2005, *Design Considerations for Datacom Equipment Centers* (ASHRAE Datacom Series), ASHRAE, Atlanta, GA.
[33] ASHRAE, 2006, *Liquid Cooling Guidelines for Datacom Equipment Centers* (ASHRAE Datacom Series), ASHRAE, Atlanta, GA.
[34] ASHRAE, 2008, *Structural and Vibration Guidelines for Datacom Equipment Centers* (ASHRAE Datacom Series), ASHRAE, Atlanta, GA.
[35] ASHRAE, 2008, *Best Practices for Datacom Facility Energy Efficiency* (ASHRAE Datacom Series), ASHRAE, Atlanta, GA.
[36] ASHRAE, 2008, *High Density Data Centers—Case Studies and Best Practices* (ASHRAE Datacom Series), ASHRAE, Atlanta, GA.

New Bio-Inspired, Multiphase Forced Convection Cooling by ABS Plastic or Encapsulated Paraffin Beads

Fatemeh Hassanipour

José L. Lage

Department of Mechanical Engineering,
Bobby B. Lyle School of Engineering,
Southern Methodist University,
Dallas, TX 75275-0337

Preliminary experimental results of forced convection by octadecane paraffin (encapsulating phase-change material (EPCM)) particles, acrylonitrile butadiene styrene plastic particles, or by clear (of particulates) water flowing through a heated parallel-plates channel are reported. The objective is to investigate the mixing effect of the particles vis-à-vis the latent heat effect. The particle concentration is kept at 3% in volume. The results, in terms of surface-averaged channel temperature and heat transfer coefficient for different fluid speed and heat-flux, indicate the mixing effect to account from 19% to 68% of the heat transfer enhancement produced by using EPCM particles. Hence particle mixing, even at a very low particle concentration, is an effective convection mechanism. [DOI: 10.1115/1.4000710]

Keywords: multiphase cooling, channel convection, phase-change material, particulate flow, bio-inspired

1 Introduction

Encapsulating phase-change material (EPCM) particles, flowing with a fluid through a heat exchanger, transport energy by "storing" it in latent form (an active-to-energy transport role) and by "mixing" the flow field (a passive role). Forced convection by micro-encapsulated phase-change materials (MEPCM) slurries was investigated theoretically by Charunyakorn et al. [1], Hu and Zhang [2], Roy and co-worker [3,4], Ho and co-workers [5,6], Xin et al. [7], Hao and Tao [8], and Wang et al. [9]; and experimentally by Wang and co-workers [9,10], Yamagishi et al. [11], and Cho and Choi [12]. As a large quantity of small particles flowing together, slurry is likely to hinder the mixing effect of individual particles. When compared with MEPCM slurries, large EPCM particles can enhance mixing and reduce clogging, clustering, and settling problems common to slurries.

In this study, large EPCM particles, with a diameter similar to the size of the heated channel, are considered as a new convection mechanism. Notice in passing the recent and very interesting works by Ulusarslan and Teke [13–15] who considered the flow of discrete spherical solid capsules (ice) carried by water inside a circular pipe. Although similar, the configuration studied here is distinct in the flow channel geometry and in the particles used. The present configuration is inspired by alveolar capillaries, where red blood cells (RBCs) are discrete particles flowing with the blood plasma [16]. A characteristic of the alveolar capillaries is the similarity between the diameter of the RBCs and the size of the capillaries.

A parallel-plates channel is built for testing with an isoflux (bottom) and an adiabatic (top) surface. The particle diameter is chosen to be comparable to the channel size. Preliminary tests with EPCM particles did not allow the distinction between the latent heat and the mixing effects [17]. New tests were run using acrylonitrile butadiene styrene (ABS) plastic particles with no latent heat capacity for isolating the mixing effect. Further comparison of heat transfer performance is done considering results obtained with clear (of particles) water. The preliminary results are presented here for particle concentration ϕ_p (volume-fraction) equal to 3%, flow speed u from 3.5×10^{-3} m/s to 12×10^{-3} m/s and channel surface heat-flux q'' from 1.0 kW/m^2 to 14 kW/m^2.

Figure 1 shows a sketch of the equipment. The main component of the apparatus is the test channel, shown in the center of the figure, linked to the inlet and exit reservoirs. The channel has a height of 5.4 mm, a width of 34 mm, and an unheated entrance section of 45 mm long followed by a 121 mm heated section and a 14 mm unheated exit section.

Seven self-adhering, 15 mm by 38 mm, 45 Ω resistance electric heaters (Minco HKK5576R45) are positioned side-by-side (with 2 mm spacing) under the bottom plate of the channel (a 2 mm thin aluminum plate) to provide a uniform heat-flux to the surface. A 2.5 cm fiber insulation panel reduces heat loss (estimated at less than 8% of the dissipated heat). Thirty-two type-T thermocouples with diameter 0.05 mm are uniformly distributed along the heated surface, placed in between the heaters, and secured with a thermal paste.

All particles have a diameter of 3 ± 0.5 mm, slightly smaller than the channel height $H=5.4$ mm. The octadecane (Microtek Laboratories, Inc., Dayton, OH) has a latent heat of 270 kJ/kg and a melting range temperature from 26°C to 36°C (data provided by the manufacturer), i.e., below the maximum channel temperature (about 50°C). The ABS plastic (Horizon Group USA, Warren, NJ) has 105°C melting temperature so there was no latent heat effect. The relevant properties are summarized in Table 1.

The clogging and settling difficulties of having particles flowing with a liquid have been mitigated by including a magnetic propeller (stirrer) inside the inlet reservoir. When rotating, the propeller disperses the particles (which are less dense than water) in the reservoir and it creates a vortex. This vortex has a low pressure at the center causing a suction effect on a feeding tube placed right in the center of the reservoir. This 0.02 m diameter flexible U-tube has the other extremity placed flush with the water surface of the exit reservoir, circulating the water, and particles back to the inlet reservoir. The U-tube passes through a heat exchanger with cold water running through an adjacent circulating bath (chiller), bringing the water and particles back to the inlet temperature $T_{in}=24$°C. A camera (UNIQ Vision, UP-685CL) provides the data for the determination of speed and concentration of the particles moving through the channel.

Uncertainties are length of 1.0%, temperature of 0.2%, voltage of 1.0%, and particle travel time of 5%. For calculated quantities, using the Kline–McClintock method [18]: volume-fraction and heater power of 8%, flow speed of 4%, heat-flux of 6%, and heat transfer coefficient of 7%.

2 Experimental Results

Figures 2 and 3 illustrate the variation in average surface temperature $\overline{T_w}$ for two different flow velocities. For all heat-fluxes tested, the results indicate that the $\overline{T_w}$ is lower for EPCM than for ABS particles than for clear water.

The results for ABS particles show the mixing effect slightly more pronounced at low heat-flux. This effect is possibly because the thermal boundary layer gets thinner as the heat-flux decreases. Also, the difference between ABS and water decreases when the fluid speed increases, probably because the boundary layers get thinner in this case as well.

Observe also the difference between the temperatures for EPCM and ABS particles decreases when the heat-flux is small. In

Contributed by the Heat Transfer Division of ASME for publication in the JOURNAL OF HEAT TRANSFER. Manuscript received March 7, 2009; final manuscript received October 26, 2009; published online April 27, 2010. Assoc. Editor: Wei Tong.

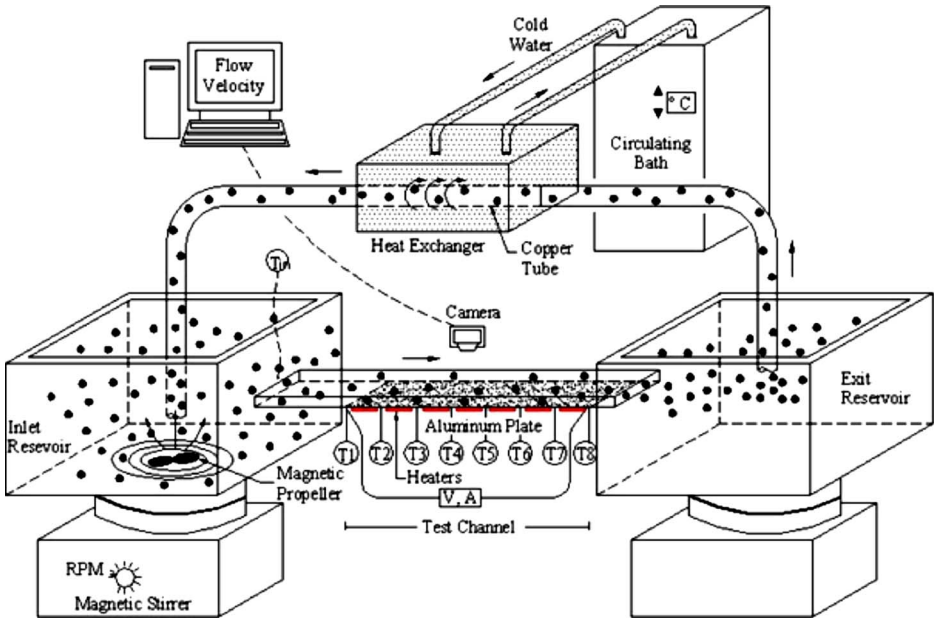

Fig. 1 Sketch of entire experimental set-up showing circulating flow of water and particles

this case, both EPCM and ABS particles behave similarly because the temperature is not high enough to melt the octadecane (no phase-change). As the speed increases from 0.0035 m/s to 0.012 m/s, the heat-flux beyond which the temperatures diverge decrease from around 5 kW/m^2 to about 3.5 kW/m^2. This behavior is believed to be due to the convection effect, which enhances the heat transfer to the flowing water and then to the particles, as the fluid speed increases.

Table 1 Properties of water and particles

	ρ (kg/m^3)	k (W/m K)	c (J/kg K)
Water at 298 K	997	0.61	4180
ABS plastic	1040	0.17	1500
Octadecane (solid)	850	0.34	1800
Octadecane (liquid)	780	0.15	2200

Finally, an average heat transfer coefficient is defined as $\overline{h} = q''/(\overline{T}_w - T_{in})$. The use of T_{in} as a representative fluid temperature is necessary as the "bulk-fluid temperature" of a flowing solid-fluid mixture would be very difficult to obtain except at the inlet.

A summary of the results is shown in Fig. 4 for $q'' = 14$ kW/m^2. Observe the ABS results indicate an increase in the heat transfer coefficient as compared with clear water. This increase can only be attributed to the mixing effect of having particles in the flow.

The phase-change effect (of using EPCM as opposed to ABS) varies from 32% for $u = 0.0055$ m/s to 81% for $u = 0.0120$ m/s of the total effect produced by EPCM particles. Notice the heat transfer coefficient increases by 9–20% as compared with the clear water results by including the EPCM particles in the flow.

3 Conclusions

The mixing effect on the heat transfer coefficient seems to grow steadily with the flow speed while the latent heat effect decreases

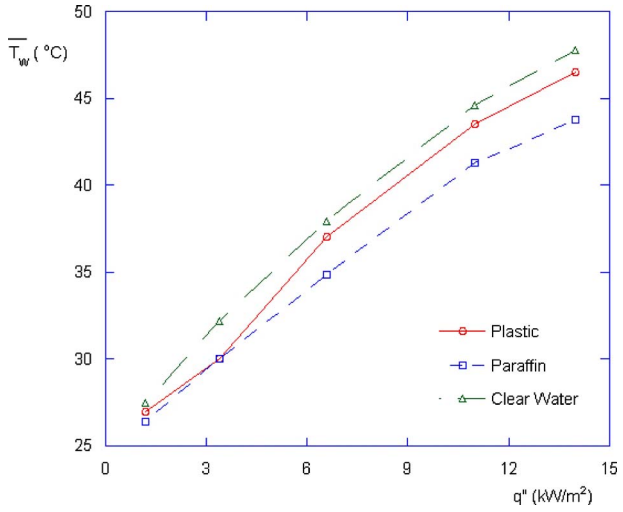

Fig. 2 Effect of heat-flux on average surface temperature for $u = 0.0035$ m/s

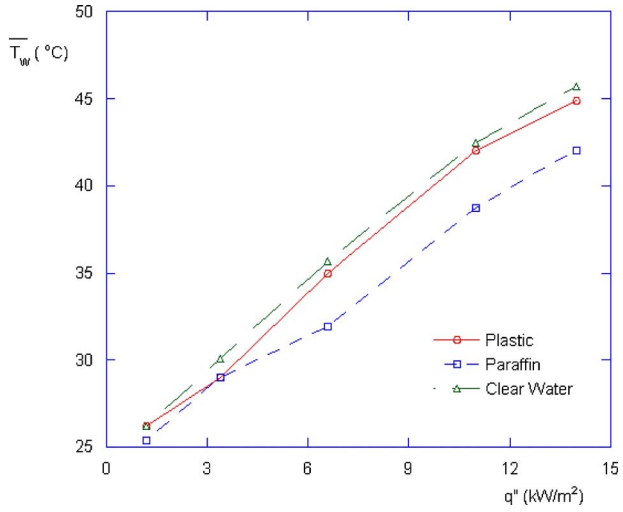

Fig. 3 Effect of heat-flux on average surface temperature for $u = 0.0120$ m/s

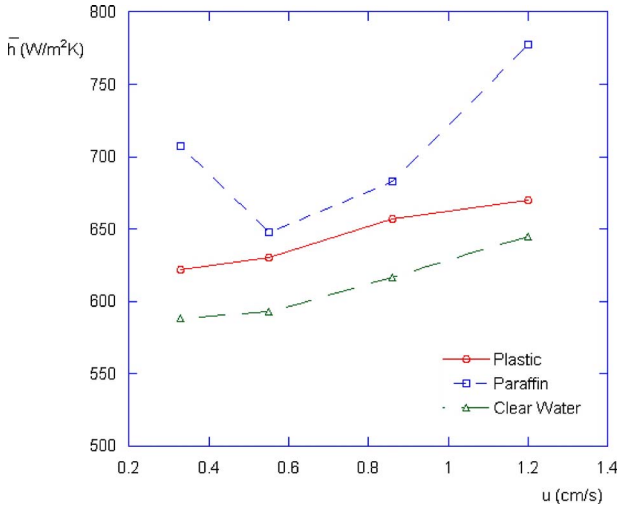

Fig. 4 Effect of flow velocity on heat transfer coefficient for $q''=14$ kW/m^2

first and then increases. Moreover, the relative importance of each effect, i.e., mixing and phase-change, varies with the flow speed. These observations likely lead to a possible optimum configuration in which the mixing and the phase-change effects are maximized, leading to an optimum heat transfer coefficient. Additional tests and analysis are necessary to evaluate this possibility.

Finally, although supercooling effects could retard the solidification of the EPCM inside the inlet reservoir then affecting the phase-change process inside the channel, this possibility is believed to be small as the particles remain flowing in the inlet reservoir for a reasonable time before entering the channel.

References

[1] Charunyakorn, P., Sengupta, S., and Roy, S., 1991, "Microencapsulated Phase Change Material Slurries Flow in Circular Ducts," Int. J. Heat Mass Transfer, **34**, pp. 819–833.

[2] Hu, X., and Zhang, Y., 2004, "Heat Transfer of Solid-Liquid Phase Change Material Suspension in Circular Pipes: Effects of Wall Conduction," Numer. Heat Transfer, Part A, **45**, pp. 171–190.

[3] Roy, S., and Avanic, B., 2001, "Laminar Forced Convection Heat Transfer With Phase Change Material Suspensions," Int. Commun. Heat Mass Transfer, **28**(7), pp. 895–904.

[4] Alisetti, L., and Roy, K., 2000, "Forced Convection Heat Transfer to Phase Change Material Slurries in Circular Ducts," Thermophysics, **14**(1), pp. 115–118.

[5] Ho, C. J., Lin, J. F., and Chiu, S. Y., 2004, "Heat Transfer of Solid-Liquid Phase Change Material Suspension in Circular Pipes: Effects of Wall Conduction," Numer. Heat Transfer, Part A, **45**, pp. 171–190.

[6] Ho, C. J., 2005, "A Continuum Model for Transport Phenomena in Convective Flow of Solid-Liquid Phase Change Material Suspensions," Appl. Math. Model., **29**, pp. 805–817.

[7] Xin, W., Yinping, Z., and Xlanxu, H., 2003, "Turbulent Heat Transfer Enhancement of Microencapsulated Phase Change Material Slurries With Constant Wall Heat Flux," J. Enhanced Heat Transfer, **11**(1), pp. 13–22.

[8] Hao, Y. L., and Tao, Y. X., 2004, "A Numerical Model for Phase-Change Suspension Flow in Microchannels," Part A, **46**, pp. 55–77.

[9] Wang, X., Niu, J., Li, Y., Wang, X., Chen, B., Zeng, R., Song, Q., and Zhang, Y., 2007, "Flow and Heat Transfer Behaviors of Phase Change Material Slurries in a Horizontal Circular Tube," Int. J. Heat Mass Transfer, **50**, pp. 2480–2491.

[10] Wang, X., Niu, J., Li, Y., Zhang, Y., Wang, X., Chen, B., Zeng, R., and Song, Q., 2008, "Heat Transfer of Microencapsulated PCM Slurry Flow in a Circular Tube," AIChE J., **54**(4), pp. 1110–1120.

[11] Yamagishi, Y., Takeuchi, H., Pyatenko, A., and Kayukawa, N., 1999, "Characteristic of Microencapsulated PCM Slurry as a Heat-Transfer Fluid," AIChE J., **45**(4), pp. 696–707.

[12] Cho, K., and Choi, S., 2000, "Thermal Characteristic of Paraffin in a Spherical Capsule During Freezing and Melting Processes," Int. J. Heat Mass Transfer, **43**, pp. 3183–3196.

[13] Teke, I., and Ulusarslan, D., 2005, "An Investigation of the Capsule Velocity, Concentration Rate and the Spacing Between the Capsules for Spherical Capsule Train Flow in a Horizontal Circular Pipe," Powder Technol., **159**, pp. 27–34.

[14] Ulusarslan, D., and Teke, I., 2006, "An Experimental Determination of Pressure Drops in the Flow of Low Density Spherical Capsule Train Inside Horizontal Pipes," Exp. Therm. Fluid Sci., **30**, pp. 233–241.

[15] Teke, I., and Ulusarslan, D., 2007, "Mathematical Expression of Pressure Gradient in the Flow of Spherical Capsules Less Dense than Water," Int. J. Multiphase Flow, **33**, pp. 658–674.

[16] Merrikh, A. A., and Lage, J. L., 2005, "Effect of Blood Flow on Gas Transport in a Pulmonary Capillary," ASME J. Biomech. Eng., **127**, pp. 432–439.

[17] Hassanipour, F., and Lage, J. L., 2008, "Bio-Inspired Particle Enhanced Capillary Heat Exchanger," *Proceedings of the Sixth International ASME Conference on Nanochannels, Microchannels and Minichannel ICNMM*, Darmstadt, Germany.

[18] Kline, S. J., and McClintock, F. A., 1953, "Describing Uncertainties in Single-Sample Experiments," Mech. Eng. (Am. Soc. Mech. Eng.), **75**, pp. 3–8.

Network Modeling of Fin-and-Tube Evaporator Performance Under Dry and Wet Conditions

Ling-Xiao Zhao
Institute of Refrigeration and Cryogenics,
Shanghai Jiaotong University,
Shanghai 200240, China

Liang Yang
Institute of Refrigeration and Cryogenics,
Shanghai Jiaotong University,
Shanghai 200240, China;
China R&D Center,
Carrier Corporation,
No. 3239 Shen Jiang Road,
Shanghai 201206, China

Chun-Lu Zhang[1]
Faculty of Mechanical Engineering,
Tongji University,
No. 4800 Cao An Road,
Shanghai 201804, China
e-mail: chunlu.zhang@gmail.com

A new neural network modeling approach to the evaporator performance under dry and wet conditions has been developed. Not only the total cooling capacity but also the sensible heat ratio and pressure drops on both air and refrigerant sides are modeled. Since the evaporator performance under dry and wet conditions is, respectively, dominated by the dry-bulb temperature and the web-bulb temperature, two neural networks are used together for capturing the characteristics. Training of a multi-input multi-output neural network is separated into training of multi-input single-output neural networks for improving the modeling flexibility and training efficiency. Compared with a well-developed physics-based model, the standard deviations of trained neural networks under dry and wet conditions are less than 1% and 2%, respectively. Compared with the experimental data, errors fall into ±5%. [DOI: 10.1115/1.4000950]

Keywords: heat exchanger, evaporator, model, neural network

1 Introduction

Fin-and-tube heat exchangers are widely used in air-conditioning and refrigeration systems as one of the key components. As an evaporator, the fin-and-tube heat exchanger has a two-phase flow boiling refrigerant inside the tubes and humid air flowing through the fins and tubes with or without water condensation.

Laboratory tests on evaporator performance are relatively expensive and time-consuming because both dry-bulb temperature and wet-bulb temperature or humidity in the testing chamber should be controlled. Therefore, many evaporator models based on the first principles and heat transfer and pressure drop correlations were developed by researchers. For instance, Liu et al. [1] developed a generic tube-by-tube model using the graph theory, which is capable to describe any flexible refrigerant circuitry and quantify the refrigerant distribution in circuits and cross fin heat conduction. The impact of heat exchanger configuration and operating conditions on the heat exchanger performance can be captured in such a model. Therefore, physics-based detailed models with certain accuracy can be used for heat exchanger design and reduction in laboratory tests. However, this kind of model is usually running slow and conditionally stable. If one wants to invoke such a model in a large-scale system simulation or optimization, it will not be practical.

Neural network (NN) is an alternative approach by which we can quickly simulate the heat exchanger performance without dealing with the detailed heat transfer physics and numerical convergence issue. Yang and co-worker [2–4] reviewed the in-depth NN applications in thermal science and engineering. Particularly for heat exchangers, the application of NN to heat exchangers is drawing more attention [2,5–11]. But an investigation on the evaporator NN modeling is still rare because of its complexity and the absence of experimental data. Pacheco-Vega et al. [10] applied NN to heat rate prediction of humid air-to-water heat exchangers using the experimental data from McQuiston [12]. As the air-to-water heat exchangers only have single-phase water flow inside tubes, its overall heat transfer process is simpler than that of the evaporator. On air side heat transfer, they found that it is difficult for a NN to learn more about the coil performance under dry and wet conditions. Pacheco-Vega et al. [11] developed a NN model of refrigerant-to-air fin-and-tube evaporators based on very limited experimental data. Only 38 experimental data are used to develop a NN model with two hidden layers, 11 inputs and one output (11-11-7-1 structure). Since the number of connection weights is much more than the number of data, although the neural network could be trained, the overfitting risk is high. In addition, the model only calculated the total cooling capacity, which is insufficient to describe the evaporator performance under dry and wet conditions.

In this work, the authors focus on NN modeling of the refrigerant-to-air fin-and-tube evaporator performance under dry and wet conditions. To completely describe the evaporator performance from system modeling perspective, multiple outputs including the total cooling capacity, sensible heat ratio, and pressure drop on both sides are considered. Note that it is not practical to get sufficient test data for NN training. At the start of such a study, the number of data points required training a good neural network is still a question. Furthermore, if the neural networks could well approximate the reference model should be answered as well. Therefore, in this preliminary investigation, to avoid blind investment on laboratory tests, the well-developed physics-based detailed model [1] is used to generate sufficient data for NN training and testing. In the end of this paper, the trained NN is compared with the limited experimental data independently.

2 Evaporator Performance Analysis

Prior to the NN modeling, basic evaporator performance analysis is important for getting right direction. The total cooling capacity of evaporator consists of the sensible cooling capacity and the latent cooling capacity. The sensible capacity Q_{sen} represents the change in temperature and the latent capacity Q_{lat} is the heat removed by the change in phase. Q_{sen} and Q_{lat} can be calculated by the air side parameters.

$$Q_{sen} = m_a c_{p,a}(T_{a,out} - T_{a,in}) \tag{1}$$

$$Q_{lat} = m_a(W_{in} - W_{out})h_{fg} \tag{2}$$

$$Q_{tot} = Q_{sen} + Q_{lat} = m_a(h_{a,in} - h_{a,out}) \tag{3}$$

where the enthalpy of moist air is $h_a = c_{p,a}T + Wh_{w,g}$.

[1]Corresponding author.

Contributed by the Heat Transfer Division of ASME for publication in the JOURNAL OF HEAT TRANSFER. Manuscript received December 25, 2008; final manuscript received December 1, 2009; published online May 5, 2010. Assoc. Editor: Sai C. Lau.

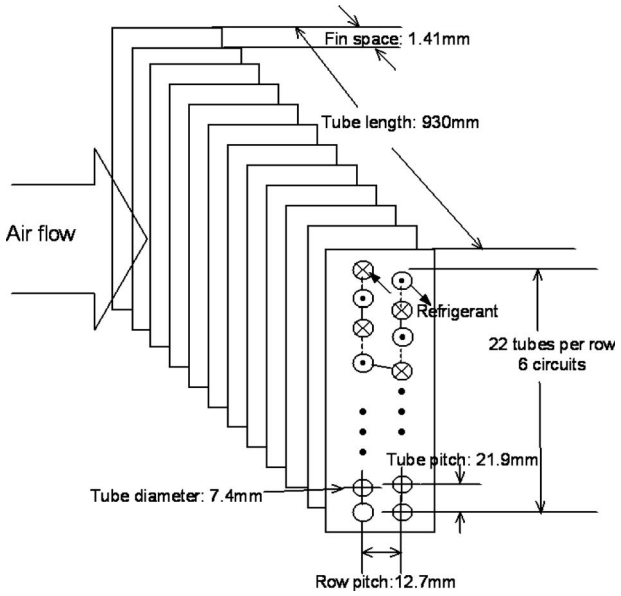

Fig. 1 Architecture of three-layer perceptron network

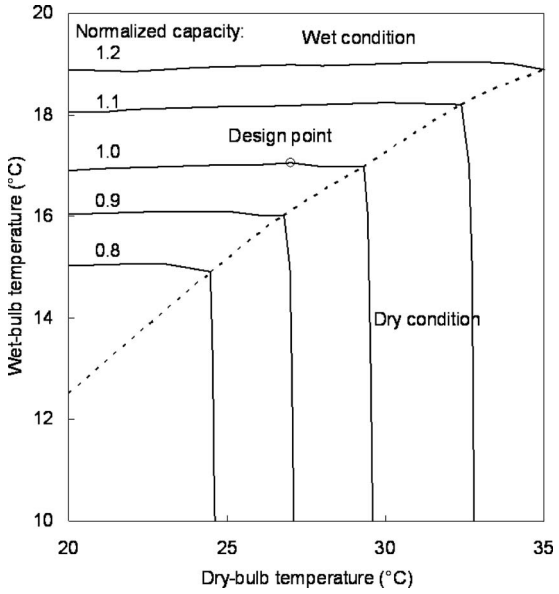

Fig. 2 Constant total cooling capacity lines under different working conditions

The sensible heat ratio (SHR) is defined as

$$\mathrm{SHR} = Q_{\mathrm{sen}}/Q_{\mathrm{tot}} \tag{4}$$

The refrigerant-side capacity Q_r is defined as

$$Q_r = m_r(h_{r,\mathrm{out}} - h_{r,\mathrm{in}}) = Q_{\mathrm{tot}} - m_a(W_{\mathrm{in}} - W_{\mathrm{out}})h_w \tag{5}$$

If air and refrigerant entering states are given, the evaporator performance (e.g., Q_{tot}, SHR, Δp_a, and Δp_r) can be found by laboratory test or modeling. All the leaving state parameters on air and refrigerant sides can be therefore calculated by the above equations together with fluid property equations.

The evaporator under dry and wet conditions shows different performance, especially Q_{tot} and SHR. As shown in Fig. 1, Q_{tot} is dominated by the dry-bulb air temperature ($T_{\mathrm{db,in}}$) under dry conditions. But when the evaporator is running wet, the wet-bulb air temperature ($T_{\mathrm{wb,in}}$) becomes the dominant one. In addition, SHR changes with $T_{\mathrm{wb,in}}$ and $T_{\mathrm{db,in}}$ under wet conditions. But once the coil dries out, SHR keeps unity and has no relationship with $T_{\mathrm{wb,in}}$ or $T_{\mathrm{db,in}}$.

Considering the remarkable difference between dry and wet conditions, it is very difficult to get the evaporator performance well trained in a single NN. A new approach is proposed in present work to solve this issue. The evaporator performance under dry and wet conditions is individually learned by two NNs. Afterward, the two NNs can be combined using the following simple relation.

$$Q_{\mathrm{tot}} = \max(Q_{\mathrm{wet}}, Q_{\mathrm{dry}}) \tag{6}$$

This approach can make good predictions under both dry and wet conditions and keep the continuity of evaporator performance between dry and wet conditions.

3 Neural Network Modeling

To reduce the overfitting risk, a simpler structure of NN is recommended. The three-layer perceptron network is therefore employed in the present work.

The schematic of the fin-and-tube evaporator investigated in this paper is shown in Fig. 2. The working fluid is R410A. The database used for NN training and testing range over the full operating parameter space, as shown in Table 1. A well-developed physics-based detailed evaporator model [1] is used to generate the database. In total, 5968 sets of data under wet conditions and 1014 sets of data under dry conditions are generated. The refrigerant properties are calculated by REFPROP Version 7.0 [13].

3.1 Selection of Input and Output Parameters. Among the given state parameters, a group of independent parameters, which have significant impact on the evaporator performance will be selected as the inputs of NNs. When selecting NN outputs, the refrigeration system level design requirements are taken into account, namely, Q_{tot}, SHR (for wet conditions only), Δp_a, and Δp_r. According to the analysis in above, except common inputs ($T_{s,\mathrm{in}}, x_{\mathrm{in}}, m_r, V_a$) for each output, under dry conditions $T_{\mathrm{db,in}}$ are chosen for Q_{tot} and Δp_r, and under wet conditions $T_{\mathrm{wb,in}}$, is chosen for Q_{tot} and Δp_r. Besides, both $T_{\mathrm{db,in}}$ and $T_{\mathrm{wb,in}}$ are chosen for SHR and Δp_a.

3.2 Separation of MIMO NN Into MISO NNs. There are two reasons to separate multi-input multi-output (MIMO) NN into multi-input single-output (MISO) NNs. One is the flexibility of modeling. Another is the ease of NN training.

The flexibility of modeling is a nature of NN. Usually, NN applies the same transfer function for all neurons at the same layer. In other words, for different outputs in a MIMO NN, each output must have the same combination of transfer functions. In reality, there are many kinds of neurons taking charge of different functions of a human body. The activation functions of different types of neurons should be different. Therefore, it is natural to customize the transfer function layer-by-layer for each output, which can be carried out by separating the MIMO NN into MISO NNs.

The ease of training is important when the NN size goes up. Compared with a MISO NN, a MIMO NN consists of much more

Table 1 Data range of input and output parameters

Input	Range	Output	Range
$T_{s,\mathrm{in}}$	−3–15°C	Q_{tot}	1.82–15.24 kW
x_{in}	0.05–0.33	SHR	0.34–1.0
m_r	0.01–0.1 kg/s	Δp_a	0.85–1.98 mm H_2O
$T_{\mathrm{db,in}}$	20–32°C	Δp_r	1.3–179.7 kPa
$T_{\mathrm{wb,in}}$	10–30°C		
V_a	0.26–0.39 m^3/s		

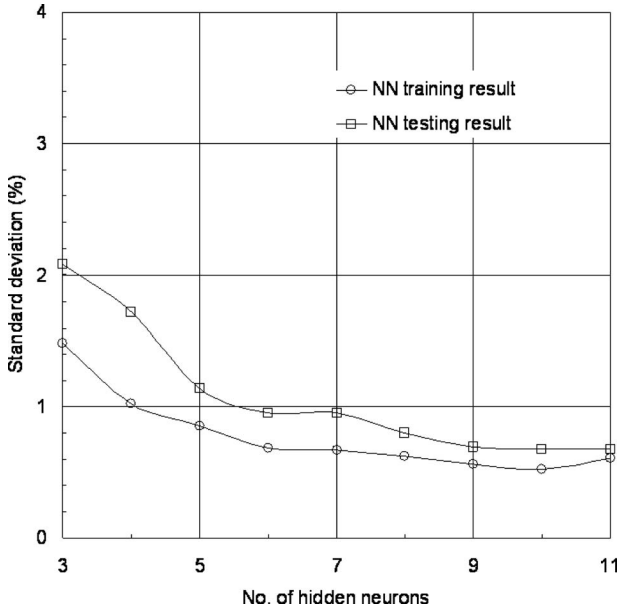

Fig. 3 Standard deviation of the total cooling capacity under wet conditions versus number of hidden neurons

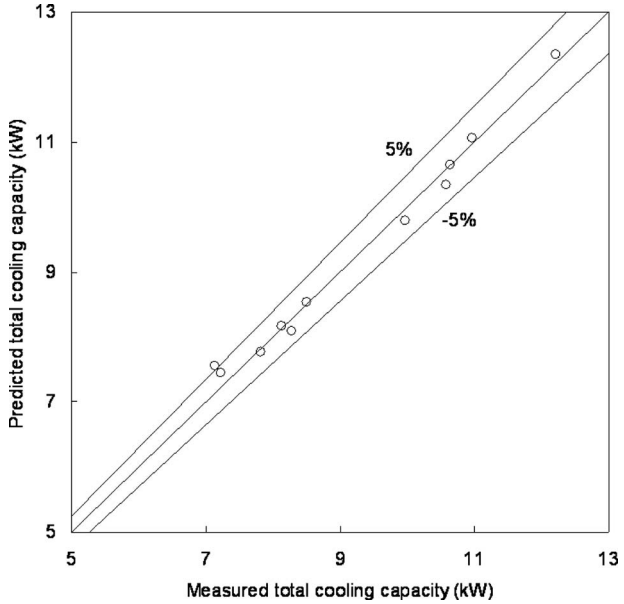

Fig. 4 Model validation of trained neural network with lab test data

neurons in the hidden and output layers, which brings more calculations and lower learning rate. Therefore, the separation of a MIMO NN into MISO NNs is helpful in improving NN training. Besides, when one more output is required, using MISO NNs method is easy to get it trained without retraining the existing part of the NN.

In the evaporator modeling, seven MISO NNs are trained under dry and wet conditions.

3.3 Training of MISO NNs. Two thousand and twenty-four sets of data under wet conditions and 332 sets of data under dry conditions are randomly chosen to train MISO NNs and the rests will be used to test the trained NNs.

The log sigmoid transfer function is adopted in the hidden layer for all NNs. The pure linear transfer function is applied in the output layer for all MISO NNs except for SHR, which chooses the log sigmoid transfer function after benchmarking. The log sigmoid and the pure linear transfer function are defined as follows.

$$g_{\log}(x) = \frac{1}{1+e^{-x}} \tag{7}$$

$$g_{\text{linear}}(x) = x \tag{8}$$

The Bayesian-Regulation back-propagation algorithm (trainbr) is chosen because of its high efficiency. More details can be found in commercial software MATLAB 7.

The neuron number in the hidden layer is optimized by a trial-and-error method. Taking Q_{tot} under wet conditions as an example, Fig. 3 demonstrates the model results along with a number of hidden neurons. As a trade-off of model accuracy and model complexity, nine neurons in the hidden layer are recommended for Q_{tot} under wet conditions. The average deviation (AD) and the standard deviation (SD) are defined as below.

$$\text{AD} = \frac{1}{N}\sum_{N} \frac{y_{\text{predicted}} - y_{\text{desired}}}{y_{\text{desired}}} \tag{9}$$

$$\text{SD} = \sqrt{\frac{1}{N-1}\sum_{N}\left(\frac{y_{\text{predicted}} - y_{\text{desired}}}{y_{\text{desired}}} - \text{AD}\right)^2} \tag{10}$$

Finally, under dry conditions, four, one, and two hidden neurons are employed in the NNs of Q_{tot}, Δp_a, and Δp_r, respectively. Under wet conditions, nine, seven, six, and five hidden neurons are employed in the NNs of Q_{tot}, SHR, Δp_a, and Δp_r, respectively.

4 Results and Analysis

Statistically, the comparison between the trained NNs and the physics-based evaporator model [1] shows respective less than 1% and 2% standard deviations of the evaporator performance under dry and wet conditions. Results under dry conditions are a little better than that under wet conditions, which is reasonable because the heat transfer physics under wet conditions is more complex. Compared with the limited experimental data of cooling capacity, as those dots shown in Fig. 4, 91% NN predictions fall into $\pm 5\%$ error band. The experimental data were from a calibrated psychrometric room where the measurement uncertainty of cooling capacity is $\pm 4\%$.

At last, trained MISO NNs can be combined to form a MIMO NN with some void connections. Since different transfer functions are adopted in the output layer under wet conditions, it is not applicable to train the combined MIMO NN directly. For comparison, The MIMO NN under dry conditions with seven hidden neurons is retrained. A little better result is obtained since the void connection weights get involved this time.

5 Conclusions

In the present work, the evaporator performance under dry and wet conditions has been modeled by three-layer perceptron NNs. One MIMO NN is used to capture the evaporator performance under wet conditions and another MIMO NN is trained for predicting the evaporator performance under dry conditions. Two trained MIMO NNs work together to decide whether the evaporator is running under dry or wet condition. To improve the NN modeling flexibility and training efficiency, the MIMO NNs are separated into MISO NNs for individual training and reunited afterward. Compared with the physics-based model and experimental data, the trained NN model gave both good quantitative and qualitative results. Experimental data or advanced physics-based modeling data are required for NN training in order for the presented technique to be dependable for applications. The further research will concentrate on the minimum data requirement for the NN training.

Nomenclature

c_p = specific heat at constant pressure, $kJ/kg_a\ K$
Q = capacity, W
h = enthalpy, kJ/kg
h_{fg} = latent enthalpy, kJ/kg
T = temperature, °C
V = volume flow rate, m^3/s
W = humidity ratio, kg_w/kg_a
x = variable; vapor quality
Δp_a = pressure drop on air side, mm H_2O
Δp_r = pressure drop on refrigerant-side, kPa

Subscripts and Superscripts

a = air
db = dry-bulb
g = gas
lat = latent
r = refrigerant
s = saturated
sen = sensible
tot = total
w = water
wb = wet-bulb

References

[1] Liu, J., Wei, W. J., Ding, G. L., Zhang, C. L., Fukaya, M., Wang, K. J., and Inagaki, T., 2004, "A General Steady State Mathematical Model for Fin-and-Tube Heat Exchanger Based on Graph Theory," Int. J. Refrig., **27**, pp. 965–973.

[2] Yang, K. T., 2008, "Artificial Neural Networks (ANNs): A New Paradigm for Thermal Science and Engineering," ASME J. Heat Transfer, **130**, p. 093001.

[3] Yang, K. T., 2007, "Role of Artificial Intelligence (AI) in Thermal Sciences and Engineering," ASME Paper No. HT-2007-32042.

[4] Sen, M., and Yang, K. T., 2000, "Applications of Artificial Neural Networks and Genetic Algorithms in Thermal Engineering," Section 4.24, *The CRC Handbook of Thermal Engineering*, F. Kreith, ed., CRC, Boca Raton, FL, pp. 620–661.

[5] Xie, G. N., Wang, Q. W., Zeng, M., and Luo, L. Q., 2007, "Heat Transfer Analysis for Shell-and-Tube Heat Exchangers With Experimental Data by Artificial Neural Networks Approach," Appl. Therm. Eng., **27**, pp. 1096–1104.

[6] Islamoglu, Y., 2003, "A New Approach for the Prediction of the Heat Transfer Rate of the Wire-on-Tube Type Heat Exchanger—Use of an Artificial Neural Network Model," Appl. Therm. Eng., **23**, pp. 243–249.

[7] Wu, Z. G., Zhang, J. Z., Tao, Y. B., He, Y. L., and Tao, W. Q., 2008, "Application of Artificial Neural Network Method for Performance Prediction of a Gas Cooler in a CO_2 Heat Pump," Int. J. Heat Mass Transfer, **51**, pp. 5459–5464.

[8] Diaz, G., Sen, M., Yang, K. T., and McClain, R. L., 1999, "Simulation of Heat Exchanger Performance by Artificial Neural Networks," HVAC&R Res., **5**(3), pp. 195–208.

[9] Díaz, G., Sen, M., Yang, K. T., and McClain, R. L., 2001, "Dynamic Prediction and Control of Heat Exchangers Using Artificial Neural Networks," Int. J. Heat Mass Transfer, **44**(9), pp. 1671–1679.

[10] Pacheco-Vega, A., Diaz, G., Sen, M., Yang, K. T., and McClain, R. L., 2001, "Heat Rate Predictions in Humid Air-Water Heat Exchanger Using Correlations and Neural Networks," ASME J. Heat Transfer, **123**, pp. 348–354.

[11] Pacheco-Vega, A., Sen, M., Yang, K. T., and McClain, R. L., 2001, "Neural Network Analysis of Fin-Tube Refrigerating Heat Exchanger With Limited Experimental Data," Int. J. Heat Mass Transfer, **44**, pp. 763–770.

[12] McQuiston, F. C., 1978, "Heat, Mass and Momentum Transfer Data for Five Plate-Fin-Tube Heat Transfer Surfaces," ASHRAE Trans., **84**(1), pp. 266–293.

[13] 2002, REFPROP version 7.0, Reference Fluid Thermodynamic and Transport Properties, NIST Standard Reference Database 23, Gaithersburg, MD.

The Onset of Convection in a Layer of Cellular Porous Material: Effect of Temperature-Dependent Conductivity Arising From Radiative Transfer

D. A. Nield
Department of Engineering Science,
University of Auckland,
Private Bag 92019,
Auckland 1142, New Zealand
e-mail: d.nield@auckland.ac.nz

A. V. Kuznetsov
Department of Mechanical and Aerospace Engineering,
North Carolina State University,
Campus Box 7910,
Raleigh, NC 27695-7910
e-mail: avkuznet@eos.ncsu.edu

The onset of convection in a horizontal layer of a cellular porous material heated from below is investigated. The problem is formulated as a combined conductive-convective-radiative problem in which radiative heat transfer is treated as a diffusion process. The problem is relevant to cellular foams formed from plastics, ceramics, and metals. It is shown that the variation of conductivity with temperature above that of the cold boundary leads to an increase in the critical Rayleigh number (based on the conductivity of the fluid at that boundary temperature) and an increase in the critical wave number. On the other hand, the critical Rayleigh number based on the conductivity at the mean temperature decreases with increase in the thermal variation parameter if the radiative contribution to the effective conductivity is sufficiently large compared with the nonradiative component.
[DOI: 10.1115/1.4001125]

Keywords: cellular porous medium, radiative heat transfer, temperature-dependent conductivity, onset of convection, Horton–Rogers–Lapwood problem

1 Introduction

Radiative transfer in cellular porous materials has been recently reviewed by Viskanta [1]. He noted that such materials of high porosity are finding increased uses as thermal insulations, sound absorbers, electrodes, regenerative heat exchangers, burners for combustion enhancements, and in many other applications. The foamlike open-cellular porous materials typically consist of hollow three-dimensional dodecahedronlike cells with pentagonal or hexagonal walls. They are characterized by high porosity, large surface area per unit volume, large volumetric heat transfer coefficient, large radiation extinction coefficient, and low pressure drop. Further information about these materials is given by Zhao et al. [2].

Viskanta [1] further noted that cellular foams formed from plastics, ceramics, and metals are strongly attenuating, and radiative transfer in foams even of small thickness can often be treated as a diffusion process. This is particularly convenient as combined conduction and radiation in a porous material can be treated as an effective conduction process.

For example, in one dimension, the combined conductive heat flux in the x-direction can be expressed as

$$q_x'' = -(k_c + k_r)\frac{\partial T}{\partial x} = -k_{\text{eff}}\frac{\partial T}{\partial x} \tag{1}$$

where the radiative conductivity k_r is approximated by

$$k_r = \frac{16\sigma T^3}{3\beta_R} \tag{2}$$

where β_R is the Rosseland mean extinction (absorption + scattering) coefficient and σ is the Stefan–Boltzmann constant.

Thus it is of interest to investigate combined conductive-convective-radiative problems using this approach. In this paper we investigate using linear stability analysis the effect of radiation on the onset of natural convection in a saturated cellular porous material modeled using Darcy's law. Numerous studies have been published on the case where radiation is negligible (the Horton–Rogers–Lapwood problem), and these have been surveyed in Chapter 6 of the book by Nield and Bejan [3].

Since the thermal conductivity enters as a coefficient in the thermal energy equation in which the temperature is the dependent variable, the inclusion of the radiative conductivity term automatically makes that equation intrinsically nonlinear in the temperature. Normally it would not be possible to find an analytic solution for such an equation, and it would have to be solved numerically. However, in the present situation, we are able to obtain an approximate analytical expression for the critical Rayleigh number.

The Horton–Rogers–Lapwood problem is paradigmatic for natural convection in an enclosure. The authors have written companion papers for forced convection in a parallel plate channel (a typical example of confined forced convection) [4] and for the Cheng–Minkowycz problem (an exemplar for external natural convection) [5].

2 Analysis

We select a coordinate frame in which the z-axis is aligned vertically upwards. We consider a horizontal layer of a cellular porous material confined between the planes $z^*=0$ and $z^*=H$. Asterisks are now used to denote dimensional variables. Each boundary wall is assumed to be impermeable and perfectly thermally conducting. The temperatures at the lower and upper walls are taken to be T^*_h and T^*_c, the former being the greater. For simplicity, Darcy's law is assumed to hold and the Oberbeck–Boussinesq approximation is employed. Homogeneity and local thermal equilibrium in the porous medium are each assumed. The reference temperature is taken to be T^*_c. In the linear theory being applied here the temperature change in the fluid is assumed to be small in comparison with T^*_c.

The permeability is denoted by K. The Darcy velocity is denoted by $\mathbf{v}^\star$. We treat a steady state flow. The following three field equations embody the conservation of total mass, momentum, and thermal energy, respectively:

$$\nabla^* \cdot \mathbf{v}^* = 0 \tag{3}$$

$$0 = -\nabla^* p^* - \frac{\mu}{K}\mathbf{v}^* - \beta(T^* - T_\infty^*)\mathbf{g} \tag{4}$$

$$(\rho c)_m \frac{\partial T^*}{\partial t^*} + (\rho c)_f \mathbf{v}^* \cdot \nabla T^* = \nabla^* \cdot (k_m \nabla T^*) \tag{5}$$

Here ρ, μ, β, and c are the density, viscosity, volumetric expansion coefficient, and specific heat of the fluid, and $(\rho c)_m$ is the effective heat capacity of the porous medium. The gravitational acceleration is denoted by $\mathbf{g}$, and the pressure p^* is the excess

Contributed by the Heat Transfer Division of ASME for publication in the JOURNAL OF HEAT TRANSFER. Manuscript received September 27, 2009; final manuscript received January 3, 2010; published online May 5, 2010. Assoc. Editor: Peter Vadasz.

pressure over the hydrostatic value. We have introduced the effective thermal conductivity k_m of the porous medium. This is now a function of temperature.

We write $\mathbf{v}^* = (u^*, v^*, w^*)$.

The boundary conditions are

$$w^* = 0, \quad T^* = T_h^* \quad \text{at} \quad z^* = 0 \tag{6}$$

$$w^* = 0, \quad T^* = T_c^* \quad \text{at} \quad z^* = H \tag{7}$$

We introduce dimensionless variables as follows. We define

$$(x,y,z) = (x^*,y^*,z^*)/H, \quad t = t^*\alpha_{m0}/\sigma H^2,$$

$$(u,v,w) = (u^*,v^*,w^*)H/\alpha_{m0}$$

$$p = p^*K/\mu\alpha_{m0}, \quad T = \frac{T^* - T_c^*}{T_h^* - T_c^*} \tag{8}$$

where

$$\alpha_{m0} = \frac{k_{m0}}{(\rho c)_f} \tag{9}$$

and k_{m0} is a reference value of k_m.

Then Eqs. (3)–(7) take the form

$$\nabla \cdot \mathbf{v} = 0 \tag{10}$$

$$0 = -\nabla p - \mathbf{v} + \mathrm{Ra}\ T\hat{\mathbf{e}}_z \tag{11}$$

$$\frac{\partial T}{\partial t} + \mathbf{v} \cdot \nabla T = \nabla \cdot [F(T)\,\nabla\, T] \tag{12}$$

$$w = 0, \quad T = 1 \quad \text{at} \quad z = 0 \tag{13}$$

$$w = 0, \quad T = 0 \quad \text{at} \quad z = 1 \tag{14}$$

Here Ra is the familiar thermal Rayleigh–Darcy number defined as

$$\mathrm{Ra} = \frac{\rho g \beta K H (T_h^* - T_c^*)}{\mu \alpha_{m0}} \tag{15}$$

and we have introduced the function

$$F(T) = \frac{k_m}{k_{m0}} = \frac{\alpha_m}{\alpha_{m0}} \tag{16}$$

The basic time-independent quiescent solution of Eqs. (10)–(14) is given by

$$\mathbf{v}_b = 0, \quad T_b = 1 - z \tag{17}$$

We now approximate $F(T)$ by $F(T_b)$. (In effect we are assuming that, in the subsequent perturbation analysis, the conductivity is a function of the horizontally averaged temperature.)

We now superimpose perturbations on the basic solution. We write

$$\mathbf{v} = \mathbf{v}', \quad p = p_b + p', \quad T = T_b + T' \tag{18}$$

substitute in Eqs. (10)–(14), and linearize by neglecting products of primed quantities. The following equations are obtained:

$$\nabla \cdot \mathbf{v}' = 0 \tag{19}$$

$$0 = -\nabla p' - \mathbf{v}' + \mathrm{Ra}\ T'\hat{\mathbf{e}}_z \tag{20}$$

$$\frac{\partial T'}{\partial t} - w' = \nabla \cdot (F(T_b)\,\nabla\, T') \tag{21}$$

The boundary conditions are now

$$w' = 0, \quad T' = 0 \quad \text{at} \quad z = 0 \quad \text{and} \quad \text{at} \quad z = 1 \tag{22}$$

The five unknowns u', v', w', p', and T' can be reduced to two by operating on Eq. (20) with $\hat{\mathbf{e}}_z \cdot$curl curl and using the identity curl curl $\equiv$ grad div $-\nabla^2$ together with Eq. (19).

The result is

$$\nabla^2 w' = \mathrm{Ra}\ \nabla_H^2 T' \tag{23}$$

Here ∇_H^2 is the two-dimensional Laplacian operator in the horizontal plane. Differential equations (21) and (23), and boundary condition (22) constitute a linear boundary-value problem that can be solved using the method of normal modes.

We write

$$(w', T') = [W(z), \Theta(z)]\exp(st + ilx + imy) \tag{24}$$

and substitute into the differential equations to obtain

$$(D^2 - \alpha^2)W + \mathrm{Ra}\ \alpha^2\Theta = 0 \tag{25}$$

$$W + (D(G(z)D) - \alpha^2 - s)\Theta = 0 \tag{26}$$

where, consistent with the definition of $F(T)$ in Eq. (16) and the assumption that $F(T)$ can be approximated by $F(T_b)$, we have written

$$G(z) = \frac{\overline{k_m}(z)}{k_{m0}} \tag{27}$$

where $\overline{k_m}(z)$ is the horizontal average of k_m,

$$W = 0, \quad \Theta = 0 \quad \text{at} \quad z = 0 \quad \text{and} \quad \text{at} \quad z = 1 \tag{28}$$

$$D \equiv \frac{d}{dz} \quad \text{and} \quad \alpha = (l^2 + m^2)^{1/2} \tag{29}$$

Thus α is a dimensionless horizontal wave number.

For neutral stability the real part of s is zero. In the present problem the principle of exchange of stabilities is valid (so oscillatory instability can be ruled out) and hence we can set $s=0$ at neutral stability.

We now employ a Galerkin-type weighted residual method to obtain an approximate solution to the system of Eqs. (25)–(28). We choose as trial functions (satisfying the boundary conditions)

$$W_p = \Theta_p = \sin p\pi z, \quad p = 1,2,3,\ldots \tag{30}$$

We then write

$$W = \sum_{p=1}^{N} A_p W_p, \quad \Theta = \sum_{p=1}^{N} B_p \Theta_p \tag{31}$$

substitute into Eqs. (25) and (26), and make the expressions on the left-hand sides of those equations (the residuals) orthogonal to the trial functions, thereby obtaining a system of $2N$ linear algebraic equations in the $2N$ unknowns A_p, B_p; $p=1,2,\ldots,N$. The vanishing of the determinant of coefficients produces the eigenvalue equation for the system. One can regard Ra as the eigenvalue. Thus Ra is found in terms of the other parameters.

We now turn to the particular case where

$$k_m = k_c + \frac{16\sigma T^{*3}}{3\beta_R} \tag{32}$$

In a practical situation the absolute temperature T^* will be in the range from 300 K to 800 K, well away from absolute zero. It is convenient to take the cold wall temperature T_c^* as a reference temperature and make an expansion about this value, thus obtaining the expression

$$T^{*3} = T_c^{*3} + 3T_c^{*2}(T^* - T_c^*) + 3T_c^*(T^* - T_c^*)^2 + (T^* - T_c^*)^3 \tag{33}$$

We can then write

Table 1 Values of (a) the critical Rayleigh number Ra_c and (b) the corresponding critical wave number α_c for various values of the temperature variation parameter T_r, for various levels of the Galerkin approximation

	$N=1$	$N=2$	$N=3$	$N=4$
(a)				
$T_r=0$	39.5	39.5	39.5	39.5
0.2	46.1	45.8	45.7	45.7
0.4	54.2	52.7	52.7	52.7
0.6	63.9	60.4	60.4	60.3
0.8	75.3	69.0	68.7	68.6
1.0	88.5	78.4	77.9	77.6
1.2	103.7	88.8	87.8	87.3
1.4	120.9	100.2	98.5	97.7
1.6	140.4	112.7	110.1	108.9
(b)				
$T_r=0$	3.14	3.14	3.14	3.14
0.2	3.38	3.37	3.37	3.37
0.4	3.64	3.59	3.59	3.59
0.6	3.90	3.81	3.80	3.80
0.8	4.17	4.02	4.01	4.01
1.0	4.44	4.23	4.22	4.21
1.2	4.70	4.44	4.42	4.41
1.4	4.97	4.65	4.62	4.61
1.6	5.23	4.86	4.82	4.80

$$k_m = k_{m0}(1 + 3T_rT + 3T_r^2T^2 + T_r^3T^3) \tag{34}$$

where

$$k_{m0} = k_c + \frac{16\sigma T_c^{*3}}{3\beta_R} \tag{35}$$

$$T_r = \frac{T_h^* - T_c^*}{T_c^*} \tag{36}$$

We refer to T_r as the temperature variation parameter. Clearly it is a positive quantity. Since in practice both T_h^* and T_c^* will be in the range [300 K, 800 K], the value of T_r will normally lie in the range [0, 5/3].

On taking horizontal averages, and invoking Eq. (17), Eq. (34) then gives

$$\overline{k_m} = k_{m0}[1 + 3T_r(1-z) + 3T_r^2(1-z)^2 + T_r^3(1-z)^3] \tag{37}$$

Hence we are especially interested in the case where

$$G(z) = 1 + 3T_r(1-z) + 3T_r^2(1-z)^2 + T_r^3(1-z)^3 \tag{38}$$

One can employ MATHEMATICA with a one-term Galerkin expansion to obtain the expression

$$\mathrm{Ra} = \frac{(\pi^2+\alpha^2)}{\alpha^2}\left[\pi^2 + \alpha^2 + \frac{3\pi^2}{2}T_r + \frac{2\pi^2+3}{2}T_r^2 + \frac{\pi^2+3}{4}T_r^3\right] \tag{39}$$

For the case $T_r=0$, Eq. (39) reduces to

$$\mathrm{Ra} = \frac{(\pi^2+\alpha^2)^2}{\alpha^2} \tag{40}$$

which takes the minimum value $4\pi^2$ when $\alpha=\pi$. These are the well known results for the critical Rayleigh number Ra_c and the corresponding critical wave number α_c for the Horton–Rogers–Lapwood problem. Thus for this case the $N=1$ Galerkin approximation happens to yield the exact result (the trial functions are the exact eigenfunctions). For the case of nonzero values of T_r the Galerkin approximation is expected to give upper bounds on the values of Ra_c and α_c. This is confirmed by the results reported in Table 1.

It is clear that both Ra_c and α_c increase as T_r increases. At the same time the accuracy of the Galerkin approximation decreases. The increase in the value of Ra_c is as expected, since for simplicity we have defined Ra in terms of the conductivity at the temperature of the cold boundary. In the bulk of the fluid the conductivity is greater than this value, and increase in thermal diffusivity leads to increased stability. However, for a fair comparison, one should consider a Rayleigh number Rm based on conductivity at the mean temperature $\overline{T^*}=(T_c^*+T_h^*)/2$ and so related to Ra by

$$\mathrm{Rm} = \frac{\mathrm{Ra}}{1 + \lambda\left(\frac{3}{2}T_r + \frac{3}{4}T_r^2 + \frac{1}{8}T_r^3\right)} \tag{41}$$

where

$$\lambda = \frac{1}{1 + \frac{3\beta_R k_c}{16\sigma T_c^{*3}}} \tag{42}$$

This follows since from Eqs. (35) and (36) one has

$$\overline{T^*} = T_c^*(1 + T_r/2) \tag{43}$$

and

$$\frac{k_m(\overline{T^*})}{k_{m0}} = \frac{k_c + \frac{16\sigma\overline{T^*}^3}{3\beta_R}}{k_c + \frac{16\sigma T_c^{*3}}{3\beta_R}} \tag{44}$$

The parameter λ takes its maximum value of unity in the limit as the radiative contribution to the conductivity dominates the conductive contribution. For example, when λ and T_r each take the value 1, Eq. (41) gives Rm=Ra/3.375. According to the last column of Table 1(a) an increase in T_r leads to a twofold increase in Ra, but the net effect on Rm is a 40% decrease. Thus in this extreme case the variation of conductivity with temperature results in a decrease in stability relative to the constant conductivity situation. At the other extreme, as λ tends to zero, the distinction between Rm and Ra vanishes, and one concludes that the variation of conductivity with temperature results in an increase in stability.

3 Conclusions

The Horton–Rogers–Lapwood problem for a layer of cellular porous material has been investigated, and the approximate analytical expression for a critical Rayleigh number has been obtained. It has been established that both the critical Rayleigh number (based on the conductivity at the temperature of the cold boundary) and the corresponding critical wave number increase as the temperature variation parameter increases. The critical Rayleigh number based on the conductivity at the mean temperature decreases with increase in the thermal variation parameter if the radiative contribution to the effective conductivity is sufficiently large compared with the nonradiative component.

Nomenclature

c = specific heat of the fluid
$F(T)$ = function defined by Eq. (16)
$\mathbf{g}$ = gravity vector
$G(z)$ = function defined by Eq. (27)
H = layer depth
k_c = molecular thermal conductivity
k_{eff} = effective thermal conductivity (conduction +radiation)
k_m = effective thermal conductivity of the porous medium
k_{m0} = reference value of k_m

k_r = radiative conductivity defined by Eq. (2)
K = permeability
p^* = pressure in excess of its hydrostatic value
p = dimensionless pressure, $p^*K/\mu\alpha_{m0}$
q''_x = combined conductive heat flux in the x-direction
Ra = thermal Rayleigh–Darcy number defined by Eq. (15)
Rm = Rayleigh number based on conductivity at the mean temperature, defined by Eq. (41)
t = dimensionless time, $t^*\alpha_{m0}/\sigma H^2$
t^* = time
T = dimensionless temperature, $(T^*-T^*_c)/(T^*_h-T^*_c)$
T^* = temperature
T^*_c = temperature at the upper wall
T^*_h = temperature at the lower wall
T_r = temperature variation parameter defined by Eq. (36)
(u,v,w) = dimensionless Darcy velocity components, $(u^*,v^*,w^*)H/\alpha_{m0}$
$\mathbf{v}$ = dimensionless Darcy velocity
$\mathbf{v}^*$ = dimensional Darcy velocity, (u^*,v^*,w^*)
(x,y,z) = dimensionless Cartesian coordinates, $(x^*,y^*,z^*)/H$; z is the vertically upward coordinate
(x^*,y^*,z^*) = Cartesian coordinates

Greek Symbols

α_m = thermal diffusivity of the porous medium, $k_m/(\rho c_p)_f$
α_{m0} = reference value of α_m defined by Eq. (9)
β = volumetric expansion coefficient of the fluid
β_R = Rosseland mean extinction (absorption+scattering) coefficient
λ = parameter defined by Eq. (42)
μ = fluid viscosity
ρ = fluid density
$(\rho c)_m$ = effective heat capacity of the porous medium
σ = Stefan–Boltzmann constant

Subscripts

b = basic time-independent quiescent solution
f = fluid

Superscripts

* = dimensional variable

References

[1] Viskanta, R., 2009, "Overview of Radiative Transfer in Cellular Porous Materials," *Proceedings of the ASME 2009 Heat Transfer Summer Conference*, San Francisco, CA, Jul. 19–23.
[2] Zhao, C. Y., Tassou, S. A., and Lu, T. J., 2008, "Analytical Considerations of Thermal Radiation in Cellular Metal Foams With Open Cells," Int. J. Heat Mass Transfer, **51**, pp. 929–940.
[3] Nield, D. A., and Bejan, A., 2006, *Convection in Porous Media*, 3rd ed., Springer, New York.
[4] Nield, D. A., and Kuznetsov, A. V., "Forced Convection in Cellular Porous Materials: Effect of Temperature-Dependent Conductivity Arising From Radiative Transfer," Int. J. Heat Mass Transfer, in press.
[5] Kuznetsov, A. V., and Nield, D. A., "The Cheng-Minkowycz Problem for Cellular Porous Materials: Effect of Temperature-Dependent Conductivity Arising From Radiative Transfer," Int. J. Heat Mass Transfer, in press.